Web of Science™

Web of Science CV
Prepared on March 11th 2026

# Andrijana Šolajić

https://www.webofscience.com/wos/author/rid/AAH-2072-2019
Web of Science ResearcherID: AAH-2072-2019
ORCiD: 0000-0002-0553-0858

Current affiliation:

- Institute of Physics - University of Belgrade

## Publication Metrics

For manuscripts published from date range March 2017 - March 2026

| | |
|---|---|
| 6 | 197 |
| H-index | Sum of Times Cited |
| 19 | 16 |
| Total Publications | Web of Science Core Collection Publications |

For all time

| | |
|---|---|
| 6 | 197 |
| H-index | Sum of Times Cited |
| 19 | 16 |
| Total Publications | Web of Science Core Collection Publications |

## Publication Impact Over Time

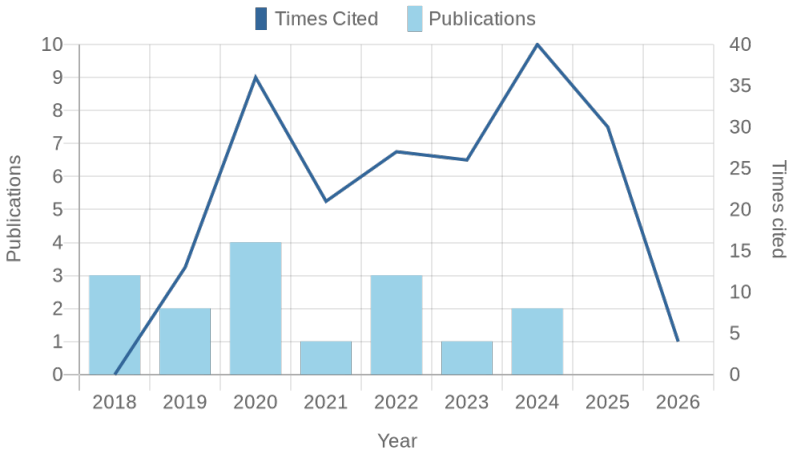

## Publications

| For manuscripts published from date range March 2017 - March 2026 (16) | Times Cited (All time) |
|---|---|
| Strain-induced modulation of electronic and optical properties in hBN/InSe heterostructure<br>Authors (2): Solajic, Andrijana; Pesic, Jelena<br>Published: Jun 2024 in Optical and Quantum Electronics<br>DOI: 10.1007/S11082-024-06837-2 | 1 |
| Tailoring electronic and optical properties of hBN/InTe and hBN/GaTe heterostructures through biaxial strain engineering<br>Authors (2): Solajic, A.; Pesic, J.<br>Published: Jan 2024 in Scientific Reports<br>DOI: 10.1038/S41598-024-51303-4 | 4 |
| Spin-phonon interaction and short-range order in Mn3Si2Te6<br>Authors (9): Mijin, S. Djurdjic; Solajic, A. ... Lazarevic, N.<br>Published: Feb 2023 in Physical Review B<br>DOI: 10.1103/PHYSREVB.107.054309 | 13 |
| Evolution of lattice, spin, and charge properties across the phase diagram of FeSe1-xSx<br>Authors (15): Lazarevic, N.; Baum, A. ... Hackl, R.<br>Published: Sep 2022 in Physical Review B<br>DOI: 10.1103/PHYSREVB.106.094510 | 4 |
| Novel wide spectrum light absorber heterostructures based on hBN/In(Ga)Te<br>Authors (2): Solajic, A.; Pesic, J.<br>Published: Aug 2022 in Journal of Physics: Condensed Matter<br>DOI: 10.1088/1361-648X/AC7996 | 4 |
| Structural and optical characterization of titanium-carbide and polymethyl methacrylate based nanocomposite<br>Authors (7): Pesic, Jelena; Solajic, Andrijana ... Romcevic, Nebojsa<br>Published: Jun 2022 in Optical and Quantum Electronics<br>DOI: 10.1007/S11082-022-03674-Z | 2 |
| Probing charge density wave phases and the Mott transition in 1T-TaS2I by inelastic light scattering<br>Authors (12): Mijin, S. Djurdjic; Baum, A. ... Lazarevic, N.<br>Published: Jun 2021 in Physical Review B<br>DOI: 10.1103/PHYSREVB.103.245133 | 10 |
| Peculiar symmetry-protected electronic dispersions in two-dimensional materials<br>Authors (6): Damljanovic, V; Lazic, N. ... Damnjanovic, M.<br>Published: Nov 2020 in Journal of Physics: Condensed Matter<br>DOI: 10.1088/1361-648X/ABAAD1 | 4 |

| | |
|---|---|
| Short-Range Order in VI3<br>Authors (9): Mijin, Sanja Djurdjic; Abeykoon, A. M. Milinda ... Lazarevic, Nenad<br>Published: Nov 2020 in Inorganic Chemistry<br>DOI: 10.1021/ACS.INORGCHEM.0C02060 | 3 |
| Vacancies and spin-phonon coupling in CrSi0.8Ge0.1Te3<br>Authors (9): Milosavljevic, Ana; Solajic, Andrijana ... Lazarevic, Nenad<br>Published: Nov 2020 in Journal of Raman Spectroscopy<br>DOI: 10.1002/JRS.5962 | 4 |
| Optical and mechanical properties and electron-phonon interaction in graphene doped with metal atoms<br>Authors (3): Solajic, Andrijana; Pesic, Jelena; Gajic, Rados<br>Published: Mar 2020 in Optical and Quantum Electronics<br>DOI: 10.1007/S11082-020-02300-0 | 1 |
| Lattice dynamics and phase transitions in Fe3-xGeTe2<br>Authors (9): Milosavljevic, A.; Solajic, A. ... Popovic, Z., V<br>Published: Jun 2019 in Physical Review B<br>DOI: 10.1103/PHYSREVB.99.214304 | 27 |
| Ab Initio Study of the Electronic, Vibrational, and Mechanical Properties of the Magnesium Diboride Monolayer<br>Authors (7): Pesic, Jelena; Popov, Igor ... Gajic, Rados<br>Published: Jun 2019 in Condensed Matter<br>DOI: 10.3390/CONDMAT4020037 | 10 |
| Evidence of spin-phonon coupling in CrSiTe3<br>Authors (7): Milosavljevic, A.; Solajic, A. ... Popovic, Z. V.<br>Published: Sep 2018 in Physical Review B<br>DOI: 10.1103/PHYSREVB.98.104306 | 57 |
| Lattice dynamics and phase transition in CrI3 single crystals<br>Authors (9): Djurdjic-Mijin, S.; Solajic, A. ... Popovic, Z. V.<br>Published: Sep 2018 in Physical Review B<br>DOI: 10.1103/PHYSREVB.98.104307 | 51 |
| Ab-initio calculations of electronic and vibrational properties of Sr and Yb intercalated graphene<br>Authors (3): Solajic, Andrijana; Pesic, Jelena; Gajic, Rados<br>Published: Jul 2018 in Optical and Quantum Electronics<br>DOI: 10.1007/S11082-018-1541-X | 2 |

## Verified Reviews

### Reviewer Summary

For manuscripts reviewed from date range March 2017 - March 2026

| | |
|---|---|
| (3) Journal of Electronic Materials | (2) Physica E: Low-dimensional Syst... |

(2) Electronic Structure

(1) Journal of Computational Electro…

**8 REVIEWS OF 6 MANUSCRIPTS**

For manuscripts published from date range March 2017 - March 2026

Influence of non-metal doping and biaxial strain on the photovoltaic characteristics of monolayer 1T-PtSe2
Reviewed: Feb 2025 for Journal of Computational Electronics

Structure-Property Relationship and Electronic Structure Calculation of Cubic YSZ Solid Electrolyte for Electrochemical Applications
2 rounds from Sep 2024 to Nov 2024 for Journal of Electronic Materials

Strain Engineering on the Electronic Structure and Optical Properties of Monolayer WSi2X4 (X = N, P, As)
Reviewed: Jun 2024 for Journal of Electronic Materials

Phonons from density-functional perturbation theory using the all-electron full-potential linearized augmented plane-wave method FLEUR
Reviewed: Nov 2023 for Electronic Structure

Structural, Mechanical and Thermodynamic Properties of Two-dimensional Be3X2 (X = C, Si, Ge and Sn) Materials Using First Principles Calculations
Reviewed: Sep 2020 for Electronic Structure

Tunable electronic and magnetic properties of substitutionally doped graphene
2 rounds from Dec 2019 to Jan 2020 for Physica E: Low-dimensional Systems and Nanostructures

Montanuniversität Leoben

**Department of Physics, Mechanics and Electrical Engineering**
Chair of Physics
Ass. Prof. Priv.-Doz. Dr Aleksandar Matkovic
Franz Josef Strasse 18
8700 Leoben
Phone.: +43 3842 402 4664
aleksandar.matkovic@unileoben.ac.at

*Leoben, 3.11.2025*

To:
***Dr. Andrijana Solajic***
***Laboratory for 2D materials,***
***Institute of Physics,***
***University of Belgrade***

# Invitation Letter

Dear Andrijana,

> It is my great pleasure **to invite you to give a seminar lecture on the topic of your choosing** at our University's **Seminar Series on Semiconductor Physics and Nanotechnology**, in the current winter semester (WS 25-26).

As we have previously discussed via email, the best suiting dates for the seminar would be in the first or the second week of December. I would suggest 01.12.2025 as the preliminary date. The seminar is advertised University wide via all our chairs, departments, and institutes, targeting research staff, professors, and also graduate students (mandatory for the Materials Science curriculum). The timeslot is 45min talk and 15-30min questions. The seminar will be hybrid (online via Zoom). The list of previous speakers and their abstracts you can find on our web page: https://physik.unileoben.ac.at/home/seminars

Also, as discussed per email, our joint bilateral exchange grant should cover all the expenses of you and anyone else from your team that might be joining the stay.

If you agree, please send me per email a one-page abstract in an editable format (e.g. MS word, google doc, latex, or plain text) and please fix the seminar date. Looking forward to your reply.

Sincerely,

***Ass. Prof. Priv.-Doz. Dr Aleksandar Matkovic***
***Senior Group Leader – Matkovic's Lab***
*Vice-head of the Chair of Physics,*
*Department Physics, Mechanics and Electrical Engineering,*
*Montanuniversität Leoben, Austria*
https://www.unileoben.ac.at/matkovics-lab/

Montanuniversität Leoben

# Lehrstuhl für Physik

Department Physik, Mechanik und Elektrotechnik
Montanuniversität Leoben

A-8700 LEOBEN, Franz Josef Straße 18, Austria
Tel: +43 3842 402-4601
e-mail: physics@unileoben.ac.at

Chair of Physics

## S E M I N A R
## on
## Semiconductor Physics and Nanotechnology

**Mo, 01.12.2025, 11:15 Uhr,**

**Seminar in**
**person in the Physics lecture hall *or* via Zoom**

## "Tuning the Optical Response of 2D Materials through Strain Engineering"

## Dr. Andrijana Šolajić

*Institute of Physics Belgrade, University of Belgrade, Belgrade, Serbia*

Two-dimensional (2D) materials represent a versatile platform for tailoring electronic and optical properties at the atomic scale. Their remarkable mechanical flexibility makes them ideal candidates for strain engineering, where external deformation serves as a precise and reversible tool for tuning structural, electronic, and optical properties. Such an approach enables the design of materials with adjustable characteristics suitable for a wide range of optoelectronic and photonic applications.

In this seminar, the influence of strain on the optical response of 2D materials and heterostructures will be discussed, with an emphasis on their potential as novel ultraviolet (UV) absorbers. The role of strain in modifying band structures and excitonic behavior will be outlined, together with examples of strain-induced tuning of the absorption edge and enhancement of light-matter interactions in van der Waals systems. Representative *ab initio* results obtained for group III monochalcogenides and their heterostructures with hexagonal boron nitride (hBN) will be presented, demonstrating the extent to which strain affects their electronic and optical spectra.

Finally, possible applications of strain-engineered 2D materials in flexible and wearable optoelectronics and UV photodetectors will be highlighted, illustrating the potential of this approach for the development of next-generation, lightweight, and energy-efficient devices.

***Zoom – Link:***
https://zoom.us/j/96375934537?pwd=RTlKTWhSdzRHU211YTY1bGFxTUtpZz09
Meeting-ID: 963 7593 4537
Kenncode: =r=4YQ

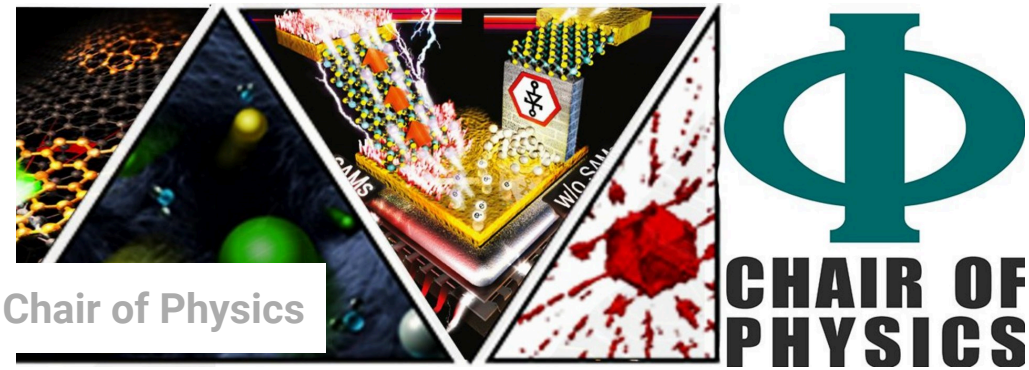


# Chair of Physics



## Seminars

### Wintersemester 2025/26

| | | |
|---|---|---|
| Mo, 2. Februar 2026 11:15 Uhr | **Seminar in person in the seminar room D *or* via Zoom** | **Prof. Dr. Stephanos Konstantinidis**<br>Plasma - Surface Interaction Chemistry, University of Mons, Belgium<br>**"Can we use magnetron sputtering to engineer 1D and 0D nanomaterials ?"**<br>Abstract |
| Mo, 26. Jänner 2026 11:15 Uhr | | ..... |
| Mo, 19. Jänner 2026 11:15 Uhr | **Seminar in person in the Physics lecture hall *or* via Zoom** | **Dr. Max Ritter**<br>Wood Materials Science group , Institute for Building Materials, Dep. Of Civil, Environmental and Geomatic Engineering, ETH Zurich, Switzerland<br>**"Wood-Based Functional Materials for Mechanical Energy Harvesting and Conductive Interfaces"**<br>Abstract |
| Mo, 12. Jänner 2025 11:15 Uhr | | ..... |





| | | |
|---|---|---|
| Do, 18. Dezember 2025 | Montanuniversität Leoben (Chair of Physics together with the Department General, Analytical and Physical Chemistry)<br>**Aula of the Montanuniversität Leoben** | **COLLOQUIUM ON THE NOBEL PRIZES 2025 from Physics and Chemistry**<br>**3:00 p.m.** – Lecture on the Nobel Prize in Physics<br>**Prof. Wolfgang Lang**<br>Faculty of Physics, University of Vienna, AUSTRIA<br>***„Macroscopic quantum tunneling: artificial atoms - big enough to get one's grubby fingers on"***<br>The Nobel Prize in Physics 2025 was awarded jointly to **John Clarke, Michael H. Devore**t and **John M. Martins** for the discovery of macroscopic quantum mechanical tunnelling and energy quantisation in an electric circuit.<br>*4:15 p.m. - Coffee Break*<br>**4:45 p.m.** – Lecture on the Nobel Prize in Chemistry<br>**Prof. Paolo Falcaro**<br>Institute of Physical and Theoretical Chemistry, Graz University of Technology, AUSTRIA<br>***„The art of tailoring space in solid crystals"***<br>The Nobel Prize in Chemistry 2025 was awarded jointly to **Susumu Kitagawa, Richard Robson** and **Omar M. Yaghi** for the development of metal-organic frameworks.<br>Poster |
| Mo, 15. Dezember 2025 11:15 Uhr | **Seminar in person in the Physics lecture hall *or* via Zoom** | **Dr. Lukas Legenstein**<br>Chair of Physics, Department Physics, Mechanics and Electrical Engineering, Technical University of Leoben, Austria<br>**"Modelling Heat Conduction in Crystalline Organic Semiconductors"**<br>Abstract |
| Mo, 01. Dezember 2025 11:15 Uhr | **Seminar in person in the Physics lecture hall *or* via Zoom** | **Dr. Andrijana Šolajić**<br>Institute of Physics Belgrade, University of Belgrade, Belgrade, Serbia<br>**"Tuning the Optical Response of 2D Materials through Strain Engineering"**<br>Abstract |
| Mo, 24. November 2025 11:15 Uhr | **Seminar in person in the Physics lecture hall *or* via Zoom** | **Assoz. Prof. Dr. Stefan Kowarik**<br>Department of Chemistry, Physical and Theoretical Chemistry, University of Graz, Austria<br>**"In situ X-Ray analysis of thin-film deposition: Bridging microsecond experiments, analysis with(generative) AI, and FAIR Data"**<br>Abstract |
| Fr, 21. November 2025 14:00 Uhr | **Seminar in person in the Physics lecture hall *or* via Zoom** | ***Defensio:***<br>**Muhammad Khan, M.Sc.**<br>Chair of Physics, Department Physics, Mechanics and Electrical Engineering, Technical University of Leoben, Austria<br>**"Two-dimensional Phyllosilicates as an Air-stable Platform for Layered Magnetic Materials"**<br>Abstract |
| Mo, 17. November 2025 15:00 Uhr | **Seminar in person in the Physics lecture hall *or* via Zoom** | **Prof. Georg S. Duesberg**<br>Institute of Physics, Faculty of Electrical Power Systems and Information Technology& SENS Research Center, University of the Bundeswehr Munich, Neubiberg, Germany<br>**"Not-so-perfect 2D materials in vertical heterostructures and scalable devices"**<br>Abstract |
| Mo, 10. November 2025 11:15 Uhr | **Seminar in person in the Physics lecture hall *or* via Zoom** | **Dr. Rainer T. Lechner**<br>Chair of Physics, Department Physics, Mechanics and Electrical Engineering, Technical University of Leoben, Austria<br>**"Investigations of Colloidal Nanocrystals using X-ray Scattering Techniques with Lab and Synchrotron Sources"**<br>Abstract |

# PROTOCOL

of the Fourth Meeting of the Serbian-Austrian Joint Commission for Scientific and Technological Cooperation implementing the Agreement between the Government of the Republic of Serbia and the Government of the Republic of Austria on Scientific and Technological Cooperation, concluded in Vienna, on 13 July 2010

Belgrade and Vienna, 17 June 2024

The 4rd Meeting of the Serbian-Austrian Joint Commission for Scientific and Technological Cooperation in accordance with Article 5 of the Agreement between the Government of the Republic of Serbia and the Government of the Republic of Austria on Scientific and Technological Cooperation of 13 July 2010 took place in Belgrade and Vienna, 17th of June 2024.

The Serbian delegation was headed by Ms. Vukašinović, Ministry of Science, Technological Development and Innovation of the Republic of Serbia.

The Austrian delegation was headed by Mr. Christian Gollubits, Federal Ministry of Education, Science and Research of the Republic of Austria.

The set-up of the two delegations can be found in Annex 1.

The Joint Commission adopted the following agenda:

1. Exchange of information on science and research
2. Discussion and adoption of the Work Programme
3. Selection of projects for the period 2024-2026
4. Next meeting and call for project proposals for the period 2026-2027
5. Adoption and Effectiveness of the Protocol

**Ad 1 Exchange of information on science and research**

Both sides supplied information on current developments of their national research policies. The Joint Commission expressed its confidence that the implementation of the bilateral programme will further contribute to the development of beneficial links between scientific institutions and scientists of both countries and will enable them to use their scientific potential more efficiently and fruitfully in regional as well as multilateral projects. Both sides reached an understanding to encourage their researchers to jointly participate in EU projects.

**Ad 2 Adoption of the Work Programme**

The Joint Commission discussed and adopted the Work Programme for the years 2024 - 2026.

The Work Programme includes regulations about the forms and aspects of cooperation, general administrative regulations, the administration of the exchange of scientists and experts as well as financial regulations.

A copy of the Work Programme for the years 2024 - 2026 is attached as part of this Protocol as Annex 2.

**Ad 3 Selection of projects for the period 2024-2026**

The Joint Committee agreed upon financing mobility costs of 27 cooperation projects lasting from 1st of July 2024 to 30th of June 2026 listed in Annex 3.

The Serbian side supports each bilateral project up to an amount of EUR 4,000.-.

The Austrian side supports each bilateral project up to an amount of EUR 9,000.-.

**Ad 4 Next meeting and call for project proposals for the period 2026-2028**

The Joint Commission has reached an understanding that upcoming calls for proposals will be published in principal on a biennial basis by the responsible institutions at least six months prior to the meetings of the Joint Commission for Scientific and Technological Cooperation.

The Parties also agreed to send the list of eligible proposals received on their side within 20 working days from the closure of the call.

The call for project proposals will be open from 2 October 2026 to 30 November 2026.

Both parties have reached an understanding to hold the 5th Meeting of the Joint Commission in Vienna in the first half of 2026. The exact date will be agreed upon through diplomatic channels.

**Ad 5 Adoption and Effectiveness of the Protocol**

This Protocol will remain effective until 30th of June 2026. It will remain effective beyond this date until a new Protocol becomes effective for a maximum period of another year.

Done in Belgrade and Vienna, on 17th of June 2024 in two English original copies.

Head of the Serbian delegation

Ms. Ivana Vukašinović

Ministry of Science, Technological Development and Innovation of the Republic of Serbia

Head of the Austrian delegation

Mr. Christian Gollubits

Federal Ministry of Education, Science and Research of the Republic of Austria

**Work Programme**
**for the Years 2024-2026**

Adopted on the occasion of the 4th Meeting of the Joint Commission for Scientific and Technological Cooperation, held on-line in Belgrade and Vienna on 17 June 2024, implementing the Agreement between the Government of the Republic of Serbia and the Government of the Republic of Austria on Scientific and Technological Cooperation, signed in Vienna, on 13 July 2010.

1. Forms of Cooperation
2. Aspects of Cooperation
3. General Administrative Regulations
4. Financial Regulations

## 1. Forms of Cooperation

1.1 According to Article 2 of the Agreement, joint cooperation projects in the field of science and technology between Serbian and Austrian researchers will be supported by funding the mobility of researchers.

1.2 The Joint Commission will select joint research projects for funding on the basis of public calls for project proposals. The project duration will be two years.

1.3 The costs arising from joint cooperation projects should be balanced between the two sides.

## 2. Aspects of Cooperation

2.1 The Joint Commission agreed to support cooperation projects in all research fields.

2.2 Project applications with the potential for follow-up applications in bilateral and multilateral cooperation programs in Serbia, Austria and the EU will be favoured.

2.3 Project applications submitted by early-stage researchers as well as project applications with involvement of PhD/doctoral students and/or female researchers will be prioritized.

## 3. General Administrative Regulations

3.1 Responsible Institutions:

3.1.1 In Serbia:

The Ministry of Science, Technological Development and Innovation of the Republic of Serbia - NITRA, on behalf of the Serbian side, shall be the coordinating body for the implementation of the Work Programme.

Ministry of Science, Technological Development and Innovation

Nemanjina 22-26, 11000 Belgrade

Telephone: +381 11 3616 589

Fax: +381 11 3616 589

Email: snezana.omic@nitra.gov.rs

Internet: www.nitra.gov.rs

3.1.2 In Austria:

The mobility funding programme will be implemented by the OeAD - Austria's Agency for Education and Internationalisation

Ebendorferstrasse 7, 1010 Vienna

Telephone: +43 1 53408-472

Email: wtz@oead.at

Internet: http://www.oead.at/wtz

The OeAD GmbH is an institution commissioned by the Austrian Federal Ministry of Education, Science and Research to implement this funding programme.

Federal Ministry of Education, Science and Research

Rosengasse 2-6, 1014 Vienna

Telephone: +43 53120 7132

Email: christian.gollubits@bmbwf.gv.at

Internet: http://www.bmbwf.gv.at

3.2 Selection procedure of cooperation projects and administration

3.2.1 The upcoming calls for will be published on a biennial basis by the responsible institutions (3.1) at least six months prior to the meetings of the Joint Commission.

3.2.2 Submitted project applications have to include:

- Topic
- Names and contact information of the cooperating Austrian and Serbian institutions, Austrian and Serbian Principal Investigators and research team members
- Project description (subject, objective and methodology)
- Work plan
- Qualifications of the Principal Investigators and research team members
- Project budget
- Further cooperation perspective

3.2.3 Project applications have to be prepared jointly by the Austrian and Serbian Principal Investigators and have to be submitted to both respective responsible institutions (3.1) according to the criteria defined in the call text.

3.2.4 Only project applications received in time by both respective responsible institutions (3.1) will be eligible for evaluation. The responsible institutions will exchange the lists of eligible applications received within 20 working days after the closure of the call and the results of national evaluations at least 10 working days before the selection meeting.

3.2.5 Evaluation criteria for applications:

In Serbia:

- Quality and scientific relevance
- Importance and attainability of the proposed goals
- Compatibility of the methodology and the plan of activities
- Achievements and the applicability of the results
- Perspective for further joint cooperation and participation of the Serbian young researchers

In Austria:

- Scientific quality of the proposed research project incl.
  - Feasibility of the joint research plan
  - Adequacy of the scientific method
  - Qualification of the scientist's/research teams involved
- Perspective for further joint cooperation activities
- Project applications will receive up to 10 points additionally,
  - Either if submitted by early-stage researchers
  - Or if involving doctoral students/early-stage researchers and/or female researchers

3.2.6 The responsible institutions (3.1) will provide the Joint Commission with a joint short list of evaluated project applications as a basis for the selection meeting.

3.2.7 The Joint Commission will take the final funding decision, either at a physical meeting or via exchange of Emails.

3.2.8 A brief midterm report has to be submitted to and adopted by the respective responsible institutions (3.1) after the first year of the project duration as a precondition for further funding.

3.2.9 A final report about the results of their research activities has to be submitted no more than 3 months after the expiration of the project duration by the Principal Investigators to the respective responsible institutions (3.1).

3.2.10 The exploitation, possible patent registration and publication of project results are subject to the respective national and international laws that are applicable to both sides.

3.3 Administration of the Exchange of Researchers and Experts

3.3.1 The project partners have to agree on the date and duration of a stay at the host institution at least three weeks prior to the intended date of visit.

3.3.2 The Serbian Principal Investigator will notify the Austrian researcher in question at the responsible institution in Serbia (3.1.1).

3.3.3 The Austrian Principal Investigator will notify the Serbian researcher in question at the responsible institution in Austria (3.1.2).

## 4. Financial Regulations

4.1 Each side will cover the travel expenses as well as the accommodation costs of its researchers.

4.2 Grants in Serbia

4.2.1 Travel expenses (economy class) of the Serbian researchers will be reimbursed based on submitted invoices. Reimbursement of travel expenses by private car will be made on the basis of the Law on the Use of an Official Vehicle.

4.2.2 Accommodation expenses of the Serbian researchers and Young researchers: EUR 100.- per working day for up to 14 days or EUR 1,400. - per month for long-term stays between 14 days and 3 months maximum.

4.3 Grants in Austria

4.3.1 Travel expenses (economy class) of the Austrian researchers will be reimbursed based on submitted invoices.

4.3.2 Accommodation Expenses of the Austrian researchers: EUR 100.- per working day for up to 14 days or EUR 1,400. - per month for long-term stays between 14 days and 3 months maximum. PhD/Doctoral students: EUR 100.- per working day for up to 12 days or EUR 1,250. - per month for long-term stays between 12 days and 3 months maximum.

4.3.3 Project related material costs: max. EUR 3000.- as part of the granted maximum budget based on submitted invoices.

4.4 Health insurance:

The sending side will assure that outgoing personnel is sufficiently insured for health.

Annex 3 - List of Projects 2024-2026

| Project Title | SRB Project Leader - First Name | SRB Project Leader - Surname | SRB Organisation | AT Project Leader - First Name | AT Project Leader - Surname | AT Organisation |
|---|---|---|---|---|---|---|
| Human Rights and border policies – a comparison of Serbia and Austria | Maja | NASTIĆ | University of Nis; Faculty of Law | Philip | CZECH | Paris Lodron Universität Salzburg; |
| Learning from mosses: the roles of tri saccharides for plant survival in extreme climate conditions | Aneta | SABOVLEJEVIĆ | University of Belgrade; Faculty of Biology | Ingeborg | LANG | Universität Wien; |
| Green micro-reinforced building composites with agricultural by-products | Slobodan | ŠUPIĆ | University of Novi Sad; Faculty of technical sciences;Institute for testing of materials; | Ildiko | MERTA | Technische Universität Wien; |
| Exchanging Laboratory Practices in Air Radioactivity Monitoring | Jelena | AJTIĆ | University of Belgrade; Faculty of Veterinary Medicine | Claudia | LANDSTETTER | AGES - Agentur für Gesundheit und Ernährungssicherheit; |
| Exploring spectroscopic fingerprints of defects and dopants in two dimensional magnetic insulators | Andrijana | ŠOLAJIĆ | Institute of Physics Belgrade; | Aleksandar | MATKOVIC | Montanuniversität Leoben; |
| DEVELOPING A PREDICTIVE ANTIBODY TEST FOR EARLY DETECTION OF TUBAL FACTOR INFERTILITY AND TRACHOMA | Marijana | STOJANOVIĆ | University of Belgrade; Institute for Biological Research "Siniša Stanković", National Institute of the Republic of Serbia | Aleksandra | INIC-KANADA | Medizinische Universität Wien; |
| What's in a verb? Mapping Serbian verbs borrowed into Romani | Mirjana | MIRIĆ | Institute for Balkan Studies SASA; | Marko | SIMONOVIC | Universität Graz; |
| Impact of Defects on Electronic, Magnetic, and Topological Properties in Semimetallic van der Waals Transition Metal Dichalcogenides | Jelena | PEŠIĆ | University of Belgrade; Institute of Physics Belgrade | Rajdeep | ADHIKARI | Johannes Kepler Universität Linz; |
| Non-targeted speciation analysis in Asparagus officinalis and Boletus edulis by HPLC-ICPMS/MS | Ivan | MILOVANOVIĆ | University of Belgrade; Innovation Centre of the Faculty of Technology and Metallurgy | Bassam | LAJIN | Universität Graz; |
| Migrants in Need? The Sociocultural Effects of Contemporary Crises on Serbian Migrants in Austria and Returnees in Serbia | Marija | BRUJIĆ | University of Belgrade; Faculty of Philosophy | Eva Tamara | ASBOTH | Johannes Kepler Universität Linz; Österreichische Akademie der Wissenschaften; Paris Lodron Universität Salzburg; |

| | | | | | | |
|---|---|---|---|---|---|---|
| Towards reconstructing the Triassic-Jurassic eastern continental margin of the Vardar Ocean: Triassic-Jurassic tectonostratigraphy of the Carpatho-Balkanides/Serbo-Macedonides (Serbia) | Uros | STOJADINOVIĆ | University of Belgrade; Faculty of Mining and Geology | Hans-Jürgen | GAWLICK | Montanuniversität Leoben; |
| In vitro and in vivo models development for the prediction of sensitization to food | Marija | GAVROVIĆ-JANKULOVIĆ | University of Belgrade; Faculty of Chemistry | Michelle | EPSTEIN | Medizinische Universität Wien; |
| Anticoagulation and inflammation monitoring in patients after heart and vascular interventions: Prospective | Dragana | UNIĆ-STOJANOVIĆ | University of Belgrade; Institute for Cardiovascular Diseases Dedinje | Sasa | RAJSIC | Medizinische Universität Innsbruck; |
| Activated flux fusion for wire based plasma additive manufacturing (AS Fusion) | Sebastian | BALOŠ | University of Novi Sad; Faculty of Technical Sciences | Norbert | ENZINGER | Technische Universität Graz; |
| Data Story about Dementia | Anđelka | ZEČEVIĆ | Serbian Academy of Sciences and Arts; Mathematical Institute | Elma | DERVIC | Complexity Science Hub Vienna; |
| CREATING VALUABLE (SEMI)PRODUCTS FROM BLACK RASPBERRY POMACE | Katarina | ŠAVIKIN | Institute for Medicinal Plants Research "Dr Josif Pančić" (IPLB); | Heidrun | HALBWIRTH | Technische Universität Wien; |
| Safety Climate and Performance Appraisal of Heavy Machinery Supply Chain Members in Austria and Serbia as a Resilience Enhancement Tool – SAFECORNER | Vesna | SPASOJEVIĆ BRKIĆ | University of Belgrade; Faculty of Mechanical Engineering | Bernd Markus | ZUNK | Technische Universität Graz; |
| Small Polaron: from Models to Real Materials | Darko | TANASKOVIĆ | Institute of Physics Belgrade; | Michele | RETICCIOLI | Universität Wien; |
| From peels to peroxidase: obtaining commercial enzyme preparation from agro-industrial waste | Milica | SVETOZAREVIĆ ARSOVIĆ | University of Belgrade; Innovation Center of the Faculty of Technology and | Eva | PRADA | Technische Universität Wien; |
| Preventing LPMO from self-destruction by oxidative damage | Dejan | MILENKOVIĆ | The State University in Novi Pazar; University of Kragujevac Institute for Information Technologies | Peter | POLIAK | Universität für Bodenkultur Wien; |
| Comparative housing studies – commodification and financialisation in contemporary housing in Vienna and Belgrade | Ivan | RATKAJ | University of Belgrade; Faculty of Geography | Robert | MUSIL | Österreichische Akademie der Wissenschaften; |
| Space weather and monitoring the effects of extraterrestrial radiation | Aleksandra | NINA | University of Belgrade; Institute of Physics Belgrade; | Hans | EICHELBERGER | Österreichische Akademie der Wissenschaften; |

Annex 3 - List of Projects 2024-2026

| | | | | | | |
|---|---|---|---|---|---|---|
| Helen – a Catholic Noblewoman, Serbian Queen and Interreligious Donor connecting East and West in the 13th/14th Centuries (IDCEW) | Branka | VRANEŠEVIĆ | University of Belgrade; Faculty of Philosophy | Mihailo | POPOVIC | Österreichische Akademie der Wissenschaften; |
| Insights in co-infections with Pneumocystis spp. and canine distemper virus, canine parvovirus-2, canine coronavirus, pseudorabies virus, and flaviviruses in Serbian wild carnivore species | Branislav | KURELJUŠIĆ | Institute of Veterinary Medicine of Serbia; | Christiane | WEISSENBACHER-LANG | Veterinärmedizinische Universität Wien; |
| Effective interactions between charged Janus colloids beyond mean-field | Nataša | ADŽIĆ | University of Belgrade; Institute of Physics Belgrade; | Emanuela | BIANCHI | Technische Universität Wien; |
| COMPARING THE REMNANTS OF THE CENERIAN OROGEN IN AUSTRIA AND SERBIA | Bojan | KOSTIĆ | University of Belgrade; Faculty of Mining and Geology | FRIEDRICH | FINGER | Paris Lodron Universität Salzburg; Universität Graz; |
| Clean and Green hydraulic fluids: ionic liquids approach | Milan | VRANEŠ | University of Novi Sad; Faculty of Sciences | Christian | SCHRÖDER | Universität Wien; |

scientific reports

Check for updates

OPEN

# Tailoring electronic and optical properties of hBN/InTe and hBN/GaTe heterostructures through biaxial strain engineering

A. Šolajić[1]✉ & J. Pešić[1,2]

**In this research study, we systematically investigate the electronic and optical properties of van der Waals heterostructures (HSs) consisting of InTe (GaTe) and hBN monolayers, subjected to controlled biaxial strain. Our analysis demonstrates that the application of strain induces noteworthy alterations in the electronic band structure, enabling precise manipulation of the band gap and augmentation of the absorption properties of these structures. Employing density functional theory, we conduct a comprehensive examination of the influence of strain on the electronic and optical characteristics of these HSs. Our investigation showcases the remarkable potential of strain engineering in rendering these heterostructures into efficient and robust wide-range absorbers, particularly optimised for the visible spectrum, underscoring their relevance in various photonic and optoelectronic applications, paving the way for integration into advanced nanodevices.**

Van der Waals (vdW) heterostructures (HSs), a class of materials composed of stacked two-dimensional materials held together by van der Waals forces, have attracted significant attention in recent years due to their unique electronic and optical properties[1–3]. A noteworthy advantage inherent to vdW HSs is their remarkable amenability to precise manipulation and customisation. The weak nature of vdW forces allows the layers to be easily separated and manipulated, allowing the creation of an unlimited number of different structures with precise control over the electronic, optical, and mechanical properties. This makes it possible to design and fabricate materials with specific desired characteristics, offering countless new possibilities for their applications in modern nanodevices[4]. With their high-performance electronic and optical properties, novel HSs can be used for transistors[5], solar cells[6,7], lithium ion batteries[8,9], light emitting devices[10,11], photodetectors[12–15], various sensors[16–18], and many more. Recent research has further illuminated their promising potential as candidates for quantum computing applications[19].

Delving deeper into the mechanisms of manipulation for vdW HSs not only enhances their properties but also unlocks a wider array of possibilities for applications in devices that fulfil the growing demands of today's market, such as sensors and switches. The modulation of electrical properties in such structures can be achieved in many ways, with the most common approaches being doping, strain application, or the use of external electric or magnetic field. The study of strain in 2D materials and vdW HSs represents a dynamically evolving research frontier, granting us an additional level of precision in controlling material properties[20–22].

Group III–VI monochalcogenide-based HSs have emerged as focal points of research attention, offering substantial promise for a broad spectrum of cutting-edge device applications. They find utility as Schottky barriers, high-performance 2D and flexible electronics, sensors, photodetectors, and more. Materials within the class of two-dimensional III–VI monochalcogenides are known for their high electron mobility, broad absorption spectra, and favourable elastic properties. Notably, the single-layer InTe is predicted to exhibit exceptional thermoelectric performance due to its remarkably low thermal conductance, boasting the highest merit figure, $ZT = 2.03$ at 300 K, among the III–VI monochalcogenide family[23]. Recent study was discussing electronic transport and thermoelectric properties of doped InTe, showing that p-type InTe doped with Bi, Ag, Mn, Sn or Sb exhibits the enhanced thermoelectric performance, mainly induced by reduced thermal conductivity[24]. Additionally, the InTe monolayer demonstrates a broad absorption spectrum, covering the ultraviolet to visible regions, with an absorption coefficient of up to $10^{-5}$ $cm^{-1}$. In most recent report, two-dimensional InTe

[1]Laboratory for 2D materials, Center for Solid State Physics and New Materials, Institute of Physics Belgrade, University of Belgrade, Pregrevica 118, 11080 Belgrade, Serbia. [2]Chair of Physics, Department Physics, Mechanics and Electrical Engineering, Montanuniversität Leoben, 8700 Leoben, Austria. ✉email: solajic@ipb.ac.rs

was synthesized in large-scale samples, as centimeter-scale 2D films on $SiO_2$/Si substrates[25]. InTe also exists in tetragonal phase, and its electronic band structure has a highly anisotropic character[26] , marking it of high interest for electronic and thermoelectric applications. In that phase, structure has quasi-one-dimensional form, where one-dimensional $In^{1+}$ chains are observed, and additionally, the presence of $In^{1+}$ induces a localized gap state, responsible for the high intrinsic p-type doping of InTe[27]. Similarly to InTe , the monolayer GaTe exhibits comparable absorbing properties[28], along with excellent UV light absorption. In the realm of single-layer materials, each member of this material family exhibits remarkable and distinctive properties. Nonetheless, single layer III–VI monochalcogenides possess one noteworthy limitation in their pristine form. The majority of these materials display sensitivity to oxidation upon exposure to ambient air[29–31], especially in their single layer form, and need adequate material for passivisation and mechanical protection. Non-reactive with most chemicals, stable in air and resistant to oxidation, hBN is already known as an effective coating material in the form of thin films or monolayers[32–34], and has been demonstrated successful for protection against oxidation and even for improving the electronic and optical properties of few-layered InSe and GaSe[35].

Motivated by these results, in our previous work, we designed and investigated two novel heterostructures, hBN/InTe and hBN/GaTe, as detailed in[36]. These heterostructures displayed favourable electronic properties and an excellent broad absorption spectrum, enhanced and protected by the hBN layer, making them promising candidates for applications in photodetectors or field-effect transistors. Given the experimentally favourable binding energies and stacking versatility of both hBN/InTe and hBN/GaTe heterostructures, this study further delves into the intriguing potential of fine-tuning their properties through the application of controlled strain. In the following sections, we present a computational study of hBN/InTe and hBN/InTe under biaxial strain. The application of uniform biaxial strain does not alter the symmetry of the structure; instead, it allows us to tune the band structure and optical absorption.

## Computational methods

Calculations were carried out using density functional theory (DFT), as implemented in the Quantum Espresso (QE) software package[37], based on plane waves and pseudopotentials. In all calculations, the Perdew–Burke–Ernzerhof (PBE) exchange correlation functional[38] is used, along with norm-conserving pseudopotentials. The energy cutoff of 80 Ry was set for both structures after the convergence tests.

The Monkhorst pack of $16 \times 16 \times 1$ mesh for k-point sampling is used in geometric optimisation, total energy, and phonon calculations. For calculations of p-DOS and optical properties, a refined $64 \times 64 \times 1$ mesh is used. The band structure is calculated on 440 k-points along Γ-M-K-Γ direction. To simulate the 2D structure, a vacuum of 20 Å was added along the z-direction to avoid interactions between the layers. Geometry optimisation of the positions of the atoms and the lattice parameters is performed using the BFGS algorithm, with criteria for the maximum forces allowed between atoms of $10^{-6}$ Ry/Å. To properly account for van der Waals force effects, the Grimme-D2 correction[39,40] was included to obtain more accurate lattice constants and forces. The optical properties were calculated using the epsilon.x code in QE software, based on the random phase approximation (RPA).

## Results and discussion

As discussed in our previous work[36], the unit cells of InTe and GaTe monolayer are $a = 4.371$ Å and $a = 4.048$ Å, respectively. The unit cell of hBN is $a = 2.515$ Å, and for both structures, constructing the heterostructure consisting of a $\sqrt{3} \times \sqrt{3}$ supercell of hBN rotated for 30o on top of $1 \times 1$ unit cell of InTe or GaTe provides an excellent match. After complete optimisation of the lattice parameters and atom positions within the unit cell, the obtained unit cell is hexagonal, with a lattice constant of $a = 4.336$ Å for hBN/InTe and $a = 4.309$ Å for hBN/GaTe. Resulting unit cell of hBN/InTe has induced strain of 0.8% on InTe layer and 0.3% on hBN layer, showing that HS constructed as described is almost an ideal match. The resulting unit cell of hBN/GaTe induces strain of 6% on GaTe and 0.8% on hBN which is slightly less perfect than hBN/InTe HS, but still agreeable. The top view of the structures is presented in Fig. 1. With all three types of stacking being energetically close to each other, we consider H-top stacking (the In(Ga) atom above the centre of the hBN hexagon), which has slightly lower total energy and binding energy compared to the B-top and N-top types. All constituting materials (hBN, InTe, GaTe) exhibit outstanding mechanical properties, demonstrating the ability to withstand significant biaxial strain strengths of more than 10%[23,28,41] . From an experimental standpoint, achieving a controllable and precise strain beyond a few percent in complex structures like van der Waals (vdW) heterostructures is often challenging, if not impossible. Taking this into account, we chose to set the maximum absolute strain values at 5% even though both systems theoretically possess the capacity for higher strain tolerance. The uniform biaxial strain of − 5 to 5% is applied to both structures, with the step of 1%, and the geometry optimisation of the positions of the atoms within the unit cell is performed for all strained structures. The binding energies $E_b$ are calculated for all structures as follows:

$$E_b = E_{heterostr.} - E_{In(Ga)Te} - E_{hBN}, \quad (1)$$

where $E_{heterostr.}$, $E_{In(Ga)Te}$ and $E_{hBN}$ represent the total energy of hBN/In(Ga)Te heterostructure, InTe or GaTe monolayer and hBN monolayer, respectively. Total and binding energies, $E_{tot}$ and $E_b$, along with the distance between the hBN and In(Ga)Te layers $d$ and the width of the layer $h$ are given in Table in the Supplementary file. First, the binding energies are negative in all cases, suggesting that all strained structures are experimentally feasible. It can be seen from and Fig. 2 that the total energy is lowest for HS without strain and increases exponentially with both positive and negative strains, as expected, since the initial system without strain was fully relaxed with respect to the lattice constants and atom positions within the unit cell. The distance between layers and the bond lengths change with different values of applied strain. Although the bonds in the InTe (GaTe) layer are slightly shortened when compressive strain is applied (mainly the In(Ga)–Te bonds), a significant difference

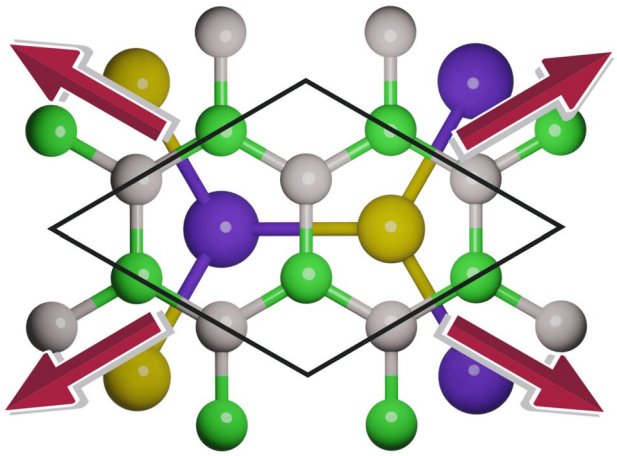

**Figure 1.** Top view of heterostructures, with arrows showing the tensile biaxial strain. B and N atoms are represented with a grey and green colour, In/Ga and Te atoms are coloured purple and yellow.

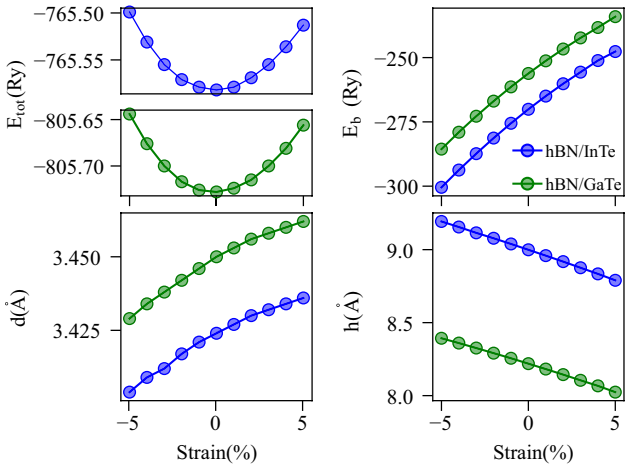


**Figure 2.** Dependence of total energy $E_{tot}$, binding energy $E_b$. distance between the layers $d$ and the thickness of HSs $h$ on applied strain. The blue lines and markers correspond to hBN/InTe, and green lines and markers correspond to hBN/GaTe.

is present in the angle of the In(Ga)–Te bond with respect to the horizontal plane, so the In(Ga)Te layer width is increased, and the inner Te atoms are positioned slightly closer to the hBN layer. In the case of tensile strain, the In(Ga)Te bonds are stretched, causing the layer width to decrease and the distance between the inner Te atoms and the hBN layer to increase. The complete data are given in Table 1 in the Supplementary file.

Before the introduction of strain into any structure, it is essential to conduct a thorough analysis of its mechanical characteristics. We used the Thermo pw code[42] to compute the elastic constants. The code calculates the non-zero components of the stress tensor for a set of strains and obtains the elastic constants from the first derivative of the stress with respect to the strain. In this way, we can gain a solid basis to understand the relationship between strain and the mechanical reaction of the structure. For 2D systems, nonzero elastic constants follows the Hooke's law under plane stress conditions:

$$\begin{bmatrix} \sigma_1 \\ \sigma_2 \\ \sigma_3 \end{bmatrix} = \begin{vmatrix} c_{11} & c_{12} & 0 \\ 0 & c_{22} & 0 \\ 0 & 0 & c_{66} \end{vmatrix} \cdot \begin{bmatrix} \varepsilon_1 \\ \varepsilon_2 \\ \varepsilon_3 \end{bmatrix}. \tag{2}$$

For a hexagonal lattice, $C_{11} = C_{22}$ and $C_{12} = C_{21}, C_{66} = (C_{11} - C_{22})/2$, so there are only two independent elastic constants. In that case, Young's modulus, Poisson's ratio, and shear modulus are obtained from the following relations:

$$E_Y = C_{11} - \frac{C_{12}^2}{C_{11}}, \ \nu_{xy} = \frac{C_{12}}{C_{11}}, \ G_{xy} = C_{66}. \tag{3}$$

For hexagonal 2D systems, layer modulus that represents the resistance of a sheet to stretching is calculated by following[43]:

$$\gamma^{2D} = \frac{C_{11} + C_{12}}{2}. \quad (4)$$

Calculated elastic constants and moduli are given in Table 1. Obtained elastic constants of single layer InTe and GaTe are in range of other III–VI monochalcogenides[44]. Constants $C_{11} = 45.36$ N/m and $C_{12} = 11.76$ N/m for InTe are close to constants of single layer InSe, and $C_{11} = 65.62$ N/m and $C_{12} = 15.30$ N/m for GaTe close to results for single layer GaSe. We calculated the elastic constants of hBN in order to validate our results, and obtained values are in agreement with the literature[43,45]. When the HSs are formed, all constants and moduli are significantly increased. Elastic constants $C_{11}$ and $C_{12}$ for hBN/InTe are $C_{11} = 338.3$ N/m and $C_{12} = 72.08$ N/m; $C_{11} = 340$ N/m and $C_{12} = 75.48$ for hBN/GaTe, and their values are roughly similar to the sum of individual constants of each layer in the heterostructure. Young modulus is increased to 323 N/m in HSs, which are high almost as in graphene (342–366 N/m for Young modulus and 206–212 N/m for layer modulus, according to the literature[43,46]), indicating high resistance to unidirectional compression as well to stretching. The results suggest that the presence of the hBN layer in our heterostructures not only shields the delicate monochalcogenide layers from oxidation but also provides effective mechanical protection, at the same time rendering the system more robust and resistant to deformations.

In our investigation, we computed the band structures of both heterostructures (HSs) under various compressive and tensile strain conditions, building upon the foundation laid out in our previous study[36]. The band structures for HSs under − 4%, 0% and 4% strain are visually represented in Fig. 3. The band structures for all values of strain, from − 5 to 5%, are represented in Figures S1 and S2 in supplementary file. In their pristine, unstrained states, hBN/InTe and hBN/GaTe exhibit band gaps of $E_g = 1.53$ eV and $E_g = 0.76$ eV, respectively. Notably, both HSs display an indirect band gap configuration, with the valence band maximum (VBM) positioned near the Γ point and the conduction band minimum (CBM) precisely at the Γ point.

When the application of strain is introduced, significant alterations occur in both the band gap and the shape of the bands within the heterostructures. In the case of the hBN/GaTe heterostructure subjected to compressive strain, the band gap widens as the strain magnitude increases, reaching a maximum value of $E_g = 1.49$ eV at −5% strain. Importantly, the valence band retains its shape while shifting downward to lower energy levels. In contrast, the conduction band exhibits distinct behaviour: the Γ-valley expands, whereas the energy level of the M-valley remains relatively stable. This results in both valleys having nearly identical energies at −4% strain. Conversely, the introduction of tensile strain leads to a contrasting effect. The upper region of the valence band near the Γ point shifts upward, while the lower region of the conduction band at the Γ point experiences a substantial descent. Consequently, at + 5% strain, the band gap narrows to only 0.24 eV.

The relationship between band gap and strain is systematically explored and plotted in Fig. 6. Remarkably, across the entire range of applied strains, from −5 to + 5%, the dependence closely approximates a linear decrease.

Turning our attention to the hBN/InTe heterostructure, we observe similar trends in band gap modulation under strain. However, a significant disparity arises in the conduction band behaviour, particularly under compressive strain. Here, the valence band also shifts downward as compressive strain intensifies, eventually falling below the group of bands situated around −0.5 eV at the Γ point. Initially, in the relaxed state, the conduction band minimum (CBM) resides at the Γ point, while the bottom of the M valley maintains nearly the same energy. However, as compressive strain is applied, the Γ-valley remains relatively stable in terms of energy, while the M-valley experiences a downward shift. Consequently, the CBM transitions from the Γ to the M-point as strain surpasses −1%. This intricate interplay between the valence and conduction bands results in a band gap expansion, peaking at $E_g = 1.69$ eV at −2% strain before gradually reducing to 1.39 eV at −5% strain.

In the case of tensile strain, the behaviour mirrors that of the hBN/GaTe heterostructure. The valence band shifts upward, and the CBM descends with increasing tensile strain, leading to a reduced band gap, which ultimately reaches a minimum of 0.70 eV at + 5% strain.

The shifts in the position of valleys within the conduction band in response to varying strain values are not uncommon and have been observed in InTe and GaTe monolayers subjected to biaxial strain[28,47,48]. Furthermore, our analysis of the density of states (DOS) reveals that the bands closest to the Fermi level predominantly arise from the In(Ga) and Te states. DOS for HSs with − 4%, 0% and 4% strain are presented in Figs. 4 and 5 . Complete

| 1 | InTe | GaTe | hBN | hBN/InTe | hBN/GaTe |
|---|---|---|---|---|---|
| $C_{11}$ | 45.36 | 65.62 | 290.77 | 338.30 | 340.00 |
| $C_{12}$ | 11.76 | 15.30 | 63.93 | 72.08 | 75.48 |
| $C_{66}$ | 16.52 | 25.16 | 113.42 | 132.94 | 132.26 |
| $E_y$ | 42.31 | 62.05 | 276.41 | 322.94 | 323.24 |
| $\nu_{xy}$ | 0.26 | 0.23 | 0.22 | 0.21 | 0.22 |
| $G_{xy}$ | 16.52 | 25.16 | 113.42 | 132.94 | 132.26 |
| $\gamma^{2D}$ | 28.56 | 40.46 | 177.35 | 205.19 | 207.74 |

**Table 1.** Elastic constants, Young modulus, Poisson ratio, shear modulus and layer modulus for HSs and pristine InTe and GaTe monolayers. Units are given in N/m.

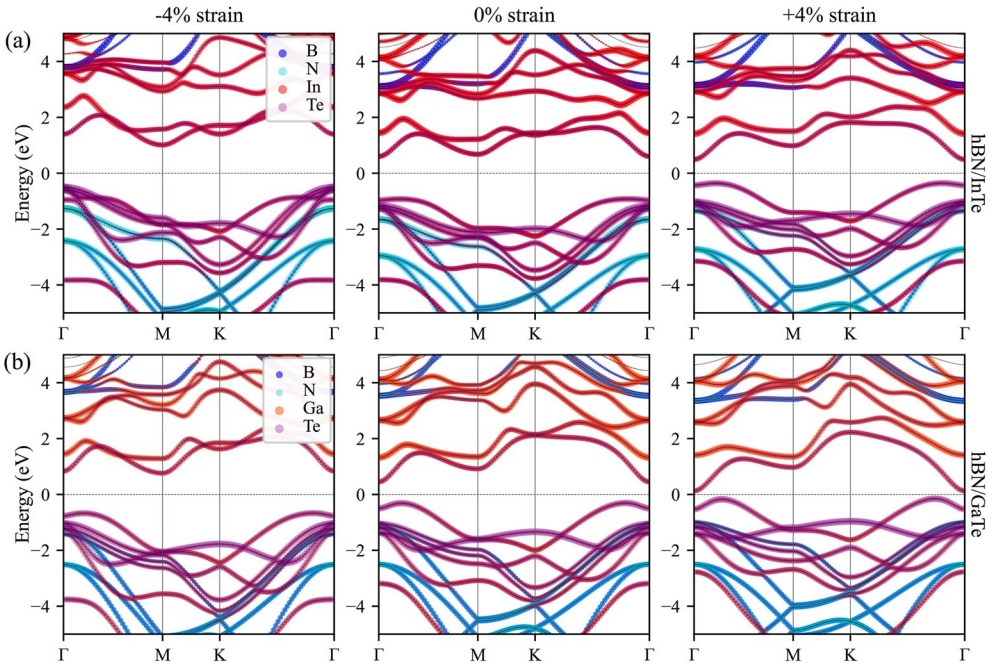


**Figure 3.** Band structure of (**a**) hBN/InTe HS and (**b**) hBN/GaTe. The width of the lines is proportional to the contribution of different atoms/states. The line width is proportional to the magnitude of projections of wavefunctions over atomic orbitals. The contributions from different atomic orbitals are presented in different colours, as shown in the legend.

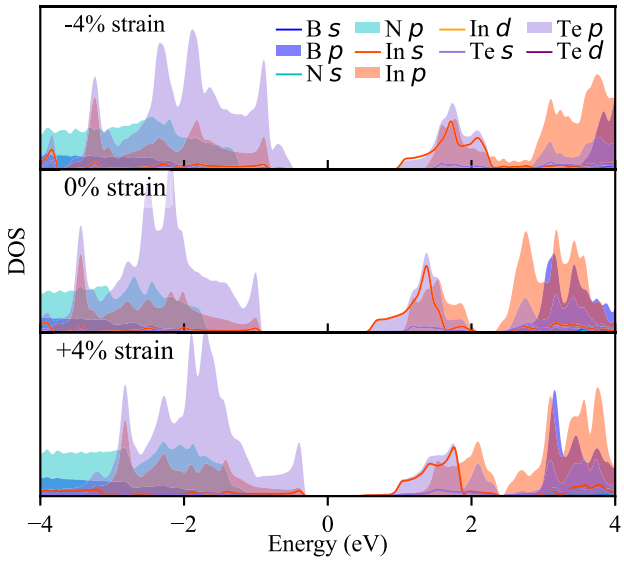


**Figure 4.** Projected density of states of hBN/InTe HS. Contributions from different atoms and states are represented with colours as in legend.

data with DOS for all strain values are shown in Figure S3 in supplementary file. The uppermost bands below the Fermi level primarily originate from the Te states, while the bands above comprise a combination of In(Ga) and Te states. Consequently, it can be inferred that the changes in the conduction band shape predominantly result from the influence of strain on the InTe(GaTe) layer itself, rather than being an inherent characteristic of the formed heterostructure. These findings underscore the profound influence of strain engineering on the electronic properties of these heterostructures, offering a promising avenue for precise control and modulation of their behaviour for tailored optoelectronic applications.

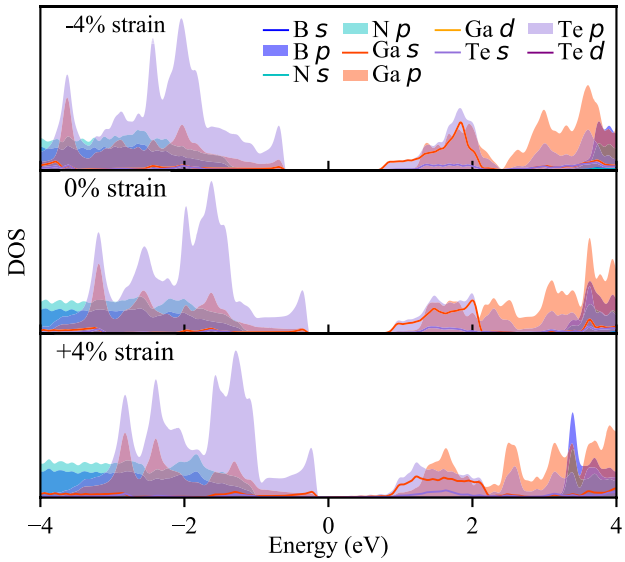


**Figure 5.** Projected density of states of hBN/GaTe HS. Contributions from different atoms and states are represented with colours as in legend.

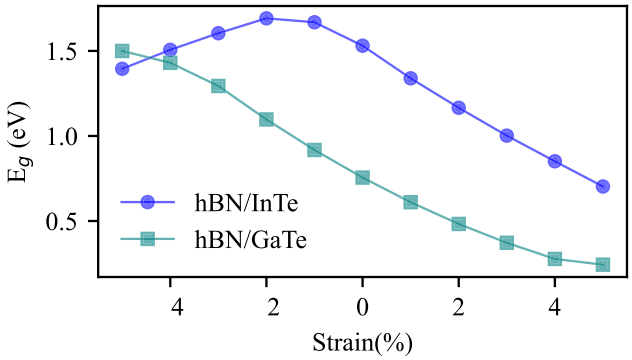


**Figure 6.** Band gap of hBN/InTe (indicated as blue line and circles) and hBN/GaTe (indicated as green line and squares) as a function of applied strain.

Significant variations in both the band gap and the shape of the bands can drastically alter dielectric function and absorption. The complex dielectric function $\epsilon(\omega) + \epsilon_R(\omega) + i\epsilon_I(\omega)$ is obtained from DFT calculations in the RPA framework. The absorption coefficient $\alpha(\omega)$ is obtained directly from the dielectric function as follows:

$$\alpha(\omega) = \sqrt{2}\frac{\omega}{c}\sqrt{\sqrt{\epsilon_R^2(\omega) + \epsilon_I^2(\omega)} - \epsilon_I(\omega)}. \tag{5}$$

Calculation of optical properties were performed within RPA. Optical properties of group III monochalcogenide members and similar structures as well of hBN were previously studied both with GW and RPA based methods, and it is shown that RPA can provide reasonably good results of dielectric function and its qualitative description[49–53]. In[54], heterostructure of InSe with silicene, germanene and antimonene, imaginary part of the dielectric function calculated both with RPA over GGA and GW, and main difference observed is the shift of the dielectric function for 0.5–1 eV due to larger calculated band gap. The absorption coefficients of both HSs under different strain strengths are presented in Figs. 7 and 8, respectively. The band gap width variations induced by strain strength exhibit a notable influence on the absorption properties of both HSs. Specifically, compressive strain causes the absorption function to shift towards higher energies, while tensile strain results in a shift towards lower energies, a behaviour consistently observed in both HSs. However, the most striking disparity in absorption behaviour occurs in hBN/InTe, where the application of compressive strain induces the formation of a pronounced peak at approximately 3 eV for z-polarisation. This striking alteration is attributed to the significant reduction of the M-valley in hBN/InTe and is absent in hBN/GaTe under similar strain conditions. This study highlights the intricate interplay between strain and the optical properties of these heterostructures. The observed differences in absorption behaviour underscore the nuanced effects that strain engineering can exert, offering a pathway towards fine-tuning the optical characteristics of these materials for tailored optoelectronic applications.

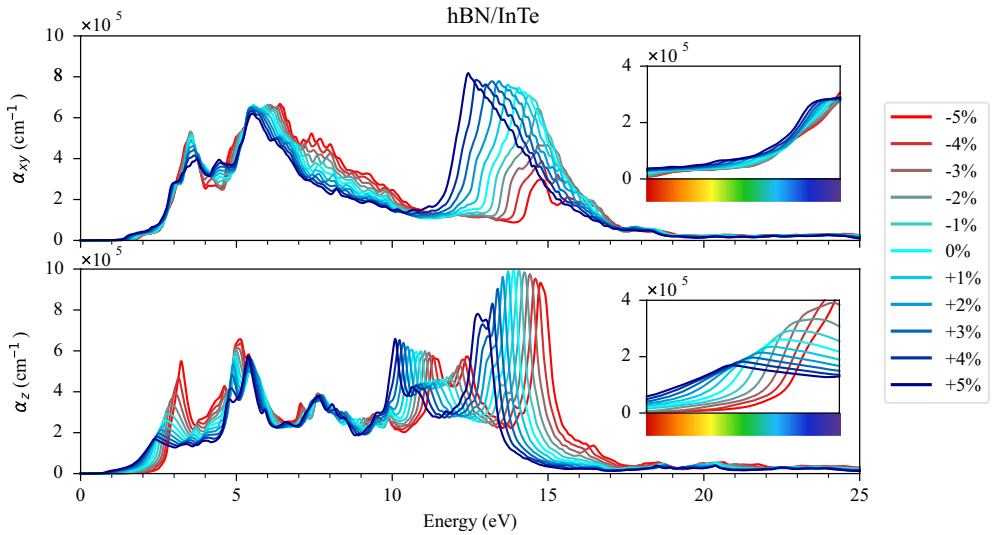


**Figure 7.** Absorption function of hBN/InTe HS for (**a**) in-plane ($\alpha_{xy}$) and (**b**) out-of-plane ($\alpha_z$) polarisations. Each colour represents a different value of the induced strain, from red (− 5% of strain) to blue (+ 5% of strain). The visible part of the spectrum is enlarged in the inset.

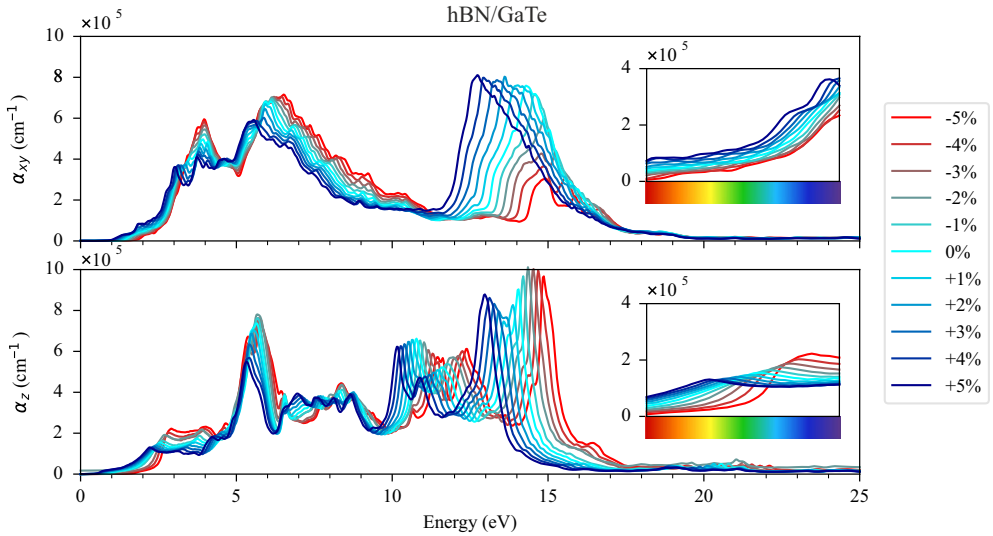


**Figure 8.** Absorption function of hBN/GaTe HS for (**a**) in-plane ($\alpha_{xy}$) and (**b**) out-of-plane ($\alpha_z$) polarisations. Each colour represents a different value of the induced strain, from red (− 5% of strain) to blue (+ 5% of strain). The visible part of the spectrum is enlarged in the inset.

## Conclusions

In this study, we systematically investigated the impact of biaxial strain on recently designed HSs composed of InTe (GaTe) and hBN monolayers using DFT. All the considered strained structures were found to be experimentally feasible, characterised by negative binding energies. Our band structure analysis revealed that strain offers a powerful tool for the precise manipulation of the band gap in these structures.

In the case of hBN/GaTe, we observed an almost linear relationship between band gap and strain, with band gap values increasing under compressive strain and decreasing under tensile strain. Specifically, the largest band gap of $E_g = 1.49$ eV was achieved at − 5% strain, while it reduced to 0.24 eV at + 5% strain. In hBN/InTe, the manipulation of strain led to a decrease in the M-valley's energy, effectively positioning it below the Γ-valley. This resulted in a band gap that decreased under strain stronger than − 2%, with band gap energies falling within the range of 0.70–1.69 eV.

Additionally, we examined the optical properties by calculating the dielectric functions and found that tensile strain substantially enhanced absorption in the low-energy spectrum, particularly in the visible spectrum.

On the contrary, compressive strain increased absorption at 3 eV, but shifted the absorption function towards higher energies.

Our findings underscore the pivotal role of strain engineering in these HSs, offering precise control over their electronic and optical properties. Furthermore, these tunable properties open up possibilities for their utilisation in various sensor and switch applications.

## Data availibility

The datasets used and/or analysed during the current study are available from the corresponding author on reasonable request.

Received: 27 October 2023; Accepted: 3 January 2024
Published online: 11 January 2024

## References

1. Geim, A. K. & Grigorieva, I. V. Van der waals heterostructures. *Nature* **499**, 419–425 (2013).
2. Novoselov, K., Mishchenko, O. A., Carvalho, O. A. & Neto, A. C. 2d materials and van der waals heterostructures. *Science* **353**, 25 (2016).
3. Liu, Y. *et al.* Van der waals heterostructures and devices. *Nat. Rev. Mater.* **1**, 1–17 (2016).
4. Liang, S.-J., Cheng, B., Cui, X. & Miao, F. Van der waals heterostructures for high-performance device applications: Challenges and opportunities. *Adv. Mater.* **32**, 1903800 (2020).
5. Huo, N. *et al.* Novel and enhanced optoelectronic performances of multilayer MOS2-WS2 heterostructure transistors. *Adv. Funct. Mater.* **24**, 7025–7031 (2014).
6. Furchi, M. M. *et al.* Device physics of van der waals heterojunction solar cells. *NPJ 2D Mater. Appl.* **2**, 1–7 (2018).
7. Zheng, X. *et al.* Pn/pas-wse2 van der waals heterostructures for solar cell and photodetector. *Sci. Rep.* **10**, 1–9 (2020).
8. Zhou, W. *et al.* Epitaxial growth of branched $\alpha$-fe2o3/sno2 nano-heterostructures with improved lithium-ion battery performance. *Adv. Funct. Mater.* **21**, 2439–2445 (2011).
9. Chen, C. *et al.* Mos2-on-mxene heterostructures as highly reversible anode materials for lithium-ion batteries. *Angew. Chem. Int. Ed.* **57**, 1846–1850 (2018).
10. Withers, F. *et al.* Light-emitting diodes by band-structure engineering in van der waals heterostructures. *Nat. Mater.* **14**, 301–306 (2015).
11. Zong, X. *et al.* Black phosphorus-based van der waals heterostructures for mid-infrared light-emission applications. *Light Sci. Appl.* **9**, 1–8 (2020).
12. Qin, S. *et al.* Robust, flexible and broadband photodetectors based on van der waals graphene/c60 heterostructures. *Carbon* **167**, 668–674 (2020).
13. Dong, T., Simoes, J. & Yang, Z. Flexible photodetector based on 2d materials: Processing, architectures, and applications. *Adv. Mater. Interfaces* **7**, 1901657 (2020).
14. Chen, Y. *et al.* High-performance photovoltaic detector based on mote2/mos2 van der waals heterostructure. *Small* **14**, 1703293 (2018).
15. Cui, B. *et al.* Ultrahigh photoresponsive photodetector based on graphene/sns2 van der waals heterostructure. *Phys. Status Solidi (a)* **218**, 2100228 (2021).
16. Stutzmann, M. *et al.* Gan-based heterostructures for sensor applications. *Diam. Relat. Mater.* **11**, 886–891 (2002).
17. Bag, A. & Lee, N.-E. Gas sensing with heterostructures based on two-dimensional nanostructured materials: A review. *J. Mater. Chem. C* **7**, 13367–13383 (2019).
18. Hou, H.-L., Anichini, C., Samorì, P., Criado, A. & Prato, M. 2d van der waals heterostructures for chemical sensing. *Adv. Funct. Mater.* **20**, 2207065 (2022).
19. Scappucci, G., Taylor, P., Williams, J., Ginley, T. & Law, S. Crystalline materials for quantum computing: Semiconductor heterostructures and topological insulators exemplars. *MRS Bull.* **46**, 596–606 (2021).
20. Xiong, P. *et al.* Strain engineering of two-dimensional multilayered heterostructures for beyond-lithium-based rechargeable batteries. *Nat. Commun.* **11**, 1–12 (2020).
21. Zhang, J., Lang, X., Zhu, Y. & Jiang, Q. Strain tuned inse/mos 2 bilayer van der waals heterostructures for photovoltaics or photocatalysis. *Phys. Chem. Chem. Phys.* **20**, 17574–17582 (2018).
22. Postorino, S. *et al.* Strain-induced effects on the electronic properties of 2d materials. *Nanomater. Nanotechnol.* **10**, 1847980420902569 (2020).
23. Li, M.-S., Chen, K.-X., Mo, D.-C. & Lyu, S.-S. Predicted high thermoelectric performance in a two-dimensional indium telluride monolayer and its dependence on strain. *Phys. Chem. Chem. Phys.* **21**, 24695–24701 (2019).
24. Song, L., Zhang, J., Mamakhel, A. & Iversen, B. B. Crystal structure, electronic transport, and improved thermoelectric properties of doped inte. *ACS Appl. Electron. Mater.*https://doi.org/10.1021/acsaelm.3c01064 *(2023).*
25. Yang, Z. *et al.* Large-scale synthesis of two-dimensional indium telluride films for broadband photodetectors. *Mater. Design* **233**, 112218. https://doi.org/10.1016/j.matdes.2023.112218 (2023).
26. Kremer, G. *et al.* Direct observation of highly anisotropic electronic and optical nature in indium telluride. *Phys. Rev. Mater.* **7**, 074601. https://doi.org/10.1103/PhysRevMaterials.7.074601 (2023).
27. Bouaziz, M. *et al.* Intrinsic defects and mid-gap states in quasi-one-dimensional indium telluride. *Phys. Rev. Res.* **5**, 033152. https://doi.org/10.1103/PhysRevResearch.5.033152 (2023).
28. Vi, V. T., Hieu, N. N., Hoi, B. D., Binh, N. T. & Vu, T. V. Modulation of electronic and optical properties of gate monolayer by biaxial strain and electric field. *Superlattices Microstruct.* **140**, 106435 (2020).
29. Rahaman, M., Rodriguez, R. D., Monecke, M., Lopez-Rivera, S. A. & Zahn, D. R. T. GaSe oxidation in air: From bulk to monolayers. *Semicond. Sci. Technol.* **32**, 105004 (2017).
30. Guo, Y., Zhou, S., Bai, Y. & Zhao, J. Defects and oxidation of group-iii monochalcogenide monolayers. *J. Chem. Phys.* **147**, 104709 (2017).
31. Guo, Y., Zhou, S. & Zhao, J. Oxidation behaviors of two-dimensional metal chalcogenides. *ChemNanoMat* **6**, 838–849 (2020).
32. Tang, X. *et al.* Direct growth of hexagonal boron nitride nanofilms on stainless steel for corrosion protection. *ACS Appl. Nano Mater.* **4**, 12024–12033 (2021).
33. Liu, Z. *et al.* Ultrathin high-temperature oxidation-resistant coatings of hexagonal boron nitride. *Nat. Commun.* **4**, 2541 (2013).
34. Li, X., Yin, J., Zhou, J. & Guo, W. Large area hexagonal boron nitride monolayer as efficient atomically thick insulating coating against friction and oxidation. *Nanotechnology* **25**, 105701 (2014).
35. Arora, H. *et al.* Effective hexagonal boron nitride passivation of few-layered inse and gase to enhance their electronic and optical properties. *ACS Appl. Mater. Interfaces* **11**, 43480–43487 (2019).

36. Šolajić, A. & Pešić, J. Novel wide spectrum light absorber heterostructures based on hbn/in (ga) te. *J. Phys. Condens. Matter* **34**, 345301 (2022).
37. Giannozzi, P. *et al.* Quantum espresso: A modular and open-source software project for quantum simulations of materials. *J. Phys. Condensed Matter* **21**(395502), 19 (2009).
38. Perdew, J. P., Burke, K. & Ernzerhof, M. Generalized gradient approximation made simple. *Phys. Rev. Lett.* **77**, 3865–3868. https://doi.org/10.1103/PhysRevLett.77.3865 (1996).
39. Grimme, S. Semiempirical gga-type density functional constructed with a long-range dispersion correction. *J. Comput. Chem.* **27**, 1787–1799 (2006).
40. Barone, V. *et al.* Role and effective treatment of dispersive forces in materials: Polyethylene and graphite crystals as test cases. *J. Comput. Chem.* **30**, 934–939 (2009).
41. Falin, A. *et al.* Mechanical properties of atomically thin boron nitride and the role of interlayer interactions. *Nat. Commun.* **8**, 15815 (2017).
42. Dal Corso, A. Thermopw: A python package to calculate the electronic thermal conductivity from first principles. https://dalcorso.github.io/thermo_pw/ (2023). Accessed 6 Oct 2023.
43. Andrew, R. C., Mapasha, R. E., Ukpong, A. M. & Chetty, N. Mechanical properties of graphene and boronitrene. *Phys. Rev. B* **85**, 125428. https://doi.org/10.1103/PhysRevB.85.125428 (2012).
44. Li, W. & Li, J. Piezoelectricity in two-dimensional group-iii monochalcogenides. *Nano Res.* **8**, 3796–3802 (2015).
45. Peng, Q., Ji, W. & De, S. Mechanical properties of the hexagonal boron nitride monolayer: Ab initio study. *Comput. Mater. Sci.* **56**, 11–17 (2012).
46. Singh, S., Espejo, C. & Romero, A. H. Structural, electronic, vibrational, and elastic properties of graphene/mos 2 bilayer heterostructures. *Phys. Rev. B* **98**, 155309 (2018).
47. Touski, S. B., Ariapour, M. & Hosseini, M. Electrical and electronic properties of strained mono-layer inte. *Physica E* **118**, 113875 (2020).
48. Huang, L., Chen, Z. & Li, J. Effects of strain on the band gap and effective mass in two-dimensional monolayer gax (x= s, se, te). *RSC Adv.* **5**, 5788–5794 (2015).
49. Shang, J. *et al.* Tunable electronic and optical properties of inse/inte van der waals heterostructures toward optoelectronic applications. *J. Mater. Chem. C* **6**, 7201–7206 (2018).
50. Do, T.-N., Vi, V. T., Binh, N. T., Hieu, N. N. & Hieu, N. V. Computational study on strain and electric field tunable electronic and optical properties of inte monolayer. *Superlattices Microstruct.* **151**, 106816. https://doi.org/10.1016/j.spmi.2021.106816 (2021).
51. Jalilian, J. & Safari, M. Electronic and optical properties of $\alpha$-inx (x=s, se and te) monolayer: Under strain conditions. *Phys. Lett. A* **381**, 1313–1320. https://doi.org/10.1016/j.physleta.2017.01.024 (2017).
52. Liao, Y., Liu, H., Yuan, G., Huang, Z. & Qi, X. Electronic and optical properties of novel graphene-like inte monolayer: First principle calculations. *Cryst. Res. Technol.* **55**, 2000102 (2020).
53. Zólyomi, V., Drummond, N. D. & Fal'ko, V. I. Electrons and phonons in single layers of hexagonal indium chalcogenides from ab initio calculations. *Phys. Rev. B* **89**, 205416. https://doi.org/10.1103/PhysRevB.89.205416 (2014).
54. Sengupta, A., Dominguez, A. & Frauenheim, T. Photo-absorption properties of van der waals heterostructure of monolayer inse with silicene, germanene and antimonene. *Appl. Surf. Sci.* **475**, 774–780. https://doi.org/10.1016/j.apsusc.2019.01.054 (2019).


## Acknowledgements

The authors acknowledge funding provided by the Institute of Physics Belgrade through the Grant by the Ministry of Science, Technological Development and Innovations of the Republic of Serbia, and by Austrian Science Fund (FWF der Wissenschaftsfonds) through START Grant number Y1298-N. DFT calculations were performed using computational resources at Johannes Kepler University (Linz, Austria).

## Author contributions

A.Š. did the calculations and prepared figures. Both authors wrote the main manuscript text and reviewed the manuscript.

## Competing interests

The authors declare no competing interests.

## Additional information

**Supplementary Information** The online version contains supplementary material available at https://doi.org/10.1038/s41598-024-51303-4.

**Correspondence** and requests for materials should be addressed to A.Š.

**Reprints and permissions information** is available at www.nature.com/reprints.

**Publisher's note** Springer Nature remains neutral with regard to jurisdictional claims in published maps and institutional affiliations.

Optical and Quantum Electronics (2024) 56:1186
https://doi.org/10.1007/s11082-024-06837-2

# Strain-induced modulation of electronic and optical properties in hBN/InSe heterostructure

**Andrijana Šolajić**[1] · **Jelena Pešić**[1]

Received: 31 December 2023 / Accepted: 13 March 2024 / Published online: 16 June 2024


**Abstract**
Our study delves into the nuanced effects of strain on hBN/InSe heterostructures, known for their exceptional wide-spectrum absorption capabilities. Employing uniform biaxial strain in the range of −6% to 6%, our investigation reveals a powerful method for manipulating the band gap. Notably, intense tensile strain leads to the near-complete elimination of the band gap—an outcome with profound implications. Comparison with hBN/InTe and hBN/GaTe heterostructures underscores the unique behaviour of hBN/InSe, showing a striking resemblance to hBN/GaTe but achieving lower band gap values under tensile strain. These findings provide crucial insights for experimental work and serve as a guide for more intricate theoretical explorations. With its outstanding electronic properties, tunable band gap, and remarkable absorption characteristics, hBN/InSe emerges as a key player in the development of future novel devices.

**Keywords** VdW heterostructures · DFT · InSe · Electronic structure · Optical properties · 2D

## 1 Introduction

Two-dimensional (2D) materials and van der Waals (vdW) heterostructures (HSs) have captured immense attention within the scientific community in recent years, owing to their distinctive physical properties that distinguish them from their bulk counterparts (Novoselov et al. 2016; Geim and Grigorieva 2013; Liu et al. 2016). Their remarkable electronic, optical, and mechanical attributes open up numerous possibilities for applications in modern devices. The exhaustive research in this field has underscored the special advantage of 2D materials and vdW heterostructures—they offer a plenty of options for customization and precise manipulation of their properties, enabling their use in a wide array of applications including transistors, solar cells, lithium-ion batteries, photodetectors (Liang et al.

✉ Andrijana Šolajić
solajic@ipb.ac.rs

Jelena Pešić
yelena@ipb.ac.rs

[1] Laboratory for 2D materials, Center for Solid State Physics and New Materials, Institute of Physics Belgrade, University of Belgrade, Pregrevica 118, 11080 Belgrade, Serbia

2020; Huo et al. 2014; Furchi et al. 2018; Zhou et al. 2011; Withers et al. 2015; Bag and Lee 2019). The current needs of nanoelectronics, optoelectronics and spintronics necessitate use of materials and components with diverse characteristics, coupled with the imperative of their minimization. In this context, 2D materials and vdW heterostructures emerge as promising contributors to fulfilling these demands.

As for tuning their properties, various effective methods have emerged, including doping and controlled introduction of defects, application of external electric or magnetic fields, and the utilization of strain. Notably, strain has proven exceptionally efficient for the precise control of the electronic and optical properties of 2D materials, offering a means to tailor these properties without fundamentally altering the material's characteristics (Xiong et al. 2020; Postorino et al. 2020). In the realm of van der Waals (vdW) materials and heterostructures, in-plane strain is commonly employed to modulate the electronic band structure. However, its utility extends beyond this, as it has been demonstrated to influence spin-orbit coupling (Zhuang et al. 2016), alter magnetic ordering (Šiškins et al. 2020; Wang et al. 2020; Webster and Yan 2018), and introduce various other novel effects (Miao et al. 2021). This multidimensional impact of strain, giving rise to the evolving field of straintronics, has sparked a new wave of research in the manipulation and optimization of material properties for advanced applications.

Within the 2D materials landscape, group III monochalcogenides have emerged as a focal point of extensive research, distinguished by their unique and promising properties. Recent investigations highlight their high electron mobility, a critical parameter for electronic devices, surpassing $10^3$ $cm^2V^{-1}s^{-1}$ (Chen et al. 2019). Notably, their band gap is easily tunable by adjusting the number of layers or applying strain Song et al. (2018); Li et al. (2018); Ma et al. (2013). Moreover, these materials exhibit substantial optical absorption across the UV, visible, and infrared regions (Wang et al. 2019; Lei et al. 2013; Hu et al. 2012), showcasing their potential in photonic applications. The nonlinear optical properties of group III monochalcogenides have been explored (Jie et al. 2015; Zhou et al. 2015), adding another layer of versatility to their applications. A significant advantage lies in their ease of exfoliation through mechanical or chemical methods (Yang et al. 2017; Aitzhanov et al. 2022; Qi et al. 2021; Harvey et al. 2015; Yang et al. 2023). Notably, InSe, one of the pioneering members, has been extensively studied, revealing a plethora of extraordinary properties. For instance, InSe demonstrates excellent thermoelectric performance (Hung et al. 2017) and high electron mobility (Bandurin et al. 2017; Sucharitakul et al. 2015; Feng et al. 2014), underlining its significance in the realm of 2D materials and beyond.

The exploration of heterostructures based on group III monochalcogenides is a thriving area of research. When combined with graphene, these heterostructures demonstrate exceptional tunable Schottky diode characteristics (Kim et al. 2016; Pham et al. 2019; Zhang et al. 2020). Specifically, InSe/InTe heterostructures exhibit enhanced optical absorption intensity compared to isolated monolayers (Shang et al. 2018). Another noteworthy application is observed in Sb/InSe heterostructures, where practical utilization allows for dipole control of Rashba spin splitting. The incorporation of hBN layers in these heterostructures goes beyond enhancing the inherent properties of monochalcogenides. It provides robust mechanical protection and passivation for the fragile monochalcogenides (Tang et al. 2021; Liu et al. 2013; Li et al. 2014), which are susceptible to oxidation when exposed to air (Guo et al. 2017, 2020). This engineering approach not only improves the performance of the HSs but also ensures the stability and longevity of the delicate monochalcogenide components.

Computational predictions suggest that encapsulating an InSe layer between two hBN capping layers significantly boosts electron mobility compared to pristine InSe films (Kang

et al. 2017). The high mobility and on/off ratio exhibited by InSe/hBN/graphite heterostructures, especially when integrated onto flexible substrates, make them compelling candidates for flexible electronics (Wu et al. 2020).

The theoretical exploration of InSe/hBN heterostructures extends beyond their electrical properties to their optical characteristics. Studies indicate that the construction of the heterostructure enhances absorption, concurrently reducing the band gap (Shen et al. 2022) - The band gap of bulk InSe lies in range from 1.3 to 1.4 eV (Gürbulak et al. 2014; Politano et al. 2017; Sang et al. 2019), but in monolayer, the gap is increased to 2.37 eV (Lei et al. 2014; Zhuang and Hennig 2013), resulting in limited applications for optoelectronic devices, as it is too large to be usable for absorbing IR and visible part of the spectrum. This dual enhancement in optical properties further underscores the multifaceted advantages offered by InSe/hBN heterostructures, making them compelling candidates for diverse applications.

Leveraging these insights, our work aims to comprehensively investigate the impact of strain on InSe/hBN heterostructures. Furthermore, the theoretical findings on the optical properties of InSe/hBN heterostructures, indicating enhanced absorption and a reduced band gap, inspire our exploration into the nuanced effects of strain. Understanding how strain influences the electronic and optical properties of InSe/hBN heterostructures is pivotal for optimizing their performance and unlocking their full potential for future technological applications.

## 2 Computational Methods

Density functional theory (DFT) were performed in the Quantum Espresso (QE) software package (Giannozzi 2009), based on plane waves and pseudopotentials. The Perdew-Burke-Ernzerhof (PBE) exchange correlation functional (Perdew et al. 1996) is used along with norm-conserving pseudopotentials. The energy cutoff of 90 Ry was set after the convergence tests.

The Monkhorst pack of 16x16x1 mesh for k-point sampling is used in geometric optimisation and total energy calculations. For calculations of p-DOS and optical properties, a refined 48x48x1 mesh is used. The band structure is calculated on 440 k-points along Γ -M-K-Γ direction. A vacuum of 20 Å is added along the z-direction to avoid interactions between the layers and simulate 2D structure. Geometry optimisation of the positions of the atoms and the lattice parameters is performed using the BFGS algorithm, with criteria for the maximum forces allowed between atoms of $10^{-6}$Ry/Å. To properly account for van der Waals force effects, the Grimme-D2 correction (Grimme 2006; Barone et al. 2009) was included to obtain more accurate lattice constants and forces. The optical properties were calculated using the epsilon.x code in QE software, based on the random phase approximation (RPA).

## 3 Results

Similarly to hBN/InTe and hBN/GaTe HSs reported in our previous work (Šolajić and Pešić 2022; šolajić and Pešić 2023), hBN/InSe HS is modelled as supercell composed of 1x1 unit cell of InSe, with $\sqrt{3} \times \sqrt{3}$ supercell of hBN rotated for 30° on top of InSe. Drawing parallels with our previous studies, this approach ensures consistency in our methodology.

For hBN, the unit cell's lattice constant ($a$) is 2.51Å, while the constructed $\sqrt{3} \times \sqrt{3}$ supercell has a lattice constant of 4.34Å. Comparatively, the calculated lattice constant for InSe is 4.03Å, closely mirroring the values obtained for GaTe in our earlier research (Šolajić and Pešić 2022), where $a = 4.05$Å.

Searching for an energetically most favourable configuration, the constructed heterostructure undergoes relaxation, adjusting both the lattice parameter and atomic positions within the unit cell. The optimized lattice parameter for the hBN/InSe heterostructure converges to $a = 4.29$Å. Notably, this relaxation induces a 1% strain on the hBN layer and a 6% strain on InSe. This pattern aligns with observations in our studies of hBN/GaTe and hBN/InTe, where the preference is for GaTe (InTe) to experience more significant strain than the hBN layer. Such strain variation arise from the different elastic properties inherent in the combined materials, providing valuable insights into the mechanical interplay within these heterostructures. Namely, the elastic constants of hBN are roughly 3 times larger than ones of InSe, as well the Young and layer modulus (Li and Li 2015; Šolajić and Pešić 2022), similar as in GaTe, leading to different strain strengths induced in each layer.

The application of uniform tensile and compressive biaxial strain, with a maximum amplitude of 6%, to the heterostructure induces significant transformations in its structural parameters. In the unstrained, relaxed configuration, the distance between the hBN layer and InSe, denoted as $d$, measures 3.29 Å. Under compressive strain, $d$ slightly decreases, reaching 3.26 Å for −6% strain, while under tensile strain, it increases, peaking at 3.30 Å for 6%. The bond lengths also undergo alterations with strain. In the absence of strain, the In-In bond length is 2.82 Å, the In-Se bond is 2.73 Å, and the In-Se-In angle is 103°. Under compressive strain, these bond lengths reduce: the In-In bond shortens to 2.79 Å, the In-Se bond contracts to 2.66 Å, and the In-Se-In angle decreases to 98.7°. Conversely, tensile strain leads to elongation of bonds and widening of angles. At 6% strain, the In-In bond extends to 2.85 Å, the In-Se bond increases to 2.80 Å, and the angle expands to 108°. These variations in geometry and covalent bond distances are anticipated to exert a profound influence on the heterostructure's band structure and band gap, providing crucial insights into the structural modifications induced by strain.

### 3.1 Electronic structure

In the absence of applied strain, representing the relaxed structure, band gap of hBN/InSe heterostructure is calculated to be $E_g = 0.56$ eV , which is less than the band gaps observed in both the hBN/InTe and hBN/GaTe heterostructures. To validate our results, we also calculated the band gap of the InSe monolayer, obtaining $E_g = 1.49$ eV, consistent with previous results using the same methodology (Hu et al. 2017). It is important to note that DFT calculations with standard functionals such as PBE often underestimate the band gap in semiconductors. For a more accurate assessment of the band gap, hybrid functionals (e.g. HSE06) are commonly employed. However, it has been observed that in group III monochalcogenides and related structures, the difference in band structures obtained using PBE and hybrid functionals primarily stems from variations in the width of the band gap, which tends to be larger (and more accurate) with hybrids. Notably, the valence bands remain largely unchanged within both methods, while the conduction bands are shifted upwards, largely preserving their shape. Taking into account the qualitatively similar band structures obtained using both methods, we opted for the PBE functional in this manuscript for our calculations. This decision was made due to the significant computational demands associated with calculations employing hybrid

functionals, especially in studies of systems under strain, where a large number of calculations are necessitated. The estimated error introduced in band gaps in our research is approximately in the range of 0.6–0.9 eV. Specifically, our calculations yield a band gap of 1.49 eV in InSe monolayer and 0.56 eV in hBN/InSe heterostructure without introduced strain; when hybrid functionals are used, band gaps of 2.37 eV and 1.16 eV are obtained for monolayer InSe and hBN/InSe heterostructure, respectively. A similar deviation in the band structure is expected in strained structures.

Figure 1 illustrates the relationship between band gap and strain for the hBN/InSe heterostructure, alongside the previously studied hBN/InTe and hBN/GaTe heterostructures for comparative analysis. In contrast to the behaviour observed in hBN/InTe, where the band gap enlarges up to 2% strain before declining, the band gap in hBN/InSe mirrors the trend observed in hBN/GaTe. Notably, it exhibits an almost linear dependence on applied strain. The widest band gap, $E_g = 1.37$ eV, is achieved under −6% strain. Conversely, tensile strain diminishes the band gap, reaching near-zero values at 6% strain. At this point, the energy level at the bottom of the valley in the Γ point of the valence band aligns closely with the energy level at the top of the conduction band valleys located between the Γ and M point, and between K and Γ point, leaving only the indirect gap between the valleys.

Analysing deeper the behaviour of bands proximate to the Fermi level and the composition of associated states reveals several key features, we present the band structure for different strain values illustrated in Fig. 2. Band structure is calculated along the Γ -M-K-Γ direction, and given that heterostructure consisted only of single-layered hBN and InSe is essentially two dimensional, hence the Brillouin zone is practically flat, and negligible contribution exist in the out-of-plane directions. Primarily, the valence band predominantly comprises states contributed by In and Se. Under compressive strain, the valley in the Γ point expands, while under tensile strain, it contracts, influencing the entire band. The conduction band behaviour is more peculiar. For tensile strain, the top of the conduction band rises, and the band closest to the Fermi level is predominantly composed from In and Se states. Conversely, with compressive strain, where top of the conduction band located between the Γ and M/K points is decreasing, at -4% strain, top of the conduction band relocates to the Γ point, and is predominantly composed of N states.

The projected density of states illustrated in Fig. 3 is showing more clear picture of atoms/states composition near the Fermi level. Near the Fermi level we predominantly

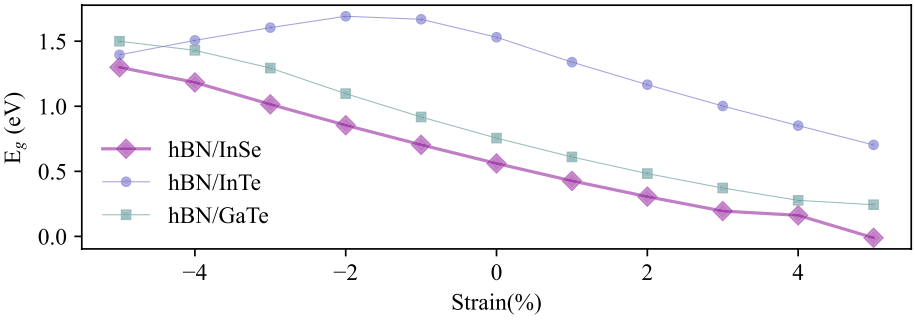


**Fig. 1** Band gap as a function of strain for hBN/InSe (purple line with rhomboid markers), along with hBN/InTe (green line and square markers) and hBN/GaTe (blue line, circle markers) for comparison

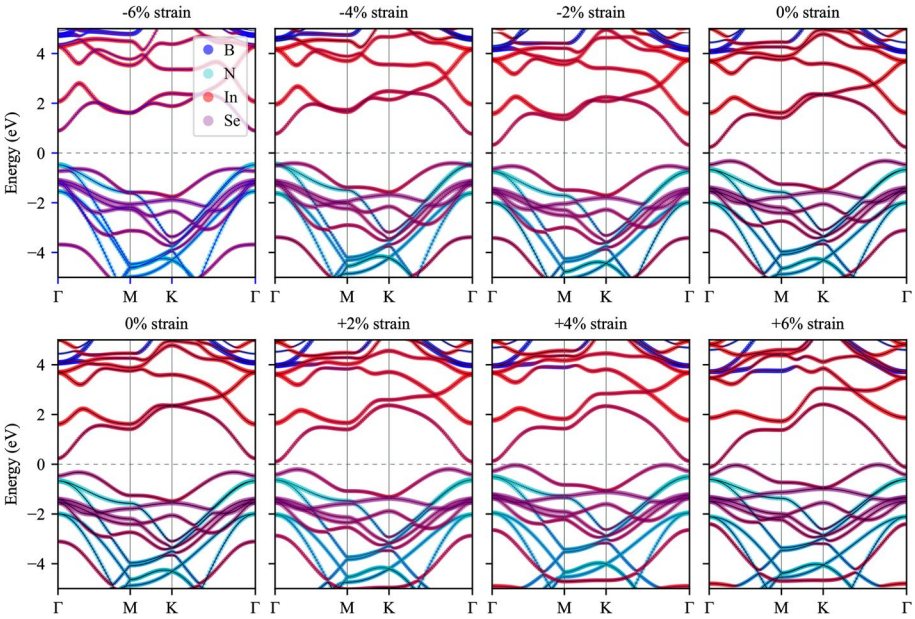


**Fig. 2** Projected bandstructure of hBN/InSe HS for different values of applied strain, from −6% to +6%. Contribution from different atoms/states are represented in different colours as in legend

observe Se $p$ and In $s$ states, for strain strengths in range of -4% to +6%. For compressive strain of -4% and stronger, N $p$ states are dominant below the Fermi level, and above the Fermi level, group of In $p$ states is moved closer to the bottom of valence band.

### 3.2 Optical properties

Consistent with our previous research, the optical properties were calculated within the random phase approximation (RPA). We were mostly interested to study how does the strain influence the absorption of heterostructure, and RPA was previously displayed as good performer for qualitative description of optical properties (Jalilian and Safari 2017; Liao et al. 2020; Zólyomi et al. 2014; Shang et al. 2018; Do et al. 2021; Sengupta et al. 2019). The complex dielectric function $\epsilon(\omega) + \epsilon_R(\omega) + i\epsilon_I(\omega)$ is calculated first. From there, we can get the absorption function as follows:

$$\alpha(\omega) = \sqrt{2}\frac{\omega}{c}\sqrt{\sqrt{\epsilon_R^2(\omega) + \epsilon_I^2(\omega)} - \epsilon_I(\omega)}. \tag{1}$$

Real and imaginary part of dielectric function are presented in Figs. 4 and 5.

In general, both the real and imaginary components of the dielectric function undergo shifts to the right under negative strain and to the left under positive strain, accompanied by alterations in peak amplitudes. However, notable deviations become evident. Under positive strain, specifically at +4% and beyond, the imaginary part of the dielectric function diverges to infinity at 0 eV. Concurrently, at the same energy, the real part of the dielectric function diverges towards $-\infty$, indicative of a transition towards a metallic character. In

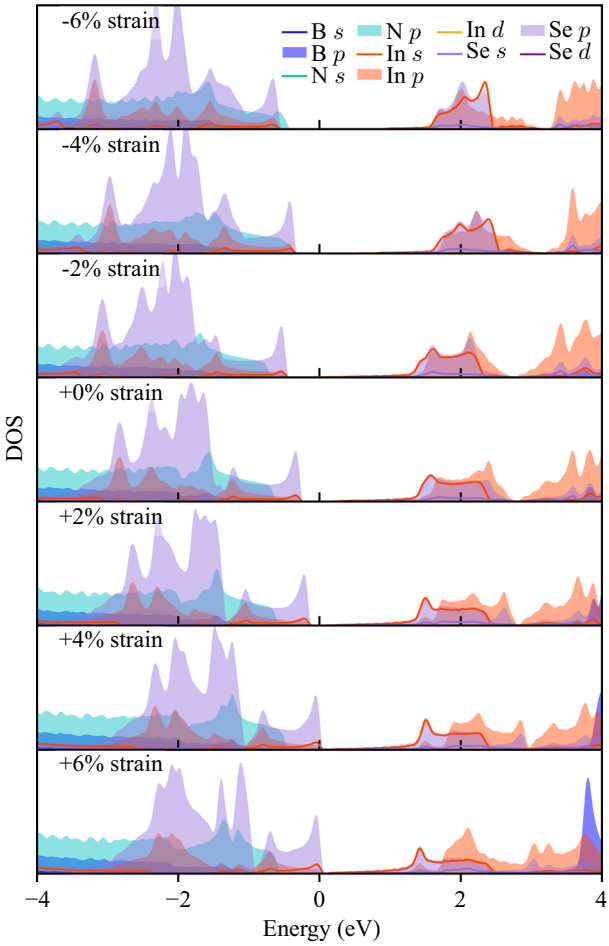


**Fig. 3** Projected density of states of hBN/InSe for different strain values. States from different atoms are presented as in legend

the case of $z$ polarization, additional peaks in the imaginary part of $\epsilon(\omega)$ emerge above +4% strain at approximately 0.5 eV, subsequently dropping to zero at 1.25 eV and 3.75 eV. These distinct features in the dielectric response under strain provide valuable insights into the evolving electronic structure and the potential transition towards metallic behaviour.

Building on prior investigations of hBN/InSe (Shen et al. 2022), which showcased exceptional absorption across a broad spectrum comparable to hBN/InTe and hBN/GaTe, our focus turns to manipulating these properties through strain-induced enhancements. Figure 6 presents the absorption profile of the hBN/InSe heterostructure, considering in-plane ($xy$) and out-of-plane ($z$) polarizations. The observed behavior is in agreement with our findings in previously studied heterostructures. Our results affirm the outstanding wide-spectrum absorptive capabilities of hBN/InSe, consistent with the reported values in (Shen et al. 2022), where absorption peaks reach up to $8 \times 10^5$ cm$^{-1}$, as well with hBN/In(Ga)Te HSs which showcase similar magnitude. In the $xy$ polarization, compressive strain enhances absorption in the part of UV spectrum (6 eV to 11 eV), while the peak at 15 eV slowly diminishes. Conversely, tensile strain shifts this peak towards the left without losing its amplitude. Notably, tensile strains of +5% and above introduce a small peak in

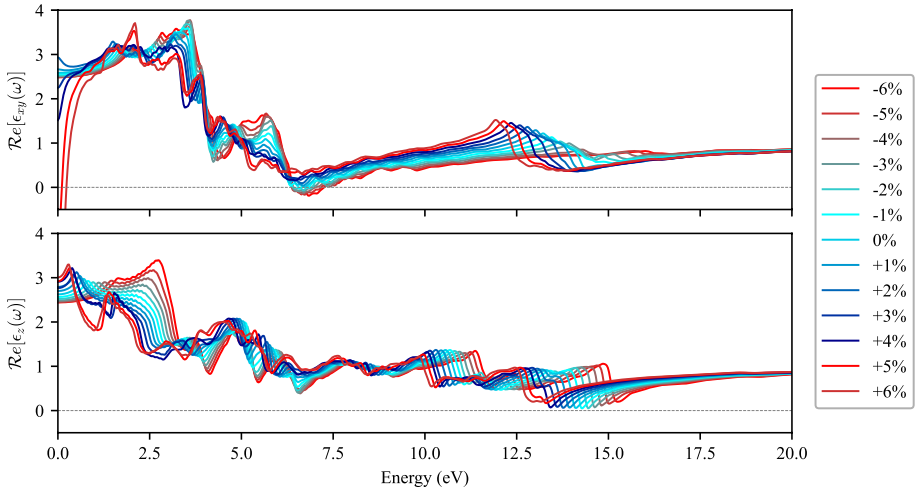


**Fig. 4** Real part of complex dielectric function for (a) *xy* and (b) *z* polarization, for different values of strain

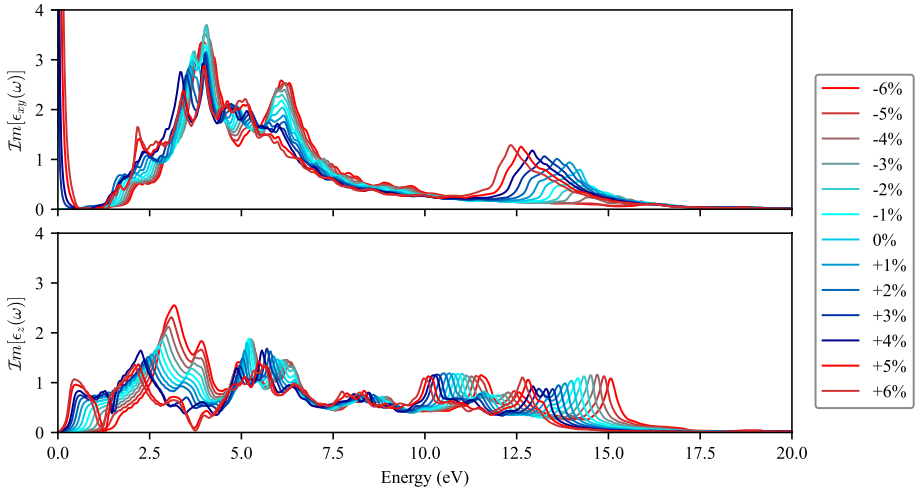


**Fig. 5** Imaginary part of complex dielectric function for (a) *xy* and (b) *z* polarization, for different values of strain

the IR spectrum and enhance absorption in the visible range. In out-of-plane polarization, tensile strain shifts the absorption function leftward, slightly improving absorption in the visible spectrum, while compressive strains enhance the 2.5 eV to 4.5 eV region. However, stronger tensile strains of 5% and 6% result in a drop to zero absorption at 1.5 eV and 3.8 eV, a feature which is not observed in previously studied HSs. Most of those effects are ascribed to the change in the band gap as a function of strain, but also to different behaviour of specific band and the shape of their valleys, e.g. rising of N *p* states near the Fermi level at strong compressive strain. These substantial changes in absorption as a function of

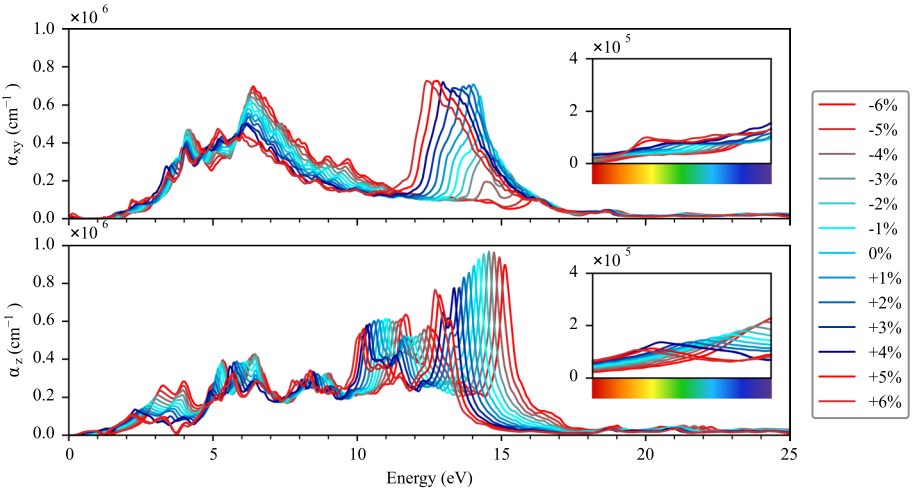


**Fig. 6** Absorption function of hBN/InSe for *xy* and *z* polarization, for different values of strain. The inset shows the enlarged part within the visible-light part of the spectrum

strain offer a promising avenue for tailoring the properties of hBN/InSe for specific applications, particularly in the development of sensors and detectors.

## 4 Conclusion

In conclusion, we systematically explored the impact of strain on hBN/InSe heterostructures—an already established exceptional wide-spectrum absorber. Recognized for its promising electronic and mechanical properties, hBN/InSe emerges as a strong contender for future electronic and optoelectronic devices. Applying uniform biaxial strain in the range of −6% to 6%, our results unveil a highly effective method for manipulating the band gap, showcasing a particularly noteworthy outcome: near-complete elimination of the band gap under intense tensile strain. Comparing our findings with previous investigations on strain effects in hBN/InTe and hBN/GaTe heterostructures, hBN/InSe exhibits a striking resemblance to hBN/GaTe. However, the hBN/InSe system demonstrates a distinct trend of reaching lower band gap values under tensile strain, concurrently enhancing absorption in the low-energy spectrum. These outcomes bear considerable significance for guiding subsequent experimental endeavours and serve as a roadmap for more intricate theoretical explorations. With its established outstanding electronic and transport properties, coupled with highly tunable band gap and remarkable absorption characteristics, hBN/InSe stands poised to make a substantial impact on the advancement of future novel devices.

**Acknowledgements** The authors acknowledge funding provided by the Institute of Physics Belgrade through the grant by the Ministry of Science, Technological Development and Innovations of the Republic of Serbia, and European Cooperation in Science and Technology (COST) Action CA21159 PhoBioS. DFT calculations were performed using computational resources at Johannes Kepler University (Linz, Austria).

**Author's contribution** AS performed calculations and prepared figures. Both authors wrote and reviewed the manuscript.

**Funding** The authors acknowledge funding provided by the Institute of Physics Belgrade through the grant by the Ministry of Science, Technological Development and Innovations of the Republic of Serbia.

**Data availibility Statement** The datasets generated during and/or analysed during the current study are available from the corresponding author on request.

## Declarations

**Conflict of interest** The authors have no relevant financial or non-financial interests to disclose.

## References

Aitzhanov, M., Guseinov, N., Nemkayeva, R., Sagidolda, Y., Tolepov, Z., Prikhodko, O., Mukhametkarimov, Y.: Growth and liquid-phase exfoliation of gase1- xsx crystals. Materials **15**(20), 7080 (2022)

Bag, A., Lee, N.-E.: Gas sensing with heterostructures based on two-dimensional nanostructured materials: a review. J. Mater. Chem. C **7**(43), 13367–13383 (2019)

Bandurin, D.A., Tyurnina, A.V., Geliang, L.Y., Mishchenko, A., Zólyomi, V., Morozov, S.V., Kumar, R.K., Gorbachev, R.V., Kudrynskyi, Z.R., Pezzini, S.: High electron mobility, quantum hall effect and anomalous optical response in atomically thin inse. Nat. Nanotechnol **12**(3), 223–227 (2017)

Barone, V., Casarin, M., Forrer, D., Pavone, M., Sambi, M., Vittadini, A.: Role and effective treatment of dispersive forces in materials: Polyethylene and graphite crystals as test cases. J. Comput. Chem. **30**(6), 934–939 (2009)

Chen, J., Tan, X., Lin, P., Sa, B., Zhou, J., Zhang, Y., Wen, C., Sun, Z.: Comprehensive understanding of intrinsic mobility in the monolayers of iii–vi group 2d materials. Phys. Chem. Chem. Phys. **21**(39), 21898–21907 (2019)

Do, T.-N., Vi, V.T.T., Binh, N.T.T., Hieu, N.N., Hieu, N.V.: Computational study on strain and electric field tunable electronic and optical properties of inte monolayer . Superlatt. Microstruct. **151**, 106816 (2021). https://doi.org/10.1016/j.spmi.2021.106816

Feng, W., Zheng, W., Cao, W., Hu, P.: Back gated multilayer inse transistors with enhanced carrier mobilities via the suppression of carrier scattering from a dielectric interface. Adv. Mater. **26**(38), 6587–6593 (2014)

Furchi, M.M., Höller, F., Dobusch, L., Polyushkin, D.K., Schuler, S., Mueller, T.: Device physics of van der waals heterojunction solar cells . npj 2D Mater. Appl. **2**(1), 1–7 (2018)

Geim, A.K., Grigorieva, I.V.: Van der waals heterostructures. Nature **499**(7459), 419–425 (2013)

Giannozzi, P.: Quantum espresso: a modular and open-source software project for quantum simulations of materialsend. J. Phys. Condensed Matter **21**(39), 395502–395519 (2009)

Grimme, S.: Semiempirical gga-type density functional constructed with a long-range dispersion correction. J. Comput. Chem. **27**(15), 1787–1799 (2006)

Guo, Y., Zhou, S., Bai, Y., Zhao, J.: Defects and oxidation of group-iii monochalcogenide monolayers. J. Chem. Phys. **147**(10), 104709 (2017)

Guo, Y., Zhou, S., Zhao, J.: Oxidation behaviors of two-dimensional metal chalcogenides. ChemNanoMat **6**(6), 838–849 (2020)

Gürbulak, B., Şata, M., Dogan, S., Duman, S., Ashkhasi, A., Keskenler, E.F.: Structural characterizations and optical properties of inse and inse: Ag semiconductors grown by bridgman/stockbarger technique. Phys. E Low-dimensional Syst. Nanostruct. **64**, 106–111 (2014)

Harvey, A., Backes, C., Gholamvand, Z., Hanlon, D., McAteer, D., Nerl, H.C., McGuire, E., Seral-Ascaso, A., Ramasse, Q.M., McEvoy, N.: Preparation of gallium sulfide nanosheets by liquid exfoliation and their application as hydrogen evolution catalysts. Chem. Mater. **27**(9), 3483–3493 (2015)

Hu, P., Wen, Z., Wang, L., Tan, P., Xiao, K.: Synthesis of few-layer gase nanosheets for high performance photodetectors. ACS Nano **6**(7), 5988–5994 (2012)

Hu, T., Zhou, J., Dong, J.: Strain induced new phase and indirect-direct band gap transition of monolayer inse. Phys. Chem. Chem. Phys. **19**(32), 21722–21728 (2017)

Hung, N.T., Nugraha, A.R., Saito, R.: Two-dimensional inse as a potential thermoelectric material. Appl. Phys. Lett. **111**(9) (2017)

Huo, N., Kang, J., Wei, Z., Li, S.-S., Li, J., Wei, S.-H.: Novel and enhanced optoelectronic performances of multilayer mos2-ws2 heterostructure transistors. Adv. Funct. Mater. **24**(44), 7025–7031 (2014)

Jalilian, J., Safari, M.: Electronic and optical properties of $\alpha$-inx (x=s, se and te) monolayer: Under strain conditions. Phys. Lett. A **381**(15), 1313–1320 (2017). https://doi.org/10.1016/j.physleta.2017.01.024

Jie, W., Chen, X., Li, D., Xie, L., Hui, Y.Y., Lau, S.P., Cui, X., Hao, J.: Layer-dependent nonlinear optical properties and stability of non-centrosymmetric modification in few-layer gase sheets. Angewandte Chemie International Edition **54**(4), 1185–1189 (2015)

Kang, P., Michaud-Rioux, V., Kong, X., Yu, G., Guo, H.: Calculated carrier mobility of h-bn/$\gamma$-inse/h-bn van der waals heterostructures . 2D Mater. **4**(4), 045014 (2017)

Kim, W., Li, C., Chaves, F.A., Jiménez, D., Rodriguez, R.D., Susoma, J., Fenner, M.A., Lipsanen, H., Riikonen, J.: Tunable graphene-gase dual heterojunction device. Adv. Mater. **28**(9), 1845–1852 (2016)

Lei, S., Ge, L., Liu, Z., Najmaei, S., Shi, G., You, G., Lou, J., Vajtai, R., Ajayan, P.M.: Synthesis and photoresponse of large gase atomic layers. Nano Lett. **13**(6), 2777–2781 (2013)

Lei, S., Ge, L., Najmaei, S., George, A., Kappera, R., Lou, J., Chhowalla, M., Yamaguchi, H., Gupta, G., Vajtai, R.: Evolution of the electronic band structure and efficient photo-detection in atomic layers of inse. ACS Nano **8**(2), 1263–1272 (2014)

Li, Y., Wang, T., Wu, M., Cao, T., Chen, Y., Sankar, R., Ulaganathan, R.K., Chou, F., Wetzel, C., Xu, C.-Y., : Ultrasensitive tunability of the direct bandgap of 2d inse flakes via strain engineering . 2D Mater. **5**(2), 021002 (2018)

Li, W., Li, J.: Piezoelectricity in two-dimensional group-iii monochalcogenides. Nano Res. **8**, 3796–3802 (2015)

Li, X., Yin, J., Zhou, J., Guo, W.: Large area hexagonal boron nitride monolayer as efficient atomically thick insulating coating against friction and oxidation. Nanotechnology **25**(10), 105701 (2014)

Liang, S.-J., Cheng, B., Cui, X., Miao, F.: Van der waals heterostructures for high-performance device applications: challenges and opportunities. Adv. Mater. **32**(27), 1903800 (2020)

Liao, Y., Liu, H., Yuan, G., Huang, Z., Qi, X.: Electronic and optical properties of novel graphene-like inte monolayer: first principle calculations. Crystal Res. Technol. **55**(12), 2000102 (2020)

Liu, Z., Gong, Y., Zhou, W., Ma, L., Yu, J., Idrobo, J.C., Jung, J., MacDonald, A.H., Vajtai, R., Lou, J.: Ultrathin high-temperature oxidation-resistant coatings of hexagonal boron nitride. Nat. Commun. **4**(1), 2541 (2013)

Liu, Y., Weiss, N.O., Duan, X., Cheng, H.-C., Huang, Y., Duan, X.: Van der waals heterostructures and devices. Nat. Rev. Mater. **1**(9), 1–17 (2016)

Ma, Y., Dai, Y., Guo, M., Yu, L., Huang, B.: Tunable electronic and dielectric behavior of gas and gase monolayers. Phys. Chem. Chem. Phys. **15**(19), 7098–7105 (2013)

Miao, F., Liang, S.-J., Cheng, B.: Straintronics with van der waals materials. npj Quant. Mater. **6**(1), 59 (2021)

Novoselov, K., Mishchenko, O.A., Carvalho, O.A., Neto, A.C.: 2d materials and van der waals heterostructures. Science **353**(6298) (2016)

Perdew, J.P., Burke, K., Ernzerhof, M.: Generalized gradient approximation made simple. Phys. Rev. Lett. **77**, 3865–3868 (1996) https://doi.org/10.1103/PhysRevLett.77.3865

Pham, K.D., Vu-Quang, H., Nguyen, C.V.: Modulation of electronic properties and schottky barrier in the graphene/gas heterostructure by electric gating. Phys. B Condensed Matter **555**, 69–73 (2019)

Politano, A., Campi, D., Cattelan, M., Ben Amara, I., Jaziri, S., Mazzotti, A., Barinov, A., Gürbulak, B., Duman, S., Agnoli, S.: Indium selenide: an insight into electronic band structure and surface excitations. Sci. Rep. **7**(1), 3445 (2017)

Postorino, S., Grassano, D., D'Alessandro, M., Pianetti, A., Pulci, O., Palummo, M.: Strain-induced effects on the electronic properties of 2d materials. Nanomater. Nanotechnol. **10**, 1847980420902569 (2020)

Qi, X., Gao, M., Ding, C., Zhang, W., Qu, R., Guo, Y., Gao, H., Zhang, Z.: Simple exfoliation of bulk gallium selenide to single/few layers by a temperature-adjustment bath-ultrasonic treatment. Phys. Status Solidi (RRL) Rapid Res. Lett. 15(8), 2100052 (2021)

Sang, D.K., Wang, H., Qiu, M., Cao, R., Guo, Z., Zhao, J., Li, Y., Xiao, Q., Fan, D., Zhang, H.: Two dimensional $\beta$-inse with layer-dependent properties: band alignment, work function and optical properties. Nanomaterials **9**(1), 82 (2019)

Sengupta, A., Dominguez, A., Frauenheim, T.: Photo-absorption properties of van der waals heterostructure of monolayer inse with silicene, germanene and antimonene. Appl. Surf. Sci. **475**, 774–780 (2019). https://doi.org/10.1016/j.apsusc.2019.01.054

Shang, J., Pan, L., Wang, X., Li, J., Deng, H.-X., Wei, Z.: Tunable electronic and optical properties of inse/inte van der waals heterostructures toward optoelectronic applications. J. Mater. Chem. C **6**(27), 7201–7206 (2018)

Shen, N.-f., Yang, X.-d., Wang, X.-x., Wang, G.-h., Wan, J.-g.: Two-dimensional van der waals heterostructure of indium selenide/hexagonal boron nitride with strong interlayer coupling. Chem. Phys. Lett. **749**, 137430 (2020)

Šiškins, M., Lee, M., Mañas-Valero, S., Coronado, E., Blanter, Y.M., Zant, H.S., Steeneken, P.G.: Magnetic and electronic phase transitions probed by nanomechanical resonators. Nat. Commun. **11**(1), 2698 (2020)
šolajić, A., Pešić, J.: Tailoring electronic and optical properties of /inte and hbn /gate heterostructures through biaxial strain engineering. PREPRINT (2023). Version 1
Šolajić, A., Pešić, J.: Novel wide spectrum light absorber heterostructures based on hbn/in (ga) te. J. Phys. Condensed Matter **34**(34), 345301 (2022)
Song, C., Fan, F., Xuan, N., Huang, S., Zhang, G., Wang, C., Sun, Z., Wu, H., Yan, H.: Largely tunable band structures of few-layer inse by uniaxial strain. ACS Appl. Mater. Interfaces **10**(4), 3994–4000 (2018)
Sucharitakul, S., Goble, N.J., Kumar, U.R., Sankar, R., Bogorad, Z.A., Chou, F.-C., Chen, Y.-T., Gao, X.P.: Intrinsic electron mobility exceeding 103 cm2/(v s) in multilayer inse fets. Nano Lett. **15**(6), 3815–3819 (2015)
Tang, X., Wang, H., Liu, C., Zhu, X., Gao, W., Yin, H.: Direct growth of hexagonal boron nitride nanofilms on stainless steel for corrosion protection. ACS Appl. Nano Mater. **4**(11), 12024–12033 (2021)
Wang, H., Qin, G., Yang, J., Qin, Z., Yao, Y., Wang, Q., Hu, M.: First-principles study of electronic, optical and thermal transport properties of group iii–vi monolayer mx (m = ga, in; x = s, se). J. Appl. Phys. **125**(24) (2019)
Wang, Y., Wang, C., Liang, S.-J., Ma, Z., Xu, K., Liu, X., Zhang, L., Admasu, A.S., Cheong, S.-W., Wang, L.: Strain-sensitive magnetization reversal of a van der waals magnet. Adv. Mater. **32**(42), 2004533 (2020)
Webster, L., Yan, J.-A.: Strain-tunable magnetic anisotropy in monolayer $CrCl_3$, $CrBr_3$, and $CrI_3$. Phys. Rev. B **98**(14), 144411 (2018)
Withers, F., Del Pozo-Zamudio, O., Mishchenko, A., Rooney, A., Gholinia, A., Watanabe, K., Taniguchi, T., Haigh, S., Geim, A., Tartakovskii, A.: Light-emitting diodes by band-structure engineering in van der waals heterostructures. Nat. Mater. **14**(3), 301–306 (2015)
Wu, L., Shi, J., Zhou, Z., Yan, J., Wang, A., Bian, C., Ma, J., Ma, R., Liu, H., Chen, J.: Inse/hbn/graphite heterostructure for high-performance 2D electronics and flexible electronics. Nano Res. **13**, 1127–1132 (2020)
Xiong, P., Zhang, F., Zhang, X., Wang, S., Liu, H., Sun, B., Zhang, J., Sun, Y., Ma, R., Bando, Y.: Strain engineering of two-dimensional multilayered heterostructures for beyond-lithium-based rechargeable batteries. Nat. Commun. **11**(1), 1–12 (2020)
Yang, Z., Jie, W., Mak, C.-H., Lin, S., Lin, H., Yang, X., Yan, F., Lau, S.P., Hao, J.: Wafer-scale synthesis of high-quality semiconducting two-dimensional layered inse with broadband photoresponse. ACS Nano **11**(4), 4225–4236 (2017)
Yang, Z., Guo, J., Li, H., Du, X., Zhao, Y., Chen, H., Chen, W., Zhang, Y.: Large-scale synthesis of two-dimensional indium telluride films for broadband photodetectors. Mater. Des. **233**, 112218 (2023)
Zhang, W., Shi, C., He, C., Bai, M.: External-strain induced transition from schottky to ohmic contact in graphene/ins and graphene/janus in2sse heterostructures. J. Solid State Chem. **289**, 121511 (2020)
Zhou, W., Cheng, C., Liu, J., Tay, Y.Y., Jiang, J., Jia, X., Zhang, J., Gong, H., Hng, H.H., Yu, T.: Epitaxial growth of branched $\alpha$-fe2o3/sno2 nano-heterostructures with improved lithium-ion battery performance. Adv. Funct. Mater. **21**(13), 2439–2445 (2011)
Zhou, X., Cheng, J., Zhou, Y., Cao, T., Hong, H., Liao, Z., Wu, S., Peng, H., Liu, K., Yu, D.: Strong second-harmonic generation in atomic layered gase. J. Am. Chem. Soc. **137**(25), 7994–7997 (2015)
Zhuang, H.L., Hennig, R.G.: Single-layer group-iii monochalcogenide photocatalysts for water splitting. Chem. Mater. **25**(15), 3232–3238 (2013)
Zhuang, H.L., Kent, P., Hennig, R.G.: Strong anisotropy and magnetostriction in the two-dimensional stoner ferromagnet fe 3 gete 2. Phys. Rev. B **93**(13), 134407 (2016)
Zólyomi, V., Drummond, N.D.: Fal'ko, V.I.: Electrons and phonons in single layers of hexagonal indium chalcogenides from ab initio calculations. Phys. Rev. B **89**, 205416 (2014). https://doi.org/10.1103/PhysRevB.89.205416

PAPER

# Novel wide spectrum light absorber heterostructures based on hBN/In(Ga)Te

IOP Publishing Journal of Physics: Condensed Matter
J. Phys.: Condens. Matter **34** (2022) 345301 (9pp) https://doi.org/10.1088/1361-648X/ac7996

# Novel wide spectrum light absorber heterostructures based on hBN/In(Ga)Te

**A Šolajić*** and **J Pešić**

Center for Solid State Physics and New Materials, Institute of Physics Belgrade, University of Belgrade, Pregrevica 118, 11080 Belgrade, Serbia

E-mail: solajic@ipb.ac.rs

Received 20 April 2022, revised 2 June 2022
Accepted for publication 16 June 2022
Published 28 June 2022

**Abstract**

Two-dimensional group III monochalcogenides have recently attracted quite attention for their wide spectrum of optical and electric properties, being promising candidates for optoelectronic and novel electrical applications. However, in their pristine form they are extremely sensitive and vulnerable to oxygen in air and need good mechanical protection and passivization. In this work we modeled and studied two newly designed van der Waals (vdW) heterostructures based on layer of hexagonal boron nitride (hBN) and GaTe or InTe monolayer. Using density functional theory, we investigate electronic and optical properties of those structures. Their moderate band gap and excellent absorption coefficient makes them ideal candidate for broad spectrum absorbers, covering all from part of IR to far UV spectrum, with particularly good absorption of UV light. The hBN layer, which can be beneficial for protection of sensitive GaTe and InTe, does not only preserve their optical properties but also enhances it by changing the band gap width and enhancing absorption in low-energy part of spectrum. Calculated binding energies prove that all three stacking types are possible to obtain experimentally, with H-top as the preferable stacking position. Moreover, it is shown that type of stacking does not affect any relevant properties and bandstructure does not reveal any significant change for each stacking type.

Keywords: heterostructures, hBN, 2D materials, InTe, GaTe, light absorption, DFT

(Some figures may appear in colour only in the online journal)

## 1. Introduction

Enormous attention given to the exploration and researching of two-dimensional materials in the past decade has started a whole new era in materials science and countless possibilities for novel devices emerged. After successful exfoliation and experimental confirmation of graphene's extraordinary properties, many van der Waals (vdW) layered materials were regaining the attention, being extensively exploited in order to find more possible 2D structures [1]—hexagonal boron nitride [2, 3], silicene [4, 5], germanene [6, 7], transition metal dichalcogenides (TMD's) [8–13], MXenes [14, 15]. As a result, many possibilities emerged for more innovations and research of more complex systems such are 2D vdW heterostructures. Those layered structures often have new rich physics and enhanced properties, particularly attractive for countless applications in nanoelectronic [16–18] and optoelectronic devices such are Light-emitting diodes based on vdW heterostructures [19], solar cells [20, 21] and flexible broad-spectrum photodetectors [22, 23].

In last few years, two-dimensional group IIIa monochalcogenides have been extensively researched [24–27]. In their bulk form, they are layered structures with weak vdW binding forces, suitable for mechanical exfoliation down to a single layer. With a wide spectrum of exceptional electronic and

* Author to whom any correspondence should be addressed.

 

optical properties in their two dimensional form, they became very desirable candidates for further research and applications. One of the most outstanding materials in this 2D family, InSe, exhibits very high electron mobility [28] and superb optical properties. Previous work revealed it as very promising material for a highly stable field effect transistors [29]. Excellent absorption properties mark InSe favorable for use in broad spectrum flexible photodetectors, covering wide range from UV to the near IR region [30]. With the idea to further enhance their properties to be more suitable for particular devices, research of vdW heterostructures based on 2D group IIIa monochalcogenides brought notable attention. Various combinations of group III monochalcogenides and graphene emerged as an effective and tunable Schottky barrier [31–35] with many possible ways to precisely control the electronic properties—via electric field, external strain or controlling the interlayer distance. Recent work on heterostructures based on InSe/hBN revealed them as excellent absorbers of the visible and UV part of spectrum.

Two members of group III monochalcogenides were more recently explored and theoretically proposed as new 2D structures—monolayers of InTe and GaTe. Both materials are indirect band gap semiconductors with moderate band gaps of 1.29 and 1.75 eV, respectively. In addition to good electrical and optical properties [36–40], those materials also excel in elastic properties, being able to sustain considerable values of both tensile and compressive strain [36, 40, 41], which is already proven as very effective and convenient way to precisely tune electronic and optical properties of 2D materials [42–44]. Suitable for various applications in novel electronic and optoelectronic devices, research of heterostructures based on those materials is very attractive, with huge expectations for achieving new effects or enhancing desired properties of the 2D structures alone. However, pristine monochalcogenides, especially in form of thin films or as a single layer, are very sensitive and vulnerable to oxygen in air—many studies reveal that single layers are oxidized almost instantly after exposure to the air [45–48]. The issue of their challenging stability can be overcome by passivization with adequate material which would ensure the safe encapsulation of monochalcogenides as well as good mechanical protection. One of materials particularly good and widely used for this purpose is hexagonal boron nitride (hBN). Experimental studies confirmed it as effective for protection and passivization of few layers InSe and GaSe, while their electronic and optical properties are preserved or even enhanced [49] hence the similar effects can be expected for different members of the group III monochalcogenide family.

In the next sections, we present newly designed heterostructures, hBN/GaTe and hBN/InTe, based on a single layer of GaTe or InTe and a layer of hBN. Using the density functional theory (DFT), we explore their electronic and optical properties and analyze the influence of hBN layer on GaTe and InTe. Given the facts stated in previous paragraphs, our motivation was to model stable, mechanically protected structures based on those materials, which would excel in their electronic and optical properties in broad spectrum. Based on their lattice parameters, we expect to obtain structures with good lattice matching, suitable for experimental realization.

## 2. Theoretical methods

Results are obtained using DFT implemented in Quantum Espresso (QE) software package [50], based on plane waves and pseudopotentials. Perdew–Burke–Ernzerhof (PBE) functional [51] and PAW pseudopotentials [52] were used in all calculations. After convergence tests, the energy cutoff for the wavefunction and the charge density were set to 44 Ry and 364 Ry for hBN/InTe heterostructure, and 60 Ry and 480 Ry for hBN/GaTe heterostructure. The Monkhorst–Pack of $16 \times 16 \times 1$ mesh for k-point sampling is used in geometric optimization, total energy and phonon calculations. For calculations of p-DOS and optical properties, refined mesh of $64 \times 64 \times 1$ is used. The bandstructure is calculated on 440 k-points along $\mathbf{\Gamma}$–M–K–$\mathbf{\Gamma}$ direction. In order to simulate 2D structure, a vacuum of 20 Å was added along the z-direction to avoid interactions between the layers. Geometry optimization of both atom positions and lattice parameters is performed using BFGS algorithm, with criteria for maximum allowed forces between atoms of $10^{-6}$ Ry Å$^{-1}$. As the GGA functionals do not take into consideration long range forces as the van der Waals force, Grimme-D2 correction was included to obtain more accurate lattice constants and forces. Optical properties were calculated using epsilon.x code in QE software, based on the random phase approximation (RPA).

## 3. Results and discussion

Both GaTe (InTe) and hBN have hexagonal lattices with $D_{3h}^{1}$ symmetry. Lattice constants obtained after the geometric optimizations of $a = 4.371$ Å for InTe, $a = 4.047$ Å for GaTe and 2.515 Å for hBN are in agreement with previous reports [25, 37, 40, 53]. The unit cell of In(Ga)Te/hBN heterostructure is modeled as a supercell which contain one layer of InTe($1 \times 1$) or GaTe($1 \times 1$) on top of layer of hBN($\sqrt{3} \times \sqrt{3}$) supercell, resulting in hexagonal unit cell with $C_3^1$ symmetry. The lattice constant of $\sqrt{3} \times \sqrt{3}$ supercell of hBN is $a = 4.347$ Å. In case of hBN/InTe heterostructure, lattice constants of InTe and hBN supercell are excellent matches with close values of 4.371 and 4.347 Å. After geometric optimization, obtained lattice constant of formed heterostructure is $a = 4.336$ Å. That results in almost ideal lattice matching with induced strain of 0.8% on InTe layer and 0.3% on hBN layer, making this heterostructure a great candidate for experimental realization. With lattice constant of $a = 4.047$ Å, monolayer of GaTe is a less perfect match with $a = 4.347$ Å of hBN supercell. However, the obtained lattice constant of formed hBN/GaTe heterostructure is $a = 4.309$ Å which induces strains of 6.1% on GaTe layer and 0.8% on hBN, making them still possible for fabrication. Hence, both heterostructures are promising in terms of lattice matching and can be modeled with proposed supercell. Phonon dispersion for both heterostructures is also calculated and presented in figure 1 in order to

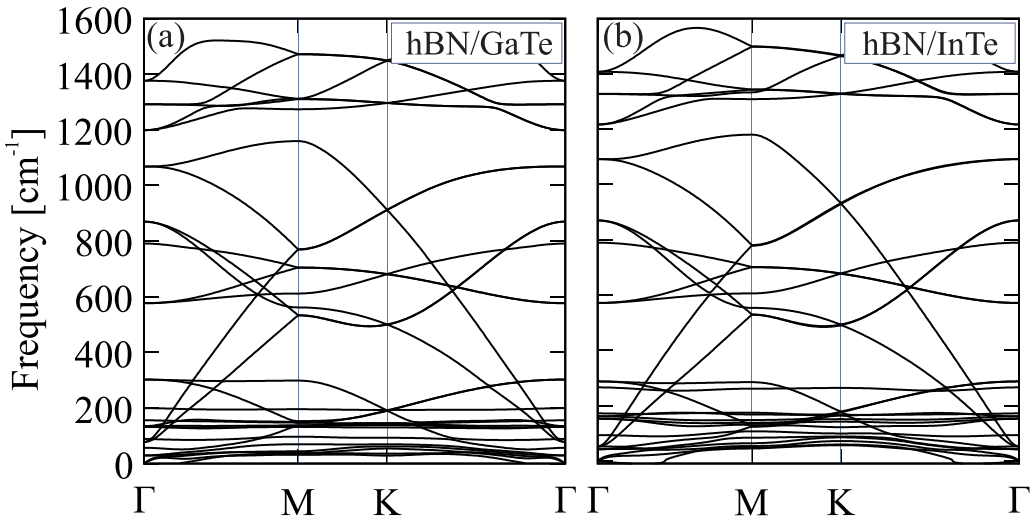


**Figure 1.** Phonon dispersion of (a) hBN/InTe and (b) hBN/GaTe.

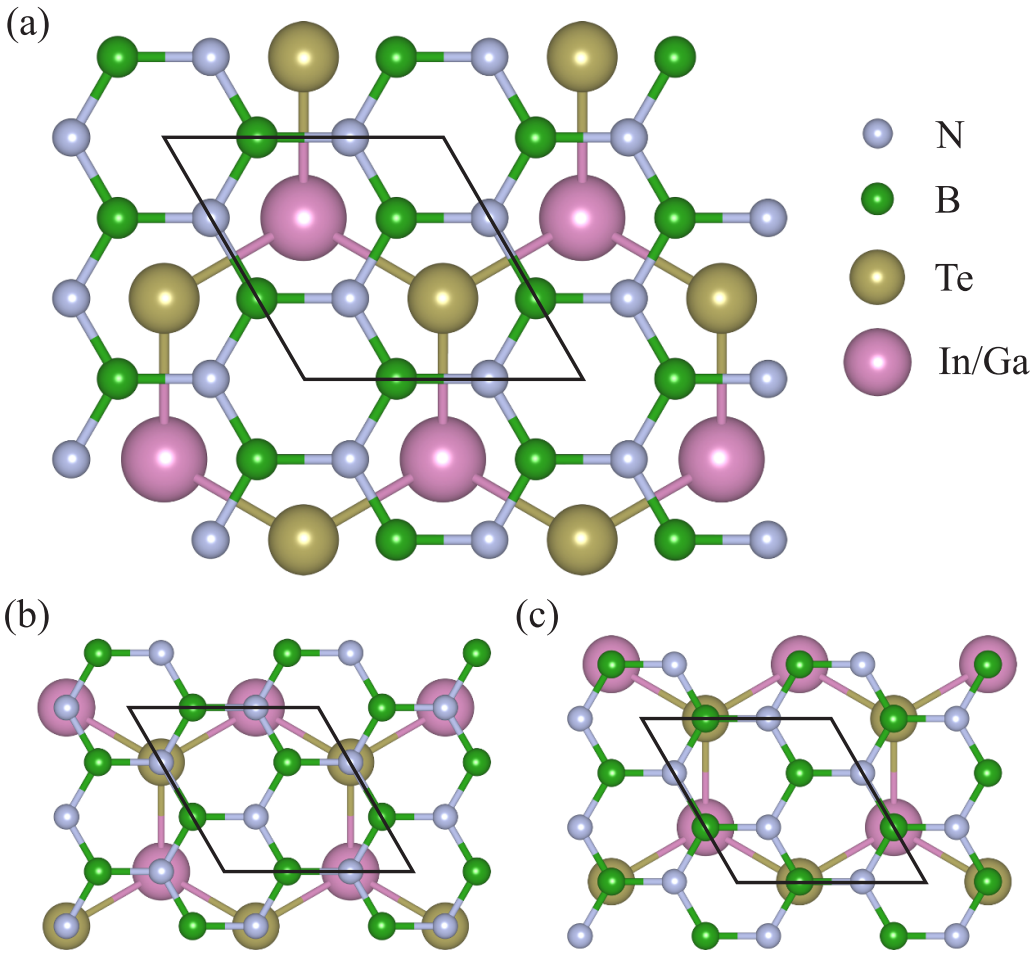


**Figure 2.** Top view of three possible stacking types, (a) H-top, (b) N-top and (c) B-top.

confirm the structural stability. We do not observe imaginary frequencies, except the small kinks near the Gamma point with low negative values, which are often emerging in calculations of phonons in 2D materials, being a numerical issue and not the real instabilities.

Three possible stacking types are presented in figure 2, the H-top (In/Ga atom being in the center of hBN hexagon), B-top (In/Ga atom above the B atom of hBN) and N-top (In/Ga atom above the N atom of hBN). We investigated all three types of structure in order to determine the favorable stacking, as well whether the properties are affected by type of stacking, e.g. bandstructure. The optimal distance between the hBN layer and InTe(GaTe) layers ($d$) for both heterostructures and each of their stacking types are obtained previously during the

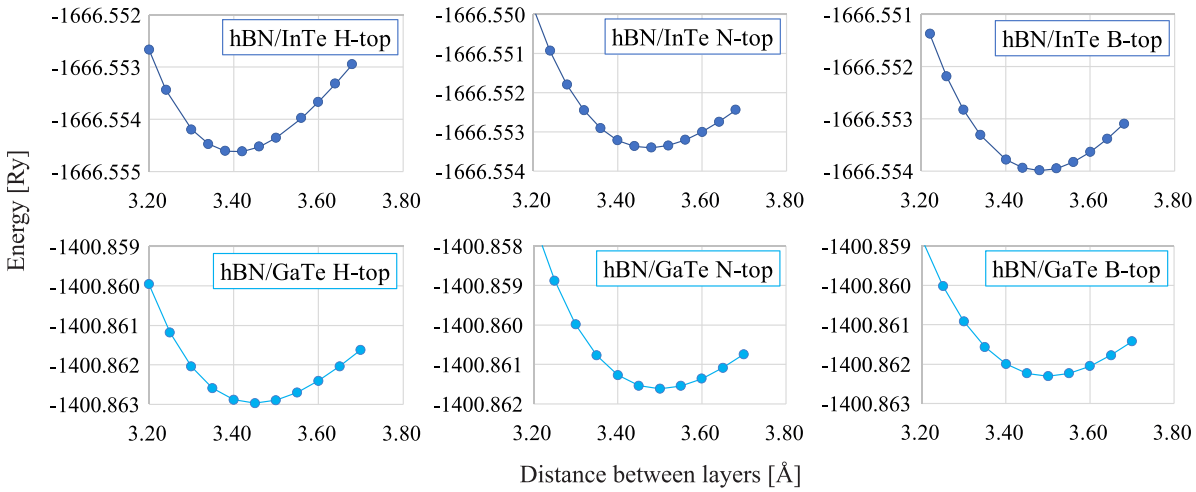


**Figure 3.** Total energy of the system as a function of the distance between hBN and InTe(GaTe) for different stacking types for hBN/InTe and hBN/GaTe.

geometry optimization, with resulting distances of 3.43–3.52 Å for different stacking positions of hBN/InTe and 3.45–3.52 Å for hBN/GaTe. Total energy of the structure in function of the interlayer distance is shown in figure 3.

In order to confirm the stability of the structures and prove they can be experimentally obtained, we calculated their binding energies ($E_b$) by the following equation:

$$E_b = E_{heterostr.} - E_{In(Ga)Te} - E_{hBN}, \quad (1)$$

where $E_{heterostr.}$, $E_{In(Ga)Te}$ and $E_{hBN}$ represent the total energy of hBN/In(Ga)Te heterostructure, InTe or GaTe monolayer and hBN monolayer, respectively. Binding energies, interlayer distance and lattice parameters obtained for each configuration of hBN/InTe and hBN/GaTe heterostructures are summarized in table 1. Negative values of binding energies suggest that both heterostructures are energetically feasible in all stacking configurations. The favorable stacking type for both hBN/InTe and hBN/GaTe heterostructures is H-top with the lowest value of binding energy, but also the total energy of H-top configuration for both heterostructures is ≈8 and ≈17 meV lower than in N-top and B-top configurations, respectively. However, the total and binding energies for H-top, N-top and B-top stacking configurations differ just for 10 meV, making all systems convenient for fabrication.

From our calculations, both InTe and GaTe monolayers have an indirect band gap of $E_g = 1.38$ eV and $E_g = 1.75$ eV respectively, while hBN has a large direct band gap of 4.63 eV. These results are in agreement with previous theoretical results obtained using the PBE functional [24, 36, 37, 40]. As the PBE functional underestimates the band gap in semiconductors, hybrid functionals such as Heyd–Scuseria–Ernzerhof (HSE) must be used in order to obtain accurate electronic properties. Reports on similar structures show that employing the HSE functional does not change the bandstructure qualitatively, the most significant difference comes from shifted bands above the Fermi level and thus an enlargement of the band gap. Large difference in band gap of InTe(GaTe) and hBN

**Table 1.** Lattice parameters, distance between hBN and In(Ga)Te layers ($d$) and binding energy for all three possible stacking types of hBN/InTe and hBN/GaTe.

| | hBN/InTe | | |
|---|---|---|---|
| | H-top | N-top | B-top |
| $a$ (Å) | 4.346 | 4.337 | 4.337 |
| $d$ (Å) | 3.429 | 3.523 | 3.479 |
| $E_b$ (meV) | −269.64 | −255.49 | −259.63 |
| | hBN/GaTe | | |
| | H-top | N-top | B-top |
| $a$ (Å) | 4.309 | 4.309 | 4.311 |
| $d$ (Å) | 3.451 | 3.516 | 3.503 |
| $E_b$ (meV) | −255.62 | −241.76 | −246.61 |

as well their alignment of bands make both systems a type-I heterojunctions. This can be also confirmed from the density of states of pristine single layer hBN, InTe and GaTe and projected density of states for both heterostructures, presented in figure 4. As in similar heterostructures [54], the bandstructure does not change with the stacking almost at all—zones near the Fermi level are nearly identical, the band gap does not change and only minor differences can be observed e.g. slightly changed position of some zones below the Fermi level and far above the Fermi level. Bandstructure plots for all three stacking types are shown in figure 5. In further discussion we will focus on the H-top stacking in both hBN/InTe and hBN/GaTe heterostructures.

Atom-decomposed bandstructures of hBN/InTe and hBN/GaTe are presented in figures 6 and 7, alongside their pristine monolayer compounds, InTe and GaTe for easier comparison. Fermi level is set to zero and shown in green line in all figures. Both GaTe and InTe pristine monolayers are indirect band gap semiconductors with valence band maxima close to the Γ point and conduction band minima (CBM) at the M point for GaTe

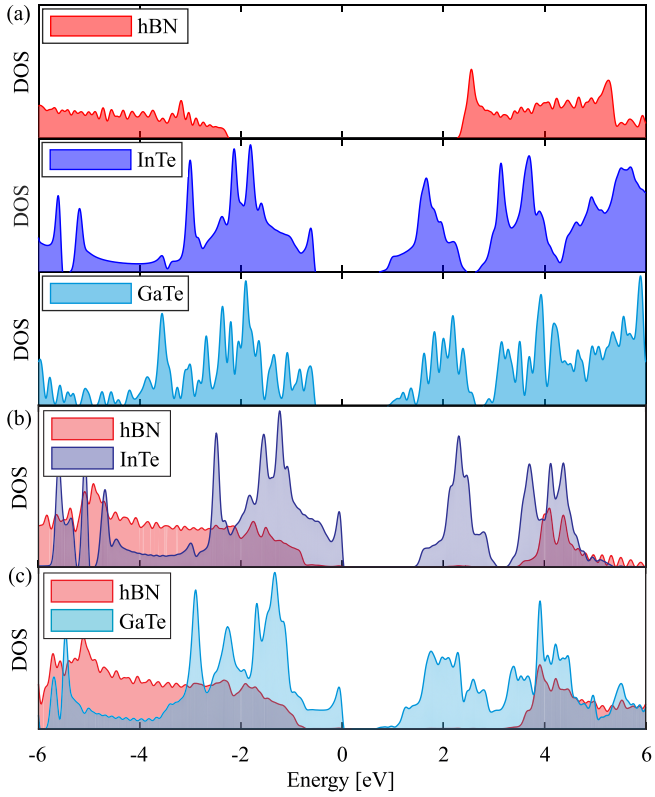


**Figure 4.** Projected density of states for (a) single layer hBN, InTe and GaTe, (b) hBN/InTe heterostructure and (c) hBN/GaTe heterostructure. The contribution from hBN is shown in red lines and red shaded area, while dark blue and turquoise lines and area represent contribution from InTe and GaTe, respectively.

and Γ and M points for InTe. After stacking into heterostructure, the band gap is slightly changed from original GaTe and InTe structures. CBM are shifted to the Γ point in both heterostructures. In the hBN/InTe band gap is slightly enlarged, from 1.38 eV in pure InTe monolayer to 1.54 eV in the heterostructure. This change in band gap is barely visible and bands near the Fermi level have the same shape as in pristine InTe. Hence, upon forming the hBN/InTe heterostructure, there are no important differences in the band structure. States around the Fermi level are almost completely formed by InTe, while the hBN contributions are observed below −2 eV and above 3 eV, similar as in pristine hBN.

More changes can be observed in the second structure—gap of single layer GaTe is 1.59 eV, but after the heterostructure is formed, band gap is reduced to just 0.79 eV. Upon forming the heterostructure, in the vicinity of the Γ point, there are many mixed states around −1 eV, originated from 5p states of Te atoms and 2p states of N atoms, as result of interaction between the hBN and GaTe layers. In addition, valence band is heavily lifted, separating previously grouped states around the Γ point for more than 0.5 eV and significantly reducing the band gap.

The reduction of band gap along with interfacial states can be useful for applications in optoelectronics so we proceeded to analyze the optical properties of these heterostructures. We calculated the absorption coefficients, expecting both structures to have good absorption properties. The complex dielectric function $\epsilon(\omega) + \epsilon_R(\omega) + i\epsilon_I(\omega)$ is obtained from calculations in the RPA framework. From these results, we can obtain the absorption coefficient $\alpha(\omega)$ as the following:

$$\alpha(\omega) = \sqrt{2}\frac{\omega}{c}\sqrt{\sqrt{\epsilon_R^2(\omega) + \epsilon_I^2(\omega)} - \epsilon_I(\omega)}. \tag{2}$$

Results are shown in figure 8 for hBN/InTe and figure 9 for hBN/GaTe heterostructures, both plotted alongside their pristine monolayer compounds. Both structures have very good absorption properties, being able to absorb visible, near and far UV spectrum—the absorption of hBN/GaTe even slightly extends to the IR spectrum. As the PBE functional underestimates band gap, some shift in energy would be noticed compared to HSE calculations. The results though would not be significantly changed, only the reduction in capabilities of absorbing the IR and red part of the visible light is expected.

The highest peaks in absorption function are near 6 eV, primarily originating from the InTe/GaTe, at 11 and at 14 eV as a contribution from hBN layer, with peaks up to $8 \times 10^5\,\mathrm{cm}^{-1}$. As a result of smaller band gap in hBN/GaTe heterostructure, slightly enhanced absorption is observed in very low energy region of 1–2 eV. The difference is though, not significant, which is not unexpected as the bandstructures of hBN/InTe and hBN/GaTe do not differ much qualitatively, and band gap

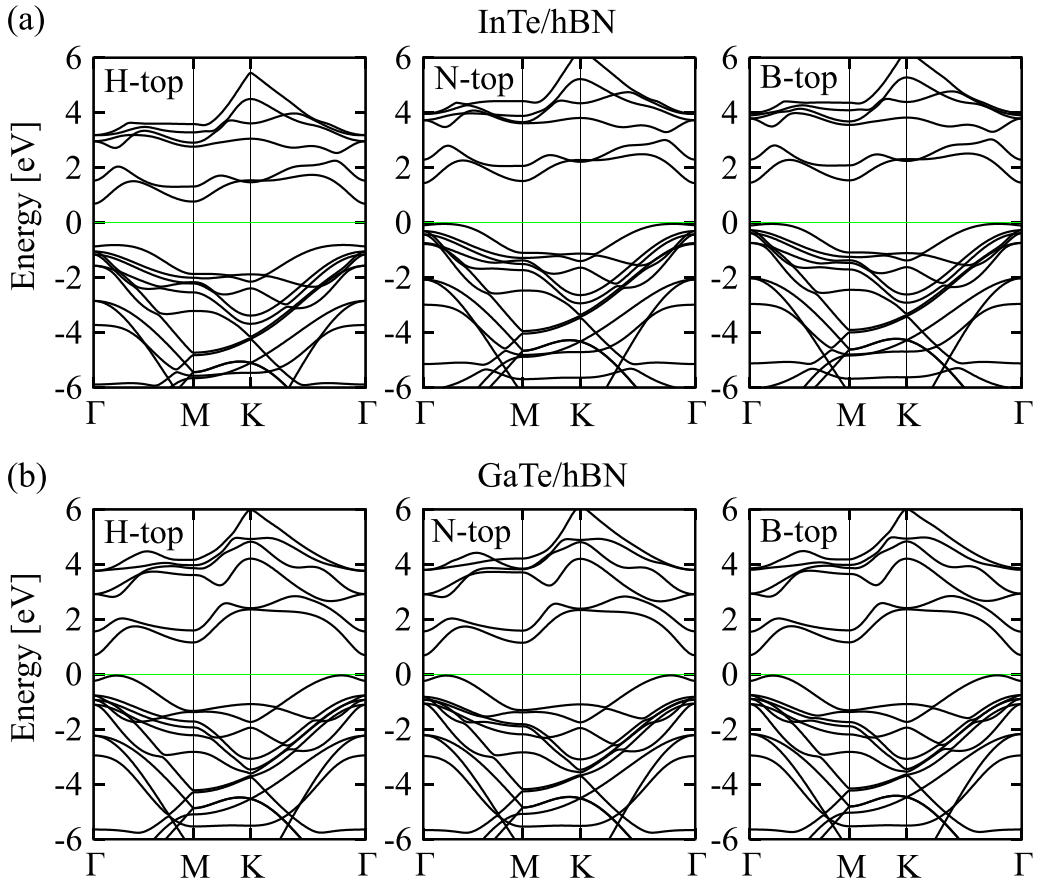


**Figure 5.** Bandstructure for different types of stacking for (a) hBN/InTe and (b) hBN/GaTe heterostructure.

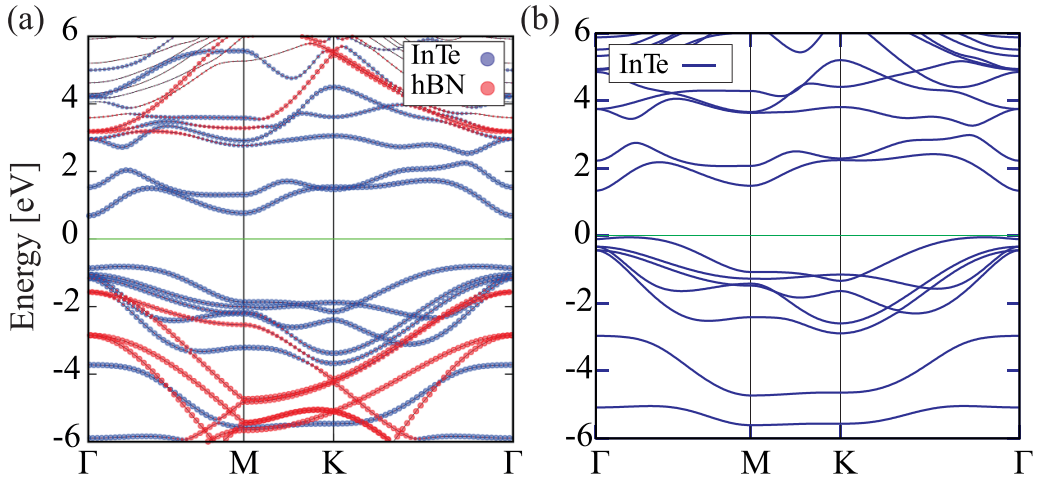


**Figure 6.** (a) Projected bandstructure of hBN/InTe heterostructure and (b) bandstructure of InTe monolayer. The size of circles on the left graph indicate the magnitude of projections of wavefunctions over atomic orbitals—contribution from different atomic orbitals are presented in different colors as shown in the legend.

in GaTe/hBN is primarily reduced due to one single shifted band below the Fermi level. In addition, results obtained using RPA calculations have contribution just from transitions in ground state, any exciton effects cannot be observed. In energy range from 3 to 15 eV, both heterostructures have exceptional values of absorption of 2–8 $\times 10^5$ cm$^{-1}$, giving them a huge potential for light absorbers in near and far UV spectrum. This makes both heterostructures excellent candidates for light absorption-relevant photoelectric applications, such are modern photodetectors. Further, we calculated the reflectance for our heterostructures. The real and imaginary part of dielectric function are related with a complex index of refraction $n^*(\omega) = n(\omega) + i\kappa(\omega)$ by:

$$\epsilon_R = 2n\kappa, \epsilon_I = n^2 - \kappa^2. \quad (3)$$

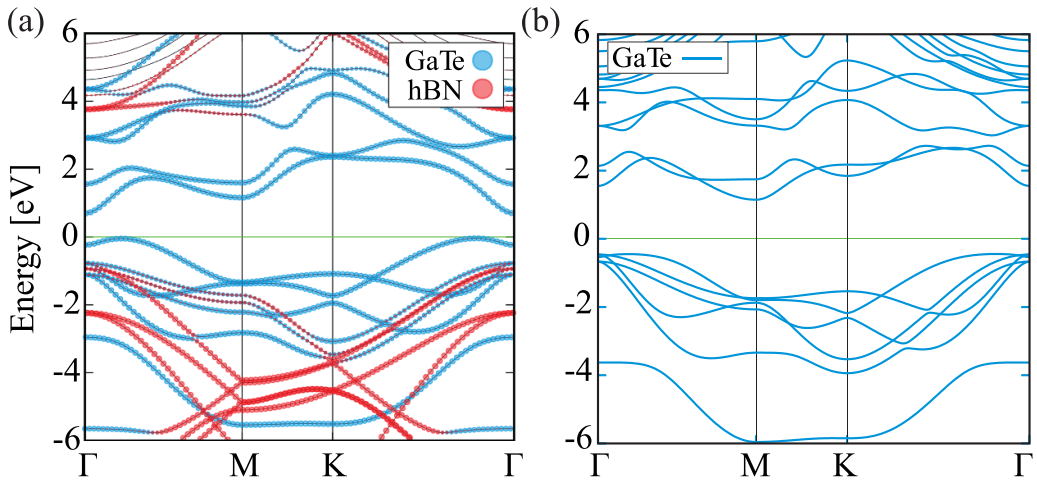


**Figure 7.** (a) Projected bandstructure of hBN/GaTe heterostructure and (b) bandstructure of GaTe monolayer. The size of circles on the left graph indicate the magnitude of projections of wavefunctions over atomic orbitals—contribution from different atomic orbitals are presented in different colors as shown in the legend.

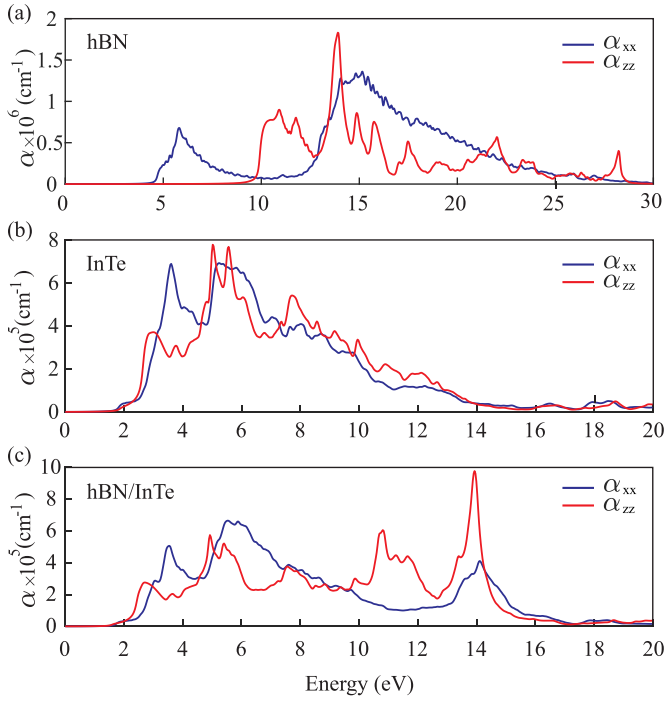


**Figure 8.** Absorption coefficient of (a) hBN, (b) InTe, (c) hBN/InTe heterostructure for in-plane ($\alpha_{xx}$) and out-of-plane ($\alpha_{zz}$) polarizations.

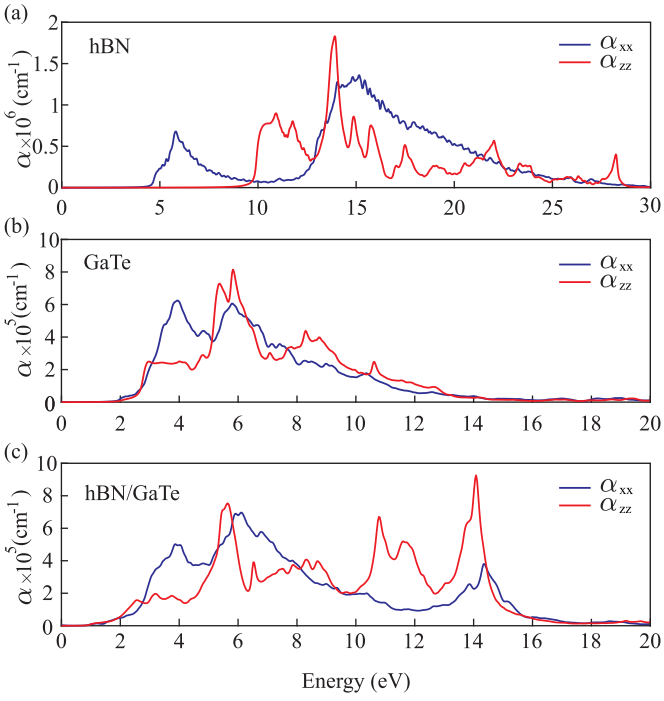


**Figure 9.** Absorption coefficient of (a) hBN, (b) GaTe, (c) hBN/GaTe heterostructure for in-plane ($\alpha_{xx}$) and out-of-plane ($\alpha_{zz}$) polarizations.

The reflectance is now given by:

$$\frac{(n-1)^2+\kappa^2}{(n+1)^2+\kappa^2}. \tag{4}$$

Figure 10 presents calculated reflectance of hBN/InTe and hBN/GaTe heterostructures. Reflectance of both materials are no larger than 30% for any energy, and are especially low in the low-energy region with 10%, confirming that only a small amount of light is being reflected at any incidence angle. As both heterostructures have qualitatively similar bandstructures, their reflectances are not much different. However, for z polarization, the small peak at 2.5 eV is flattened in hBN/GaTe dropping to nearly constant values of around 10% in region up to 5 eV, while the peak at 6 eV is narrowed and higher than in hBN/InTe. That can be ascribed as a result of differences in shape and positions of certain bands and different values of band gap.

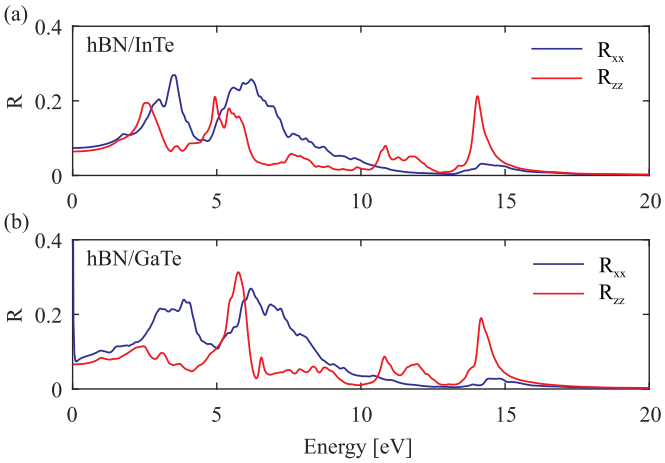


**Figure 10.** Reflectance of (a) hBN/InTe heterostructure and (b) hBN/GaTe, for in-plane ($\alpha_{xx}$) and out-of-plane ($\alpha_{zz}$) polarizations.

## 4. Conclusions

We report the study of two new heterostructures based on hexagonal boron nitride and InTe/GaTe, by employing first principle calculations. We confirm the structural stability of those systems and show that stacking type does not affect any of the relevant properties and all types of stacking are feasible for fabrication. We investigate their electronic and optical properties, showing the benefit of forming heterostructures of InTe/GaTe with hBN layer. Formation of heterostructure slightly changes the band gap in comparison with pristine monolayer InTe and GaTe, which also enhances absorption in the low-energy region of the spectrum. Both heterostructures have good broad spectrum absorption, with exceptionally good absorbing of the UV light. Hence, their electronic and optical properties reveal them as excellent candidates for field effect transistors based on vdW heterostructures, or modern optoelectronic devices such are flexible broad spectrum photodetectors, solar cells . From the previous studies, the hBN layer is also proven to be beneficial for mechanical protection of sensitive and vulnerable single layers of monochalcogenides like InTe and GaTe, while as we showed, electronic and optical properties are not only preserved but even enhanced. Of special interest is hBN/InTe heterostructure for its remarkably good lattice constant matching between InTe and hBN layers which yields less than 1% of induced strain between the layers. This places hBN/InTe beneficial over similar studied heterostructures with comparable electronic and absorption properties (e.g. hBN/InSe) with significant advantage for future fabrication and experiments as well for their further mechanical manipulation. As both InTe (GaTe) and hBN can withstand a moderate strain, electronic and optical properties can be tuned by applying the strain on the heterostructure or by including electric field, giving these materials a huge value for further research and applications.

## Data availability statement

All data that support the findings of this study are included within the article (and any supplementary files).

## Acknowledgments

The authors acknowledge funding provided by the Institute of Physics Belgrade through the grant by the Ministry of Education, Science and Technological Development of the Republic of Serbia. DFT calculations were performed using computational resources at Johannes Kepler University (Linz, Austria).

## ORCID iDs

A Šolajić https://orcid.org/0000-0002-0553-0858
J Pešić https://orcid.org/0000-0002-8600-7187

## References

[1] Liu B and Zhou K 2019 *Prog. Mater. Sci.* **100** 99–169
[2] Zhang K, Feng Y, Wang F, Yang Z and Wang J 2017 *J. Mater. Chem.* C **5** 11992–2022
[3] Song L *et al* 2010 *Nano Lett.* **10** 3209–15
[4] Kara A, Enriquez H, Seitsonen A P, Voon L L Y, Vizzini S, Aufray B and Oughaddou H 2012 *Surf. Sci. Rep.* **67** 1–18
[5] Zhao J *et al* 2016 *Prog. Mater. Sci.* **83** 24–151
[6] Acun A *et al* 2015 *J. Phys.: Condens. Matter* **27** 443002
[7] Derivaz M, Dentel D, Stephan R, Hanf M C, Mehdaoui A, Sonnet P and Pirri C 2015 *Nano Lett.* **15** 2510–6
[8] Fu Q *et al* 2021 *Adv. Mater.* **33** 1907818
[9] Li Y, Wang H, Xie L, Liang Y, Hong G and Dai H 2011 *J. Am. Chem. Soc.* **133** 7296–9
[10] Splendiani A, Sun L, Zhang Y, Li T, Kim J, Chim C Y, Galli G and Wang F 2010 *Nano Lett.* **10** 1271–5
[11] Li H, Zhang Q, Yap C C R, Tay B K, Edwin T H T, Olivier A and Baillargeat D 2012 *Adv. Funct. Mater.* **22** 1385–90
[12] Zhao W, Ghorannevis Z, Chu L, Toh M, Kloc C, Tan P H and Eda G 2013 *ACS Nano* **7** 791–7
[13] Li H, Lu G, Wang Y, Yin Z, Cong C, He Q, Wang L, Ding F, Yu T and Zhang H 2013 *Small* **9** 1974–81
[14] Anasori B, Lukatskaya M R and Gogotsi Y 2017 *Nat. Rev. Mater.* **2** 1–17
[15] Pang J, Mendes R G, Bachmatiuk A, Zhao L, Ta H Q, Gemming T, Liu H, Liu Z and Rummeli M H 2019 *Chem. Soc. Rev.* **48** 72–133
[16] Geim A K and Grigorieva I V 2013 *Nature* **499** 419–25
[17] Novoselov K, Mishchenko o A, Carvalho o A and Neto A C 2016 *Science* **353** 14
[18] Liu Y, Weiss N O, Duan X, Cheng H C, Huang Y and Duan X 2016 *Nat. Rev. Mater.* **1** 1–17
[19] Withers F *et al* 2015 *Nat. Mater.* **14** 301–6
[20] Furchi M M, Höller F, Dobusch L, Polyushkin D K, Schuler S and Mueller T 2018 *npj 2D Mater. Appl.* **2** 1–7
[21] Zheng X, Wei Y, Pang K, Kaner Tolbert N, Kong D, Xu X, Yang J, Li X and Li W 2020 *Sci. Rep.* **10** 1–9
[22] Qin S, Du Q, Dong R, Yan X, Liu Y, Wang W and Wang F 2020 *Carbon* **167** 668–74
[23] Dong T, Simoes J and Yang Z 2020 *Adv. Mater. Interfaces* **7** 1901657

[24] Ren C, Wang S, Tian H, Luo Y, Yu J, Xu Y and Sun M 2019 *Sci. Rep.* **9** 1–6
[25] Demirci S, Avazl N, Durgun E and Cahangirov S 2017 *Phys. Rev.* B **95** 115409
[26] Yang Z and Hao J 2019 *Adv. Mater. Technol.* **4** 1900108
[27] Chen J, Cai S, Xiong R, Sa B, Wen C, Wu B and Sun Z 2020 *Phys. Chem. Chem. Phys.* **22** 7039–47
[28] Bandurin D A *et al* 2017 *Nat. Nanotechnol.* **12** 223–7
[29] Jiang J, Li J, Li Y, Duan J, Li L, Tian Y, Zong Z, Zheng H, Feng X, Li Q 2019 *npj 2D Mater. Appl.* **3** 1–8
[30] Tamalampudi S R, Lu Y-Y, Rajesh Kumar U, Sankar R, Liao C-D, Cheng C-H, Chou F C and Chen Y-T 2014 *Nano Lett.* **14** 2800–6
[31] Li H, Zhou Z and Wang H 2020 *Nanotechnology* **31** 335201
[32] Li H, Zhou Z, Zhang K and Wang H 2019 *Nanotechnology* **30** 405207
[33] Pham K D, Vu-Quang H and Nguyen C V 2019 *Physica* B **555** 69–73
[34] Pham K D, Hieu N N, Phuc H V, Fedorov I, Duque C, Amin B and Nguyen C V 2018 *Appl. Phys. Lett.* **113** 171605
[35] Gao X, Shen Y, Ma Y, Wu S and Zhou Z 2019 *Comput. Mater. Sci.* **170** 109200
[36] Touski S B, Ariapour M and Hosseini M 2020 *Physica* E **118** 113875
[37] Liao Y, Liu H, Yuan G, Huang Z and Qi X 2020 *Cryst. Res. Technol.* **55** 2000102
[38] Li K, Xian X, Wang J and Yu N 2019 *Appl. Surf. Sci.* **471** 18–22
[39] Ariapour M and Touski S B 2019 *Mater. Res. Express* **6** 076402
[40] Vi V T, Hieu N N, Hoi B D, Binh N T and Vu T V 2020 *Superlattices Microstruct.* **140** 106435
[41] Jalilian J and Safari M 2017 *Phys. Lett.* A **381** 1313–20
[42] Zhang J, Lang X, Zhu Y and Jiang Q 2018 *Phys. Chem. Chem. Phys.* **20** 17574–82
[43] Xiong P *et al* 2020 *Nat. Commun.* **11** 1–12
[44] Postorino S, Grassano D, D'Alessandro M, Pianetti A, Pulci O and Palummo M 2020 *Nanomater. Nanotechnol.* **10** 1847980420902569
[45] Rahaman M, Rodriguez R D, Monecke M, Lopez-Rivera S A and Zahn D R T 2017 *Semicond. Sci. Technol.* **32** 105004
[46] Guo Y, Zhou S and Zhao J 2020 *ChemNanoMat* **6** 838–49
[47] Guo Y, Zhou S, Bai Y and Zhao J 2017 *J. Chem. Phys.* **147** 104709
[48] Afaneh T, Fryer A, Xin Y, Hyde R H, Kapuruge N and Gutierrez H R 2020 *ACS Appl. Nano Mater.* **3** 7879–87
[49] Arora H, Jung Y, Venanzi T, Watanabe K, Taniguchi T, Hubner R, Schneider H, Helm M, Hone J C and Erbe A 2019 *ACS Appl. Mater. Interfaces* **11** 43480–7
[50] Giannozzi P *et al* 2009 *J. Phys.: Condens. Matter* **21** 395502
[51] Perdew J P, Burke K and Ernzerhof M 1996 *Phys. Rev. Lett.* **77** 3865–8
[52] Dal Corso A 2014 *Comput. Mater. Sci.* **95** 337–50
[53] Wickramaratne D, Weston L and Van de Walle C G 2018 *J. Phys. Chem.* C **122** 25524–9
[54] Shen N F, Yang X D, Wang X X, Wang G H and Wan J G 2020 *Chem. Phys. Lett.* **749** 137430

# Strain-Induced Corrugation and Its Impact on Electronic and Optical Properties of hBN-GaS, -GaSe, and -InS heterostructures

**Andrijana Šolajić**

solajic@ipb.ac.rs

Institute of Physics Belgrade

**Jelena Pešić**

Institute of Physics Belgrade

**Research Article**

**Keywords:** 2d materials, heterostructures, dft, strain engineering

**Posted Date:** January 12th, 2026

**DOI:** https://doi.org/10.21203/rs.3.rs-8491186/v1



**Additional Declarations:** No competing interests reported.

# Strain-Induced Corrugation and Its Impact on Electronic and Optical Properties of hBN-GaS, -GaSe, and -InS heterostructures

Andrijana Šolajić[1*] and Jelena Pešić[1]

[1*]Center for Solid State Physics and New Materials, Institute of Physics Belgrade, University of Belgrade, Pregrevica 118, Belgrade, 11080, Serbia.

*Corresponding author(s). E-mail(s): solajic@ipb.ac.rs;

**Abstract**

Two dimensional group IIIa monochalcogenides are promising two-dimensional semiconductors, known for their high carrier mobility and strong optical absorption in the visible and UV range. When integrated with hexagonal boron nitride (hBN) in van der Waals heterostructures, these materials benefit from the atomically flat and inert nature of hBN, which helps preserve their intrinsic electronic quality and enhances overall device performance. In our previous studies, hBN-based heterostructures with these monolayers exhibited favorable band alignment and optoelectronic characteristics.

In this work, we investigate the role of strain in shaping the structural and electronic behavior of hBN/GaS, hBN/GaSe, and hBN/InS heterostructures using first-principles DFT calculations. Contrary to heterostructures previously reported in the literature, these three systems develop a pronounced corrugated geometry as a result of compressive strain and lattice mismatch. We analyze how this strain-induced out-of-plane distortion modifies interlayer coupling, charge redistribution, band structure, and optical absorption spectra.

**Keywords:** 2d materials, heterostructures, dft, strain engineering

## 1 Introduction

The rapid development of materials science in the past two decades has been strongly driven by the discovery and exploration of two-dimensional (2D) materials. Owing

to their reduced dimensionality and unique electronic structure, 2D materials exhibit physical properties that differ fundamentally from those of their bulk counterparts, enabling a wide range of potential applications in nanoelectronics, optoelectronics, and sensing technologies [1, 2]. The isolation of graphene in 2004 marked a turning point in condensed matter physics, demonstrating the stability of atomically thin crystals and stimulating extensive research into other layered materials.

Following graphene, numerous 2D systems have been identified and investigated, including hexagonal boron nitride (hBN) [3, 4], silicene [5, 6], germanene [7, 8], transition metal dichalcogenides [9–11], MXenes [12, 13], and group-III monochalcogenides [14–17]. Many of these materials exhibit tunable band gaps, strong light-matter interaction, and excellent mechanical flexibility, making them promising building blocks for next-generation electronic and optoelectronic devices.

Among them, group-III monochalcogenides ($M^{III}X^{VI}$, where M = Ga, In and X = S, Se, Te) have attracted considerable attention due to their favorable electronic and optical properties. These materials possess direct or quasi-direct band gaps, high carrier mobilities, and strong optical absorption across a wide spectral range. For example, few-layer InSe exhibits electron mobilities exceeding 1000 $cm^2/Vs$ at room temperature [18], comparable to or even surpassing those of many transition metal dichalcogenides and approaching values observed in strained silicon-based devices [19]. In addition, III-VI monochalcogenides show excellent performance in photodetection applications, with efficient absorption extending from the ultraviolet to the near-infrared region [20].

Despite these advantages, the practical application of III-VI monochalcogenides is severely limited by their chemical instability. In particular, monolayer and few-layer GaS, GaSe, and InS are prone to rapid oxidation when exposed to ambient conditions, leading to degradation of their electronic and optical properties [21–24]. This issue can be effectively mitigated by encapsulation using chemically inert materials. Hexagonal boron nitride has proven to be especially suitable for this purpose, providing excellent environmental protection while preserving the intrinsic properties of the encapsulated layers [25, 26]. Moreover, hBN offers an atomically flat, mechanically robust, and electrically insulating substrate, making it an ideal component for van der Waals heterostructures (HSs).

Van der Waals (vdW) HSs formed by stacking different 2D materials enable precise control over electronic and optical properties without the constraints of lattice matching typical for conventional HSs [1, 2, 27]. In HSs based on III-VI monochalcogenides and hBN, the combination of strong optical absorption, mechanical flexibility, and chemical stability makes these systems particularly attractive for optoelectronic applications. In addition, their layered nature allows for the application of external strain as an efficient tool for tuning electronic structure and optical response. Our previous works on hBN/GaTe, hBN/InTe and hBN/InSe HSs highlight their potential as wide-spectrum absorbers, being able to absorb visible light as well the UV part of the spectrum [28–30].

Sometimes, in lattice-mismatched HSs, strain relaxation does not occur solely through in-plane deformation but may also involve out-of-plane structural relaxation.

In systems composed of GaS, GaSe, or InS combined with hBN, this can lead to the formation of slight corrugation or buckling of the layers. Although subtle, such structural distortions influence interlayer spacing, orbital hybridization, and band alignment, thereby affecting the electronic and optical properties of the HS. These effects become increasingly relevant under applied biaxial strain and must be considered for a realistic description of strain-dependent behavior.

In this work, we present a systematic first-principles study of hBN/GaS, hBN/-GaSe, and hBN/InS HSs under biaxial strain ranging from -6% to +6%. We investigate their structural response, with particular attention to the emergence of out-of-plane relaxation, and analyze how strain affects the electronic band structure and optical properties. Special emphasis is placed on the evolution of the band gap, the character of band-edge states, and the resulting absorption and reflectance spectra. By comparing HSs based on different monochalcogenides, we elucidate how chemical composition and lattice flexibility govern strain accommodation and determine the optoelectronic response.

The results demonstrate that hBN/III-VI HSs represent a versatile platform for strain-engineered optoelectronic applications. Their combination of strong optical absorption, mechanical robustness, and tunable electronic structure highlights their potential for future devices such as photodetectors, flexible electronics, and strain-sensitive optoelectronic components.

## 2 Computational Methods

First-principles calculations were performed within the framework of density functional theory (DFT) using the *Quantum ESPRESSO* package [31, 32]. The exchange-correlation effects were treated within the generalized gradient approximation (GGA), employing the Perdew-Burke-Ernzerhof (PBE) functional [33], along with Norm-conserving pseudopotentials. The energy cutoff of 86 Ry was set for hBN/GaSe HS and 80 Ry for hBN/InS and hBN/GaS HSs.

To model the two-dimensional nature of the investigated systems and avoid spurious interactions between periodic replicas, a vacuum spacing of 20 Å was introduced along the out-of-plane ($z$) direction. All HSs were fully relaxed prior to electronic and optical calculations by optimizing both lattice parameters and internal atomic positions using the Broyden-Fletcher-Goldfarb-Shanno (BFGS) algorithm. The convergence criterion for the residual forces acting on atoms was set to $10^{-6}$ RyÅ$^{-1}$.

Brillouin zone integrations were carried out using a Monkhorst-Pack $k$-point mesh of $16 \times 16 \times 1$ for structural relaxation and total energy calculations. Denser $k$-point grids, up to $64 \times 64 \times 1$, were employed for calculations of the projected density of states (PDOS) and optical properties. The electronic band structures were calculated along high-symmetry paths in the hexagonal Brillouin zone, following the $\Gamma - \mathrm{M} - \mathrm{K} - \Gamma$ trajectory.

Since standard GGA functionals do not accurately account for long-range dispersion interactions, van der Waals forces were included using the Grimme D2 correction scheme [34, 35]. This approach ensures a more reliable description of interlayer distances and binding characteristics in van der Waals HSs.

Biaxial strain was applied uniformly in the plane of the HSs by varying the in-plane lattice constant according to

$$\varepsilon = \frac{a - a_0}{a_0}, \tag{1}$$

where $a_0$ and $a$ denote the equilibrium and strained lattice constants, respectively. Both compressive and tensile strain were considered in the range from -6% to +6%, while preserving the hexagonal symmetry of the lattice. For each strain value, the atomic positions were fully relaxed with fixed in-plane lattice parameters.

Optical properties were calculated within the random phase approximation (RPA) using the *epsilon.x* module of the *Quantum ESPRESSO* package. The frequency-dependent complex dielectric function was obtained, from which absorption coefficients and reflectance spectra were derived. For visualisation of crystal structures, VESTA software was used [36].

## 3 Results and Discussion

The van der Waals HSs considered in this work, hBN/GaS, hBN/GaSe, and hBN/InS, were modeled following the same approach as previously described for hBN/InTe, hBN/GaTe, and hBN/InSe [28–30]. In those systems, the unit cell consisted of 10 atoms, combining a single unit cell of III-VI monochalcogenide layer and a $\sqrt{3} \times \sqrt{3}$ hBN supercell, enabling minimal lattice mismatch while preserving hexagonal symmetry.

For the present systems, due to the specific lattice constants of GaS, GaSe, and InS, the optimal unit cells are slightly larger. Specifically, the hBN/GaS HS requires 34 atoms per unit cell, while hBN/GaSe and hBN/InS contain 26 atoms, as shown in Figure 1. These supercells provide a good compromise between minimizing induced interlayer strain (below 3% for GaS and 1% for GaSe and InS) and computational efficiency. As in previous studies, the layers were stacked without rotation whenever

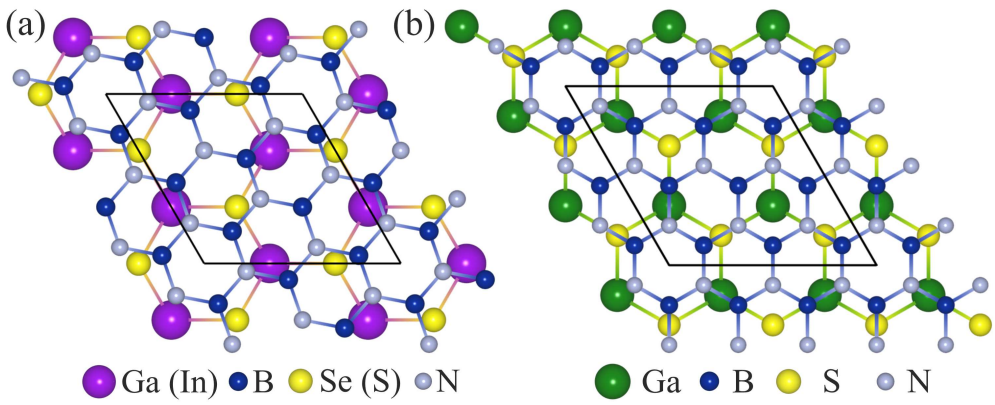


**Fig. 1** The unit cell of (a) hBN/GaSe and hBN/InS, and (b) hBN/GaS HSs.

possible, except for the hBN/GaSe and hBN/InS systems, which require a small rotational alignment of approximately 10.89° between the monochalcogenide supercell and the hBN layer. This configuration preserves the overall hexagonal symmetry while allowing for lattice mismatch relaxation.

## 3.1 Structural Properties and Strain Response

The structural properties of the hBN/GaS, hBN/GaSe, and hBN/InS HSs were first analyzed in their fully relaxed configurations. The optimized lattice constants obtained after full structural relaxation are $a = 7.44$ Å for hBN/GaS, $a = 6.61$ Å for hBN/GaSe, and $a = 6.59$ Å for hBN/InS.

In the relaxed, unstrained configurations, the formation of the HSs does not significantly distort the individual layers. Only a slight reduction in the thickness of the III-VI layers is observed, on the order of 0.1 Å, accompanied by minor shortening of Ga-Ga or In-In bonds.

Unlike systems where strain is accommodated predominantly through uniform in-plane deformation, the present HSs exhibit a more complex relaxation mechanism, particularly under compressive strain. Upon relaxation, out-of-plane corrugation develops in the form of buckling of the hBN layer, a strain-relief mechanism commonly observed in lattice-mismatched van der Waals HSs. Besides the relative position of B and N atoms to the monochalcogenide atoms, this behavior also originates from the competition between in-plane elastic energy and relatively weak interlayer van der Waals interactions, leading to partial strain release through vertical atomic displacements and a non-planar geometry.

The degree of buckling depends on the chemical composition and intrinsic lattice stiffness of the monochalcogenide layer, as well as on the magnitude and sign of the applied biaxial strain. Consequently, GaS-, GaSe-, and InS-based HSs exhibit distinct structural responses, reflected in differences in interlayer spacing and local atomic environments.

Although weak, corrugation is already present in the relaxed HSs and is further modulated by applied strain. Compressive strain enhances out-of-plane deformation, while tensile strain tends to flatten the HSs.

In hBN/GaS, the largest out-of-plane displacements occur in hBN hexagons where N atoms are positioned nearly above S atoms. In contrast, in hBN/GaSe and hBN/InS the maximum heights correspond to B atoms located above the centers of GaSe/InS hexagons, accompanied by three neighboring N atoms positioned close to S/Se atoms. The corrugation patterns for all three HSs are illustrated in Figure 2.

Buckling becomes more pronounced under compressive strain, reaching a maximum at -6%, where the height difference between the lowest and highest atoms in the hBN layer approaches 1 Å. At lower compressive strain (-2%), this effect is much weaker, while in the unstrained HSs buckling is almost negligible. Nevertheless, even in the relaxed configurations a perfectly flat hBN layer is not achieved, in contrast to hBN/In(Ga)Te and hBN/InSe HSs.

In previously studied systems where all atoms of the $M^{III}X^{VI}$ layers are located exactly at the centers of hBN hexagons, no buckling was observed. The presence of

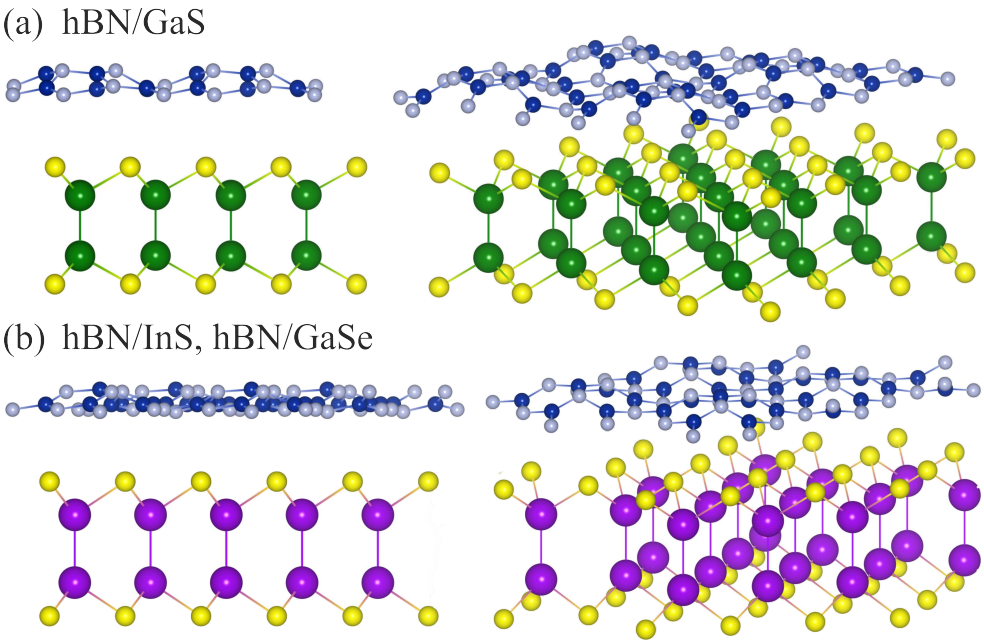


**Fig. 2** The buckling occuring in studied HSs, (a) hBN/GaS and (b) hBN/InSe or hBN/GaSe, illustrated for structures under -6% strain.

corrugation in the present systems does not indicate structural instability, as all structures were successfully relaxed with residual forces below $10^{-6}$ Ry/Å. Such rippled geometries are common in many 2D materials and vdW HSs [37–40]; however, for intrinsically flat systems they may complicate experimental fabrication and increase the likelihood of defect formation.

The calculated adsorption energies are negative for all structures, ranging from 17 to -28 meV, confirming their energetic stability over the entire strain range. Stronger interlayer binding is found for hBN/InTe and hBN/GaTe, with adsorption energies between -23 and -30 meV. Although dynamical stability is commonly assessed through phonon dispersion calculations, such calculations are computationally demanding for systems of this size and were therefore not performed in the present work.

## 3.2 Electronic Structure

The electronic properties of the hBN/GaS, hBN/GaSe, and hBN/InS HSs were analyzed through their band structures and projected density of states. While the electronic structure of isolated III-VI monochalcogenide monolayers is highly sensitive to strain and thickness, the weak interlayer interaction with hBN largely preserves their intrinsic features, introducing only moderate changes in band alignment and dispersion.

In lattice-mismatched HSs, out-of-plane relaxation plays an important role. Buckling modifies the local interlayer distance and orbital overlap, leading to strain-dependent shifts of the band edges. These effects become particularly pronounced under compressive strain, where structural deformation and electronic response are strongly coupled.

The calculated band structures for -6%, 0%, and +6% strain are shown in Figure 3. Band structure for remaining strain values, are provided in Supplementary material.

In the unstrained systems, the band gaps remain close to those of the isolated monolayers: in hBN/GaS the gap decreases from 2.35 to 1.95 eV, in hBN/InSe it slightly increases from 1.66 to 1.72 eV, while in hBN/GaSe it remains nearly unchanged at 1.77 eV.

Under compressive strain, enhanced buckling leads to more pronounced band-gap modifications. Increased out-of-plane deformation alters orbital hybridizationand shifts the VBM and CBM. Tensile strain, in contrast, partially suppresses corrugation and produces smoother band-gap variations.

For hBN/GaSe, the band structure resembles that of hBN/InTe and hBN/GaTe, but with a larger band gap. A distinctive feature is the presence of N-derived states already around -1 eV. The VBM originates mainly from Se $p$ states and is located between the Γ-M and Γ-K points, shifting to Γ under -4% and -6% strain. The CBM lies at Γ, with the M valley approaching it at higher compression. The band gap increases up to 2.11 eV at -6% strain and decreases to 0.65 eV under +6% tensile strain.

In hBN/GaS, the electronic structure differs more significantly due to the relative position of hBN-derived states. While the B and N atom states in previous HSs were far from the Fermi level, the VBM in hBN/GaS at the Γ point is formed by N $p$ states, with S $p$ states nearby. The CBM remains at the Γ point, mainly composed of Ga and S states. With compressive strain, the VBM in Γ further separates from S states, which approach a set of nearly degenerate S states at around -2 eV, so the VBM and its vicinity are primarily of N atom origin. Compression also modifies the CBM shape and the relative positions of bands above the Fermi level, so at -6% strain the CBM shifts to the K point. The band gap increases with compressive strain, reaching 2.45 eV at -6%. Tensile strain shifts the VBM away from Γ and lowers the CBM, reducing the band gap to 0.66 eV at +6%.

A similar trend is observed for hBN/InS. The valence band in the InS layer exhibits deep valleys at the M and K points relative to the Γ point, while the VBM lies between Γ and M and between K and Γ. In the HS, this band is shifted by N states forming the VBM at the K point, while the shape of this band is fairly flat. The CBM remains at the Γ point, with the M-point valley nearby. Under compressive strain, the N-derived band further separates as the highest S $p$ state decreases in energy with increasing compression. This effect is evident from the projected density of states for various strains: at -6% strain, the VBM consists of N $p$ states at K and S $p$ states at Γ, while the CBM valley at M is nearly degenerate with Γ. The band gap reaches 2.01 eV at -6% strain. Under tensile strain, the N-derived VBM remains nearly unchanged, while the S $p$ band flattens and rises energetically, equalizing the VBM energy between Γ-M and Γ-K, and the CBM at Γ lowers, yielding a band gap of 1.16 eV at +6% strain.

The projected density of states provides further insight into the origin of the states near the Fermi level. In agreement with the band-structure analysis, the electronic states near the Fermi level are dominated by contributions from the III-VI monochalcogenide layers, while hBN contributes mainly at deeper valence and higher conduction energies (Figure 4). For all systems, the valence band maximum is primarily composed of chalcogen $p$ orbitals, whereas the conduction band minimum originates mainly from metal $s$ and $p$ states. The relative weight of these contributions varies with applied strain, reflecting strain-induced redistribution of electronic states. Under compressive strain, enhanced buckling leads to stronger hybridization and increased competition between valleys located at the Γ, M, and K points, which is particularly pronounced in hBN/GaS and hBN/InS.

In contrast, hBN/GaSe shows a more moderate redistribution of states near the band edges. Overall, these results indicate that the strain-dependent evolution of the electronic structure is determined by the combined effect of lattice mismatch, out-of-plane relaxation, and the orbital character of the monochalcogenide layers.

### 3.3 Optical properties

Strain-induced modifications of the electronic structure directly affect the optical response of the hBN/GaS, hBN/GaSe, and hBN/InS HSs. The optical properties were analyzed through the frequency-dependent dielectric function, from which the absorption coefficient and reflectance spectra were obtained.

In all three systems, optical absorption in the low-energy region is governed primarily by electronic transitions within the III-VI monochalcogenide layers, while the contribution of hBN is negligible due to its wide band gap. Consequently, the absorption edge closely follows the strain-dependent evolution of the band gap discussed in the previous section. The calculated absorption spectra are shown in Figure 5.

For hBN/GaSe, the absorption coefficient exceeds $10^5$ cm$^{-1}$ over most of the spectrum, with pronounced peaks reaching up to $8 \times 10^5$ cm$^{-1}$. The overall spectral shape remains relatively stable under applied strain, with only moderate shifts in peak positions and intensities, reflecting the weaker structural deformation and lower sensitivity to buckling compared to the other two HSs.

In hBN/GaS, compressive strain induces more pronounced changes in the absorption spectra. Enhanced buckling leads to increased absorption in the 6-15 eV range for in-plane polarization, as well as the emergence of a distinct peak around 4 eV for out-of-plane polarization, reaching $8 \times 10^5$ cm$^{-1}$ at -6% strain. At the same time, absorption in the visible range is reduced due to the widening of the band gap. In contrast, tensile strain enhances visible-range absorption and increases intensity in the 11-15 eV region, accompanied by a smoother evolution of the spectra.

A similar behavior is observed for hBN/InS. Although notable strain-induced changes occur in the electronic structure, the overall absorption profile remains comparable to that of hBN/GaS, with slightly enhanced features around 4 eV. The absorption coefficient reaches values of approximately $5 \times 10^5$ cm$^{-1}$ in the UV region and somewhat lower values in the visible range. Compressive strain shifts the absorption toward higher photon energies and enhances selected peaks, whereas tensile strain enhances absorption in the visible region with only minor spectral shifts.

The corresponding reflectance spectra are shown in Figure 6. For all three HSs, the reflectance remains relatively low, typically between 0.1 and 0.3, indicating that no more than 30% of incident light is reflected. In hBN/GaS and hBN/InS, the reflectance remains below 0.2 over most of the spectrum, except for distinct features in the 4-6 eV (in-plane) and 13-16 eV (out-of-plane) ranges. These features shift systematically with applied strain, with more pronounced changes observed under compressive strain due to enhanced buckling.

Overall, the combined analysis of absorption and reflectance shows that the optical response of hBN/GaS, hBN/GaSe, and hBN/InS HSs is primarily governed by strain-induced modifications of the electronic structure. While changes in the band gap set the overall energy scale of optical transitions, the resulting spectra remain robust and highly tunable, underscoring the potential of these systems for strain-engineered optoelectronic applications.

# 4 Conclusion

In this work, we performed a comprehensive first-principles investigation of the structural, electronic, and optical properties of hBN/GaS, hBN/GaSe, and hBN/InS van der Waals HSs under biaxial strain. The study was focused on understanding how strain and structural relaxation influence their electronic structure and optical response, with particular emphasis on their applicability in optoelectronic devices.

The results demonstrate that all three HSs exhibit strong and broadband optical absorption, extending from the visible to the ultraviolet spectral region, with absorption coefficients reaching values on the order of $10^5$-$10^6$ $cm^{-1}$. Such high absorption efficiency, combined with the atomically thin nature of the systems, makes these HSs especially attractive for applications in photodetectors, phototransistors, and other optoelectronic components requiring efficient light-matter interaction.

The electronic structure analysis shows that the band gap can be effectively tuned by biaxial strain, enabling control over both its magnitude and character. Tensile strain generally leads to smoother band-gap modulation and enhanced absorption in the visible range, while compressive strain induces stronger changes in the electronic structure. These effects originate from the combined influence of strain and out-of-plane relaxation, which modifies orbital hybridization and redistributes electronic states near the band edges.

Although buckling emerges as a natural strain-relief mechanism in these lattice-mismatched HSs, it does not compromise their optical performance. On the contrary, the optical response remains robust over the entire strain range, indicating that efficient light absorption is preserved even in the presence of structural corrugation. This is particularly important for realistic device conditions, where perfect planarity is rarely achieved.

These HSs can be viewed as atomically thin optical metamaterials, where strain-induced corrugation and interlayer coupling enable engineered anisotropy and tunable dielectric response beyond that of the individual layers. Such controllable, sub-wavelength modulation of electronic and optical properties positions these HSs as

promising building blocks for 2D metasurfaces, adaptive photonic components, and strain-programmable optoelectronic metamaterials.

Overall, the present study demonstrates that hBN/GaS, hBN/GaSe, and hBN/InS HSs combine strong and tunable optical absorption with good structural stability under strain. The interplay between strain, electronic structure, and optical response provides a powerful route for engineering their properties, positioning these systems as promising candidates for strain-tunable and flexible optoelectronic applications. The insights obtained here contribute to a deeper understanding of structure-property relationships in van der Waals HSs and support their further development for next-generation nanoscale optoelectronic devices.

**Acknowledgements.** The authors acknowledge funding provided by the Institute of Physics Belgrade through the grant by the Ministry of Science, Technological Development and Innovations of the Republic of Serbia. DFT calculations were performed using computational resources at Johannes Kepler University (Linz, Austria).

# References

[1] Geim, A. K. & Grigorieva, I. V. Van der waals heterostructures. *Nature* **499**, 419–425 (2013).

[2] Withers, F. *et al.* Light-emitting diodes by band-structure engineering in van der waals heterostructures. *Nature materials* **14**, 301–306 (2015).

[3] Zhang, K., Feng, Y., Wang, F., Yang, Z. & Wang, J. Two dimensional hexagonal boron nitride (2d-hbn): synthesis, properties and applications. *Journal of Materials Chemistry C* **5**, 11992–12022 (2017).

[4] Song, L. *et al.* Large scale growth and characterization of atomic hexagonal boron nitride layers. *Nano letters* **10**, 3209–3215 (2010).

[5] Kara, A. *et al.* A review on silicene - new candidate for electronics. *Surface science reports* **67**, 1–18 (2012).

[6] Zhao, J. *et al.* Rise of silicene: A competitive 2d material. *Progress in Materials Science* **83**, 24–151 (2016).

[7] Acun, A. *et al.* Germanene: the germanium analogue of graphene. *Journal of physics: Condensed matter* **27**, 443002 (2015).

[8] Derivaz, M. *et al.* Continuous germanene layer on al (111). *Nano letters* **15**, 2510–2516 (2015).

[9] Splendiani, A. *et al.* Emerging photoluminescence in monolayer mos2. *Nano letters* **10**, 1271–1275 (2010).

[10] Li, H. *et al.* From bulk to monolayer mos2: evolution of raman scattering. *Advanced Functional Materials* **22**, 1385–1390 (2012).

[11] Zhao, W. *et al.* Evolution of electronic structure in atomically thin sheets of ws2 and wse2. *ACS nano* **7**, 791–797 (2013).

[12] Anasori, B., Lukatskaya, M. R. & Gogotsi, Y. 2d metal carbides and nitrides (mxenes) for energy storage. *Nature Reviews Materials* **2**, 1–17 (2017).

[13] Pang, J. *et al.* Applications of 2d mxenes in energy conversion and storage systems. *Chemical Society Reviews* **48**, 72–133 (2019).

[14] Ren, C. *et al.* First-principles investigation on electronic properties and band alignment of group iii monochalcogenides. *Scientific reports* **9**, 1–6 (2019).

[15] Demirci, S., Avazlı, N., Durgun, E. & Cahangirov, S. Structural and electronic properties of monolayer group iii monochalcogenides. *Physical Review B* **95**, 115409 (2017).

[16] Yang, Z. & Hao, J. Recent progress in 2d layered iii–vi semiconductors and their heterostructures for optoelectronic device applications. *Advanced Materials Technologies* **4**, 1900108 (2019).

[17] Chen, J. *et al.* High-performance iii–vi monolayer transistors for flexible devices. *Physical Chemistry Chemical Physics* **22**, 7039–7047 (2020).

[18] Feng, W., Zheng, W., Cao, W. & Hu, P. Back gated multilayer inse transistors with enhanced carrier mobilities via the suppression of carrier scattering from a dielectric interface. *Advanced materials* **26**, 6587–6593 (2014).

[19] Gomez, L., Aberg, I. & Hoyt, J. Electron transport in strained-silicon directly on insulator ultrathin-body n-mosfets with body thickness ranging from 2 to 25 nm. *IEEE electron device letters* **28**, 285–287 (2007).

[20] Tamalampudi, S. R. *et al.* High performance and bendable few-layered inse photodetectors with broad spectral response. *Nano letters* **14**, 2800–2806 (2014).

[21] Rahaman, M., Rodriguez, R. D., Monecke, M., Lopez-Rivera, S. A. & Zahn, D. R. T. GaSe oxidation in air: from bulk to monolayers. *Semiconductor Science and Technology* **32**, 105004 (2017).

[22] Guo, Y., Zhou, S. & Zhao, J. Oxidation behaviors of two-dimensional metal chalcogenides. *ChemNanoMat* **6**, 838–849 (2020).

[23] Guo, Y., Zhou, S., Bai, Y. & Zhao, J. Defects and oxidation of group-iii monochalcogenide monolayers. *The Journal of chemical physics* **147**, 104709 (2017).

[24] Afaneh, T. *et al.* Large-area growth and stability of monolayer gallium monochalcogenides for optoelectronic devices. *ACS Applied Nano Materials* **3**, 7879–7887 (2020).

[25] Bandurin, D. A. *et al.* High electron mobility, quantum hall effect and anomalous optical response in atomically thin inse. *Nature nanotechnology* **12**, 223–227 (2017).

[26] Arora, H. & Erbe, A. Recent progress in contact, mobility, and encapsulation engineering of InSe and GaSe. *InfoMat* **3**, 662–693 (2021).

[27] Liu, Y. *et al.* Van der waals heterostructures and devices. *Nature Reviews Materials* **1**, 1–17 (2016).

[28] Šolajić, A. & Pešić, J. Novel wide spectrum light absorber heterostructures based on hBN/In(Ga)Te. *Journal of Physics: Condensed Matter* **34**, 345301 (2022).

[29] Šolajić, A. & Pešić, J. Strain-induced modulation of electronic and optical properties in hBN/InSe heterostructure. *Optical and Quantum Electronics* **56**, 1186 (2024).

[30] Šolajić, A. & Pešić, J. Tailoring electronic and optical properties of hBN/InTe and hBN/GaTe heterostructures through biaxial strain engineering. *Scientific Reports* **14**, 1081 (2024).

[31] Giannozzi, P. *et al.* Quantum espresso: a modular and open-source software project for quantum simulations of materials. *Journal of Physics: Condensed Matter* **21**, 395502 (19pp) (2009). URL http://www.quantum-espresso.org.

[32] Giannozzi, P. *et al.* Advanced capabilities for materials modelling with quantum espresso. *Journal of Physics: Condensed Matter* **29**, 465901 (2017). URL http://stacks.iop.org/0953-8984/29/i=46/a=465901.

[33] Perdew, J. P., Burke, K. & Ernzerhof, M. Generalized gradient approximation made simple. *Phys. Rev. Lett.* **77**, 3865–3868 (1996).

[34] Grimme, S. Semiempirical gga-type density functional constructed with a long-range dispersion correction. *Journal of computational chemistry* **27**, 1787–1799 (2006).

[35] Barone, V. *et al.* Role and effective treatment of dispersive forces in materials: Polyethylene and graphite crystals as test cases. *Journal of computational chemistry* **30**, 934–939 (2009).

[36] Momma, K. & Izumi, F. Vesta 3 for three-dimensional visualization of crystal, volumetric and morphology data. *Journal of applied crystallography* **44**, 1272–1276 (2011).

[37] Zihlmann, S. *et al.* Out-of-plane corrugations in graphene based van der waals heterostructures. *Phys. Rev. B* **102**, 195404 (2020). URL https://link.aps.org/doi/10.1103/PhysRevB.102.195404.

[38] Arias, P., Abdulslam, A., Ebnonnasir, A., Ciobanu, C. V. & Kodambaka, S. Bifurcation and orientation-dependence of corrugation of 2D hexagonal boron nitride on palladium. *2D Materials* **5**, 045001 (2018). URL https://doi.org/10.1088/2053-1583/aacd71.

[39] Geng, W. T., Wang, V., Liu, Y. C., Ohno, T. & Nara, J. Moire potential, lattice corrugation, and band gap spatial variation in a twist-free $MoTe_2/MoS_2$ heterobilayer. *The Journal of Physical Chemistry Letters* **11**, 2637–2646 (2020). URL https://doi.org/10.1021/acs.jpclett.0c00605. PMID: 32188242.

[40] Li, W., Brumme, T. & Heine, T. Relaxation effects in transition metal dichalcogenide bilayer heterostructures. *npj 2D Materials and Applications* **8**, 43 (2024).

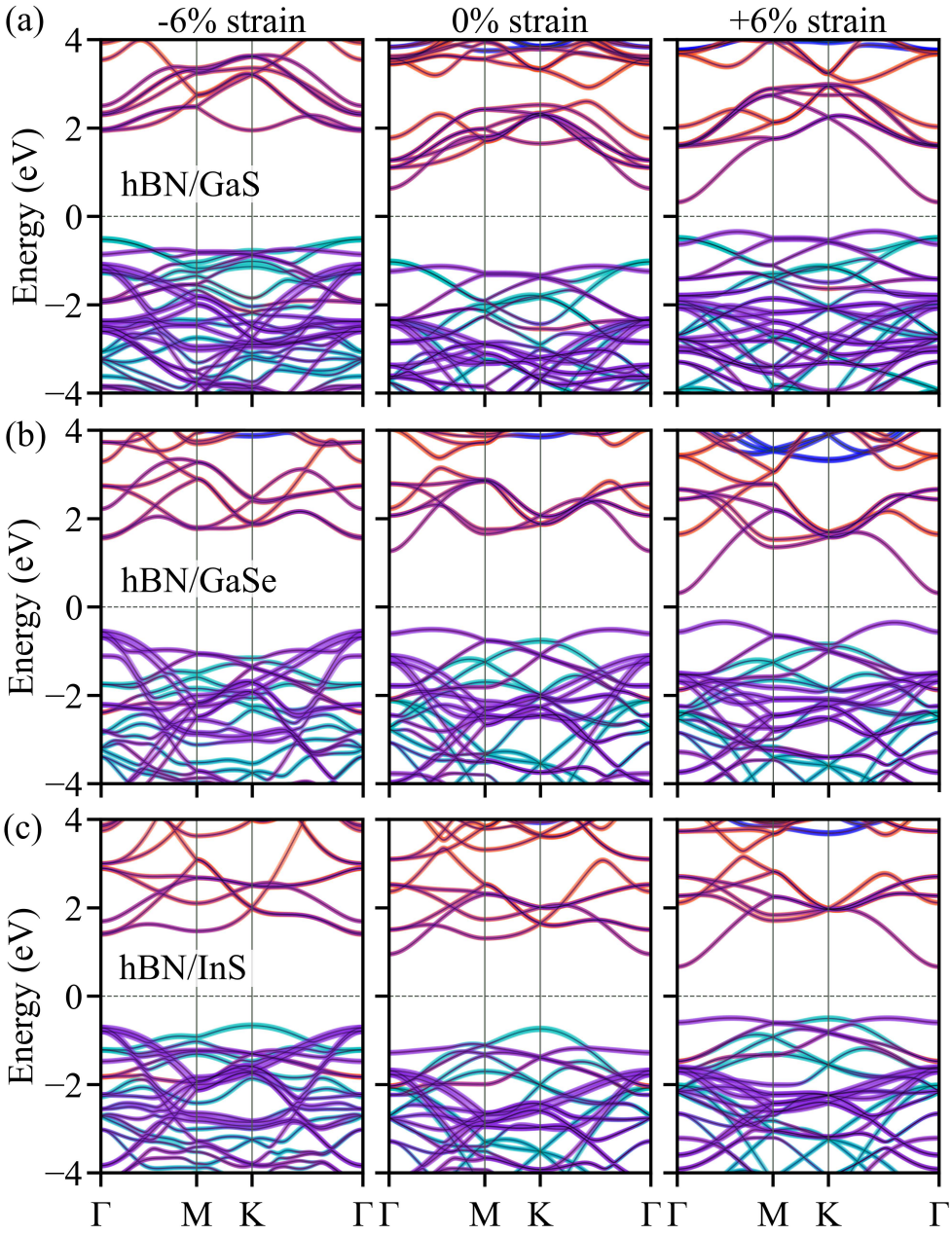


**Fig. 3** Projected band structure of hBN/GaS, hBN/GaSe and hBN/InS HSs, for -6%, 0% and +6% of applied strain. The line width is proportional to the contribution of different atoms/states.

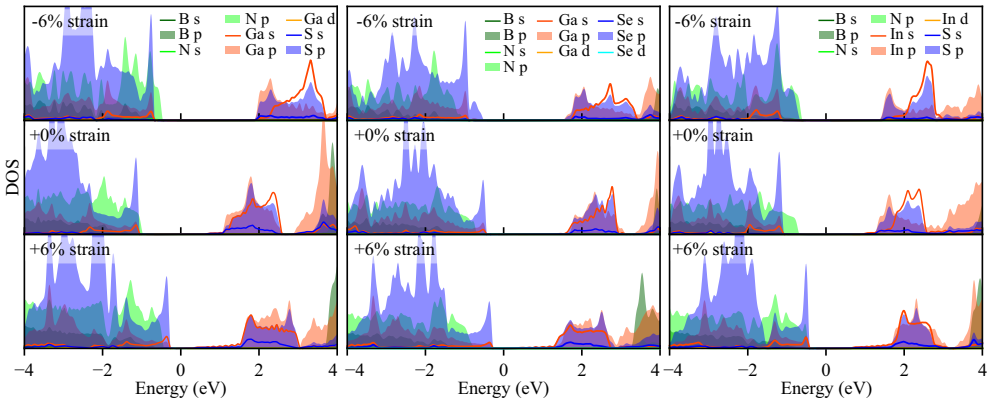


**Fig. 4** Projected density of states (PDOS) of hBN/GaS, hBN/GaSe, and hBN/InS HSs calculated for compressive (-6%), unstrained (0%), and tensile (+6%) configurations. The states near the Fermi level are dominated by contributions from the III-VI monochalcogenide layers, while hBN states appear mainly at deeper valence and higher conduction energies. Strain-induced redistribution of orbital contributions reflects the influence of buckling and modified interlayer coupling, particularly pronounced under compressive strain. PDOS for remaining strain values are presented in Supplementary material.

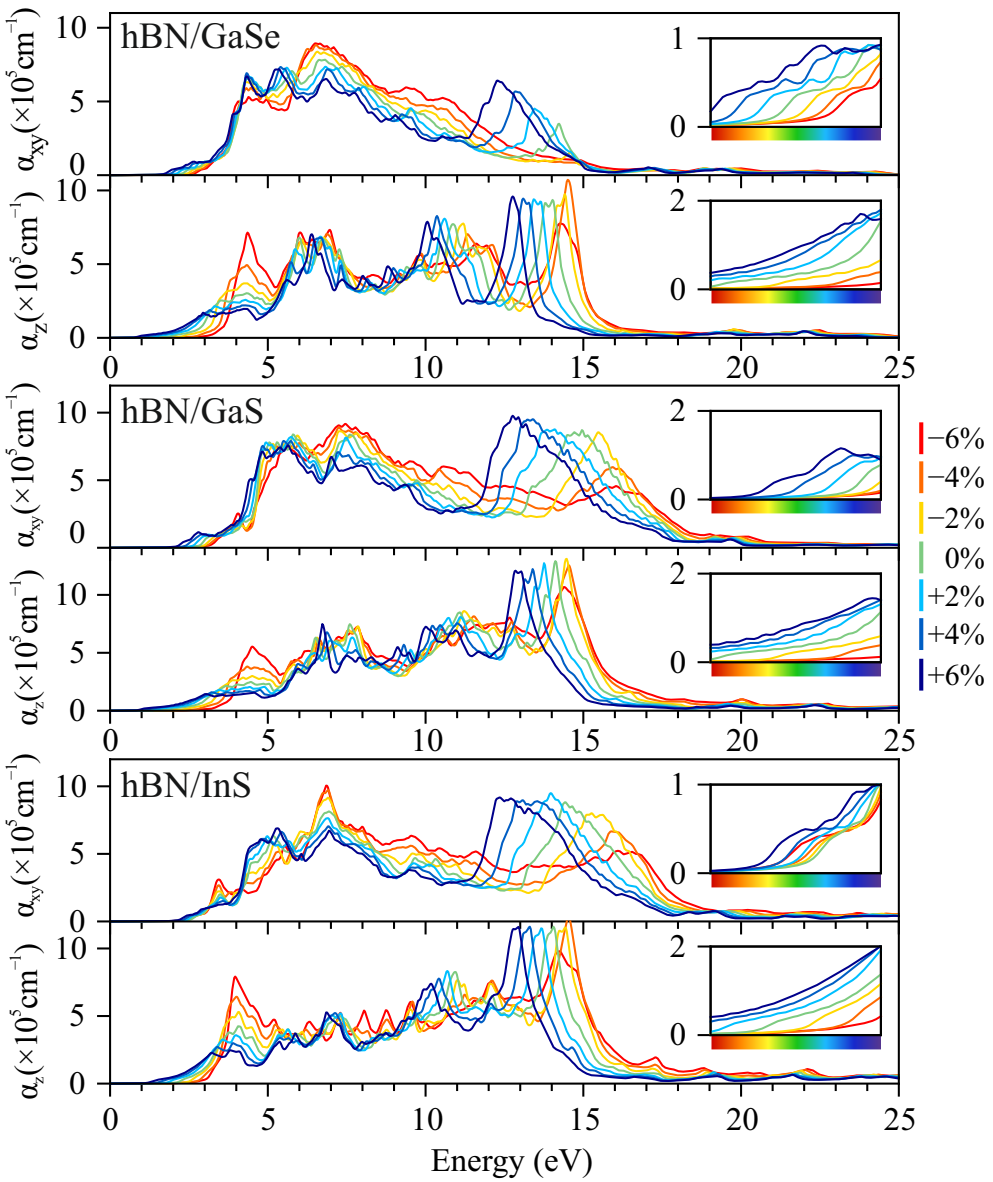


**Fig. 5** Absorption spectra of hBN/GaSe, hBN/GaS, and hBN/InS HSs calculated for biaxial strain values ranging from -6% to +6%. Different colors correspond to different strain levels, as indicated in the legend. The spectra illustrate the strain-induced shifts of absorption features and the modulation of absorption intensity resulting from changes in the electronic structure.

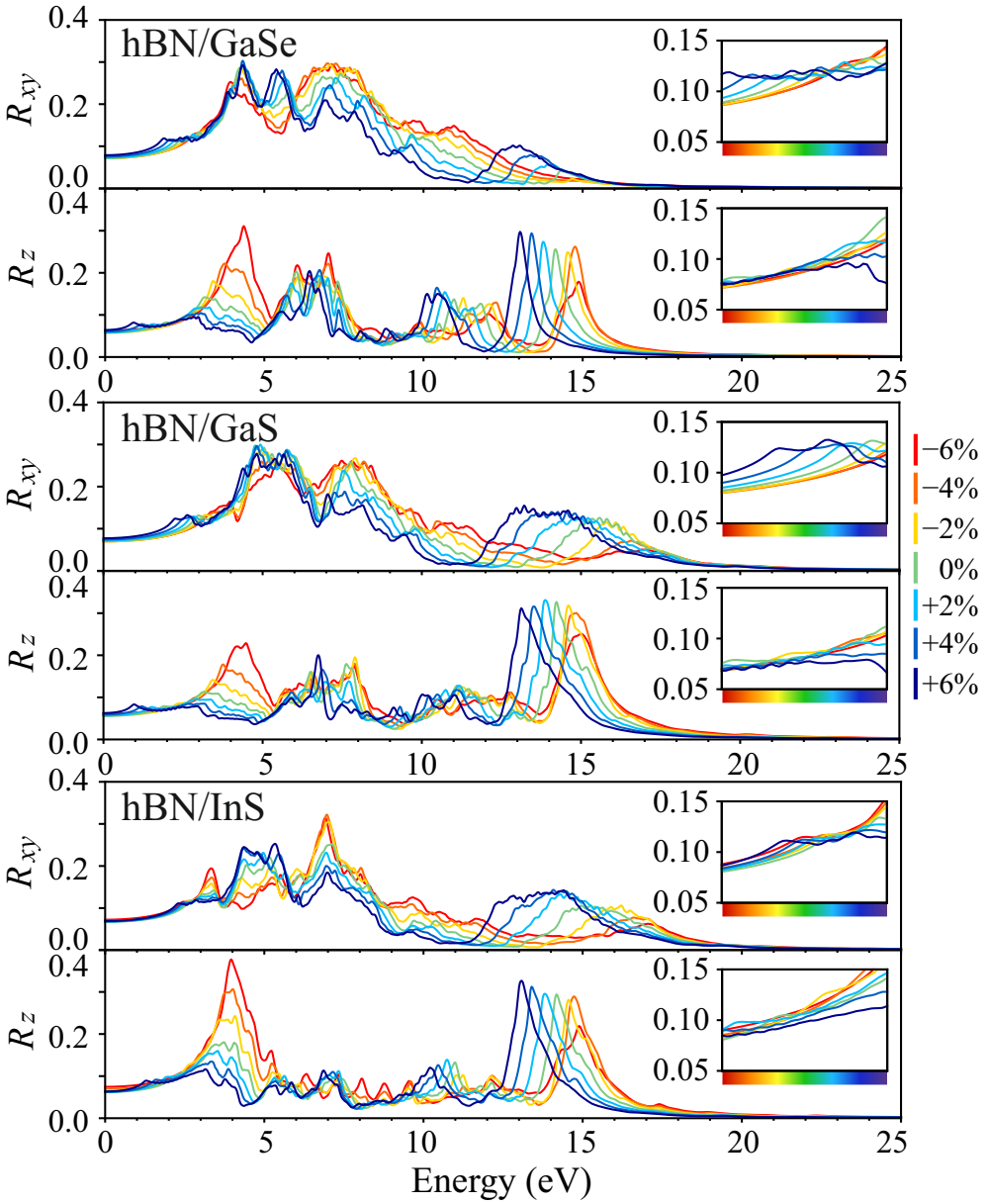


**Fig. 6** Reflectance spectra of hBN/GaSe, hBN/GaS, and hBN/InS HSs under biaxial strain from -6% to +6%. The evolution of spectral features reflects strain-induced modifications of the electronic structure and enhanced sensitivity to out-of-plane relaxation under compressive strain.

## Supplementary Files

This is a list of supplementary files associated with this preprint. Click to download.

- supp.pdf

# Phonon frequency comb close to an isolated Einstein mode in $InSiTe_3$

**Tea Belojica[1], Jovan Blagojević[1], Sanja Djurdjić Mijin[1,2], Andrijana Šolajić[1], Jelena Pešić[1], Emil S. Bozin[1], Bojana Višić[1,3], Yu Liu[4,5], Cedomir Petrovic[4,6,7,8], Zoran V. Popović[9], Rudi Hackl[10,11], Ana Milosavljević[1,*], and Nenad Lazarević[1]**

[1]Center for Solid State Physics and New Materials, Institute of Physics Belgrade, Pregrevica 118, 11080 Belgrade, Serbia
[2]Departamento de Física de Materiales, Facultad de Ciencias, Universidad Autónoma de Madrid, 28049 Madrid, Spain
[3]Department of Condensed Matter Physics, Jozef Stefan Institute, Jamova cesta 39, Ljubljana 1000, Slovenia
[4]Shanghai Advanced Research in Physical Sciences (SHARPS), Shanghai 201203, China
[5]Center for Correlated Matter and School of Physics, Zhejiang University, Hangzhou 310058, People's Republic of China
[6]Center for High Pressure Science & Technology Advanced Research (HPSTAR) - Beijing 100094, China
[7]Condensed Matter Physics and Materials Science Department, Brookhaven National Laboratory, Upton, NY 11973-5000, USA
[8]Department of Nuclear and Plasma Physics, Vinca Institute of Nuclear Sciences, University of Belgrade, Belgrade 11001, Serbia
[9]Serbian Academy of Sciences and Arts, Kneza Mihaila 35, 11000 Belgrade, Serbia
[10]School of Natural Sciences, Department of Physics E51, Technische Universität München, 85748 Garching, Germany
[11]IFW Dresden, Helmholtzstrasse 20, 01069 Dresden, Germany
[*]ana.milosavljevic@ipb.ac.rs

## ABSTRACT

The emergence of phonon frequency combs exemplifies a rare and intriguing phenomenon in quantum solids. Materials with distinctive phonon band structures are especially promising for hosting such states, as their vibrational dispersion landscape across the Brillouin zone can facilitate the formation of long-lived, collective lattice excitations. In the layered Van der Waals compound $InSiTe_3$, polarization-resolved Raman spectroscopy reveals a pronounced anharmonicity in symmetry-predicted modes and the formation of a self-organized frequency domain structure (coherent-like state), in the range of a localized high-energy $A_{1g}$ phonon mode near 500 $cm^{-1}$. This strong phonon-phonon coupling manifests itself as an anomalous temperature dependence around 200 K, coinciding with the appearance of higher-order excitations within the phonon density of states gap. These findings position $InSiTe_3$ as an unconventional platform where intrinsic highly structured phonon spectral correlations and unusually strong anharmonic effects coexist, opening new avenues for exploring emergent vibrational phenomena in low-dimensional materials.

## Introduction

Femtosecond pump–probe spectroscopy has long been the primary tool for generating and studying coherent phonons. In these experiments, an ultrashort laser pulse excites the lattice, initiating collective vibrational motion that can be tracked in real time.[1–4]When a femtosecond laser pulse reshapes the electronic potential, the equilibrium atomic positions are displaced, leaving the atoms to oscillate coherently around the new minimum. This displacive excitation mechanism inherently favors fully symmetric modes. As a result, materials like bismuth and antimony consistently exhibit strong $A_{1g}$ coherent phonons in pump–probe experiments, while lower-symmetry modes appear only under special conditions.[5–7] In contrast, finding equidistant closely separated phonon lines or a phonon comb without femtosecond excitation is unusual and reflects a nonlinear lattice potential.

Layered Van der Waals (VdW) materials, with their quasi–low-dimensional character, provide an important platform for studying emergent lattice, electronic, and magnetic phenomena.[8,9] The class is broad, from transition metal trihalides ($CrI_3$, $VI_3$),[10–14] transition metal trichalcogenides ($CrSiTe_3$, $CrGeTe_3$),[15–18] iron-based tellurides ($Fe_3GeTe_2$)[19] to transition metal

dichalcogenides ($VSe_2$, $MnSe_2$).[20,21] The acceleration in the discovery of such quasi-2D systems provides many opportunities to study phonon correlations and nonlinear phenomena as an intrinsic property of the lattice and at the same time to consider their potential for future applications.[22–25] During the course of this research, Chen *et al.* reported the spontaneous formation of phonon frequency combs in $CrSiTe_3$ and $CrGeTe_3$,[26] emphasizing the growing interest in the vibrational properties of ternary VdW trichalcogenides. These developments further emphasize the relevance of exploring related compounds such as $InSiTe_3$, where nonlinearities of the lattice potential may entail unconventional vibrational dynamics.

The first report of $InSiTe_3$ single-crystal synthesis appeared more than three decades ago.[27] Since then, its related compounds such as $CrSiTe_3$, $CrGeTe_3$, $InGeTe_3$, and $AlSiTe_3$ have been extensively studied, both theoretically and experimentally, for their magnetic, electronic, and vibrational properties.[28–33] By contrast, only a few studies have addressed the fundamental properties of $InSiTe_3$.[28,29,34,35] Nevertheless, it has already been applied in broadband photodetectors with ultrafast response times[36] which makes a deeper understanding of its lattice dynamics particularly relevant. Low-temperature experiments have not been performed on $InSiTe_3$, leaving certain aspects of the physical phenomena below room temperature unexplored.

In this work, we investigate the lattice dynamics of the VdW compound $InSiTe_3$ using temperature-dependent polarization-resolved Raman scattering combined with density functional theory (DFT) calculations. Our study reveals a pronounced anharmonicity and the formation of frequency-domain phonon comb associated with a localized high-energy $A_{1g}$ mode near 500 $cm^{-1}$. This state reflects a frequency-locked spectral response of the $SiTe_3$ tetrahedra, linked to a flat and isolated phonon branch. The temperature-dependent analysis further uncovers anomalous linewidth behavior around 200 K, together with large values of $A_{1g}$ phonon coupling constants. Upon heating to this temperature, broad features emerge in the parallel scattering configuration within the gap of the calculated phonon density of states (PDOS), consistent with overtone excitations. These findings identify $InSiTe_3$ as an important member of the of VdW family and underscore the role of anharmonic interactions in VdW trichalhogenides.

## Results

The Raman measurements were performed on freshly cleaved surfaces. As shown in Fig. 1 scanning electron microscopy (SEM) reveals a flat surface of at least $0.5 \times 0.5$ $mm^2$. The individual maps obtained with energy dispersive spectroscopy (EDS) as displayed on the left hand side of Fig. 1 demonstrate the uniformity of the sample over several tens of microns and corroborate the atomic ratio of In:Si:Te to be 1:1:3. No impurities, contaminations and vacancies could be detected.

For the phonon analysis, the symmetry positions of the atoms in the lattice are relevant. The factor group analysis for the $P\bar{3}1m$ space group (No. 162)[37] yields the symmetry allowed phonons in the center of the Brillouin zone (BZ). The corresponding Raman tensors that govern selection rules are listed in Tab. 1. In our experiment, the plane of incidence is the *ab*-plane, where $|a| = |b|$ and $\measuredangle(a,b) = 120°$. This plane is oriented perpendicular to the optical axis of the spectrometer, so that the light propagates along the *c*-axis. The incident and scattered light polarizations, $\mathbf{e}_i$ and $\mathbf{e}_s$, respectively, lie in the *ab*-plane, with $\mathbf{e}_i \parallel \mathbf{e}_s$ corresponding to $\theta = 0°$ and $\mathbf{e}_i \perp \mathbf{e}_s$ corresponding to $\theta = 90°$. In these two scattering configurations all allowed Raman active modes ($3A_{1g} + 5E_g$) can be observed. The doubly degenerate $E_g$ modes are observable in both parallel and crossed polarizations, whereas the fully symmetric $A_{1g}$ modes vanish in configurations with crossed polarization. In

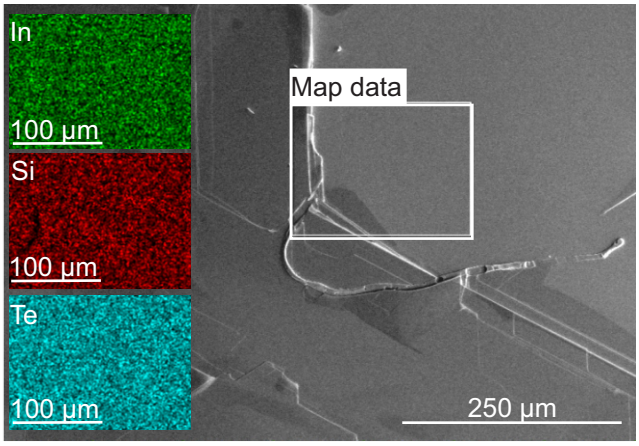


**Figure 1.** SEM and EDS mapping of a freshly cleaved surface of an $InSiTe_3$ single crystal. The right part of the figure shows a flat surface over an extended area. The white rectangle indicates the area in which the EDS mapping was performed. The green, red, and turquoise areas on the left demonstrate the homogeneous distributions of the elements.

**Table 1.** Atoms, Wyckoff positions, related Γ point phonons, and Raman tensors for the $P\bar{3}1m$ space group.

| Atoms (Wyckoff positions) | Irreducible representations |
|---|---|
| In ($2d$) | $A_{2u}+E_u+E_g$ |
| Si ($2e$) | $A_{2u}+E_u+A_{1g}+E_g$ |
| Te ($6k$) | $2A_{2u}+3E_u+2A_{1g}+3E_g$ |

Raman tensors

$$A_{1g}=\begin{pmatrix} a & 0 & 0\\ 0 & a & 0\\ 0 & 0 & b\end{pmatrix}$$

$$^1E_g=\begin{pmatrix} c & 0 & 0\\ 0 & -c & d\\ 0 & d & 0\end{pmatrix} \qquad ^2E_g=\begin{pmatrix} 0 & -c & -d\\ -c & 0 & 0\\ -d & 0 & 0\end{pmatrix}$$

**Table 2.** Phonon symmetry, activity, experimental (80 K) and theoretical phonon frequencies (0 K) calculated using experimental crystallographic data. All values are given in $cm^{-1}$. Silent modes are indicated by an asterisk.

| Space group: $P\bar{3}1m$ (No. 162) | | | | |
|---|---|---|---|---|
| Even ($g$) | | | Odd ($u$) | |
| Symmetry | Exp. | Calc. | Symmetry | Calc. |
| $A_{2g}^{(1)*}$ | - | 25.5 | $A_{2u}^{(1)}$ | 0 |
| $E_g^{(1)}$ | 58.5 | 57.7 | $E_u^1$ | 0 |
| $E_g^{(2)}$ | - | 77.0 | $A_{2u}^{(2)}$ | 67.1 |
| $E_g^{(3)}$ | 107.8 | 100.0 | $E_u^{(2)}$ | 69.1 |
| $A_{1g}^{(1)}$ | 113.4 | 108.4 | $A_{1u}^{(1)*}$ | 89.9 |
| $A_{2g}^{(2)*}$ | - | 118.2 | $E_u^{(3)}$ | 92.1 |
| $E_g^{(4)}$ | 124.9 | 123.8 | $E_u^{(4)}$ | 111.9 |
| $A_{1g}^{(2)}$ | 148.3 | 145.5 | $A_{2u}^{(3)}$ | 154.1 |
| $E_g^{(5)}$ | - | 360.4 | $A_{2u}^{(4)}$ | 239.4 |
| $A_{1g}^{(3)}$ | 498.0 | 486.4 | $E_u^{(5)}$ | 360.1 |

addition to the experiments, density-functional theory (DFT) calculations were performed. The resulting frequencies of the optical phonons are in good agreement with the experimental values obtained at 80 K, as summarized in Tab. 2.

Representative Raman spectra of $InSiTe_3$ at 80 K and 300 K obtained for both parallel ($\theta = 0°$) and crossed ($\theta = 90°$) polarization configurations are shown in Fig. 2 (a) and (b), respectively. All three $A_{1g}$ modes and three out of the five expected $E_g$ modes appear as narrow lines. At 80 K the Raman spectrum in parallel scattering configuration [Fig. 2 (a)] reveals two extra peaks in the energy range 450 to 500 $cm^{-1}$ labeled as $A_{1g}^{(3'')}$ and $A_{1g}^{(3')}$. Although weak in intensity, they are still distinctly observable on the low-energy side of the Raman-active $A_{1g}^{(3)}$ mode. These additional two peaks and the $A_{1g}^{(3)}$ phonon are equidistant and persist up to high temperatures, although they cannot be resolved any further as separate lines [Fig. 2 (b) and Fig. 6]. As seen in Fig. 2(b), at 300 K additional excitations are observed in the parallel scattering configuration, appearing

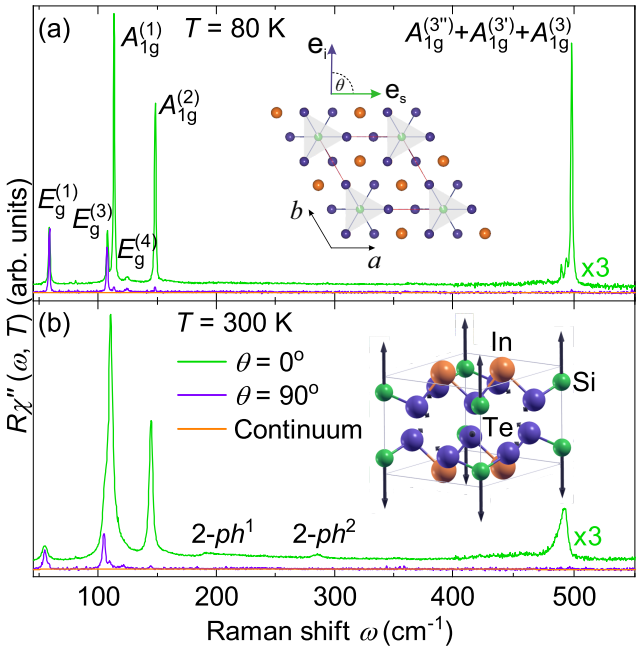


**Figure 2.** Raman spectra of $InSiTe_3$ in parallel ($\theta = 0°$) and cross ($\theta = 90°$) polarization configurations at (a) 80 K and (b) 300 K. The orange lines represent the phenomenological continua (see text). Inset of (a) $InSiTe_3$ crystallographic unit cell with vectors of incident and scattered light polarizations $\mathbf{e}_i$ and $\mathbf{e}_s$, respectively. For symmetry reasons the orientation of the polarizations with respect to the crystal axes $a$ and $b$ is irrelevant. Inset of (b) displacement pattern of $A_{1g}^{(3)}$ mode. The arrow lengths are proportional to the square root of the inter-atomic forces. For this mode only the Si atoms move.

slightly below 200 $cm^{-1}$ and 300 $cm^{-1}$.

For the quantitative analysis, the phonon peaks were modeled using a Voigt line shape, defined as the convolution of a Lorentzian and a Gaussian function. The Gaussian component, which accounts for the instrumental resolution of the spectrometer, was fixed to a linewidth of $\Gamma_G = 1$ $cm^{-1}$. To this end, the continuum was modeled phenomenologically using a Drude function together with a linear term: $\chi''_{\text{continuum}}(\omega) \propto A\Gamma\omega/(\omega^2+\Gamma^2)+B\omega$ (orange lines in Fig. 2) and was subtracted from the raw data, where $A$, $B$, and $\Gamma$ are temperature dependent phenomenological parameters. The resulting continuum is very weak and essentially constant within the phonon energy range. Fig. 3 displays the results of the phonon analysis in parallel scattering configuration at 80 K.

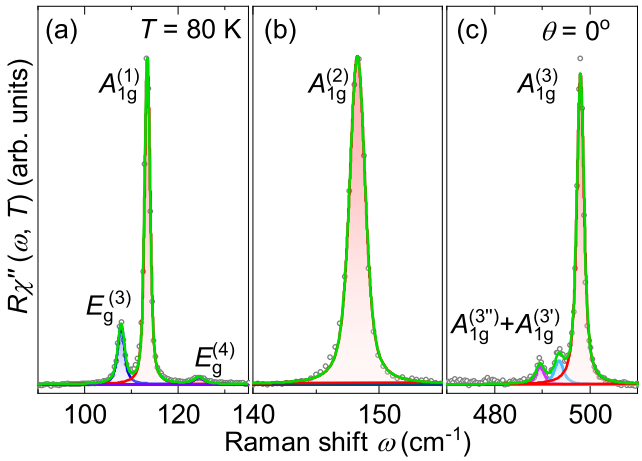


**Figure 3.** (a)-(c) Phonon excitations modeled with Voigt profiles in parallel ($\theta = 0°$) polarization configuration where phonons of both $A_{1g}$ and $E_g$ symmetry are observed. The spectra are recorded at 80 K.

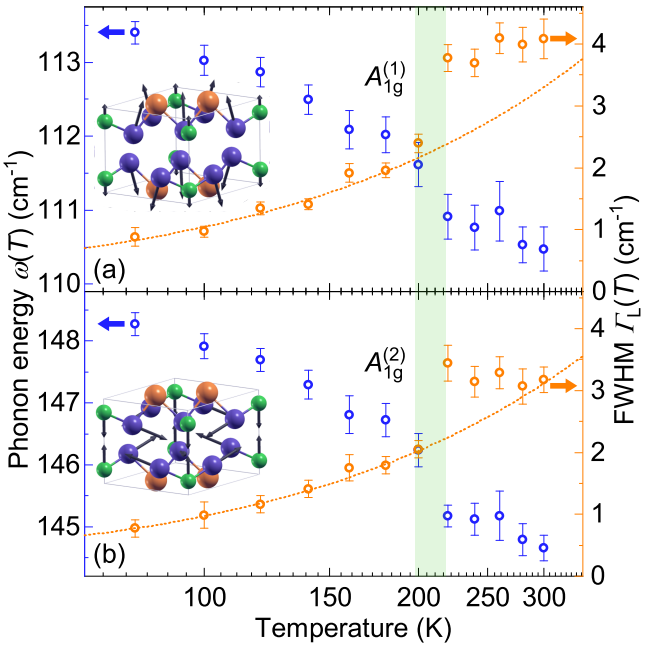


**Figure 4.** Temperature dependences of the energies and Lorentzian linewidths of the $A_{1g}^{(1)}$ and $A_{1g}^{(2)}$ phonons. There are discontinuities of both the energies and linewidths close to 200 K. The dashed lines represent fits to the data below 200 K. The linewidths and energies are well described by anharmonic phonon decay (Eq. 1) and thermal expansion, respectively.

We first focus on the low-lying $A_{1g}$ modes, labeled $A_{1g}^{(1)}$ and $A_{1g}^{(2)}$. The temperature dependencies of their energies and linewidths are displayed in Fig. 4, with the vibration patterns shown in insets. For describing the linewidths, we use the Klemens model of symmetric anharmonic decay,[38]

$$\Gamma_{\mathrm{L}}(T) = \Gamma_{\mathrm{L}}(0)\left(1 + \frac{2\lambda_{\mathrm{ph-ph}}}{\frac{\hbar\omega_0}{e^{2k_{\mathrm{B}}T}} - 1}\right), \tag{1}$$

where $\Gamma_{\mathrm{L}}(0)$ and $\omega_0$ were obtained by extrapolating linewidths and energies to the zero temperature limit. The phonon-phonon coupling parameter $\lambda_{\mathrm{ph-ph}}$ parametrizes the interaction between the optical (here Raman-active) phonon and the acoustical modes at $\pm\mathbf{k}$ and $\hbar\omega/2$. The interaction may be mediated by electrons, spins or fluctuations.

At low temperatures $A_{1g}^{(1)}$ and $A_{1g}^{(2)}$ exhibit linewidths in the range of $\Gamma_L < 1$ cm$^{-1}$ providing further evidence of the excellent crystal quality. Across the measured temperature range, the linewidths of $A_{1g}^{(1)}$ and $A_{1g}^{(2)}$ increase nearly by a factor of four. Up to 200 K the linewidths are well described by the symmetric anharmonic decay as described by Klemens[38] and described in Eq. 1. The temperature dependence indicates strong phonon–phonon coupling beyond 1, $\lambda_{\mathrm{ph-ph}}\left(A_{1g}^{(1)}\right) = 1.6$ and $\lambda_{\mathrm{ph-ph}}\left(A_{1g}^{(2)}\right) = 1.7$.[39] In both cases, the next data points at 220 K is offset by more than a wavenumber, well beyond the statistical uncertainty. Up to room temperature the linewidths are essentially temperature independent. A similar (and consistent) discontinuity is observed for the energies. The cause of these discontinuities is presently unresolved, with no phase transition reported in this temperature range to the best of our knowledge.

Even so, the Raman spectra in the range between 80 cm$^{-1}$ and 350 cm$^{-1}$ exhibit an intensity anomaly in the same temperature range as shown in Fig. 5. New features at 200 cm$^{-1}$ and 280 cm$^{-1}$ emerge with increasing temperature. Between 80 and 200 K these broad structures gain intensity slowly and gradually, while they double in intensity between 200 and 220 K and then remain constant up to 300 K. Upon inspecting the phonon dispersion and density of states (PDOS) (see inset of Fig. 5) we conclude that these bands derive from the relatively flat bands in the range of 100 cm$^{-1}$ and the nearly dispersionless band slightly below 150 cm$^{-1}$, mainly deriving from Te vibrations, and may be identified as 2-phonon excitations in the gaps of the phonon bands. Since these 2-phonon bands derive from phonons with energies on the scale of the thermal energy (140 cm$^{-1}$ $\approx$ 200 K), one may speculate that thermally excited quasiparticles mediate an enhanced coupling between the low-energy Te modes. Then, the $A_{1g}^{(1)}$ and $A_{1g}^{(2)}$ Raman modes which just probe this increased coupling get more damped, and

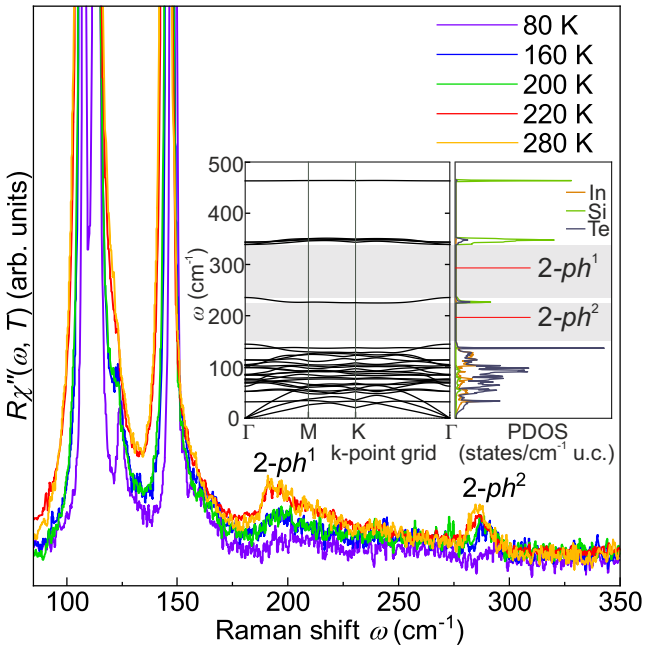


**Figure 5.** Raman spectra in the range between 80 cm$^{-1}$ and 350 cm$^{-1}$ at temperatures as indicated. The overtone excitations increase abruptly between 200 and 220 K in intensity. Inset: Calculated phonon dispersion along the high-symmetry directions as indicated and PDOS. The shaded area marks the gap in the PDOS.

the linewidths increase while the energies decrease. Similar as for the Raman-active phonons, the coupling of all other modes increases across the entire Brillouin zone and boosts the two-phonon DOS. This electron-mediated coupling scenario would be consistent with the absence of any signature in the structure.

The three equidistant lines in the range of the $A_{1g}^{(3)}$ mode predicted by DFT are fitted with Voigt profiles and shown in Fig. 3. In Fig. 6 they are presented on an expanded energy scale for more temperatures, both along with Voigt profiles and the frequency combs model to be described below. DFT calculations suggest that the $A_{1g}^{(3)}$ mode is an Einstein phonon with only Si atoms involved far above all other lines (see inset of Fig. 5). However, instead of an isolated line we observe three equidistant lines in the energy range of the $A_{1g}^{(3)}$ mode. All three $A_{1g}^{(3)}$ peaks move to lower energy with increasing temperature. While the distances between the modes are essentially temperature independent, the widths increase substantially. Above 200 K the lines cannot be resolved as separate lines in the spectra but only via the fitting procedure (see Fig. 6). When the resulting linewidths and energies are plotted as a function of temperature, no anomalies can be observed, as shown in Fig. 7.

The temperature dependences of all modes are well described by the Klemens model [Fig. 7(b)–(d)]. The linewidths increase by almost a factor of three over the investigated temperature range. The resulting phonon–phonon coupling parameters, $\lambda_{\mathrm{ph-ph}}\left(A_{1g}^{(3)}\right) = 2.8$, $\lambda_{\mathrm{ph-ph}}\left(A_{1g}^{(3')}\right) = 2.5$, and $\lambda_{\mathrm{ph-ph}}\left(A_{1g}^{(3'')}\right) = 2.8$, are exceptionally large but consistent with the values found recently for phonon combs in $CrSiTe_3$.[26] The absolute magnitude of $\lambda_{\mathrm{ph-ph}}$ is not universal and may, in addition to the specific decay channels of the Klemens model, depend on the lattice potential, particularly at high temperature, or even on other decay channels.[39–42] As a matter of fact, the lines become very narrow already at 80 K, the lowest temperature accessible in our experiment, indicating strongly reduced damping. Simultaneously, the lines in the comb become discernible and gain intensity.

On the basis of the increasing intensity and the equidistance of these lines, we employ a coherent-state formalism as a spectral description of the observed frequency-domain features to our spectra as proposed by Chen and coworkers.[26] Coherent states proposed first by Schrödinger[43] are widely used as a mathematical framework in superconductivity and laser physics to describe the superposition of a large number of oscillators. In the present context, this approach provides an effective description of the frequency components observed in the Raman spectra but does not imply the existence of a time-dependent coherent phonon expectation value in thermal equilibrium. Rather, it implies the simultaneous excitation of several oscillators[44] having a very long lifetime. This coherent state is described by an infinite superposition of oscillators,

$$|\langle x\rangle_\omega|^2 = (2\pi)^2 e^{-2|\alpha_0|^2} \sum_{n=0}^{\infty} \frac{|\alpha_0|^{4n+2}}{(n!)^2} [\delta(\omega' - \omega + A + An) + \delta(\omega' - \omega + A - An)], \tag{2}$$

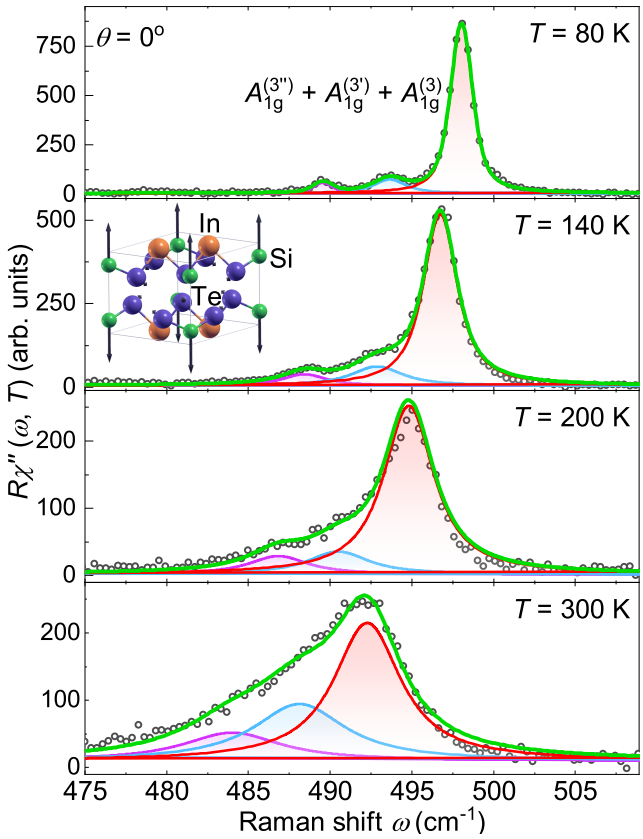


**Figure 6.** Raman spectra in the range of the $A_{1g}^{(3)}$ mode at temperatures as indicated. The solid lines represent a Voigt profile fit to the data. All lines become wider with increasing temperature and shift simultaneously to lower energies while maintaining the distance. Inset: Localized vibrations of Te in the $SiTe_3$ tetrahedra associated to the $A_{1g}^{(3)}$ mode.

where $|\alpha_0|$ represents an effective parameter controlling the relative weight of the frequency components in the coherent-state-based spectral description. $A$ is proportional to the degree of anharmonicity $\lambda^2$ in the Hamiltonian (See Supplementary Material). Eq. 2 provides the intensity of the frequency components and describes the distribution of the discrete frequencies $\omega' = \omega - A - An$ and $\omega' = \omega - A + An$. To apply this model to describe our data, we replaced the Dirac delta with a Lorentzian having a finite linewidth (convoluted with a Gaussian for the resolution). The extracted energies and linewidths obtained from both the empirical fit and the applied model were nearly identical to within the error margins. A detailed comparison between the two approaches is presented in Fig. 8.

## Discussion

Coherent optical phonons are typically induced by ultrashort pump pulses. They oscillate in phase and produce distinct signatures in optical and Raman spectra.[45] However, equilibrium Raman spectroscopy probes frequency-domain phonon correlations. If the lattice potential has sufficiently strong anharmonic contributions and the phonons are long-lived, coherent-like spectral responses may arise in the absence of ultrafast excitation.[26]

In the case of $InSiTe_3$, the only phonon expected in the energy range around 500 cm$^{-1}$ is a motion of the Si atoms with a negligible involvement of the $SiTe_3$ tetrahedra (Inset of Fig. 6). DFT predicts an isolated high-energy Einstein phonon as shown in the Inset of Fig. 5. However, instead of a single isolated line a series of equidistant peaks is observed in the Raman spectra (Fig. 6), reflecting the underlying nonlinear lattice dynamics. Phonon frequency combs have recently been reported in $CrSiTe_3$ and $CrGeTe_3$.[26] The comb-like structure was associated with the nonlinear response of a high-energy optical phonon that is spectrally well separated from other phonon states. In $InSiTe_3$, the $A_{1g}^{(3)}$ mode is separated by a sufficiently large gap in PDOS. Because of this spectral isolation, the mode remains long-lived, as the available decay channels are strongly limited. As a consequence equidistant spectral components emerge.

An alternative explanation for persistent equidistant peak structure may be thermal "hot-band" progression arising from anharmonic vibrational ladders. For an anharmonic potential in second order perturbation theory we get relatively closely

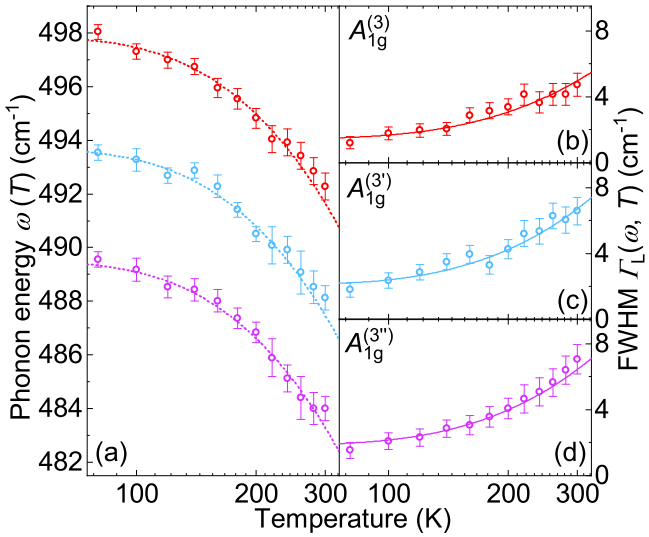


**Figure 7.** Temperature dependences of energies and linewidths of the $A_{1g}^{(3)}$ mode and its satellites, $A_{1g}^{(3'')}$ and $A_{1g}^{(3')}$ derived from three independent Voigt lineshapes. The equidistant colored dotted lines in (a) represent guide to the eye, with the theoretical difference of 4.2 $cm^{-1}$ of neighboring peaks. Solid lines in (b) represent the fit of the linewidth data to the anharmonic model (Eq. 1).

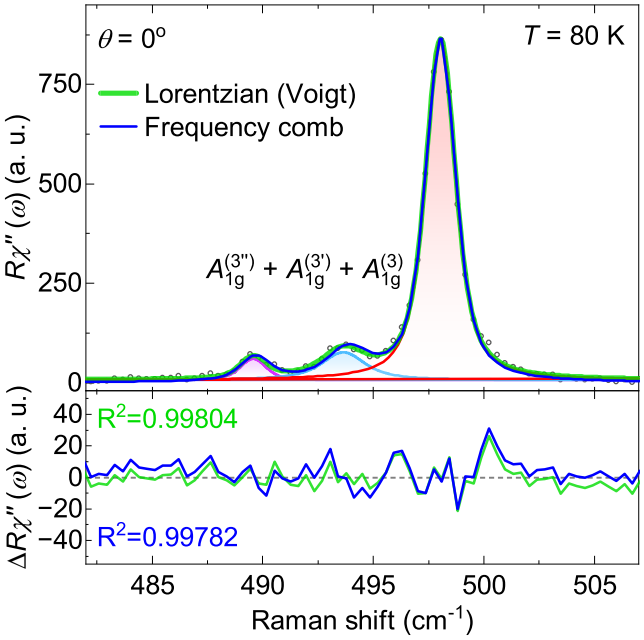


**Figure 8.** Comparison of coherent-state–based spectral model and individual line model. At 80 K the statistical quality of the frequency comb is only marginally below that of the combination of the three individual lines. (see also Fig. 6 and Supplementary).

spaced energies at distances $\Delta\omega$. The intensity of the $n$-th satellite is expected to scale as $I_n/I_0 \propto \exp(-(\hbar\omega - n\hbar\Delta\omega)/k_BT)$, where $\omega = 498.0$ $cm^{-1}$ corresponds to the energy of the $A_{1g}^{(3)}$ phonon ($n = 0$) at 80 K, and $\Delta\omega = 4.2$ $cm^{-1}$. As shown in Supplementary Fig. S1, the experimentally observed temperature dependences of the sattellites at 493.8 $cm^{-1}$ ($n = 1$) and 489.6 $cm^{-1}$ ($n = 2$) deviate strongly from this expectation. This discrepancy allows us to exclude a thermal hot-band origin of the observed phonon frequency comb.

In addition, mechanisms based on the thickness or layer dependent quantization can be excluded in the present case.

All Raman measurements reported here were performed on bulk single crystals, where the macroscopic sample dimensions prevent the formation of discrete low-energy standing acoustic modes associated with finite-size confinement. In such confined geometries, the characteristic mode spacing is expected to scale with sample thickness or number of layers. No such dependence is observed here.

The satellite peaks observed in $InSiTe_3$ are not related to phonon beating either. Phonon beating requires the coexistence of multiple distinct phonon modes with closely spaced frequencies, as demonstrated, for example, for the $A_{1g}$ modes in $Cd_3As_2$ induced by helix vacancies.[46] In contrast, for $InSiTe_3$ one expects a single isolated $A_{1g}^{(3)}$ optical phonon branch (Fig. 6) with no nearby modes that could give rise to beating. The observed satellites therefore originate from the nonlinear lattice potential leading to additional eigenstates in second order perturbation theory[26] rather than independent phonon excitations.

In $Cr_2Ge_2Te_6$ comb-like structures in the phonon spectra were observed recently and interpreted in terms isotope shifts.[47] In $InSiTe_3$, the isotope satellites were to be expected at 9 $cm^{-1}$ and 17 $cm^{-1}$ below the main line at 500 $cm^{-1}$ as opposed to 4.2 and 8.4 $cm^{-1}$ here, and their intensities and linewidths exhibit a systematic temperature evolution different from that expected for isotopes.

Finally, we wish to address the dilemma of the strong phonon-phonon coupling of the 500 $cm^{-1}$ modes derived via the Klemens model (Eq. 1), suggesting a rapid decay, and the long lifetime required for phase coherence. As already pointed out above symmetric decay is not the only mechanism for line broadening. In an anharmonic potential the lines may get broader also by a stronger shift of a the resonance frequencies at elevated temperatures and a superposition of lines at different energies. At low temperatures there are barely any channels for the isolated Einstein mode (and possible satellites) to decay into low-energy phonons as obvious from the DFT phonon dispersion (Inset of Fig. 5). The separation from the continuum of other vibrational states by a sufficiently large gap in the PDOS quenches all decay channels for symmetric decay. We conclude that the distortion of the harmonic potential required for the formation of the observed frequency comb does not originate from the anharmonic decay of the Einstein-like mode.

The temperature dependences of the fully symmetric low-energy peaks, $A_{1g}^{(1)}$ and $A_{1g}^{(2)}$, change discontinuously in the vicinity of 200 K (Fig. 4). Specifically the line widths do not follow the expected anharmonic variation any longer, indicating a change in phonon–phonon coupling. Along with these discontinuities at 200 K, two-phonon excitations (see Fig. 5) become more pronounced. In the Raman spectra, structures beyond the allowed lines may originate either from defect-induced scattering, in which case the spectral features follow a projected PDOS, or from interactions in the material.[39] A comparison of the spectra with the calculated PDOS, in addition to the SEM analysis allow us to rule out the defect scenario. The fact that the two-phonon excitations appear exclusively in the $A_{1g}$ channel is consistent with the selection rules for two-phonon scattering, where the direct product of two phonon symmetries always contains the totally symmetric representation.[39] The unusually strong coupling of the $A_{1g}$ modes in $InSiTe_3$ further enhances multi-phonon scattering in this channel, making the overtone features particularly pronounced. As the thermal phonon population and electron occupation increase, these higher-order processes become more probable and the overtones emerge clearly within the PDOS gap. By comparing their positions with the calculated phonon dispersion, the two-phonon features can be linked to low-energy PDOS maxima at roughly half the energies of 2-$ph^1$ and 2-$ph^2$ ($\approx 95$ and $\approx 145$ $cm^{-1}$, respectively), indicating contributions from acoustic or low-lying optical branches (Inset of Fig. 5).

These observations reveal that the lattice dynamics of $InSiTe_3$ are dominated by strong phonon–phonon interactions and give rise to pronounced anomalies near 200 K. Although a microscopic model for these features is still lacking, we propose that the thermal population of phononic and electronic states in this narrow-gap semiconductor drives these interactions. The appearance of overtone excitations within a PDOS gap supports this interpretation. The formation of a frequency comb, generated by coherent-like phonons and persisting across the full temperature range studied, suggests that the well-isolated Einstein phonon in $InSiTe_3$ plays a central role in stabilizing highly structured vibrational spectrum. Together with recent reports of coherent-like phonon states in $CrSiTe_3$ and $CrGeTe_3$,[26] our findings position Van der Waals trichalcogenides as promising platforms for discovering frequency combs in phonon spectra.

## Methods

### Experimental methods

Single crystals of $InSiTe_3$ were synthesized by melting stoichiometric mixture of In (5N, Alfa Aesar) chunk, Si (5N, Alfa Aesar) lump, and Te (5N, Alfa Aesar) shot. The starting materials were vacuum-sealed in a quartz tube, heated to 1100°C over 20 hours, held at 1100°C for 12 hours and then cooled to 700°C at rate of 1°C/h.

Scanning electron microscopy was performed using FEI HeliosNanolab 650 scanning electron microscope (SEM) equipped with an Oxford Instruments energy dispersive spectroscopy (EDS) system with an X-max SSD detector operating at 20 kV. Measurements were performed on as-cleaved samples deposited on a graphite tape. To determine the presence of different elements, an area about the size of 100 $\times$ 100 $\mu$m was selected on the deposited material where the EDS analysis was performed.

Inelastic scattering measurements of $InSiTe_3$ were conducted using Tri Vista 557 Raman spectrometer in the subtractive backscattering configuration, with the combination of gratings 1800/1800/2400 grooves/mm. As an excitation source $Ar^+/Kr^+$ ion laser with 514 nm line was used. In this scattering configuration plane of incidence is *ab* plane ($|a| = |b|$, $\measuredangle(a,b) = 120°$) with incident/scattered light propagation direction along crystallographic *c*-axis. The samples were cleaved right before being placed in a high vacuum ($10^{-6}$ mbar), which was achieved with a KONTI CryoVac continuous Helium Flow cryostat with 0.5 mm thick window. Laser beam focusing was accomplished using microscope objective with $\times 50$ magnification to a spot size of approximately $8\,\mu$m. All Raman spectra were corrected for the Bose factor.

### Theoretical methods

First-principles calculations based on density functional theory (DFT) were carried out using the Quantum ESPRESSO package.[48] The Perdew–Burke–Ernzerhof revised for solids (PBEsol) exchange-correlation functional[49] within the generalized gradient approximation (GGA) was employed to better describe lattice parameters in crystalline solids. The cutoff for wavefunctions and the charge density were set to 50 Ry and 400 Ry, respectively. The *k*-points were sampled using the Monkhorst-Pack scheme, on a $12\times12\times12$ $\Gamma$ - centered grid. For accurate treatment of interlayer interactions, the Van der Waals interactions is included using the Grimme-D2 correction. Phonon frequencies were calculated with the linear response method, as implemented in Phonon package of the Quantum Espresso. The initial atomic structure of $InSiTe_3$ was obtained from an experimental CIF file and used as the starting point for first-principles calculations. According to experimental crystallographic data, $InSiTe_3$ exhibits trigonal symmetry and belongs to the $P\bar{3}1m$ (No. 162) space group. All calculations correspond to the harmonic approximation at zero temperature and do not include anharmonic or finite-temperature effects.

## Data availability

Data are available upon reasonable request from the corresponding author.

## References


1. Zeiger, H. J. *et al.* Theory for displacive excitation of coherent phonons. *Phys. Rev. B* **45**, 768–778, 10.1103/PhysRevB.45.768 (1992).
2. Vialla, F. & Fatti, N. D. Time-Domain Investigations of Coherent Phonons in van der Waals Thin Films. *Nanomaterials* **10**, 10.3390/nano10122543 (2020).
3. Misochko, O. V. Coherent phonons and their properties. *J. Exp. Theor. Phys.* **92**, 246–259, 10.1134/1.1354682 (2001).
4. Melnikov, A. A., Selivanov, Y. G. & Chekalin, S. V. Anharmonic coherent dynamics of the soft phonon mode of a PbTe crystal. *Phys. Rev. B* **108**, 224309, 10.1103/PhysRevB.108.224309 (2023).
5. Ishioka, K., Kitajima, M. & Misochko, O. V. Coherent $A_{1g}$ and $E_g$ phonons of antimony. *J. Appl. Phys.* **103**, 123505, 10.1063/1.2940130 (2008).
6. Ishioka, K., Kitajima, M. & Misochko, O. V. Temperature dependence of coherent $A_{1g}$ and $E_g$ phonons of bismuth. *J. Appl. Phys.* **100**, 093501, 10.1063/1.2363746 (2006).
7. Garrett, G. A., Albrecht, T. F., Whitaker, J. F. & Merlin, R. Coherent THz Phonons Driven by Light Pulses and the Sb Problem: What is the Mechanism? *Phys. Rev. Lett.* **77**, 3661–3664, 10.1103/PhysRevLett.77.3661 (1996).
8. Lazarević, N. & Hackl, R. Fluctuations and pairing in Fe-based superconductors: light scattering experiments. *J. Physics: Condens. Matter* **32**, 413001, 10.1088/1361-648X/ab8849 (2020).
9. Wang, Q. H. *et al.* The Magnetic Genome of Two-Dimensional van der Waals Materials. *ACS Nano* **16**, 6960–7079, 10.1021/acsnano.1c09150 (2022). PMID: 35442017.
10. Liu, Y. & Petrovic, C. Three-dimensional magnetic critical behavior in $CrI_3$. *Phys. Rev. B* **97**, 014420, 10.1103/PhysRevB.97.014420 (2018).
11. Huang, B. *et al.* Layer-dependent ferromagnetism in a van der Waals crystal down to the monolayer limit. *Nature* **546**, 270–273, 10.1038/nature22391 (2017).
12. Wang, Y.-P. & Long, M.-Q. Electronic and magnetic properties of van der Waals ferromagnetic semiconductor $VI_3$. *Phys. Rev. B* **101**, 024411, 10.1103/PhysRevB.101.024411 (2020).
13. Djurdjić Mijin, S. *et al.* Short-Range Order in $VI_3$. *Inorg. Chem.* **59**, 16265–16271, 10.1021/acs.inorgchem.0c02060 (2020).

**14.** Djurdjić Mijin, S. *et al.* Lattice dynamics and phase transition in $CrI_3$ single crystals. *Phys. Rev. B* **98**, 104307, 10.1103/PhysRevB.98.104307 (2018).

**15.** Ouvrard, G., Sandre, E. & Brec, R. Synthesis and crystal structure of a new layered phase: The chromium hexatellurosilicate $Cr_2Si_2Te_6$. *J. Solid State Chem.* **73**, 27–32, 10.1016/0022-4596(88)90049-7 (1988).

**16.** Zhang, X. *et al.* Magnetic anisotropy of the single-crystalline ferromagnetic insulator $Cr_2Ge_2Te_6$. *Jpn. J. Appl. Phys.* **55**, 033001, 10.7567/jjap.55.033001 (2016).

**17.** Milosavljević, A. *et al.* Evidence of spin-phonon coupling in $CrSiTe_3$. *Phys. Rev. B* **98**, 104306, 10.1103/PhysRevB.98.104306 (2018).

**18.** Milosavljević, A. *et al.* Vacancies and spin–phonon coupling in $CrSi_{0.8}Ge_{0.1}Te_3$. *J. Raman Spectrosc.* **51**, 2153–2160, 10.1002/jrs.5962 (2020).

**19.** Fei, Z. *et al.* Two-dimensional itinerant ferromagnetism in atomically thin $Fe_3GeTe_2$. *Nat. Mater.* **17**, 778–782, 10.1038/s41563-018-0149-7 (2018).

**20.** Bonilla, M. *et al.* Strong room-temperature ferromagnetism in $VSe_2$ monolayers on van der Waals substrates. *Nat. Nanotechnol.* **13**, 289–293, 10.1038/s41565-018-0063-9 (2018).

**21.** O'Hara, D. J. *et al.* Room Temperature Intrinsic Ferromagnetism in Epitaxial Manganese Selenide Films in the Monolayer Limit. *Nano Lett.* **18**, 3125–3131, 10.1021/acs.nanolett.8b00683 (2018).

**22.** Sierra, J. F., Fabian, J., Kawakami, R. K., Roche, S. & Valenzuela, S. O. Van der Waals heterostructures for spintronics and opto-spintronics. *Nat. Nanotechnol.* 10.1038/s41565-021-00936-x (2021).

**23.** Yang, S., Zhang, T. & Jiang, C. van der Waals Magnets: Material Family, Detection and Modulation of Magnetism, and Perspective in Spintronics. *Adv. Sci.* **8**, 2002488, 10.1002/advs.202002488 (2021).

**24.** Glavin, N. R. *et al.* Emerging Applications of Elemental 2D Materials. *Adv. Mater.* **32**, 1904302, 10.1002/adma.201904302 (2020).

**25.** Khan, K. *et al.* Recent advances in two-dimensional materials and their nanocomposites in sustainable energy conversion applications. *Nanoscale* **11**, 21622–21678, 10.1039/C9NR05919A (2019).

**26.** Chen, L. *et al.* Spontaneously formed phonon frequency combs in van der Waals solid $CrGeTe_3$ and $CrSiTe_3$. *Nat. Commun.* **16**, 5795, 10.1038/s41467-025-61173-7 (2025).

**27.** E. Sandre and V. Carteaux and A.M. Marie and G. Ouvrard. ChemInform Abstract: A New Lamellar Tellurosilicate, $InSiTe_3$. *ChemInform* **23**, 10.1002/chin.199234029 (1992).

**28.** Korkmaz, M. A., Deligoz, E. & Ozisik, H. Strong Elastic Anisotropy of Low-Dimensional Ternary Compounds: $InXTe_3$ (X = Si, Ge). *J. Electron. Mater.* **50**, 2779–2788, 10.1007/s11664-021-08784-0 (2021).

**29.** Lefevre, R. *et al.* Layered tellurides: Stacking faults induce low thermal conductivity in the new $In_2Ge_2Te_6$ and thermoelectric properties of related compounds. *J. Mater. Chem. A* **5**, 19406–19415, 10.1039/C7TA04810F (2017).

**30.** E. Sandre and V. Carteaux and A.M. Marie and G. Ouvrard. Structural determination of a new lamellar tellurosilicate, $AlSiTe_3$. *J. Alloy. Compd.* **204**, 145–149, 10.1016/0925-8388(94)90083-3 (1994).

**31.** Casto, L. D. *et al.* Strong spin-lattice coupling in $CrSiTe_3$. *APL Mater.* **3**, 041515, 10.1063/1.4914134 (2015).

**32.** Bhoi, D. *et al.* Nearly Room-Temperature Ferromagnetism in a Pressure-Induced Correlated Metallic State of the van der Waals Insulator $CrGeTe_3$. *Phys. Rev. Lett.* **127**, 217203, 10.1103/PhysRevLett.127.217203 (2021).

**33.** Watson, M. D. *et al.* Direct observation of the energy gain underpinning ferromagnetic superexchange in the electronic structure of $CrGeTe_3$. *Phys. Rev. B* **101**, 205125, 10.1103/PhysRevB.101.205125 (2020).

**34.** Suriwong, T., Kurosaki, K. & Thongtem, S. Thermoelectric properties of phosphorus-doped indium tellurosilicate: $InSiTe_3$. *J. Alloy. Compd.* **735**, 75–80, 10.1016/j.jallcom.2017.11.093 (2018).

**35.** Debbichi, L., Kim, H., Björkman, T., Eriksson, O. & Lebègue, S. First-principles investigation of two-dimensional trichalcogenide and sesquichalcogenide monolayers. *Phys. Rev. B* **93**, 245307, 10.1103/PhysRevB.93.245307 (2016).

**36.** Chen, J. *et al.* A Submicrosecond-Response Ultraviolet–Visible–Near-Infrared Broadband Photodetector Based on 2D Tellurosilicate $InSiTe_3$. *ACS Nano* **16**, 7745–7754, 10.1021/acsnano.1c11628 (2022). PMID: 35499232.

**37.** Jin, Y., Wang, R. & Xu, H. Recipe for Dirac Phonon States with a Quantized Valley Berry Phase in Two-Dimensional Hexagonal Lattices. *Nano Lett.* **18**, 7755–7760, 10.1021/acs.nanolett.8b03492 (2018).

**38.** Klemens, P. G. Anharmonic decay of optical phonons. *Phys. Rev.* **148**, 845–848, 10.1103/PhysRev.148.845 (1966).

**39.** Baum, A. *et al.* Phonon anomalies in FeS. *Phys. Rev. B* **97**, 054306, 10.1103/PhysRevB.97.054306 (2018).

**40.** Kumar, D., Kumar, V., Kumar, R., Kumar, M. & Kumar, P. Electron-phonon coupling, thermal expansion coefficient, resonance effect, and phonon dynamics in high-quality CVD-grown monolayer and bilayer $MoSe_2$. *Phys. Rev. B* **105**, 085419, 10.1103/PhysRevB.105.085419 (2022).

**41.** Tiwari, A. *et al.* Spin-phonon-charge coupling in the two-dimensional honeycomb lattice compound $Ni_2Te_3O_8$. *Phys. Rev. B* **108**, 075113, 10.1103/PhysRevB.108.075113 (2023).

**42.** Poojitha, B., Shaji, A., Badola, S. & Saha, S. Spin–phonon coupling in ferrimagnet spinel $CoMn_2O_4$. *The J. Chem. Phys.* **156**, 184701, 10.1063/5.0087770 (2022).

**43.** Schrödinger, E. Der stetige Übergang von der Mikro-zur Makromechanik. *Naturwissenschaften* **14**, 664–666 (1926).

**44.** Martin, R. M. & Varma, C. M. Cascade Theory of Inelastic Scattering of Light. *Phys. Rev. Lett.* **26**, 1241–1244, 10.1103/PhysRevLett.26.1241 (1971).

**45.** Zhai, Y., Gong, P., Hasaien, J., Zhou, F. & Zhao, J. Coherent phonons in correlated quantum materials. *Prog. Surf. Sci.* **99**, 100761, 0.1016/j.progsurf.2024.100761 (2024).

**46.** Sun, F. *et al.* Coherent helix vacancy phonon and its ultrafast dynamics waning in topological Dirac semimetal $Cd_3As_2$. *Phys. Rev. B* **95**, 235108, 10.1103/PhysRevB.95.235108 (2017).

**47.** Krasucki, G. *et al.* Spin-phonon coupling and isotope-related pseudo-molecule vibrations in layered $Cr_2Ge_2Te_6$ ferromagnet (2025). 2510.01881.

**48.** Giannozzi, P. *et al.* Quantum espresso: a modular and open-source software project for quantum simulations of materials. *J. Phy. Condens. Mat.* **21**, 395502, 10.1088/0953-8984/21/39/395502 (2009).

**49.** Perdew, J. P., Burke, K. & Ernzerhof, M. Generalized Gradient Approximation Made Simple. *Phys. Rev. Lett.* **77**, 3865–3868, 10.1103/PhysRevLett.77.3865 (1996).


## Acknowledgements


Authors are grateful to Vladimir Damljanović for insightful discussions.


## Funding


The authors acknowledge funding provided by the Institute of Physics Belgrade, through a grant from the Ministry of Science, Technological Development and Innovation of the Republic of Serbia, Project F-134 of the Serbian Academy of Sciences and Arts. This research was supported by the Science Fund of the Republic of Serbia, 10925, Dynamics of CDW transition in strained quasi-1D systems - DYNAMIQS. This work has received funding from the European Union's Horzion Europe research and innovation programme under grant agreement No 101185375 (HIP-2D-QM). The collaboration between the Institute of Physics Belgrade and the IFW Dresden was supported by the German Academic Exchange Service (DAAD) through project 57703419 and the Ministry of Science, Technological Development and Innovations of the Republic of Serbia. DFT calculations were performed using computational resources at Johannes Kepler University (Linz, Austria). Materials synthesis was supported by the U.S. DOE-BES, Division of Materials Science and Engineering, under Contract DE-SC0012704 (BNL). Electron microscopy was performed at Jozef Stefan Institute, Ljubljana, Slovenia, under Slovenian Research Agency contract P1-0099. C.P. acknowledges financial support from Shanghai Key Laboratory of MFree, China (No. 22dz2260800) and Shanghai Science and Technology Committee, China (No. 22JC1410300).


## Author contributions statement

A.M., S. Dj. M., T.B., J.B., R.H. and N.L. conducted the Raman experiments and analyzed the results. B.V. performed SEM measurements and analyzed the results. A.Š. and J.P. performed theoretical calculations. Y.L. and C.P. synthesized the sample and analyzed the results. E.S.B. and Z.V.P. analyzed the results. All authors were included in the writing and review of the manuscript.

## Competing interests

The authors declare no competing interests.

# Spin-phonon interaction and short-range order in $Mn_3Si_2Te_6$

S. Djurdjić Mijin,[1] A. Šolajić,[1] J. Pešić,[1,*] Y. Liu,[2,†] C. Petrovic,[2] M. Bockstedte,[3] A. Bonanni,[4] Z. V. Popović,[1,5] and N. Lazarević[1]

[1]*Institute of Physics Belgrade, University of Belgrade, Pregrevica 118, 11080 Belgrade, Serbia*
[2]*Condensed Matter Physics and Materials Science Department, Brookhaven National Laboratory, Upton, New York 11973-5000, USA*
[3]*Institute for Theoretical Physics, Johannes Kepler University Linz, Altenbergerstrasse 69, 4040 Linz, Austria*
[4]*Institute of Semiconductor and Solid-State Physics, Johannes Kepler University Linz, Altenbergerstrasse 69, 4040 Linz, Austria*
[5]*Serbian Academy of Sciences and Arts, Knez Mihailova 35, 11000 Belgrade, Serbia*

(Received 7 September 2022; revised 31 January 2023; accepted 3 February 2023; published 21 February 2023)

The vibrational properties of ferrimagnetic $Mn_3Si_2Te_6$ single crystals are investigated using Raman spectroscopy and density functional theory calculations. Eighteen Raman-active modes are identified, 14 of which are assigned according to the trigonal symmetry. Four additional peaks, obeying the $A_{1g}$ selection rules, are attributed to the overtones. The unconventional temperature evolution of the $A^5_{1g}$ mode self-energy suggests a competition between different short-range magnetic correlations that significantly impact the spin-phonon interaction in $Mn_3Si_2Te_6$. The research provides comprehensive insight into the lattice properties, studies their temperature dependence, and shows arguments for the existence of competing short-range magnetic phases in $Mn_3Si_2Te_6$.

DOI: 10.1103/PhysRevB.107.054309

## I. INTRODUCTION

Layered magnetic van der Waals materials have lately received widespread attention due to their potential application in spintronics, magnetoelectronics, data storage, and biomedicine [1–7]. Recent experimental confirmation of a long-range magnetism persisting down to a monolayer in $CrI_3$ [8] further affirmed these materials as a platform for magneto-optoelectronic devices [9], and as candidates for studying low-dimensional magnetism [10].

$Mn_3Si_2Te_6$ single crystals were first synthesized in 1985 [11]. However, few studies were carried out on this compound since. It was only recently that the attention has shifted to them, mainly through comparisons with quasi-two-dimensional materials, specifically $CrSiTe_3$. The vast majority of recent studies were focused on explaining the magnetism in $Mn_3Si_2Te_6$ and determining its crystal structure. It was revealed that $Mn_3Si_2Te_6$ crystallizes in a trigonal structure described by the $P\bar{3}1c$ (No. 163) space group [11,12]. According to various magnetization studies, $Mn_3Si_2Te_6$ is an insulating ferrimagnetic with Curie temperature $T_c$ between 74 and 78 K [12–15]. First-principles calculations suggested a competition between the ferrimagnetic ground state and three additional magnetic configurations, originating from the antiferromagnetic exchange for the three nearest Mn-Mn pairs [15]. Additionally, both magnetization and diffuse neutron scattering experiments point at the existence of strong spin correlations well above $T_c$, which may be associated with short-range order or to the preserved correlated excitations in the paramagnetic region [12,15].

Here, we present an experimental and theoretical Raman scattering study of $Mn_3Si_2Te_6$ single crystals, with the focus on phonon properties in the temperature range from 80 to 320 K. Out of 18 observed modes, 14 ($5A_{1g} + 9E_g$) are identified and assigned in agreement with the $P\bar{3}1c$ space group. Phonon energies are in a good agreement with the theoretical predictions. Two most prominent Raman modes, $A^4_{1g}$ and $A^5_{1g}$, are used to study the temperature evolution of phonon properties, and reveal three subsequent phase transitions at $T_1 = 142.5$ K, $T_2 = 190$ K, and $T_3 = 285$ K. Furthermore, the $A^5_{1g}$ mode exhibits strong asymmetry, most likely originating from enhanced spin-phonon coupling. Interestingly, the $A^5_{1g}$ phonon line is symmetric in the temperature range $T_1$–$T_2$, while becoming more asymmetric above $T_3$, potentially indicating that the strength of spin-phonon interaction changes with temperature. We speculate that the observed phenomenon, shown in the $A^5_{1g}$ phonon, originates from the shift in dominance between competing magnetic states, that are found to be very close in energy [15].

## II. EXPERIMENTAL AND COMPUTATIONAL DETAILS

The $Mn_3Si_2Te_6$ single-crystal samples used in this study are prepared according to the procedure described in Ref. [12]. The Raman spectra have been obtained with a Tri Vista 557 spectrometer (Teledyne Princeton Instruments, Trenton, NJ, USA) with a 1800/1800/2400 grooves/mm diffraction grating combination in a backscattering configuration. The 514-nm line of a Coherent $Ar^+/Kr^+$ ion laser (Coherent, Santa Clara, CA, USA) is utilized as the excitation source. The direction of the incident (scattered) light coincides with

*Corresponding author: jelena.pesic@ipb.ac.rs
†Present address: Los Alamos National Laboratory, Los Alamos, New Mexico 87545, USA.

 

TABLE I. Wyckoff positions of atoms and their contributions to the Γ-point phonons together with the corresponding Raman tensors for the $P\bar{3}1c$ space group of $Mn_3Si_2Te_6$.

| Space group: $P\bar{3}1c$ | |
|---|---|
| Atoms | Irreducible representations |
| Mn ($2c$) | $A_{2g} + A_{2u} + E_g + E_u$ |
| Mn ($4f$) | $A_{1g} + A_{1u} + A_{2g} + A_{2u} + 2E_g + 2E_u$ |
| Si ($4e$) | $A_{1g} + A_{1u} + A_{2g} + A_{2u} + 2E_g + 2E_u$ |
| Te ($12i$) | $3A_{1g} + 3A_{1u} + 3A_{2g} + 3A_{2u} + 6E_g + 6E_u$ |

Raman tensors

$$A_{1g} = \begin{pmatrix} a & & \\ & a & \\ & & b \end{pmatrix}$$

$$^1E_g = \begin{pmatrix} c & & \\ & -c & d \\ & d & \end{pmatrix} \qquad ^2E_g = \begin{pmatrix} & -c & -d \\ -c & & \\ d & & \end{pmatrix}$$

the crystallographic $c$ axis. Laser-beam focusing is achieved through a microscope objective with 50× magnification. The temperature-dependent Raman scattering measurements have been performed under high vacuum ($10^{-6}$ mbar), with the sample being placed inside of a KONTI CryoVac continuous helium flow cryostat (CryoVac GmbH & Co. KG, Troisdorf, Germany) with a 0.5-mm-thick window. The samples are cleaved in air before being placed into the cryostat. The obtained Raman spectra are corrected by a Bose factor. The spectrometer resolution is comparable to a Gaussian width of 1 $cm^{-1}$.

The calculations are based on the density functional theory (DFT) formalism as implemented in the Vienna *ab initio* simulation package (VASP) [16–19], with the plane-wave basis truncated at a kinetic energy of 520 eV, using the Perdew-Burke-Ernzehof (PBE) exchange-correlation functional [20] and projector augmented-wave (PAW) method [19,21]. The Monkhorst and Pack scheme of $k$-point sampling is employed to integrate over the first Brillouin zone with 12 × 12 × 10 at the Γ-centered grid. The convergence criteria for energy and force have been set to $10^{-6}$ eV and 0.001 eV $Å^{-1}$, respectively. The DFT-D2 method of Grimme is employed for van der Waals (vdW) corrections [22]. The vibrational modes are calculated using density functional perturbation theory implemented in VASP and PHONOPY [23]. Previous DFT results found the energy of the ferrimagnetic state to be well above an eV per Mn below that of the nonmagnetic state [15], thus this configuration is considered in this study.

## III. RESULTS AND DISCUSSION

### A. Polarization measurements

$Mn_3Si_2Te_6$ crystallizes in a trigonal $P\bar{3}1c$ crystal structure [11,12]. The Wyckoff positions of the atoms and their contributions to the Γ-point phonons, together with the corresponding Raman tensors, are listed in Table I. In total, there are 16 Raman-active modes ($5A_{1g} + 11E_g$) and 17 infrared-active modes ($6A_{2u} + 11E_u$). According to the Raman tensors presented in Table I, in our scattering configuration and with

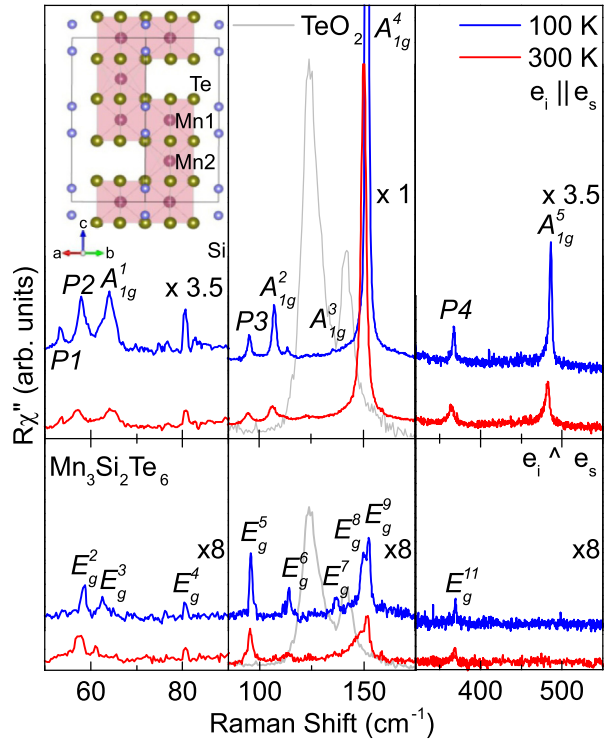


FIG. 1. Raman spectra of $Mn_3Si_2Te_6$ single crystal measured in two scattering geometries at $T = 100$ K (blue solid line) and $T = 300$ K (red solid lines) with incident light being directed along [100]. Peaks observed in both geometries are identified as $E_g$ modes, whereas peaks observed only for the parallel polarization configuration are assigned as $A_{1g}$ modes. Gray line: $TeO_2$ spectrum at 300 K, scaled for clarity. The crystal structure of $Mn_3Si_2Te_6$ viewed laterally along the $c$ axis is presented in the inset.

Raman scattering events within the crystallographic *ab* plane, $E_g$ symmetry modes can be observed in the Raman spectra measured in both parallel and crossed polarization configurations, whereas $A_{1g}$ modes arise only for those in parallel polarization configuration.

As depicted in Fig. 1, nine phonon lines are observed in a parallel polarization configuration only, and identified as $A_{1g}$ symmetry modes. According to the symmetry analysis only five $A_{1g}$ symmetry modes are expected, resulting in four excess modes at 53.3, 57.9, 95.3, and 366.7 $cm^{-1}$. These modes may arise from infrared/silent phonons activated by disorder and from the relaxation of the symmetry selection rules [24–27]. However, it is more likely they are overtones. Overtones, which are always observable in $A$ symmetries, but can also be observed in other symmetries, can become observable in Raman spectra due to disorder and/or enhanced coupling of the phonons to other excitations such as in the case of spin-phonon coupling [28].

Aside from the discussed $A_{1g}$ symmetry modes, our spectra host nine modes which obey the $E_g$ selection rules. Therefore, nine out of the expected 11 $E_g$ modes have been singled out and identified. The absence of two $E_g$ modes might be attributed to their low intensity and/or the finite resolution of the spectrometer.

Calculated and experimental phonon energies are collected in Table II, and are found to be in good agreement with each

TABLE II. Phonon symmetries and phonon frequencies of $Mn_3Si_2Te_6$ phonons. The experimental values are determined at 100 K. All calculations have been performed at zero 0 K. The experimental uncertainty is 0.3 $cm^{-1}$.

| Space group $P\bar{3}1c$ | | | |
|---|---|---|---|
| $n_0$ | Symm. | Expt. ($cm^{-1}$) | Calc. ($cm^{-1}$) |
| 1 | $E_g^1$ | | 53.1 |
| 2 | $P1$ | 53.3 | |
| 3 | $P2$ | 57.9 | |
| 4 | $E_g^2$ | 58.7 | 58.5 |
| 5 | $E_g^3$ | 62.6 | 61.8 |
| 6 | $A_{1g}^1$ | 64.2 | 62.3 |
| 7 | $E_g^4$ | 80.4 | 82.7 |
| 8 | $P3$ | 95.3 | |
| 9 | $E_g^5$ | 95.9 | 90.3 |
| 10 | $A_{1g}^2$ | 107.3 | 104.3 |
| 11 | $E_g^6$ | 114.0 | 106.5 |
| 12 | $A_{1g}^3$ | 135.4 | 134.2 |
| 13 | $E_g^7$ | 136.6 | 136.1 |
| 14 | $E_g^8$ | 149.8 | 143.4 |
| 15 | $A_{1g}^4$ | 151.8 | 147.3 |
| 16 | $E_g^9$ | 152.6 | 146.6 |
| 17 | $E_g^{10}$ | | 352.7 |
| 18 | $P4$ | 366.7 | |
| 19 | $E_g^{11}$ | 368.7 | 354.5 |
| 20 | $A_{1g}^5$ | 486.7 | 475.8 |

other, with the discrepancy being below 8% for all observed modes.

Our data significantly differ from those presented in Ref. [14] where two Raman-active modes were reported, one at 118.4 $cm^{-1}$ and the other at 136.9 $cm^{-1}$, assigned as $E_g$ and $A_{1g}$, respectively. The $E_g$ and $A_{1g}$ modes in our spectra closest (in terms of energy) to those reported in Ref. [14] are the peaks at ∼114.3 and 135.4 $cm^{-1}$ (Table II). Although the discrepancy in phonon energy is not significant, the observed phonon linewidths strongly deviate from those presented in Ref. [14]. A possible explanation for the discrepancy is the presence of $TeO_2$ in samples presented in Ref. [14], as the peaks reported there match rather well with the Raman response of $TeO_2$ (Fig. 1). In order to avoid potential contamination in our study, measurements have been repeated on multiple crystals, and no oxide traces have been identified in the spectra.

### B. Temperature dependence

Some of the modes represented in Fig. 1 exhibit an asymmetric line shape. Although the appearance of a mode asymmetry can be attributed to the presence of defects [29], this would have a significant impact also on the linewidths of other modes in the spectrum, which is not the case here. The asymmetry may arise from coupling between the phonon and other elementary excitations [30–32]. The line shape originating from such a coupling is given by the Fano

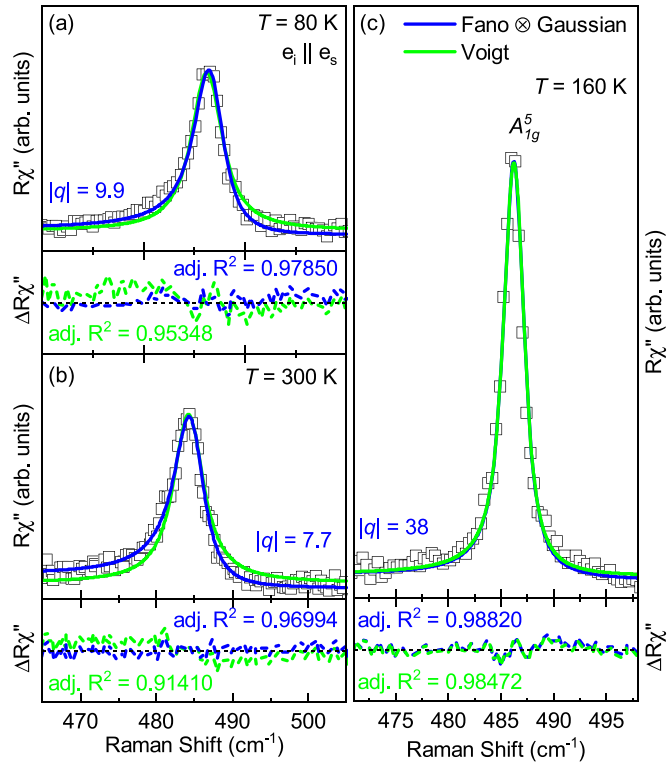


FIG. 2. Raman response as a function of the Raman shift. Quantitative analysis of the $A_{1g}^5$ mode at temperatures as indicated. (a) and (b) The blue solid lines represent the line shape obtained as a convolution of Fano profiles and Gaussian, whereas the green solid lines represent Voigt profiles. (c) Comparison between asymmetric (deep blue) and symmetric (light blue) line shapes obtained as a Fano-Gaussian convolution and a Voight profile. Experimental data are represented by open squares.

profile [33–36]

$$I(\omega) = I_0 \frac{(q+\epsilon)^2}{1+\epsilon^2},$$

where $\epsilon(\omega) = 2(\omega - \omega_0)/\Gamma$. Here, $\omega_0$ is the phonon frequency in the absence of interaction, $\Gamma$ is the full width at half maximum (FWHM), $I_0$ is the amplitude, and $q$ is the Fano parameter. The Fano parameter and FWHM depend on the interaction strength between the phonon and the elementary excitation, and therefore can be used as its indicator. To include the finite spectral resolution of the experimental setup, the Fano profile is convoluted with a Gaussian function as demonstrated in Ref. [28].

The high-intensity peak at 486.7 $cm^{-1}$, identified as the $A_{1g}^5$ symmetry mode, does not overlap with any other mode. The quantitative analysis of this peak is performed using both the symmetric Voigt profile and the Fano-Gaussian convolution mentioned above. The comparison between the two models and the experimental data at 80 and 300 K are presented in Figs. 2(a) and 2(b), respectively. The asymmetric line shapes provide a satisfactory description of the measured phonon line shape, suggesting the presence of an additional scattering mechanism in $Mn_3Si_2Te_6$.

The spectral region of the $A_{1g}^5$ Raman-active mode in the temperature range of interest is presented in Fig. 3(a). The

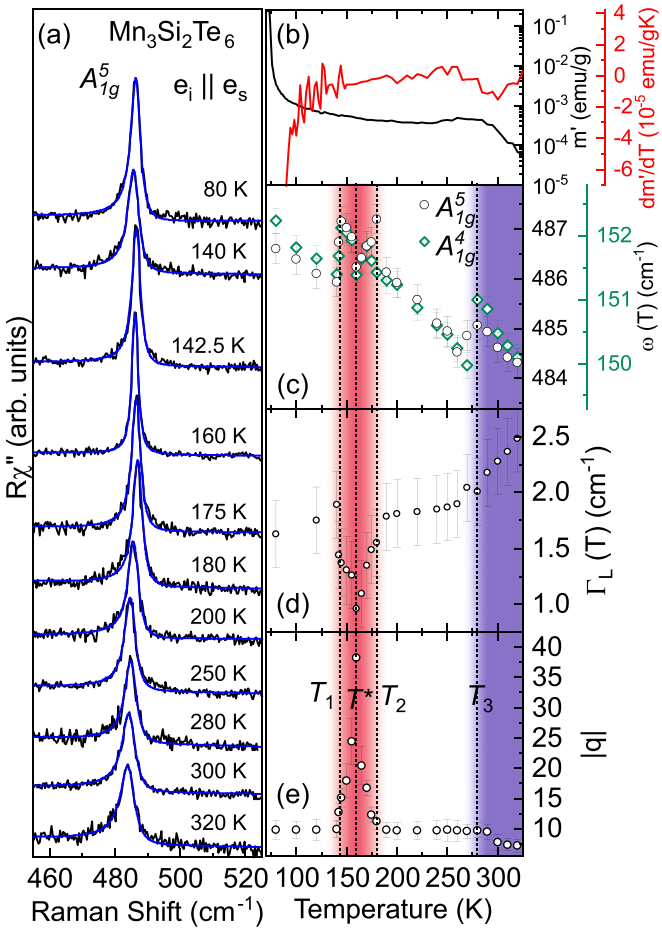


FIG. 3. (a) The spectral region of the $A^5_{1g}$ Raman-active mode of $Mn_3Si_2Te_6$ at indicated temperatures measured in the parallel polarization configuration. Green solid lines represent line shapes obtained as a convolution of the Fano line shape and Gaussian, calculated to fit the experimental data. (b) Temperature dependence of ac susceptibility real part $m'(T)$ and its temperature derivative plotted as a function of temperature with **H** ∥ **ab**. Temperature dependence of (c) the energy of the $A^4_{1g}$ and $A^5_{1g}$ as well as (d) the linewidth, and (e) the Fano parameter $|q|$ of the $A^5_{1g}$ mode.

blue solid lines represent fits to the experimental data obtained using the Fano-Gaussian line shape. The temperature dependence of the phonon energy, linewidth, and the Fano parameter $|q|$ of the $A^5_{1g}$ mode are depicted in Figs. 3(c)–3(e), respectively. By increasing the temperature above 80 K, the $A^5_{1g}$ mode broadens and softens up to $T_1 = 142.5$ K, where it abruptly narrows and shifts to higher energies followed by further softening and narrowing up to $T^* = 160$ K. Additional heating leads to a broadening and hardening before the drop in phonon energy at $\sim T_2 = 190$ K. In the region $T_2$ the mode softens and broadens with an additional jump in phonon energy at $T_3 = 285$ K. A similar trend is also observed for the $A^4_{1g}$ mode, as evidenced in Fig. 3(b).

This intriguing temperature dependence is also manifested in the asymmetry, i.e., the Fano parameter $|q|$ [Fig. 3(d)] of the $A^5_{1g}$ peak. At the lowest experimental temperature, 80 K, the $A^5_{1g}$ mode exhibits strong asymmetry with a Fano parameter $|q| = 9.9$. Upon heating the sample to $\sim T_1$ a Fano parameter remains nearly constant before the significant increase in the temperature range between $T_1$ and $T^*$ resulting in a symmetric line shape [$|q| = 38$, Fig. 3(c)]. A further temperature increase leads to a strong decrease of $|q|$ up to $T_2$, where the asymmetry is restored ($|q| = 9.9$), remaining almost constant up to $T_3$. At higher temperatures, the line shape becomes more asymmetric, reaching $|q| \sim 8$ at the highest experimentally accessible temperature $T = 320$ K.

While the ferrimagnetic order in $Mn_3Si_2Te_6$ is established only at $T_c = 78$ K [12,14], the asymmetry of the mode can be observed at all experimental temperatures. Based on the research done on $Mn_3Si_2Te_6$ and related materials, the most probable scenario is the one in which the observed asymmetry can be traced to an enhanced spin-phonon interaction related to short-range correlations, that can survive up to temperatures well above $T_c$ [24,37–39]. We may speculate, according to the results presented in Ref. [15], that these short-range correlations are likely in terms of the antiferromagnetic exchange interaction between the three nearest Mn-Mn pairs (as depicted in Fig. 1) in the paramagnetic background. However, this alone cannot explain sudden changes in the properties of the $A^5_{1g}$ phonon mode. Rather, the existence of competing short-range magnetic phases may be responsible for the observed behavior of the phonon modes. The first phonon mode anomaly at $T_3 = 285$ K corresponds to the anomaly in $m'(T)_{ab}$ [Fig. 3(b)] and can be seen as the outlet of additional short-range order in the paramagnetic domains [40] and possibly change of their nature of previously established ones. The onset in temperature with the magnetization anomaly near 330 K [14,41] is likely the consequence of local disorder. At $T_2$, $Mn_3Si_2Te_6$ becomes locally magnetically frustrated, resulting in the change in magnetostriction and a rapid decrease of the spin-phonon interaction that is manifested in the strong evolution of the phonon self-energy (Fig. 3). At this temperature both the magnetoresistance and nonlinearity of Hall resistance become observable [41]. In this scenario, by further lowering the temperature, at $T_1$ a new short-range magnetic order and the strong spin-phonon interaction are established. The new magnetic order is most likely antiferromagnetic [15]. In order to fully understand the complex evolution of the short-range magnetic correlation in $Mn_3Si_2Te_6$ that is manifested through the anomalous temperature development of the $A^5_{1g}$ mode, further investigations are required.

## IV. CONCLUSION

The lattice dynamic in single-crystalline $Mn_3Si_2Te_6$ using Raman spectroscopy in analyzed. Five $A_{1g}$ modes and nine $E_g$ modes are observed and assigned according to the $P\bar{3}1c$ symmetry group. Four additional peaks to the ones assigned to the $P\bar{3}1c$ symmetry group, obeying $A_{1g}$ selection rules, are attributed to overtones. There is a pronounced asymmetry of the $A^5_{1g}$ phonon mode at 100 and 300 K. The unconventional temperature evolution of the $A^5_{1g}$ Raman mode reveals three successive, possibly magnetic, phase transitions that may significantly impact the strength of the spin-phonon interaction in $Mn_3Si_2Te_6$. These are likely caused by the competition between the various magnetic states, close in energy. This paper provides comprehensive insight into the lattice properties, their temperature dependence, and shows arguments

for the existence of competing short-range magnetic phases in $Mn_3Si_2Te_6$.

## ACKNOWLEDGMENTS

The authors acknowledge funding provided by the Institute of Physics Belgrade, through a grant from the Ministry of Science, Technological Development and Innovations of the Republic of Serbia, the Serbian Academy of Sciences and Arts - Project No. F-134, the Science Fund of the Republic of Serbia, PROMIS, 6062656, StrainedFeSC, Austrian Science Fund (FWF) through Project No. P31423, and the support of Austrian Academy of Sciences' Joint Excellence in Science and Humanities (JESH) Program (J.P.). DFT calculations were performed using computational resources at Johannes Kepler University (Linz, Austria). Materials synthesis was supported by the U.S. DOE-BES, Division of Materials Science and Engineering, under Contract No. DE-SC0012704 (BNL). The authors would like to thank Dr. Rudi Hackl for useful discussions that contributed to the finalized version of the manuscript.

[1] Z. Guguchia, Unconventional magnetism in layered transition metal dichalcogenides, Condensed Matter **5**, 42 (2020).
[2] Q. H. Wang, K. Kalantar-Zadeh, A. Kis, J. N. Coleman, and M. S. Strano, Electronics and optoelectronics of two-dimensional transition metal dichalcogenides, Nat. Nanotechnol. **7**, 699 (2012).
[3] W. Han, R. K. Kawakami, M. Gmitra, and J. Fabian, Graphene spintronics, Nat. Nanotechnol. **9**, 794 (2014).
[4] W. Zhang, R. Mazzarello, M. Wuttig, and E. Ma, Designing crystallization in phase-change materials for universal memory and neuro-inspired computing, Nat. Rev. Mater. **4**, 150 (2019).
[5] C. Zhu, G. Yang, H. Li, D. Du, and Y. Lin, Electrochemical sensors and biosensors based on nanomaterials and nanostructures, Anal. Chem. **87**, 230 (2015).
[6] X. J. Zhou, Magnetism in medicine: A handbook, second completely revised and enlarged edition, Med. Phys. **34**, 4978 (2007).
[7] Q. H. Wang, A. Bedoya-Pinto, M. Blei, A. H. Dismukes, A. Hamo, S. Jenkins, M. Koperski, Y. Liu, Q.-C. Sun, E. J. Telford, H. H. Kim, M. Augustin, U. Vool, J.-X. Yin, L. H. Li, A. Falin, C. R. Dean, F. Casanova, R. F. L. Evans, M. Chshiev *et al.*, The magnetic genome of two-dimensional van der Waals materials, ACS Nano **16**, 6960 (2022).
[8] B. Huang, G. Clark, E. Navarro-Moratalla, D. R. Klein, R. Cheng, K. L. Seyler, D. Zhong, E. Schmidgall, M. A. McGuire, D. Cobden, W. Yao, D. Xiao, P. Jarillo-Herrero, and X. Xu, Layer-dependent ferromagnetism in a van der Waals crystal down to the monolayer limit, Nature (London) **546**, 270 (2017).
[9] S. Jiang, L. Li, Z. Wang, K. F. Mak, and J. Shan, Controlling magnetism in 2D $CrI_3$ by electrostatic doping, Nat. Nanotechnol. **13**, 549 (2018).
[10] N. Sethulakshmi, A. Mishra, P. Ajayan, Y. Kawazoe, A. K. Roy, A. K. Singh, and C. S. Tiwary, Magnetism in two-dimensional materials beyond graphene, Mater. Today **27**, 107 (2019).
[11] H. Vincent, D. Leroux, and D. Bijaoui, Crystal structure of $Mn_3Si_2Te_6$, J. Solid State Chem. **63**, 349 (1986).
[12] Y. Liu and C. Petrovic, Critical behavior and magnetocaloric effect in $Mn_3Si_2Te_6$, Phys. Rev. B **98**, 064423 (2018).
[13] R. Rimet, C. Schlenker, and H. Vincent, A new semiconducting ferrimagnet: A silicon manganese telluride, J. Magn. Magn. Mater. **25**, 7 (1981).
[14] L. M. Martinez, H. Iturriaga, R. Olmos, L. Shao, Y. Liu, T. T. Mai, C. Petrovic, A. R. Hight Walker, and S. R. Singamaneni, Enhanced magnetization in proton irradiated $Mn_3Si_2Te_6$ van der Waals crystals, Appl. Phys. Lett. **116**, 172404 (2020).
[15] A. F. May, Y. Liu, S. Calder, D. S. Parker, T. Pandey, E. Cakmak, H. Cao, J. Yan, and M. A. McGuire, Magnetic order and interactions in ferrimagnetic $Mn_3Si_2Te_6$, Phys. Rev. B **95**, 174440 (2017).
[16] G. Kresse and J. Hafner, *Ab initio* molecular dynamics for liquid metals, Phys. Rev. B **47**, 558 (1993).
[17] G. Kresse and J. Furthmüller, Efficiency of ab-initio total energy calculations for metals and semiconductors using a plane-wave basis set, Comput. Mater. Sci. **6**, 15 (1996).
[18] G. Kresse and J. Furthmuller, Efficient iterative schemes for *ab initio* total-energy calculations using a plane-wave basis set, Phys. Rev. B **54**, 11169 (1996).
[19] G. Kresse and D. Joubert, From ultrasoft pseudopotentials to the projector augmented-wave method, Phys. Rev. B **59**, 1758 (1999).
[20] J. P. Perdew, K. Burke, and M. Ernzerhof, Generalized Gradient Approximation Made Simple, Phys. Rev. Lett. **77**, 3865 (1996).
[21] P. E. Blöchl, Projector augmented-wave method, Phys. Rev. B **50**, 17953 (1994).
[22] S. Grimme, Semiempirical GGA-type density functional constructed with a long-range dispersion correction, J. Comput. Chem. **27**, 1787 (2006).
[23] A. Togo and I. Tanaka, First principles phonon calculations in materials science, Scr. Mater. **108**, 1 (2015).
[24] F. Jin, N. Lazarević, C. Liu, J. Ji, Y. Wang, S. He, H. Lei, C. Petrovic, R. Yu, Z. V. Popović, and Q. Zhang, Phonon anomalies and magnetic excitations in $BaFe_2Se_2O$, Phys. Rev. B **99**, 144419 (2019).
[25] M. Moskovits and D. Dilella, Surface-enhanced Raman spectroscopy of benzene and benzene-$d_6$ adsorbed on silver, J. Chem. Phys. **73**, 6068 (1980).
[26] A. Dubroka, J. Humlíček, M. V. Abrashev, Z. V. Popović, F. Sapiña, and A. Cantarero, Raman and infrared studies of $La_{1-y}Sr_yMn_{1-x}M_xO_3$ ($M$ = Cr, Co, Cu, Zn, Sc, or Ga): Oxygen disorder and local vibrational modes, Phys. Rev. B **73**, 224401 (2006).
[27] A. G. Souza Filho, J. L. B. Faria, I. Guedes, J. M. Sasaki, P. T. C. Freire, V. N. Freire, J. Mendes Filho, M. M. Xavier, F. A. O. Cabral, J. H. de Araújo, and J. A. P. da Costa, Evidence of magnetic polaronic states in $La_{0.70}Sr_{0.30}Mn_{1-x}Fe_xO_3$ manganites, Phys. Rev. B **67**, 052405 (2003).
[28] A. Baum, A. Milosavljević, N. Lazarević, M. M. Radonjić, B. Nikolić, M. Mitschek, Z. I. Maranloo, M. Šćepanović, M. Grujić-Brojčin, N. Stojilović, M. Opel, A. Wang, C. Petrovic,

Z. V. Popović, and R. Hackl, Phonon anomalies in FeS, Phys. Rev. B **97**, 054306 (2018).

[29] N. Lazarević, M. Radonjić, M. Šćepanović, H. Lei, D. Tanasković, C. Petrovic, and Z. V. Popović, Lattice dynamics of $KNi_2Se_2$, Phys. Rev. B **87**, 144305 (2013).

[30] M. Balkanski, K. P. Jain, R. Beserman, and M. Jouanne, Theory of interference distortion of Raman scattering line shapes in semiconductors, Phys. Rev. B **12**, 4328 (1975).

[31] D. Olego and M. Cardona, Self-energy effects of the optical phonons of heavily doped *p*-GaAs and *p*-Ge, Phys. Rev. B **23**, 6592 (1981).

[32] E. H. Hasdeo, A. R. T. Nugraha, M. S. Dresselhaus, and R. Saito, Breit-Wigner-Fano line shapes in Raman spectra of graphene, Phys. Rev. B **90**, 245140 (2014).

[33] U. Fano, Effects of configuration interaction on intensities and phase shifts, Phys. Rev. **124**, 1866 (1961).

[34] P. H. M. van Loosdrecht, J. P. Boucher, G. Martinez, G. Dhalenne, and A. Revcolevschi, Inelastic Light Scattering from Magnetic Fluctuations in $CuGeO_3$, Phys. Rev. Lett. **76**, 311 (1996).

[35] M. Braden, B. Hennion, W. Reichardt, G. Dhalenne, and A. Revcolevschi, Spin-Phonon Coupling in $CuGeO_3$, Phys. Rev. Lett. **80**, 3634 (1998).

[36] J. W. Ager, W. Walukiewicz, M. McCluskey, M. A. Plano, and M. I. Landstrass, Fano interference of the Raman phonon in heavily boron-doped diamond films grown by chemical vapor deposition, Appl. Phys. Lett. **66**, 616 (1995).

[37] S. Djurdjić Mijin, A. M. M. Abeykoon, A. Šolajić, A. Milosavljević, J. Pešić, Y. Liu, C. Petrovic, Z. V. Popović, and N. Lazarević, Short-range order in $VI_3$, Inorg. Chem. **59**, 16265 (2020).

[38] L. J. Sandilands, Y. Tian, K. W. Plumb, Y.-J. Kim, and K. S. Burch, Scattering Continuum and Possible Fractionalized Excitations in $\alpha$-$RuCl_3$, Phys. Rev. Lett. **114**, 147201 (2015).

[39] A. Milosavljević, A. Šolajic, J. Pešić, Y. Liu, C. Petrovic, N. Lazarević, and Z. V. Popović, Evidence of spin-phonon coupling in $CrSiTe_3$, Phys. Rev. B **98**, 104306 (2018).

[40] Y. Liu, Z. Hu, M. Abeykoon, E. Stavitski, K. Attenkofer, E. D. Bauer, and C. Petrovic, Polaronic transport and thermoelectricity in $Mn_3Si_2Te_6$ single crystals, Phys. Rev. B **103**, 245122 (2021).

[41] Y. Ni, H. Zhao, Y. Zhang, B. Hu, I. Kimchi, and G. Cao, Colossal magnetoresistance via avoiding fully polarized magnetization in the ferrimagnetic insulator $Mn_3Si_2Te_6$, Phys. Rev. B **103**, L161105 (2021).

# Evolution of lattice, spin, and charge properties across the phase diagram of $FeSe_{1-x}S_x$

N. Lazarević,[1,*] A. Baum,[2,3,*] A. Milosavljević,[1] L. Peis,[2,3,†] R. Stumberger,[2,3,‡] J. Bekaert,[4] A. Šolajić,[1] J. Pešić,[1] Aifeng Wang,[5] M. Šćepanović,[1] A. M. Milinda Abeykoon,[6] M. V. Milošević,[4] C. Petrovic,[7] Z. V. Popović,[1,8] and R. Hackl[2,3,9]

[1]*Center for Solid State Physics and New Materials, Institute of Physics Belgrade, University of Belgrade, Pregrevica 118, 11080 Belgrade, Serbia*

[2]*Walther Meissner Institut, Bayerische Akademie der Wissenschaften, 85748 Garching, Germany*

[3]*Fakultät für Physik, Technische Universität München, 85478 Garching, Germany*

[4]*Department of Physics, University of Antwerp, Groenenborgerlaan 171, B-2020 Antwerp, Belgium*

[5]*School of Physics, Chongqing University, Chongqing 400044, China*

[6]*National Synchrotron Light Source II, Brookhaven National Laboratory, Upton, New York 11973, USA*

[7]*Condensed Matter Physics and Materials Science Department, Brookhaven National Laboratory, Upton, New York 11973-5000, USA*

[8]*Serbian Academy of Sciences and Arts, Kneza Mihaila 35, 11000 Belgrade, Serbia*

[9]*IFW Dresden, Helmholtzstr. 20, 01069 Dresden, Germany*

(Received 9 March 2022; revised 27 July 2022; accepted 26 August 2022; published 19 September 2022)

A Raman scattering study covering the entire substitution range of the $FeSe_{1-x}S_x$ solid solution is presented. Data were taken as a function of sulfur concentration $x$ for $0 \leqslant x \leqslant 1$, of temperature and of scattering symmetry. All types of excitations including phonons, spins, and charges are analyzed in detail. It is observed that the energy and width of the iron-related $B_{1g}$ phonon mode vary continuously across the entire range of sulfur substitution. The $A_{1g}$ chalcogenide mode disappears above $x = 0.23$ and reappears at a much higher energy for $x = 0.69$. In a similar way the spectral features appearing at finite doping in $A_{1g}$ symmetry vary discontinuously. The magnetic excitation centered at approximately 500 $cm^{-1}$ disappears above $x = 0.23$ where the $A_{1g}$ lattice excitations exhibit a discontinuous change in energy. The low-energy mode associated with fluctuations displays maximal intensity at the nematostructural transition and thus tracks the phase boundary.

DOI: 10.1103/PhysRevB.106.094510

## I. INTRODUCTION

Iron-based compounds are widely believed to host unconventional superconductivity, thus being similar to cuprates or heavy fermion systems. All are characterized by competing phases including magnetism, crystal symmetry breaking or nematicity, and fluctuations of charge and spin prior to superconductivity [1–3]. While long-range magnetic ordering was found in the majority of the compounds, it is absent in the binary compound FeSe. Yet a nematic and structural phase transition occurs simultaneously at 90 K [4–6]. Below $T_c = 9$ K superconductivity is observed [7]. Upon applied pressure $T_c$ increases to approximately 37 K [8]. By substituting sulfur for selenium, the transition temperature to the nematic phase is suppressed to zero for $x \sim 0.2$ [9], suggesting the existence of a quantum critical point (QCP), and a depression of $T_c$ to approximately 2 K. For $x > 0.2$, $T_c$ increases again and reaches 5 K at $x = 1$ [10]. Surprisingly enough, FeS displays a metallic variation of the resistivity and a high residual resistivity ratio RRR of approximately 30, and neither structural nor nematic phase transitions occur [11]. Thus, $FeSe_{1-x}S_x$ uniquely offers access to instabilities and critical points and the disappearance thereof while superconductivity survives.

FeSe and FeS are isostructural, thus providing us with the opportunity to probe the evolution of competing order by isoelectronic substitution. We wish to address the question as to which extent the properties and, specifically, superconductivity are interrelated with the other instabilities and how the electronic properties affect the phonons. We employ inelastic light scattering to probe evolution with composition of lattice spin and charge excitations in $FeSe_{1-x}S_x$ [12]. We identify the $A_{1g}$ and $B_{1g}$ modes, a two-phonon scattering process as well as additional modes that can be traced to either defect-induced or second-order scattering. The obtained experimental results are in good agreement with numerical calculations. Phonons self-energy temperature dependence supports the results reported in Refs. [13,14] where emerging short-range magnetic order at approximately 20 K was reported.

## II. EXPERIMENT

Single crystals of $FeSe_{1-x}S_x$ were synthesized as described elsewhere [15]. Before the experiment the samples were cleaved in air.

Inelastic light scattering on phonons was performed using a Tri Vista 557 Raman spectrometer with the first

[*]These authors contributed equally to this work.

[†]Present Address: IFW Dresden, Helmholtzstr. 20, 01069 Dresden, Germany.

[‡]Present Address: Robert Bosch GmbH, Robert-Bosch-Platz 1, 70839 Gerlingen, Germany.

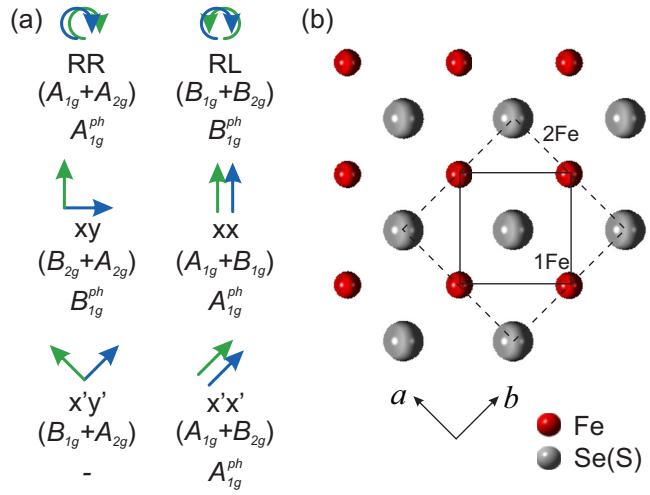


FIG. 1. Crystal structure and selection rules for FeSe(S). Solid and dashed lines represent the 1-Fe and the crystallographic 2-Fe unit cell, respectively. The crystallographic axes are $a$ and $b$. In FeSe and FeS only one $A_{1g}$ and one $B_{1g}$ phonon is expected as indicated by $A_{1g}^{ph}$ and $B_{1g}^{ph}$, respectively. The symmetries projected with the polarizations indicated symbolically with respect to the 1-Fe cell are relevant for electronic and spin excitations. The symmetries of the phonons are in brackets.

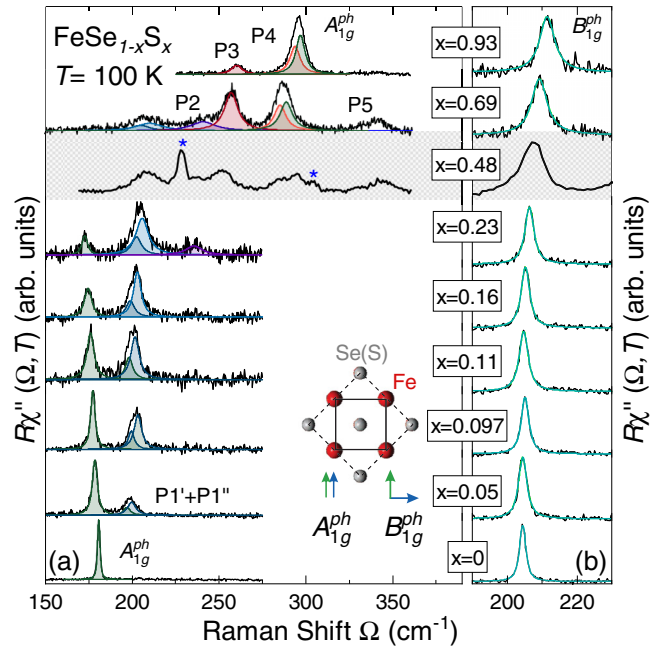


FIG. 2. Phonon spectra of $FeSe_{1-x}S_x$ measured at 100 K. We show $xx$ and $xy$ spectra where $x$ and $y$ are rotated by 45° with respect to the 2-Fe unit cell, as indicated in the inset, and project $A_{1g}^{ph}$ and $B_{1g}^{ph}$, respectively. (a) $A_{1g}^{ph}$ spectra. Only for pure FeSe ($x = 0$), a single line is observed at the $A_{1g}$ energy of 165 $cm^{-1}$ expected from lattice dynamics. Above $x = 0.23$ the Se(S) vibration becomes unobservable and reappears only for $x \geqslant 0.69$ at a much higher energy of approximately 290 $cm^{-1}$ similar to that in pure FeS. The spectrum at $x = 0.48$ was measured on the scanning spectrometer and is therefore shaded. There may be an indication of the $A_{1g}^{ph}$ phonon at about 290 $cm^{-1}$. The peaks other than Raman-active phonons are labeled P1–P5 with increasing energy. Those with asterisks correspond to maxima in the phonon density of states (Fig. 6). Solid lines represent the best fits to the data using Voigt profiles. (b) $B_{1g}^{ph}$ spectra. Energy and linewidth vary continuously with sulfur content.

two monochromators coupled subtractively and the grating combination 1800/1800/2400 grooves/mm. For excitation a Coherent Verdi G solid state laser was used emitting at 532 nm. The samples were mounted in a KONTI CryoVac continuous helium flow cryostat having a 0.5-mm-thick window. The vacuum was pumped to the range of $10^{-6}$ mbar using a turbo molecular pump. The laser was focused to a spot size of approximately 8 $\mu$m using a microscope objective lens with $\times 50$ magnification. The power absorbed by the sample was $P_a = 0.75$ mW. In backscattering configuration as used here, the incident and scattered photons propagate parallel to the crystallographic $c$ axis. All Raman spectra were divided by the Bose factor.

Fluctuations and two magnon excitations were probed with a calibrated scanning spectrometer. The samples were attached to the cold finger of a He-flow cryostat having a vacuum of better than $10^{-6}$ mbar. A diode-pumped solid state laser emitting at 575 nm (Coherent GENESIS) was used as an excitation source. The laser beam was focused on the sample at an angle of incidence of 66° to a spot of $2r_f \approx 50$ $\mu$m. Polarization and power of the incoming light were adjusted in a way that the light inside the sample had the proper polarization state and a power of $P_a = 4$ mW independent of polarization. The ratio $P_a/r_f$ is similar for the $\mu$ setup and thus the local heating for both experiments can be estimated to be in the range 3–5 K. All four symmetries of the $D_{4h}$ group, $A_{1g}$, $A_{2g}$, $B_{1g}$, and $B_{2g}$, can be accessed using appropriate in-plane polarizations of the incident and scattered light.

The selection rules are dictated by the crystal structure. Here, only polarizations in the $ab$ plane are relevant, as shown in Fig. 1, with solid and dashed lines representing 1-Fe and 2-Fe unit cells, respectively. For the tetragonal system there are six principal scattering geometries and each probes two symmetry channels. We align our laboratory system with the 1-Fe unit cell. As a consequence, the $B_{1g}$ phonon ($B_{1g}^{ph}$) is observable in the $xy$ configuration which corresponds to the $B_{2g}$ symmetry channel in the 2-Fe cell (Fig. 1). We decided to use this orientation since our main focus here is electronic and spin excitations for which the 1-Fe unit cell is more appropriate. $A_{1g}^{ph}$ is the fully symmetric in-phase Se(S) mode with elongations along the $c$ axis; $B_{1g}^{ph}$ corresponds to the out-of-phase vibration of the Fe atoms parallel to the $c$ axis.

## III. RESULTS AND DISCUSSION

### A. Lattice excitations

First, the focus is placed on lattice excitations observable in the $xx$ and $xy$ scattering configuration projecting $A_{1g}^{ph}$ and $B_{1g}^{ph}$ in the spectral range characteristic for phonons. Figure 2 shows the evolution of the spectra with doping $x$, where $x$ indicates the sulfur concentration. Additional spectra for $x = 0.48$ and, for convenience, $x = 1$ are shown in Fig. 7. In order to minimize the thermal broadening of the modes while staying above the nematic phase transition, the spectra

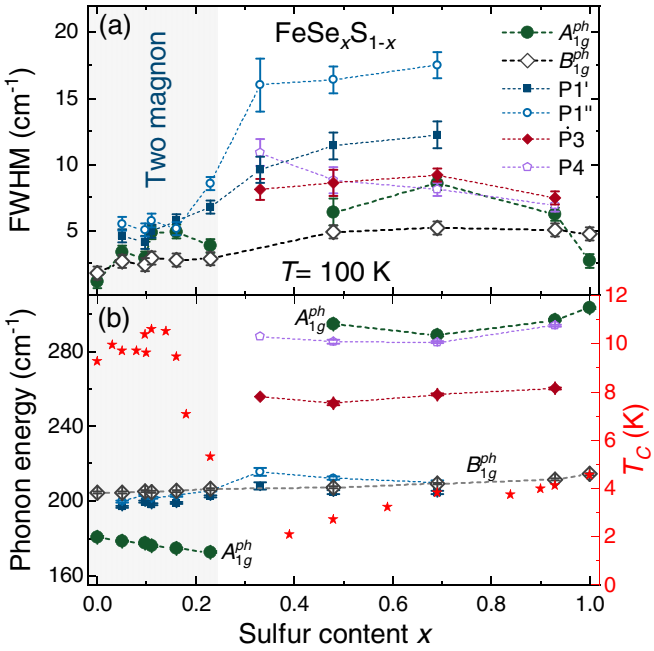


FIG. 3. Energies and linewidths of the Raman-active modes and $T_c$ in $FeSe_{1-x}S_x$ as a function of sulfur content $x$ at 100 K. (a) Peak widths (FWHM) and (b) energies as obtained from the fits (left axis). The $T_c$ values of the corresponding solid solution are taken from Ref. [16].

were recorded at 100 K. In pure stoichiometric compounds only one $A_{1g}^{ph}$ and one $B_{1g}^{ph}$ phonon mode is expected (see Fig. 1). This is indeed the case for FeSe [Fig. 2(a), bottom] as described by Gnezdilov *et al.* [17] and corroborated here. In contrast, in pure FeS ($x = 1$) additional modes exist in the $xx$ spectrum which were assigned to two-phonon scattering (265 cm$^{-1}$) and a projection of the phonon density of states (PDOS) (∼300 cm$^{-1}$) [18] as reproduced in Fig. 7(b). The $xy$ spectra show only the $B_{1g}^{ph}$ mode for all doping levels displayed here [see also Fig. 7(a)]. It hardens monotonously and exhibits a weak maximum of the linewidth at $x = 0.69$ and $x = 0.93$ highlighting the effect of disorder as summarized in Figs. 3(a) and 3(b).

The $xx$ spectra display a much more complex doping dependence. Upon substituting only a small amount of sulfur ($x = 0.05$) for selenium an additional structure appears at about 200 cm$^{-1}$ [Fig. 2(a)]. Closer inspection of the $FeSe_{0.95}S_{0.05}$ spectra reveals that this feature consists of two peaks denoted as P1′ and P1″. With increasing $x$, these structures gain intensity and harden slightly, whereas the $A_{1g}$ phonon softens, gradually loses intensity, and becomes undetectable at concentrations above $x = 0.23$. It reappears as a clear peak only for $x \geqslant 0.69$ at a much higher energy characteristic for FeS [18] and possibly as a remnant structure in the spectrum for $x = 0.48$ [Fig. 7(a)]. As in FeS the $A_{1g}^{ph}$ peak overlaps with a weaker structure which is compatible with the PDOS (P4). At $x = 0.69$ P4 is approximately as strong as the $A_{1g}$ phonon. Here [and at $x = 0.48$, Fig. 7(a)] there is also a broad feature at 340 cm$^{-1}$ (P5). For $x = 0.93$ similar to $x = 1$ there is another structure at 250 cm$^{-1}$ (P3) which gains intensity toward $x = 0.69$ where it has a weak companion at 235 cm$^{-1}$ (P2) being present down to $x = 0.23$. As expected, the increase of crystalline disorder due to substitution leads to a broadening of all observed modes to some maximum value before the trend reverses for compositions close to pure FeS. The widths and energies of the stronger modes are summarized in Fig. 3. As opposed to the $B_{1g}^{ph}$ phonon in $xy$ configuration, all modes in $xx$ polarization including the Raman-active phonon depend quasidiscontinuously on substitution.

This dichotomy of the substitution dependence of the phonon part in $xx$ and $xy$ configuration is the most remarkable effect of this study. Whereas the continuous evolution of the Fe $B_{1g}$ line by and large tracks the degree of disorder and lattice contraction, the Se/S $A_{1g}$ mode varies counterintuitively. Naively one would expect a continuous (not necessarily trivial) increase in the phonon frequency and maximal broadening for doping levels around $x = 0.5$ similar to what is observed in isotopically substituted semiconductors [19]. However, the line disappears after a continuous loss of intensity at approximately $x = 0.23$ and 172 cm$^{-1}$ and reappears (presumably) at $x = 0.48$ slightly below 300 cm$^{-1}$. At low doping the $A_{1g}$ energy decreases by 4% although S is lighter than Se by a factor of 2.13 and the lattice contracts. Above $x = 0.48$ the energy of the $A_{1g}$ phonon varies as expected [see Fig. 3(b)].

The structures appearing in addition to the allowed phonons are rather difficult to interpret in detail. There are essentially two possibilities for intensity to appear in addition to the phonons: defect-induced scattering projecting the PDOS on the site of the defect or overtone (combination) scattering [20]. In FeS one of the peaks (P3) is in the gap between the acoustic and the optical branches and was therefore assigned to an overtone, whereas P4 may originate from the PDOS [18]. The two features depend in the same fashion on doping as the $A_{1g}$ phonon, and the assignment may be maintained. This is plausible on the basis of the PDOS (Fig. 6) although the PDOS of a solid solution cannot be calculated straightforwardly. If we argue that the extra lines vary as discontinuously as the phonon, P1′ and P1″ would have both an overtone and a PDOS component. Interestingly, P1′ and P1″ have the expected doping dependence [see Fig. 3(b)].

The anomalous doping dependence of the $A_{1g}$ phonon may indicate an enhanced electron-phonon coupling which manifests itself also in the linewidth (on top of the inhomogeneous broadening) [Fig. 3(a)]. The slightly enhanced electron-phonon coupling may boost $T_c$ a little bit until the structure becomes unstable and $T_c$ decreases rapidly for $x >$ 0.16. There is, in fact, a kink in the $c/a$ ratio at $x = 0.23$ which may be related to the structural instability [15]. In a recent preprint the collapse of $T_c$ is almost precipitous and coincides with the end of the nematic phase [21], and one may speculate about the position of the quantum critical point and its impact. Yet, further work is necessary to finally clarify the issue.

### B. Spin excitations and fluctuations

Second, we focus on the electronic $B_{1g}$ symmetry channel projected in the $x'y'$ (1-Fe) configuration. Figure 4 shows the doping dependence of the high-energy Raman spectra at approximately 4 K. The $A_{2g}$ contribution can be neglected in these materials [22]. A broad excitation centered at about

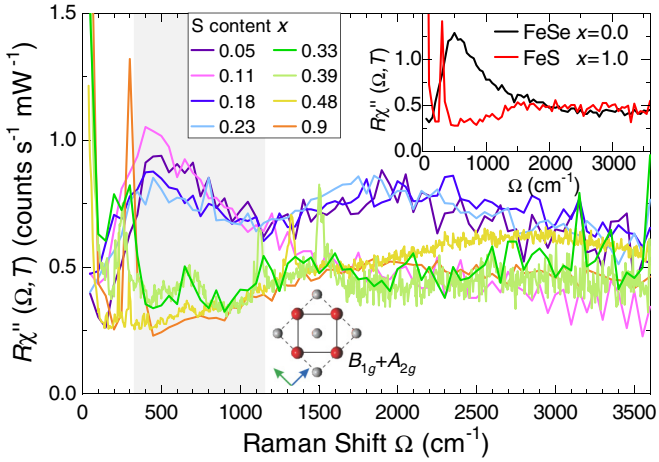


FIG. 4. Doping dependence of the high-energy spectra of $FeSe_{1-x}S_x$ in $xy$ (2-Fe) configuration at 4 K, except for $x = 0.33$, $x = 0.39$, and $x = 0.48$ which were obtained at 100 K. For the electronic unit cell (full line in Fig. 1) relevant here the $B_{1g}$ and $A_{2g}$ symmetries are projected where $A_{2g}$ is negligibly weak. The doping levels are indicated. The inset compares the high-energy spectra of pure FeSe [22] and FeS. The maximum in the range 500 $cm^{-1}$ is compatible with two-magnon scattering [23], whereas the broad shoulder around 2000 $cm^{-1}$ appearing in three out of ten (including all doping levels) spectra was identified as luminescence by using various laser lines for excitation. The peaks in the range 700–1550 $cm^{-1}$ observed only for the doping levels $x = 0.33$, $x = 0.39$, and $x = 0.48$ may originate from either overtones of the phonon density of states [20,24] or from magnetic excitations in the paramagnetic state above the magnetic phase which was observed recently below 20–40 K [25,26]. Since the measuring temperature is well above the magnetic transition the former is more likely.

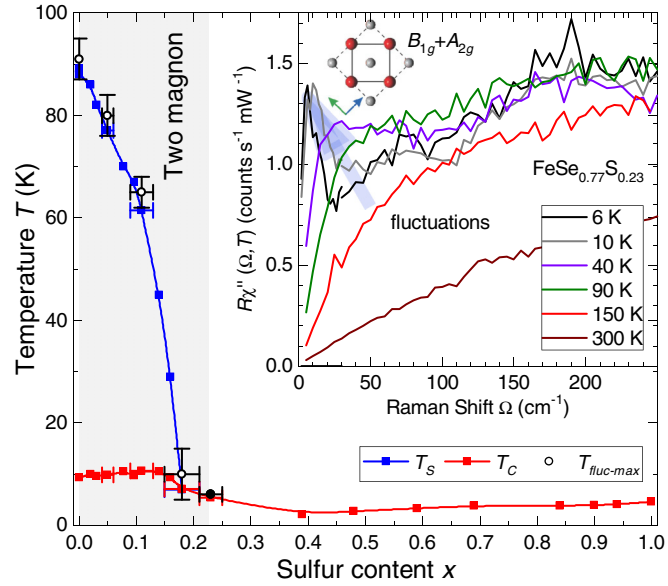


FIG. 5. Phase diagram of $FeSe_{1-x}S_x$ with $T_{fluct,max}$ tracing $T_S$ in the region where the two-magnon feature was observed in the Raman scattering experiment. $T_c$ taken from Ref. [15]. The full circle represents the lowest accessible temperature. Inset: Low-energy Raman spectrum showing the temperature dependence of the fluctuation contribution at $x = 0.23$. Spectra for all doping levels $0 \leqslant x \leqslant 0.23$ are shown in Fig. 8.

500 $cm^{-1}$ dominates the spectrum at $x = 0$ which was interpreted in terms of two-magnon scattering [22]. Since the ratio of the nearest to the next-nearest-neighbor exchange coupling $J1$ and $J2$ is close to 0.5 [27] the system is a nearly frustrated antiferromagnet. Consequently the two-magnon Raman peak is pushed to energies well below $3J1$ [23]. No comparable feature is observed in FeS (see inset in Fig. 4).

Upon doping, the two-magnon peak remains relatively robust up to $x = 0.23$ and is absent for higher doping levels. This goes in line with the fact that for $x = 0$, the Fermi velocity in the $d_{xy}$ band, $v_F^{(xy)}$, is significantly smaller than $v_F^{(xz)}$ or $v_F^{(yz)}$ and increases by only 10% for $x \leqslant 0.20$. For $x > 0.20$ $v_F^{(xy)}$ increases significantly towards FeS [28]. Generally, $v_F^{(xy)}$ in FeSe is smaller than $v_F^{(xy)}$ in $Ba(Fe_{1-x}Co_x)_2As_2$ for instance [29], in agreement with theoretical predictions [30–32]. Thus FeSe is close to the localization limit, and the two-magnonlike response may result from the rather slow carriers on the $d_{xy}$ band. In contrast, the more itinerant carriers in the pnictides condense into a stripelike spin density wave (SDW) which becomes manifest in a gap and a coherence peak [22,33].

In the energy region $\Omega < 200$ $cm^{-1}$ extra intensity is observed for low temperatures. In FeSe it becomes clearly visible below 200 K and fills the spectral gap below the magnon at 500 $cm^{-1}$. Below approximately 100 K an isolated peak may be observed for $x = 0$ which continuously softens above the structural transformation at $T_s = 90$ K, fades away below $T_s$, and almost vanishes at 21 K [22,34]. The line shape and the temperature dependence above $T_s$ can be described quantitatively in terms of critical fluctuations in a similar fashion as in $Ba(Fe_{1-x}Co_x)_2As_2$ [22,33,35]. For increasing doping, this extra intensity starts to develop at lower temperatures. However, remarkably enough the temperature where this peak's intensity is maximal, $T_{fluct,max}$, always coincides with the respective transition temperature $T_s(x)$. At $x = 0.23$ the fluctuation response gains intensity down to the lowest accessible temperatures as presented in the inset of Fig. 5. Thus, the phase transition line of the nematic phase can also be tracked by the Raman response. For $x = 0.33$ (the next available doping level) the fluctuation response cannot be observed any further. Concomitantly, the two-magnon excitation at 500 $cm^{-1}$ becomes unobservable. The most likely explanation of this coincidence is that the two phenomena have the same origin and result from spin excitations. However, there is no consensus on that view in the literature, and Zhang *et al.* [36] and Chibani *et al.* [34] interpret the same experimental observation in terms of quadrupolar charge fluctuations. Yet, one certainly has to answer the question as to why the fluctuations are not found in the simulations [23].

Most probably, the length scale the simulations can deal with limits the applicability of the exact diagonalization method. Since it was intended to study the temperature dependence the cluster had to be sufficiently small ($4 \times 4$) to keep the time for the simulations finite [23]. For the two-magnon excitations, the $4 \times 4$ cluster is sufficient because only nearest-neighbor spins are important. However, close to

the transition the correlation length of fluctuations diverges making them inaccessible for the small clusters tractable numerically. Actually, well above the transition there is a shoulder on the low-energy side of the two-magnon peak which may be associated with the fluctuations but the shoulder is lost close to $T_s$. Thus, although there are experimental arguments in favor of spin fluctuations at low energy there is no theoretical support for this conjecture.

The last question we wish to address concerns the origin of possible local or quasilocal spin order in $FeSe_{1-x}S_x$ for $x < 0.3$. It was observed a while ago that the width of the various bands derived from the orbitals close to the Fermi surface varies by approximately a factor of 3 or more. There are itinerant $yz$ and $xz$ bands crossing the Fermi surface at $E_F$ and a weakly dispersing $xy$ band just below $E_F$ [29] on which the nearly localized spins may reside [30,32]. It is an important question to which extent the fluctuations at low energy are related to these spins. As a matter of fact, Ba122 displays itinerant SDW magnetism as manifested by a gap and a coherence peak along with fluctuations [22,33], whereas FeSe exhibits signatures of local spins and also fluctuations at low energies as shown here. In $FeSe_{1-x}S_x$ both phenomena disappear together above $x > 0.23$.

## IV. CONCLUSION

Raman results covering the entire substitution range $0 \leqslant x \leqslant 1$ in $FeSe_{1-x}S_x$ were presented. The main goal was the study of the physics around the QCP where the nematic instability approached zero transition temperature in the range $0.16 \leqslant x \leqslant 0.23$. We find a striking signature of this transition in both the phonon and the electronic spectra. Whereas the $B_{1g}$ phonon varies continuously with S substitution, the $A_{1g}$ phonon and all structures in the $xx$ spectra show a discontinuity above $x = 0.23$. Similarly, the electronic spectra dominated by spin excitations change abruptly here. Both the two-magnon excitations and the low-energy fluctuations disappear. We argue that they are interrelated. Since we could not observe gap excitation for $x > 0$, statements about the evolution of the superconducting pairing are currently not possible. Another issue is the exact position of the quantum critical transition and its sharpness.

## ACKNOWLEDGMENTS

We acknowledge valuable discussions with T. Böhm and D. Jost. The authors acknowledge funding provided by the Institute of Physics Belgrade through a grant by the Ministry of Education, Science and Technological Development of the Republic of Serbia and and SASA Project No. F-134. The work was supported by the Science Fund of the Republic of Serbia, PROMIS, No. 6062656, StrainedFeSC, by Research Foundation-Flanders (FWO), and COST actions CA16218 and CA21144. Further support came from the German research foundation (DFG) via projects Ha2071/8-1, Ha2071/12-1, and 107745057-TRR 80 and from the DAAD via the project-related personal exchange program PPP with Serbia Grant No. 57449106. J.B. is Senior Postdoctoral Fellow of the FWO, and further acknowledges the Erasmus+ program for staff mobility and training (KA107, 2018) for a research stay at the Institute of Physics Belgrade. The computational resources and services used for the first-principles calculations in this work were provided by the VSC (Flemish Supercomputer Center), funded by the FWO and the Flemish Government, department EWI. Work at Brookhaven National Laboratory is supported by the U.S. DOE under Contract No. DESC0012704 (materials synthesis).

## APPENDIX A: PHONON DISPERSION AND DENSITY OF STATES

We have performed density functional theory (DFT) calculations as implemented in the ABINIT package [38]. We have used the Perdew-Burke-Ernzerhof functional tailored for solids [39] and optimized norm-conserving pseudopotentials [40,41], where Fe $3s^2 3p^6 3d^6 4s^2$, S $3s^2 3p^4$, and Se $3d^{10} 4s^2 4p^4$ are treated as valence electrons. The energy cutoff for the plane-wave basis was set to 50 Ha. The lattice parameters and atomic positions used in the calculations were directly obtained from our x-ray diffraction measurements (performed at 300 K). Following previous first-principles studies on phonons in, for example, FeS [18], the crystal structures were not further relaxed, to achieve optimal characterization of the phonon frequencies. Here, both FeS and FeSe adopt the simple tetragonal space group $P4/nmm$ (No. 129), where Fe occupies Wyckoff position $2a$ and S/Se position $2c$. The latter comprises an additional degree of freedom, namely, the height of the chalcogen atoms S and Se with respect to the Fe plane, denoted as $z$. An overview of the lattice parameters that were used in the calculations is provided in Table I.

Subsequently, the phonon dispersions were obtained from density functional perturbation theory (DFPT) calculations, also within ABINIT. Here, we have used a $15 \times 15 \times 9$ $k$-point grid for the electron wave vectors and a $5 \times 5 \times 3$ $q$-point grid for the phonon wave vectors. For the electronic occupation we employed Fermi-Dirac smearing with broadening factor $\sigma = 0.01$ Ha.

The results of these calculations are shown in Fig. 6. FeS is found to have phonon frequencies stretching up to 344 $cm^{-1}$ [Fig. 6(a)], which is significantly higher than the maximum phonon value of 273 $cm^{-1}$ obtained for FeSe [Fig. 6(b)], owing to the higher atomic mass of Se compared to S. The atom-resolved phonon densities of states (DOS) of both compounds reveal a mixture of iron and chalcogen contribution throughout the entire phonon spectrum [Figs. 6(c) and 6(d)]. Interestingly, there is a change of dominant phonon character, with the lower modes dominated by Fe in FeS, while the lower modes have predominant Se character in FeSe. This reversal can be understood from the fact that the atomic number of Fe ($Z = 26$) lies in between those of S ($Z = 16$) and Se ($Z = 34$). These differences in atomic masses lead moreover

TABLE I. Lattice parameters, obtained from x-ray diffraction measurements, used in the DFT and DFPT calculations.

| Compound | $a$ (Å) | $c$ (Å) | $z$ (units of $c$) |
|---|---|---|---|
| FeS | 3.6795 | 5.0321 | 0.2578 |
| FeSe | 3.7707 | 5.5202 | 0.2671 |

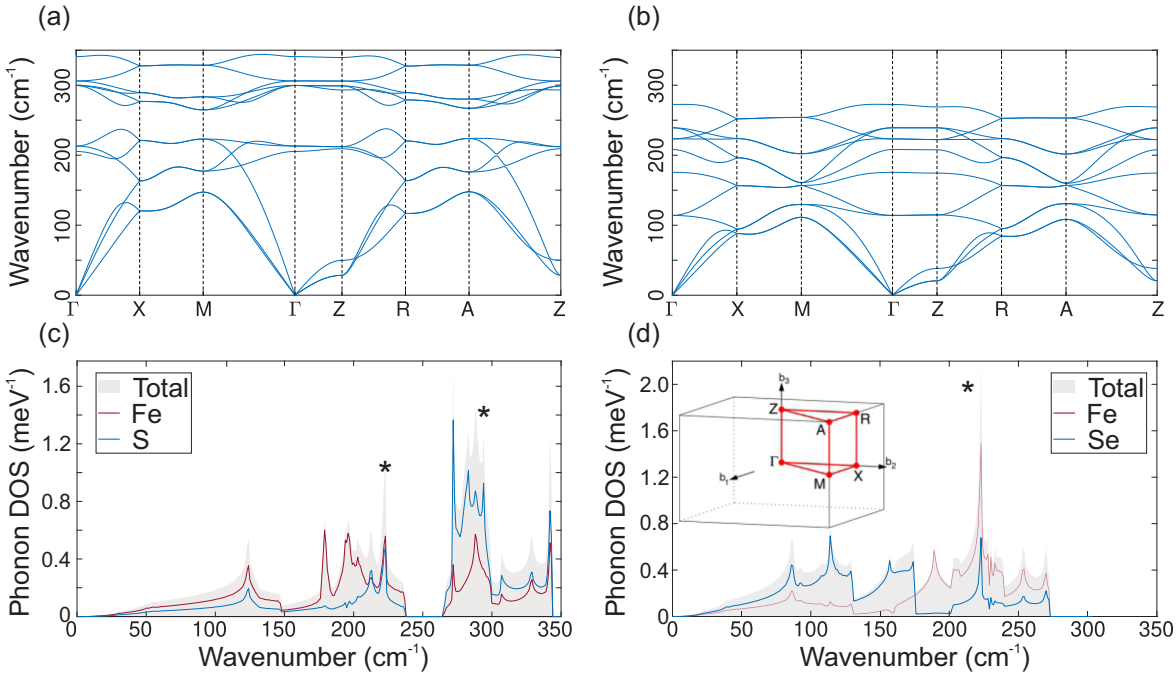


FIG. 6. Calculated phonon band structures of (a) FeS and (b) FeSe. Phonon DOS of (c) FeS and (d) FeSe, including partial contributions from Fe and S/Se. The Brillouin zone of both structures depicted in black is shown in the inset of (d), with the irreducible Brillouin zone, along which the band structures are plotted, in red [37]. The energies of the extra peaks in Fig. 7 are also indicated here by asterisks.

to a small energy gap between Fe- and S-dominated modes in FeS (between 238 and 265 cm$^{-1}$), which is entirely absent in FeSe.

### APPENDIX B: $FeSe_{0.52}S_{0.48}$ AND FeS

For convenience we show here additional doping levels in Fig. 7. The spectrum for $x = 1$ in panel (b) was already published elsewhere [18]. Note that for $x'x'$ both $A_{1g}^{ph}$ and $B_{1g}^{ph}$ are projected and that the labels for the symmetry-forbidden peaks P3 and P4 are different from those in the earlier paper [18]. $x = 0.48$ [Fig. 7(a)] is in the middle between FeSe and FeS, and one can therefore expect the strongest contribution from defect-induced scattering. This interpretation is supported by the presence of structures in both configurations. All peaks resolved at $x = 0.69$ in $xx$ configuration are also observed here. In addition there are two lines marked by asterisks which appear only at $x = 0.48$. Since they appear also for $x'x'$ we interpret them in terms of contributions from the PDOS as shown in Fig. 6 where the respective energies correspond to a high DOS of either FeSe or FeS. Structure P5 may be related to the high-energy part of FeS.

### APPENDIX C: FLUCTUATION RESPONSE

The Raman response from fluctuations was studied by various authors [22,36,42]. While the experiments agree by and large, the interpretation is still controversial. Here we show that the fluctuations appear along with the two-magnon excitations at approximately 500 cm$^{-1}$ from a frustrated spin system [22,23]. Above $x = 0.23$ we could neither observe fluctuations nor two-magnon excitations (see Fig. 4). We cannot entirely exclude that the fluctuations are masked by insufficient stray-light rejection in the more disordered samples but consider it unlikely.

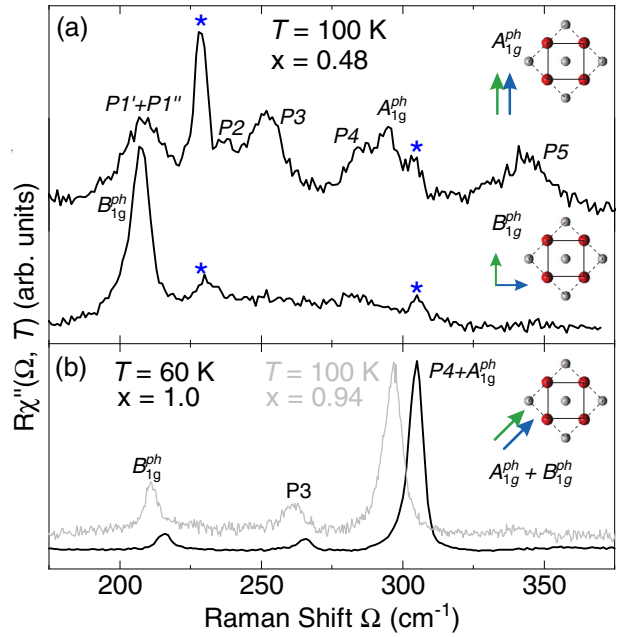


FIG. 7. $FeSe_{1-x}S_x$ for $x = 0.48$, $x = 0.94$, and $x = 1$. (a) $A_{1g}^{ph}$ ($xx$) and $B_{1g}^{ph}$ ($xy$) spectra for $FeSe_{0.52}S_{0.48}$. In addition to the phonons and the structures observed at the other doping levels there are two relatively sharp lines (marked by asterisks) which we associate with the PDOS. They may also arise from a nearly ordered superstructure close to 50% doping.

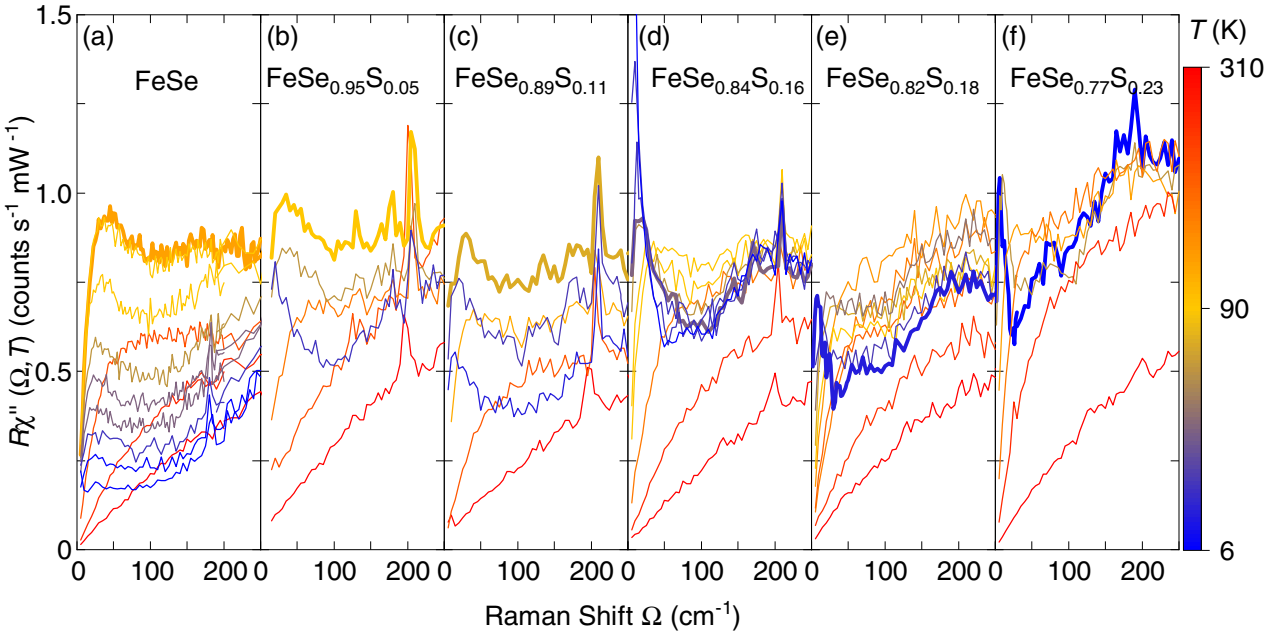


FIG. 8. Fluctuation response of $FeSe_{1-x}S_x$ for $0 \leqslant x \leqslant 0.23$. The spectra with the maximal intensity in the fluctuations are highlighted. The respective temperatures are (a) 91 K, (b) 80 K, (c) 65 K, (d) 25 K, (e) 10 K, and (f) 6 K, where 6 K was the lowest accessible temperature. The temperatures are compiled in Fig. 5 and track the transition to the nematic phase.

If excitations are very close to zero energy one encounters two difficulties: (1) The experimentally accessible quantity is the differential cross section, $d^2\sigma/(d\Omega\, d\omega) \propto S(q=0,\omega)$. The dynamical structure factor or Van Hove function $S(q=0,\omega)$ is related to the imaginary part of the Raman response function $\mathrm{Im}\chi(q=0,\omega)$ through the fluctuation-dissipation theorem as $S(q=0,\omega) = \pi^{-1}\{1 + n(\omega,T)\}\mathrm{Im}\chi(q=0,\omega)$ [43]. The Bose factor $1 + n(\omega,T)$ increases rapidly towards $\omega = 0$ for $\hbar\omega < k_\mathrm{B}T$ and conceals all spectral features below $k_\mathrm{B}T$. Since the fluctuation-dissipation theorem is derived on purely statistical arguments the response function contains exactly the same information as the structure factor but makes features at low energy visible. Thus it is sensible to show $\mathrm{Im}\chi(q=0,\omega)$ rather than $S(q=0,\omega)$. (2) If the surface is not atomically flat there is stray light from insufficient rejection of the laser. The problem is aggravated when atoms of the residual gas accumulate on the surface at low temperature. In panels (a), (b), and (d) of Fig. 8 this effect can be observed. Fortunately, it can be distinguished from the desired response which always goes through zero linearly for causality reasons. (a) In FeSe only the spectra at 10 K show a slight increase which, however, is separated from the fluctuation peak at finite energy. (b) The increase at 10 K is partially resulting from stray light but the maximal intensity is already observed at 80 K. (c) There is little contribution from stray light. (d) Here the stray light becomes strong below 20 K. In (e) and (f) the stray light is negligible.

Remarkably, the overall intensity of all spectra is approximately the same, whereas the maximal intensity in the fluctuation peak is observed at different temperatures as indicated in Fig. 8. These temperatures compare well with the boundary of the nematic phase as shown in Fig. 5.


[1] D. J. Scalapino, A common thread: The pairing interaction for unconventional superconductors, Rev. Mod. Phys. **84**, 1383 (2012).

[2] E. Fradkin, S. A. Kivelson, and J. M. Tranquada, *Colloquium*: Theory of intertwined orders in high temperature superconductors, Rev. Mod. Phys. **87**, 457 (2015).

[3] S. Lederer, Y. Schattner, E. Berg, and S. A. Kivelson, Enhancement of Superconductivity near a Nematic Quantum Critical Point, Phys. Rev. Lett. **114**, 097001 (2015).

[4] A. E. Böhmer, T. Arai, F. Hardy, T. Hattori, T. Iye, T. Wolf, H. v. Löhneysen, K. Ishida, and C. Meingast, Origin of the Tetragonal-to-Orthorhombic Phase Transition in FeSe: A Combined Thermodynamic and NMR Study of Nematicity, Phys. Rev. Lett. **114**, 027001 (2015).

[5] T. M. McQueen, A. J. Williams, P. W. Stephens, J. Tao, Y. Zhu, V. Ksenofontov, F. Casper, C. Felser, and R. J. Cava, Tetragonal-to-Orthorhombic Structural Phase Transition at 90 K in the Superconductor $Fe_{1.01}Se$, Phys. Rev. Lett. **103**, 057002 (2009).

[6] M. D. Watson, T. K. Kim, A. A. Haghighirad, N. R. Davies, A. McCollam, A. Narayanan, S. F. Blake, Y. L. Chen, S. Ghannadzadeh, A. J. Schofield *et al.*, Emergence of the nematic electronic state in FeSe, Phys. Rev. B **91**, 155106 (2015).

[7] F.-C. Hsu, J.-Y. Luo, K.-W. Yeh, T.-K. Chen, T.-W. Huang, P. M. Wu, Y.-C. Lee, Y.-L. Huang, Y.-Y. Chu, D.-C. Yan, and M.-K. Wu, Superconductivity in the PbO-type structure $\alpha$-FeSe, Proc. Natl. Acad. Sci. USA **105**, 14262 (2008).

[8] S. Medvedev, T. M. McQueen, I. A. Troyan, T. Palasyuk, M. I. Eremets, R. J. Cava, S. Naghavi, F. Casper, V. Ksenofontov, G. Wortmann, and C. Felser, Electronic and magnetic phase diagram of $\beta$-$Fe_{1.01}Se$ with superconductivity at 36.7 K under pressure, Nat. Mater. **8**, 630 (2009).

[9] Y. Sato, S. Kasahara, T. Taniguchi, X. Xing, Y. Kasahara, Y. Tokiwa, Y. Yamakawa, H. Kontani, T. Shibauchi, and Y. Matsuda, Abrupt change of the superconducting gap structure at the nematic critical point in $FeSe_{1-x}S_x$, Proc. Natl. Acad. Sci. USA **115**, 1227 (2018).

[10] X. Lai, H. Zhang, Y. Wang, X. Wang, X. Zhang, J. Lin, and F. Huang, Observation of superconductivity in tetragonal FeS, J. Am. Chem. Soc. **137**, 10148 (2015).

[11] U. Pachmayr, N. Fehn, and D. Johrendt, Structural transition and superconductivity in hydrothermally synthesized Fe*X* ($X$ = S, Se), Chem. Commun. **52**, 194 (2016).

[12] N. Lazarević and R. Hackl, Fluctuations and pairing in Fe-based superconductors: Light scattering experiments, J. Phys.: Condens. Matter **32**, 413001 (2020).

[13] S. Holenstein, U. Pachmayr, Z. Guguchia, S. Kamusella, R. Khasanov, A. Amato, C. Baines, H.-H. Klauss, E. Morenzoni, D. Johrendt, and H. Luetkens, Coexistence of low-moment magnetism and superconductivity in tetragonal FeS and suppression of $T_c$ under pressure, Phys. Rev. B **93**, 140506(R) (2016).

[14] F. K. K. Kirschner, F. Lang, C. V. Topping, P. J. Baker, F. L. Pratt, S. E. Wright, D. N. Woodruff, S. J. Clarke, and S. J. Blundell, Robustness of superconductivity to competing magnetic phases in tetragonal FeS, Phys. Rev. B **94**, 134509 (2016).

[15] A. Wang, A. Milosavljevic, A. M. M. Abeykoon, V. Ivanovski, Q. Du, A. Baum, E. Stavitski, Y. Liu, N. Lazarevic, K. Attenkofer *et al.*, Suppression of superconductivity and nematic order in $Fe_{1-y}Se_{1-x}S_x(0 \leqslant x \leqslant 1; y \leqslant 0.1)$ crystals by anion height disorder, Inorg. Chem. **61**, 11036 (2022).

[16] A. Wang, L. Wu, V. N. Ivanovski, J. B. Warren, J. Tian, Y. Zhu, and C. Petrovic, Critical current density and vortex pinning in tetragonal $FeS_{1-x}Se_x$ ($x = 0, 0.06$), Phys. Rev. B **94**, 094506 (2016).

[17] V. Gnezdilov, Y. G. Pashkevich, P. Lemmens, D. Wulferding, T. Shevtsova, A. Gusev, D. Chareev, and A. Vasiliev, Interplay between lattice and spin states degree of freedom in the FeSe superconductor: Dynamic spin state instabilities, Phys. Rev. B **87**, 144508 (2013).

[18] A. Baum, A. Milosavljević, N. Lazarević, M. M. Radonjić, B. Nikolić, M. Mitschek, Z. I. Maranloo, M. Šćepanović, M. Grujić-Brojčin, N. Stojilović *et al.*, Phonon anomalies in FeS, Phys. Rev. B **97**, 054306 (2018).

[19] M. Cardona and M. L. W. Thewalt, Isotope effects on the optical spectra of semiconductors, Rev. Mod. Phys. **77**, 1173 (2005).

[20] G. Turrell, *Infrared and Raman Spectra of Crystals* (Academic, London/New York, 1972).

[21] Y. Mizukami, M. Haze, O. Tanaka, K. Matsuura, D. Sano, J. Böker, I. Eremin, S. Kasahara, Y. Matsuda, and T. Shibauchi, Thermodynamics of transition to BCS-BEC crossover superconductivity in $FeSe_{1-x}S_x$, arXiv:2105.00739.

[22] A. Baum, H. N. Ruiz, N. Lazarević, Y. Wang, T. Böhm, R. Hosseinian Ahangharnejhad, P. Adelmann, T. Wolf, Z. V. Popović *et al.*, Frustrated spin order and stripe fluctuations in FeSe, Commun. Phys. **2**, 14 (2019).

[23] H. Ruiz, Y. Wang, B. Moritz, A. Baum, R. Hackl, and T. P. Devereaux, Frustrated magnetism from local moments in FeSe, Phys. Rev. B **99**, 125130 (2019).

[24] W. Spengler and R. Kaiser, First and second order Raman scattering in transition metal compounds, Solid State Commun. **18**, 881 (1976).

[25] F. Nabeshima, Y. Kawai, N. Shikama, Y. Sakishita, A. Suter, T. Prokscha, S. E. Park, S. Komiya, A. Ichinose, T. Adachi, and A. Maeda, Sulfur-induced magnetism in $Fese_{1-x}s_x$ thin films on $LaAlO_3$ revealed by muon spin rotation/relaxation, Phys. Rev. B **103**, 184504 (2021).

[26] X. Yi, X. Xing, L. Qin, J. Feng, M. Li, Y. Zhang, Y. Meng, N. Zhou, Y. Sun, and Z. Shi, Hydrothermal synthesis and complete phase diagram of $FeSe_{1-x}S_x(0 \leqslant x \leqslant 1)$ single crystals, Phys. Rev. B **103**, 144501 (2021).

[27] J. K. Glasbrenner, I. I. Mazin, H. O. Jeschke, P. J. Hirschfeld, R. M. Fernandes, and R. Valentí, Effect of magnetic frustration on nematicity and superconductivity in iron chalcogenides, Nat. Phys. **11**, 953 (2015).

[28] A. I. Coldea, Electronic nematic states tuned by isoelectronic substitution in bulk $FeSe_{1-x}S_x$, Frontiers Phys. **8**, 594500 (2021).

[29] M. Yi, Z.-K. Liu, Y. Zhang, R. Yu, J.-X. Zhu, J. Lee, R. Moore, F. Schmitt, W. Li, S. Riggs *et al.*, Observation of universal strong orbital-dependent correlation effects in iron chalcogenides, Nat. Commun. **6**, 7777 (2015).

[30] Z. P. Yin, K. Haule, and G. Kotliar, Kinetic frustration and the nature of the magnetic and paramagnetic states in iron pnictides and iron chalcogenides, Nat. Mater. **10**, 932 (2011).

[31] K. M. Stadler, Z. P. Yin, J. von Delft, G. Kotliar, and A. Weichselbaum, Dynamical Mean-Field Theory Plus Numerical Renormalization-Group Study of Spin-Orbital Separation in a Three-Band Hund Metal, Phys. Rev. Lett. **115**, 136401 (2015).

[32] S. L. Skornyakov, V. I. Anisimov, D. Vollhardt, and I. Leonov, Effect of electron correlations on the electronic structure and phase stability of FeSe upon lattice expansion, Phys. Rev. B **96**, 035137 (2017).

[33] F. Kretzschmar, T. Böhm, U. Karahasanović, B. Muschler, A. Baum, D. Jost, J. Schmalian, S. Caprara, M. Grilli, C. Di Castro *et al.*, Critical spin fluctuations and the origin of nematic order in $Ba(Fe_{1-x}Co_x)_2As_2$, Nat. Phys. **12**, 560 (2016).

[34] S. Chibani, D. Farina, P. Massat, M. Cazayous, A. Sacuto, T. Urata, Y. Tanabe, K. Tanigaki, A. E. Böhmer, P. C. Canfield *et al.*, Lattice-shifted nematic quantum critical point in $FeSe_{1-x}S_x$, npj Quantum Mater. **6**, 37 (2021).

[35] U. Karahasanovic, F. Kretzschmar, T. Böhm, R. Hackl, I. Paul, Y. Gallais, and J. Schmalian, Manifestation of nematic degrees of freedom in the Raman response function of iron pnictides, Phys. Rev. B **92**, 075134 (2015).

[36] W. Zhang, S. Wu, S. Kasahara, T. Shibauchi, Y. Matsuda, and G. Blumberg, Quadrupolar charge dynamics in the nonmagnetic $FeSe_{1-x}S_x$ superconductors, Proc. Natl. Acad. Sci. USA **118**, e2020585118 (2021).

[37] W. Setyawan and S. Curtarolo, High-throughput electronic band structure calculations: Challenges and tools, Comput. Mater. Sci. **49**, 299 (2010).

[38] X. Gonze, B. Amadon, G. Antonius, F. Arnardi, L. Baguet, J.-M. Beuken, J. Bieder, F. Bottin, J. Bouchet, E. Bousquet *et al.*, The ABINIT project: Impact, environment and recent developments, Comput. Phys. Commun. **248**, 107042 (2020).

[39] J. P. Perdew, A. Ruzsinszky, G. I. Csonka, O. A. Vydrov, G. E. Scuseria, L. A. Constantin, X. Zhou, and K. Burke, Restoring the Density-Gradient Expansion for Exchange in Solids and Surfaces, Phys. Rev. Lett. **100**, 136406 (2008).

[40] D. R. Hamann, Optimized norm-conserving Vanderbilt pseudopotentials, Phys. Rev. B **88**, 085117 (2013).

[41] M. van Setten, M. Giantomassi, E. Bousquet, M. Verstraete, D. Hamann, X. Gonze, and G.-M. Rignanese, The PseudoDojo: Training and grading a 85 element optimized norm-conserving pseudopotential table, Comput. Phys. Commun. **226**, 39 (2018).

[42] P. Massat, D. Farina, I. Paul, S. Karlsson, P. Strobel, P. Toulemonde, M.-A. Méasson, M. Cazayous, A. Sacuto, S. Kasahara *et al.*, Charge-induced nematicity in FeSe, Proc. Natl. Acad. Sci. USA **113**, 9177 (2016).

[43] L. D. Landau and E. M. Lifshitz, *Electrodynamics of Continuous Media* (Pergamon, Oxford, 1960), p. 377.

Optical and Quantum Electronics (2022) 54:354
https://doi.org/10.1007/s11082-022-03674-z

# Structural and optical characterization of titanium–carbide and polymethyl methacrylate based nanocomposite

**Jelena Pešić[1] · Andrijana Šolajić[1] · Jelena Mitrić[1] · Martina Gilić[1] · Ivan Pešić[2] · Novica Paunović[1] · Nebojša Romčević[1]**

Received: 11 October 2021 / Accepted: 10 March 2022 / Published online: 12 May 2022


## Abstract

The rich chemistries and unique morphologies of titanium carbide MXenes, made them strong candidates for many applications like sensors and electronic device materials. During the synthesis procedure, chemical etching, oxidation occurs and residual materials, like titanium-dioxide nanocrystals and nanosheets are often present in resulting material. As titanium-carbide MXenes are suggested to be used as additive in organic polymer matrices for production of nanocomposites, it is essential to consider the presence of the oxides and other residuals together with MXene flakes in synthesis results, and consequently in produced nanocomposite. In this study we present structural and optical characterization of such polymer nanocomposite titanium carbide/PMMA (Polymethyl methacrylate) consisting of $Ti_3C_2$, $TiC_2$ MXenes and TiC, and $TiO_2$ residues of synthesis in PMMA matrix, as a multicomponent nanocomposite. Using XRD, infra-red and Raman spectroscopy, followed by comparative study on the vibrational properties using density functional theory calculations, we characterize this nanocomposite. Further, the SEM measurements are performed, demonstrating the produced titanium-carbide-based flakes in nanocomposite are well defined and separated to nanosized grains, allowing us to use Maxwell–Garnet model to analyse infrared spectrum. This enables us to determine the presence of the optical modification of polymer matrices corresponding to a volume fraction of 0.25.

**Keywords** Titanium-carbide nanoparticles · PMMA composite · Multicomponent nanocompostite

This article is part of the Topical Collection on Photonics:Current Challenges and Emerging Applications.

Guest edited byJelena Radovanovic, Dragan Indjin, Maja Nesic, Nikola Vukovic andMilena Milosevic.

✉ Jelena Pešić
yelena@ipb.ac.rs

[1] Institute of Physics Belgrade, University of Belgrade, Pregrevica 118, Belgrade 11080, Serbia

[2] Faculty of Technology and Metallurgy, University of Belgrade, Belgrade 11000, Serbia

## 1 Introduction

Nanocomposites are the combination of two or more different materials where a minimum of one of the components has dimension less than 100 nm Twardowski (2007). The polymer nanocomposites are made of organic polymer matrix (in this research, polymethyl methacrylate—PMMA) and inorganic components (titanium carbide nanoparticles). The properties of the obtained nanocomposites depend on the individual properties of each component, morphology and the interface characteristics. In an attempt to improve the properties of conventional polymer materials and extend the fields of their applications, functionalization has emerged as important method in improvement of their not satisfactory electronic, thermal and mechanical properties Tamborra et al. (2004); Hussain et al. (2006). In addition to typical advantages of polymers (such are light-weight, low cost, and good processability), the improvement of electrical properties (e.g., electrical conductivity) with the addition of a small amount of conductive fillers into polymer matrices have promoted polymer nanocomposites into versatile multifunctional materials. Many applications like household electronics, memory and microwave devices are potentially available with addition of metal oxide nanoparticles to polymer. This enables the modification of the polymer's physical properties as well as the implementation of new features in the polymer matrix creating new type of materials known as the polymer nanocomposites. PMMA as a thermoplastic polymer, has many extraordinary properties, like great transparency and ultraviolet resistance, high abrasion resistance, hardness and stiffness and making it widely used in many applications ranging from everyday items to high tech devices. Further, PMMA is nondegradable and biocompatible which makes it an excellent candidate in medical applications like tissue engineering with typical applications such as fracture fixation, intraocular lenses and dentures Peppas and Langer (1994).

Multicomponent nanocomposites based of layered and 2D materials have drawn significant attention in past decade with promises of various applications. Reduction of dimensionality of the system to the truly atomic-scale 2D is related to the occurrence of all new amazing properties in low-dimensional material, since the reduction of available phase space and decreased screening lead to enhancement of quantum effects and increased correlations. Low-dimensional materials have been studied intensively both for their fundamental properties and insight in basic principles of matter but as well for their colossal potential for applications. A discovery of true two-dimensional material graphene Novoselov et al. (2004) and its remarkable properties like and experimental observation of Klein tunnelling, quantum Hall effect and superconductivity Novoselov et al. (2004); Katsnelson et al. (2006); Zhang et al. (2005); Durajski et al. (2019); Pešić et al. (2014); Margine et al. (2016); Durajski et al. (2020) paved the way for investigation of a new family of materials in low-dimensional physics. The new field of two-dimensional materials research has arose and investigated not only graphene but many more crystal structures where, just like in graphene, cells are connected in at least one direction by the van der Waals' forces Novoselov et al. (2016).

Transition metal carbides are important group of materials for applications since they possess some desired characteristics such as thermal stability, wear and corrosion resistance, electronic, magnetic as well as catalytic properties. Titanium-carbide powders are generally used for manufacturing cutting tools, used in treatment of metals and as abrasive-resistant materials. In 2011 Naguib et al. (2011), the group of early transition metal carbides and/or carbo-nitrides labeled as MXenes. MXenes are produced by the etching out of the A layers from MAX phases Naguib et al. (2011, 2012, 2013). Name MAX phase

comes from its chemical composition: $M_{n+1}AX_n$, where M is an early transition metal, A is mainly a group IIIA or IVA (i.e., groups 13 or 14) element, X is carbon and/or nitrogen, and n = 1, 2, or 3.

During the synthesis of titanium-carbide MXenes by chemical etching, oxidation can occur which results in presence of $TiO_2$ consisted of nanosheets and numerous $TiO_2$ nanocrystals Naguib et al. (2014). There are several studies Zhu et al. (2016); Gao et al. (2015) whose researched is focused in possible applications of $TiO_2$-MXene structures. It is demonstrated the joint effects of $Ti_3C_2$ and $TiO_2$ endowed $TiO_2$-$Ti_3C_2$ nanocomposites with excellent properties and improved functionalities Zhu et al. (2016). In this work we investigate the structural and optical properties of polymer nanocomposites prepared by the incorporation of titanium-carbide nanoparticles consisting of $Ti_3C_2$, $TiC_2$ TiC and $TiO_2$ into the matrices of polymer PMMA. The sample of nanocomposite material was prepared, the PMMA matrix with titanium-carbide particles, PMMA/TiC. As for similar materials Shan et al. (2021, 2020, 2021); Tan et al. (2021); Jafari et al. (2020); Tan et al. (2021) proper understanding of composition of materials used in composite is crucial and XRD analysis for the titanium-carbide flakes. The structural and morphology studies of the nanocomposites were carried out by SEM and Raman spectroscopy. Infrared spectroscopy is a very powerful technique in analysis of various nanoparticle and nanocomposite materials prepared in various techiques Dastan (2015); Dastan and Chaure (2014); Dastan et al. (2014); Dastan and Chaure (2017). To further understand properties of our inhomogenious nanocomposite we used infrared spectroscopy with Maxwell–Garnet model. To further support optical characterization, calculations based on density functional theory were performed.

## 2 Samples preparation and structural characterization

### 2.1 Titan-carbide/PMMA composite synthesis

In this work, titanium-carbide/PMMA nanocomposite sample was made from mixture of MXene based titanium-carbide nanoflakes in PMMA matrix. Production of layered titan-carbide flakes is based on MXene synthesis by selective etching of Al atomic layers from $Ti_3AlC_2$ MAX phase, we used the so-called 'mild' method with lithium fluoride (LiF) and hydrochloric acid (HCl) Tu et al. (2018). This method was described in Naguib et al. (2011). Procedure of composite preparation is described in Fig. 1.

Commercially available PMMA Acryrex CM205 (Chi Mei Corp. Korea, (Mw ≈ 90400 g/mol, $n = 1.49$, $\lambda = 633$ nm) pellets were used as a matrix for sample preparation. $Ti_3AlC_2$ MAX phase was processed and kindly donated from Layered Solids Group, Drexel University. Titanium-carbide flakes were obtained by sonification in the water and drying the supernatant in a Petri dish in the oven for 30 minutes on 90◦C.

Composite was prepared with 10 wt% PMMA solution in acetone (Carlo Erbe Reagents, Spain) and added dried titanium-carbide flakes. After stirring the solution was poured in Petri dish Cao et al. (2017) and dried in oven 24h on 40 °C. Content of titanium-carbide flakes in the sample was 1.7 wt%.

The morphology of the produced composite has been investigated by FESEM using high resolution electron microscope MIRA3 TESCAN. Samples display separated nano-sized grains. Fig. 2a presents FESEM image of MXene flakes delaminated in water showing morphology of obtained flakes, b FESEM image of the PMMA/titanium-carbide

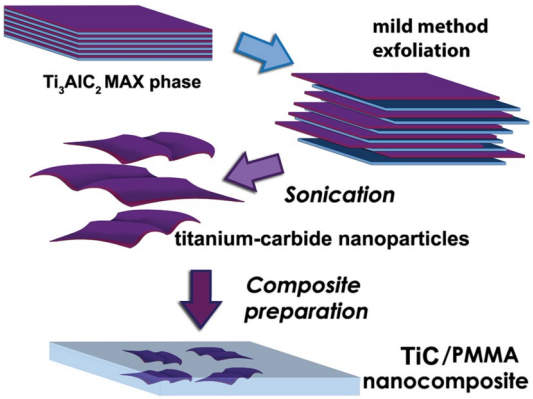


**Fig. 1** Schematic describing the synthesis process of MXenes from MAX phases and preparation of composite

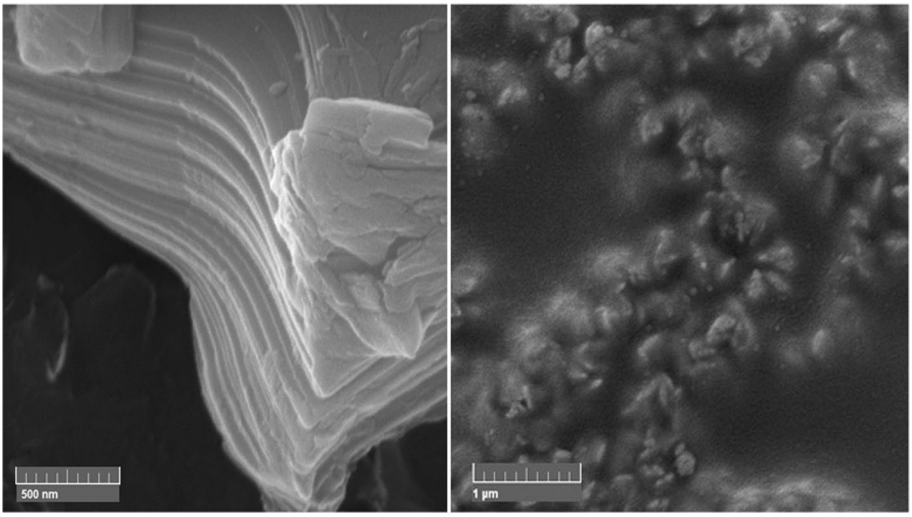


**Fig. 2** FESEM photos of **a** Flakes delaminated in water; **b** PMMA composite prepared with titanium-carbide flakes

nanocomposite. Characteristic layered structure of MXenes is visible on FESEM image and confirming success of delamination and exfoliation procedures. Obtained flakes demonstrate multilayered structure with few $\mu m$ in diameter. In Fig. 2b typical accordion like structure can be indicated in nanosize grain-like structures, clustered in PMMA matrix.

## 2.2 XRD

X–ray diffraction powder (XRD) technique was used to determine structural characteristics of titanium-carbide based flakes to be used in composites. Philips PW 1050 diffractometer equipped with a PW 1730 generator was used. The same conditions were used for all samples, 40 kV×20 mA, using Ni filtered Co K$\alpha$ radiation of 0.1778897 nm at room temperature. Measurements were carried out in the $2\theta$ range of 20–80° with a scanning step

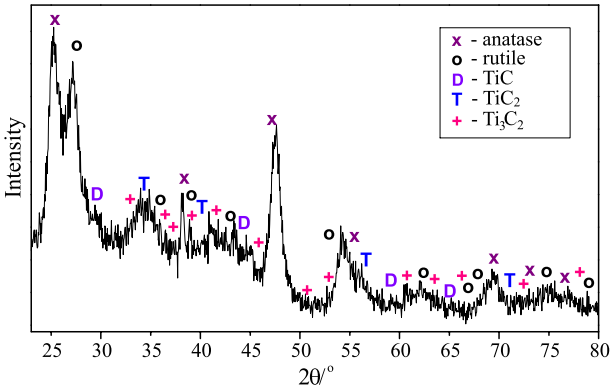


**Fig. 3** XRD pattern for titanium-carbide flakes, starting material for PMMA/TiC composite

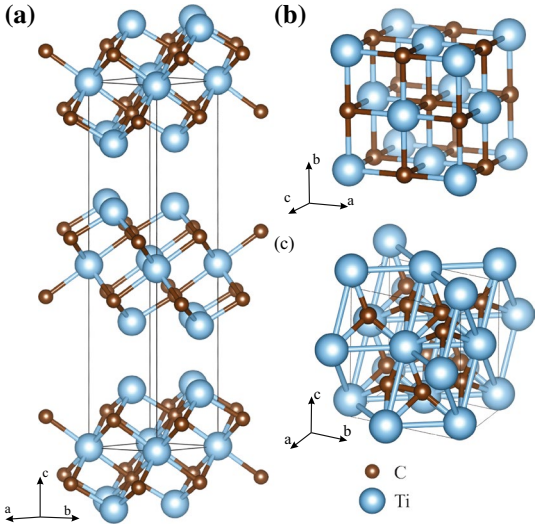


**Fig. 4** Schematic representation of Titanum-carbide structures present at composite **a** $Ti_3C_2$, **b** TiC and **c** $TiC_2$

of 0.05° and 10 s scanning time per step. In Fig. 3 is presented XRD pattern for titanium-carbide flakes, starting material for composite. The different phases of titanium carbide can be noticed from diffractogram—$Ti_3C_2$, TiC and $TiC_2$ together with $TiO_2$. $TiO_2$ is widely present as anatase and rutile. All peaks obtained correspond to the structures of $Ti_3C_2$, TiC, $TiC_2$, anatase and rutile and it is confirmed that they belong to space groups $P6_3/mmc$ (194), $Fm\bar{3}m$ (225) Fm2m (42), $I4_1/amd$ (141), $P4_2/mnm$ (136), respectively. The unit cells of MXene structures $Ti_3C_2$, TiC and $TiC_2$ are presented in Fig. 4. These structures were further used in DFT analysis of optical spectroscopy results in Sect. 3.3.

## 3 Results and discussion

### 3.1 Raman spectroscopy

The micro-Raman spectra were taken in the backscattering configuration and analyzed by the TriVista 557 system equipped with a nitrogen cooled charge-coupled-device

detector. As an excitation source, we used the 532 nm line of Ti:Sapphire laser. Excitation energy is in the off-resonance regime for all the considered materials. The Raman spectra of the PMMA, PMMA/TiC, and titanium-carbide flakes, measured in the spectral range of 100-1100 $cm^{-1}$ at room temperature, are presented in Fig. 5.

The Raman spectrum of PMMA is presented in Fig. 5a. Intense modes at 235, 300, 362, 400, 484, 560, 603, 660, 733, 815, 839, 864, 911, 967, 985, 1063 and 1091 $cm^{-1}$ were detected. The obtained results are in a good agreement with the values given in the literature Willis et al. (1969); Thomas et al. (2008); Ćurčić et al. (2020).

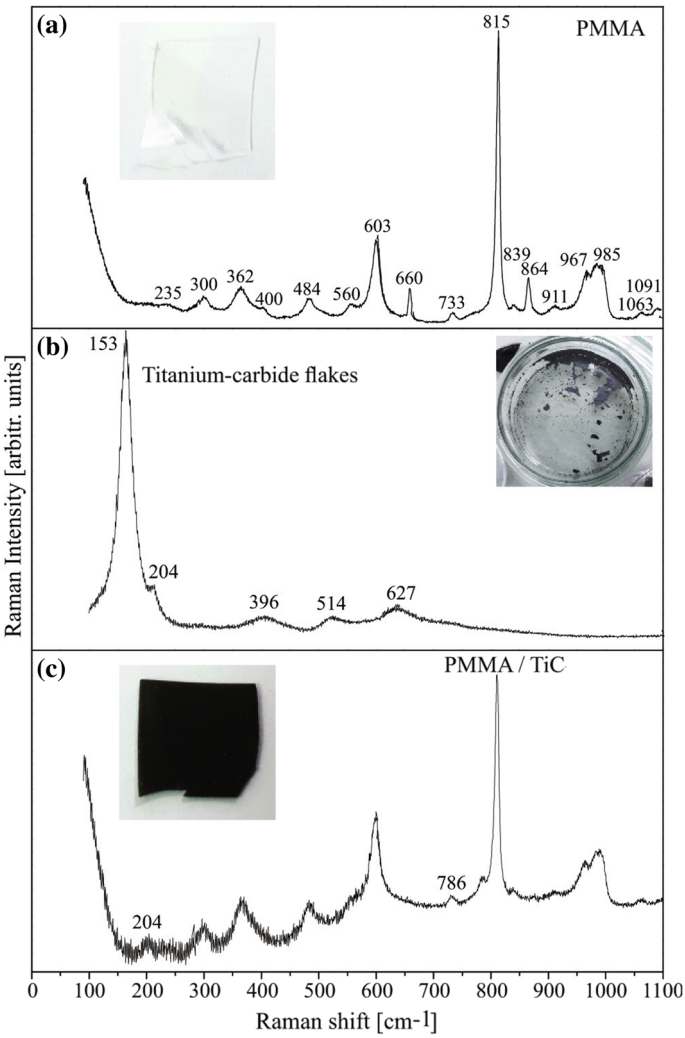


**Fig. 5** Raman spectra with photo of the sample of **a** PMMA, **b** Titanium-carbide flakes, **c** PMMA/TiC composite. Only titanium-carbide related peaks are marked in this spectrum. Unassigned peaks correspond to PMMA from **a** spectrum

In Fig. 5b spectrum of titanium-carbide flakes after etching procedure is presented. Several characteristic peaks can be distinguished on 153 $cm^{-1}$, 204 $cm^{-1}$, 396 $cm^{-1}$, 514 $cm^{-1}$ and 627 $cm^{-1}$. Peaks at 153 $cm^{-1}$ and 627 $cm^{-1}$ correspond to doubly degenerated $E_{2g}$ modes of $Ti_3C_2$. The frequency associated with $E_{2g}$ modes is calculated to be at 161 $cm^{-1}$ for the bare $Ti_3C_2$. Since their main contribution is from in-plane vibrations of Ti and C atoms, it can be influenced by the vibrations of the terminal atoms (as a residue of synthesis procedure) weaken the in-plane motion of the Ti and C atoms, hence there is shift to lower frequency. The terminal groups play significant roles for the vibrational modes: the terminal atoms weakening the motions in which the surface Ti atoms are involved while strengthening the out-of-plane vibration of the C atoms; the corresponding vibrational frequencies dramatically change with the various terminal atoms Zhao et al. (2016). This is consistent with XRD results suggesting significant amount of $TiO_2$ as a residue of synthesis procedure as described in introduction. This can be also visible in Raman spectrum of titanium-carbide flakes on 204 $cm^{-1}$ and 514 $cm^{-1}$. The doubly degenerated modes at 621 $cm^{-1}$ correspond to the in-plane vibration of the C atoms Hu et al. (2015). In Fig. 5c spectrum of PMMA/TiC is presented, only titanium-carbide related peaks at 204 and 786 $cm^{-1}$ are marked in this spectrum. Unassigned peaks correspond to PMMA peaks marked on a) panel.

As XRD analysis demonstrated, obtained flakes contain both MXene flakes and titanium-dioxide as the residue of synthesis procedure. To further understand and assign this spectra we performed theoretical analysis of all materials identified in XRD pattern using density functional theory calculations. Calculations provided us a guide for identification of peaks and all results are summarized in Table 1.

### 3.2 Far-infrared spectroscopy

Far-infrared reflection spectra were measured at room temperature in the spectral range from 40 to 600 $cm^{-1}$, carried out with a BOMEM DA 8 spectrometer. The experimental data are represented at Fig. 6a and by circles at Fig. 6b–d. As expected, the reflection spectra of nanocomposites are by intensity placed between the starting composites. In order to analyse far-infrared spectra we have used the classical oscillator model with free carrier contribution, as a base for Maxwell–Garnet effective medium approximation Abstreiter (1984); Carter and Bate (1971). The low-frequency dielectric properties of single crystals are described by classical oscillators corresponding to the TO modes, to which the Drude part is superimposed to take into account the free carrier contribution:

$$\epsilon_s(\omega) = \epsilon_\infty + \sum_{k=1}^{l} \frac{\epsilon_\infty S_k}{\omega_{TOk}^2 - \omega^2 - i\gamma_{TOk}\omega} - \frac{\epsilon_\infty \omega_P^2}{\omega(\omega + i\Gamma_P)}, \tag{1}$$

where $\epsilon_\infty$ is the bound charge contribution and it is assumed to be a constant, $\omega_{TOk}^2$ is the transverse optical-phonon frequency, $\omega_P^2$ the plasma frequency, $\gamma_{TOk}$ is damping, $\Gamma_P$ is the plasmon mode damping coefficient, and $S_k$ is the oscillator strength.

In general, the optical properties of an inhomogeneous material are described by the complex dielectric function that depends on 3D distribution of constituents. The investigated mixture consists of two materials with two different dielectric components. One is treated as a host, and the other as the inclusions. The characterization of the inhomogeneous material by the two dielectric functions is not useful, since one need to know the exact geometrical arrangement of the constituents of the material. However, if the wavelength of

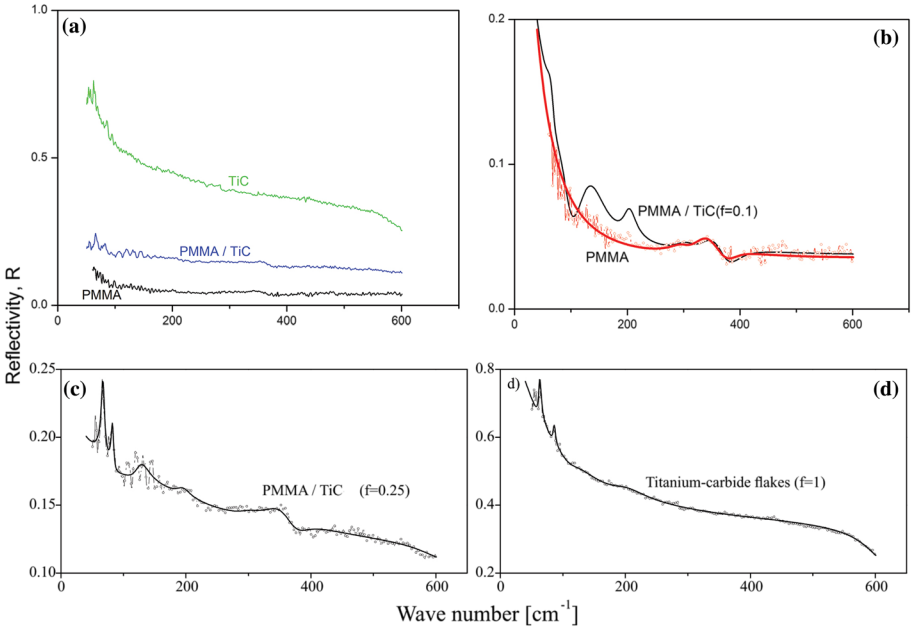


**Fig. 6** Infrared analysis: **a** Infrared spectra of Titanium-carbide flakes (green) and composites PMMA/TiC (blue) and pure PMMA (black), **b**, **c**, and **d** circles represent experimental data and solid lines are fit obtained by Maxwell–Garnet model as described in Sect. 3.2

**Table 1** Raman and infrared spectrum analysis and modes assignation for synthesized titanium-carbide flakes and PMMA/TiC composite

| | Titanium-carbide flakes | | PMMA/TiC | | Description |
|---|---|---|---|---|---|
| | Raman | IR | Raman | IR | |
| $\omega_1$ | | 62.4 | | 66 | $E_u$, $Ti_3C_2$ |
| $\omega_2$ | | 85.8 | | 81 | $B_1$, $TiO_2$ rutile |
| $\omega_3$ | | 119 | | 127 | $A_{2u}$, $Ti_3C_2$ and $B_1$ $TiC_2$ |
| $\omega_4$ | 153 | | | | $E_g$, $Ti_3C_2$ |
| $\omega_5$ | 204 | 200 | 204 | 195 | E, $TiO_2$ anatase |
| $\omega_6$ | 396 | | | | $A_2$, $TiC_2$; E, $TiO_2$ anatase |
| $\omega_7$ | 514 | | | | $A_1$, $TiO_2$ anatase |
| $\omega_8$ | | 620 | | 615 | $E_u$, $Ti_3C_2$ |
| $\omega_9$ | 627 | | | | $E_g$, $Ti_3C_2$ |
| $\omega_{10}$ | | | 786 | | $A_g$, $TiO_2$ rutile |
| $\omega_P$ | | 80 | | 150 | |
| f | | 1 | | 0.25 | |

Infrared modes fit is obtained by Maxwell–Garnet model. Modes assignation is performed using values obtained in DFT calculations

the electromagnetic radiation is much larger than the size of inclusions, classical theories of inhomogeneous material presume that the material can be treated as a homogeneous substance with an effective dielectric function. In the literature, many mixing models can

be found for the effective permittivity of such mixture. Some are present in ref Sihvola (1999). Optical properties of such materials depend upon the properties of constituents, as well as their volume fraction. Since our samples are well defined and separated nanosized grains (as demonstrated on FESEM images, Fig. 2), we used Maxwell–Garnet model for present case. For the spherical inclusions case, the prediction of the effective permittivity of mixture, $\epsilon_{eff}$, according to the Maxwell–Garnet mixing rule is Garnett (1904):

$$\epsilon_{eff} = \epsilon_1 + 3f\epsilon_1 \frac{\epsilon_2 - \epsilon_1}{\epsilon_2 + 2\epsilon_1 - f(\epsilon_2 - \epsilon_1)} \tag{2}$$

Here, spheres of permittivity $\epsilon_2$ (Titanium-carbide) are located randomly in homogeneous environment $\epsilon_1$ (PMMA) and occupy a volume fraction *f*.

Solid lines in Fig. 6 are calculated spectra obtained by a fitting procedure based on the previously presented model. The agreement of the theoretical model obtained in this manner with the experimental results is excellent.

To demonstrate the model, together with the infrared spectrum of PMMA, Fig. 6b is given the theoretical spectrum of PMMA/TiC nanocomposites for f = 0.1. The properties of TiC structures are clearly visible. A larger share of TiC structures leads to the spectrum in Fig 6c, which was obtained for f = 0.25. In Fig. 6d, for f=1 of course there is no effect from PMMA.

### 3.3 Discussion

In Table 1 are summarized results from spectroscopic measurements of obtained nanocomposites. As stated above, for infrared measurements the agreement of the theoretical model with obtained spectra is excellent and best fit parameters are presented in this table.

To further support our results we performed DFT based calculations and calculated vibrational frequencies in Γ point for all materials present after titanium-carbide flakes exfoliation, which we determined are present using XRD, Fig. 3. Obtained values are compared to experimental Raman and infrared spectrum and modes have been assigned. Results are summarized in Table 1. We presented only modes that can be assigned to peaks from the spectra. In infrared spectra we can notice good agrement with theoretical calculations, specially for low-energy $E_u$ and $A_{2u}$ mode of $Ti_3C_2$ which is present the composite spectrum (Fig. 6b, c) as in starting titanium-carbide material (Fig. 6d). As shown in XRD we notice peaks originating from $TiO_2$ and $TiC_2$ in mid-energy region. High-energy mode $E_u$ on 620 $cm^{-1}$ is present in spectrum of PMMA/TiC. In Table 2 are summarized calculated optical modes for $Ti_3C_2$ with symmetry 194 group used in analysis.

DFT calculations were performed using the Quantum Espresso software package Giannozzi (2009), based on the plane waves and pseudopotentials. The PBE (Perdew, Burke and Ernzehof) Perdew et al. (1996) exchange-correlation functional was employed and PAW (Projector augmented waves) pseudopotentials were used. Energy cutoff for wavefunctions and charge density were set to 52 Ry and 575 Ry to ensure the convergence. The Brillouin zone was sampled using the Monkhorst-Pack scheme, with 8×8×8 k-points mesh for $TiC_2$, 8×8×4 for $Ti_3C_2$, 12×12×12 for TiC, and 8×8×8 for $TiO_2$ (Rutile and Anatase structures). Phonon frequencies are calculated within the DPFT (Density Functional Perturbation Theory) implemented in Quantum Espresso Baroni et al. (2001). In order to obtain the lattice parameters more accurately, van der Waals forces were treated using the Grimme-D2 correction Grimme (2006)

**Table 2** Vibrational modes for $Ti_3C_2$ with symmetry group 194, calculated from the measured data

| $Ti_3C_2$ ($P6_3/mmc$) | | |
|---|---|---|
| $cm^{-1}$ | Symmetry | Raman or IR active |
| 65.0 | $E_u$ | I |
| 135.2 | $A_{2u}$ | I |
| 160.6 | $E_g$ | R |
| 161.4 | $E_g$ | R |
| 229.9 | $A_{1g}$ | R |
| 269.3 | $A_{1g}$ | R |
| 271.1 | $E_u$ | I |
| 271.7 | $E_u$ | I |
| 371.4 | $A_{2u}$ | I |
| 382.4 | $A_{2u}$ | I |
| 549.1 | $A_{2u}$ | I |
| 554.4 | $A_{2u}$ | I |
| 611.2 | $E_g$ | R |
| 620.4 | $E_g$ | R |
| 624.1 | $E_u$ | I |
| 626.4 | $E_u$ | I |
| 653.2 | $A_{1g}$ | R |
| 658.3 | $A_{1g}$ | R |

Optical spectroscopy results supported with the DFT numerical calculation confirm that produced composites PMMA/TiC show optical modification comparing to pure PMMA. Our X-ray diffraction investigation of synthesized nanomaterials identified presence of $Ti_3C_2$ and $TiC_2$ MXenes and residual $TiO_2$ and TiC from the synthesis procedure, which can be also supported from the optical spectroscopy results.

## 4 Conclusion

In this paper, we present results of optical and structural investigation of composite based on titanium-carbide nanoflakes ($Ti_3C_2$, $TiC_2$ TiC and $TiO_2$)in PMMA matrix. X-ray diffraction (XRD) investigation of synthesized nanomaterials identified presence of $Ti_3C_2$ and $TiC_2$ MXenes and residual $TiO_2$ and TiC from the synthesis procedure. The optical properties were studied by Raman and infrared spectroscopy at room temperature. The analysis of the Raman spectra was made by the fitting procedure. For analysis of infrared spectra we used Maxwell–Garnet model. In order to identify and assign vibrational modes, vibrational frequencies of all identified materials were calculated using density functional theory, and compared with experimental results. We confirmed optical modification in composite structure compared to pure PMMA. Further analysis that goes beyond the scope of this publication studies mechanical properties of composite materials, confirming improvements compared to pure PMMA. The obtained composite showed enhanced hardness, elastic modulus and tensile strength compared with pure PMMA Pesic et al. (2019).

**Acknowledgements** The authors acknowledge funding provided by the Institute of Physics Belgrade and Faculty of Technology and Metallurgy, through the grant by the Ministry of Education, Science and Technological Development of the Republic of Serbia. All calculations were performed using computational resources at Johannes Kepler University, Linz, Austria.

**Author Contributions** Conceptualization, JP and NR; investigation JP, AŠ, JM, MG, IP, NP; validation, JP, NP, NR; formal analysis, JP, AŠ, JM, MG, NP, NR; writing JP and AŠ; writing–review and editing, JP, AŠ, NP, NR; visualization, AŠ; supervision, NR; project administration, NR; funding acquisition, NR. All authors have read and agreed to the published version of the manuscript.

**Funding** The authors acknowledge funding provided by the Institute of Physics Belgrade and Faculty of Technology and Metallurgy, through the grant by the Ministry of Education, Science and Technological Development of the Republic of Serbia.

**Data availability** All additional material is available at authors on request.

**Code availability** Not applicable.

## Declarations

**Conflict of interest** The Authors declare no conflict of interest.

**Ethical approval** Not applicable.

**Informed consent** Not applicable.

**Consent for publication** All authors consent to publication results presented in manuscript.

## References

Abstreiter, G.: Light Scattering in Solids IV. Springer, New York (1984)

Baroni, S., de Gironcoli, S., Dal Corso, A., Giannozzi, P.: Phonons and related crystal properties from density-functional perturbation theory. Rev. Mod. Phys. **73**, 515–562 (2001)

Cao, Y., Deng, Q., Liu, Z., Shen, D., Wang, T., Huang, Q., Du, S., Jiang, N., Lin, C.-T., Yu, J.: Enhanced thermal properties of poly (vinylidene fluoride) composites with ultrathin nanosheets of mxene. RSC Adv. **7**(33), 20494–20501 (2017)

Carter, D.L., Bate, R.T.: The Physics of Semimetals and Narrow-gap Semiconductors: Proceedings, vol. 32. Pergamon, Texas, USA (1971)

Ćurčić, M., Hadžić, B., Gilić, M., Radojević, V., Bjelajac, A., Radović, I., Timotijević, D., Romčević, M., Trajić, J., Romcevic, N.: Surface optical phonon (sop) mode in ZnS/poly (methylmethacrylate) nanocomposites. Physica E **115**, 113708 (2020)

Dastan, D.: Nanostructured anatase titania thin films prepared by sol-gel dip coating technique. J. Atom. Mol. Condens. Matter Nano Phys. **2**, 109–114 (2015)

Dastan, D., Chaure, N.B.: Influence of surfactants on $TiO_2$ nanoparticles grown by sol-gel technique. Int. J. Mater. Mech. Manuf. **2**, 21 (2014)

Dastan, D., Chaure, N.: Kartha: Surfactants assisted solvothermal derived titania nanoparticles: synthesis and simulation. J. Mater. Sci. **28**, 7784–7796 (2017)

Dastan, D., Londhe, P.U., Chaure, N.B.: Characterization of $TiO_2$ nanoparticles prepared using different surfactants by sol-gel method. J. Mater. Sci. **25**, 3473–3479 (2014)

Durajski, A.P., Skoczylas, K.M., Szczaeniak, R.: Superconductivity in bilayer graphene intercalated with alkali and alkaline earth metals. Phys. Chem. Chem. Phys. **21**, 5925–5931 (2019). https://doi.org/10.1039/C9CP00176J

Durajski, A.P., Auguscik, A.E., Szczeaniak, R.: Tunable electronic and magnetic properties of substitutionally doped graphene. Physica E **119**, 113985 (2020). https://doi.org/10.1016/j.physe.2020.113985

Gao, Y., Wang, L., Zhou, A., Li, Z., Chen, J., Bala, H., Hu, Q., Cao, X.: Hydrothermal synthesis of $TiO_2/Ti_3C_2$ nanocomposites with enhanced photocatalytic activity. Mater. Lett. **150**, 62–64 (2015)

Garnett, J.M.: XII. Colours in metal glasses and in metallic films. Philosoph. Trans. R. Soc. Lond. Ser. A **203**, 385–420 (1904)
Giannozzi, P., et al.: QUANTUM ESPRESSO: a modular and open-source software project for quantum simulations of materials. J. Phys. Condens. Matter **21**(39), 395502 (2009)
Grimme, S.: Semiempirical GGA-type density functional constructed with a long-range dispersion correction. J. Comput. Chem. **27**(15), 1787–1799 (2006)
Hu, T., Wang, J., Zhang, H., Li, Z., Hu, M., Wang, X.: Vibrational properties of $ti_3c_2$ and $ti_3c_2t_2$(t= o, f, oh) monosheets by first-principles calculations: a comparative study. Phys. Chem. Chem. Phys. **17**(15), 9997–10003 (2015)
Hussain, F., Hojjati, M., Okamoto, M., Gorga, R.E.: Review article: polymer-matrix nanocomposites, processing, manufacturing, and application: an overview. J. Compos. Mater. **40**(17), 1511–1575 (2006). https://doi.org/10.1177/0021998306067321
Jafari, A., Tahani, K., Dastan, D., Asgary, S., Shi, Z., Yin, X.-T., Zhou, W.-D., Garmestani, H.: Ştefan Ţălu: Ion implantation of copper oxide thin films; statistical and experimental results. Surf. Interfaces **18**, 100463 (2020)
Katsnelson, M.I., Novoselov, K.S., Geim, A.K.: Chiral tunnelling and the Klein paradox in graphene. Nat. Phys. **2**, 620–625 (2006)
Margine, E.R., Lambert, H., Giustino, F.: Electron-phonon interaction and pairing mechanism in superconducting ca-intercalated bilayer graphene. Sci. Rep. **6**, 21414 (2016)
Naguib, M., Kurtoglu, M., Presser, V., Lu, J., Niu, J., Heon, M., Hultman, L., Gogotsi, Y., Barsoum, M.W.: Two-dimensional nanocrystals produced by exfoliation of $ti_3alc_2$. Adv. Mater. **23**(37), 4248–4253 (2011). https://doi.org/10.1002/adma.201102306
Naguib, M., Mashtalir, O., Carle, J., Presser, V., Lu, J., Hultman, L., Gogotsi, Y., Barsoum, M.W.: Two-dimensional transition metal carbides. ACS Nano **6**(2), 1322–1331 (2012). https://doi.org/10.1021/nn204153h
Naguib, M., Halim, J., Lu, J., Cook, K.M., Hultman, L., Gogotsi, Y., Barsoum, M.W.: New two-dimensional niobium and vanadium carbides as promising materials for li-ion batteries. J. Am. Chem. Soc. **135**(43), 15966–15969 (2013). https://doi.org/10.1021/ja405735d
Naguib, M., Mashtalir, O., Lukatskaya, M.R., Dyatkin, B., Zhang, C., Presser, V., Gogotsi, Y., Barsoum, M.W.: One-step synthesis of nanocrystalline transition metal oxides on thin sheets of disordered graphitic carbon by oxidation of mxenes. Chem. Commun. **50**, 7420–7423 (2014)
Novoselov, K.S., Geim, A.K., Morozov, S.V., Jiang, D., Zhang, Y., Dubonos, S.V., Grigorieva, I.V., Firsov, A.A.: Electric field effect in atomically thin carbon films. Science **306**(5696), 666–669 (2004). https://doi.org/10.1126/science.1102896
Novoselov, K.S., Mishchenko, A., Carvalho, A., Castro Neto, A.H.: 2d materials and van der Waals heterostructures. Science **353**, 6298 (2016). https://doi.org/10.1126/science.aac9439
Peppas, N., Langer, R.: New challenges in biomaterials. Science **263**(5154), 1715–1720 (1994). https://doi.org/10.1126/science.8134835
Perdew, J.P., Burke, K., Ernzerhof, M.: Generalized gradient approximation made simple. Phys. Rev. Lett. **77**, 3865–3868 (1996)
Pesic, I., Radojevic, V., Barsoum, N. M. Tomic, Romcevic, N.: Preparation, characterization and mechanical properties of mxene/pmma composite. TechConnect World Innovation Conference and Expo, Boston, MA, USA. https://www.techconnectworld.com/World2019/wednesday.htmlW6.26 (2019)
Pešić, J., Gajić, R., Hingerl, K., Belić, M.: Strain-enhanced superconductivity in li-doped graphene. EPL (Europhys. Lett.) **108**(6), 67005 (2014). https://doi.org/10.1209/0295-5075/108/67005
Shan, K., Yi, Z.-Z., Yin, X.-T., Dastan, D., Dadkhah, S., Coates, B.T., Garmestani, H.: Mixed conductivities of a-site deficient Y, Cr-doubly doped srtio3 as novel dense diffusion barrier and temperature-independent limiting current oxygen sensors. Adv. Powder Technol. **31**(12), 4657–4664 (2020)
Shan, K., Yi, Z.-Z., Yin, X.-T., Cui, L., Dastan, D., Garmestani, H., Alamgir, F.M.: Diffusion kinetics mechanism of oxygen ion in dense diffusion barrier limiting current oxygen sensors. J. Alloy. Compd. **855**, 157465 (2021)
Shan, K., Zhai, F., Yi, Z.-Z., Yin, X.-T., Dastan, D., Tajabadi, F., Jafari, A., Abbasi, S.: Mixed conductivity and the conduction mechanism of the orthorhombic CAZRO3 based materials. Surf. Interfaces **23**, 100905 (2021)
Sihvola, A.H.: Electromagnetic Mixing Formulas and Applications, vol. 47. IET, UK (1999)
Tamborra, M., Striccoli, M., Comparelli, R., Curri, M., Petrella, A., Agostiano, A.: Optical properties of hybrid composites based on highly luminescent CDS nanocrystals in polymer. Nanotechnology **15**(4), 240 (2004)

Tan, G.-L., Tang, D., Dastan, D., Jafari, A., Shi, Z., Chu, Q.-Q., Silva, J.P.B., Yin, X.-T.: Structures, morphological control, and antibacterial performance of tungsten oxide thin films. Ceram. Int. **47**(12), 17153–17160 (2021)

Tan, G.-L., Tang, D., Dastan, D., Jafari, A., Silva, J.P.B., Yin, X.-T.: Effect of heat treatment on electrical and surface properties of tungsten oxide thin films grown by HFCVD technique. Mater. Sci. Semicond. Process. **122**, 105506 (2021)

Thomas, K., Sheeba, M., Nampoori, V., Vallabhan, C., Radhakrishnan, P.: Raman spectra of polymethyl methacrylate optical fibres excited by a 532 nm diode pumped solid state laser. J. Opt. A Pure Appl. Opt. **10**(5), 055303 (2008)

Tu, S., Jiang, Q., Zhang, X., Alshareef, H.N.: Large dielectric constant enhancement in mxene percolative polymer composites. ACS Nano **12**(4), 3369–3377 (2018)

Twardowski, T.E.: Introduction to Nanocomposite Materials: Properties, Processing. Characterization, DEStech Publications Inc, Lancaster, USA (2007)

Willis, H., Zichy, V., Hendra, P.: The laser-Raman and infra-red spectra of poly (methyl methacrylate). Polymer **10**, 737–746 (1969)

Zhang, Y., Tan, Y.-W., Stormer, H.L., Kim, P.: Experimental observation of the quantum hall effect and Berry's phase in graphene. Nature **438**, 201–204 (2005)

Zhao, T., Zhang, S., Guo, Y., Wang, Q.: $Tic_2$: a new two-dimensional sheet beyond mxenes. Nanoscale **8**(1), 233–242 (2016)

Zhu, J., Tang, Y., Yang, C., Wang, F., Cao, M.: Composites of tio2 nanoparticles deposited on ti3c2 mxene nanosheets with enhanced electrochemical performance. J. Electrochem. Soc. **163**(5), 785–791 (2016)

# Probing charge density wave phases and the Mott transition in 1$T$-$TaS_2$ by inelastic light scattering

S. Djurdjić Mijin,[1] A. Baum,[2] J. Bekaert,[3] A. Šolajić,[1] J. Pešić,[1] Y. Liu,[4,*] Ge He,[2] M. V. Milošević,[3] C. Petrovic,[4] Z. V. Popović,[1,5] R. Hackl,[2] and N. Lazarević[1]

[1]*Center for Solid State Physics and New Materials, Institute of Physics Belgrade, University of Belgrade, Pregrevica 118, RS-11080 Belgrade, Serbia*

[2]*Walther Meissner Institut, Bayerische Akademie der Wissenschaften, D-85748 Garching, Germany*

[3]*Department of Physics, University of Antwerp, Groenenborgerlaan 171, B-2020 Antwerp, Belgium*

[4]*Condensed Matter Physics and Materials Science Department, Brookhaven National Laboratory, Upton, New York 11973-5000, USA*

[5]*Serbian Academy of Sciences and Arts, Knez Mihailova 35, RS-11000 Belgrade, Serbia*

(Received 10 March 2021; revised 14 June 2021; accepted 16 June 2021; published 22 June 2021)

We present a polarization-resolved, high-resolution Raman scattering study of the three consecutive charge density wave (CDW) regimes in 1$T$-$TaS_2$ single crystals, supported by *ab initio* calculations. Our analysis of the spectra within the low-temperature commensurate (C-CDW) regime shows $P\bar{3}$ symmetry of the system, thus excluding the previously proposed triclinic stacking of the "star-of-David" structure, and promoting trigonal or hexagonal stacking instead. The spectra of the high-temperature incommensurate (IC-CDW) phase directly project the phonon density of states due to the breaking of the translational invariance, supplemented by sizable electron-phonon coupling. Between 200 and 352 K, our Raman spectra show contributions from both the IC-CDW and the C-CDW phases, indicating their coexistence in the so-called nearly commensurate (NC-CDW) phase. The temperature dependence of the symmetry-resolved Raman conductivity indicates the stepwise reduction of the density of states in the CDW phases, followed by a Mott transition within the C-CDW phase. We determine the size of the Mott gap to be $\Omega_{gap} \approx 170$–$190$ meV, and track its temperature dependence.

DOI: 10.1103/PhysRevB.103.245133

## I. INTRODUCTION

Quasi-two-dimensional transition metal dichalcogenides (TMDs), such as the various structures of $TaSe_2$ and $TaS_2$, have been in the focus of various scientific investigations over the last 30 years, mostly due to the plethora of charge density wave (CDW) phases [1,2]. Among all TMD compounds 1$T$-$TaS_2$ stands out because of its unique and rich electronic phase diagram [3–6]. It experiences phase transitions at relatively high temperatures, making it easily accessible for investigation and, mainly for the hysteresis effects, attractive for potential applications such as data storage [7], information processing [8], or voltage-controlled oscillators [9].

The cascade of phase transitions as a function of temperature includes the transition from the normal metallic to the incommensurate CDW (IC-CDW) phase, the nearly commensurate CDW (NC-CDW) phase, and the commensurate CDW (C-CDW) phase occurring at around $T_{IC} = 554$ K, $T_{NC} = 355$ K, and in the temperature range from $T_{C\downarrow} = 180$ K to $T_{C\uparrow} = 230$ K, respectively. Recent studies indicate the possibility of yet another phase transition in 1$T$-$TaS_2$ at $T_H = 80$ K, named the hidden CDW state [10–12]. This discovery led to a new boost in attention for 1$T$-$TaS_2$.

Upon lowering the temperature to $T_{IC} = 554$ K, the normal metallic state structure, described by the space group $P\bar{3}m1$ ($D^d_{3d}$) [13], transforms into the IC-CDW state. As will be demonstrated here, the IC-CDW domains shrink upon further temperature reduction until they gradually disappear, giving place to the C-CDW ordered state. This region in the phase diagram between 554 and roughly 200 K is characterized by the coexistence of the IC-CDW and C-CDW phases and is often referred to as NC-CDW. At the transition temperature $T_C$, IC-CDW domains completely vanish [14] and a new lattice symmetry is established. There is a general consensus about the formation of "star-of-David" clusters with in-plane $\sqrt{13}a \times \sqrt{13}a$ lattice reconstruction, whereby 12 Ta atoms are grouped around the 13th Ta atom [15,16]. In the absence of any external strain fields, this can be achieved in two equivalent ways (by either clockwise or counterclockwise rotations) thus yielding domains [17]. Despite extensive investigations, both experimental and theoretical, it remains an open question whether the stacking of star-of-David clusters is triclinic, trigonal, hexagonal, or a combination thereof [15,16,18–20]. The C-CDW phase is believed to be an insulator [3,21–23] with a gap of around 100 meV [13]. Very recent theoretical studies based on density-functional theory (DFT) find an additional ordering pattern along the crystallographic $c$ axis. The related gap has a width of approximately 0.5 eV along $k_z$ and becomes gapped at the Fermi energy $E_F$ in the C-CDW phase [24,25].

Nearly all of the previously reported results for optical phonons in 1$T$-$TaS_2$ are based on Raman spectroscopy on the C-CDW phase and on temperature-dependent measurements in a narrow range around the NC-CDW to C-CDW phase transition [13,15,18–20]. In this paper we present temperature-dependent polarization-resolved Raman

*Present address: Los Alamos National Laboratory, Los Alamos, New Mexico 87545, USA.

 

measurements in the temperature range from 4 to 370 K covering all three CDW regimes of $1T$-$TaS_2$. Our analysis of the C-CDW phase confirms the symmetry to be $P\bar{3}$, while the NC-CDW phase is confirmed as a mixed regime of commensurate and incommensurate domains. The Raman spectra of the IC-CDW phase mainly project the phonon density of states due to the breaking of translation invariance and sizable electron-phonon coupling. The growth of the CDW gap upon cooling, followed by the opening of the Mott gap, is traced via the initial slope of the symmetry-resolved spectra. The size of 170–190 meV and the temperature dependence of the Mott gap are directly determined from high-energy Raman data.

## II. EXPERIMENTAL AND NUMERICAL METHODS

The preparation of the studied $1T$-$TaS_2$ single crystals is described elsewhere [26–29]. Calibrated customized Raman scattering equipment was used to obtain the spectra. Temperature-dependent measurements were performed with the sample attached to the cold finger of a He-flow cryostat. The sample was cooled down to the lowest temperature and then heated. In either case the rates were less than $\pm 1$ K/min. All measurements were performed in a high vacuum of approximately $5 \times 10^{-5}$ Pa.

The 575-nm laser line of a diode-pumped Coherent GENESIS MX-SLM solid state laser was used as an excitation source. Additional measurements with the 458- and 514-nm laser lines were performed with a Coherent Innova 304C argon ion laser. The absorbed power was set at 4 mW. All spectra shown are corrected for the sensitivity of the instrument and the Bose factor, yielding the imaginary part of the Raman susceptibility $R\chi''$, where $R$ is an experimental constant. An angle of incidence of $\Theta_i = 66.0 \pm 0.4^\circ$ and atomically flat cleaved surfaces enable us to measure at energies as low as 5 $cm^{-1}$ without a detectable contribution from the laser line since the directly reflected light does not reach the spectrometer. The corresponding laser spot has an area of roughly $50 \times 100$ $\mu m^2$ which prevents us from observing the possible emergence of the domains [17,30]. The inelastically scattered light is collected along the surface normal (crystallographic $c$ axis) with an objective lens having a numerical aperture of 0.25. In the experiments presented here, the linear polarizations of the incident and scattered light are denoted as $\mathbf{e}_i$ and $\mathbf{e}_s$, respectively. For $\mathbf{e}_i$ horizontal to the plane of incidence there is no projection on the crystallographic $c$ axis. For the low numerical aperture of the collection optics $\mathbf{e}_s$ is always perpendicular to the $c$ axis. Low-energy data up to 550 $cm^{-1}$ were acquired in steps of $\Delta\Omega = 1$ $cm^{-1}$ with a resolution of $\sigma \approx 3$ $cm^{-1}$. The symmetric phonon lines were modeled using Voigt profiles where the width of the Gaussian part is given by $\sigma$. For spectra up to higher energies the step width and resolution were set at $\Delta\Omega = 50$ $cm^{-1}$ and $\sigma \approx 20$ $cm^{-1}$, respectively. The Raman tensors for the $D_{3d}$ point group are given in Table I. Accordingly, parallel linear polarizations project both $A_{1g}$ and $E_g$ symmetries, while crossed linear polarizations only project $E_g$. The pure $A_{1g}$ response then can be extracted by subtraction.

We have performed DFT calculations as implemented in the ABINIT package [31]. We have used the Perdew-Burke-Ernzerhof (PBE) functional, an energy cutoff of 50 Ha for the plane-wave basis, and we have included spin-orbit coupling by means of fully relativistic Goedecker pseudopotentials [32,33], where Ta-$5d^3 6s^2$ and S-$3s^2 3p^4$ states are treated as valence electrons. The crystal structure was relaxed so that forces on each atom were below 10 $\mu$eV/Å and the total stress on the unit cell below 1 bar, yielding lattice parameters $a = 3.44$ Å and $c = 6.83$ Å. Subsequently, the phonons and the electron-phonon coupling (EPC) were obtained from density-functional perturbation theory (DFPT) calculations, also within ABINIT [34]. Here, we have used an $18 \times 18 \times 12$ **k**-point grid for the electron wave vectors and a $6 \times 6 \times 4$ **q**-point grid for the phonon wave vectors. For the electronic occupation we employed Fermi-Dirac smearing with broadening factor $\sigma_{FD} = 0.01$ Ha, which is sufficiently high to avoid unstable phonon modes related to the CDW phases.

TABLE I. Raman tensors for trigonal systems (point group $D_{3d}$).

$$A_{1g} = \begin{pmatrix} a & 0 & 0 \\ 0 & a & 0 \\ 0 & 0 & b \end{pmatrix} \quad {}^1E_g = \begin{pmatrix} c & 0 & 0 \\ 0 & -c & d \\ 0 & d & 0 \end{pmatrix} \quad {}^2E_g = \begin{pmatrix} 0 & -c & -d \\ -c & 0 & 0 \\ -d & 0 & 0 \end{pmatrix}$$

## III. RESULTS AND DISCUSSION

### A. Lattice dynamics of the charge-density wave regimes

Temperature-dependent symmetry-resolved Raman spectra of $1T$-$TaS_2$ are presented in Fig. 1. It is obvious that their evolution with temperature is divided into three distinct ranges (IC-CDW, NC-CDW, and C-CDW) as indicated. The lattice dynamics for each of these ranges will be treated separately in the first part of the section. In the second part we address the electron dynamics.

#### *1. C-CDW phase*

At the lowest temperatures $1T$-$TaS_2$ exists in the commensurate C-CDW phase. Here, the atoms form so-called star-of-David clusters. Different studies report either triclinic stacking of these clusters leading to $P\bar{1}$ unit cell symmetry [16], or trigonal or hexagonal stacking and $P\bar{3}$ unit cell symmetry [15,18–20]. A factor group analysis predicts 57 $A_g$ Raman-active modes with an identical polarization dependence for $P\bar{1}$ unit cell symmetry, and alternatively 19 $A_g$+19 $E_g$ Raman-active modes for $P\bar{3}$ unit cell symmetry [13] Our polarized Raman scattering measurements at $T = 4$ K, measured in two scattering channels, together with the corresponding cumulative fits are shown in Fig. 2. As it can be seen, we have observed modes of two different symmetries in the related scattering channels. This result indicates trigonal or hexagonal stacking of the star-of-David clusters. The symmetric phonon lines can be described by Voigt profiles, the best fit of which is shown as blue (for parallel light polarizations) and red (crossed polarizations) lines. After fitting Voigt profiles to the Raman spectra, 38 phonon modes were singled out. Following the selection rules for $A_g$ and $E_g$ symmetry modes, 19 were assigned as $A_g$ and 19 as $E_g$ symmetry, meaning all expected modes could be identified. The contribution from each mode to the cumulative fit is presented in Fig. 2 as green

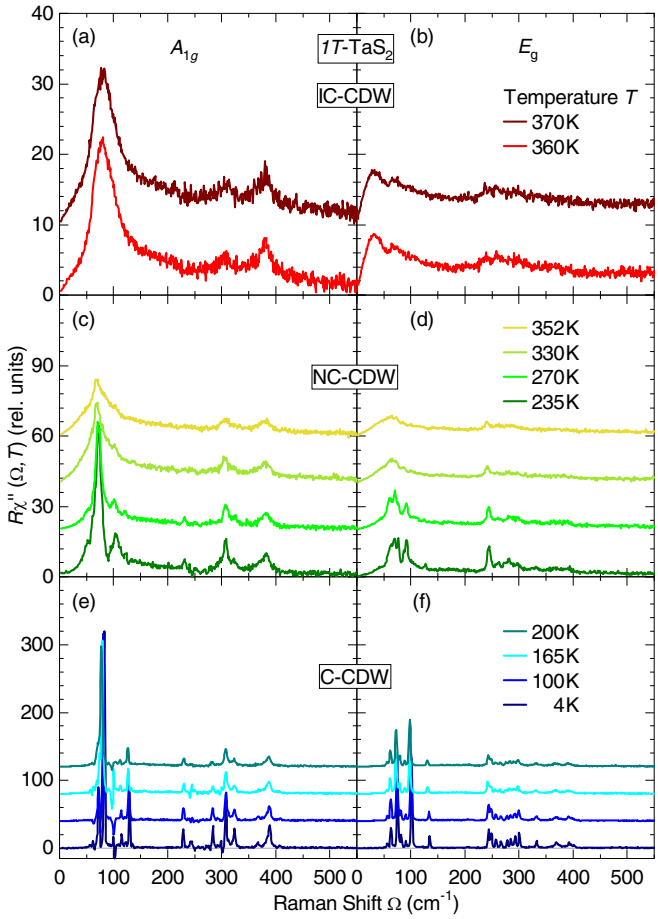


FIG. 1. Symmetry-resolved Raman spectra of $1T$-$TaS_2$ at temperatures as indicated. Both C-CDW (blue lines) and IC-CDW (red lines) domains yield significant contributions to the Raman spectra of the NC-CDW phase (green lines).

TABLE II. $A_{1g}$ and $E_g$ Raman mode energies experimentally obtained at $T = 4$ K.

| $n_o$ | $\omega_{A_g}$ (cm$^{-1}$) | $\omega_{E_g}$ (cm$^{-1}$) |
|---|---|---|
| 1 | 62.6 | 56.5 |
| 2 | 73.3 | 63.3 |
| 3 | 83.4 | 75.3 |
| 4 | 114.9 | 82.0 |
| 5 | 121.9 | 90.5 |
| 6 | 129.5 | 101.1 |
| 7 | 228.7 | 134.8 |
| 8 | 244.1 | 244.0 |
| 9 | 271.9 | 248.9 |
| 10 | 284.2 | 257.5 |
| 11 | 298.6 | 266.6 |
| 12 | 307.2 | 278.3 |
| 13 | 308.2 | 285.0 |
| 14 | 313.0 | 292.9 |
| 15 | 321.2 | 300.5 |
| 16 | 324.2 | 332.7 |
| 17 | 332.0 | 369.2 |
| 18 | 367.2 | 392.6 |
| 19 | 388.4 | 397.7 |

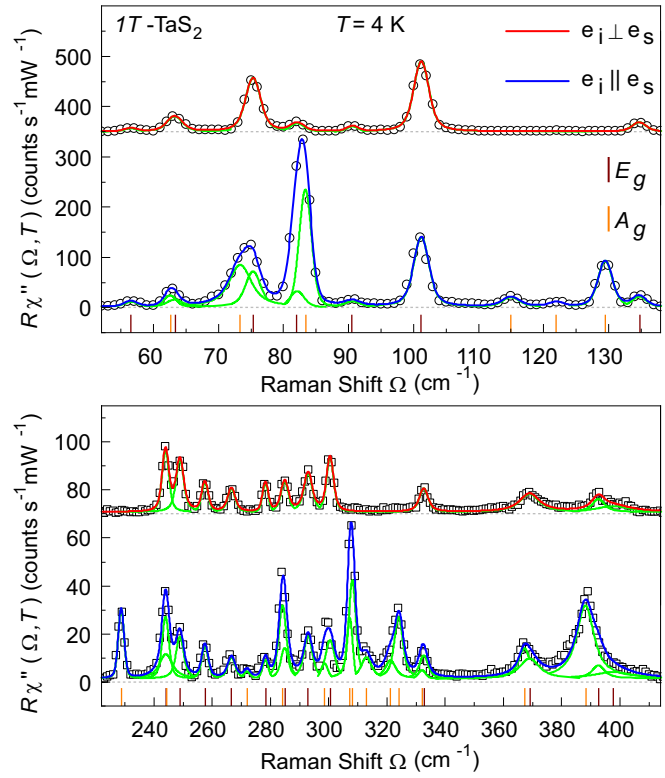


FIG. 2. Raman spectra at $T = 4$ K, i.e., in the C-CDW phase, for parallel and crossed light polarizations. Red and blue solid lines represent fits of the experimental data using Voigt profiles. Spectra are offset for clarity. The short vertical lines depict central frequencies obtained from the data analysis. The exact energy values are presented in Table II.

lines, whereas the complete list of the corresponding phonon energies can be found in Table II.

### *2. IC-CDW phase*

At the highest experimentally accessible temperatures $1T$-$TaS_2$ adopts the IC-CDW phase. Data collected by Raman scattering at $T = 370$ K, containing all symmetries, are shown as a blue solid line in Fig. 3. As $1T$-$TaS_2$ is metallic in this phase [25] we expect the phonon lines to be superimposed on a continuum of electron-hole excitations which we approximate using a Drude spectrum shown as a dashed line [35,36].

Since the IC-CDW phase arises from the normal metallic phase, described by space group $P\bar{3}m1$ [13,37], it is interesting to compare our Raman results on the IC-CDW phase to an *ab initio* calculation of the phonon dispersion in the normal phase, shown as an inset in Fig. 3. Four different optical modes were obtained at Γ: $E_u$ at 189 cm$^{-1}$ (double degenerate), $E_g$ at 247 cm$^{-1}$ (double degenerate), $A_{2u}$ at 342 cm$^{-1}$, and $A_{1g}$ at 346 cm$^{-1}$. A factor group analysis shows that two of these are Raman active, namely $E_g$ and $A_{1g}$ [13].

We observe that the calculated phonon eigenvalues of the simple metallic phase at Γ do not closely match the observed peaks in the experimental spectra of the IC-CDW phase. Rather, these correspond better to the calculated phonon density of states (PDOS), depicted in Fig. 3. There are essentially three different ways to project the PDOS in a Raman

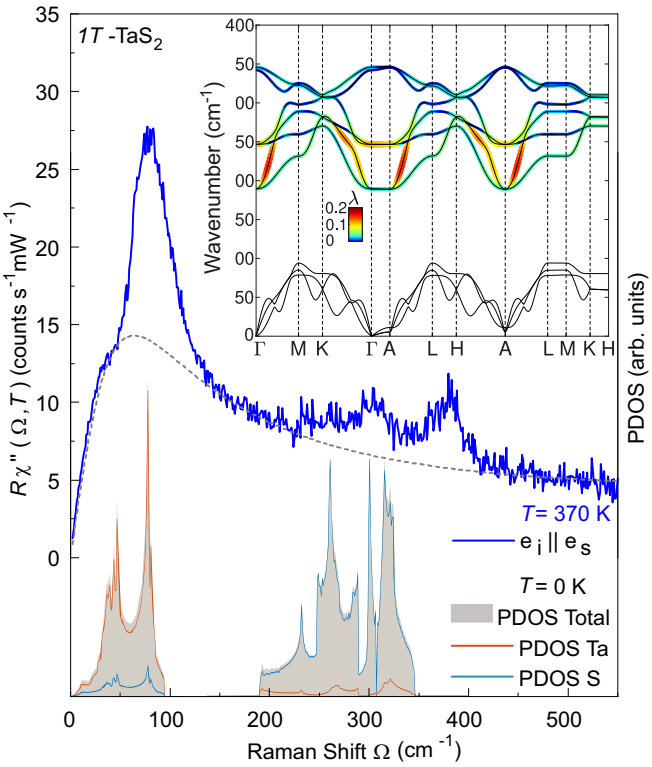


FIG. 3. Raman response for parallel light polarizations in the IC-CDW phase at 370 K (blue line). The dashed line depicts the possible electronic continuum. The contributions of the Ta (dark brown) and S atoms (light brown) to the calculated PDOS (gray area) are shown below. The inset shows the calculated phonon dispersion of $1T$-$TaS_2$ in the simple metallic phase, with the electron-phonon coupling ($\lambda$) of the optical branches indicated through the color scale.

experiment and to overcome the $q \approx 0$ selection given by the small momentum of visible light: (i) scattering on impurities [38], (ii) enhanced electron-phonon coupling [39], and (iii) breaking of the translational symmetry in the IC-CDW phase. (i) We rule out chemical impurity scattering, expected to exist at all temperatures, as the low-temperature spectra (Fig. 2) show no signs thereof. (ii) The additional scattering channel may come from the electron-phonon coupling (EPC). The calculated EPC, $\lambda$, in the optical modes (inset of Fig. 3) is limited, yet not negligible, reaching maxima of $\sim$0.2 in the lower optical branches around the Brillouin zone (BZ) points $\Gamma$ and $A$. The calculated atom-resolved PDOS shows the acoustic modes to be predominantly due to Ta and the optical modes due to S, as a result of their difference in atomic mass. The acoustic modes display several dips that are signatures of the latent CDW phases, for which the EPC cannot be reliably determined. Significant EPC in the optical modes of $1T$-$TaS_2$ is furthermore supported by experimental results linking a sharp increase in the resistivity above the IC-CDW transition temperature to the EPC [37]. It also corroborates calculated [14] and experimentally obtained [13] values of the CDW gap, which correspond to intermediate to strong EPC [37]. (iii) Although EPC certainly contributes we believe that the majority of the additional scattering channels can be traced back to the incommensurate breaking of the translational invariance upon entering IC-CDW. Thus the "weighted" PDOS is projected into the Raman spectrum [see Figs. 1(a) and 1(b)]. These "weighting" factors depend on the specific symmetries along the phonon branches as well as the "new periodicity" and go well beyond the scope of this paper.

#### *3. NC-CDW phase*

The nearly commensurate phase is seen as a mixed phase consisting of regions of commensurate and incommensurate CDWs [40,41]. This coexistence of high- and low-temperature phases is observable in our temperature-dependent data as shown in Fig. 1. The spectra for the IC-CDW (red curves) and C-CDW phase (blue curves) are distinctly different, as also visible in the data shown above (Figs. 2 and 3). The spectra of the NC-CDW phase (235 K $< T <$ 352 K) comprise contributions from both phases. As 352 K is the highest temperature at which the contributions from the C-CDW phase can be observed in the spectra, we suggest that the phase transition temperature from IC-CDW to NC-CDW phase is somewhere in between 352 and 360 K. This conclusion is in good agreement with experimental results regarding this transition [4–6].

### B. Gap evolution

The opening of a typically momentum-dependent gap in the electronic excitation spectrum is a fundamental property of CDW systems which has also been observed in $1T$-$TaS_2$ [13,37,42]. Here, in addition to the CDW, a Mott transition at the onset of the C-CDW phase leads to an additional gap opening in the bands close to the $\Gamma$ point [21,43]. Symmetry-resolved Raman spectroscopy can provide additional information here using the momentum resolution provided by the selection rules. To this end, we look at the initial slopes of the electronic part of the spectra.

As shown in Figs. 4(a)–4(c), different symmetries project individual parts of the BZ [36,44]. The vertices given by the hexagonal symmetry of $1T$-$TaS_2$ are derived in Appendix C. The $A_{1g}$ vertex mainly highlights the area around the $\Gamma$ point while the $E_g$ vertices predominantly project the BZ boundaries. The opening of a gap at the Fermi level reduces $N_F$, leading to an increase of the resistivity in the case of $1T$-$TaS_2$. This reduction of $N_F$ manifests itself also in the Raman spectra which, to zeroth order, are proportional to $N_F$ [35,44]. As a result, the initial slope changes as shown Figs. 4(d) and 4(e), which zoom in on the low-energy region of the spectra from Fig. 1. The initial slope of the Raman response is $R \lim_{\Omega\to 0} \frac{\partial \chi''}{\partial \Omega} \propto N_F \tau_0$, where $R$ incorporates only experimental factors [44]. The electronic relaxation $\Gamma_0^* \propto (N_F \tau_0)^{-1}$ is proportional to the dc resistivity $\rho(T)$ [45]. If a gap opens up there is vanishing intensity at $T = 0$ below the gap edge for an isotropic gap. At finite temperature there are thermally excited quasiparticles which scatter. Thus, there is a linear increase at low energies [35]. The black lines in Figs. 4(d)–4(g) represent the initial slopes and their temperature dependences. The lines comprise carrier relaxation and gap effects, and we focus only on the relative changes.

Starting in the IC-CDW phase at $T = 370$ K [Fig. 4(d)] the initial slope is higher for the $E_g$ spectrum than for $A_{1g}$ symmetry. While the CDW gap started to open already at

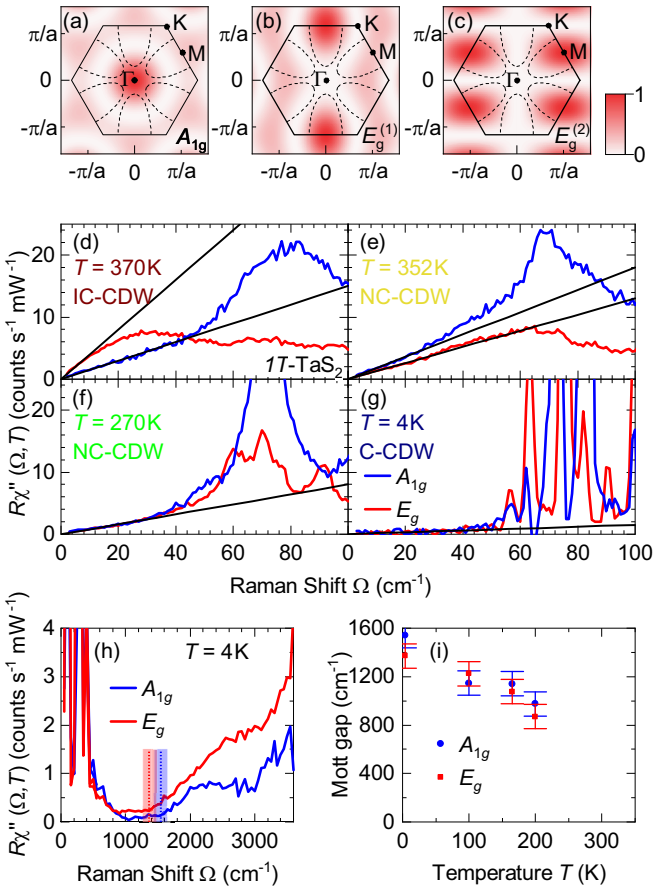


FIG. 4. Evolution of the gaps. (a)–(c) Squared Raman vertices and Fermi surface of $1T$-$TaS_2$ for the indicated symmetries in the normal phase above $T_{IC}$. The derivation of Raman vertices is presented in Appendix C. (d)–(g) Low-energy Raman spectra for $A_{1g}$ symmetry (blue) and $E_g$ symmetries (red) at temperatures as indicated. The spectra shown are zooms on the data shown in Fig. 1. The black lines highlight the initial slope of the spectra. (h) High-energy spectra at 4 K. Vertical dashed lines and colored bars indicate the approximate size and error bars of the Mott gap for the correspondingly colored spectrum. (i) Temperature dependence of the Mott gap $\Delta_\mu$ ($\mu = A_{1g}, E_g$).

554 K around the $M$ points [43], which are highlighted by the $E_g$ vertex, the Fermi surface projected by the $E_g$ vertex continues to exist. Thus, we may interpret the different slopes as a manifestation of a momentum-dependent gap in the IC-CDW phase and assume overall intensity effects to be symmetry independent for all temperatures. At $T = 352$ K [Fig. 4(e)] the slope for $E_g$ symmetry is substantially reduced to below the $A_{1g}$ slope due to a strong increase of the CDW gap in the commensurate regions [43] which emerge upon entering the NC-CDW phase. Further cooling also decreases the slope for the $A_{1g}$ spectrum, as the Mott gap around the Γ point starts to open within the continuously growing C-CDW domains [40,41]. Below $T = 270$ K the initial slopes are identical for both symmetries and decrease with temperature. Apparently, the Mott gap opens up on the entire Fermi surface in direct correspondence with the increase of the resistivity by approximately an order of magnitude [3]. Finally, at the lowest temperature close to 4 K the initial slopes drop to almost zero

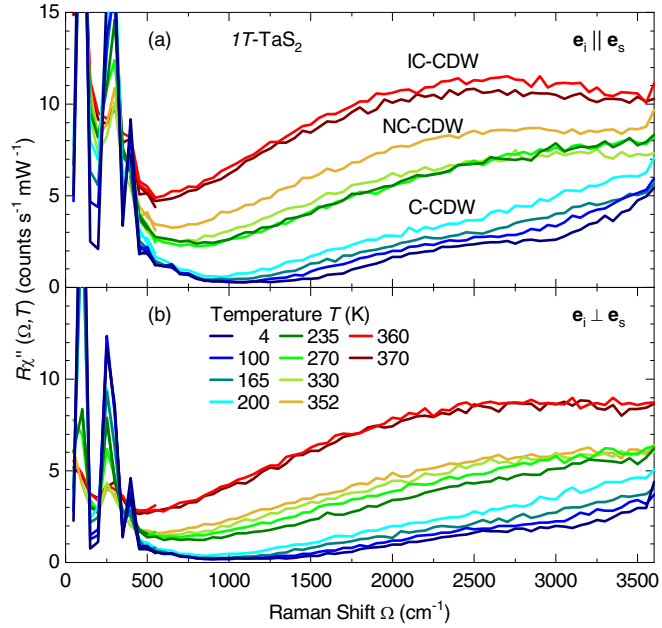


FIG. 5. Raman spectra up to high energies for (a) parallel and (b) crossed polarizations of the incident and scattered light at temperatures as given in the legend.

[Fig. 4(g)], indicating vanishing conductivity or fully gapped bands in the entire BZ.

Concomitantly, and actually more intuitive for the opening of a gap, we observe the loss of intensity in the Raman spectra below a threshold at an energy $\Omega_{gap}$. Below 30 $cm^{-1}$ the intensity is smaller than 0.2 counts(mW s)$^{-1}$ [Fig. 4(g)] and still smaller than 0.3 counts(mW s)$^{-1}$ up to 1500 $cm^{-1}$ [Fig. 4(h)]. For a superconductor or a CDW system the threshold is given by $2\Delta$, where $\Delta$ is the single-particle gap, and a pileup of intensity for higher energies, $\Omega > 2\Delta$ [44]. A pileup of intensity cannot be observed here. Rather, the overall intensity is further reduced with decreasing temperature as shown in Figs. 5 and 6 in Appendixes A and B. In particular, the reduction occurs in distinct steps between the phases and continuous inside the phases with the strongest effect in the C-CDW phase below approximately 210 K (Fig. 5). In a system as clean as $1T$-$TaS_2$ the missing pileup in the C-CDW phase is surprising and argues for an alternative interpretation.

In a Mott system, the gap persists to be observable but the pileup is not a coherence phenomenon and has not been observed yet. In fact, the physics is quite different, and the conduction band is split symmetrically about the Fermi energy $E_F$ into a lower and a upper Hubbard band. Thus in the case of Mott-Hubbard physics the experimental signatures are more such as those expected for an insulator or semiconductor having a small gap, where at $T = 0$ there is a range without intensity and an interband onset with a band-dependent shape. At finite temperature there are thermal excitations inside the gap. For $1T$-$TaS_2$ at the lowest accessible temperature, both symmetries exhibit a flat, nearly vanishing electronic continuum below a slightly symmetry-dependent threshold (superposed by the phonon lines at low energies). Above the threshold a weakly structured increase is observed. We interpret this onset as the distance of the lower

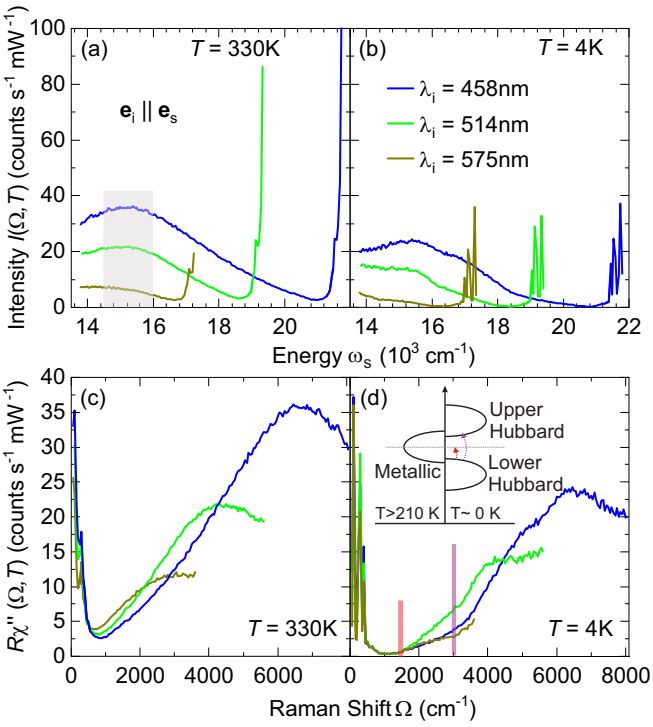


FIG. 6. Luminescence contribution to the Raman data. (a), (b) Intensity as a function of the absolute frequency for (a) $T = 330$ K and (b) $T = 4$ K. The approximate peak maximum of the contribution attributed to luminescence is highlighted by the gray shaded area. (c), (d) Raman susceptibility calculated from (a) and (b), respectively, shown as a function of frequency (Raman) shift. The luminescence peak appears at different Raman shifts depending on the wavelength of the laser light. At $T = 4$ K the spectra are identical up to 1600 $cm^{-1}$ for all laser light wavelengths.

Hubbard band from the Fermi energy $E_F$ or half of the distance between the lower and the upper Hubbard band, shown as vertical dashed lines at 1350–1550 $cm^{-1} \equiv$ 170–190 meV [Fig. 4(h)]. The energy is in good agreement with gap obtained from the in-plane angle-resolved photoemission spectroscopy (ARPES) [43], scanning tunneling spectroscopy [46], and infrared spectroscopy [13] which may be compared directly with our Raman results measured with in-plane polarizations. Upon increasing the temperature the size of the gap shrinks uniformly in both symmetries [Fig. 4(i)] and may point to an onset above the C-CDW phase transition, consistent with the result indicated by the initial slope. However, we cannot track the development of the gap into the NC-CDW phase as an increasing contribution of luminescence (see Appendix B) overlaps with the Raman data.

Recently, it was proposed on the basis of DFT calculations that 1$T$-$TaS_2$ orders also along the $c$ axis perpendicular to the planes in the C-CDW state [24,25]. This quasi-one-dimensional (1D) coupling is unexpectedly strong and the resulting metallic band is predicted to have a width of approximately 0.5 eV. For specific relative ordering of the star of David patterns along the $c$ axis this band develops a gap of 0.15 eV at $E_F$ [25], which is intriguingly close to the various experimental observations. However, since our light polarizations are strictly in plane, we have to conclude that the gap observed here (and presumably in the other experiments) is an in-plane gap. Our experiment cannot detect an out-of-plane gap. Thus, neither a quasimetallic dispersion along the $c$ axis nor a gap in this band along $k_z$ may be excluded in the C-CDW phase. However, there is compelling evidence for a Mott-like gap in the layers rather than a CDW gap.

## IV. CONCLUSIONS

We have presented a study of the various charge density wave regimes in 1$T$-$TaS_2$ by inelastic light scattering, supported by *ab initio* calculations. The spectra of lattice excitations in the commensurate CDW (C-CDW) phase determine the unit cell symmetry to be $P\bar{3}$, indicating trigonal or hexagonal stacking of the "star-of-David" structure. The high-temperature spectra of the incommensurate CDW (IC-CDW) state are dominated by a projection of the phonon density of states caused by either a significant electron-phonon coupling or, more likely, the superstructure. The intermediate nearly commensurate (NC-CDW) phase is confirmed to be a mixed regime of commensurate and incommensurate regions contributing to the phonon spectra below an onset temperature $T_{NC} \approx$ 352–360 K, in good agreement with previously reported values. At the lowest measured temperatures, the observation of a virtually clean gap without a redistribution of spectral weight from low to high energies below $T_C$ argues for the existence of a Mott metal-insulator transition at a temperature of order 100 K. The magnitude of the gap is found to be $\Omega_{gap} \approx$ 170–190 meV and has little symmetry, thus momentum, dependence, in agreement with earlier ARPES results [37]. At 200 K, on the high-temperature end of the C-CDW phase, the gap shrinks to ∼60% of its low-temperature value. Additionally, the progressive filling of the CDW gaps by thermal excitations is tracked via the initial slope of the spectra, and indicates that the Mott gap opens primarily on the parts of the Fermi surface closest to the Γ point.

Our results demonstrate the potential of using inelastic light scattering to probe the momentum dependence and energy scale of changes in the electronic structure driven by low-temperature collective quantum phenomena. This opens perspectives to investigate the effect of hybridization on collective quantum phenomena in heterostructures composed of different 2D materials, e.g., alternating $T$ and $H$ monolayers as in the 4$Hb$-$TaS_2$ phase [47].

## ACKNOWLEDGMENTS

The authors acknowledge funding provided by the Institute of Physics Belgrade through the grant by the Ministry of Education, Science and Technological Development of the Republic of Serbia. The work was supported by the Science Fund of the Republic of Serbia, PROMIS, No. 6062656, StrainedFeSC, and by Research Foundation-Flanders (FWO). J.B. acknowledges support of a postdoctoral fellowship of the FWO, and of the Erasmus + program for staff mobility and training (KA107, 2018) for a research stay at the Institute of Physics Belgrade, during which part of the work was carried out. The computational resources and services used for the first-principles calculations in this work were provided by the VSC (Flemish Supercomputer Center), funded by the

FWO and the Flemish Government – department EWI. Work at Brookhaven is supported by the U.S. DOE under Contract No. DESC0012704. A.B. and R.H. acknowledge support by the German research foundation (DFG) via Projects No. Ha2071/12-1 and No. 107745057 – TRR 80 and by the DAAD via the project-related personal exchange program PPP with Serbia Grant No. 57449106.

## APPENDIX A: RAW DATA

Figure 5 shows Raman spectra at temperatures ranging from $T = 4$ to 370 K for parallel [Fig. 5(a)] and crossed [Fig. 5(b)] in-plane light polarizations. The spectra were measured in steps of $\Delta\Omega = 50\ \mathrm{cm}^{-1}$ and a resolution of $\sigma \approx 20\ \mathrm{cm}^{-1}$. Therefore neither the shapes nor the positions of the phonon lines below 500 $\mathrm{cm}^{-1}$ may be resolved. All spectra reach a minimum in the range from 500 to 1600 $\mathrm{cm}^{-1}$. At energies above 500 $\mathrm{cm}^{-1}$ the overall intensities are strongly temperature dependent and decreasing with decreasing temperature. Three clusters of spectra are well separated according to the phases they belong to.

In the C-CDW phase ($T \leqslant 200$ K, blue lines) the spectra start to develop substructures at 1500 and 3000 $\mathrm{cm}^{-1}$. The spectra at 200 K increase almost linearly with energy. The spectra of the NC- and IC-CDW phases exhibit a broad maximum centered in the region of 2200–3200 $\mathrm{cm}^{-1}$ which may be attributed to luminescence (see Appendix B). For clarification we measured a few spectra with various laser lines for excitation.

## APPENDIX B: LUMINESCENCE

Figure 6 shows Raman spectra measured with parallel light polarizations for three different wavelengths $\lambda_i$ of the incident laser light. Figures 6(a) and 6(b) depict the measured intensity $I$ (without the Bose factor) as a function of the absolute frequency $\tilde{\nu}$ of the scattered light.

At high temperature [$T = 330$ K, Fig. 6(a)] a broad peak can be seen for all $\lambda_i$ which is centered at a fixed frequency of 15 200 $\mathrm{cm}^{-1}$ of the scattered photons (gray shaded area). The peak intensity decreases for increasing $\lambda_i$ (decreasing energy). Correspondingly, this peak's center depends on the laser wavelength in the spectra shown as a function of the Raman shift [Fig. 6(c)]. This behavior indicates that the origin of this excitation is likely to be luminescence where transitions at fixed absolute final frequencies are expected.

At low temperature [Fig. 6(b)] we can no longer find a structure at a fixed absolute energy. Rather, as already indicated in the main part, the spectra develop additional, yet weak, structures which are observable in all spectra but are particularly pronounced for blue excitation. For green and yellow excitation the spectral range of the spectrometer, limited to 732 nm, is not wide enough for a deeper insight into the luminescence contributions (at energies different from those at high temperature) and no maximum common to all three spectra is observed. If these spectra are plotted as a function of the Raman shift, the changes in slope at 1500 and 3000 $\mathrm{cm}^{-1}$ are found to be in the same position for all $\lambda_i$, values thus arguing for inelastic scattering rather than luminescence. Since we do currently not have the appropriate experimental tools for an in-depth study, our interpretation is preliminary although supported by the observations in Fig. 6(d).

As shown in the inset of Fig. 6(d) we propose a scenario on the basis of Mott physics. In the C-CDW phase the reduced bandwidth is no longer the largest energy and the Coulomb repulsion $U$ becomes relevant [22] and splits the conduction band into a lower and upper Hubbard band. We assume that the onset of scattering at 1500 $\mathrm{cm}^{-1}$ corresponds to the distance of the highest energy of the lower Hubbard band to the Fermi energy $E_F$. The second onset corresponds then to the distance between the highest energy of the lower Hubbard band and the lowest energy of the upper Hubbard band. An important question needs to be answered: Into which unoccupied states right above $E_F$ does the first process scatter electrons? We may speculate that some DOS is provided by the metallic band dispersing along $k_z$ or by the metallic domain walls between the different types of ordering patterns along the $c$ axis observed recently by tunneling spectroscopy [46]. These quasi-1D domain walls would provide the states required for the onset of scattering at high energy but are topologically too small for providing enough density of states for a measurable intensity at low energy [Fig. 4(g)] in a location-integrated experiment such as Raman scattering.

## APPENDIX C: DERIVATION OF THE RAMAN VERTICES

Phenomenologically, the Raman vertices can be derived based on lattice symmetry, which are proportional to the Brillouin zone harmonics. They are a set of functions that exhibit the symmetry and periodicity of the lattice structure proposed by Allen [48]. These functions make the $k$-space sums and energy integrals more convenient than that of the Cartesian basis or the spherical harmonics basis, especially for those materials who have anisotropic and/or multiple Fermi pockets. The three Cartesian components of the Fermi velocity $v_k$ are recommended to generate this set of functions since they inherit the symmetry and periodicity of the crystal lattice naturally. However, in most cases, we do not know the details of band dispersion. A phenomenological method is needed to construct such a set of basis functions. Here, we demonstrate a method based on the group theory. The Brillouin zone harmonics can be obtained by the projection operation on specific trial functions.

For a certain group $G$ with symmetry elements $R$ and symmetry operators $\hat{P}_R$, it can be described by several irreducible representations $\Gamma_n$, where $n$ labels the representation. For each irreducible representation, there are corresponding basis functions $\Phi^j_{\Gamma_n}$ that can be used to generate representation matrices for a particular symmetry. Here, $j$ labels the component or partner of the representations. For an arbitrary function $F$, we have

$$F = \sum_{\Gamma_n} \sum_{j} f_j^{\Gamma_n} \Phi^j_{\Gamma_n}. \tag{C1}$$

According to the group theory, we can always define a projection operator by the relation [49]

$$\hat{P}^{\Gamma_n} = \frac{d}{N} \sum_{R} \chi^{\Gamma_n}(R) * \hat{P}_R, \tag{C2}$$

TABLE III. Symmetry operations $\hat{P}_R$ and corresponding character table of the$D_{3d}$ point group.

| $\hat{P}_R$ | $x'$ | $y'$ | $z'$ | $\chi^{\Gamma_n}(R)$ | |
|---|---|---|---|---|---|
| | | | | $A_{1g}$ | $E_g$ |
| $E$ | $x$ | $y$ | $z$ | 1 | 2 |
| $C_3^1$ | $-\frac{1}{2}x+\frac{\sqrt{3}}{2}y$ | $-\frac{\sqrt{3}}{2}x-\frac{1}{2}y$ | $z$ | 1 | $-1$ |
| $C_3^{-1}$ | $-\frac{1}{2}x-\frac{\sqrt{3}}{2}y$ | $\frac{\sqrt{3}}{2}x-\frac{1}{2}y$ | $z$ | 1 | $-1$ |
| $C_2'$ | $x$ | $-y$ | $-z$ | 1 | 0 |
| $C_2''$ | $-\frac{1}{2}x+\frac{\sqrt{3}}{2}y$ | $\frac{\sqrt{3}}{2}x+\frac{1}{2}y$ | $-z$ | 1 | 0 |
| $C_2'''$ | $-\frac{1}{2}x-\frac{\sqrt{3}}{2}y$ | $-\frac{\sqrt{3}}{2}x+\frac{1}{2}y$ | $-z$ | 1 | 0 |
| $I$ | $-x$ | $-y$ | $-z$ | 1 | 2 |
| $S_6^1$ | $\frac{1}{2}x-\frac{\sqrt{3}}{2}y$ | $\frac{\sqrt{3}}{2}x+\frac{1}{2}y$ | $-z$ | 1 | $-1$ |
| $S_6^{-1}$ | $\frac{1}{2}x+\frac{\sqrt{3}}{2}y$ | $-\frac{\sqrt{3}}{2}x+\frac{1}{2}y$ | $-z$ | 1 | $-1$ |
| $\sigma_v'$ | $-x$ | $y$ | $z$ | 1 | 0 |
| $\sigma_v''$ | $\frac{1}{2}x-\frac{\sqrt{3}}{2}y$ | $-\frac{\sqrt{3}}{2}x-\frac{1}{2}y$ | $z$ | 1 | 0 |
| $\sigma_v'''$ | $\frac{1}{2}x+\frac{\sqrt{3}}{2}y$ | $\frac{\sqrt{3}}{2}x-\frac{1}{2}y$ | $z$ | 1 | 0 |

that satisfies the relation

$$\hat{P}^{\Gamma_n}F=\sum_j f_j^{\Gamma_n}\Phi_{\Gamma_n}^j, \tag{C3}$$

where $d$ is the dimensionality of the irreducible representation $\Gamma_n$, $N$ is the number of symmetry operators in the group, and $\chi^{\Gamma_n}(R)$ is the character of the matrix of symmetry operator $R$ in irreducible representation $\Gamma_n$. By projection operation on a certain irreducible representation $\Gamma_n$, we can directly get its basis functions $\Phi_{\Gamma_n}^j$.

The basis functions are not unique. In specific physical problems, it is useful to use physical insight to guess an appropriate arbitrary function to find the basis functions for specific problems. $1T$-$TaS_2$ belongs to the $D_{3d}$ point group. There are 12 symmetry operators in this group, i.e., $E$, $C_3^1$, $C_3^{-1}$, $C_2'$, $C_2''$, $C_2'''$, $I$, $S_6^1$, $S_6^{-1}$, $\sigma_v'$, $\sigma_v''$, $\sigma_v'''$. The coordinate transformations after symmetry operations and the corresponding character table are listed in Table III.

In order to simulate the periodicity of the Brillouin zone, trigonometric functions are used as trial functions. According to the parity of the irreducible representations, we can choose an appropriate trigonometric function, e.g., a sine function for odd parity representation and cosine function for even parity representation. The combinations of them are also available.

Here, we use $F=\cos(k_x a)$ as a trial function, where $a$ is the in-plane crystal constant. The basis function of $A_{1g}$ can be derived as

$$\Phi_{A_{1g}}(\mathbf{k})=\frac{1}{3}\left[\cos(k_x a)+2\cos\left(\frac{1}{2}k_x a\right)\cos\left(\frac{\sqrt{3}}{2}k_y a\right)\right]. \tag{C4}$$

With the same method, we obtain a basis function of $E_g$ as

$$\Phi_{E_g^1}(\mathbf{k})=\frac{2}{3}\left[\cos(k_x a)-\cos\left(\frac{1}{2}k_x a\right)\cos\left(\frac{\sqrt{3}}{2}k_y a\right)\right]. \tag{C5}$$

Since the $E_g$ is a two-dimensional representation, the projection operation provides only one of the two basis functions of the corresponding subspace. The second function is found based on the subspace invariance under the symmetry operations (e.g., if we operate $\Phi_{E_g^1}$ with $C_3^1$ symmetry, the result can be presented as a linear combination of $\Phi_{E_g^1}$ and $\Phi_{E_g^2}$). Thus we obtain

$$\Phi_{E_g^2}(\mathbf{k})=2\sin\left(\frac{1}{2}k_x a\right)\sin\left(\frac{\sqrt{3}}{2}k_y a\right). \tag{C6}$$


[1] J. C. Tsang, J. E. Smith, M. W. Shafer, and S. F. Meyer, Raman spectroscopy of the charge-density-wave state in $1T$- and $2H$-$TaSe_2$, Phys. Rev. B **16**, 4239 (1977).

[2] C. J. Sayers, H. Hedayat, A. Ceraso, F. Museur, M. Cattelan, L. S. Hart, L. S. Farrar, S. Dal Conte, G. Cerullo, C. Dallera, E. Da Como, and E. Carpene, Coherent phonons and the interplay between charge density wave and Mott phases in $1T$-$TaSe_2$, Phys. Rev. B **102**, 161105(R) (2020).

[3] A. J. Wilson, J. F. D. Salvo, and S. Mahajan, Charge-density waves and superlattices in the metallic layered transition metal dichalcogenides, Adv. Phys. **24**, 117 (1975).

[4] C. B. Scruby, P. M. Williams, and G. S. Parry, The role of charge density waves in structural transformations of $1T$-$TaS_2$, Philos. Mag. **31**, 255 (1975).

[5] R. E. Thomson, B. Burk, A. Zettl, and J. Clarke, Scanning tunneling microscopy of the charge-density-wave structure in $1T$-$TaS_2$, Phys. Rev. B **49**, 16899 (1994).

[6] W. Wen, C. Dang, and L. Xie, Photoinduced phase transitions in two-dimensional charge-density-wave $1T$-$TaS_2$, Chin. Phys. B **28**, 058504 (2019).

[7] D. Svetin, I. Vaskivskyi, S. Brazovskii, Mertelj, and D. Mihailovic, Three-dimensional resistivity and switching between correlated electronic states in $1T$-$TaS_2$, Sci. Rep. **7**, 46048 (2017).

[8] D. Svetin, I. Vaskivskyi, P. Sutar, E. Goreshnik, J. Gospodaric, T. Mertelj, and D. Mihailovic, Transitions between photoinduced macroscopic quantum states in $1T$-$TaS_2$ controlled by substrate strain, Appl. Phys. Express **7**, 103201 (2014).

[9] G. Liu, B. Debnath, T. R. Pope, T. T. Salguero, R. K. Lake, and A. A. Balandin, A charge-density wave oscillator based on an integrated tantalum disulfide-boron nitride-graphene device operating at room temperature, Nat. Nanotechnol. **11**, 845 (2016).

[10] R. Salgado, A. Mohammadzadeh, F. Kargar, A. Geremew, C.-Y. Huang, M. A. Bloodgood, S. Rumyantsev, T. T. Salguero, and A. A. Balandin, Low-frequency noise spectroscopy of charge-density-wave phase transitions in vertical quasi-2D $1T$-$TaS_2$ devices, Appl. Phys. Express **12**, 037001 (2019).

[11] Z. X. Wang, Q. M. Liu, L. Y. Shi, S. J. Zhang, T. Lin, T. Dong, D. Wu, and N. L. Wang, Photoinduced hidden CDW state and relaxation dynamics of $1T$-$TaS_2$ probed by time-resolved terahertz spectroscopy, arXiv:1906.01500.

[12] L. Stojchevska, I. Vaskivskyi, T. Mertelj, P. Kusar, D. Svetin, S. Brazovskii, and D. Mihailovic, Ultrafast switching to a stable

hidden quantum state in an electronic crystal, Science **344**, 177 (2014).

[13] L. V. Gasparov, K. G. Brown, A. C. Wint, D. B. Tanner, H. Berger, G. Margaritondo, R. Gaál, and L. Forró, Phonon anomaly at the charge ordering transition in 1$T$-$TaS_2$, Phys. Rev. B **66**, 094301 (2002).

[14] O. R. Albertini, R. Zhao, R. L. McCann, S. Feng, M. Terrones, J. K. Freericks, J. A. Robinson, and A. Y. Liu, Zone-center phonons of bulk, few-layer, and monolayer 1$T$-$TaS_2$: Detection of commensurate charge density wave phase through Raman scattering, Phys. Rev. B **93**, 214109 (2016).

[15] S. Uchida and S. Sugai, Infrared and raman studies on a commensurate CDW states in transition metal dichalcogenides, Physica B+C **105**, 393 (1981).

[16] R. Brouwer and F. Jellinek, The low-temperature superstructures of 1$T$-$TaSe_2$ and 2$H$-$TaSe_2$, Physica B+C **99**, 51 (1980).

[17] A. Zong, X. Shen, A. Kogar, L. Ye, C. Marks, D. Chowdhury, T. Rohwer, B. Freelon, S. Weathersby, R. Li, J. Yang, J. Checkelsky, X. Wang, and N. Gedik, Ultrafast manipulation of mirror domain walls in a charge density wave, Sci. Adv. **4**, eaau5501 (2018).

[18] J. R. Duffay and R. D. Kirby, Raman scattering from 1$T$-$TaS_2$, Solid State Commun. **20**, 617 (1976).

[19] T. Hirata and F. S. Ohuchi, Temperature dependence of the Raman spectra of 1$T$-$TaS_2$, Solid State Commun. **117**, 361 (2001).

[20] S. L. L. M. Ramos, R. Plumadore, J. Boddison-Chouinard, S. W. Hla, J. R. Guest, D. J. Gosztola, M. A. Pimenta, and A. Luican-Mayer, Suppression of the commensurate charge density wave phase in ultrathin 1$T$-$TaS_2$ evidenced by Raman hyperspectral analysis, Phys. Rev. B **100**, 165414 (2019).

[21] B. Sipos, A. F. Kusmartseva, A. Akrap, H. Berger, L. Forró, and E. Tutis, From Mott state to superconductivity in 1$T$-$TaS_2$, Nat. Mater. **7**, 960 (2008).

[22] P. Fazekas and E. Tosatti, Electrical, structural and magnetic properties of pure and doped 1$T$-$TaS_2$, Philos. Mag. B **39**, 229 (1979).

[23] E. Martino, A. Pisoni, L. Ćirić, A. Arakcheeva, H. Berger, A. Akrap, C. Putzke, P. J. W. Moll, I. Batistić, E. Tutiš, L. Forró, and K., Preferential out-of-plane conduction and quasi-one-dimensional electronic states in layered 1$T$-$TaS_2$, npj 2D Mater. Appl. **4**, 7 (2020).

[24] P. Darancet, A. J. Millis, and C. A. Marianetti, Three-dimensional metallic and two-dimensional insulating behavior in octahedral tantalum dichalcogenides, Phys. Rev. B **90**, 045134 (2014).

[25] S.-H. Lee, J. S. Goh, and D. Cho, Origin of the Insulating Phase and First-Order Metal-Insulator Transition in 1$T$-$TaS_2$, Phys. Rev. Lett. **122**, 106404 (2019).

[26] Y. Ma, Y. Hou, C. Lu, L. Li, and C. Petrovic, Possible origin of nonlinear conductivity and large dielectric constant in the commensurate charge-density-wave phase of 1$T$-$TaS_2$, Phys. Rev. B **97**, 195117 (2018).

[27] L. J. Li, W. J. Lu, X. D. Zhu, L. S. Ling, Z. Qu, and Y. P. Sun, Fe-doping induced superconductivity in the charge-density-wave system 1$T$-$TaS_2$, Europhys. Lett. **98**, 29902 (2012).

[28] Y. Liu, R. Ang, W. J. Lu, W. H. Song, L. J. Li, and Y. P. Sun, Superconductivity induced by Se-doping in layered charge-density-wave system 1$T$-$TaS_{2-x}Se_x$, Appl. Phys. Lett. **102**, 192602 (2013).

[29] R. Ang, Y. Miyata, E. Ieki, K. Nakayama, T. Sato, Y. Liu, W. J. Lu, Y. P. Sun, and T. Takahashi, Superconductivity and bandwidth-controlled Mott metal-insulator transition in 1$T$-$TaS_{2-x}Se_x$, Phys. Rev. B **88**, 115145 (2013).

[30] M. Bovet, D. Popović, F. Clerc, C. Koitzsch, U. Probst, E. Bucher, H. Berger, D. Naumović, and P. Aebi, Pseudogapped Fermi surfaces of 1$T$-$TaS_2$ and 1$T$-$TaSe_2$: A charge density wave effect, Phys. Rev. B **69**, 125117 (2004).

[31] X. Gonze, B. Amadon, P.-M. Anglade, J.-M. Beuken, F. Bottin, P. Boulanger, F. Bruneval, D. Caliste, R. Caracas, M. Côté, T. Deutsch, L. Genovese, P. Ghosez, M. Giantomassi, S. Goedecker, D. Hamann, P. Hermet, F. Jollet, G. Jomard, S. Leroux *et al.*, ABINIT: First-principles approach to material and nanosystem properties, Comput. Phys. Commun. **180**, 2582 (2009).

[32] S. Goedecker, M. Teter, and J. Hutter, Separable dual-space Gaussian pseudopotentials, Phys. Rev. B **54**, 1703 (1996).

[33] M. Krack, Pseudopotentials for H to Kr optimized for gradient-corrected exchange-correlation functionals, Theor. Chem. Acc. **114**, 145 (2005).

[34] X. Gonze, D. C. Allan, and M. P. Teter, Dielectric Tensor, Effective Charges, and Phonons in $\alpha$-Quartz by Variational Density-Functional Perturbation Theory, Phys. Rev. Lett. **68**, 3603 (1992).

[35] A. Zawadowski and M. Cardona, Theory of Raman scattering on normal metals with impurities, Phys. Rev. B **42**, 10732 (1990).

[36] N. Lazarević and R. Hackl, Fluctuations and pairing in Fe-based superconductors: Light scattering experiments, J. Phys.: Condens. Matter **32**, 413001 (2020).

[37] K. Rossnagel, On the origin of charge-density waves in select layered transition-metal dichalcogenides, J. Phys.: Condens. Matter **23**, 213001 (2011).

[38] R. Shuker and R. W. Gammon, Raman-Scattering Selection-Rule Breaking and the Density of States in Amorphous Materials, Phys. Rev. Lett. **25**, 222 (1970).

[39] A. Baum, A. Milosavljević, N. Lazarević, M. M. Radonjić, B. Nikolić, M. Mitschek, Z. I. Maranloo, M. Šćepanović, M. Grujić-Brojčin, N. Stojilović, M. Opel, A. Wang, C. Petrovic, Z. V. Popović, and R. Hackl, Phonon anomalies in FeS, Phys. Rev. B **97**, 054306 (2018).

[40] A. Spijkerman, J. L. de Boer, A. Meetsma, G. A. Wiegers, and S. van Smaalen, X-ray crystal-structure refinement of the nearly commensurate phase of 1$T$-$TaS_2$ in $(3+2)$-dimensional superspace, Phys. Rev. B **56**, 13757 (1997).

[41] R. He, J. Okamoto, Z. Ye, G. Ye, H. Anderson, X. Dai, X. Wu, J. Hu, Y. Liu, W. Lu, Y. Sun, A. N. Pasupathy, and A. W. Tsen, Distinct surface and bulk charge density waves in ultrathin 1$T$-$TaS_2$, Phys. Rev. B **94**, 201108(R) (2016).

[42] G. Grüner, The dynamics of charge-density waves, Rev. Mod. Phys. **60**, 1129 (1988).

[43] C. Sohrt, A. Stange, M. Bauer, and K. Rossnagel, How fast can a Peierls–Mott insulator be melted?, Faraday Discuss. **171**, 243 (2014).

[44] T. P. Devereaux and R. Hackl, Inelastic light scattering from correlated electrons, Rev. Mod. Phys. **79**, 175 (2007).

[45] M. Opel, R. Nemetschek, C. Hoffmann, R. Philipp, P. F. Müller, R. Hackl, I. Tüttő, A. Erb, B. Revaz, E. Walker, H. Berger, and L. Forró, Carrier relaxation, pseudogap, and superconducting

gap in high-$T_c$ cuprates: A Raman scattering study, Phys. Rev. B **61**, 9752 (2000).

[46] J. Skolimowski, Y. Gerasimenko, and R. Žitko, Mottness Collapse without Metallization in the Domain Wall of the Triangular-Lattice Mott Insulator 1$T$-$TaS_2$, Phys. Rev. Lett. **122**, 036802 (2019).

[47] A. Ribak, R. M. Skiff, M. Mograbi, P. K. Rout, M. H. Fischer, J. Ruhman, K. Chashka, Y. Dagan, and A. Kanigel, Chiral superconductivity in the alternate stacking compound 4$H$*b*-$TaS_2$, Sci. Adv. **6**, eaax9480 (2020).

[48] P. B. Allen, Fermi-surface harmonics: A general method for nonspherical problems. Application to Boltzmann and Eliashberg equations, Phys. Rev. B **13**, 1416 (1976).

[49] M. S. Dresselhaus, G. Dresselhaus, and A. Jorio, *Group Theory* (Springer, Berlin, 2008).

PAPER

# Peculiar symmetry-protected electronic dispersions in two-dimensional materials

IOP Publishing Journal of Physics: Condensed Matter
J. Phys.: Condens. Matter **32** (2020) 485501 (8pp) https://doi.org/10.1088/1361-648X/abaad1

# Peculiar symmetry-protected electronic dispersions in two-dimensional materials

**V Damljanović[1,3], N Lazić[2], A Šolajić[1], J Pešić[1], B Nikolić[2] and M Damnjanović[2]**

[1] Institute of Physics Belgrade, University of Belgrade, Pregrevica 118, 11080 Belgrade, Serbia
[2] NanoLab, Faculty of Physics, University of Belgrade, PO Box 44, Belgrade 11001, Serbia

E-mail: damlja@ipb.ac.rs

Received 16 June 2020, revised 23 July 2020
Accepted for publication 30 July 2020
Published 8 September 2020

**Abstract**

Symmetry indicates that low energy spectra of materials could be richer than well-known Dirac, semi-Dirac, or quadratic, hosting some unusual quasiparticles. Performing the systematic study of exact forms of low energy effective Hamiltonians and dispersions in high-symmetry points with fourfold degeneracy of bands, we found new, previously unreported dispersion, which we named poppy flower (PF) after its shape. This massless fermion exists in non-magnetic two-dimensional (2D) crystals with spin–orbit coupling (SOC), which are invariant under one of the proposed ten noncentrosymmetric layer groups. We suggest real three-dimensional (3D) layered materials suitable for exfoliation, having layers that belong to these symmetry groups as candidates for realization of PF fermions. In 2D systems without spin–orbit interaction, fortune teller (FT)-like fermions were theoretically predicted, and afterward experimentally verified in the electronic structure of surface layer of silicon. Herein, we show that such fermions can also be hosted in 2D crystals with SOC, invariant under additional two noncentrosymmetric layer groups. This prediction is confirmed by density functional based calculation: layered $BiIO_4$, which has been synthesized already as a 3D crystal, exfoliates to stable monolayer with symmetry $pb2_1a$, and FT fermion is observed in the band structure. Analytically calculated density of states (DOS) of the PF shows semimetallic characteristic, in contrast to metallic nature of FT having non-zero DOS at the bands contact energy. We indicate possibilities for symmetry breaking patterns which correspond to the robustness of the proposed dispersions as well as to the transition from Dirac centrosymmetric semimetal to PF.

Keywords: electronic dispersions, spin–orbit coupling, symmetry, new fermions

(Some figures may appear in colour only in the online journal)

## 1. Introduction

Electronic dispersion essentially determines crystal properties and it is well known that it is assigned by quantum numbers of the underlying symmetry group. These are space, layer (including wallpaper) or line groups, referring respectively to dimensionality of crystals: 3D, quasi-2D (Q2D), or quasi-1D. Probably the most famous example of a low-dimensional material is graphene (there are also related single layers, such as borophene [1], borophosphene [2], graphynes [3], etc), which hosts Dirac like (linear in quasi-momentum) dispersion in the vicinity of high symmetry Dirac points. Such shape of energy bands, besides being responsible for some intriguing phenomena, provides material realization of relativistic electron. This triggered numerous investigations of the connection between symmetry of materials and appearance of Dirac and Weyl points in their band structures. These points are attributed to existence of rotational [4], nonsymmorphic [5], mirror [6], space-time inversion [7, 8], time-reversal plus fractional translation [9], and generalized chiral symmetry [10]. There are also results on the search for Weyl and Dirac

[3] Author to whom any correspondence should be addressed.

 

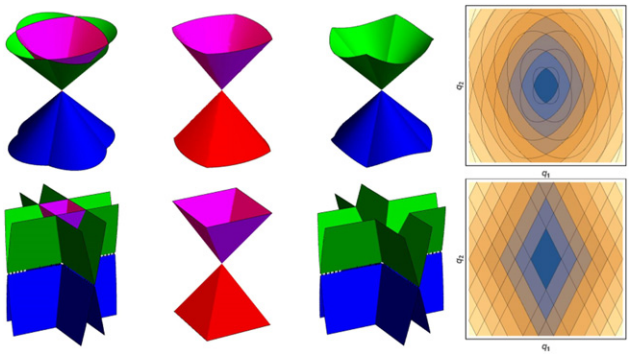

**Figure 1.** PF (up) and FT (bottom) dispersions (given by equations (3.1)): from left to right are all bands, bands $E_{\pm1,+1}$, bands $E_{\pm1,-1}$ and horizontal sections of the bands (iso-energetic lines).

points according to group theoretical criteria in Brillouin zones (BZs) of all space [11], layer [12–14] or wallpaper groups [15].

In addition, geometrical symmetries impose conditions that lead to the emergence of unconventional quasiparticles in condensed matter systems. In 3D materials, enforced by space groups, double Dirac points [16], three-component [17, 18] or hourglass fermions [19] are found, inspiring further theoretical and experimental research [20–25]. Concerning Q2D systems, besides Dirac (as in graphene [26]), there are also semi-Dirac (Dirac-like in one direction, and quadratic in the orthogonal one, as in black phosphorus [27]), quadratic (as in molybdenum disulphide [28]), and fortune teller (FT) dispersions [29], which corresponds to the coexistence of a nodal point and lines. Namely, symmetry analysis of the possible completely linear dispersions in non-magnetic, Q2D materials with negligible spin–orbit coupling (SOC) has shown that only completely massless fermions appearing in layers are Dirac and FT [29]. Recently, FT dispersion has been experimentally confirmed in a surface layer of silicon [30].

A question arises whether new types of fermions are possible in Q2D materials by inclusion of SOC? With help of layer double groups (LDGs) and time-reversal symmetry (TRS) (i.e. gray LDG), we made a quite general search for linear dispersions in the vicinity of high symmetry points (HSPs); since no reference to nonsymmorphic symmetries is made, the topological (hour-glass like) band crossing mechanisms are not *a priori* assumed, as it is usual. Indeed, it turns out that there are two peculiar types (figure 1) featuring twelve nonsymmorphic and noncentrosymmetric groups: two groups support previously predicted FT, and the remaining ones poppy flower (PF) dispersion (generalizing both FT and Dirac types).

After a brief overview of necessary group-theoretical methods, the obtained results are discussed on the basis of effective low-energy model, calculated densities of states and symmetry breaking patterns. Also, a list of material candidates supporting the new dispersions is provided. The predicted effect is justified by density functional based relaxation and band structure calculation in $BiIO_4$ monolayer. Synthesis of this layered 3D material was reported around a decade ago [31]. Numerical band structure confirms our group theoretical prediction, which may be the motivation for future laboratory synthesis of this material as monolayer.

## 2. Method

Symmetry determines Bloch Hamiltonian in the vicinity of high-symmetry BZ wave vector through the allowed irreducible representations (IRs) of the little group [32]. Allowed IRs of LDGs are subduced from the corresponding space groups IRs (found on Bilbao Crystallographic Server [33]), and also independently constructed by POLSym code [34]. Concerning LDGs with TRS, the dimensions [33, 35] of the allowed IRs (actually co-representations) are 1, 2 or 4, and for generic ones, giving bands degeneracy, this is 1 or 2. Here we focus on the band structures near quadruple points at high-symmetry momenta. Further, we do not consider generically degenerate bands, giving double degenerate Dirac dispersion (precisely, it consists of two double spinfull degenerate cones meeting at one fourfold degenerate point); this automatically excludes centrosymmetric crystals, as Kramers degeneracy in them forbids non-degenerate bands [36]. Among the remaining groups, only twelve are with special points with four-dimensional allowed (co)representation.

Analysis of all allowed IRs $R$ of little groups $G(\boldsymbol{k}_0)$ of HSPs $\boldsymbol{k}_0$ in LDG lacking the inversion symmetry gives the following conditions for quadruple point: $\boldsymbol{k}_0$ is time-reversal invariant momentum, $R$ is two-dimensional, either real or complex IR. Therefore, we consider $\hat{H}(\boldsymbol{k})$ being Hamiltonian of the system $\hat{H}_0$ (including spin–orbit) in the basis $\{|\Psi_1\rangle, |\Psi_2\rangle, |\theta\Psi_1\rangle, |\theta\Psi_2\rangle\}$, where the spinors $|\Psi_i\rangle = |\Psi_i(\boldsymbol{k})\rangle$ ($i = 1, 2$ counts two bands touching each other at $\boldsymbol{k}_0$ also in the absence of TRS) belong to $R$ at $\boldsymbol{k}_0$ and $\theta$ is an anti-unitary operator of TRS, for which we used $\theta^2 = -\hat{\sigma}_0$, since spinfull case is considered. Throughout the text $\hat{\sigma}_0$ is two-by-two unit matrix, and $\hat{\sigma}_1, \hat{\sigma}_2, \hat{\sigma}_3$ are Pauli matrices. Denoting the little group elements by $\ell = (h|\boldsymbol{r}_{\hat{h}} + \boldsymbol{b})$, where $h$ is crystallographic double point group element, while $\boldsymbol{r}_{\hat{h}}$ and $\boldsymbol{b}$ are fractional and lattice translation, respectively, one gets the conditions imposed by time-reversal and geometrical symmetries on $\hat{H}(\boldsymbol{k}_0 + \boldsymbol{q})$ in the vicinity of $\boldsymbol{k}_0$ (therefore, the wavevector $\boldsymbol{q}$ is small):

$$\hat{H}^*(\boldsymbol{k}_0 + \boldsymbol{q}) = \hat{T}^\dagger \hat{H}(\boldsymbol{k}_0 - \boldsymbol{q})\hat{T}, \tag{2.1}$$

$$\hat{H}(\boldsymbol{k}_0 + \boldsymbol{q}) = \hat{D}^\dagger(\ell)\hat{H}(\boldsymbol{k}_0 + \hat{h}'\boldsymbol{q})\hat{D}(\ell). \tag{2.2}$$

Here, $\hat{D} = \mathrm{diag}(\hat{R}, \hat{R}^*)$, and $\hat{h}'$ is an operator reduction of vector representation $\hat{h}$ to 2D BZ, while $\hat{T} = -\mathrm{i}\hat{\sigma}_2 \otimes \hat{\sigma}_0$ represents the action of $\theta$ on the basis of spinors.

To focus on the terms linear in $\boldsymbol{q}$, Hamiltonian is expanded in the form $\hat{H}(\boldsymbol{k}_0 + \boldsymbol{q}) \approx \sum_{i=1,2} q_i \frac{\partial \hat{H}(\boldsymbol{k}_0+\boldsymbol{q})}{\partial q_i}|_{\boldsymbol{q}=0}$ (energy scale is conveniently shifted such that $\hat{H}(\boldsymbol{k}_0) = 0$). To incorporate symmetry, the matrix elements of the Hamiltonian gradient are arranged into the four-by-eight matrix $\hat{W}$, which entries $w_{pq} = \left(w^1_{pq}\ w^2_{pq}\right)$ are pairs $w^i_{pq} = \frac{\partial H_{pq}(\boldsymbol{k}_0+\boldsymbol{q})}{\partial q_i}|_{\boldsymbol{q}=0}$. The form

**Table 1.** Groups providing dispersions (3.1). Notations for layer (columns 1 and 2) and space groups (columns 4, 5 and 6) are according to [37, 38] respectively. IR notation in the eighth column is as in Bilbao Crystallographic Server [33]. Effective Hamiltonian is indicated in the last column by the nonzero parameters (and their interrelations) of (2.5). For the last four groups $a = c$ while $\bar{M}_6$ and $\bar{M}_7$ are conjugated pair of IRs.

| Layer double group | | | Corresponding space double group | | | | | | |
|---|---|---|---|---|---|---|---|---|---|
| Group | | IR | Group | | | Plane | IR | Dispersion | Nonzero $v^i_{pq}$ |
| 21 | $p2_12_12$ | $\bar{S}_5$ | 18 | $P2_12_12$ | $D^3_2$ | $z=0$ | $\bar{S}_5$ | (3.1a) | $v^1_{13}, v^1_{23}, v^1_{33}, v^2_{11}, v^2_{21}, v^2_{31}$ |
| 25 | $pba2$ | $\bar{S}_5$ | 32 | $Pba2$ | $C^8_{2v}$ | $z=0$ | $\bar{S}_5$ | (3.1a) | $v^1_{13}, v^1_{23}, v^1_{33}, v^2_{11}, v^2_{21}, v^2_{31}$ |
| 28 | $pm2_1b$ | $\bar{Y}_5, \bar{S}_5$ | 26 | $Pmc2_1$ | $C^2_{2v}$ | $y=0$ | $\bar{Z}_5, \bar{U}_5$ | (3.1a) | $v^1_{11}, v^1_{21}, v^1_{31}, v^2_{10}, v^2_{20}, v^2_{30}$ |
| 29 | $pb2_1m$ | $\bar{Y}_5, \bar{S}_5$ | 26 | $Pmc2_1$ | $C^2_{2v}$ | $x=0$ | $\bar{Z}_5, \bar{T}_5$ | (3.1b) | $v^1_{02}, v^2_{10}, v^2_{20}, v^2_{30}$ |
| 30 | $pb2b$ | $\bar{Y}_5, \bar{S}_5$ | 27 | $Pcc2$ | $C^3_{2v}$ | $x=0$ | $\bar{Z}_5, \bar{T}_5$ | (3.1a) | $v^1_{11}, v^1_{21}, v^1_{31}, v^2_{10}, v^2_{20}, v^2_{30}$ |
| 32 | $pm2_1n$ | $\bar{Y}_5$ | 31 | $Pmn2_1$ | $C^7_{2v}$ | $y=0$ | $\bar{Z}_5$ | (3.1a) | $v^1_{13}, v^1_{23}, v^1_{33}, v^2_{10}, v^2_{20}, v^2_{30}$ |
| 33 | $pb2_1a$ | $\bar{Y}_5$ | 29 | $Pca2_1$ | $C^5_{2v}$ | $y=0$ | $\bar{Z}_5$ | (3.1b) | $v^1_{33}, v^2_{11}, v^2_{21}, v^2_{30}$ |
| 34 | $pb2n$ | $\bar{Y}_5$ | 30 | $Pnc2$ | $C^6_{2v}$ | $x=0$ | $\bar{Z}_5$ | (3.1a) | $v^1_{13}, v^1_{23}, v^1_{33}, v^2_{10}, v^2_{20}, v^2_{30}$ |
| 54 | $p42_12$ | $(\bar{M}_6, \bar{M}_7)$ | 90 | $P42_12$ | $D^2_4$ | $z=0$ | $(\bar{M}_6, \bar{M}_7)$ | (3.1a) | $\left\{\begin{array}{l} v^1_{02}=v^2_{02}=v^1_{31}=-v^2_{31} \\ v^1_{10}=v^2_{10}=v^1_{23}=-v^2_{23} \\ v^1_{13}=-v^2_{13}=-v^1_{20}=-v^2_{20} \end{array}\right\}$ |
| 56 | $p4bm$ | $(\bar{M}_6, \bar{M}_7)$ | 100 | $P4bm$ | $C^2_{4v}$ | $z=0$ | $(\bar{M}_6, \bar{M}_7)$ | (3.1a) | |
| 58 | $p\bar{4}2_1m$ | $(\bar{M}_6, \bar{M}_7)$ | 113 | $P\bar{4}2_1m$ | $D^3_{2d}$ | $z=0$ | $(\bar{M}_6, \bar{M}_7)$ | (3.1a) | |
| 60 | $p\bar{4}b2$ | $(\bar{M}_6, \bar{M}_7)$ | 117 | $P\bar{4}b2$ | $D^7_{2d}$ | $z=0$ | $(\bar{M}_6, \bar{M}_7)$ | (3.1a) | |

$$\hat{W} = \begin{pmatrix} w_{11} & w_{12} & w_{13} & w_{14} \\ w^*_{12} & w_{22} & w_{14} & w_{24} \\ w^*_{13} & w^*_{14} & -w_{11} & -w^*_{12} \\ w^*_{14} & w^*_{24} & -w_{12} & -w_{22} \end{pmatrix} \tag{2.3}$$

follows from the relation (2.1), together with $w^i_{pq} = w^{i*}_{qp}$ corresponding to the requirement that Hamiltonian $\hat{H}$ is a Hermitian operator. Note that the form (2.3) of $\hat{W}$ leads to the traceless Hamiltonian: it excludes the scalar term (which imposes the tilt of the bands). The geometrical symmetries are incorporated by (2.2), which is rewritten [11, 29] as an efficient fixed point condition

$$\left|\widehat{W}\right\rangle = \hat{D} \otimes \hat{D}^* \otimes \hat{h}' \left|\widehat{W}\right\rangle, \tag{2.4}$$

on the column vector $(32 \times 1)$ form $\left|\widehat{W}\right\rangle$ of $\hat{W}$. The equation (2.4) is solved with help of the group projection operators for all of the twelve noncentrosymmetric groups hosting quadruple points at high symmetry momenta; in this way, the symmetry determines form of $\hat{W}$. To explicate this, it is more convenient to use another general expansion of the effective low energy Hamiltonian,

$$\hat{H}(\boldsymbol{q}) = \sum_{p,q=0}^{3} \sum_{i=1}^{2} q_i v^i_{pq}\, \hat{\sigma}_p \otimes \hat{\sigma}_q, \tag{2.5}$$

and find the constraints imposed by symmetry on the real coefficients $v^i_{pq}$ (simply interrelated with $w^i_{pq}$).

## 3. Results and discussion

### 3.1. Symmetry adapted Hamiltonians and dispersions

Groups hosting new dispersions are listed in table 1. Besides intrinsic layer group notation (the first part), the space group of the system obtained by periodic repetition of the layer along axis perpendicular to it (column plane) according to Bilbao Crystallographic Server is also given (second part), where the directions $x$, $y$ and $z$ are along axes of orthorombic/tetragonal 3D primitive unit cell. On the other hand, in POLSym approach we used convention that layers are in $xy$-plane. Orthogonal lattice vectors $\boldsymbol{a}_1$ and $\boldsymbol{a}_2$ span primitive rectangular/square 2D unit cell, while reciprocal lattice vectors $\boldsymbol{k}_1$ and $\boldsymbol{k}_2$ satisfy $\boldsymbol{a}_j \cdot \boldsymbol{k}_l = 2\pi\delta_{j,l}$ and $q_1$, $q_2$ are projections of $\boldsymbol{q}$ along $\boldsymbol{k}_1$ and $\boldsymbol{k}_2$. Relevant BZs are in figure 2.

Effective Hamiltonians allowed by symmetry group in the special points of Brillouin's zone are presented in the last column of the table 1: the nonzero real coefficients $v^i_{pq}$ in the expansion (2.5) are specified, together with the constraints among them. The listed forms correspond to the group settings (lattice vectors and coordinate origin) and double valued irreducible co-representations obtained by POLSym code. In fact, this enabled flexibility in the choice of generators (coordinate system and translational periods), which finally results in the form of irreducible co-representations. These are chosen such to get the same form of the effective Hamiltonian whenever it is possible (for different groups). Equivalent (but different) settings (and co-representations) produce different (still equivalent with respect to dispersions) Hamiltonian forms. Clearly, the exact values of the nonzero coefficients $v^i_{pq}$ (listed in the last column of the table 1) are material dependent. The groups' generators and their representative matrices in the allowed co-representations associated to the specified high-symmetry points are in the table 2. It should be remarked that in all the considered cases this point is fixed by the whole gray group, i.e. the little group is the gray (double) group, and the allowed co-representations of the little group are simultaneously the irreducible co-representations of the gray group. The matrices of the relevant co-representations are four-dimensional. In all the cases time-reversal corresponds to the matrix $\hat{T}$; all other generators are represented by the block-diagonal

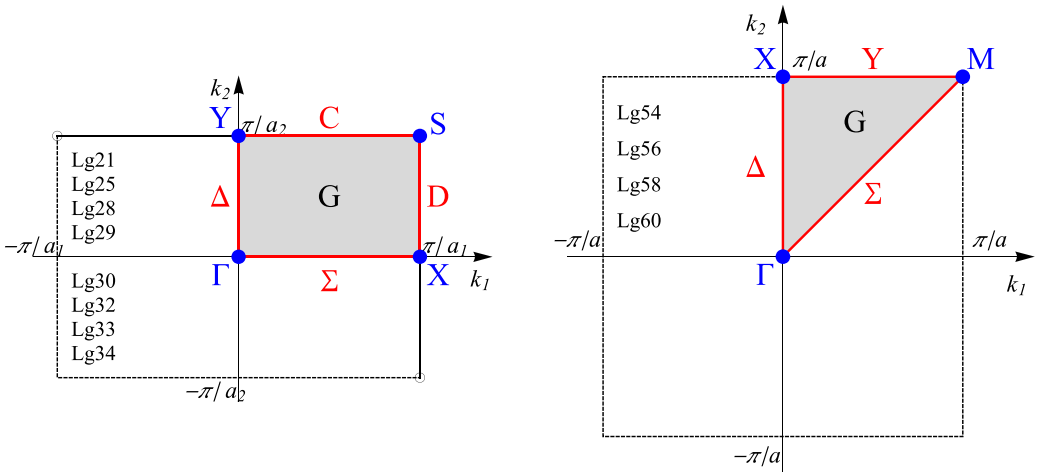


**Figure 2.** BZs of the groups (listed in table 1) supporting dispersions (3.1). For layer groups 28, 29, 30, 32, 33 and 34 vector $\boldsymbol{k}_2$ is along (screw) axis of order two.

matrices $\hat{D} = \mathrm{diag}(\hat{R}, \hat{R}^*)$, with mutually conjugated $2 \times 2$ blocks. Therefore, only this block, $\hat{R}$, is given in the table 2.

The described technique leads to two new types of dispersions (figure 1; crossings are taken at $E = 0$). The first one is PF, with four bands (obtained for $u, v = \pm 1$):

$$E_{v,u}(\boldsymbol{q}) = v\sqrt{aq_1^2 + cq_2^2 + u\,b\,|q_1 q_2|}. \tag{3.1a}$$

The expression under the square root is non-negative since $a$, $b$ and $c$ are positive quantities (functions of $v^i_{pq}$) such that $b^2 - 4ac < 0$. For quadratic layer groups (54, 56, 58, 60) $c = a$, and above dispersion degenerates to the isotropic one $E_{v,u} = v\sqrt{a\boldsymbol{q}^2 + u\,b\,|q_1 q_2|}$. Two groups, 29 and 33, enforce $b^2 - 4ac = 0$, hosting thus FT dispersions (with bands counted by $u, v = \pm 1$):

$$E_{v,u}(\boldsymbol{q}) = v\,|f\,|q_1| + u\,g\,|q_2|\,|, \tag{3.1b}$$

with $f$, $g$ positive quantities, also functions of $v^i_{pq}$. Note that on the other side, the limit $b \to 0^+$ gives Dirac dispersion.

### 3.2. Density of states

Dispersions (3.1), differing from the well-known Dirac, semi-Dirac or quadratic, impose specific physical properties. In this context, one must take into account the range of validity of these forms, describing the realistic band structures only in the vicinity of high-symmetry point. In particular, corresponding density of states (DOS) near $E = 0$ are:

$$\rho^{\mathrm{SOC}}_{\mathrm{PF}} = \frac{2|E|}{\pi\sqrt{4ac - b^2}}, \tag{3.2a}$$

$$\rho^{\mathrm{SOC}}_{\mathrm{FT}} \approx \frac{L}{4\pi^2\sqrt{f^2 + g^2}}. \tag{3.2b}$$

Unlike to PF, but similarly to 3D nodal semimetals [39], exact calculation of DOS of FT is prevented due to the non-circular iso-energetic lines (figure 1). Thus, the last expression corresponds to realistic situations where the horizontal parts of band crossing lines are of the length $L$ (this is an effective range of approximation). In non-SOC case calculation of DOS gives doubled results (3.2), since each energy is spin degenerate, which is then decoupled from the orbital one. Non zero DOS of FT near $E = 0$ is in contrast to DOS of Dirac or PF dispersions being proportional to $|E|$, as well as to semi-Dirac which is proportional to $\sqrt{|E|}$. This affects many properties, to mention only charge and spin transport. Further, it can be shown that the electron effective mass, obtained from band curvatures, for all dispersions (3.1) vanishes. Let us emphasize that the higher order terms, neglected in derivation cannot change the obtained band topology (figure 1), though may distort bands slightly.

### 3.3. Symmetry breaking

Despite the obtained dispersions are essential, i.e. resistant to symmetry preserving perturbation, an interesting additional insight is gained by considering symmetry breaking. Herein, taking into account group–subgroup relations, we discuss the possibilities of robustness or switching between various dispersions at the same BZ-point by lowering the symmetry, e.g. due to strain. It is expected that decreasing the number of symmetry elements leads to relaxing the constraints imposed on Hamiltonians, and consequently increasing (or preserving) the number of independent parameters. In this context, taking into account the number of non-zero parameters $v^i_{pq}$ of (2.5) given in table 1, it is meaningful to consider the transitions from FT to anisotropic PF, as well as from isotropic PF to FT, when the symmetry is lowered. Precisely, the allowed four-band model Hamiltonian diagonalizing in PF dispersion have six real independent parameters, which are reduced to three for quadratic groups; similarly, there are 4 real independent Hamiltonian parameters for FT. Before proceeding, let us take a brief look into the robustness of FT and PF.

Regarding groups 29 and 33 supporting FT dispersion, symmetry reduction in which either nonsymmorphic glide plane or screw axis (but not both) is retained causes that FT at the $Y$ point splits into two non-degenerate conical dispersions. Opposite out-of-plane shifts of the adjacent nuclei positioned

**Table 2.** Allowed irreducible co-representations: for each group and corresponding HSP, the generators are listed, and the block-diagonal part $\hat{R}$ of double valued co-representation $\hat{D}$ representing these generators (in the same order). Here, $C_{n\hat{n}}$ is rotation for $2\pi/n$ around axis $\hat{n}$ (which is $\hat{x}$, $\hat{y}$, $\hat{z}$, or $\hat{c} = \frac{1}{\sqrt{2}}(\hat{x} + \hat{y})$), $m_{\hat{n}}$ is vertical mirror plane which contains $\hat{n}$ axis, $m_{\mathrm{h}}$ is horizontal mirror plane, and $S_n = C_{n\hat{z}} m_{\mathrm{h}}$.

| Group | HSP | Generators | | | $\hat{R}$ | | | |
|---|---|---|---|---|---|---|---|---|
| 21 | $S$ | $(C_{2\hat{x}}\|\frac{1}{2}0)$ | $(C_{2\hat{y}}\|0\frac{1}{2})$ | | $\hat{\sigma}_3$ | $\hat{\sigma}_1$ | | |
| 25 | $S$ | $(m_{\hat{x}}\|\frac{1}{2}0)$ | $(m_{\hat{y}}\|0\frac{1}{2})$ | | $\hat{\sigma}_3$ | $\hat{\sigma}_1$ | | |
| 28 | $Y$ | $(I\|10)$ | $(C_{2\hat{y}}\|0\frac{1}{2})$ | $m_{\hat{y}}$ | $\hat{\sigma}_0$ | $-\hat{\sigma}_3$ | $-\mathrm{i}\hat{\sigma}_2$ | |
| 28 | $S$ | $(I\|10)$ | $(C_{2\hat{y}}\|0\frac{1}{2})$ | $m_{\hat{y}}$ | $-\hat{\sigma}_0$ | $-\hat{\sigma}_3$ | $-\mathrm{i}\hat{\sigma}_2$ | |
| 29 | $Y$ | $(I\|10)$ | $(C_{2\hat{y}}\|0\frac{1}{2})$ | $m_{\mathrm{h}}$ | $\hat{\sigma}_0$ | $-\hat{\sigma}_3$ | $-\mathrm{i}\hat{\sigma}_2$ | |
| 29 | $S$ | $(I\|10)$ | $(C_{2\hat{y}}\|0\frac{1}{2})$ | $m_{\mathrm{h}}$ | $-\hat{\sigma}_0$ | $-\hat{\sigma}_3$ | $-\mathrm{i}\hat{\sigma}_2$ | |
| 30 | $Y$ | $(I\|10)$ | $(m_{\hat{y}}\|0\frac{1}{2})$ | $C_{2\hat{y}}$ | $\hat{\sigma}_0$ | $-\hat{\sigma}_3$ | $-\mathrm{i}\hat{\sigma}_2$ | |
| 30 | $S$ | $(I\|10)$ | $(m_{\hat{y}}\|0\frac{1}{2})$ | $C_{2\hat{y}}$ | $-\hat{\sigma}_0$ | $-\hat{\sigma}_3$ | $-\mathrm{i}\hat{\sigma}_2$ | |
| 32 | $Y$ | $(I\|10)$ | $(m_{\mathrm{h}}\|\frac{1}{2}\frac{1}{2})$ | $m_{\hat{y}}$ | $\hat{\sigma}_0$ | $-\hat{\sigma}_3$ | $-\mathrm{i}\hat{\sigma}_2$ | |
| 33 | $Y$ | $(m_{\mathrm{h}}\|\frac{1}{2}0)$ | $(C_{2\hat{y}}\|0\frac{1}{2})$ | | $\mathrm{i}\hat{\sigma}_3$ | $\hat{\sigma}_1$ | | |
| 34 | $Y$ | $(I\|10)$ | $(m_{\mathrm{h}}\|\frac{1}{2}\frac{1}{2})$ | $C_{2\hat{y}}$ | $\hat{\sigma}_0$ | $-\hat{\sigma}_3$ | $-\mathrm{i}\hat{\sigma}_2$ | |
| 54 | $M$ | $(I\|10)$ | $(C_{2\hat{c}}\|\frac{1}{2}\frac{1}{2})$ | $C_{4\hat{z}}$ | $-\hat{\sigma}_0$ | $-\mathrm{i}\hat{\sigma}_2$ | $\mathrm{e}^{-\mathrm{i}\frac{3\pi}{4}}$ | $\mathrm{diag}(1,\mathrm{i})$ |
| 56 | $M$ | $(I\|10)$ | $(m_{\hat{c}}\|\frac{1}{2}\frac{1}{2})$ | $C_{4\hat{z}}$ | $-\hat{\sigma}_0$ | $-\mathrm{i}\hat{\sigma}_2$ | $\mathrm{e}^{-\mathrm{i}\frac{3\pi}{4}}$ | $\mathrm{diag}(1,\mathrm{i})$ |
| 58 | $M$ | $(I\|10)$ | $(m_{\hat{c}}\|\frac{1}{2}\frac{1}{2})$ | $S_4$ | $-\hat{\sigma}_0$ | $-\mathrm{i}\hat{\sigma}_2$ | $\mathrm{e}^{-\mathrm{i}\frac{3\pi}{4}}$ | $\mathrm{diag}(1,\mathrm{i})$ |
| 60 | $M$ | $(I\|10)$ | $(C_{2\hat{c}}\|\frac{1}{2}\frac{1}{2})$ | $S_4$ | $-\hat{\sigma}_0$ | $-\mathrm{i}\hat{\sigma}_2$ | $\mathrm{e}^{-\mathrm{i}\frac{3\pi}{4}}$ | $\mathrm{diag}(1,\mathrm{i})$ |

in the mirror plane, transforms mirror into a glide plane, while doubling the lattice constant; this in turn halves primitive vector $\boldsymbol{k}_1$ of the reciprocal lattice. Group 29 reduces to 33 and the $S$ point in 29 becomes $Y$ point in 33. Consequently, FT in $Y$ and $S$ points in 29 are robust against lowering the symmetry to group 33. Similarly, concerning the PF, any homogenous stretching along $\boldsymbol{a}_1$ or $\boldsymbol{a}_2$ axis deforms square primitive cell to rectangular, reducing the symmetries of layer groups 54 and 58 (56 and 60) to the group 21 (25) and causes PF to change from isotropic to anisotropic form, which implies direction-dependent electronic and related properties.

Since PF is a generalized form of FT, one could expect that the parameters of these dispersions can be interrelated by tuning. However, continuous transformation from FT to PF at the same point of the BZ is not possible, since neither of groups supporting FT is a subgroup of any of groups allowing PF, nor vice-versa. The expression (3.2a) for DOS of PF shows that the changing parameters such that PF approaches to FT results in a singularity at zero energy. In the other words, if opposite would hold, arbitrarily small displacements of nuclei, being sufficient to lower the symmetry, would cause a jump of (graphene-like) negligible DOS of PF to a finite and constant DOS of FT, which we found unlikely. At the same time, such obstruction from DOS does not forbid the transition between Dirac (double degenerate cones with four-fold degenerate point) and PF, nor it forbids splitting of FT and PF into two non-degenerate conical dispersions (with double degenerate point).

Following the above arguments, it is expected that transition from Dirac cone to PF may be realized by lowering the symmetry, since Dirac dispersions has less independent parameters than PF. According to [5] Dirac semimetals in time-reversal invariant two-dimensional systems with strong SOC are possible in nonsymmorphic groups with inversion symmetry. E.g. let us consider the layer group 46 (*pmmn*), hosting Dirac cones at $X$, $Y$ and $S$ HSPs (the BZ is the same as this one given on the left panel in figure 2). It is expected that the violation of the inversion symmetry leads to Weyl points or node [5]. However, listing all subgroups, it turns out that the two of the subgroups, 32 and 21, actually host PF in the points $Y$ and $S$, respectively. Indeed, in [46], using spinfull tight-binding model with four sites (with s-orbitals) per unit cell, authors show that at fillings 2, 6, system invariant under double layer group 21 is semimetal, which hosts one fourfold degenerate and four Weyl points. A plethora of such cases, where groups allowing PF from the table 1 are subgroups of symmetry groups of Dirac semimetals, indicates candidates for transitions between centrosymmetric and noncentrosymmetric crystals with protected four-fold band crossing point. Moreover, the existence of such essential fourfold degenerate point simultaneously with double degenerate Weyl points in the same system, makes that the layers from our list represent possible two-dimensional materials suitable for the study of their interplay.

### 3.4. Material realization

Despite the fabrication of freestanding layers is not always feasible, the above theoretical predictions required material realizations, or at least numerical simulations. To find realistic material with layer groups from table 1 we searched the list [41] of 3D layered materials, synthesis of which has been reported in the literature. In the table 3 we listed potential material candidates with symmetry groups allowing the predicted peculiar dispersions. These are laboratory fabricated 3D crystals with layered structures, which could be easily or potentially exfoliated into layers.

It is interesting to single out our group-theoretical findings indicated that dispersions (3.1) are not preserved when SOC is neglected, except for the LDG 33, which supports FT dispersion also in that case [29]. Inclusion of SOC moves FT from

**Table 3.** Material candidates: layered systems with symmetry groups hosting the dispersions (3.1). Layer and corresponding space groups are listed for materials given by a formula and materials project ID. Abbreviations EE and PE stand for easily and potentially exfoliable, respectively, according to [41].

| Layer group | | Space group | | Formula | ID | EE/PE |
|---|---|---|---|---|---|---|
| 21 | $p2_12_12$ | 18 | $P2_12_12$ | $As_2SO_6$ | mp-27230 | EE |
| | | | | $MgMoTeO_6$ | mp-1210722 | EE |
| 25 | $pba2$ | 32 | $Pba2$ | $Au_2Se_2O_7$ | mp-28095 | EE |
| | | | | $Re_2S_2O_{13}$–$I$ | mp-974650 | EE |
| 28 | $pm2_1b$ | 26 | $Pmc2_1$ | $TlP_5$ | mp-27411 | EE |
| | | | | $KO_2H_4F$ | mp-983327 | PE |
| | | | | $NaGe_3P_3$ | mp-1104707 | PE |
| 29 | $pb2_1m$ | 26 | $Pmc2_1$ | $WO_2Cl_2$ | mp-32539 | EE |
| 32 | $pm2_1n$ | 31 | $Pmn2_1$ | CuCOCl | mp-562090 | EE |
| 33 | $pb2_1a$ | 29 | $Pca2_1$ | $BiIO_4$ | mp-1191266 | PE |
| | | | | $KPSe_6$ | mp-18625 | EE |
| 58 | $p\bar{4}2_1m$ | 113 | $P\bar{4}2_1m$ | $LiReO_2F_4$ | mp-554108 | EE |

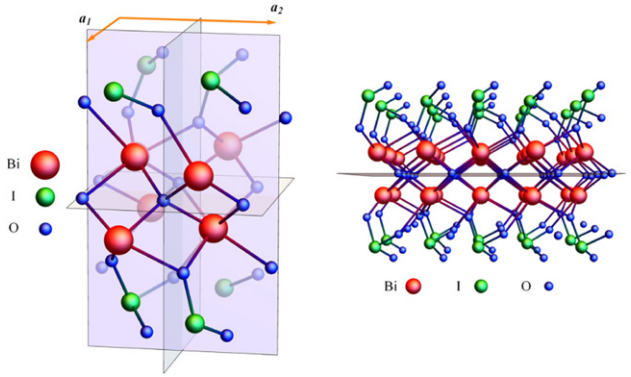


**Figure 3.** Crystal structure of $BiIO_4$ mono-layer: elementary cell (left) and a part of layer (right).

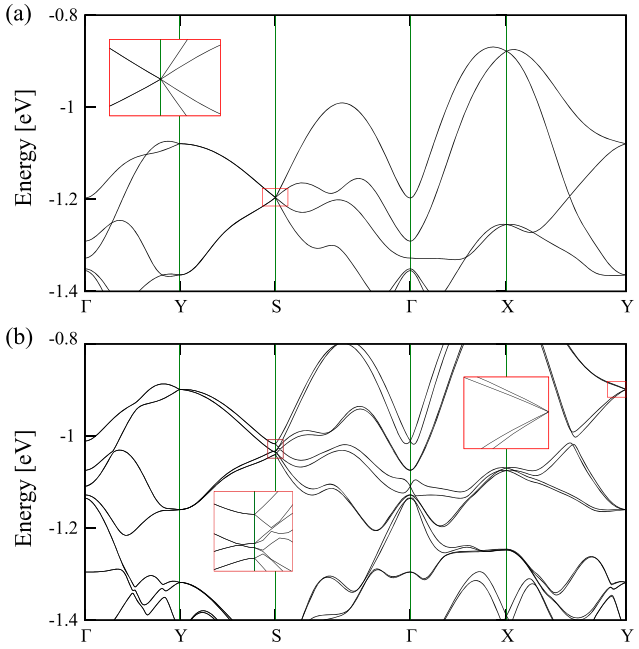


**Figure 4.** Band structure of $BiIO_4$ mono-layer without SOC (top) and with SOC (bottom), with insets showing magnified FT and split FT dispersions. The Fermi level is set to zero eV.

BZ corners to the $Y$-point. The material $BiIO_4$ belongs to corresponding space group 29 and has layers parallel to the $y = 0$ plane. Consequently, it should exfoliate to layer group 33 so we choose it for further DFT investigations, as an example of achievements of our theory. Since IRs from table 1 are the only extra IRs in these BZ points, the dispersions (3.1) are unavoidable for crystals with symmetry of these groups. On the other hand, the position of Fermi level cannot be determined solely by symmetry arguments, nor it can be guaranteed that no other bands cross or touch the Fermi level.

We determined crystal (figure 3) and band structure (figure 4) of $BiIO_4$ mono-layer configuration using DFT calculations: full relaxation and bands calculations were performed by QUANTUM ESPRESSO software package [42], full relativistic PAW pseudopotentials [43, 44], with the Perdew–Burke–Ernzerhof exchange–correlation functional [45]. The energy cutoff for electron wavefunction and charge density of 47 Ry and 476 Ry were chosen, respectively. The band structures were found in 500 $k$-points on selected path, and 2500 $k$-points for 2D band structure plots in the vicinity of HSPs.

Crystal structure of mono-layer is shown in figure 3. It belongs to rectangular lattice of the group 33, with nearly equal $a_1 = 0.566\,\text{nm}$ and $a_2 = 0.575\,\text{nm}$. Band structure of $BiIO_4$ mono-layer with and without SOC is shown in figure 4. It turns out that the system is insulating in undoped and ungated regime. The closest to Fermi level FT state is at $-0.9$ eV. When SOC is neglected energy at the point $S$ is eightfold degenerate (including spin), which gives electron filling of $8n$ that is necessary for insulating systems [40]. With inclusion of SOC the eightfold spinfull degeneracy at $S$ is lifted, but sets of eight non-degenerate bands each, form *cat's cradle* structure along $\Gamma X$ line, as predicted in reference [46]. This gives again electron filling of $8n$ [46, 47]. Our electron filling of 184, derived from DFT calculations, is indeed divisible by 8. Electron filling for DLG 33 prevents FT to be the only dispersion at the Fermi level, while for remaining groups in table 1 the filling condition necessary for Fermi surface consisting of isolated points is $\nu = 4n + 2$.

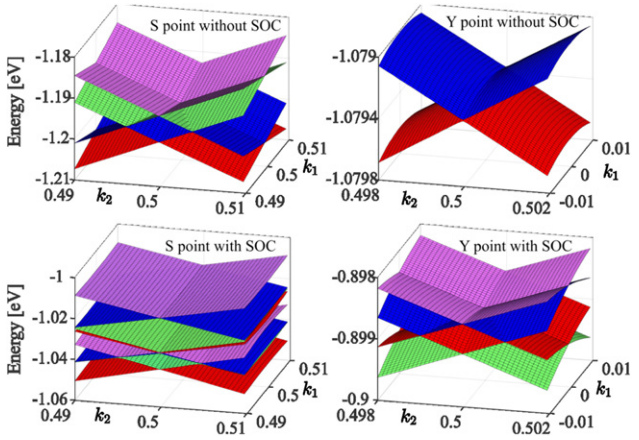


**Figure 5.** Band structures of $BiIO_4$ mono-layer without and with SOC near points *S* and *Y*. Inclusion of SOC turns FT dispersion into nodal lines in *S*, and degenerate Dirac line into FT in *Y*.

Behavior of FT states with inclusion of SOC is shown in figure 5. In non-SOC case, two pairs of Dirac lines meet at the point *S* and form the FT states. SOC splits eightfold degenerate band at *S* into four double degenerate ones. Near point *Y*, SOC splits fourfold spinfull degenerate Dirac line into one FT state. Since SOC strength is proportional to the fourth power of the atomic number [48], heavy elements in the material induced observable splitting.

## 4. Conclusions

Characterized by band crossings (touching) points (lines) at Fermi level from which energies disperse linearly, nodal metals/semimetals take an important role in investigations of various topological properties of crystals. Among them, symmetry-enforced ones represent a class of materials hosting such dispersions in HSPs due to increased degeneracy. In the language of group theory, while the spinless case is described by the ordinary group of geometrical transformations, the spinfull situation, when system is robust on spin–orbit perturbation, needs double groups. Additional inclusion of TRS leads to gray magnetic ordinary or double group. The increased degeneracy of energy is enabled by higher dimensional allowed irreducible (co)representations of the corresponding underlying crystal symmetry.

New fermions in 2D materials revealed by application of full gray double layer group symmetry contribute to the interesting physical phenomena of layered systems: two new types of dispersions beyond Dirac, PF and FT, accompany the fourfold degeneracy of bands in high-symmetry points. Our findings single out list of twelve nonsymmorphic and noncentrosymmetric layer groups that support such unusual linear electronic dispersions. As the method is not based on the topological mechanism (invoking nonsymmorphic symmetry), the result is general, verifying *a posteriori* the necessity of nonsymmorphic elements for the considered dispersions. Providing this list, numerical simulations aimed to find material realizations of the peculiar dispersions are facilitated, which is of a great importance to achieve corresponding physical properties. PF dispersion occurs in ten groups; in particular, there are single isolated HSP hosting it in the groups $p2_12_12$, $pba2$ (point *S*), $pm2_1n$, $pb2n$ (*Y*), and $p42_12$, $p4bm$, $p\bar{4}2_1m$, $p\bar{4}b2$ (*M*), while the groups $pm2_1b$ and $pb2b$ have two such points (*Y*, *S*). On the other hand, the FT type of dispersion in the group $pb2_1a$ is hosted in single (*Y*), and in the group $pb2_1m$ in two HSPs (*Y*, *S*).

Particularly interesting are groups $pb2_1a$, supporting FT dispersion both with and without SOC, as well as $pba2$ and $p4bm$, which are also wallpaper groups, preserved even when perpendicular, homogenous electric field is applied (e.g. due to gating). Moreover, coexistence of degenerate point and lines at the same energy in FT dispersion may lead to some new phenomena. FT dispersion has constant contribution to DOS, manifested as a plateau nearby zero energy in FT. This may be important in technological applications, especially when electron and/or spin transport are looked for, like materials for solar cells [49], spintronic etc. On the contrary, PF dispersion, similarly to Dirac ones, contributes by linear DOS with no states on zero energy. It has both isotropic and anisotropic forms which may be continuously transformed into each other by crystal deformations.

Our numerical calculations show that layered $BiIO_4$ 3D crystal, exfoliates to stable mono-layer having a symmetry group from our list. Band structure of $BiIO_4$ mono-layer confirms theoretical prediction, but further efforts are necessary in order to place the Fermi level at right energy.

## Acknowledgments

Authors VD, AŠ and JP acknowledge funding provided by the Institute of Physics Belgrade, through the Grant by the Ministry of Education, Science and Technological Development of the Republic of Serbia. NL, BN and MD were supported by the Serbian Ministry of Education, Science and Technological Development under Project Number OI171035. DFT calculations were performed using computational resources at Johannes Kepler University, Linz, Austria.

## ORCID iDs

V Damljanović https://orcid.org/0000-0001-7517-6439
N Lazić https://orcid.org/0000-0002-3634-0301
A Šolajić https://orcid.org/0000-0002-0553-0858
J Pešić https://orcid.org/0000-0002-8600-7187
B Nikolić https://orcid.org/0000-0002-7241-3248
M Damnjanović https://orcid.org/0000-0003-2806-253X

## References

[1] Gupta S, Kutana A and Yakobson B I 2018 Dirac cones and nodal line in borophene *J. Phys. Chem. Lett.* **9** 2757–62
[2] Zhang Y, Kang J, Zheng F, Gao P-F, Zhang S-L and Wang L-W 2019 Borophosphene: a new anisotropic Dirac cone monolayer with a high Fermi velocity and a unique self-doping feature *J. Phys. Chem. Lett.* **10** 6656–63
[3] Zhang L Z, Wang Z F, Wang Z M, Du S X, Gao H-J and Liu. F 2015 Highly anisotropic Dirac fermions in square graphynes *J. Phys. Chem. Lett.* **6** 2959–62

[4] Fang C, Gilbert M J, Dai X and Andrei Bernevig B 2012 Multi-Weyl topological semimetals stabilized by point group symmetry *Phys. Rev. Lett.* **108** 266802

[5] Young S M and Kane C L 2015 Dirac semimetals in two dimensions *Phys. Rev. Lett.* **115** 126803

[6] van Miert G and Smith C M 2016 Dirac cones beyond the honeycomb lattice: a symmetry-based approach *Phys. Rev.* B **93** 035401

[7] Wang J 2017 Antiferromagnetic Dirac semimetals in two dimensions *Phys. Rev.* B **95** 115138

[8] Kim J, Baik S S, Jung S W, Sohn Y, Ryu S H, Choi H J, Yang B-J and Kim K S 2017 Two-dimensional Dirac fermions protected by space-time inversion symmetry in black phosphorus *Phys. Rev. Lett.* **119** 226801

[9] Young S M and Wieder B J 2017 Filling-enforced magnetic Dirac semimetals in two dimensions *Phys. Rev. Lett.* **118** 186401

[10] Kawarabayashi T, Aoki H and Hatsugai Y 2019 Topologically protected doubling of tilted Dirac fermions in two dimensions *Phys. Status Solidi* B **256** 1970025

[11] Mañes J L 2012 Existence of bulk chiral fermions and crystal symmetry *Phys. Rev.* B **85** 155118

[12] Damljanović V and Gajić R 2016 Existence of Dirac cones in the Brillouin zone of diperiodic atomic crystals according to group theory *J. Phys.: Condens. Matter* **28** 085502

[13] Damljanović V and Gajić R 2016 Addendum to existence of Dirac cones in the Brillouin zone of diperiodic atomic crystals according to group theory *J. Phys.: Condens. Matter* **28** 439401

[14] Park S and Yang B-J 2017 Classification of accidental band crossings and emergent semimetals in two-dimensional noncentrosymmetric systems *Phys. Rev.* B **96** 125127

[15] Wieder B J, Bradlyn B, Wang Z, Cano J, Kim Y, Kim H-S D, Rappe A M, Kane C L and Andrei Bernevig B 2018 Wallpaper fermions and the nonsymmorphic Dirac insulator *Science* **361** 246–51

[16] Wieder B J, Kim Y, Rappe A M and Kane C L 2016 Double Dirac semimetals in three dimensions *Phys. Rev. Lett.* **116** 186402

[17] Bradlyn B, Cano J, Wang Z, Vergniory M G, Felser C, Cava R J and Andrei Bernevig B 2016 Beyond Dirac and Weyl fermions: unconventional quasiparticles in conventional crystals *Science* **353** aaf5037

[18] Zhu Z, Winkler G W, Wu QuanS, Ju L and Alexey A 2016 Soluyanov. Triple point topological metals *Phys. Rev.* X **6** 031003

[19] Wang Z, Alexandradinata A, Cava R J and Andrei Bernevig B 2016 Hourglass fermions *Nature* **532** 189–94

[20] Lv B Q *et al* 2017 Observation of three-component fermions in the topological semimetal molybdenum phosphide *Nature* **546** 627–31

[21] Barik R K, Shinde R and Singh A K 2018 Multiple triple-point fermions in Heusler compounds *J. Phys.: Condens. Matter* **30** 375702

[22] Yang Y *et al* 2019 Topological triply degenerate point with double Fermi arcs *Nat. Phys.* **15** 645–9

[23] Ma J *et al* 2017 Experimental evidence of hourglass fermion in the candidate nonsymmorphic topological insulator KHgSb *Sci. Adv.* **3** e1602415

[24] Wang S-S, Liu Y, Yu Z-M, Sheng X-L and Yang S A 2017 Hourglass Dirac chain metal in rhenium dioxide *Nat. Commun.* **8** 1844

[25] Singh B, Ghosh B, Su C, Lin H, Agarwal A and Bansil A 2018 Topological hourglass Dirac semimetal in the nonpolar phase of $Ag_2BiO_3$ *Phys. Rev. Lett.* **121** 226401

[26] Novoselov K S, Geim A K, Morozov S V, Jiang D, Zhang Y, Dubonos S V, Grigorieva I V and Firsov A A 2004 Electric field effect in atomically thin carbon films *Science* **306** 666–9

[27] Kim J *et al* 2015 Observation of tunable band gap and anisotropic Dirac semimetal state in black phosphorus *Science* **349** 723–6

[28] Wang Z M 2014 *$MoS_2$ Materials, Physics and Devices* (Berlin: Springer)

[29] Damljanović V, Popov I and Gajić R 2017 Fortune teller fermions in two-dimensional materials *Nanoscale* **9** 19337–45

[30] Kopciuszyński M, Krawiec M, Żurawek L and Zdyb R 2020 Experimental evidence of a new class of massless fermions *Nanoscale Horiz.* **5** 679–82

[31] Nguyen S D, Yeon J, Kim S-H and Shiv Halasyamani P 2011 $BiO(IO_3)$: a new polar iodate that exhibits an Aurivillius-type $(Bi_2O_2)^{2+}$ layer and a large SHG response *J. Am. Chem. Soc.* **133** 12422–5

[32] Cornwell J F 1984 *Group Theory in Physics* (New York: Academic)

[33] Elcoro L *et al* 2017 Double crystallographic groups and their representations on the Bilbao Crystallographic Server *J. Appl. Crystallogr.* **50** 1457–77

[34] Damnjanović M and Milošević I 2015 Full symmetry implementation in condensed matter and molecular physics—modified group projector technique *Phys. Rep.* **581** 1–43

[35] Litvin D B and Wike T R 1991 *Character Tables and Compatibility Relations of the Eighty Layer Groups and Seventeen Plane Groups* (New York: Plenum)

[36] Dresselhaus M S, Dresselhaus G and Jorio A 2008 *Group Theory* (Berlin: Springer)

[37] Kopsky V and Litvin D B 2002 *International Tables of Crystallography Volume E: Subperiodic Groups* (Dordrecht: Kluwer)

[38] Hahn T 2005 *International Tables of Crystallography Volume A: Space-Group Symmetry* (Berlin: Springer)

[39] Burkov A A, Hook M D and Leon B 2011 Topological nodal semimetals *Phys. Rev.* B **84** 235126

[40] Watanabe H, Po H C, Zaletel M P and Vishwanath A 2016 Filling-enforced gaplessness in band structures of the 230 space groups *Phys. Rev. Lett.* **117** 096404

[41] Mounet N *et al* 2018 Two-dimensional materials from high-throughput computational exfoliation of experimentally known compounds *Nat. Nanotechnol.* **13** 246–52

[42] Giannozzi P *et al* 2009 QUANTUM ESPRESSO: a modular and open-source software project for quantum simulations of materials *J. Phys.: Condens. Matter* **21** 395502

[43] Blöchl P E 1994 Projector augmented-wave method *Phys. Rev.* B **50** 17953–79

[44] Kresse G and Joubert D 1999 From ultrasoft pseudopotentials to the projector augmented-wave method *Phys. Rev.* B **59** 1758–75

[45] Perdew J P, Burke K and Ernzerhof M 1996 Generalized gradient approximation made simple *Phys. Rev. Lett.* **77** 3865–8

[46] Wieder B J and Kane C L 2016 Spin–orbit semimetals in the layer groups *Phys. Rev.* B **94** 155108

[47] Watanabe H, Po H C, Vishwanath A and Zaletel M 2015 Filling constraints for spin-orbit coupled insulators in symmorphic and nonsymmorphic crystals *Proc. Natl Acad. Sci.* **112** 14551–6

[48] Yang S A 2016 Dirac and Weyl materials: fundamental aspects and some spintronics applications *SPIN* **06** 1640003

[49] Boriskina S, Zhou J, Ding Z and Chen G 2018 Efficiency limits of solar energy harvesting via internal photoemission in carbon materials *Photonics* **5** 4

Optical and Quantum Electronics (2020) 52:182
https://doi.org/10.1007/s11082-020-02300-0

# Optical and mechanical properties and electron–phonon interaction in graphene doped with metal atoms

**Andrijana Šolajić[1] · Jelena Pešić[1] · Radoš Gajić[1]**

Received: 31 October 2019 / Accepted: 5 March 2020 / Published online: 14 March 2020


**Abstract**
Graphene, the first experimentally realized 2D material with outstanding mechanical and electrical properties as well an excellent optical transparency, is predicted to have many applications in various scientific fields. Furthermore, there are numerous ways for modifications of pure graphene that allow precise tuning of its properties or observation of some new effects, including the applied strain, various types of controlled defects, exposure to electrical or magnetic field, or doping. It is known that graphene with alkali metal atoms adsorbed on its surface becomes superconducting with due to enhanced electron–phonon coupling. The question remains what happens with optical and mechanical properties of such structures, can we preserve or enhance these superb properties while making graphene superconducting at the same time. Here we investigate structures based on graphene doped with several metal atoms—Sr, and some transition metal atoms such are Y and Sc. Using the density functional theory, we analyze the optical and elastic properties of those structures, discussing the influence of adsorbed atoms on these properties and calculate the electron–phonon coupling related properties.

**Keywords** Graphene · DFT · Superconductivity · Electron–phonon interaction · Optical properties · 2D materials

## 1 Introduction

Since the experimental discovery in 2004, graphene has been attracting enormous attention, not only as the first experimentally realised 2D material as the large scale samples, but mostly for its many unique properties. With this wide spectra of effects, graphene was also predicted to be suitable for various applications (Ferrari 2015; Blake et al. 2008; Todorović et al. 2015; Bonaccorso et al. 2015; Sassi et al. 2017; Liu et al. 2014). Monolayer graphene

This article is part of the Topical Collection on Advanced Photonics Meets Machine Learning.

Guest edited by Goran Gligoric, Jelena Radovanovic and Aleksandra Maluckov.

✉ Andrijana Šolajić
solajic@ipb.ac.rs

[1] Institute of Physics Belgrade, University of Belgrade, Pregrevica 118, Belgrade 11080, Serbia

formed on various metal surfaces was also extensively researched (Wintterlin and Bocquet 2009; Aizawa et al. 1990a, b; Taleb and Farías 2016) along with intercalation of these supported graphene systems (Gall et al. 1997; Shikin et al. 1998; Farías et al. 1999). Up to today, a couple of thousands papers about graphene are publicated and it is very well-known today how special graphene is and how its characteristics can be tailored to be suitable for even more suitable use. But in the long list of graphene's remarkable properties (Katsnelson et al. 2006; Gusynin and Sharapov 2005; Castro Neto et al. 2006; Lee et al. 2008), there is one notable effect missing, the superconductivity, which is absent in pristine graphene. Among many attempts to make graphene superconducting, a successful idea came from the so-called Graphite intercalation compounds (GICs). GICs are composed from graphite layers, with metallic atoms nested between. They were extensively studied since the 1960s, but with discovery of the superconductivity in some of the GICs ($CaC_6$ with $T_c = 11.5$K and $YbC_6$ with $T_c = 6.5$K), an interest in those structures has raised again. The origin of superconductivity in GICs was debated for a long time, but most suggested was that the pairing mediated by electron–phonon interactions as the mechanism (Mazin 2005; Calandra and Mauri 2005), which was later confirmed by experimental data. As it can be observed, in all superconducting GICs there is an intercalant Fermi surface at the Fermi level, and those electrons are strongly coupled to the phonons. As reported in several studies, similar effects are present when going down to the thinnest limit, case of monolayer graphene doped with alkali adatoms in a similar manner to GICs. The electron–phonon coupling constant, $\lambda$,

$$\lambda = \frac{N(0)D^2}{M\omega_{ph}^2}, \tag{1}$$

is proportional to the density of states at the Fermi level and the deformational potential $D$, and inversely proportional to effective atomic mass $M$ and the frequency of the phonon involved $\omega_{ph}$. As the DOS on the Fermi level in graphene is zero and slowly growing in its vicinity, the superconductivity in pristine graphene can not be observed, similar to pristine bulk graphite. However, the situation is changed upon doping with metallic adatoms, similar as in GICs. In the presence of adatoms, new electronic band is formed, the number of carriers is enlarged and, if the interlayer band occurs at the Fermi level, the electron–phonon coupling $\lambda$ is enhanced and the coupling to carbon out-of-plane vibrations is promoted. Besides DOS, electron–phonon coupling constant also depends on the deformation potential $D$, which is inversely related to the distance between the graphene and adatoms. Hence for occurrence of the superconductivity it is favourable for adatoms to be closer to the graphene plane. On the other hand, it was shown that too small distance would result in a complete charge transfer between the graphene and the adatoms, so the interlayer band would be completely empty, as is the case with the bulk $LiC_6$ where the strong confinement along the $z$ axis leads to interlayer band to be completely unoccupied and the superconductivity is suppressed. In contrary, in the $LiC_6$ monolayer, the quantum confinement is removed, resulting in partially occupied interlayer band and superconductivity with $T_c$ up to 8K.

Motivated by these results, we wanted to explore graphene doped with Sr atoms and also with some transition metal atoms such are Sc and Y. Besides the electron–phonon properties crucial for the superconductivity, we were interested to investigate mechanical and optical properties also in order to study effects of added adatoms, questioning can we obtain superconducting material and preserve this superb graphene's properties, which would be of great significance for many applications. Using the density functional theory, we analyse the electron–phonon interaction properties and predict the critical temperature in the framework of the

electron–phonon coupling theory. We analyse the mechanical and optical properties of these structures and discuss the influence of adatoms on these properties.

## 2 Computational details

All calculations were performed in the Quantum Espresso software package (Giannozzi et al. 2009), in the LDA approximation, which is proven to be suitable for graphene systems and often is used. We used norm-conserving pseudopotentials, with the energy cutoff for wavefunctions of 120 Ry, obtained with respect to the convergence test. The unit cell for all doped graphene structures is modelled as $\sqrt{3} \times \sqrt{3}R30°$ supercell of graphene unit cell, with adatoms positioned above the centres of carbon hexagons, the so-called H-site, as it is the most favourable site for all three atoms, according to the DFT study (Nakada and Ishii 2011). In order to avoid the interactions due to periodicity and to simulate a 2D system, the hexagonal $c$ parameter was set to be sufficiently large, more than $c = 10$ Å. Prior to any further calculations, the structures were relaxed to their minimum energy configuration, using the BFGS algorithm. The dielectric function was calculated within the framework of the random-phase approximation (RPA), as implemented in epsilon.x code of QE, on the uniform k-point grid composed of 4096 k-points. The second-order elastic constants were calculated using the ElaStic code. First, the strain type and strength is chosen, and for each deformation, total energies are calculated. From the second derivatives of energy curves, elastic constants are calculated. Here we used amplitudes of 7% positive and negative Lagrangian strain.

The grid for electron–phonon coupling was used up to $48 \times 48 \times 1$ electronic $k$-mesh and $12 \times 12 \times 1$ phonon-momentum mesh using the Monkhorst pack. The electron–phonon coupling parameter $\lambda$ and the critical temperature $T_c$ are obtained with the isotropic Eliashberg theory. The Eliashberg function is defined as

$$\alpha^2 F(\omega) = \frac{1}{N(0) N_k N_q} \sum_{n\mathbf{k},m\mathbf{q},\nu} |g^{\nu}_{n\mathbf{k},m\mathbf{k}+\mathbf{q}}|^2 \times \delta(\epsilon_{n\mathbf{k}}) \delta(\epsilon_{m\mathbf{k}+\mathbf{q}}) \delta(\omega - \omega^{\nu}_q) \tag{2}$$

where $N(0)$ is total density of states per spin, $N_k$ and $N_q$ are the total numbers of $k$ and $q$ points. $g^{\nu}_{n\mathbf{k},m\mathbf{k}+\mathbf{q}}$ is the electron–phonon matrix element, and electron eigenvalues and the band indexes are labelled with $n$ and $m$, the wavevectors $\mathbf{k}$ and $\mathbf{k} + \mathbf{q}$, the phonon frequencies with the mode number $\nu$ and the wavevector $\mathbf{q}$. From previous equation, the electron–phonon coupling coefficient is given as

$$\lambda(\omega) = 2 \int_0^{\omega} \frac{\alpha^2 F(\omega')}{\omega'} d\omega' \tag{3}$$

The total electron phonon coupling is obtained for $\omega \to \infty$. The superconducting critical temperature is estimated using the Allen–Dynes formula,

$$T_c = \frac{\omega_{log}}{1.2} \exp\left[\frac{-1.04(1+\lambda)}{\lambda(1 - 0.62\mu^*) - \mu^*}\right] \tag{4}$$

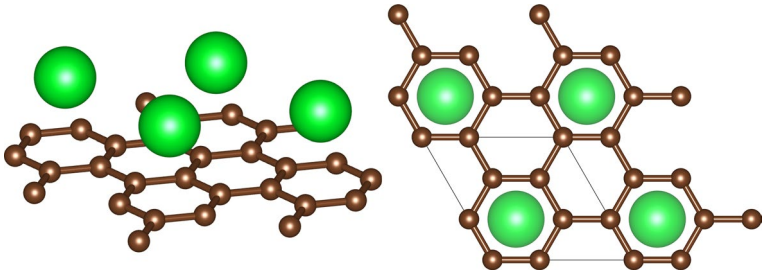

**Fig. 1** The structure of graphene with atoms adsorbed on H-site. On the right, top view of structure is shown, with unit cell marked with black line

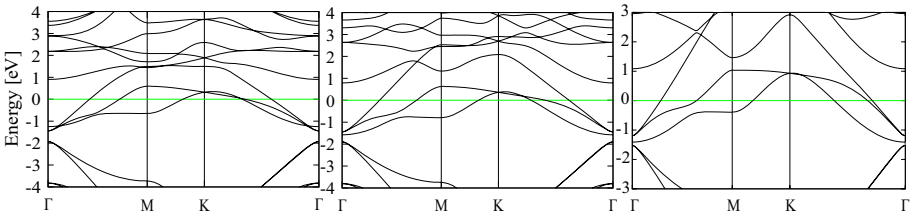


**Fig. 2** Electronic structure of $ScC_6$, $YC_6$ and $SrC_6$ along $\Gamma$-M-K-$\Gamma$ direction. Fermi level is centered on 0 eV

where $\mu^*$ is the screened Coulomb pseudopotential and

$$\omega_{log} = \exp\left[\frac{2}{\lambda}\int \frac{d\omega}{\omega}\alpha^2 F(\omega)\log\omega\right] \tag{5}$$

is the phonon frequencies logarithmic average.

## 3 Results and Discussion

The atomic structure of $SrC_6$ monolayer is consisted of graphene sheet covered with Sr adatoms positioned in the H-site, as shown in Fig. 1. Upon relaxing the systems, obtained distance between the graphene sheet and the adatom are $h = 2.22$ Å for $SrC_6$, $h = 2.04$ Å for $YC_6$, and $h = 1.76$ Å for $ScC_6$. Comparing to, for example the bulk $SrC_6$ compound, where this distance is 2.475 Å, Sr atoms are closer to the graphene plane, more nested in the centres of carbon hexagons.

The electronic structure of $SrC_6$ monolayer is discussed in details in our previous work (Šolajić et al. 2018). We have shown the interlayer band that is forming due to the presence of Sr atoms, positioned near the Fermi level, partially occupied. Carbon $\pi^*$ bands are strongly hybridized with new adatom-derived bands and also the DOS on Fermi level is significantly raised. Very similar are monolayers of $ScC_6$ and $YC_6$, without almost any qualitative difference or significant difference in position of the Fermi level. Electronic structure of all three systems are shown in Fig. 2.

Motivated with those results, we proceeded to calculate the phonon dispersion and electron phonon coupling. In Fig. 3 the phonon dispersion of $SrC_6$ and phonon density of states for all structures are shown. The adatom contribution to phonon modes is marked

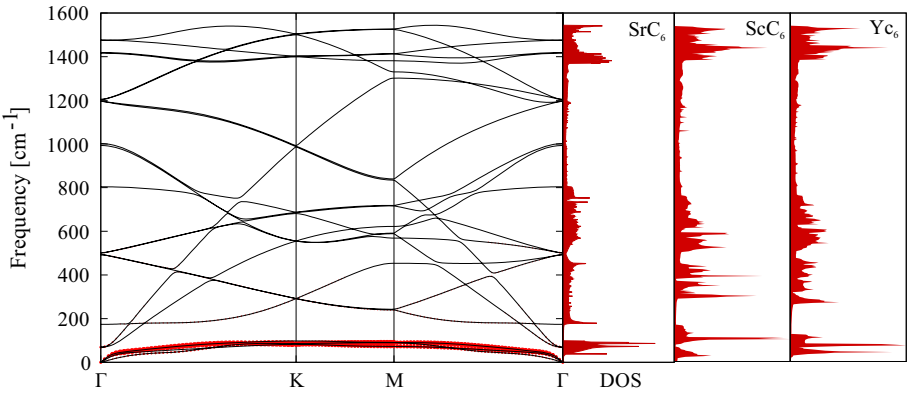


**Fig. 3** Phonon dispersion for $SrC_6$-mono and phonon density of states for all three structures

with red circles. The phonon dispersions do not show any negative modes and they suggest that systems are dynamically stable. Similar to other metal doped graphene structures, we can observe three distinguished regions. Lowest region belongs to adatom modes, in the middle region are positioned carbon out-of-plane modes, and highest modes are C–C stretching modes. Since the phonon dispersions show minor differences for all three structures, presented is only $SrC_6$. First two modes with lowest energies (degenerated one at $\approx 70\,\mathrm{cm}^{-1}$ and one at $\approx 175\,\mathrm{cm}^{-1}$) are related to pristine graphene's acoustic modes. That can be also seen in Fig 4. of our previous study (Šolajić et al. 2018), for the lowest mode at $70\,\mathrm{cm}^{-1}$, the in plane displacements of carbon atoms are like TA and LA modes, with the adatom oscillating in opposite direction, and analogue case for the mode at $175\,\mathrm{cm}^{-1}$, related to ZA graphene mode. This splitting of ZA-like mode from the lower two is similar to the case where graphene layer is formed on metal substrates, and the gap at the $\Gamma$ point is introduced due to interaction of graphene with substrate [The shift of ZA mode is seen at $48\,\mathrm{cm}^{-1}$ in graphene on Cu(111) substrate (Taleb and Farías 2016) and at $282\,\mathrm{cm}^{-1}$ for graphene on transition-metal carbides TaC(111), HfC(111) and TiC(111) (Aizawa et al. 1990b)]. We can consider that the splitting of the ZA-like mode can be described in a similar way, representing the interaction between the graphene and adsorbed metal atoms. The formed gap depends on the strength of the graphene-substrate coupling and as given in the following models. For free-standing pristine graphene, the dispersion of the acoustic ZA mode in the vicinity of the $\Gamma$ point is given by Taleb et al. (2015):

$$\omega_{ZA}^{free}(\mathbf{q}) = \sqrt{\frac{\kappa}{\rho_{2D}}}\mathbf{q}^2, \tag{6}$$

where $\rho_{2D} = 7.6 \times 10^{-8}\,\mathrm{g/cm}^2$ is the two-dimensional mass density of graphene. Coupling to the substrate introduces a gap at a frequency $\omega_0$ at the $\Gamma$ point and the dispersion relation is given by Amorim and Guinea (2013)

$$\omega_{ZA}^{free}(\mathbf{q}) = \sqrt{\frac{\kappa}{\rho_{2D}}\mathbf{q}^4 + \omega_0^2}, \tag{7}$$

where $\omega_0 = \sqrt{g/\rho_{2D}}$ and $g$ is the coupling strength between graphene and substrate. Following this model, we can approximate the similar interaction of graphene with adsorbed

metal layer and determine the $g = 0.739 \times 10^{19}$ N/m$^3$. This value is significantly smaller than for graphene on various substrates [from $g = 5.7 \times 10^{19}$ N/m$^3$ for graphene on Cu (Taleb et al. 2015), to the order of $2 \times 10^{21}$ for the (111) surface of transition metal carbides (Amorim and Guinea 2013)], as somewhat expecting given that the graphene is covered with not so dense placed Sr metal atoms and not suspended on a real surface.

The right side of Fig. 3 shows the phonon DOS for doped graphene structures. For all three structures, the phonon DOS is largest in the adatom region, as well in carbon in-plane modes area. As it can be seen in Eliashberg function, presented in Fig. 4, those modes also have significant contribution in electron–phonon coupling. The choice of adatom does not affect the phonon density of states and, in every of three systems, largest peaks are in low energy region and the highest ones with some minor difference in positions of peaks.

In the Eliashberg function calculated for $SrC_6$ monolayer, shown in Fig. 4, three distinguished peaks are present as expected, one from the lowest adatom-related modes, one wide and narrow in the middle-energy region, and the highest peak at 1400–1500 cm$^{-1}$ related to the carbon in-plane modes. Although the C–C stretching modes are strongly coupled with electronic states at Fermi level, the $\lambda$ parameter is enhanced most in the low energy region related to adatoms ($\approx 0.18$), given that it depends on the phonon energy inversely, so the low-energy modes have largest contribution to electron–phonon coupling constant. Comparing this to bulk $SrC_6$ compound (Calandra and Mauri 2006), we can observe slightly softened $Sr_z$ phonon mode, giving a larger peak in Eliashberg function. However, in the middle region, the contribution of carbon out-of-plane modes is significantly smaller and the contribution to electron–phonon coupling is drastically lowered than in bulk. Very similar case is reported with $CaC_6$ (Calandra and Mauri 2006; Profeta et al. 2012) where the carbon out-of-plane vibrations are similar in bulk and the monolayer case but overall contribution to $\lambda$ is decreased in the monolayer. This is also an opposite to the $LiC_6$ where the removal of confinement gives a rise to the $\lambda$.

Overall electron–phonon coupling constant in $SrC_6$-monolayer is $\lambda = 0.38$, with $\omega_{log} = 280.9$ cm$^{-1}$. The superconducting transition temperature, estimated using the Allen–Dynes formula with $\mu^* = 0.112$ is $T_c = 0.9$K, lower than in its bulk counterpart (3K). Both other structures have very similar electronic and phonon structure and enhanced electron–phonon coupling is expected, with critical temperatures in similar range. Further calculations of electron–phonon coupling parameter are needed to be confirmed.

Interested to see what happens with mechanical properties that are superb in graphene, we calculated the elastic constants of our doped structures and compare them

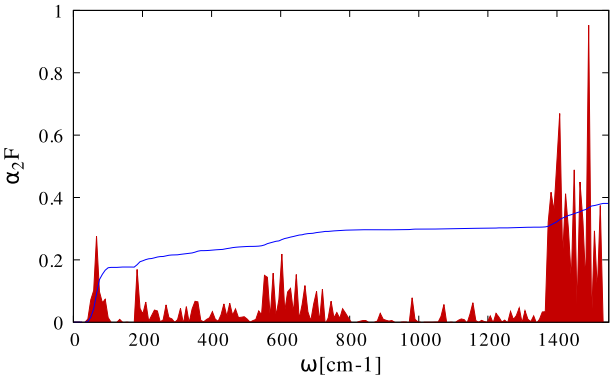


**Fig. 4** Eliashberg function with integrated electron–phonon coupling parameter for SrC6-mono

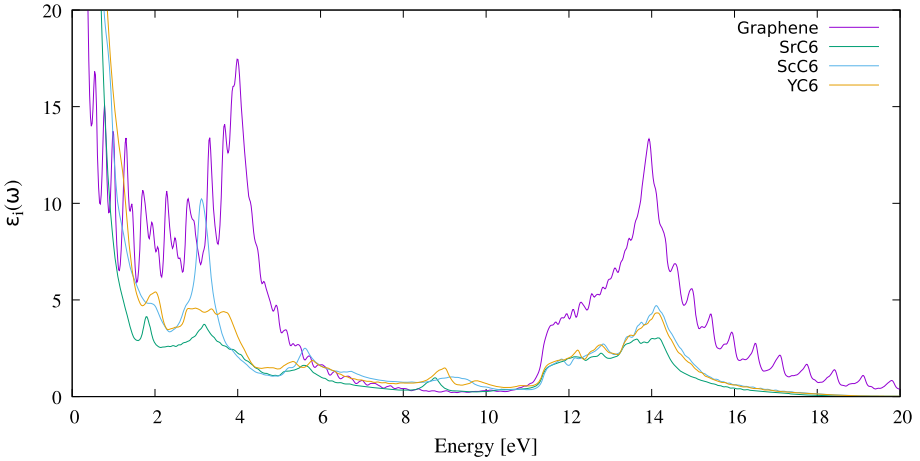


**Fig. 5** Eliashberg function with integrated electron–phonon coupling parameter for SrC6-mono

with pristine graphene, which are shown in Table 1. 2D hexagonal, square and rectangular lattices have 4 non-zero second-order elastic constants, $c_{11}$, $c_{12}$, $c_{22}$ and $c_{66}$, where due to symmetry, in case of hexagonal lattice, only two elastic constants are independent because $c_{11} = c_{22}$ and $c_{66} = \frac{1}{2}(c_{11} - c_{22})$. In this case, the Young modulus and Poisson's ratio are in defined according to Wei and Peng (2014) as $Y = \frac{c_{11}^2 - c_{12}^2}{c_{11}}$ and $\nu = \frac{c_{21}}{c_{11}}$. Obtained results for elastic properties of pristine graphene are overall in good agreement with previous experimental and theoretical studies. Calculated elastic constants $c_{11}$ and $c_{12}$ are both larger than in literature (estimated to be around 350 and 60 N/m, respectively), so the Young Modulus is also larger (experimentally measured to 342 N/m in Politano et al. 2012 and 340 N/m in Lee et al. 2008). The Poisson's ratio is however accurately obtained to 0.19, presumably due to both $c_{11}$ and $c_{12}$ similarly overestimated. Pristine graphene has extraordinary large values of elastic constants and also can be stretched up to roundly 20%. It is clearly observable that upon doping, elastic constants drop to almost half of the pristine graphene ones, as it is somewhat expected due to added adatoms on top of graphene surface. Still, that leaves these parameters very high in comparison to many other similar 2D materials. Moreover, parameters such is Young modulus remains exceptionally good. The elastic constants and Young modulus of doped graphene structures are in range of hBN and slightly larger than SiC (Andrew et al. 2012; Zhang et al. 2017), and still much larger than many other 2D structures, such are $MgB_2$ (Pešić et al. 2019) or silicene (Zhang et al. 2017). This possibility to

**Table 1** The calculated elastic constants, Young's modulus $Y$, Poisson's ratio $\nu$ and the shear modulus $G$, for pristine graphene, $ScC_6$, $YC_6$ and $SrC_6$ monolayers

| | $c_{11}$ | $c_{12}$ | $c_{66}$ | $Y$ | $\nu$ | $G$ |
|---|---|---|---|---|---|---|
| Graphene | 462.3 | 79.6 | 191.4 | 448.6 | 0.19 | 94.67 |
| $ScC_6$ | 244.8 | 37.2 | 103.8 | 239.2 | 0.15 | 103.83 |
| $SrC_6$ | 205.9 | 33.3 | 86.3 | 200.5 | 0.16 | 86.26 |
| $YC_6$ | 239.7 | 38.2 | 100.8 | 233.6 | 0.16 | 100.77 |

All parameters are given in units of N/m, except the Poisson's ratio which is dimensionless

strain graphene can be also exploited for tuning superconducting properties, as previously was shown that certain types of strain can enhance the superconducting critical temperature significantly. Pešić et al. (2014).

Calculated imaginary part of dielectric function for our doped structures and pristine graphene, for the electric field vector perpendicular to the $c$ axis, is shown in Fig. 5. Dielectric function of pristine graphene is discussed before (Marinopoulos et al. 2004) and we will not discuss it in details. Our calculations are in agreement with previous theoretical as well experimental studies, showing clear peaks at 4 eV and 14 eV, originating from $\pi \rightarrow \pi^*$ and $\sigma \rightarrow \sigma^*$ interband transitions. The singularity at zero frequency is present and shows metalicity of the system. Upon doping, two small differences can be observed. First, the first peak which is in pristine graphene at 4 eV is shifted to around 3 eV and it is lower intensity in all structures. The second peak ad 14 eV does not change position in energy, but drops to much lower intensity in all three structures. These lower intensities and changes in positions of the peaks can be related to Fermi level shift and an adatom influence on $\pi^*$ bands. Varying the type of dopants however does not make any significant changes in position or intensity of these peaks, except in case of $ScC_6$ monolayer where intensity of first peak is slightly smaller than in pristine graphene. Moreover, none of the changes in dielectric function induced by adatoms is crucial for the quality of the optical properties and they remain superb as in pristine graphene.

## 4 Conclusions

In this work we investigated the electron–phonon coupling and possibility of supeconductivity in graphene doped with Sr, Y and Sc adatoms, as well their mechanical and optical properties. The bulk $SrC_6$ which is superconducting with $T_c = 3K$, was studied theoretically as well experimentally. Moreover, previously studied electronic properties predict the monolayer as good candidate for occurrence of superconductivity. Here we expanded our research by doping with transition metals such are Sc and Y. The phonon dispersion of systems show they are dynamically stable, with no negative frequencies present. Using the isotropic Eliashberg theory, we calculated the total electron–phonon coupling parameter of $SrC_6$ monolayer, $\lambda = 0.38$. As in bulk $SrC_6$ compound, superconductivity is occurring, but with lower $T_c$, which is estimated as $T_c = 0.9K$ using the Allen–Dynes formula with $\mu^* = 0.112$. Other two discussed structures have similar electronic structure and density of states, as well the phonon dispersion too and have potential to have superconducting properties with similar critical temperatures, and need further investigation. Our calculations of elastic constants and mechanical properties show that upon doping graphene, elastic constants and other parameters like Young modulus, drop by half of pristine graphene's, which is still extraordinary good in comparison to many similar structures. Calculated imaginary parts of dielectric constants show no significant changes other than lower intensities of the peaks and slightly shifting in energy. This makes those structures an excellent candidates for potential applications.

**Acknowledgements** The authors acknowledge funding provided by the Institute of Physics Belgrade, through the grant by the Ministry of Education, Science, and Technological Development of the Republic of Serbia. DFT calculations were performed using computational resources at Johannes Kepler University, Linz, Austria.

## References


Aizawa, T., Souda, R., Otani, S., Ishizawa, Y., Oshima, C.: Anomalous bond of monolayer graphite on transition-metal carbide surfaces. Phys. Rev. Lett. **64**, 768–771 (1990a). https://doi.org/10.1103/PhysRevLett.64.768

Aizawa, T., Souda, R., Otani, S., Ishizawa, Y., Oshima, C.: Bond softening in monolayer graphite formed on transition-metal carbide surfaces. Phys. Rev. B **42**, 11469–11478 (1990b). https://doi.org/10.1103/PhysRevB.42.11469

Amorim, B., Guinea, F.: Flexural mode of graphene on a substrate. Phys. Rev. B **88**(11), 115418–115425 (2013)

Andrew, R.C., Mapasha, R.E., Ukpong, A.M., Chetty, N.: Mechanical properties of graphene and boronitrene. Phys. Rev. B **85**, 125428–125437 (2012). https://doi.org/10.1103/PhysRevB.85.125428

Blake, P., Brimicombe, P.D., Nair, R.R., Booth, T.J., Jiang, D., Schedin, F., Ponomarenko, L.A., Morozov, S.V., Gleeson, H.F., Hill, E.W., Geim, A.K., Novoselov, K.S.: Graphene-based liquid crystal device. Nano Lett. **8**(6), 1704–1708 (2008). https://doi.org/10.1021/nl080649i

Bonaccorso, F., Colombo, L., Yu, G., Stoller, M., Tozzini, V., Ferrari, A.C., Ruoff, R.S., Pellegrini, V.: Graphene, related two-dimensional crystals, and hybrid systems for energy conversion and storage. Science (2015). https://doi.org/10.1126/science.1246501

Calandra, M., Mauri, F.: Theoretical explanation of superconductivity in $c_6$ Ca. Phys. Rev. Lett. **95**, 237002–237006 (2005). https://doi.org/10.1103/PhysRevLett.95.237002

Calandra, M., Mauri, F.: Possibility of superconductivity in graphite intercalated with alkaline earths investigated with density functional theory. Phys. Rev. B **74**, 094507–094515 (2006). https://doi.org/10.1103/PhysRevB.74.094507

Castro Neto, A.H., Guinea, F., Peres, N.M.R.: Edge and surface states in the quantum hall effect in graphene. Phys. Rev. B **73**, 205408–205416 (2006). https://doi.org/10.1103/PhysRevB.73.205408

Farías, D., Shikin, A.M., Rieder, K.H., Dedkov, Y.S.: Synthesis of a weakly bonded graphite monolayer on ni(111) by intercalation of silver. J. Phys. Condens. Matter **11**(43), 8453–8458 (1999). https://doi.org/10.1088/0953-8984/11/43/308

Ferrari, A.C., et al.: Science and technology roadmap for graphene, related two-dimensional crystals, and hybrid systems. Nanoscale **7**, 4598–4810 (2015). https://doi.org/10.1039/C4NR01600A

Gall, N.R., Rut'kov, E.V., Tontegode, A.Y.: Two dimensional graphite films on metals and their intercalation. Int. J. Mod. Phys. B **11**(16), 1865–1911 (1997). https://doi.org/10.1142/S0217979920000976

Giannozzi, P., et al.: Quantum espresso: a modular and open-source software project for quantum simulations of materials. J. Phys. Condens. Matter **21**(39), 395502–395521 (2009)

Gusynin, V.P., Sharapov, S.G.: Unconventional integer quantum hall effect in graphene. Phys. Rev. Lett. **95**, 146801–146805 (2005). https://doi.org/10.1103/PhysRevLett.95.146801

Katsnelson, M., Novoselov, K., Geim, A.: Chiral tunnelling and the klein paradox in graphene. Nat. Phys. **2**(9), 620–625 (2006). https://doi.org/10.1038/nphys384

Lee, C., Wei, X., Kysar, J.W., Hone, J.: Measurement of the elastic properties and intrinsic strength of monolayer graphene. Science **321**(5887), 385–388 (2008). https://doi.org/10.1126/science.1157996

Liu, C.H., Chang, Y.C., Norris, T.B., Zhong, Z.: Graphene photodetectors with ultra-broadband and high responsivity at room temperature. Nat. Nanotechnol. **9**(4), 273–278 (2014)

Marinopoulos, A.G., Reining, L., Rubio, A., Olevano, V.: Ab initio study of the optical absorption and wave-vector-dependent dielectric response of graphite. Phys. Rev. B **69**, 245419–245431 (2004). https://doi.org/10.1103/PhysRevB.69.245419

Mazin, I.I.: Intercalant-driven superconductivity in $YbC_6$ and $CaC_6$. Phys. Rev. Lett. **95**, 227001–227005 (2005). https://doi.org/10.1103/PhysRevLett.95.227001

Nakada, K., Ishii, A.: DFT calculation for adatom adsorption on graphene. In: Gong, J.R. (ed.) Graphene Simulation. InTech, Rijeka, Croatia (2011)

Pešić, J., Gajić, R., Hingerl, K., Belić, M.: Strain-enhanced superconductivity in li-doped graphene. Europhys. Lett.: EPL **108**(6), 67005–67011 (2014)

Pešić, J., Popov, I., Šolajić, A., Damljanović, V., Hingerl, K., Belić, M., Gajić, R.: Ab initio study of the electronic, vibrational, and mechanical properties of the magnesium diboride monolayer. Condens. Matter (2019). https://doi.org/10.3390/condmat4020037

Politano, A., Marino, A.R., Campi, D., Farías, D., Miranda, R., Chiarello, G.: Elastic properties of a macroscopic graphene sample from phonon dispersion measurements. Carbon **50**(13), 4903–4910 (2012). https://doi.org/10.1016/j.carbon.2012.06.019

Profeta, G., Calandra, M., Mauri, F.: Phonon-mediated superconductivity in graphene by lithium deposition. Nat. Phys. **8**(2), 131–134 (2012)

Sassi, U., Parret, R., Nanot, S., Bruna, M., Borini, S., De Fazio, D., Zhao, Z., Lidorikis, E., Koppens, F., Ferrari, A., et al.: Graphene-based mid-infrared room-temperature pyroelectric bolometers with ultra-high temperature coefficient of resistance. Nat. Commun. **8**, 14311–14321 (2017)

Shikin, A.M., Farías, D., Rieder, K.H.: Phonon stiffening induced by copper intercalation in monolayer graphite on ni(111). Europhys. Lett.: EPL **44**(1), 44–49 (1998). https://doi.org/10.1209/epl/i1998-00432-x

Šolajić, A., Pešić, J., Gajić, R.: Ab-initio calculations of electronic and vibrational properties of sr and yb intercalated graphene. Opt. Quantum Electron. **50**(7), 276–286 (2018). https://doi.org/10.1007/s11082-018-1541-x

Taleb, A.A., Farías, D.: Phonon dynamics of graphene on metals. J. Phys. Condens. Matter **28**(10), 103005–103024 (2016). https://doi.org/10.1088/0953-8984/28/10/103005

Taleb, A.A., Yu, H.K., Anemone, G., Farías, D., Wodtke, A.M.: Helium diffraction and acoustic phonons of graphene grown on copper foil. Carbon **95**, 731–737 (2015). https://doi.org/10.1016/j.carbon.2015.08.110

Todorović, D., Matković, A., Milićević, M., Jovanović, D., Gajić, R., Salom, I., Spasenović, M.: Multilayer graphene condenser microphone. 2D Mater. **2**(4), 045013–045019 (2015)

Wei, Q., Peng, X.: Superior mechanical flexibility of phosphorene and few-layer black phosphorus. Appl. Phys. Lett. **104**(25), 251915–251920 (2014). https://doi.org/10.1063/1.4885215

Wintterlin, J., Bocquet, M.L.: Graphene on metal surfaces. Surface Science **603**(10), 1841–1852 (2009). https://doi.org/10.1016/j.susc.2008.08.037. (Special Issue of Surface Science dedicated to Prof. Dr. Dr. h.c. mult. Gerhard Ertl, Nobel-Laureate in Chemistry 2007)

Zhang, Z., Yang, Y., Penev, E.S., Yakobson, B.I.: Elasticity, flexibility, and ideal strength of borophenes. Adv. Funct. Mater. **27**(9), 1605059–1605066 (2017). https://doi.org/10.1002/adfm.201605059

Inorganic Chemistry

pubs.acs.org/IC

Article

# Short-Range Order in $VI_3$

Sanja Djurdjić Mijin, A. M. Milinda Abeykoon, Andrijana Šolajić, Ana Milosavljević, Jelena Pešić, Yu Liu, Cedomir Petrovic, Zoran V. Popović, and Nenad Lazarević*

Cite This: *Inorg. Chem.* 2020, 59, 16265−16271

Read Online

ACCESS | Metrics & More | Article Recommendations

**ABSTRACT:** We present a detailed investigation of the crystal structure of $VI_3$, a two-dimensional van der Waals material of interest for studies of low-dimensional magnetism. As opposed to the average crystal structure that features $R\bar{3}$ symmetry of the unit cell, our Raman scattering and X-ray atomic pair distribution function analysis supported by density functional theory calculations point to the coexistence of short-range ordered $P\bar{3}1c$ and long-range ordered $R\bar{3}$ phases. The highest-intensity peak, $A_{1g}^3$, exhibits a moderate asymmetry that might be traced back to the spin−phonon interactions, as in the case of $CrI_3$.

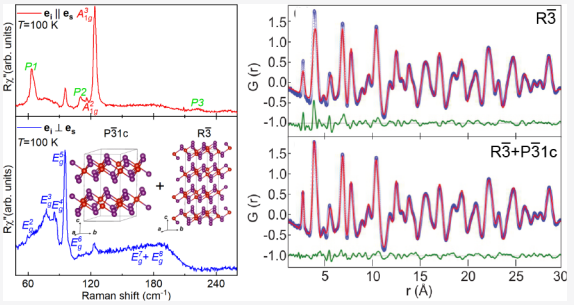


## INTRODUCTION

A well-known family of transition metal trihalides (TMTs) $MX_3$ (X = Cr, B, or I) have received a great deal of attention due to potential existence of two-dimensional (2D) ferromagnetism,[1−6] which has been confirmed in $CrI_3$.[7,8] The similar crystal structure and magnetic properties of $CrI_3$ and $VI_3$ fostered a belief that the same might be found in the latter. In fact, magnetization measurements revealed the 2D ferromagnetic nature of $VI_3$ with a Currie temperature ($T_c$) of around 50 K.[9,10] Contrary to a layer-dependent ferromagnetism in $CrI_3$,[11] the first-principles calculations predict that ferromagnetism in $VI_3$ persists down to a single layer,[9] making it a suitable candidate for engineering 2D spintronic devices. Resistivity measurements showed $VI_3$ is an insulator with an optical band gap of ∼0.6 eV.[9,12]

Whereas laboratory X-ray diffraction studies reported three possible high-temperature $VI_3$ unit cell symmetries,[9,12−14] high-resolution synchrotron X-ray diffraction confirmed a rhombohedral $R\bar{3}$ space group.[10] A very recently published Raman spectroscopy study indicated that the $VI_3$ crystal structure can be described within the $C_{2h}$ point group.[15] All results agree on the existence of a phase transition at a temperature of 79 K. However, the subtle[12] structural changes below 79 K are still under debate.

The long-range magnetic order in ultrathin 2D van der Waals (vdW) crystals stems from strong uniaxial anisotropy, in contrast to materials with isotropic exchange interactions where order parameters are forbidden.[16−18] 2D vdW magnetic materials are of interest both as examples of exotic magnetic order[19] and for potential applications in spintronic technology.[2,4,20,21]

Atomically thin flakes of $CrCl_3$ have a magnetic transition temperature that is different from that of bulk crystals possibly due to the different crystal structure of the monolayer and ultrathin crystals when compared to bulk.[22,23] Similar observations were made on $CrI_3$ monolayers.[22,24,25] It has been proposed[23] that the second anomaly in heat capacity in bulk $CrCl_3$ arises due to regions close to the surface that host a different crystal structure when compared to bulk;[26,27] however, due to the substantial mass fraction detected in heat capacity measurements, this could also reflect differences between the short-range order and long-range crystallographic order of Bragg planes. The short-range order is determined by the space group that is energetically favorable for a monolayer or a few layers, whereas the long-range crystallographic order is established over large packing lengths.

In this paper, we present an experimental Raman scattering study of the bulk $VI_3$ high-temperature structure, supported by density functional theory (DFT) calculations and the X-ray atomic pair distribution function (PDF) analysis. The comparison between the Raman experiment and DFT calculations for each of the previously reported space groups suggested that the high-temperature lattice vibrations of bulk $VI_3$ are consistent with a $P\bar{3}1c$ trigonal structure. Nine ($2A_{1g}$ + $7E_g$) of 12 observed peaks were assigned on the basis of factor group analysis (FGA) and DFT calculations. The PDF analysis indicated the coexistence of two crystallographic phases at two different interatomic distances, short-range ordered $P\bar{3}1c$ and

**Received:** July 12, 2020
**Published:** October 23, 2020

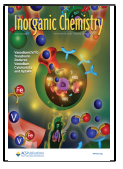









https://dx.doi.org/10.1021/acs.inorgchem.0c02060
*Inorg. Chem.* 2020, 59, 16265−16271

long-range ordered $R\bar{3}$, as two segregated phases and/or as randomly distributed short-range ordered $P\bar{3}1c$ domains in the long-range ordered $R\bar{3}$ lattice. Raman data displayed a moderate asymmetry of the $A_{1g}^3$ phonon line. This behavior was attributed to the spin−phonon interaction, similar to the case for $CrI_3$. The additional peaks in our spectra obey $A_g$ selection rules and can be described in terms of overtones, as well as the $A_{2g}$ silent modes "activated" by the symmetry breaking.

## EXPERIMENTAL AND COMPUTATIONAL DETAILS

The preparation of single-crystal $VI_3$ samples used in this study is presented elsewhere.[10] For the Raman scattering experiment, a Tri Vista 557 spectrometer was used in the backscattering micro-Raman configuration with a 1800/1800/2400 grooves/mm diffraction grating combination. A Coherent $Ar^+/Kr^+$ ion laser with a 514 nm line was used as an excitation source. Laser beam focusing was achieved through the microscope objective with 50× magnification. The direction of the incident (scattered) light coincides with the crystallographic $c$ axis. The sample, cleaved in open air, was held inside a KONTI CryoVac continuous helium flow cryostat with a 0.5 mm thick window. Raman scattering measurements were performed under high vacuum ($10^{-6}$ mbar). All of the obtained Raman spectra were corrected by the Bose factor. The spectrometer resolution is comparable to the Gaussian width of 1 $cm^{-1}$.

PDF and wide-angle X-ray scattering measurements were carried out in capillary transmission geometry using a PerkinElmer amorphous silicon area detector placed 206 and 983 mm downstream from the sample, respectively, at beamline 28-ID-1 (PDF) of National Synchrotron Light Source II at Brookhaven National Laboratory. The setup utilized a 74.3 keV ($\lambda$ = 0.1668 Å) X-ray beam.

Two-dimensional diffraction data were integrated using the Fit2D software package.[28] Data reduction was performed to obtain experimental PDFs ($Q_{max}$ = $26A^{-1}$) using the xPDFsuite software package.[29] The Rietveld and PDF analyses were carried out using GSAS-II[30] and PDFgui[31] software packages, respectively.

Density functional theory calculations were performed using the Quantum Espresso software package,[32] employing the PBE exchange-correlation functional[33] and PAW pseudopotentials.[34,35] All calculations are spin-polarized. The cutoff for wave functions and the charge density were set to 48 and 650 Ry, respectively. The $k$-points were sampled using the Monkhorst−Pack scheme, on a 6 × 6 × 6 Γ-centered grid for $R\bar{3}$ and $C2/m$ structures and a 12 × 12 × 8 grid for the $P\bar{3}1c$ structure. Optimization of the lattice parameters and atomic positions in the unit cell was performed until the interatomic forces were <$10^{-6}$ Ry/Å. To obtain more accurate lattice parameters, treatment of the van der Waals interactions is included using the Grimme-D2 correction. The correlation effects are treated with the Hubbard U correction (LDA+U), using a rotationally invariant formulation implemented in QE,[36] where $U$ = 3.68 eV. Band structure plots are calculated at 800 $k$-points on the chosen path over high-symmetry points. Phonon frequencies were calculated with the linear response method, as implemented in the -honon part of Quantum Espresso.

## RESULTS AND DISCUSSION

The first reported results for $VI_3$, dating from the 1950s,[37−39] indicated that $VI_3$ adopts a honeycomb layer-type $BiI_3$ structure described with space group $R\bar{3}$, which is a structure common in TMTs, also found in the low-temperature phase of $CrI_3$.[6,40]

There have been several proposed unit cell symmetries for $VI_3$ in the literature: $R\bar{3}$,[12,13] $C2/m$,[14] and $P\bar{3}1c$.[9] Schematic representations of the $P\bar{3}1c$, $R\bar{3}$, and $C2/m$ crystal structures are depicted in Figure 1. The corresponding crystallographic unit cell parameters, previously reported, are listed in Table 1.

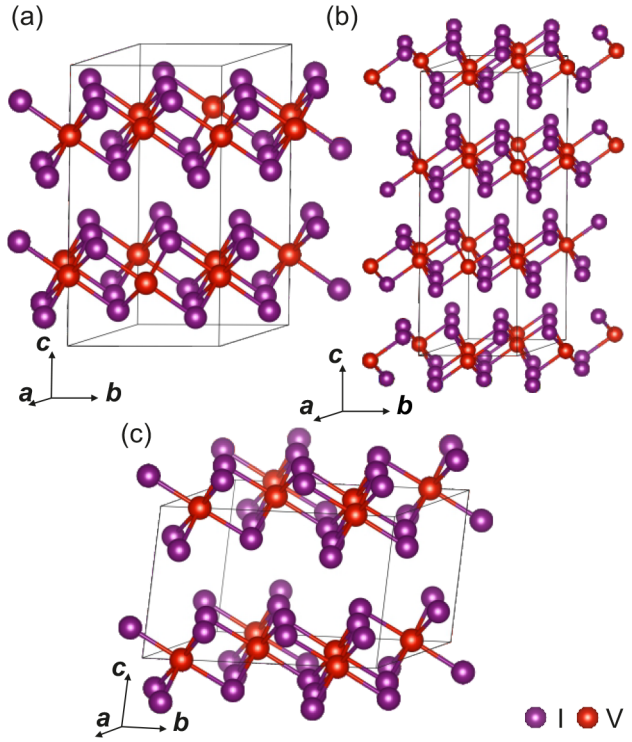


**Figure 1.** Schematic representation of the high-temperature (a) $P\bar{3}1c$, (b) $R\bar{3}$, and (c) $C2/m$ structures of $VI_3$. Black solid lines represent unit cells.

Each of the suggested symmetries implies a different distribution of Raman active modes.

According to FGA, eight ($4A_g$ + $4E_g$), 11 ($3A_{1g}$ + $8E_g$), and 12 ($6A_g$ + $6B_g$) Raman active modes are expected to be observed in the light scattering experiment for $R\bar{3}$, $P\bar{3}1c$, and $C2/m$ crystal structures, respectively. Wyckoff positions, irreducible representations, and corresponding tensors of Raman active modes for each space group are listed in Table 2.

The first step in determining the crystal symmetry from the light scattering experiment is to compare the expected and observed Raman active modes, shown in Figure 2. The red solid line represents the spectrum measured in the parallel polarization configuration, whereas the blue line corresponds to the cross polarization configuration. Five of 12 observed peaks emerge only in parallel, whereas five peaks and a broad peak-like structure can be observed for both polarization configurations. The emergence of the 123.4 $cm^{-1}$ peak in the cross polarization can be understood as a "leakage" of the $A_{1g}^3$ mode due to a possible finite $c$ axis projection and/or the presence of defects.

Now the peaks that appear only for the parallel polarization configuration can be assigned as either $A_{1g}$ or $A_g$ symmetry modes, assuming the light polarization direction along the main crystal axis of the $C2/m$ structure for the later. On the basis of the FGA for possible symmetry group candidates, the remaining Raman active modes can be either of $E_g$ or $B_g$ symmetry. The selection rules (Table 2) do not allow observation of the $B_g$ symmetry modes for the parallel polarization configuration. Consequently, the peaks that can be observed in both scattering channels were recognized as $E_g$ modes. The absence of $B_g$ modes in the Raman spectra rules out the possibility of the $AlCl_3$ type of structure (space group $C2/m$). Two possible remaining crystal symmetries ($R\bar{3}$ and


https://dx.doi.org/10.1021/acs.inorgchem.0c02060
Inorg. Chem. 2020, 59, 16265−16271

**Table 1. Previously Reported Experimental and Calculated Unit Cell Parameters for $P\bar{3}1c$, $R\bar{3}$, and $C2/m$ Structures of $VI_3$**

| | $P\bar{3}1c$ | | $R\bar{3}$ | | $C2/m$ | |
|---|---|---|---|---|---|---|
| | calcd | exp.[9] | calcd | exp.[12] | calcd | exp.[14] |
| $a$ (Å) | 6.87 | 6.89(10) | 6.69 | 6.89(3) | 7.01 | 6.84(3) |
| $b$ (Å) | 6.87 | 6.89(10) | 6.69 | 6.89(3) | 12.14 | 11.83(6) |
| $c$ (Å) | 13.224 | 13.289(1) | 19.81 | 19.81(9) | 7.01 | 6.95(4) |
| $\alpha$ (deg) | 90 | 90 | 90 | 90 | 90 | 90 |
| $\beta$ (deg) | 90 | 90 | 90 | 90 | 109.05 | 108.68 |
| $\gamma$ (deg) | 120 | 120 | 120 | 120 | 90 | 90 |
| cell volume (Å$^3$) | 559.62 | 547.74(10) | 767.71 | 814.09(8) | 563.33 | 533.66(36) |

**Table 2. Wyckoff Positions of Atoms and Their Contributions to the Γ-Point Phonons for the $R\bar{3}$, $C2/m$, and $P\bar{3}1c$ Structures and the Raman Tensors for the Corresponding Space Groups**

| space group $P\bar{3}1c$ | | space group $R\bar{3}$ | | space group $C2/m$ | |
|---|---|---|---|---|---|
| atom | irreducible representation | atom | irreducible representation | atom | irreducible representation |
| V ($2a$) | $A_{2g} + A_{2u} + E_g + E_u$ | V ($3a$) | | V ($4g$) | $A_g + A_u + 2B_g + 2B_u$ |
| V ($2c$) | $A_{2g} + A_{2u} + E_g + E_u$ | V ($6c$) | $A_g + A_u + E_g + E_u$ | I ($4i$) | $2A_g + A_u + B_g + 2B_u$ |
| I ($12i$) | $3A_{1g} + 3A_{1u} + 3A_{2g} + 3A_{2u} + 6E_g + 6E_u$ | I ($18f$) | $3A_g + 3A_u + 3E_g + 3E_u$ | I ($8j$) | $3A_g + 3A_u + 3B_g + 3B_u$ |

$$A_{1g} = \begin{pmatrix} a & & \\ & a & \\ & & b \end{pmatrix} \qquad A_g = \begin{pmatrix} a & & \\ & a & \\ & & b \end{pmatrix} \qquad A_g = \begin{pmatrix} a & & d \\ & c & \\ d & & b \end{pmatrix}$$

$$^1E_g = \begin{pmatrix} c & & \\ & -c & d \\ & d & \end{pmatrix} \; ^2E_g = \begin{pmatrix} & -c & -d \\ -c & & \\ d & & \end{pmatrix} \qquad ^1E_g = \begin{pmatrix} c & d & e \\ d & -c & f \\ e & f & \end{pmatrix} \; ^2E_g = \begin{pmatrix} d & -c & -f \\ -c & -d & e \\ -f & e & \end{pmatrix} \qquad B_g = \begin{pmatrix} & & e \\ & & f \\ e & f & \end{pmatrix}$$

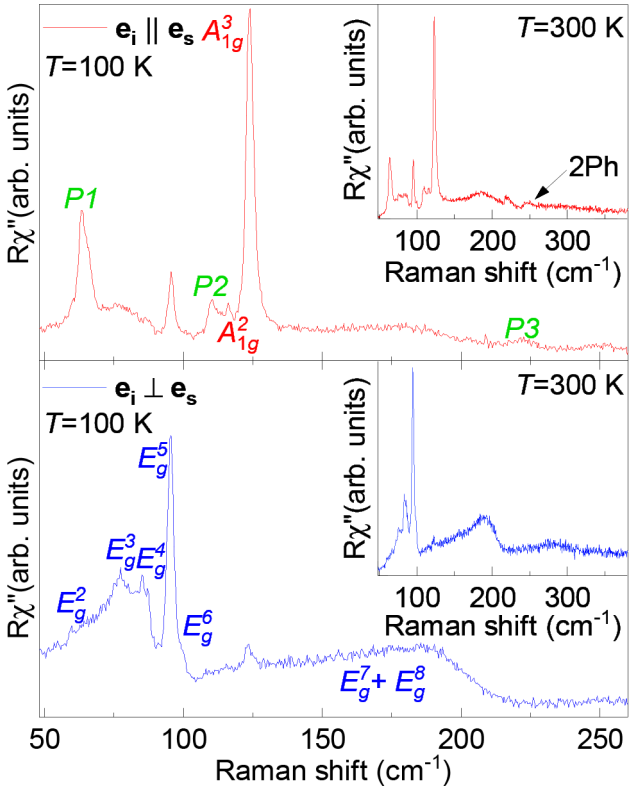


**Figure 2.** Raman spectra of the high-temperature $VI_3$ single-crystal structure measured in parallel (red solid line) and cross (blue solid line) polarization configurations at 100 K. Peaks observed in both spectra were identified as $E_g$ modes, whereas peaks observed only in the red spectrum were assigned as $A_{1g}$ modes. Additional peaks that obey pure $A_{1g}$ symmetry are marked as $P1$–$P3$.

$P\bar{3}1c$) are difficult to single out on the basis of the Raman data symmetry analysis alone. To overcome this obstacle, the DFT method was applied for each of the suggested structures.

It was reported in the literature that $P\bar{3}1c$ $VI_3$ can have two possible electronic states[9,14,41−43] that both can be obtained using DFT+U calculations by varying the smearing and mixing parameters. This approach resulted in a Mott-insulator state having a lower energy making it the electronic ground state of $VI_3$. However, the total energy difference of these two states is small and will not be mentioned further because it is outside of the scope of our analysis. For the sake of completeness, both sets of phonon energies obtained through DFT calculations for these electronic states of the $P\bar{3}1c$ structure are listed in Table 3 together with the results for the $R\bar{3}$ and $C2/m$ space groups as well as the experimental results measured at 100 K.

Now one can see that, even though the Raman mode symmetries for the case of the $R\bar{3}$ crystal structure can describe our Raman spectra, there is a stronger mismatch in calculated and experimentally determined phonon energies when compared to the results obtained for the $P\bar{3}1c$ structure. The deviation is largest for the calculated $A_g^1$ mode. The closest mode in energy, which obeys the same symmetry rules as the calculated $A_g^1$, is a peak at ∼64.1 cm$^{-1}$, yielding a deviation of ∼30%. Also, the calculated energy of the $A_g^4$ mode could not be identified within our spectrum, with the closest experimental $A_g$ peaks being within 20%. Such deviation in theory and experiment, >20%, indicates that the room-temperature phonon vibrations in $VI_3$ do not originate predominantly from the $BiI_3$ structure type either, leaving $P\bar{3}1c$ as the only candidate. This indication is further reinforced by the inability to connect the experimentally observed $E_g$ modes at ∼77 and ∼86 cm$^{-1}$ with the $R\bar{3}$-calculated modes.

Our experimental data (Table 3) are mostly supported by the phonon energies obtained for possible electronic states of


https://dx.doi.org/10.1021/acs.inorgchem.0c02060
Inorg. Chem. 2020, 59, 16265−16271

Table 3. Comparison between Calculated Values of Raman Active Phonon Energies for Insulating and Half-Metallic States of the $P\bar{3}1c$ Structure and Experimentally Obtained Values (left)[a] and Phonon Symmetries and Calculated Phonon Energies for the $R\bar{3}$ and $C2/m$ Structures of $VI_3$[b]

| space group $P\bar{3}1c$ | | | | space group $R\bar{3}$ | | space group $C2/m$ | |
|---|---|---|---|---|---|---|---|
| symmetry | calcd ($cm^{-1}$) | calcd ($cm^{-1}$) | exp. ($cm^{-1}$) | symmetry | calcd ($cm^{-1}$) | symmetry | calcd ($cm^{-1}$) |
| $E_g^1$ | 17.2 | 15.2 | – | $E_g^1$ | 45.2 | $A_g^1$ | 58.1 |
| $A_{2g}^1$ (silent) | 35.0 | 56.8 | | $E_g^2$ | 69.9 | $B_g^1$ | 60.0 |
| $E_g^2$ | 62.2 | 61.6 | 59.8 | $A_g^1$ | 99.3 | $A_g^2$ | 82.7 |
| $A_{2g}^2$ (silent) | 69.4 | 72.3 | | $E_g^3$ | 99.8 | $B_g^2$ | 82.9 |
| $E_g^3$ | 74.1 | 75.9 | 77.2 | $A_g^2$ | 105.1 | $A_g^3$ | 85.7 |
| $A_{1g}^1$ | 83.3 | 84.2 | – | $A_g^3$ | 135.5 | $B_g^3$ | 88.9 |
| $E_g^4$ | 84.9 | 86.6 | 86.7 | $A_g^4$ | 167.9 | $A_g^4$ | 99.3 |
| $E_g^5$ | 91.5 | 98.4 | 95.2 | $E_g^4$ | 176.8 | $B_g^4$ | 99.3 |
| $A_{2g}^3$ (silent) | 92.2 | 96.3 | | | | $A_g^5$ | 122.3 |
| $E_g^6$ | 97.4 | 108.3 | 100.4 | | | $B_g^5$ | 149.9 |
| $A_{1g}^2$ | 113.2 | 119.3 | 116.8 | | | $B_g^6$ | 161.0 |
| $A_{1g}^3$ | 117.1 | 123.9 | 123.4 | | | $A_g^6$ | 164.0 |
| $A_{2g}^4$ (silent) | 121.3 | 147.8 | | | | | |
| $E_g^7$ | 132.2 | 151.9 | c | | | | |
| $E_g^8$ | 149.4 | 166.9 | c | | | | |
| $A_{2g}^5$ (silent) | 185.9 | 212.1 | | | | | |

[a]The experimental values were determined at 100 K. The experimental uncertainty is 0.3 $cm^{-1}$. [b]All calculations were performed at 0 K. [c]See the text for an explanation.

the $P\bar{3}1c$ trigonal structure with deviations of around 10% and 15%. Nine of 11 Raman modes were singled out and identified, with $E_g^1$ being not observable in our experimental setup due to its low energy. The $A_{1g}^1$ mode might be missing due to its low intensity and/or the finite spectrometer resolution. The most striking was the observation of the broad feature at ~180 $cm^{-1}$, persisting up to 300 K in both scattering channels. Whereas its line shape resembles those of the two-magnon type of excitation, we believe that scenario is unlikely for a ferromagnetic material. The energy region where the feature was observed may also suggest the possibility of a two-phonon type of excitation. However, their scattering cross sections are usually small and dominated by overtones, thus mostly observed for the parallel scattering configuration.[45] For example, such an excitation was observed at ~250 $cm^{-1}$ (Figure 2). Finally, the observed feature also falls into the energy region where, as suggested by the numerical calculations, observation of the $E_g^7$ and $E_g^8$ modes is expected. We believe that it is actually a complex structure comprising $E_g^7$ and $E_g^8$ Raman modes, significantly broadened by the spin–phonon interaction, that is particularly strong on these phonon branches. The proximity of the two very broad, presumably asymmetric peaks hampers their precise assignment.

Closer inspection of other Raman peaks revealed that some of them also exhibit an asymmetric line shape. To further demonstrate this virtue, we have quantitatively analyzed the highest-intensity peak, $A_{1g}^3$, using the symmetric Voigt line shape and convolution of a Fano profile and a Gausian.[44−46] The asymmetric line shape (with a Fano parameter of $|q|$ = 12.3) gives a slightly better agreement with the experimental data, as depicted in Figure 3. Considering that the observed asymmetry in similar materials was shown to reflect the spin–phonon interaction,[46,47] we propose it as a possible scenario in $VI_3$, as well.

Our findings, based on the inelastic light scattering experiments, at first glance differ from those presented in ref 10. To resolve this discrepancy, we used synchrotron X-ray Rietveld and PDF analysis. Typically, the short-range order

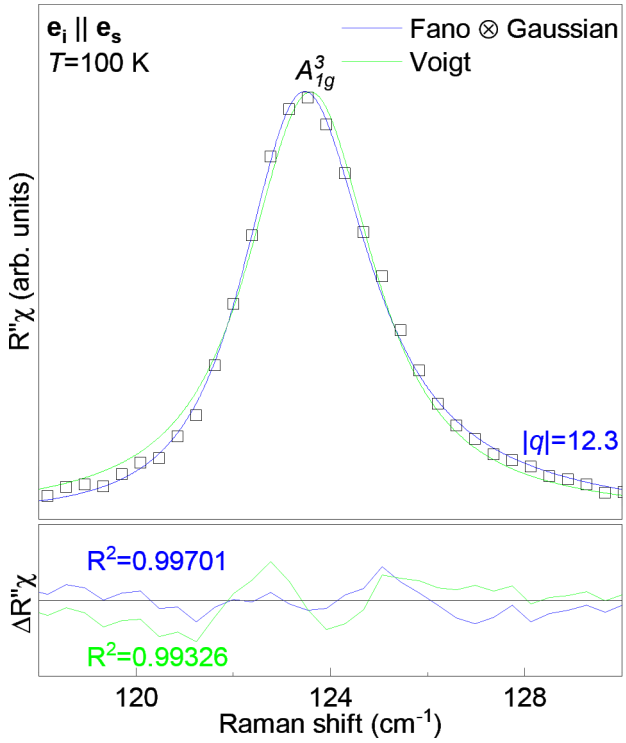


Figure 3. Quantitative analysis of the $A_{1g}^3$ mode. The blue solid line represents the line shape obtained as a convolution of the Fano line shape and the Gaussian, whereas the green one represents a Voigt profile fitted to experimental data (□). For details, see refs 44 and 45.

(SRO) contributes to diffuse scattering under the long-range order (LRO) Bragg peaks when they coexist. Because the diffuse scattering is subtracted as part of the background in the Rietveld refinement, this method is more sensitive to the average structure of materials. In contrast, PDF analysis is performed on the sine Fourier transform of the properly corrected diffraction patten, including both Bragg and diffuse


https://dx.doi.org/10.1021/acs.inorgchem.0c02060
Inorg. Chem. 2020, 59, 16265−16271

components. PDF is a real space function that provides a histogram of interatomic distances, which contain information regarding all length scales.[48−51] The 1−10 and 11−30 Å PDF length scales are more sensitive to SRO and LRO, respectively. For the $VI_3$ system, the best Rietveld fit was obtained using the $R\bar{3}$ space group (Figure 4a), in agreement with that previously

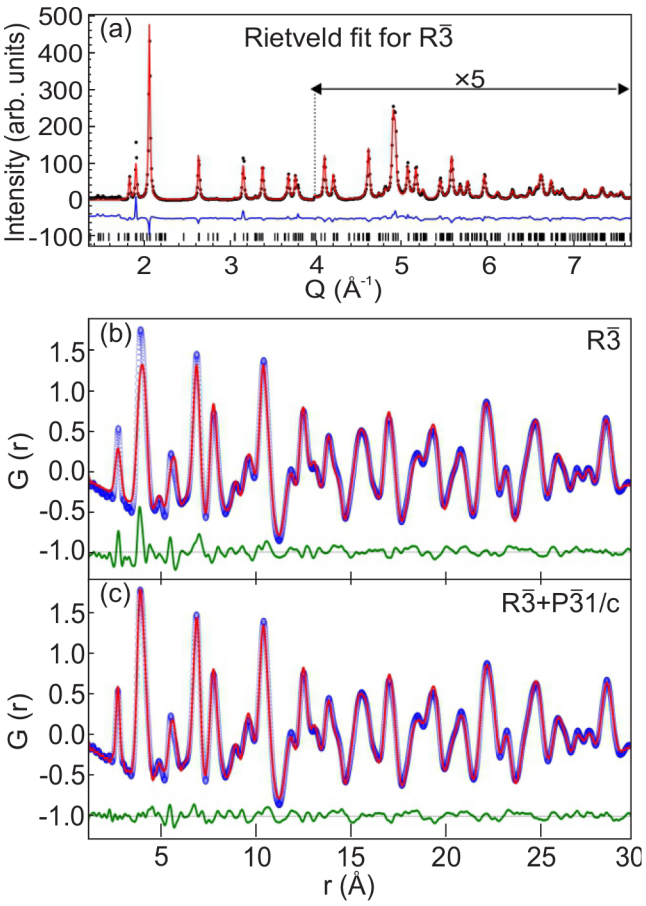


**Figure 4.** Best structural model fits to diffraction data. (a) Rietveld fit using the $R\bar{3}$ space group with black vertical bars indicating calculated peak positions. (b) PDF fit using the $R\bar{3}$ space group. (c) Two-phase PDF fit using $R\bar{3}$ and $P\bar{3}1c$ space groups to fit LRO and SRO, respectively. Black dots (XRD) and blue dots (PDF) represent experimental data, and red solid lines represent the model-based fits. The fit residues are shown at the bottom of each plot.

observed.[10] Not surprisngly, LRO obtained from the Rietveld refinement showed a good agreement on the PDF length scale of 10−30 Å. However, the $R\bar{3}$ space group gave a poor fit on the length scale of 1.5−15 Å with refined $\delta 1$ to account for correlated motion (Figure 4b). In contrast, $P\bar{3}1c$ gave a better fit to SRO, but a poor fit to LRO. The best PDF fits were obtained by refining a weighted two-phase structural model containing ∼25 wt % SRO $P\bar{3}1c$ and ∼75 wt % LRO $R\bar{3}$ phases. The refined correlation length of the SRO is ∼15−20 Å (Figure 4c). These results suggest two possible seanarios: (1) coexistence of two segregated phases, LRO $R\bar{3}$ and SRO $P\bar{3}1c$, and (2) randomly distributed short-range ordered $P\bar{3}1c$ domains in the long-range ordered $R\bar{3}$ lattice. A detailed structural analysis is required to pinpoint scenario 1 and/or 2, which is beyond the scope of this work.

In addition to the peaks already assigned to Γ-point Raman active phonons of the $P\bar{3}1c$ crystal structure (Table 2), three additional peaks at 64.2 cm$^{-1}$ ($P1$), 110.1 cm$^{-1}$ ($P2$), and 220.6 cm$^{-1}$ ($P3$) are observed (see Figure 2). According to the results of DFT, energies of these modes correspond well to those calculated for silent $A_{2g}^2$, $A_{2g}^3$, and $A_{2g}^5$ modes. Their observability in Raman data may come from the release of the symmetry selection rules by breaking of the (translation) symmetry as suggested by the PDF in both scenarios.[52−55] However, as previously discussed, these peaks obey $A_{1g}$ selection rules, indicating the possibility for them to be overtones in nature. In this less likely scenario, the phonon−phonon coupling is enhanced by the spin−phonon interaction and/or by the structural imperfections, thus enhancing the Raman scattering rate for the two-phonon processes.[45] Hence, the observed Raman modes reflect the symmetry of phonon vibrations related to the SRO.[56,57] It is interesting to note that, besides a possible short-range crystallography that is different from the average, $VI_3$ might also feature short-range magnetic order above 79 K.[14]

## CONCLUSION

In summary, room-temperature phonon vibrations of $VI_3$ stem from the $P\bar{3}1c$ symmetry of the unit cell. The PDF analysis suggested the coexistence of two phases, short-range ordered $P\bar{3}1c$ and long-range ordered $R\bar{3}$, as two segregated phases and/or as randomly distributed short-range ordered $P\bar{3}1c$ domains in the long-range ordered $R\bar{3}$ lattice. Nine of 12 observed peaks in the Raman spectra were assigned in agreement with $P\bar{3}1c$ symmetry calculations. Three additional peaks, which obey $A_{1g}$ symmetry rules, could be explained as either overtones or as activated $A_{2g}$ silent modes caused by a symmetry breaking. The asymmetry of one of the $A_{1g}$ phonon modes, together with the anomalous behavior of $E_g^7$ and $E_g^8$, indicates strong spin−phonon coupling, which has already been reported in similar 2D materials.[46,58]

## AUTHOR INFORMATION


### Corresponding Author

**Nenad Lazarević** − *Institute of Physics Belgrade, University of Belgrade, 11080 Belgrade, Serbia;* orcid.org/0000-0001-6310-9511; Email: nenadl@ipb.ac.rs

### Authors

**Sanja Djurdjić Mijin** − *Institute of Physics Belgrade, University of Belgrade, 11080 Belgrade, Serbia*

**A. M. Milinda Abeykoon** − *National Synchrotron Light Source II, Brookhaven National Laboratory, Upton, New York 11973, United States*

**Andrijana Šolajić** − *Institute of Physics Belgrade, University of Belgrade, 11080 Belgrade, Serbia*

**Ana Milosavljević** − *Institute of Physics Belgrade, University of Belgrade, 11080 Belgrade, Serbia*

**Jelena Pešić** − *Institute of Physics Belgrade, University of Belgrade, 11080 Belgrade, Serbia*

**Yu Liu** − *Condensed Matter Physics and Materials Science Department, Brookhaven National Laboratory, Upton, New York 11973-5000, United States;* orcid.org/0000-0001-8886-2876

**Cedomir Petrovic** − *Condensed Matter Physics and Materials Science Department, Brookhaven National Laboratory, Upton, New York 11973-5000, United States;* orcid.org/0000-0001-6063-1881




https://dx.doi.org/10.1021/acs.inorgchem.0c02060
Inorg. Chem. 2020, 59, 16265−16271

**Zoran V. Popović** − *Institute of Physics Belgrade, University of Belgrade, 11080 Belgrade, Serbia; Serbian Academy of Sciences and Arts, 11000 Belgrade, Serbia*

Complete contact information is available at: https://pubs.acs.org/10.1021/acs.inorgchem.0c02060

### Notes

The authors declare no competing financial interest.

## ■ ACKNOWLEDGMENTS

The authors acknowledge funding provided by the Institute of Physics Belgrade, through a grant from the Ministry of Education, Science and Technological Development of the Republic of Serbia, Project F-134 of the Serbian Academy of Sciences and Arts, and the Science Fund of the Republic of Serbia, PROMIS, 6062656, StrainedFeSC. DFT calculations were performed using computational resources at Johannes Kepler University (Linz, Austria). Materials synthesis was supported by the U.S. DOE-BES, Division of Materials Science and Engineering, under Contract DE-SC0012704 (BNL). This research used beamline 28-ID-1 of National Synchrotron Light Source II, a U.S. DOE Office of Science User Facility operated for the DOE Office of Science by Brookhaven National Laboratory under Contract DE-S.

## ■ REFERENCES

(1) Seyler, K. L.; Zhong, D.; Klein, D. R.; et al. Ligand-field helical luminescence in a 2D ferromagnetic insulator. *Nat. Phys.* **2018**, *14*, 277−281.

(2) Klein, D. R.; MacNeill, D.; Lado, J. L.; Soriano, D.; Navarro-Moratalla, E.; Watanabe, K.; et al. Probing magnetism in 2D van der Waals crystalline insulators via electron tunneling. *Science* **2018**, *360*, 1218−1222.

(3) Huang, B.; Clark, G.; Klein, D. R.; MacNeill, D.; Navarro-Moratalla, E.; Seyler, K. L.; et al. Electrical control of 2D magnetism in bilayer $CrI_3$. *Nat. Nanotechnol.* **2018**, *13*, 544−548.

(4) Jiang, S.; Li, L.; Wang, Z.; Mak, K. F.; Shan, J. Controlling magnetism in 2D $CrI_3$ by electrostatic doping. *Nat. Nanotechnol.* **2018**, *13*, 549−553.

(5) McGuire, M. A.; Clark, G.; KC, S.; Chance, W. M.; Jellison, G. E.; Cooper, V. R.; Xu, X.; Sales, B. C. Magnetic behavior and spin-lattice coupling in cleavable van der Waals layered $CrCl_3$ crystals. *Phys. Rev. Materials* **2017**, *1*, 014001.

(6) Djurdjic-Mijin, S. D.; Šolajić, A.; Pešić, J.; Šćepanović, M.; Liu, Y.; Baum, A.; et al. Lattice dynamics and phase transition in $CrI_3$ single crystals. *Phys. Rev. B: Condens. Matter Mater. Phys.* **2018**, *98*, 104307.

(7) Thiel, L.; Wang, Z.; Tschudin, M.; Rohner, D.; Gutierrez-Lezama, I. G.; Ubrig, N.; et al. Probing magnetism in 2D materials at the nanoscale with single-spin microscopy. *Science* **2019**, *364*, 973−976.

(8) Lin, G. T.; Luo, X.; Chen, F. C.; Yan, J.; Gao, J. J.; Sun, Y.; et al. Critical behavior of two-dimensional intrinsically ferromagnetic semiconductor $CrI_3$. *Appl. Phys. Lett.* **2018**, *112*, 072405.

(9) Son, S.; Coak, M. J.; Lee, N.; Kim, J.; Kim, T. Y.; Hamidov, H.; et al. Bulk properties of the van der Waals hard ferromagnet $VI_3$. *Phys. Rev. B: Condens. Matter Mater. Phys.* **2019**, *99*, 041402.

(10) Liu, Y.; Abeykoon, M.; Petrovic, C. Critical behavior and magnetocaloric effect in $VI_3$. *Phys. Rev. Research* **2020**, *2*, 013013.

(11) Huang, B.; Clark, G.; Navarro-Moratalla, E.; Klein, D. R.; Cheng, R.; Seyler, K. L.; et al. Layer-dependent ferromagnetism in a van der Waals crystal down to the monolayer limit. *Nature* **2017**, *546*, 270−273.

(12) Kong, T.; Stolze, K.; Timmons, E. I.; Tao, J.; Ni, D.; Guo, S.; et al. $VI_3$ − a New Layered Ferromagnetic Semiconductor. *Adv. Mater.* **2019**, *31*, 1808074.

(13) Doležal, P.; Kratochvílová, M.; Holý, V.; Čermak, P.; Sechovský, V.; Dušek, M.; et al. Crystal structures and phase transitions of the van der Waals ferromagnet $VI_3$. *Phys. Rev. Materials* **2019**, *3*, 121401.

(14) Tian, S.; Zhang, J.-F.; Li, C.; Ying, T.; Li, S.; Zhang, X.; et al. Ferromagnetic van der Waals Crystal $VI_3$. *J. Am. Chem. Soc.* **2019**, *141*, 5326−5333.

(15) Wang, Y.-M.; Tian, S.-J.; Li, C.-H.; Jin, F.; Ji, J.-T.; Lei, H.-C.; Zhang, Q.-M. Raman scattering study of two-dimensional magnetic van der Waals compound $VI_3$. *Chin. Phys. B* **2020**, *29*, 056301.

(16) Lee, I.; Utermohlen, F. G.; Weber, D.; Hwang, K.; Zhang, C.; van Tol, J.; Goldberger, J. E.; Trivedi, N.; Hammel, P. C. Fundamental Spin Interactions Underlying the Magnetic Anisotropy in the Kitaev Ferromagnet $CrI_3$. *Phys. Rev. Lett.* **2020**, *124*, 017201.

(17) Xu, C.; Feng, J.; Xiang, H.; Bellaiche, L. Interplay between Kitaev interaction and single ion anisotropy in ferromagnetic $CrI_3$ and $CrGeTe_3$ monolayers. *npj Comput. Mater.* **2018**, *4*, 57.

(18) Mermin, N. D.; Wagner, H. Absence of Ferromagnetism or Antiferromagnetism in One- or Two-Dimensional Isotropic Heisenberg Models. *Phys. Rev. Lett.* **1966**, *17*, 1133−1136.

(19) Pershoguba, S. S.; Banerjee, S.; Lashley, J. C.; Park, J.; Ågren, H.; Aeppli, G.; Balatsky, A. V. Dirac Magnons in Honeycomb Ferromagnets. *Phys. Rev. X* **2018**, *8*, 011010.

(20) Liu, J.; Shi, M.; Mo, P.; Lu, J. Electrical-field-induced magnetic Skyrmion ground state in a two-dimensional chromium tri-iodide ferromagnetic monolayer. *AIP Adv.* **2018**, *8*, 055316.

(21) Jiang, S.; Li, L.; Wang, Z.; Shan, J.; Mak, K. Spin tunnel field-effect transistors based on two-dimensional van der Waals heterostructures. *Nature Electronics* **2019**, *2*, 159.

(22) Klein, D. R.; MacNeill, D.; Song, Q.; Larson, D. T.; Fang, S.; Xu, M.; Ribeiro, R. A.; Canfield, P. C.; Kaxiras, E.; Comin, R.; Jarillo-Herrero, P. Enhancement of interlayer exchange in an ultrathin two-dimensional magnet. *Nat. Phys.* **2019**, *15*, 1255−1260.

(23) Wang, Z.; Gibertini, M.; Dumcenco, D.; Taniguchi, T.; Watanabe, K.; Giannini, E.; Morpurgo, A. Determining the phase diagram of atomically thin layered antiferromagnet $CrCl_3$. *Nat. Nanotechnol.* **2019**, *14*, 1116.

(24) Ubrig, N.; Wang, Z.; Teyssier, J.; Taniguchi, T.; Watanabe, K.; Giannini, E.; Morpurgo, A. F.; Gibertini, M. Low-temperature monoclinic layer stacking in atomically thin $CrI_3$ crystals. *2D Mater.* **2020**, *7*, 015007.

(25) Sun, Z.; et al. Giant nonreciprocal second-harmonic generation from antiferromagnetic bilayer $CrI_3$. *Nature* **2019**, *572*, 497−501.

(26) McGuire, M. A.; Clark, G.; KC, S.; Chance, W. M.; Jellison, G. E.; Cooper, V. R.; Xu, X.; Sales, B. C. Magnetic behavior and spin-lattice coupling in cleavable van der Waals layered $CrCl_3$ crystals. *Phys. Rev. Materials* **2017**, *1*, 014001.

(27) Kuhlow, B. Magnetic Ordering in $CrCl_3$ at the Phase Transition. *physica status solidi (a)* **1982**, *72*, 161−168.

(28) Hammersley, A. P.; Svensson, S. O.; Hanfland, M.; Fitch, A. N.; Hausermann, D. Two-dimensional detector software: From real detector to idealised image or two-theta scan. *High Pressure Res.* **1996**, *14*, 235−248.

(29) Yang, X.; Juhas, P.; Farrow, C. L.; Billinge, S. J. L. *xPDFsuite: an end-to-end software solution for high throughput pair distribution function transformation, visualization and analysis*; 2014.

(30) Toby, B. H.; Von Dreele, R. B. *GSAS-II*: the genesis of a modern open-source all purpose crystallography software package. *J. Appl. Crystallogr.* **2013**, *46*, 544−549.

(31) Farrow, C. L.; Juhas, P.; Liu, J. W.; Bryndin, D.; Božin, E. S.; Bloch, J.; Proffen, T.; Billinge, S. J. L. PDFfit2 and PDFgui: computer programs for studying nanostructure in crystals. *J. Phys.: Condens. Matter* **2007**, *19*, 335219.

(32) Giannozzi, P.; et al. QUANTUM ESPRESSO: a modular and open-source software project for quantum simulations of materials. *J. Phys.: Condens. Matter* **2009**, *21*, 395502.

(33) Perdew, J. P.; Burke, K.; Ernzerhof, M. Generalized Gradient Approximation Made Simple. *Phys. Rev. Lett.* **1996**, *77*, 3865−3868.

(34) Blöchl, P. E. Projector augmented-wave method. *Phys. Rev. B: Condens. Matter Mater. Phys.* **1994**, *50*, 17953−17979.
(35) Kresse, G.; Joubert, D. From ultrasoft pseudopotentials to the projector augmented-wave method. *Phys. Rev. B: Condens. Matter Mater. Phys.* **1999**, *59*, 1758−1775.
(36) Cococcioni, M.; de Gironcoli, S. Linear response approach to the calculation of the effective interaction parameters in the LDA + U method. *Phys. Rev. B: Condens. Matter Mater. Phys.* **2005**, *71*, 035105.
(37) Juza, D.; Giegling, D.; Schäfer, H. Über die Vanadinjodide $VJ_2$ und $VJ_3$. *Z. Anorg. Allg. Chem.* **1969**, *366*, 121−129.
(38) Berry, K. O.; Smardzewski, R. R.; McCarley, R. E. Vaporization reactions of vanadium iodides and evidence for gaseous vanadium-(IV) iodide. *Inorg. Chem.* **1969**, *8*, 1994−1997.
(39) Klemm, W.; Krose, E. Die Kristallstrukturen von $ScCl_3$, $TiCl_3$ und $VCl_3$. *Z. Anorg. Chem.* **1947**, *253*, 218−225.
(40) Liu, Y.; Petrovic, C. Three-dimensional magnetic critical behavior in $CrI_3$. *Phys. Rev. B: Condens. Matter Mater. Phys.* **2018**, *97*, 014420.
(41) He, J.; Ma, S.; Lyu, P.; Nachtigall, P. Unusual Dirac half-metallicity with intrinsic ferromagnetism in vanadium trihalide monolayers. *J. Mater. Chem. C* **2016**, *4*, 2518−2526.
(42) Wang, Y.-P.; Long, M.-Q. Electronic and magnetic properties of van der Waals ferromagnetic semiconductor $VI_3$. *Phys. Rev. B: Condens. Matter Mater. Phys.* **2020**, *101*, 024411.
(43) Li, Y.; Liu, Y.; Wang, C.; Wang, J.; Xu, Y.; Duan, W. Electrically tunable valleytronics in quantum anomalous Hall insulating transition metal trihalides. *Phys. Rev. B: Condens. Matter Mater. Phys.* **2018**, *98*, 201407.
(44) Lazarević, N.; Popović, Z. V.; Hu, R.; Petrovic, C. Evidence for electron-phonon interaction in $Fe_{1-x}M_xSb_2$ (M = Co and Cr $0 \leq x \leq 0.5$) single crystals. *Phys. Rev. B: Condens. Matter Mater. Phys.* **2010**, *81*, 144302.
(45) Baum, A.; Milosavljević, A.; Lazarević, N.; Radonjić, M. M.; Nikolić, B.; Mitschek, M.; Maranloo, Z. I.; Šćepanović, M.; Grujić-Brojčin, M.; Stojilović, N.; Opel, M.; Wang, A.; Petrovic, C.; Popović, Z. V.; Hackl, R. Phonon anomalies in FeS. *Phys. Rev. B: Condens. Matter Mater. Phys.* **2018**, *97*, 054306.
(46) Milosavljević, A.; Šolajic, A.; Pešić, J.; Liu, Y.; Petrovic, C.; Lazarević, N.; Popović, Z. V. Evidence of spin-phonon coupling in $CrSiTe_3$. *Phys. Rev. B: Condens. Matter Mater. Phys.* **2018**, *98*, 104306.
(47) McCarty, K. F.; Radousky, H. B.; Hinks, D. G.; Zheng, Y.; Mitchell, A. W.; Folkerts, T. J.; Shelton, R. N. Electron-phonon coupling in superconducting $Ba_{0.6}K_{0.4}BiO_3$: A Raman scattering study. *Phys. Rev. B: Condens. Matter Mater. Phys.* **1989**, *40*, 2662−2665.
(48) Proffen, T.; Page, K. L.; McLain, S. E.; Clausen, B.; Darling, T. W.; TenCate, J. A.; Lee, S.-Y.; Ustundag, E. Atomic pair distribution function analysis of materials containing crystalline and amorphous phases. *Z. Kristallogr.* **2005**, *220*, 1002−1008.
(49) Bordet, P. Application of the pair distribution function analysis for the study of cultural heritage materials. *C. R. Phys.* **2018**, *19*, 561−574.
(50) Bozin, E. S.; Yin, W. G.; Koch, R. J.; Abeykoon, M.; Hor, Y. S.; Zheng, H.; Lei, H. C.; Petrovic, C.; Mitchell, J. F.; Billinge, S. J. L. Local orbital degeneracy lifting as a precursor to an orbital-selective Peierls transition. *Nat. Commun.* **2019**, *10*, 3638.
(51) Egami, T.; Billinge, S. J. L. *Underneath the Bragg Peaks: Structural Analysis of Complex Materials*; 2003; p 16.
(52) Jin, F.; Lazarević, N.; Liu, C.; Ji, J.; Wang, Y.; He, S.; Lei, H.; Petrovic, C.; Yu, R.; Popović, Z. V.; Zhang, Q. Phonon anomalies and magnetic excitations in $BaFe_2Se_2O$. *Phys. Rev. B: Condens. Matter Mater. Phys.* **2019**, *99*, 144419.
(53) Moskovits, M.; Dilella, D. Surface-enhanced Raman spectroscopy of benzene and benzene-d6 adsorbed on silver. *J. Chem. Phys.* **1980**, *73*, 6068−6075.
(54) Dubroka, A.; Humlíček, J.; Abrashev, M. V.; Popović, Z. V.; Sapiña, F.; Cantarero, A. Raman and infrared studies of $La_{1-y}Sr_yMn_{1-x}M_xO_3$ ($M$ = Cr,Co,Cu,Zn,Sc or Ga): Oxygen disorder and local vibrational modes. *Phys. Rev. B: Condens. Matter Mater. Phys.* **2006**, *73*, 224401.
(55) Souza Filho, A. G.; Faria, J. L. B.; Guedes, I.; Sasaki, J. M.; Freire, P. T. C.; Freire, V. N.; Mendes Filho, J.; Xavier, M. M.; Cabral, F. A. O.; de Araújo, J. H.; da Costa, J. A. P. Evidence of magnetic polaronic states in $La_{0.70}Sr_{0.30}Mn_{1-x}Fe_xO_3$manganites. *Phys. Rev. B: Condens. Matter Mater. Phys.* **2003**, *67*, 052405.
(56) Lekgoathi, M.; Kock, L. Effect of short and long range order on crystal structure interpretation: Raman and powder X-ray diffraction of $LiPF_6$. *Spectrochim. Acta, Part A* **2016**, *153*, 651−654.
(57) Wolverton, C.; Zunger, A.; Lu, Z.-W. Long-versus short-range order in $Ni_3V$ and $Pd_3V$ alloys. *Phys. Rev. B: Condens. Matter Mater. Phys.* **1994**, *49*, 16058.
(58) Webster, L.; Liang, L.; Yan, J.-A. Distinct spin-lattice and spin-phonon interactions in monolayer magnetic $CrI_3$. *Phys. Chem. Chem. Phys.* **2018**, *20*, 23546−23555.


https://dx.doi.org/10.1021/acs.inorgchem.0c02060
*Inorg. Chem.* 2020, 59, 16265−16271

Received: 14 May 2020 | Revised: 15 July 2020 | Accepted: 22 July 2020

DOI: 10.1002/jrs.5962

RESEARCH ARTICLE

Journal of RAMAN SPECTROSCOPY WILEY

# Vacancies and spin–phonon coupling in $CrSi_{0.8}Ge_{0.1}Te_3$

**Ana Milosavljević[1] | Andrijana Šolajić[1] | Bojana Višić[1] | Marko Opačić[1] | Jelena Pešić[1] | Yu Liu[2] | Cedomir Petrovic[2] | Zoran V. Popović[1,3] | Nenad Lazarević[1]**

[1]Institute of Physics Belgrade, University of Belgrade, Pregrevica 118, Belgrade, 11080, Serbia

[2]Condensed Matter Physics and Materials Science Department, Brookhaven National Laboratory, Upton, New York, 11973-5000, USA

[3]Serbian Academy of Sciences and Arts, Knez Mihailova 35, Belgrade, 11000, Serbia

**Correspondence**
Ana Milosavljević, Institute of Physics Belgrade, University of Belgrade, Pregrevica 118, 11080 Belgrade, Serbia.
Email: ana.milosavljevic@ipb.ac.rs

**Funding information**
Serbian Academy of Sciences and Arts, Grant/Award Number: F-134; Slovenian Research Agency, Grant/Award Number: P1-0099; Ministry of Education, Science and Technological Development of the Republic of Serbia U.S. DOE-BES, Division of Materials Science and Engineering, Grant/Award Number: DE-SC0012704

**Abstract**

We report temperature-dependent Raman scattering and magnetization studies of van der Waals ferromagnetic compound $CrSi_{0.8}Ge_{0.1}Te_3$. Magnetic susceptibility measurements revealed dominant ferromagnetic interactions below $T_C$ which shift to the lower values due to the presence of vacancies. A Raman active mode, additional to the ones predicted by symmetry in the parent compounds, has been observed. This $A_g$ symmetry mode most likely emerges as a consequence of the atomic vacancies on Si/Ge site. Presence of the strong spin–phonon coupling at temperature around 210 K is indicated by deviations from conventional phonon self-energy temperature dependence of all analysed modes.

**KEYWORDS**

magnetism, phonons, raman spectroscopy, van der Waals materials

## 1 | INTRODUCTION

Considerable progress has been made in the field of material science through developing new materials and revealing their properties in the last decade. Namely, in the recent years, large family of van der Waals materials with inherent magnetism became the focus of experimental and theoretical research, because they seem suitable for numerous technical applications.[1-7] The family includes $Fe_{3-x}GeTe_2$ metallic materials with high magnetic transition temperature,[8-10] semiconductors $CrXTe_3$ (X = Si, Ge, Sn) and $CrX_3$ (X = Cl, Br, I) monolayers[2,11-13] and heterostructures.[14]

$CrSiTe_3$ and $CrGeTe_3$ are ferromagnetic (FM) semiconductors with band gap of 0.4 and 0.7 eV and Curie temperatures ($T_C$) of 32 and 61 K, respectively.[15-18] Twining of $CrSiTe_3$ single crystals along *c*-axes was revealed by X-ray diffraction experiment as well as $Cr^{3+}$ ions magnetic order.[15] Recently, through high-resolution angle-resolved photoemission spectroscopy (ARPES), it was possible to identify full electronic structure near the Fermi level. Due to spin–orbit coupling, $CrSiTe_3$ is a Mott-type FM insulator.[19] Electronic structure of $CrGeTe_3$ single crystals was also investigated by ARPES.[20] It was shown that the low-lying valence bands are centred around the Γ point and are mainly formed from Te 5*p* orbitals.

  

Raman scattering studies of $CrSiTe_3$ reveal strong spin–lattice coupling in the paramagnetic phase[15,21] as a consequence of a short-range magnetic order in this compound. In addition to renormalization of energies and linewidths of observed Raman active modes, coupling of doubly degenerate $E_g$ mode with magnetic continuum was found.[21] The coupling results in an asymmetric phonon line shape up to 180 K. Besides the splitting of two low-energy $E_g$ modes in the magnetic phase of $CrGeTe_3$ and unconventional behaviour of phonon properties around transition temperature, experimental results indicate spin–phonon coupling effect with magnetic quasi-elastic scattering.[22] Pressure-dependent Raman scattering study of $CrGeTe_3$ showed a decrease in bond length, the deviation of Cr–Te–Cr angle, and reduction of phase transition temperature.[23]

Change of the carrier concentration plays an important role in the physics of semiconducting materials as it can lead to surprising physical properties. Very small variations in dopant concentrations can lead to structural modifications and considerable changes in magnetic transition temperature. Here, we report a Raman scattering and magnetization studies of $CrSi_{0.8}Ge_{0.1}Te_3$. Our scanning electron microscopy (SEM) measurements reveal 10% of Ge atoms concentration and 10% of vacancies. Vacancies induced a decrease in $T_C$ was detected within magnetic susceptibility measurements. In the Raman scattering results, we identified three $A_g$ and four $E_g$ symmetry modes. Additional peak of the $A_g$ symmetry is also observed in our spectra. This mode may be traced to vacancies and possible inhomogeneous distribution of Ge atoms substitution on Si atomic site at nano-scale. Energies of modes predicted by symmetry analysis are found between the experimental values of parent compounds $CrSiTe_3$ and $CrGeTe_3$, reported previously in Milosavljevi et al..[21] The presence of the strong spin–phonon interaction at temperature around 210 K is indicated in small deviations from conventional temperature-dependent behaviour of the observed modes energies and linewidths, including additional one.

## 2 | EXPERIMENT AND NUMERICAL METHOD

$CrSi_{0.8}Ge_{0.1}Te_3$ single crystals were grown as described previously.[24] Magnetic properties were measured in a Quantum Design MPMS-XL5 system.

SEM measurements were performed using FEI HeliosNanolab 650. This microscope is equipped with an Oxford Instruments energy dispersive spectroscopy (EDS) system with an X-max SSD detector operating at 20 kV. Measurements were performed on as-cleaved samples deposited on a graphite tape. The elemental composition EDS mapping was obtained on crystals that appeared to be uniform for several tens of microns. The maps show the presence of Cr, Ge, Te and Si.

For Raman scattering experiment, Tri Vista 557 spectrometer was used in the subtractive backscattering micro-Raman configuration. The combination of gratings was 1800/1800/2400 grooves/mm and the entrance slit of 80 $\mu$m. Solid state laser with 532-nm line was used as an excitation source. In our scattering configuration, plane of incidence is *ab*-plane, where $|a| = |b|$ ($\measuredangle(a,b) = 120^\circ$), with incident (scattered) light propagation direction along *c*-axes. Samples were cleaved in the air before being placed in vacuum. All measurements were performed in high vacuum ($10^{-6}$ mbar) using a KONTI CryoVac continuous Helium flow cryostat with 0.5-mm thick window. Laser beam focusing was achieved using microscope objective with ×50 magnification. All spectra were corrected for Bose factor.

Spin-polarized density functional theory calculations were performed in Quantum Espresso software package,[25] based on plane waves and pseudopotentials, using Perdew–Burke–Ernzerhof (PBE) exchange-correlation functional[26] and projector augmented wave (PAW) pseudopotentials.[27,28] The cutoff for wavefunctions and the charge density of 85 and 425 Ry were chosen, respectively. The *k*-point were sampled using the Monkhorst-Pack scheme, on $8 \times 8 \times 8$ Γ centred grid used for both structures. Optimization of the lattice parameters and atomic positions in unit cell was performed until the interatomic forces were minimized down to $10^{-6}$ Ry/Å. Treatment of the van der Waals interactions is included using the Grimme-D2 correction, in order to obtain the lattice parameters more accurately. Phonon wave numbers were calculated within the linear response method, as implemented in PHonon part of Quantum Espresso.

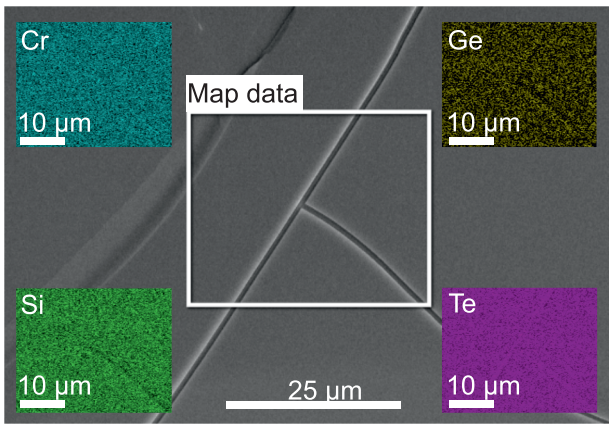


**FIGURE 1** Energy dispersive spectroscopy (EDS) mapping on a $CrSi_{0.8}Ge_{0.1}Te_3$ single crystal [Colour figure can be viewed at wileyonlinelibrary.com]

## 3 | RESULTS AND DISCUSSION

In order to investigate uniformity and elemental composition of $CrSi_{0.8}Ge_{0.1}Te_3$ sample, SEM measurements were performed on as-cleaved crystals. EDS mapping presented in Figure 1 shows that the ratio of Cr:Si:Ge:Te (averaged over 10 measurements) is 1:0.8:0.1:3. This result reveals the presence of 10% Ge atomic vacancies in the sample.

Figure 2a,b presents the temperature dependence of zero-field cooling (ZFC) magnetic susceptibility $\chi(T) = M(T)/H$ measured in 1-kOe magnetic field applied parallel to $a$ (a) and $c$ (b) crystallographic axes. Curie–Weiss law $\chi = \frac{C}{T-\theta}$ fit at high temperatures yields Weiss temperatures $\theta_a$ = 61(2) K, $\theta_c$ = 70(2) K and high temperature paramagnetic moments $\mu_{eff,a}$ = 4.14(2)$\mu_B$ and $\mu_{eff,c}$ = 3.91 (2)$\mu_B$ for $CrSi_{0.8}Ge_{0.1}Te_3$, consistent with dominant FM interactions below $T_c$ and in line with the observed FM $T_c$ and magnetic hystheresis loops.[13,24] The approximate $T_c$ value can be determined from the minima of the $d\chi/dT$ curves insets in Figure 2(a,b). It should be noted that, instead of monotonous rise, there is a weak but discernible shift to lower temperature in $d\chi/dT$ in $CrSi_{0.8}Ge_{0.1}Te_3$ when compared with $CrSiTe_3$. This small reduction in FM transition temperature is likely induced by the presence of vacancies, as suggested by the EDS data. The presence of vacancies in this class of materials usually disarrange magnetic exchange due to disorder increment, which leads to the reduction of $T_C$.[29]

Isostructural parent compounds $CrSiTe_3$ and $CrGeTe_3$ crystallize in the rhombohedral crystal structure, described with space group $R\bar{3}$ ($C_{3i}^2$).[30] According to factor group analysis, five $A_g$ and five double degenerate $E_g$ symmetry modes are expected to be observed in the light scattering experiment. Detailed symmetry analysis, phonon mode distribution and selection rules for parent compounds ($CrSiTe_3$ and $CrGeTe_3$) can be found in Milosavljević et al.[21] In our scattering configuration, the plane of incidence is $ab$ plane, where $|a| = |b|$ ($\measuredangle(a,b) = 120°$) (inset in Figure 3), and the direction of incident (scattered) light propagation is along $c$-axes. According to the selection rules for this scattering configuration,[21] all Raman active modes may be observed, having in mind that $A_g$ symmetry modes can be detected only in parallel polarization configuration. The $E_g$ symmetry modes are expected to appear in both the parallel and cross polarization configurations. Raman spectra of $CrSi_{0.8}Ge_{0.1}Te_3$, obtained by continuous change of the angle between polarization vectors of incident and

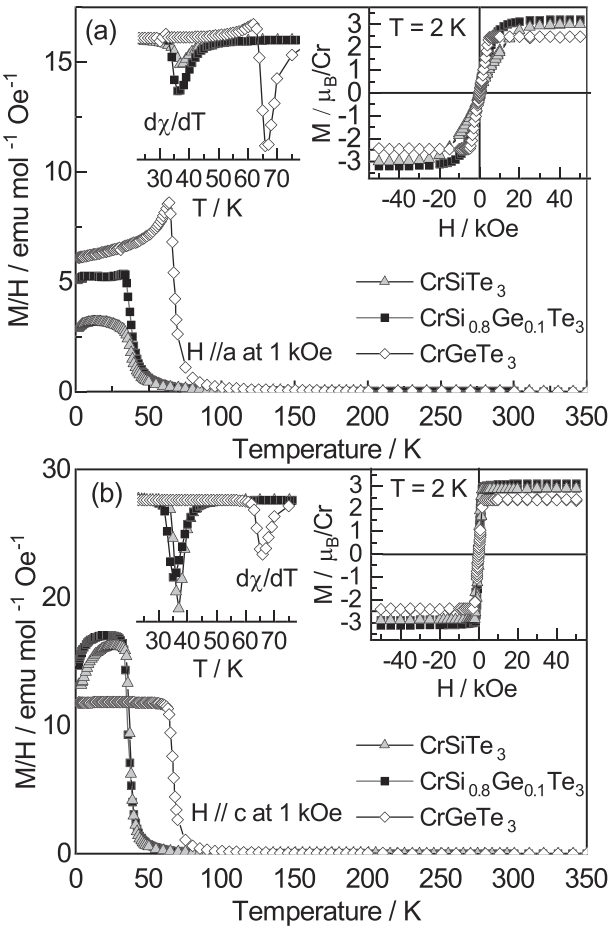


**FIGURE 2** Temperature dependence of zero-field cooling (ZFC) $\chi$=M/H for $CrSiTe_3$, $CrSi_{0.8}Ge_{0.1}Te_3$ and $CrGeTe_3$ in 1-kOe magnetic field applied in-plane (a) and along the $c$-axis (b). Insets show transition temperatures of ferromagnetic orders (d$\chi$/dT) and magnetic hystheresis loops taken at 2 K

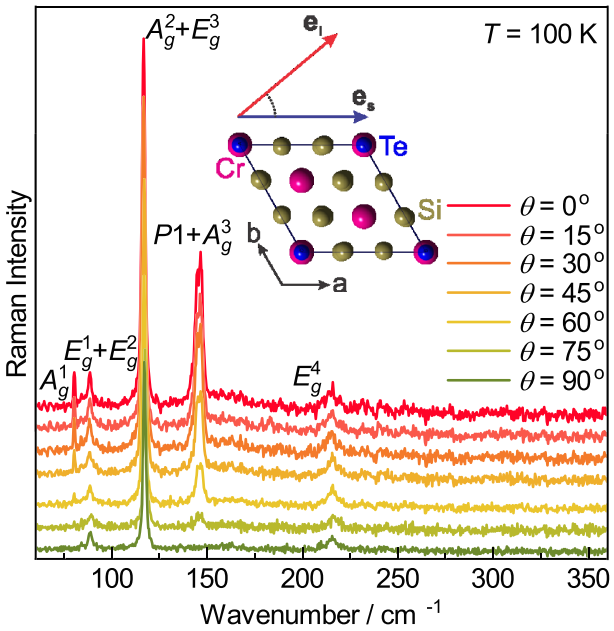


**FIGURE 3** Raman spectra of $CrSi_{0.8}Ge_{0.1}Te_3$ single crystal, measured at 100 K, as a function of angle $\theta$, between incident and scattered light polarization. Inset: schematic representation of the incident and scattered light polarization with respect to the crystal orientation [Colour figure can be viewed at wileyonlinelibrary.com]

scattered light, $\theta = \measuredangle(\mathbf{e}_i, \mathbf{e}_s)$, $(0° \leqslant \theta \leqslant 90°)$ at 100 K, are shown in Figure 3. It can be seen that by changing this angle, starting from $\theta = 0°$, the intensities of the peaks at energies 80.2, 116.4 and 145.5 $cm^{-1}$ continuously decrease and completely vanish for polarization angle of 90°. Therefore, these excitations obey pure $A_g$ symmetry. On the other hand, the peaks at energies of 84.5, 88.3, 117.2 and 215.0 $cm^{-1}$ are not influenced by change of polarization angle, so they can be identified as $E_g$ symmetry modes.

Here, one should note that the feature observed at around 117 $cm^{-1}$ in both scattering configurations is actually a two-peak structure comprising of 116.4-$cm^{-1}$ $A_g$ and 117.2-$cm^{-1}$ $E_g$ symmetry modes. Detailed analysis of the structure for two scattering configurations is presented in Figure A1 of Appendix. Furthermore, closer inspection of the data revealed that peak at energy of 145.5 $cm^{-1}$, which obeys pure $A_g$ symmetry, is also composed of two modes, $P1$ (144.6 $cm^{-1}$) and $A_g^3$ (146.7 $cm^{-1}$), as shown in Figure A2 of Appendix.

Calculated optical phonon wavenumbers of the parent compounds, $CrSiTe_3$ and $CrGeTe_3$, together with their experimental Raman active values as well as Raman mode energies of $CrSi_{0.8}Ge_{0.1}Te_3$, are compiled in Table 1. As expected, experimental values of $CrSi_{0.8}Ge_{0.1}Te_3$ Raman active modes are found between the values of the observed modes in parent compounds.[21] Figure 4a shows compositional evolution of the peaks with highest

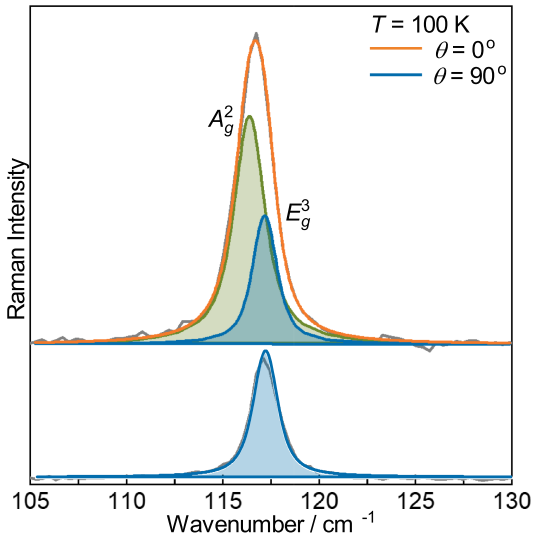


**FIGURE A1** Decomposition of unresolved $A_g^2$ and $E_g^3$ symmetry modes obtained by simultaneous modelling in parallel and cross polarization configuration. Grey line represents the measured data, Voigt line of $A_g^2$ mode is shown by green, and blue lines represent the $E_g^3$ symmetry mode in parallel (upper panel) and cross (lower panel) polarization. The orange line is the superposition of these two lines [Colour figure can be viewed at wileyonlinelibrary.com]

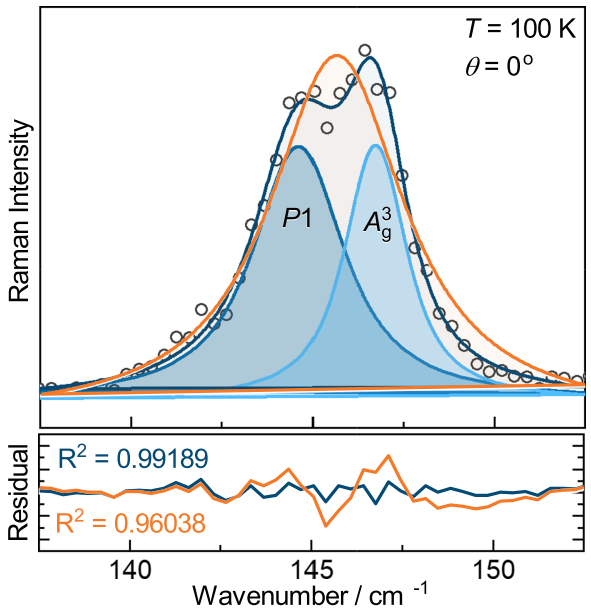


**FIGURE A2** Decomposition of phonon mode in parallel scattering configuration on two $A_g$ symmetry modes. Open circles represent the measured data and the blue one sum of two Voigt profile line shapes. Data modelled with one Voigt profile line shape (orange line) deviates significantly from measured data [Colour figure can be viewed at wileyonlinelibrary.com]

intensity, assigned as $E_g^3$ and $A_g^3$ symmetry modes in parent compounds. The $E_g^3$ mode energy changes almost linearly (Figure 4b), as a consequence of change in lattice parameters and "change of mass" effect. The observed energy shift is followed by doubling of the linewidth, dominantly induced by the significant crystalline disorder. The similar type of behaviour, with somewhat larger increase in the linewidth, was also observed for the $A_g^3$ symmetry mode. The most striking feature was the additional $A_g$ symmetry mode (denoted as $P1$, see Figure A2 of the Appendix), observed in the doped sample. Generally, both the substitutional defects and vacancies may have similar impact on the Raman modes energy and linewidth. Here, the appearance of $P1$ peak can be understood as a consequence of the presence of vacancies on Si/Ge atomic site and their inharmonious distribution at nano-scale. The mode "splitting" is detected only for the $A_g^3$ but not for other observed modes, due to the fact that different nature of these vibrations results in different values of energy shifts. In the case of other modes, the difference between the shifts for corresponding domains is smaller than the spectral resolution of the instrument (~1.8 $cm^{-1}$), and therefore, the separate modes can not be resolved.

Figure 5 shows $CrSi_{0.8}Ge_{0.1}Te_3$ Raman scattering spectra measured at various temperatures. For clarity, spectra obtained for cross polarization configuration are

**TABLE 1** Phonon symmetry, calculated ($T$= 0 K) and experimental ($T$ = 100 K) Raman active phonon wavenumbers of parent compounds $CrSiTe_3$ and $CrGeTe_3$.[21] Experimental values for Raman active phonons of $CrSi_{0.8}Ge_{0.1}Te_3$ at 100 K are shown in the last column

| Raman active modes | | | | | |
|---|---|---|---|---|---|
| | Calculations | | Experiment | | |
| Symmetry | $CrSiTe_3$ | $CrGeTe_3$ | $CrSiTe_3$ | $CrGeTe_3$ | $CrSi_{0.8}Ge_{0.1}Te_3$ |
| $A_g^1$ | 88.2 | 84.2 | — | — | 80.2 |
| $E_g^1$ | 93.5 | 82.0 | 88.9 | 83.5 | 84.5 |
| $E_g^2$ | 96.9 | 90.8 | — | — | 88.3 |
| $E_g^3$ | 118.3 | 114.2 | 118.2 | 112.2 | 117.2 |
| $A_g^2$ | 122.0 | 105.9 | — | — | 116.4 |
| $A_g^3$ | 148.0 | 134.8 | 147.4 | 137.9 | 146.7 |
| $A_g^4$ | 208.7 | 200.3 | — | — | — |
| $E_g^4$ | 219.5 | 209.6 | 217.2 | 217.5 | 215.0 |
| $E_g^5$ | 357.4 | 229.8 | — | — | — |
| $A_g^5$ | 508.9 | 290.7 | — | 296.6 | — |

*Note:* All values are given in $cm^{-1}$.

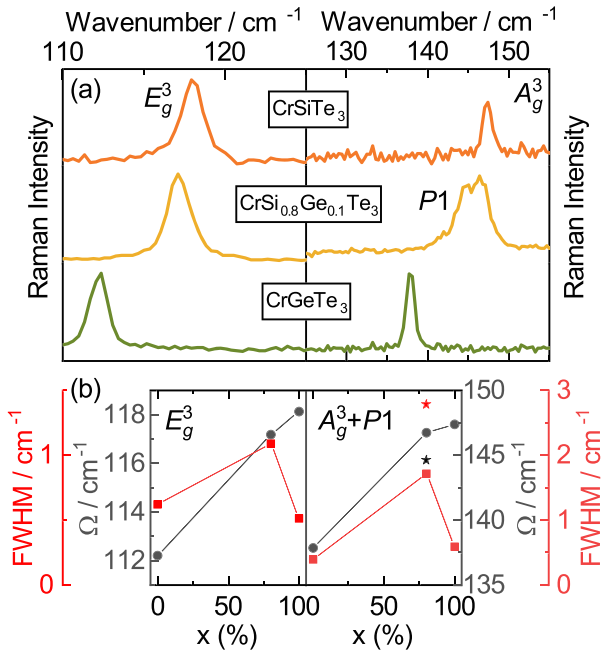


**FIGURE 4** (a) Raman scattering spectra of $E_g^3$ and $A_g^3$ phonon modes of $CrSiTe_3$ (orange line), $CrSi_{0.8}Ge_{0.1}Te_3$ (yellow line) and $CrGeTe_3$ (green line) at $T$ = 100 K measured in cross (left panel) and parallel (right panel) scattering configuration, respectively. (b) Energy (grey line) and linewidth (red line) of these two modes with respect to the percentage of Si atoms concentration. Energy and linewidth of $P1$ mode are marked with black and red star, respectively [Colour figure can be viewed at wileyonlinelibrary.com]

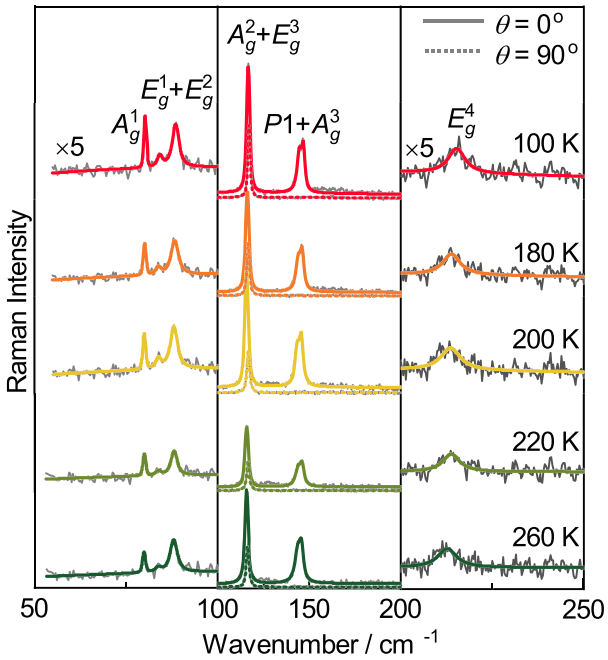


**FIGURE 5** Raman spectra of $CrSi_{0.8}Ge_{0.1}Te_3$ single crystal measured at various temperatures. The spectra were analysed by using multiple Voigt peak functions and a single $\chi''_{cont} = a\Gamma\omega/(\Gamma^2+\omega^2) + b\omega$ function, for parallel ($\theta = 0°$, solid coloured lines) and cross ($\theta = 90°$, dashed coloured lines) scattering configuration. For clarity, higher and lower energy ranges (left and right panel) are multiplied by the factor of five [Colour figure can be viewed at wileyonlinelibrary.com]

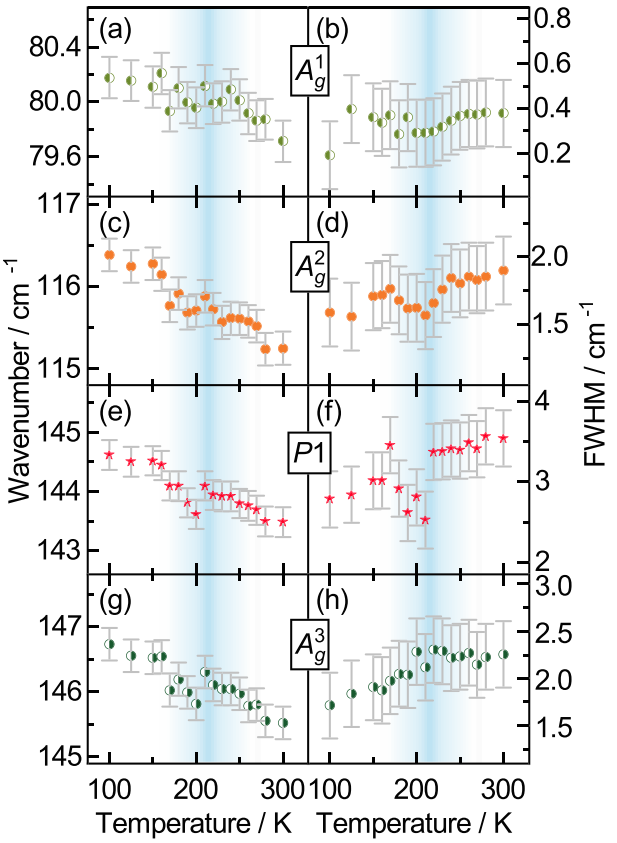


**FIGURE 6** Energy and linewidth temperature dependence of $A_g^1$ (a,b), $A_g^2$ (c,d), $P1$ (e,f) and $A_g^3$ (g,h) Raman modes [Colour figure can be viewed at wileyonlinelibrary.com]

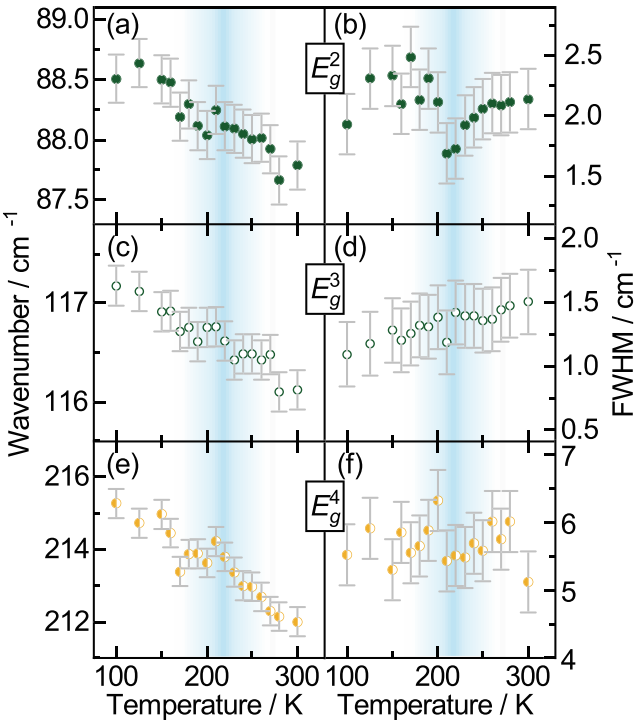


**FIGURE 7** Energy and linewidth temperature dependence of $E_g^2$ (a,b), $E_g^3$ (c,d) and $E_g^4$ (e,f) symmetry modes [Colour figure can be viewed at wileyonlinelibrary.com]

only shown for the mid-energy range. Temperature dependence of energies and linewidths of all the observed $A_g$ symmetry modes, including $P1$, are presented in Figure 6. By heating the sample from 100 K to approximately 210 K, monotonous decrease in energy of all the $A_g$ symmetry modes is present, dominantly driven by thermal expansion.[31] In the temperature region around 210 K, these modes' energy exhibit small deviation, followed by a continuous decrease up to room temperature. In the same temperature region, deviation from expected anharmonic type of behaviour is observed for all the $A_g$ symmetry modes linewidth. This effect is more pronounced for higher energy modes where the anharmonicity is expected to be higher. Similar response of analysed $E_g$ symmetry modes is present and shown in Figure 7.

Concerning previously reported strong spin–phonon coupling in $CrSiTe_3$,[15,21] which persists up to 180 K, we believe that this unconventional behaviour of energies and linewidths can be attributed to the coupling of the phonon modes to the spin system.[32] Due to the doping and presence of vacancies, strong magnetic correlations in $CrSi_{0.8}Ge_{0.1}Te_3$ are sustained up to 210 K.

## 4 | CONCLUSIONS

In summary, we presented temperature-dependent Raman scattering and magnetization studies of doped van der Waals ferromagnet $CrSi_{0.8}Ge_{0.1}Te_3$. SEM measurements revealed the presence of 10% vacancies on Si/Ge atomic site. As a consequence, magnetization measurements detected small but clear decrease in $T_C$. Seven out of 10 Raman active modes have been assigned in our Raman spectra. Temperature dependence of all the observed modes shows the persistence of magnetic correlations up to 210 K. In addition, the results revealed the appearance of the peak that obey pure $A_g$ symmetry, which is attributed to the possible inhomogeneous distribution of Ge atoms and vacancies at nano-scale. This study provides an insight into the impact of doping and presence of vacancies on magnetic and lattice properties in this class of materials.

## ACKNOWLEDGEMENTS

This work was supported by the Ministry of Education, Science and Technological Development of the Republic of Serbia and project no F-134 of the Serbian Academy of Sciences and Arts. DFT calculations were performed using computational resources at Johannes Kepler University, Linz, Austria. Electron microscopy was performed at Jozef Stefan Institute, Ljubljana, Slovenia,

under Slovenian Research Agency contract P1-0099 (B. V.). Work at BNL (crystal synthesis and magnetic characterization) was supported by the U.S. DOE-BES, Division of Materials Science and Engineering, under Contract No. DE-SC0012704.

## ORCID

*Ana Milosavljević* https://orcid.org/0000-0002-8654-0475

## REFERENCES

[1] F. Hellman, A. Hoffmann, Y. Tserkovnyak, G. S. Beach, E. E. Fullerton, C. Leighton, A. H. MacDonald, D. C. Ralph, D. A. Arena, H. A. Dürr, P. Fischer, *Rev. Mod. Phys.* **2017**, *89*, 025006.
[2] N. Sivadas, M. W. Daniels, R. H. Swendsen, S. Okamoto, D. Xiao, *Phys. Rev. B.* **2015**, *91*, 235425.
[3] K. S. Novoselov, A. K. Geim, S. V. Morozov, D. Jiang, Y. Zhang, S. V. Dubonos, I. V. Grigorieva, A. A. Firsov, *Science* **2004**, *306*(5696), 666.
[4] Q. H. Wang, K. Kalantar-Zadeh, A. Kis, J. N. Coleman, M. S. Strano, *Nat. Nanotechnol.* **2012**, *7*, 699.
[5] G. Cheng, L. Lin, L. Zhenglu, J. Huiwen, S. Alex, X. Yang, C. Ting, B. Wei, W. Chenzhe, W. Yuan, Z. Q. Qiu, R. J. Cava, G. L. Steven, X. Jing, Z. Xiang, *Nature* **2017**, *546*, 265.
[6] B. Huang Bevin, G. Clark, E. Navarro-Moratalla, D. R. Klein, R. Cheng, K. L. Seyler, D. Zhong, E. Schmidgall, M. A. McGuire, D. H. Cobden, W. Yao, *Nature* **2017**, *546*, 270.
[7] K. S. Burch, D. Mandrus, J.-G. Park, *Nature* **2018**, *563* (7729), 47.
[8] J.-X. Zhu, M. Janoschek, D. Chaves, S. J. C. Cezar, T. Durakiewicz, F. Ronning, Y. Sassa, M. Mansson, B. L. Scott, N. Wakeham, E. D. Bauer, J. D. Thompson, *Phys. Rev. B.* **2016**, *93*, 144404.
[9] B. Chen, J. H. Yang, H. D. Wang, M. Imai, H. Ohta, C. Michioka, K. Yoshimura, M. H. Fang, *J. Phys. Soc. Japan* **2013**, *82*(12), 124711.
[10] A. Milosavljević, A. Šolajić, S. Djurdjić-Mijin, J. Pešić, B. Višić, Y. Liu, C. Petrovic, N. Lazarević, Z. V. Popović, *Phys. Rev. B.* **2019**, *99*, 214304.
[11] M. A. McGuire, H. Dixit, V. R. Cooper, B. C. Sales, *Chem. Mat.* **2015**, *27*(2), 612.
[12] H. L. Zhuang, Y. Xie, P. R. C. Kent, P. Ganesh, *Phys. Rev. B.* **2015**, *92*, 035407.
[13] G. T. Lin, H. L. Zhuang, X. Luo, B. J. Liu, F. C. Chen, J. Yan, Y. Sun, J. Zhou, W. J. Lu, P. Tong, Z. G. Sheng, *Phys. Rev. B.* **2017**, *95*, 245212.
[14] M. Gibertini, M. Koperski, A. F. Morpurgo, K. S. Novoselov, *Nat. Nanotech.* **2019**, *14*(5), 408.
[15] L. D. Casto, A. J. Clune, M. O. Yokosuk, J. L. Musfeldt, T. J. Williams, H. L. Zhuang, M.-W. Lin, K. Xiao, R. G. Hennig, B. C. Sales, J.-Q. Yan, D. Mandrus, *APL Mat.* **2015**, *3*(4), 041515.
[16] X. Zhang, Y. Zhao, Q. Song, S. Jia, J. Shi, W. Han, *JJpn. J. Appl. Phys.* **2016**, *55*(3), 033001.
[17] B. Siberchicot, S. Jobic, V. Carteaux, P. Gressier, G. Ouvrard, *Phys. J. Chem.* **1996**, *100*(14), 5863.
[18] V. Carteaux, F. Moussa, M. Spiesser, *EPL.* **1995**, *29*(3), 251.
[19] J. Zhang, X. Cai, W. Xia, A. Liang, J. Huang, C. Wang, L. Yang, H. Yuan, Y. Chen, S. Zhang, Y. Guo, *Phys. Rev. Lett.* **2019**, *123*, 047203.
[20] Y. F. Li, W. Wang, W. Guo, C. Y. Gu, H. Y. Sun, L. He, J. Zhou, Z. B. Gu, Y. F. Nie, X. Q. Pan, *Phys. Rev. B.* **2018**, *98*, 125127.
[21] A. Milosavljević, A. Šolajić, J. Pešć, Y. Liu, C. Petrovic, N. Lazarević, Z. V. Popović, *Phys. Rev. B.* **2018**, *98*, 104306.
[22] Y. Tian, M. J. Gray, H. Ji, R. J. Cava, K. S. Burch, *2D Mater.* **2016**, *3*(2), 025035.
[23] Y. Sun, R. C. Xiao, G. T. Lin., R. R. Zhang, L. S. Ling, Z. W. Ma, X. Luo, W. J. Lu, Y. P. Sun, Z. G. Sheng, *Appl. Phys. Lett.* **2018**, *112*(7), 072409.
[24] Y. Liu, C. Petrovic, *Phys. Rev. Mater.* **2019**, *3*, 014001.
[25] P. Giannozzi, S. Baroni, N. Bonini, M. Calandra, R. Car, C. Cavazzoni, D. Ceresoli, G. L. Chiarotti, M. Cococcioni, I. Dabo, A. Dal Corso, *J. Phys. Condens. Matter.* **2009**, *21*(39), 395502.
[26] J. P. Perdew, K. Burke, M. Ernzerhof, *Phys. Rev. Lett.* **1996**, *77*, 3865.
[27] P. E. Blöchl, *Phys. Rev. B.* **1994**, *50*, 17953.
[28] G. Kresse, D Joubert, *Phys. Rev. B.* **1999**, *59*, 1758.
[29] F. A. May, S. Calder, C. Cantoni, H. Cao, M. A. McGuire, *Phys. Rev. B* **2016**, *93*, 014411.
[30] R. E. Marsh, *J. Solid State Chem.* **1988**, *77*(1), 190.
[31] M. Opačić, N. Lazarević, M. Šćepanović, H. Ryu, H. Lei, C. Petrovic, Z. V. Popović, *J. Phys. Condens. Matter.*, *48*(27), 485701.
[32] F. Feng, N. Lazarević, C. Liu, J. Ji, Y. Wang, S. He, H. Lei, C. Petrovic, R. Yu, Z. V. Popović, Q. Zhang, *Phys. Rev. B.* **2019**, *99*, 144419.

**How to cite this article:** Milosavljević A, Šolajić A, Višić B, et al. Vacancies and spin–phonon coupling in $CrSi_{0.8}Ge_{0.1}Te_3$. *J Raman Spectrosc*. 2020;51:2153–2160. https://doi.org/10.1002/jrs.5962

## APPENDIX: A DECOMPOSITION OF UNRESOLVED MODES

Analysing the spectra of $CrSi_{0.8}Ge_{0.1}Te_3$ single crystal, in different polarization configurations (Figure 3), in the energy range around 117 $cm^{-1}$, becomes clear that lower energy part completely disappears in cross polarization configuration, whereas higher energy part persists. Enlarged part of this energy region is shown in Figure A1, in parallel and cross polarization configuration at temperature of 100 K. After simultaneous modelling of these spectra becomes clear that they consist of the $A_g^2$ and $E_g^3$ modes, at energies 116.4 and 117.2 $cm^{-1}$, respectively. This is completely supported with theoretical calculations presented in Table 1.

On the other hand, existence of *P*1 is not predicted by theoretical calculations, as Raman active peak. Only closer inspection and detailed analysis, presented in Figure A2, shows that much better agreement with experimental results gives modelling as a superposition of two Voigt lines.

condensed matter

MDPI

Article

# Ab Initio Study of the Electronic, Vibrational, and Mechanical Properties of the Magnesium Diboride Monolayer

**Jelena Pešić [1,*], Igor Popov [1,2], Andrijana Šolajić [1], Vladimir Damljanović [1], Kurt Hingerl [3], Milivoj Belić [4] and Radoš Gajić [1]**

1 Laboratory for graphene, other 2D materials and ordered nanostructures, Center for Solid State Physics and New Materials, Institute of Physics Belgrade, University of Belgrade, 11080 Belgrade, Serbia; popov@ipb.ac.rs (I.P.); solajic@ipb.ac.rs (A.Š.); damlja@ipb.ac.rs (V.D.); rgajic@ipb.ac.rs (R.G.)
2 Institute for Multidisciplinary Research, University of Belgrade, Kneza Višeslava 1, 11030 Belgrade, Serbia
3 Center for Surface and Nanoanalytics, Johannes Kepler University, 4040 Linz, Austria; Kurt.Hingerl@jku.at
4 Science Program, Texas A&M University at Qatar, Doha P.O. Box 23874, Qatar; milivoj.belic@qatar.tamu.edu
* Correspondence: yelena@ipb.ac.rs

Received: 15 March 2019; Accepted: 1 April 2019; Published: 2 April 2019


**Abstract:** Magnesium diboride gained significant interest in the materials science community after the discovery of its superconductivity, with an unusually high critical temperature of 39 K. Many aspects of the electronic properties and superconductivity of bulk $MgB_2$ and thin sheets of $MgB_2$ have been determined; however, a single layer of $MgB_2$ has not yet been fully theoretically investigated. Here, we present a detailed study of the structural, electronic, vibrational, and elastic properties of monolayer $MgB_2$, based on ab initio methods. First-principles calculations reveal the importance of reduction of dimensionality on the properties of $MgB_2$ and thoroughly describe the properties of this novel 2D material. The presence of a negative Poisson ratio, higher density of states at the Fermi level, and a good dynamic stability under strain make the $MgB_2$ monolayer a prominent material, both for fundamental research and application studies.

**Keywords:** magnesium diboride; 2D materials; density functional theory

**PACS:** 71.15.Mb; 74.70.Ad

## 1. Introduction

Magnesium diboride was first synthesized and had its structure confirmed in 1953 [1]. An interest in its properties has grown ever since 2001, when it was discovered that $MgB_2$ exhibits the highest superconducting transition temperature $T_c$ of all metallic superconductors. It is an inter-metallic s-wave compound superconductor with a quasi-two dimensional character [2] and a critical temperature of superconductive transition at $T_c$ = 39 K. The experimental confirmation of the isotope effect [3] in $MgB_2$ indicated that it is a phonon-mediated BCS superconductor. A better definition would describe $MgB_2$ as self-doped semimetal with a crucial $\sigma$-bonding band that is nearly filled [4]. The basic aspects of the electronic structure and pairing is in a rather strong coupling of high frequency boron–boron stretch modes to the bonding electronic boron–boron states at the Fermi surface. The phonon-mediated mechanism with different coupling strengths between a particular phonon mode and selected electronic bands, boron $\sigma$- and $\pi$-bands [5–13], results in the presence of two superconducting gaps at the Fermi level. $MgB_2$ has already been fabricated in bulk, as single crystals, and as a thin film, and shows potential for practical applications.

The discovery of graphene in 2004 [14] sparked an interest in 2D materials and their properties. A variety of new properties, which distinguished graphene from graphite [14–22], inspired a search for other low-dimensional limits of layered materials and possibilities they offered. Interest in a low-dimensional limit of $MgB_2$ has arisen in past years, showing that it is superconductive even in a monolayer [23,24].

$MgB_2$ has a distinct layer structure, where boron atoms form a honeycomb layer and magnesium atoms are located above the center of the hexagons, between every boron plane. The boron layers alternate with a triangular lattice of magnesium layers. There is a noticeable structural similarity of $MgB_2$ to graphite-intercalated compounds (GICs), some of which also exhibit superconductivity [25–29]. Both monolayer and two-layer graphene, decorated/intercalated with atoms of alkali and alkaline earth metals, exhibit superconductivity and have been thoroughly studied using ab initio methods and isotropic and anisotropic Eliashberg theory [30–32].

Furthermore, a similarity in the electronic structure between GICs and $MgB_2$ exists. The peculiar and unique property of $MgB_2$ is a consequence of the incomplete filling of two $\sigma$ bands corresponding to strongly covalent $sp^2$-hybrid bonding within the graphite-like boron layers [33].

Here, we present a comprehensive study of the electronic, vibrational, and mechanical properties of $MgB_2$ using ab initio methods, in order to provide its detail description.

## 2. Computational Details

$MgB_2$ has a hexagonal unit cell and consists of graphite-like $B_2$ layers stacked with the Mg atoms in between, as shown in Figure 1. The first-principles calculations were performed within the density functional theory (DFT) formalism, using a general gradient approximation (GGA) to calculate the electronic structure. For all electronic and phonon structure, the Quantum Espresso software package [34] was used with ultra-soft pseudopotentials and a plane-wave cutoff energy of 30 Ry. All calculated structures are relaxed to their minimum energy configuration, following the internal force on atoms and stress tensor of the unit cell. We used the Monkhorst-Pack $48 \times 48 \times 48$ and $40 \times 40 \times 1$ k-meshes, for the calculations of the electronic structure of the $MgB_2$ bulk and $MgB_2$ monolayer, respectively. The phonon frequencies are calculated using Density Functional Perturbation Theory (DPFT) on the $12 \times 12 \times 12$ and $20 \times 20 \times 1$ phonon wave vector mesh for the bulk and monolayer structures, respectively. In two-dimensional systems, the van der Waals (vdW) interaction was found to play an important role on the electronic structure [35]; however, as this is study on monolayer $MgB_2$, we do not treat vdW interactions, especially since, in this case, the effects are minor and including them would add additional computational costs but would not yield more accurate results.

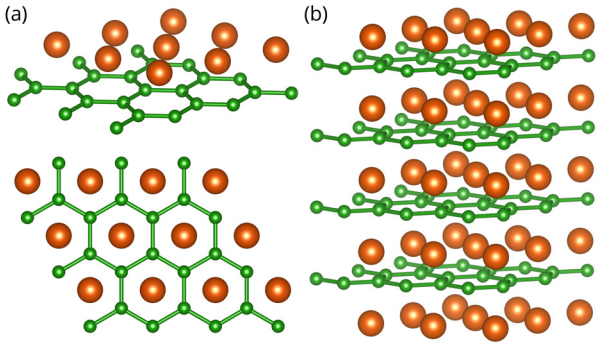


**Figure 1.** Crystal structure of the $MgB_2$ monolayer (**a**) and bulk $MgB_2$ (**b**), with a hexagonal unit cell. Green (orange) spheres represent Boron (Magnesium) atoms. Color online.

The crystal structure of $MgB_2$ and the $MgB_2$ monolayer are presented in Figure 1. The lattice parameters for the bulk $MgB_2$ are in agreement with the experimental results, $a = 3.083$ Å and

$c/a = 1.142$ [9]. In order to avoid an interlayer interaction due to the periodicity and to simulate a 2D material, an artificial vacuum layer was set to be 25 Å. When the monolayer is modelled, the structure is geometrically optimized, allowing the atoms to reach a minimum potential energy state. The bond length between neighbouring atoms remained to be 1.78 Å, but the distance from the boron layer to the Mg atoms changed from $h = 1.76$ Å to $h = 1.60$ Å.

For the molecular dynamics (MD) study, the Siesta code was utilized [36]. The super-cell is built by repeating the unit cell three times in both in-plane directions, whereas the lattice vector in the perpendicular direction is 15 Å, providing a large enough vacuum space between the 2D material and its periodic replica in order to avoid their mutual interaction. The lattice parameters and the geometry of the unit cell are initially optimized using the conjugate gradient method. The Perdew-Burke-Ernzerhof form of the exchange-correlation functional [37], the double-zeta polarized basis set, and the Troulier-Martins pseudopotentials [38] were used in all MD calculations.

The second-order elastic constants were calculated using the ElaStic software package [39]. First, the direction is projected from the strain tensor and total energies for each deformation are calculated. Elastic constants are then calculated using the second derivatives of the energy curves, dependent on the parameter $\eta$. In our calculations, the maximum positive and negative amplitudes of 5% Lagrangian strain were applied, with a step of 0.1%.

For the 2D square, rectangular, or hexagonal lattices, the non-zero second-order elastic constants, in Voigt notation, are $c_{11}$, $c_{22}$, $c_{12}$, and $c_{66}$. Due to symmetry, in hexagonal structures $c_{11} = c_{22}$ and $c_{66} = \frac{1}{2}(c_{11} - c_{12})$; so, we have 2 independent elastic constants. The layer modulus, which represents the resistance of a 2D material to stretching, is given as

$$\gamma = \frac{1}{4}(c_{11} + c_{22} + 2c_{12}).$$

The 2D Young modulus $Y$ for strains in the (10) and (01) directions, Poisson's ratio $\nu$ and the shear modulus $G$ are obtained from the following relations,

$$Y = \frac{c_{11}^2 - c_{12}^2}{c_{11}}, \ \nu = \frac{c_{12}}{c_{22}}, \ G = c_{66}.$$

Units for elastic constants and those parameters are N/m.

## 3. Results and Discussion

In order to determine the stability of a single layer of $MgB_2$, we perform MD simulations based on DFT and the super-cell approach. Besides the system with optimized (pristine) lattice parameters, we also consider a biaxially stretched system (up to 3% of tensile strain) and biaxially compressed system (up to 5% of compressive strain). The MD simulations are conducted in the range of temperatures between 50–300 K, with a step of 50 K, using the Nosé–Hoover thermostat [40].

Figure 2a shows the average distance between Mg and B atomic layers, as evolved over a time of 1 ps. Throughout the simulation time, there is no further evolution of the z-coordinate and the Mg atom shows only oscillatory movement around the equilibrium positions (as is shown in Figure 2) Importantly, the separation indicates that the Mg atoms do not leave the surface of the $MgB_2$ crystal. The plane in which the Mg atoms reside shifts away from the plane of the B atoms on average by 0.09 Å in a compressed crystal, while the distance between the planes decreases on average by 0.42 Å in the stretched system. This (relatively larger) shift in the latter case can be understood by analysing the details of the $MgB_2$ atomic structure. When the crystal is biaxially stretched, its Mg–B bond lengths increase, which is partially compensated by the nesting of the Mg atoms in the hollow sites closer to the B sublattice. Despite these atomic shifts, the MD simulations show the structural stability of the system. The stability from the MD simulations can be further quantitatively derived from the global Lindemann index, the dependence of which on temperature is shown in Figure 2b. It is calculated

for the pristine crystal, with a compressive strain of 5% and a tensile strain of 3%, from the local Lindemann indices, given by the formula

$$q_i = \frac{1}{N-1} \sum_{j \neq i} \frac{\sqrt{\langle r_{ij}^2 \rangle - \langle r_{ij} \rangle^2}}{\langle r_{ij} \rangle},$$

by averaging over all atoms. Here $q_i$ is the local Lindemann index of atom $i$, N is number of atoms, $r_{ij}$ is a separation between atoms $i$ and $j$, and the angle brackets denote averaging over time (i.e., MD steps) [41]. The linear behaviour of the Lindemann indices indicate that systems are stable, at least up to room temperature.

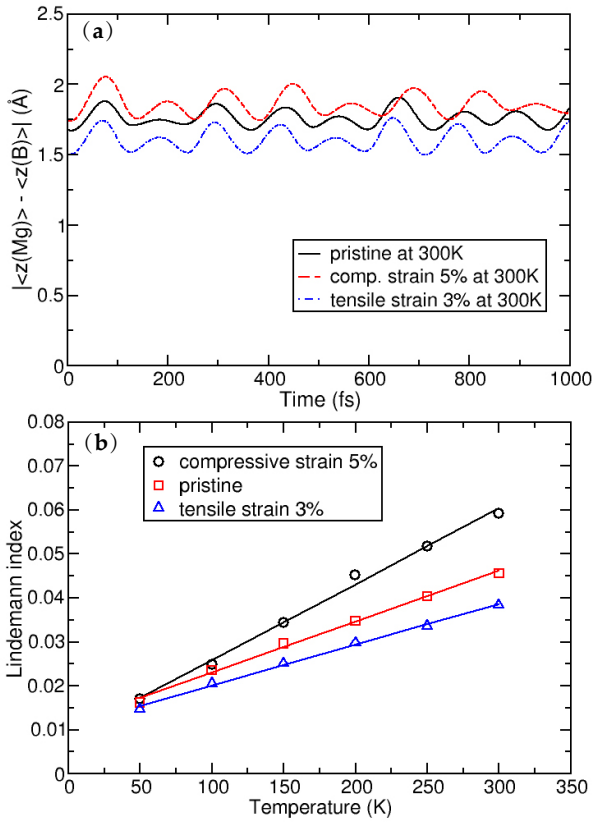


**Figure 2.** (**a**): Average distance between the Mg and B atomic layers; and (**b**): the dependence of the global Lindemann index as a function of temperature.

The calculated second-order elastic constants and other structural parameters for monolayer $MgB_2$ are given in Table 1. All elastic constants related to the bulk material (those that have 3, 4, or 5 in their subscripts), are calculated close to zero, as is expected for the monolayer. Compared to similar 2D materials, the layer modulus of $MgB_2$ of 30.18 N/m is relatively small (in the range of Silicene and Germanene), roughly five times smaller than that of graphene or h–BN, for example [42,43]. Similar results are obtained for the Young modulus. Compared to borophene (two-dimensional boron sheets with rectangular structures) [44], which is a hard and brittle 2D material that exhibits an extremely large Young's modulus of 398 N/m along the $a$ direction [45], the $MgB_2$ monolayer has a significantly smaller value of 63.29 N/m. The most interesting observation in the elastic properties of the MgB2 monolayer is that the $c_{12}$ constant is negative, which gives a negative Poisson ratio in the $a$ and $b$ directions, too—although, with a very small negative value of $-0.05$. However, compared to 2D borophene, which has an out-of-plane negative Poisson's ratio (that effectively holds the strong boron bonds lying along the $a$ direction and makes the boron sheet show superior mechanical flexibility along

the $b$ direction [46]), we obtain similar values [45]. For comparison, graphene has a Young modulus of 352.2 N/m and a Poisson ratio of 0.185 [42]. After confirming its stability and determining the elastic properties of the $MgB_2$ monolayer, we study its electronic properties. In Figure 3, the electronic structures of bulk $MgB_2$ and the $MgB_2$ monolayer are presented. The band structures for the bulk along the high-symmetry points Γ-K-M-Γ-A-L, and for the monolayer along Γ-K-M-Γ were calculated. The Fermi level is set to zero. The band structure of the bulk is in full agreement with previous studies [10,47–49]. The two bands crossing the Fermi level play a crucial role in the electronic properties of $MgB_2$. The density of the states around $E_f$ are predominantly related to the B atoms and their $p$-orbitals, whereas the Mg atom contribution is negligible in this region. Previous studies described Mg as fully ionized and showed that the electrons donated to the system are not localized on the anion but, rather, are distributed over the whole crystal [6]. A similarity to graphite can be observed, with three $\sigma$ bands, corresponding to the in-plane $sp_xp_y$ ($sp^2$) hybridization in the boron layer and two $\pi$-bands of boron $p_z$ orbitals [33]. Boron $p_{x(y)}$ and $p_z$ orbitals contribute as $\sigma$ and $\pi$ states. Analysing projected DOS, one concludes that the $\sigma$ states are considerably involved in the total density of states at the Fermi level, while the $\pi$ states have only a partial contribution. It is worth emphasizing that the bulk bands of this material at the K-point above the Fermi level present a formation similar to the Dirac cones in graphene.

In the monolayer, there is an increase in the total density of states at the Fermi level from $N(E_f)_{bulk}$ = 0.72 states/eV to $N(E_f)_{mono}$ = 0.97 states/eV. In the same manner as in the bulk, the monolayer Mg atoms negligibly contribute to the density of states at the Fermi level, and the main contribution comes from the B p-orbitals. The characteristic Dirac cone-like structure is still present and closer to the Fermi level. Dg77, as the symmetry group of the $MgB_2$ monolayer, hosts a Dirac-like dispersion in the vicinity of the K-point in the hexagonal Brillouin zone, if the orbital wave functions belong to the 2D representation E of the $C_{3v}$ point group of the wave vector [50,51]. In the tight-binding case, the $p_x$ and $p_y$ orbitals of two boron ions give rise to one E-representation (and to two one-dimensional representations), while the s-orbitals form a basis for one E-representation and $p_z$-orbitals form a basis for one E-representation as well. This explains the presence of the Dirac cones at the K-point in the band structure of the $MgB_2$ monolayer (as shown in Figure 3b).

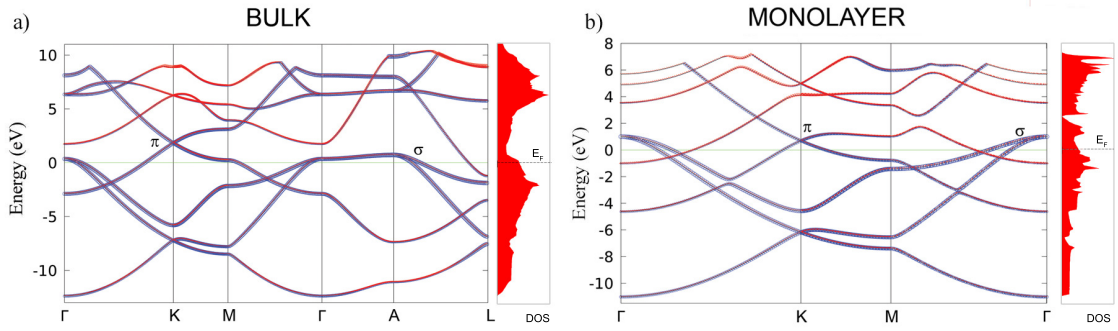


**Figure 3.** The electronic band structure and total density of states in bulk $MgB_2$ (**a**) and the $MgB_2$ monolayer (**b**). The blue and red colors represent the B and Mg atoms contributions to the electronic dispersion, respectively.

**Table 1.** The calculated elastic stiffness constants, layer modulus $\gamma$, Young's modulus $Y$, Poisson's ratio $\nu$, and shear modulus $G$ for the $MgB_2$ monolayer. All parameters are in units of N/m.

| $c_{11}$ | $c_{12}$ | $c_{66}$ | $\gamma$ | $Y$ | $\nu$ | $G$ |
|---|---|---|---|---|---|---|
| 63.4 | −3.1 | 33.3 | 30.18 | 63.29 | −0.05 | 33.3 |

Figure 4 shows the phonon dispersions for both the bulk and monolayer. For the bulk (in Figure 4a), there are four optical modes at the Γ point. Due to the light atomic mass of the B

atoms and the strong B–B coupling, the two high-frequency modes almost have a pure boron character. The in-plane stretching mode $E_{2g}$ and the out-of-plane mode (where the atoms move in opposite directions $B_{1g}$) are the boron atom modes. $E_{2g}$ is a doubly-degenerate Raman active mode and experimental studies [6,9] showed that this mode is very sensitive to structural changes and it has a strong electron-phonon coupling. The low-frequency modes ($A_{2u}$) and double degenerate ($E_{1u}$) are infrared active and they do not involve changes on in-plane bonds. In Figure 4b, the phonon dispersion of the $MgB_2$ monolayer is presented. In the phonon spectrum there are no imaginary frequencies, which confirms, once again, the dynamical stability of the system (also demonstrated earlier by the MD calculations).

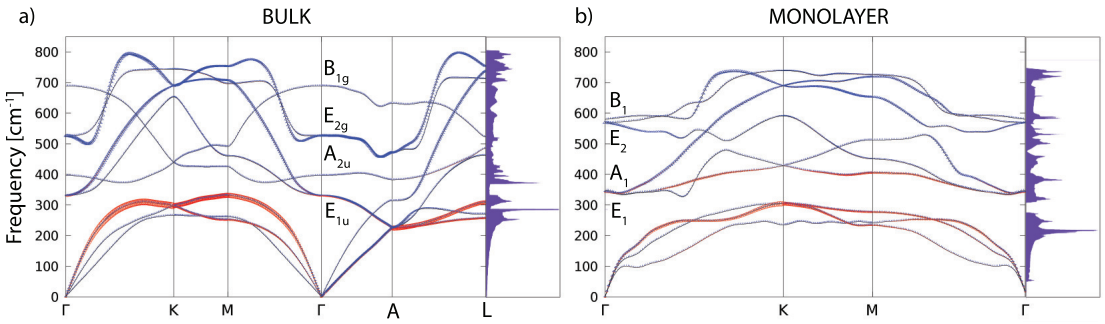


**Figure 4.** The phonon dispersion and the phonon density of states for the $MgB_2$ bulk (**a**) and monolayer (**b**). The blue and red colours represent the B and Mg atom contributions in the phonon dispersion, respectively.

At the Γ point, there are three acoustic and six optical modes (from which two pairs are doubly degenerate). The optical modes $A_1$, $B_1$, $E_1$, and $E_2$ are related to the optical modes of the parent material. Two significant differences between the bulk and monolayer spectrum can be observed: The $E_1$ and $A_1$ mode become energy degenerate in the monolayer, resulting in either a slight softening (hardening) of the modes which leads to nearly equal frequencies, which opens a gap in the phonon density of states (DOS) between the acoustic and optical modes. A more significant effect concerns the softening of the $B_1$ mode and hardening of the $E_2$ mode. As in the bulk $E_{2g}$ mode, the monolayer $E_2$ mode is strongly coupled to electrons, causing the superconductivity in the monolayer in a similar fashion as in the bulk. In Figure 5, the vibrational frequencies and normal coordinates for the $MgB_2$ monolayer are presented. The symmetry group is $C_{6v}$, and the acoustic modes are $A_1$ and $E_1$. The optical modes at the Γ point are $A_1$, $B_1$, $E_1$, and $E_2$, where the infrared-active ones are $A_1$ and $E_1$. The Raman-active modes are $A_1$, $E_1$, and $E_2$, and $B_1$ is silent. In Table 2, the Raman tensor for the $MgB_2$ monolayer is presented [52]. Similar to graphene, the phonon eigenvectors and the normal coordinates at the Γ-point are determined by symmetry rules and, therefore, are a model independent.

**Table 2.** Raman tensor of the $MgB_2$ monolayer.

| | **Raman Tensors** | | | | |
|---|---|---|---|---|---|
| **$MgB_2$-mono**<br>$Dg77 = TC_{6v}$<br>$O_z \,\|\|\, C_6$<br>$O_x \,\|\|\, \sigma_v$ | $A_1$<br>$\begin{pmatrix} a & 0 & 0 \\ 0 & a & 0 \\ 0 & 0 & b \end{pmatrix}$ | $E_1$<br>$\begin{pmatrix} 0 & 0 & c \\ 0 & 0 & 0 \\ c & 0 & 0 \end{pmatrix}$ | $\begin{pmatrix} 0 & 0 & 0 \\ 0 & 0 & c \\ 0 & c & 0 \end{pmatrix}$ | $E_2$<br>$\begin{pmatrix} d & 0 & 0 \\ 0 & -d & 0 \\ 0 & 0 & 0 \end{pmatrix}$ | $\begin{pmatrix} 0 & -d & 0 \\ -d & 0 & 0 \\ 0 & 0 & 0 \end{pmatrix}$ |

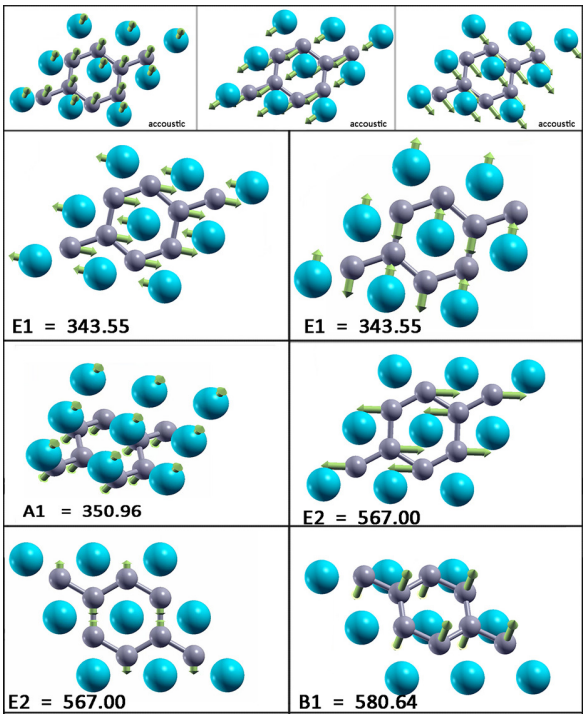


**Figure 5.** Vibrational frequencies (in wavenumbers) and the vibration normal coordinates at Γ for the $MgB_2$ monolayer.

## 4. Conclusions

The electronic band structure, density of states, phonon dispersion, and elastic constants have been calculated for the $MgB_2$ monolayer and compared to the bulk material, using first-principles calculations within the DFT framework. We demonstrated an increase of electronic density of states at the Fermi level in the monolayer (compared to the bulk) and determined its stability under various strains. These two features are crucial for the enhancement of electron–phonon coupling and they enable significant mechanical modification that increases the critical superconducting temperature. Establishing stability and offering insight into this novel 2D material, we focus on the effects of ultimate lowering of the dimensionality. The question of reduction of dimensionality to its limit, a truly atomic-scale 2D system, and the consequences of this [53–61] are highly relevant, not only to fundamental science but also to applications in nanotechnology.

**Author Contributions:** Conceptualization, J.P. and R.G.; Validation, K.H., M.B., R.G.; Investigation, J.P., I.P., A.Š. and V.D.; Writing—Original Draft Preparation, J.P., I.P., A.Š. and V.D.; Writing—Review & Editing, J.P.; Supervision, R.G.; Funding Acquisition, K.H., M.B. and R.G.

**Funding:** This research is supported by Serbian Ministry of Education, Science and Technological Development under projects OI 171005, III 45018, and III 45016 and by the Qatar National Research Fund, cycle 11, under grant number NPRP 11S-1126-170033. K.H. acknowledges the support of the European Commission under the H2020 grant TWINFUSYON.GA692034.

**Acknowledgments:** The DFT calculations were performed using the computational resources at Johannes Kepler University, Linz, Austria. This work was supported by the Serbian Ministry of Education, Science and Technological Development under projects OI 171005, III 45018, and III 45016.

**Conflicts of Interest:** The authors declare no conflict of interest.

## References


1. Jones, M.E.; Marsh R.E. The preparation and structure of magnesium boride, $MgB_2$. *J. Am. Chem. Soc.* **1953**, *76*, 5. [CrossRef]
2. Nagamatsu, J.; Nakagawa, N.; Muranaka, T.; Zenitani, Y.; Akimitsu, J. Superconductivity at 39 K in magnesium diboride. *Nature* **2001**, *410*, 63. [CrossRef] [PubMed]
3. Bud'ko, S.L.; Lapertot, G.; Petrovic, C.; Cunningham, C.E.; Anderson, N.; Canfield, P.C. Boron Isotope Effect in Superconducting $MgB_2$. *Phys. Rev. Lett.* **2001**, *86*, 1877. [CrossRef] [PubMed]
4. Pickett, W. Superconductivity: 2D Physics, Unknown Mechanisms, Current Puzzles. *Emerg. Phenom. Correl. Matter Lect. Notes Autumn School Corr. Electron.* **2013**, *2013*, 45.
5. Choi, H.J.; Roundy, D.; Sun, H.; Cohen, M.L.; Steven Louie, G. The origin of the anomalous superconducting properties of $MgB_2$. *Nature* **2002**, *418*, 758. [CrossRef]
6. Kortus, J.; Mazin, I.I.; Belaachenko, K.D.; Antropov, V.P.; Boyer, L.L. Superconductivity of Metallic Boron in $MgB_2$. *Phys. Rev. Lett.* **2001**, *86*, 4656. [CrossRef]
7. An, J.M.; Pickett, W.E. Superconductivity of $MgB_2$: Covalent Bonds Driven Metallic. *Phys. Rev. Lett.* **2001**, *86*, 4366. [CrossRef] [PubMed]
8. Liu, A.Y.; Mazin, I.I.; Kortus, J. Beyond Eliashberg Superconductivity in $MgB_2$: Anharmonicity, Two-Phonon Scattering, and Multiple Gaps. *Phys. Rev. Lett.* **2001**, *87*, 087005. [CrossRef] [PubMed]
9. Kong, Y.; Dolgov, O.V.; Jepsen, O.; Andersen, O.K. Electron-phonon interaction in the normal and superconducting states of $MgB_2$. *Phys. Rev. B* **2001**, *64*, 020501. [CrossRef]
10. Bohnen, K.-P.; Heid, R.; Renker, B. Phonon Dispersion and Electron-Phonon Coupling in $MgB_2$ and $AlB_2$. *Phys. Rev. Lett.* **2001**, *86*, 5771. [CrossRef] [PubMed]
11. Kunc, K.; Loa, I.; Syassen, K.; Kremer, R.K.; Ahn, K. $MgB_2$ under pressure: phonon calculations, Raman spectroscopy, and optical reflectance. *J. Phys. Condens. Matter* **2001**, *13*, 9945. [CrossRef]
12. Choi, H.J.; Roundy, D.; Sun, H.; Cohen, M.L.; Louie, S.G. First-principles calculation of the superconducting transition in MgB2 within the anisotropic Eliashberg formalism. *Phys. Rev. B* **2002**, *66*, 020513. [CrossRef]
13. Canfield, P.C.; Crabtree, G.W. Magnesium Diboride: Better Late than Never. *Phys. Today* **2003**, *56*, 34. [CrossRef]
14. Novoselov, K.S.; Geim, A.K.; Morozov, S.V.; Jiang, D.; Zhang, Y.; Dubonos, S.V.; Grigorieva, I.V.; Firsov, A.A. Electric Field Effect in Atomically Thin Carbon Films. *Science* **2004**, *306*, 666–669. [CrossRef]
15. Katsnelson, M.I.; Novoselov, K.S.; Geim, A.K. Chiral tunnelling and the Klein paradox in graphene. *Nat. Phys.* **2006**, *2*, 620–625. [CrossRef]
16. Katsnelson, M.I. Zitterbewegung, chirality, and minimal conductivity in graphene. *Eur. Phys. J. B* **2006**, *51*, 157–160. [CrossRef]
17. Rusin, T.M.; Zawadzki, W. Zitterbewegung of electrons in graphene in a magnetic field. *Phys. Rev. B* **2008**, *78*, 125419. [CrossRef]
18. Pisana, S.; Lazzeri, M.; Casiraghi, C.; Novoselov, K.S.; Geim, A.K.; Ferrari, A.C.; Mauri, F. Breakdown of the adiabatic Born-Oppenheimer approximation in graphene. *Nat. Mater.* **2007**, *6*, 198–201. [CrossRef] [PubMed]
19. Piscanec, S.; Lazzeri, M.; Mauri, F.; Ferrari, A.C.; Robertson, J. Kohn Anomalies and Electron-Phonon Interactions in Graphite. *Phys. Rev. Lett.* **2004**, *93*, 85503. [CrossRef]
20. Novoselov, K.S.; Jiang, Z.; Zhang, Y.; Morozov, S.V.; Stormer, H.L.; Zeitler, U.; Maan, J.C.; Boebinger, G.S.; Kim, P.; Geim, A.K. Room-temperature quantum Hall effect in graphene. *Science* **2007**, *315*, 1379. [CrossRef]
21. Zhou, S.Y.; Gweon, G.-H.; Fedorov, A.V.; First, P.N.; de Heer, W.A.; Lee, D.-H.; Guinea, F.; Castro Neto, A.H.; Lanzara, A.; et al. Substrate-induced bandgap opening in epitaxial graphene. *Nat. Mater.* **2007**, *6*, 770–775. [CrossRef]
22. Zhang, Y.; Tan, Y.; Stormer, H.L.; Kim, P. Experimental observation of the quantum Hall effect and Berry's phase in graphene. *Nature* **2005**, *438*, 201–204. [CrossRef]
23. Bekaert, J.; Aperis, A.; Partoens, B. Oppeneer, P.M.; Milošević, M.V. Evolution of multigap superconductivity in the atomically thin limit: Strain-enhanced three-gap superconductivity in monolayer MgB2 *Phys. Rev. B* **2017**, *96*, 094510.
24. Morshedloo, T.; Roknabadi, M.R.; Behdani, M. First-principles study of the superconductivity in $MgB_2$ bulk and in its bilayer thin film based on electron–phonon coupling. *Physica C* **2015**, *509*. [CrossRef]

25. Calandra, M.; Profeta, G.; Mauri, F. Superconductivity in metal-coated graphene. *Phys. Status Solidi (b)* **2012**, *249*, 2544. [CrossRef]
26. Ludbrook, B.M.; Levy, G.; Nigge, P.; Zonno, M.; Schneider, M.; Dvorak, D.J.; Veenstra, C.N.; Zhdanovich, S.; Wong, D.; Dosanjh, P.; et al. Evidence for superconductivity in Li-decorated monolayer graphene. *Proc. Natl. Acad. Sci. USA* **2015**, *112*, 11795. [CrossRef] [PubMed]
27. Profeta, G.; Calandra, M.; Mauri, F. Phonon-mediated superconductivity in graphene by lithium deposition. *Nat. Phys.* **2012**, *8*, 131–134. [CrossRef]
28. Pešić, J.; Gajić, R.; Hingerl, K.; Belić, M. Strain-enhanced superconductivity in Li-doped graphene. *Europhys. Lett.* **2014**, *108*, 67005. [CrossRef]
29. Szczesniak, D.; Durajski, A.P.; Szczesniak, R. Influence of lithium doping on the thermodynamic properties of graphene based superconductors. *J. Phys-Condens. Mat.* **2014**, *26*, 255701. [CrossRef]
30. Durajski, A.; Skoczylas, K.; Szczesniak, R. Superconductivity in bilayer graphene intercalated with alkali and alkaline earth metals. *Phys. Chem. Chem. Phys.* **2019**, *21*, 5925. [CrossRef] [PubMed]
31. Zheng, J.-J.; Margine, E.R. First-principles calculations of the superconducting properties in Li-decorated monolayer graphene within the anisotropic Migdal-Eliashberg formalism. *Phys. Rev. B* **2016**, *94*, 064509. [CrossRef]
32. Margine, E.R.; Lambert, H.; Giustino, F. Electron-phonon interaction and pairing mechanism in superconducting Ca-intercalated bilayer graphene. *Sci. Rep.* **2016**, *6*, 21414. [CrossRef]
33. Mazin, I.I.; Antropov, V.P. Electronic structure, electron–phonon coupling, and multiband effects in $MgB_2$. *Phys. C Supercond.* **2003**, *385*, 49–65. [CrossRef]
34. Giannozzi, P.; Andreussi, O.; Brumme, T.; Bunau, O.; Buongiorno, N.M.; Calandra, M.; Car, R.; Cavazzoni, C.; Ceresoli, D.; Cococcioni, M. et al. Quantum espresso: A modular and open-source software project for quantum simulations of materials. *J. Phys. Condensed Matter* **2009**, *21*, 395502. [CrossRef] [PubMed]
35. Lu, N.; Guo, H.; Zhuo, Z.; Wang, L.; Wu, X.; Zeng, X.C. Twisted $MX_2/MoS_2$ heterobilayers: effect of van der Waals interaction on the electronic structure. *Nanoscale* **2017**, *9*, 19131–19138. [CrossRef] [PubMed]
36. Soler, J.M.; Artacho, E.; Gale, J.D.; García, A.; Junquera, J.; Ordejón, P.; Sánchez-Portal, D. The SIESTA method for ab initio order-N materials simulation. *J. Phys. Condens. Matter.* **2002**, *14*, 2745. [CrossRef]
37. Perdew, J.P.; Burke, K.; Ernzerhof, M. Generalized Gradient Approximation Made Simple. *Phys. Rev. Lett.* **1996**, *77*, 3865–3868. [CrossRef]
38. Troullier, N.; Martins, J.L. Efficient pseudopotentials for plane-wave calculations. *Phys. Rev. B* **1991**, *43*, 1993–2006. [CrossRef]
39. Golesorkhtabar, R.; Pavone, P.; Spitaler, J.; Puschnig, P.; Draxl, C.ElaStic: A tool for calculating second-order elastic constants from first principles. *Comput. Phys. Commun.* **2013**, *184*, 1861–1873. [CrossRef]
40. Nosé, S. A unified formulation of the constant temperature molecular dynamics methods. *J. Chem. Phys.* **1984**, *81*, 511. [CrossRef]
41. Lindemann, F.A. The calculation of molecular vibration frequencies. *Phys. Z.* **1910**, *11*, 609.
42. Andrew, R.C.; Mapasha, R.E.; Ukpong, A.M.; Chetty, N. Mechanical properties of graphene and boronitrene. *Phys. Rev. B* **2012**, *85*, 125428. [CrossRef]
43. Zhang, Z.; Yang, Y.; Penev, E.S.; Yakobson, B.I. Elasticity, Flexibility, and Ideal Strength of Borophenes. *Adv. Func. Mater.* **2017**, *27*, 1605059. [CrossRef]
44. Zhong, H.; Huang, K.; Yu, G.; Yuan, S. Electronic and mechanical properties of few-layer borophene. *Phys. Rev. B* **2018**, *98*, 054104. [CrossRef]
45. Mannix, A.J.; Zhou, X.F.; Kiraly, B.; Wood, J.D.; Alducin, D.; Myers, B.D.; Liu, X.; Fisher, B.L.; Santiago, U.; Guest, J.R.; et al. Synthesis of borophenes: Anisotropic, two-dimensional boron polymorphs. *Science* **2015**, *350*, 1513–1516. [CrossRef]
46. Wang, H.; Li, Q.; Gao, Y.; Miao, F.; Zhou, X.-F.; Wan, X.G. Strain effects on borophene: Ideal strength, negative Possion's ratio and phonon instability. *New J. Phys.* **2016**, *18*, 073016. [CrossRef]
47. De la Pena-Seaman, O.; de Cross, R.; Heid, R.; Bohnen, K.-P. Effects of Al and C doping on the electronic structure and phonon renormalization in $MgB_2$. *Phys. Rev. B* **2009**, *79*, 134523. [CrossRef]
48. Ponce, S.; Margine E.R., Verdi, C.; Giustino, F. EPW: Electron-phonon coupling, transport and superconducting properties using maximally localized Wannier functions. *Comp. Phys. Commun.* **2016**, *209*, 116–133. [CrossRef]

49. Margine, E.R.; Giustino, F. Anisotropic Migdal-Eliashberg theory using Wannier functions. *Phys. Rev. B* **2013**, *87*, 024505. [CrossRef]
50. Damljanovic, V.; Gajic, R. Existence of Dirac cones in the Brillouin zone of diperiodic atomic crystals according to group theory. *J. Phys. Condens. Matter* **2016**, *28*, 085502. [CrossRef]
51. Damljanovic, V.; Gajic, R. Addendum to 'Existence of Dirac cones in the Brillouin zone of diperiodic atomic crystals according to group theory'. *J. Phys. Condens. Matter* **2016**, *28*, 439401. [CrossRef]
52. Poulet, H.; Mathieu, J.P. *Vibration Spectra and Symmetry of Crystals*; Gordon and Breach: New York, NY, USA, 1976.
53. Szalowski, K. Critical temperature of $MgB_2$ ultrathin superconducting films: BCS model calculations in the tight-binding approximation. *Phys. Rev. B* **2006**, *74*, 094501. [CrossRef]
54. Zhang, C.; Wang, Y.; Wang, D.; Zhang, Y.; Liu, Z.-H.; Feng, Q.-R.; Gan, Z.-Z. Suppression of superconductivity in epitaxial MgB2 ultrathin films. *J. Appl. Phys.* **2013**, *114*, 023903. [CrossRef]
55. Ao, B.; Zhang, Z.; Tang, T.; Zhao, Y. Potential enhancement of superconductivity in $MgB_2$ nanosheets: First-principles calculations. *Chem. Phys. Lett.* **2014**, *591*, 185–188. [CrossRef]
56. Romero-Bermudez, A.; Garcıa-Garcıa, A.M. Shape resonances and shell effects in thin-film multiband superconductors. *Phys. Rev. B* **2014**, *89*, 024510. [CrossRef]
57. Romero-Bermudez, A.; Garcıa-Garcıa, A.M. Size effects in superconducting thin films coupled to a substrate. *Phys. Rev. B* **2014**, *89*, 064508. [CrossRef]
58. Acharya, N.; Wolak, M.A.; Cunnane, D.P.; Karasik, B.S.; Xi, X.X. MgB2 ultrathin films fabricated by hybrid physical chemical vapor deposition and ion milling. *APL Mater.* **2016**, *4*, 086114. [CrossRef]
59. Valentinis, D.; van der Marel, D.; Berthod, C. Rise and fall of shape resonances in thin films of BCS superconductors. *Phys. Rev. B* **2016**, *94*, 054516. [CrossRef]
60. Narlikar, A.V. Small Superconductors: Introduction. In *The Oxford Handbook of Small Superconductors*, 1st ed.; Narlikar, A.V., Ed.; Oxford University Press: Oxford, UK, 2017.
61. Gariglio, S.; Scheurer, M.; Schmalian, J.; Monteiro, A.M.R.V.L.; Goswami, S.; Caviglia, A. Surface and Interface Superconductivity. In *The Oxford Handbook of Small Superconductors*, 1st ed.; Narlikar, A.V., Ed.; Oxford University Press: Oxford, UK, 2017.


# Lattice dynamics and phase transitions in $Fe_{3-x}GeTe_2$

A. Milosavljević,[1] A. Šolajić,[1] S. Djurdjić-Mijin,[1] J. Pešić,[1] B. Višić,[1] Yu Liu (刘育),[2] C. Petrovic,[2] N. Lazarević,[1] and Z. V. Popović[1,3]

[1]*Center for Solid State Physics and New Materials, Institute of Physics Belgrade, University of Belgrade, Pregrevica 118, 11080 Belgrade, Serbia*

[2]*Condensed Matter Physics and Materials Science Department, Brookhaven National Laboratory, Upton, New York 11973-5000, USA*

[3]*Serbian Academy of Sciences and Arts, Knez Mihailova 35, 11000 Belgrade, Serbia*

(Received 23 April 2019; published 17 June 2019)

We present Raman spectroscopy measurements of the van der Waals bonded ferromagnet $Fe_{3-x}GeTe_2$, together with lattice dynamics. Four out of eight Raman active modes are observed and assigned, in agreement with numerical calculations. The energies and linewidths of the observed modes display an unconventional temperature dependence at about 150 and 220 K, followed by the nonmonotonic evolution of the Raman continuum. Whereas the former can be related to the magnetic phase transition, the origin of the latter anomaly remains an open question.

DOI: 10.1103/PhysRevB.99.214304

## I. INTRODUCTION

A novel class of magnetism hosting van der Waals bonded materials has recently become of great interest, since the materials are suitable candidates for numbers of technical applications [1–5]. Whereas $CrXTe_3$ ($X$ = Si, Ge, Sn) and $CrX_3$ ($X$ = Cl, Br, I) classes maintain low phase transition temperatures [1,6–9] even in a monolayer regime [10], $Fe_{3-x}GeTe_2$ has a high bulk transition temperature, between 220 and 230 K [11,12], making it a promising applicant.

The $Fe_{3-x}GeTe_2$ crystal structure consists of $Fe_{3-x}Ge$ sublayers stacked between two sheets of Te atoms, and a van der Waals gap between neighboring Te layers [13,14]. Although the structure contains two different types of Fe atoms, it is revealed that vacancies take place only in the Fe2 sites [13,15].

Neutron diffraction, thermodynamic and transport measurements, and Mössbauer spectroscopy were used to analyze the magnetic and functional properties of $Fe_{3-x}GeTe_2$, with an Fe atom deficiency of $x \approx 0.1$ and $T_C = 225$ K. It is revealed that at a temperature of 1.5 K, magnetic moments of $1.95(5)\mu_B$ and $1.56(4)\mu_B$ are directed along the easy magnetic $c$ axes [16]. In chemical vapor transport (CVT) grown $Fe_3GeTe_2$ single crystals, besides the ferromagnetic (FM)-paramagnetic (PM) transition at a temperature of 214 K, FM layers order antiferromagnetically at 152 K [17]. Close to a ferromagnetic transition temperature of 230 K, a possible Kondo lattice behavior, i.e., coupling of traveling electrons and periodically localized spins, is indicated at $T_K = 190 \pm 20$ K, which is in good agreement with theoretical predictions of 222 K [18].

Lattice parameters, as well as the magnetic transition temperature, vary with Fe ion concentration. Lattice parameters $a$ and $c$ follow the opposite trend, whereas the Curie temperature $T_C$ decreases with an increase of Fe ion concentration [15]. For flux-grown crystals, the critical behavior was investigated by bulk dc magnetization around the ferromagnetic phase transition temperature of 152 K [13]. The anomalous Hall effect was also studied, where a significant amount of defects produces bad metallic behavior [19].

Theoretical calculations predict a dynamical stability of $Fe_3GeTe_2$ single-layer, uniaxial magnetocrystalline anisotropy that originates from spin-orbit coupling [20]. Recently, anomalous Hall effect measurements on single-crystalline metallic $Fe_3GeTe_2$ nanoflakes with different thicknesses are reported, with a $T_C$ near 200 K and strong perpendicular magnetic anisotropy [21].

We report $Fe_{3-x}GeTe_2$ single-crystal lattice dynamic calculations, together with Raman spectroscopy measurements. Four out of eight Raman active modes were observed and assigned. Phonon energies are in a good agreement with theoretical predictions. Analyzed phonon energies and linewidths reveal fingerprint of a ferromagnetic phase transition at a temperature around 150 K. Moreover, discontinuities in the phonon properties are found at temperatures around 220 K. Consistently, in the same temperature range, the Raman continuum displays nonmonotonic behavior.

## II. EXPERIMENT AND NUMERICAL METHOD

$Fe_{3-x}GeTe_2$ single crystals were grown by the self-flux method as previously described [13]. Samples for scanning electron microscopy (SEM) were cleaved and deposited on graphite tape. Energy dispersive spectroscopy (EDS) maps were collected using a FEI Helios NanoLab 650 instrument equipped with an Oxford Instruments EDS system, equipped with an X-max SSD detector operating at 20 kV. The surface of the as-cleaved $Fe_{3-x}GeTe_2$ crystal appears to be uniform for several tens of microns in both directions, as shown in Fig. 4 of Appendix A. Additionally, the elemental composition maps of Fe, Ge, and Te show a distinctive homogeneity of all the three elements (Fig. 5 of Appendix A).

For Raman scattering experiments, a Tri Vista 557 spectrometer was used in the backscattering micro-Raman configuration. As an excitation source, a solid state laser with a 532 nm line was used. In our scattering configuration, the plane of incidence is the $ab$ plane, where $|a| = |b|$ ($\measuredangle(a, b) = 120°$), with the incident (scattered) light propagation direction

 

TABLE I. Top panel: The type of atoms, Wyckoff positions, each site's contribution to the phonons in the Γ point, and corresponding Raman tensors for the $P6_3/mmc$ space group of $Fe_{3-x}GeTe_2$. Bottom panel: Phonon symmetry, calculated optical Raman active phonon frequencies (in $cm^{-1}$) for the magnetic (M) phase, and experimental values for Raman active phonons at 80 K.

Space group $P6_3/mmc$ (No. 194)

| | |
|---|---|
| Fe1 (4*e*) | $A_{1g} + E_{1g} + E_{2g} + A_{2u} + E_{1u}$ |
| Fe2 (2*c*) | $E_{2g} + A_{2u} + E_{1u}$ |
| Ge (2*d*) | $E_{2g} + A_{2u} + E_{1u}$ |
| Te (2*c*) | $A_{1g} + E_{1g} + E_{2g} + A_{2u} + E_{1u}$ |

Raman tensors

$$A_{1g} = \begin{pmatrix} a & 0 & 0 \\ 0 & a & 0 \\ 0 & 0 & b \end{pmatrix} \quad E_{1g} = \begin{pmatrix} 0 & 0 & -c \\ 0 & 0 & c \\ -c & c & 0 \end{pmatrix} \quad E_{2g} = \begin{pmatrix} d & -d & 0 \\ -d & -d & 0 \\ 0 & 0 & 0 \end{pmatrix}$$

Raman active modes

| Symmetry | Calculations (M) | Experiment (M) |
|---|---|---|
| $E^1_{2g}$ | 50.2 | |
| $E^1_{1g}$ | 70.3 | |
| $E^2_{2g}$ | 122.2 | 89.2 |
| $A^1_{1g}$ | 137.2 | 121.1 |
| $E^2_{1g}$ | 209.5 | |
| $E^3_{2g}$ | 228.6 | 214.8 |
| $A^2_{1g}$ | 233.4 | 239.6 |
| $E^4_{2g}$ | 334.3 | |

along the *c* axes. Samples were cleaved in the air, right before being placed in the vacuum. All the measurements were performed in the high vacuum ($10^{-6}$ mbar) using a KONTI CryoVac continuous helium flow cryostat with a 0.5 mm thick window. To achieve laser beam focusing, a microscope objective with ×50 magnification was used. A Bose factor correction of all spectra was performed. More details can be found in Appendix C.

Density functional theory (DFT) calculations were performed with the QUANTUM ESPRESSO (QE) software package [22]. We used the projector augmented-wave (PAW) pseudopotentials [23,24] with the Perdew-Burke-Ernzerhof (PBE) exchange-correlation functional [25]. The electron wave function and charge density cutoffs of 64 and 782 Ry were chosen, respectively. The *k* points were sampled using the Monkhorst-Pack scheme, with an 8 × 8 × 4 Γ-centered grid. Both magnetic and nonmagnetic calculations were performed, using the experimentally obtained lattice parameters and the calculated values obtained by relaxing the theoretically proposed structure. In order to obtain the lattice parameters accurately, a treatment of the van der Waals interactions is introduced. The van der Waals interaction was included in all calculations using the Grimme-D2 correction [26]. Phonon frequencies in the Γ point are calculated within the linear response method implemented in QE.

## III. RESULTS AND DISCUSSION

$Fe_{3-x}GeTe_2$ crystallizes in a hexagonal crystal structure, described with the $P6_3/mmc$ ($D^4_{6h}$) space group. The atom type, site symmetry, each site's contribution to the phonons in the Γ point, and corresponding Raman tensors for the $P6_3/mmc$ space group are presented in Table I.

Calculated displacement patterns of Raman active modes, which can be observed in our scattering configuration, are presented in Fig. 1(a). Since the Raman tensor of the $E_{1g}$ mode contains only the *z* component (Table I), by selection rules, it cannot be detected when measuring from the *ab* plane in the backscattering configuration. Whereas $A_{1g}$ modes include vibrations of Fe and Te ions along the *c* axis, $E_{2g}$ modes include in-plane vibrations of all four atoms. The Raman spectra of $Fe_{3-x}GeTe_2$ in the magnetic phase (M), at 80 K, and nonmagnetic phase (NM), at 280 K, in a parallel scattering configuration ($\mathbf{e}_i \parallel \mathbf{e}_s$), are presented in Fig. 1 (b). As it can be seen, four peaks at 89.2, 121.1, 214.8, and 239.6 $cm^{-1}$ can be clearly observed at 80 K. According to numerical calculations (see Table I), peaks at 89.2 and 239.6 $cm^{-1}$ correspond to two out of four $E_{2g}$ modes, whereas peaks at 121.1 and 239.6 $cm^{-1}$ can be assigned as two $A_{1g}$ symmetry modes. One should note that numerical calculations performed by using experimentally obtained lattice parameters in the magnetic phase yield a better agreement with experimental values. This is not surprising since the calculations are performed for the stoichiometric compound as opposed to the nonstoichiometry of the sample. Furthermore, it is known that lattice parameters strongly depend on the Fe atom deficiency [15]. All calculated Raman and infrared phonon frequencies, for the magnetic and nonmagnetic phase of $Fe_{3-x}GeTe_2$, using relaxed and experimental lattice parameters, together with experimentally observed Raman active modes, are summarized in Table II of Appendix D.

After assigning all observed modes we focused on their temperature evolution. Having in mind finite instrumental

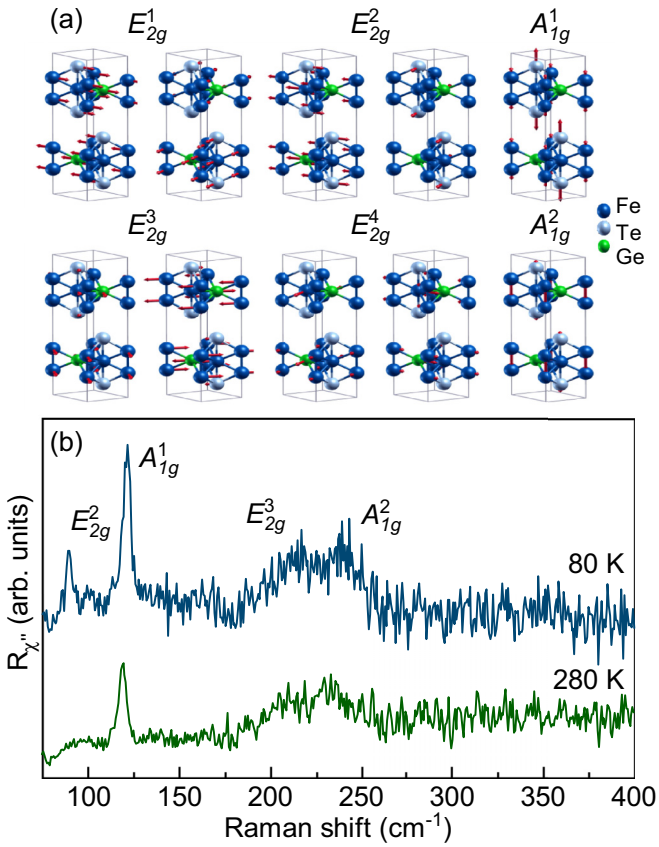


FIG. 1. (a) Displacement patterns of $A_{1g}$ and $E_{2g}$ symmetry modes. (b) Raman spectra of $Fe_{3-x}GeTe_2$ single crystal measured at different temperatures in a parallel polarization configuration.

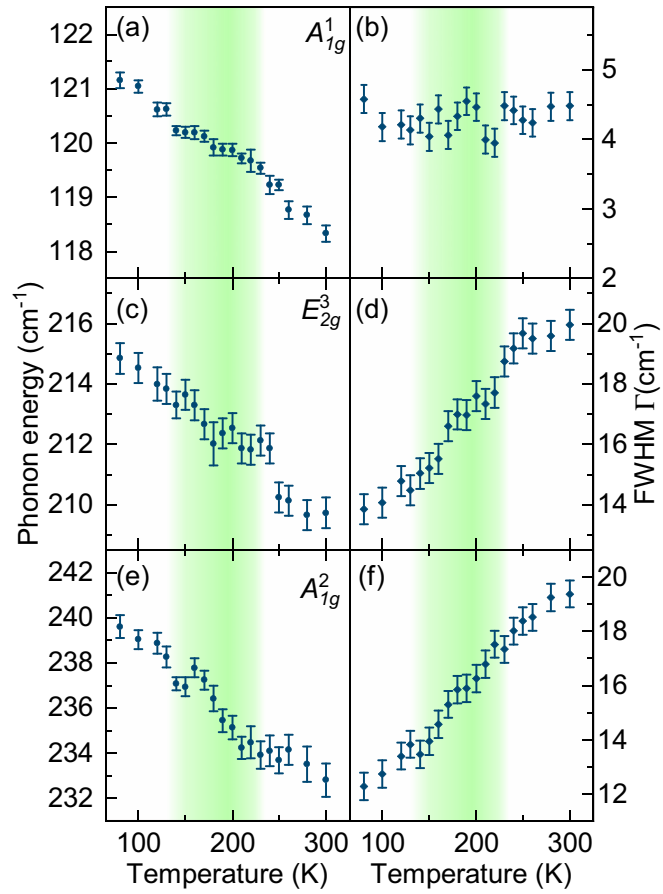


FIG. 2. Energy and linewidth temperature dependence of $A^1_{1g}$ [(a) and (b)], $E^3_{2g}$ [(c) and (d)], and $A^2_{1g}$ [(e) and (f)] phonon modes in $Fe_{3-x}GeTe_2$.

broadening, the Voigt line shape was used for the data analysis [27,28]. The modeling procedure is described in detail in Appendix B and presented in Fig. 6. Figure 2 shows the temperature evolution of the energy and linewidth of the $A^1_{1g}$, $E^3_{2g}$, and $A^2_{1g}$ modes between 80 and 300 K. Upon heating the sample, both the energy and linewidth of $A^1_{1g}$ and $A^2_{1g}$ symmetry modes exhibit a small but sudden discontinuity at about 150 K [Figs. 2(a) and 2(e)]. An apparent discontinuity in energy of all analyzed Raman modes is again present at temperatures around 220 K. In the same temperature range the linewidths of these Raman modes show a clear deviation from the standard anharmonic behavior [27–31].

Apart from the anomalies in the phonon spectra, a closer inspection of the temperature-dependent Raman spectra measured in the parallel polarization configuration reveals a pronounced evolution of the Raman continuum [Fig. 3(a)]. For the analysis we have used a simple model including a damped Lorentzian and linear term, $\chi''_{\text{cont}} \propto a\Gamma\omega/(\omega^2 + \Gamma^2) + b\omega$ [32], where $a$, $b$, and $\Gamma$ are temperature-dependent parameters. Figure 3(b) summarizes the results of the analysis with the linear term omitted (most likely originating from a luminescence). At approximately the same temperatures, where phonon properties exhibit discontinuities, the continuum temperature dependence manifests nonmonotonic behavior. The maximum positions of the curve were obtained by integrating those shown in Fig. 3(b). The inset of Fig. 3(b) shows the temperature evolution of their displacements. This analysis confirms the presence of discontinuities in the electronic continuum at temperatures around 150 and 220 K, which leaves a trace in the phonon behavior around these temperatures (Fig. 2). While we do not have evidence for the Kondo effect in the $Fe_{3-x}GeTe_2$ crystals we measured, a modification of the electronic background at FM ordering due to localization or the Kondo effect cannot be excluded.

The temperature evolutions of the phonon self-energies and the continuum observed in the Raman spectra of $Fe_{3-x}GeTe_2$ suggest the presence of phase transition(s). Magnetization measurements of the samples were performed as described in Ref. [13], revealing a FM-PM transition at 150 K. Thus, the discontinuity in the observed phonon properties around this temperature can be traced back to the weak to moderate spin-phonon coupling. The question remains open regarding the anomaly observed at about 220 K. As previously reported, the Curie temperature of the $Fe_{3-x}GeTe_2$ single crystals grown by the CVT method is between 220 and 230 K [11,12,14], varying with the vacancy concentration, i.e., a decrease in the vacancy content will result an increment of $T_C$ [15]. On the other hand, the $Fe_{3-x}GeTe_2$ crystals grown by the self-flux method usually have a lower Curie temperature, since the

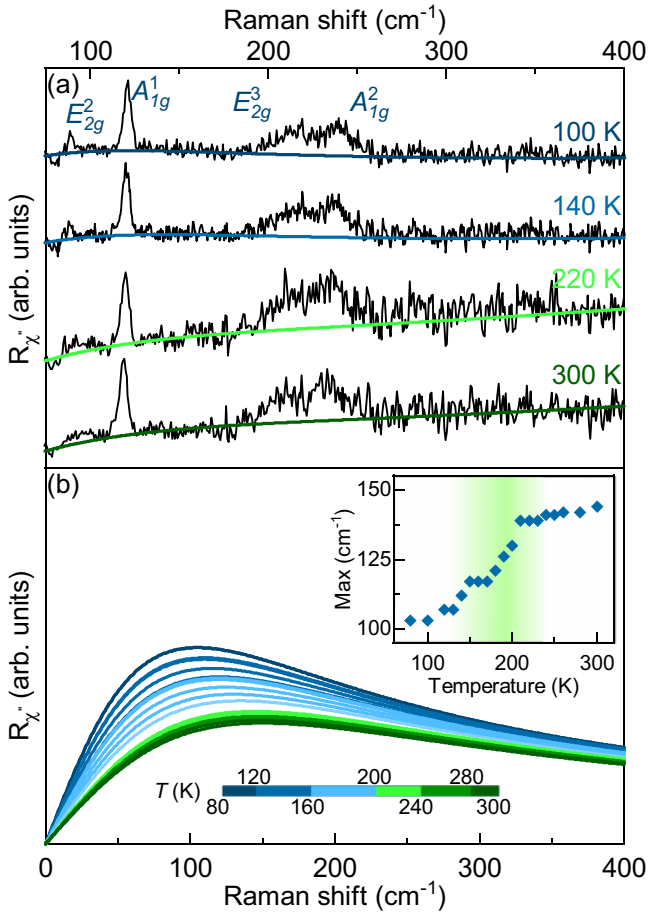


FIG. 3. (a) Raman spectra of $Fe_{3-x}GeTe_2$ at four temperatures measured in a parallel polarization configuration. Solid lines represent the theoretical fit to the experimental data. (b) Temperature evolution of the electronic continuum after omitting the linear term. Inset: Displacement of the maximum of fitted curves.

vacancy content is higher [13,15]. Crystals used in the Raman scattering experiment presented here were grown by the self-flux method with a Fe vacancy content of $x \approx 0.36$ [13]. This is in good agreement with our EDS results of $x = 0.4 \pm 0.1$, giving rise to the FM-PM transition at 150 K. Nevertheless,

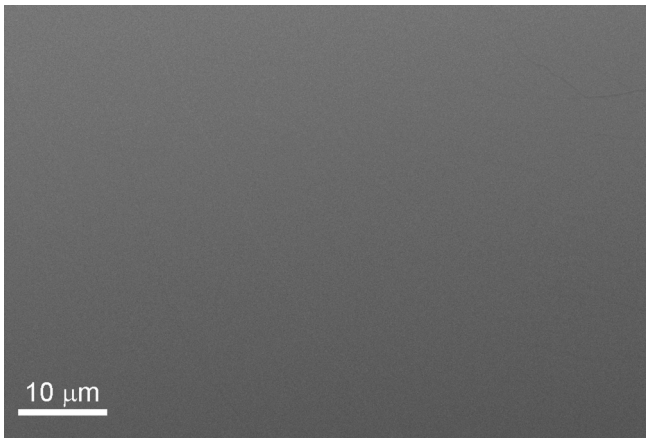


FIG. 4. SEM image of a $Fe_{3-x}GeTe_2$ single crystal.

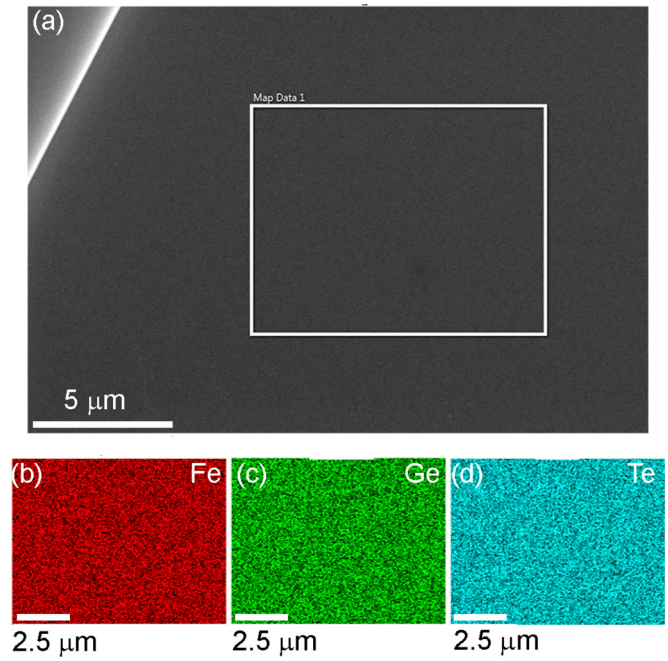


FIG. 5. EDS mapping on a $Fe_{3-x}GeTe_2$ single crystal. (a) Secondary electron image of the crystal with the mapping performed within the rectangle. (b)–(d) Associated EDS maps for Fe, Ge, and Te, respectively.

an inhomogeneous distribution of vacancies may result the formation of vacancy depleted "islands" which in turn would result in an anomaly at 220 K similar to the one observed in our Raman data. However, the EDS data (see Fig. 5) do not support this possibility. At this point we can only speculate that while the long-range order temperature is shifted to a lower temperature by the introduction of vacancies, short-range correlations may develop at 220 K.

## IV. CONCLUSION

We have studied the lattice dynamics of flux-grown $Fe_{3-x}GeTe_2$ single crystals by means of Raman spectroscopy and DFT. Four out of eight Raman active modes, two $A_{1g}$ and two $E_{2g}$, have been observed and assigned. DFT calculations are in good agreement with experimental results. The temperature dependence of the $A^1_{1g}$, $E^3_{2g}$, and $A^2_{1g}$ mode properties reveals a clear fingerprint of spin-phonon coupling, at a temperature of around 150 K. Furthermore, the anomalous behavior in the energies and linewidths of the observed phonon modes is present in the Raman spectra at temperatures around 220 K with the discontinuity also present in the electronic continuum. Its origin still remains an open question, and requires further analysis.

## ACKNOWLEDGMENTS

The work was supported by the Serbian Ministry of Education, Science and Technological Development under Projects No. III45018 and No. OI171005. DFT calculations were performed using computational resources at Johannes Kepler University, Linz, Austria. Materials synthesis was supported

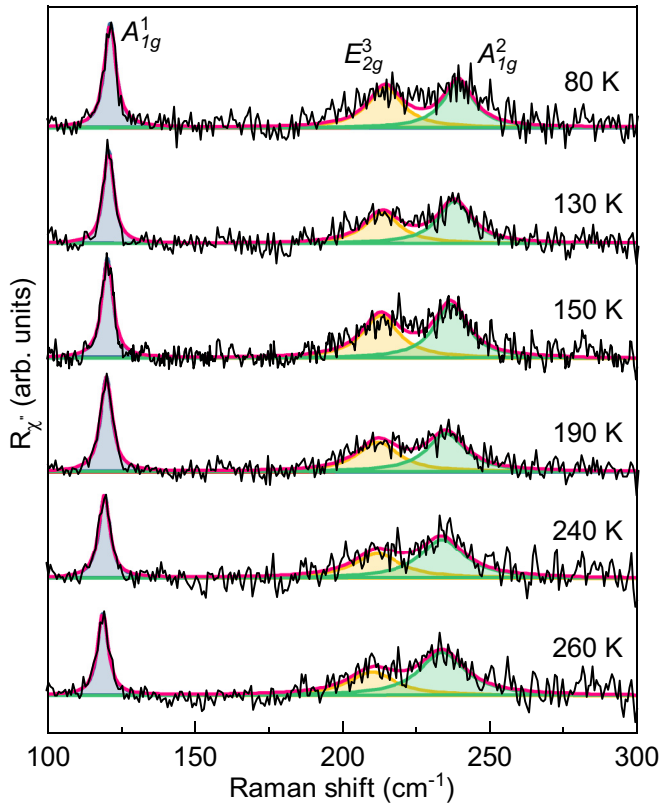


FIG. 6. Modeled Raman spectra of $Fe_{3-x}GeTe_2$ single crystal, after subtracting continuum contributions, obtained at various temperatures. For experimental data modeling, the Voigt line shape was used.

TABLE II. Top panel: Comparison of calculated energies of Raman active phonons using relaxed (R) and experimental [nonrelaxed (NR)] lattice parameters for the magnetic (M) and nonmagnetic phase (NM), given in cm$^{-1}$. Obtained experimental values in the magnetic phase at a temperature of 80 K are given in the last column. Bottom panel: Comparison of calculated energies of infrared optical phonons of $Fe_{3-x}GeTe_2$.

| Raman active modes | | | | | |
|---|---|---|---|---|---|
| | Calculations | | | | |
| Sym. | NM-R | M-R | NM-NR | M-NR | Experiment (M) |
| $E^1_{2g}$ | 28.4 | 49.6 | 33.9 | 50.2 | |
| $E^1_{1g}$ | 79.2 | 70.2 | 71.7 | 70.3 | |
| $E^2_{2g}$ | 115.5 | 121.0 | 100.0 | 122.2 | 89.2 |
| $A^1_{1g}$ | 151.7 | 139.2 | 131.7 | 137.2 | 121.1 |
| $E^2_{1g}$ | 225.5 | 206.0 | 194.3 | 209.5 | |
| $E^3_{2g}$ | 238.0 | 232.6 | 204.9 | 228.6 | 214.8 |
| $A^2_{1g}$ | 272.0 | 262.6 | 235.7 | 233.4 | 239.6 |
| $E^4_{2g}$ | 362.0 | 337.6 | 315.4 | 334.7 | |
| Infrared active modes | | | | | |
| $A^1_{2u}$ | 70.7 | 96.6 | 73.5 | 92.7 | |
| $E^1_{1u}$ | 112.5 | 121.2 | 89.4 | 121.6 | |
| $A^2_{2u}$ | 206.0 | 162.5 | 183.1 | 153.7 | |
| $E^2_{1u}$ | 226.4 | 233.6 | 192.1 | 231.3 | |
| $A^3_{2u}$ | 271.8 | 248.6 | 240.8 | 241.0 | |
| $E^3_{1u}$ | 361.1 | 336.6 | 314.7 | 334.7 | |

by the US Department of Energy, Office of Basic Energy Sciences as part of the Computation Material Science Program (Y.L. and C.P.). Electron microscopy was performed at Jozef Stefan Institute, Ljubljana, Slovenia under Slovenian Research Agency Contract No. P1-0099 (B.V.). This work has received funding from the European Union's Horizon 2020 research and innovation program under the Marie Sklodowska-Curie Grant Agreement No. 645658 (DAFNEOX Project).

## APPENDIX A: ELECTRON MICROSCOPY

In order to examine the uniformity of $Fe_{3-x}GeTe_2$, Scanning electron microscopy (SEM) was performed on as-cleaved crystals. It can be seen from Fig. 4 that the crystals maintain uniformity for several tens of microns. Furthermore, the elemental composition was obtained using EDS mapping, as shown in Fig. 5. The atomic percentage, averaged over ten measurements, is 47%, 17%, and 36% (±2%) for Fe, Ge, and Te, respectively, with the vacancy content $x = 0.4 \pm 0.1$. The maps associated with the selected elements appear homogeneous, as they are all present uniformly with no apparent islands or vacancies.

## APPENDIX B: DATA MODELING

In order to obtain the temperature dependence of the energies and linewidths of the observed $Fe_{3-x}GeTe_2$ phonon modes, the Raman continuum, shown in colored lines in Fig. 3(a), was subtracted for simplicity from the raw Raman susceptibility data (black line). The spectra obtained after the subtraction procedure are presented in Fig. 6 (black line) for various temperatures. Because of the finite resolution of the spectrometer and the fact that line shapes of all the observed phonons are symmetric, the Voigt line shape ($\Gamma_G = 0.8$ cm$^{-1}$) was used for data modeling. Blue, yellow, and green lines in Fig. 6 represent fitting curves for $A^1_{1g}$, $E^3_{2g}$, and $A^2_{1g}$ phonon modes, respectively, whereas the overall spectral shape is shown in the red line.

## APPENDIX C: EXPERIMENTAL DETAILS

Before being placed in a vacuum and being cleaved, the sample was glued to a copper plate with GE varnish in order to achieve good thermal conductivity and prevent strain effects. Silver paste, as a material with high thermal conductivity, was used to attach the copper plate with the sample to the cryostat. The laser beam spot, focused through an Olympus long-range objective of × 50 magnification, was approximately 6 $\mu$m in size, with a power less than 1 mW at the sample surface. A TriVista 557 triple spectrometer was used in the subtractive mode, with a diffraction grating combination of 1800/1800/2400 grooves/mm and the entrance and second intermediate slit set to 80 $\mu$m, in order to enhance stray light rejection and attain good resolution.

## APPENDIX D: CALCULATIONS

In Table II the results of DFT calculations are presented for magnetic (M) and nonmagnetic (NM) relaxed and experimental lattice parameters. For comparison, the experimental results are shown in the last column. Since the lattice parameters strongly depend on the Fe atom deficiency, the best agreement with experimental results gives the magnetic nonrelaxed solution.


[1] N. Sivadas, M. W. Daniels, R. H. Swendsen, S. Okamoto, and D. Xiao, Magnetic ground state of semiconducting transition-metal trichalcogenide monolayers, Phys. Rev. B **91**, 235425 (2015).

[2] K. S. Novoselov, A. K. Geim, S. V. Morozov, D. Jiang, Y. Zhang, S. V. Dubonos, I. V. Grigorieva, and A. A. Firsov, Electric field rffect in atomically thin carbon films, Science **306**, 666 (2004).

[3] Q. H. Wang, K. Kalantar-Zadeh, A. Kis, J. N. Coleman, and M. S. Strano, Electronics and optoelectronics of two-dimensional transition metal dichalcogenides, Nat. Nanotechnol. **7**, 699 (2012).

[4] C. Gong, L. Li, Z. Li, H. Ji, A. Stern, Y. Xia, T. Cao, W. Bao, C. Wang, Y. Wang, Z. Q. Qiu, R. J. Cava, S. G. Louie, J. Xia, and X. Zhang, Discovery of intrinsic ferromagnetism in two-dimensional van der Waals crystals, Nature (London) **546**, 265 (2017).

[5] B. Huang, G. Clark, E. Navarro-Moratalla, D. R. Klein, R. Cheng, K. L. Seyler, D. Zhong, E. Schmidgall, M. A. McGuire, D. H. Cobden, W. Yao, D. Xiao, P. Jarillo-Herrero, and X. Xu, Layer-dependent ferromagnetism in a van der Waals crystal down to the monolayer limit, Nature (London) **546**, 270 (2017).

[6] M. A. McGuire, H. Dixit, V. R. Cooper, and B. C. Sales, Coupling of crystal structure and magnetism in the layered, ferromagnetic insulator $CrI_3$, Chem. Mater. **27**, 612 (2015).

[7] H. L. Zhuang, Y. Xie, P. R. C. Kent, and P. Ganesh, Computational discovery of ferromagnetic semiconducting single-layer $CrSnTe_3$, Phys. Rev. B **92**, 035407 (2015).

[8] G. T. Lin, H. L. Zhuang, X. Luo, B. J. Liu, F. C. Chen, J. Yan, Y. Sun, J. Zhou, W. J. Lu, P. Tong, Z. G. Sheng, Z. Qu, W. H. Song, X. B. Zhu, and Y. P. Sun, Tricritical behavior of the two-dimensional intrinsically ferromagnetic semiconductor $CrGeTe_3$, Phys. Rev. B **95**, 245212 (2017).

[9] L. D. Casto, A. J. Clune, M. O. Yokosuk, J. L. Musfeldt, T. J. Williams, H. L. Zhuang, M.-W. Lin, K. Xiao, R. G. Hennig, B. C. Sales, J.-Q. Yan, and D. Mandrus, Strong spin-lattice coupling in $CrSiTe_3$, APL Mater. **3**, 041515 (2015).

[10] M.-W. Lin, H. L. Zhuang, J. Yan, T. Z. Ward, A. A. Puretzky, C. M. Rouleau, Z. Gai, L. Liang, V. Meunier, B. G. Sumpter, P. Ganesh, P. R. C. Kent, D. B. Geohegan, D. G. Mandrus, and K. Xiao, Ultrathin nanosheets of $CrSiTe_3$: A semiconducting two-dimensional ferromagnetic material, J. Mater. Chem. C **4**, 315 (2016).

[11] J.-X. Zhu, M. Janoschek, D. S. Chaves, J. C. Cezar, T. Durakiewicz, F. Ronning, Y. Sassa, M. Mansson, B. L. Scott, N. Wakeham, E. D. Bauer, and J. D. Thompson, Electronic correlation and magnetism in the ferromagnetic metal $Fe_3GeTe_2$, Phys. Rev. B **93**, 144404 (2016).

[12] B. Chen, J. H. Yang, H. D. Wang, M. Imai, H. Ohta, C. Michioka, K. Yoshimura, and M. H. Fang, Magnetic properties of layered itinerant electron ferromagnet $Fe_3GeTe_2$, J. Phys. Soc. Jpn. **82**, 124711 (2013).

[13] Y. Liu, V. N. Ivanovski, and C. Petrovic, Critical behavior of the van der Waals bonded ferromagnet $Fe_{3-x}GeTe_2$, Phys. Rev. B **96**, 144429 (2017).

[14] H.-J. Deiseroth, K. Aleksandrov, C. Reiner, L. Kienle, and R. K. Kremer, $Fe_3GeTe_2$ and $Ni_3GeTe_2$ - Two new layered transition-metal compounds: Crystal structures, HRTEM investigations, and magnetic and electrical properties, Eur. J. Inorg. Chem. **2006**, 1561 (2006).

[15] A. F. May, S. Calder, C. Cantoni, H. Cao, and M. A. McGuire, Magnetic structure and phase stability of the van der Waals bonded ferromagnet $Fe_{3-x}GeTe_2$, Phys. Rev. B **93**, 014411 (2016).

[16] V. Yu. Verchenko, A. A. Tsirlin, A. V. Sobolev, I. A. Presniakov, and A. V. Shevelkov, Ferromagnetic order, strong magnetocrystalline anisotropy, and magnetocaloric effect in the layered telluride $Fe_{3-\delta}GeTe_2$, Inorg. Chem. **54**, 8598 (2015).

[17] J. Yi, H. Zhuang, Q. Zou, Z. Wu, G. Cao, S. Tang, S. A. Calder, P. R. C. Kent, D. Mandrus, and Z. Gai, Competing antiferromagnetism in a quasi-2D itinerant ferromagnet: $Fe_3GeTe_2$, 2D Mater. **4**, 011005 (2016).

[18] Y. Zhang, H. Lu, X. Zhu, S. Tan, W. Feng, Q. Liu, W. Zhang, Q. Chen, Y. Liu, X. Luo, D. Xie, L. Luo, Z. Zhang, and X. Lai, Emergence of Kondo lattice behavior in a van der Waals itinerant ferromagnet, $Fe_3GeTe_2$, Sci. Adv. **4**, eaao6791 (2018).

[19] Y. Liu, E. Stavitski, K. Attenkofer, and C. Petrovic, Anomalous Hall effect in the van der Waals bonded ferromagnet $Fe_{3-x}GeTe_2$, Phys. Rev. B **97**, 165415 (2018).

[20] H. L. Zhuang, P. R. C. Kent, and R. G. Hennig, Strong anisotropy and magnetostriction in the two-dimensional Stoner ferromagnet $Fe_3GeTe_2$, Phys. Rev. B **93**, 134407 (2016).

[21] C. Tan, J. Lee, S.-G. Jung, T. Park, S. Albarakati, J. Partridge, M. R. Field, D. G. McCulloch, L. Wang, and C. Lee, Hard magnetic properties in nanoflake van der Waals $Fe_3GeTe_2$, Nat. Commun. **9**, 1554 (2018).

[22] P. Giannozzi *et al.*, QUANTUM ESPRESSO: A modular and open-source software project for quantum simulations of materials, J. Phys.: Condens. Matter **21**, 395502 (2009).

[23] P. E. Blöchl, Projector augmented-wave method, Phys. Rev. B **50**, 17953 (1994).

[24] G. Kresse and D. Joubert, From ultrasoft pseudopotentials to the projector augmented-wave method, Phys. Rev. B **59**, 1758 (1999).

[25] J. P. Perdew, K. Burke, and M. Ernzerhof, Generalized Gradient Approximation Made Simple, Phys. Rev. Lett. **77**, 3865 (1996).

[26] S. Grimme, Semiempirical GGA-type density functional constructed with a long-range dispersion correction, J. Comput. Chem. **27**, 1787 (2006).

[27] A. Milosavljević, A. Šolajić, J. Pešić, Y. Liu, C. Petrovic, N. Lazarević, and Z. V. Popović, Evidence of spin-phonon coupling in $CrSiTe_3$, Phys. Rev. B **98**, 104306 (2018).

[28] A. Baum, A. Milosavljević, N. Lazarević, M. M. Radonjić, B. Nikolić, M. Mitschek, Z. I. Maranloo, M. Šćepanović, M. Grujić-Brojčin, N. Stojilović, M. Opel, A. Wang,

C. Petrovic, Z. V. Popović, and R. Hackl, Phonon anomalies in FeS, Phys. Rev. B **97**, 054306 (2018).

[29] M. Opačić, N. Lazarević, M. M. Radonjić, M. Šćepanović, H. Ryu, A. Wang, D. Tanasković, C. Petrovic, and Z. V. Popović, Raman spectroscopy of $K_xK_{2-y}Se_2$ single crystals near the ferromagnet–paramagnet transition, J. Phys.: Condens. Matter **28**, 485401 (2016).

[30] Z. V. Popović, N. Lazarević, S. Bogdanović, M. M. Radonjić, D. Tanasković, R. Hu, H. Lei, and C. Petrovic, Signatures of the spin-phonon coupling in $Fe_{1+y}Te_{1-x}Se_x$ alloys, Solid State Commun. **193**, 51 (2014).

[31] Z. V. Popović, M. Šćepanović, N. Lazarević, M. Opačić, M. M. Radonjić, D. Tanasković, H. Lei, and C. Petrovic, Lattice dynamics of $BaFe_2X_3$ ($X$ = S, Se) compounds, Phys. Rev. B **91**, 064303 (2015).

[32] T. P. Devereaux and R. Hackl, Inelastic light scattering from correlated electrons, Rev. Mod. Phys. **79**, 175 (2007).

# Lattice dynamics and phase transition in $CrI_3$ single crystals

S. Djurdjić-Mijin,[1] A. Šolajić,[1] J. Pešić,[1] M. Šćepanović,[1] Y. Liu (刘育),[2] A. Baum,[3,4] C. Petrovic,[2] N. Lazarević,[1] and Z. V. Popović[1,5]

[1]*Center for Solid State Physics and New Materials, Institute of Physics Belgrade, University of Belgrade, Pregrevica 118, 11080 Belgrade, Serbia*

[2]*Condensed Matter Physics and Materials Science Department, Brookhaven National Laboratory, Upton, New York 11973-5000, USA*

[3]*Walther Meissner Institut, Bayerische Akademie der Wissenschaften, 85748 Garching, Germany*

[4]*Fakultät für Physik E23, Technische Universität München, 85748 Garching, Germany*

[5]*Serbian Academy of Sciences and Arts, Knez Mihailova 35, 11000 Belgrade, Serbia*

(Received 9 July 2018; published 18 September 2018; corrected 28 March 2019)

The vibrational properties of $CrI_3$ single crystals were investigated using Raman spectroscopy and were analyzed with respect to the changes of the crystal structure. All but one mode are observed for both the low-temperature $R\bar{3}$ and the high-temperature $C2/m$ phase. For all observed modes the energies and symmetries are in good agreement with DFT calculations. The symmetry of a single layer was identified as $p\bar{3}1/m$. In contrast to previous studies we observe the transition from the $R\bar{3}$ to the $C2/m$ phase at 180 K and find no evidence for coexistence of both phases over a wide temperature range.

DOI: 10.1103/PhysRevB.98.104307

## I. INTRODUCTION

Two-dimensional layered materials have gained attention due to their unique properties, the potential for a wide spectrum of applications, and the opportunity for the development of functional van der Waals heterostructures. $CrI_3$ is a member of the chromium-trihalide family which are ferromagnetic semiconductors [1]. Recently they have received significant attention as candidates for the study of magnetic monolayers. The experimental realization of $CrI_3$ ferromagnetic monolayers [1] motivated further efforts towards their understanding. $CrI_3$ features electric field controlled magnetism [2] as well as a strong magnetic anisotropy [3,4]. With the main absorption peaks lying in the visible part of the spectrum, it is a great candidate for low-dimensional semiconductor spintronics [5]. In its ground state, $CrI_3$ is a ferromagnetic semiconductor with a Curie temperature of 61 K [1,6] and a band gap of 1.2 eV [6]. It was demonstrated that the magnetic properties of $CrI_3$ mono- and bilayers can be controlled by electrostatic doping [2]. Upon cooling, $CrI_3$ undergoes a phase transition around 220 K from the high-temperature monoclinic ($C2/m$) to the low-temperature rhombohedral ($R\bar{3}$) phase [3,7]. Although the structural phase transition is reported to be first order, it was suggested that the phases may coexist over a wide temperature range [3]. Raman spectroscopy can be of use here due to its capability to simultaneously probe both phases in a phase-separated system [8–10].

A recent theoretical study predicted the energies of all Raman active modes in the low-temperature and high-temperature structure of $CrI_3$ suggesting a near degeneracy between the $A_g$ and $B_g$ modes in the monoclinic ($C2/m$) structure. Their energies match the energies of $E_g$ modes in the rhombohedral ($R\bar{3}$) structure [7].

In this article we present an experimental and theoretical Raman scattering study of $CrI_3$ lattice dynamics. In both phases all but one of the respective modes predicted by symmetry were observed. The energies for all modes are in good agreement with the theoretical predictions for the assumed crystal symmetry. Our data suggest that the first-order transition occurs at $T_s \approx 180$ K without evidence for phase coexistence over a wide temperature range.

## II. EXPERIMENT AND NUMERICAL METHOD

The preparation of the single crystal $CrI_3$ sample used in this study is described elsewhere [11]. The Raman scattering experiment was performed using a Tri Vista 557 spectrometer in backscattering micro-Raman configuration with a 1800/1800/2400 groves/mm diffraction grating combination. The 532 nm line of a Coherent Verdi G solid state laser was used for excitation. The direction of the incident light coincides with the crystallographic $c$ axis. The sample was oriented so that its principal axis of the $R\bar{3}$ phase coincides with the $x$ axis of the laboratory system. A KONTI CryoVac continuous helium flow cryostat with a 0.5-mm-thick window was used for measurements at all temperatures under high vacuum ($10^{-6}$ mbar). The sample was cleaved in air before being placed into the cryostat. The obtained Raman spectra were corrected by the Bose factor and analyzed quantitatively by fitting Voigt profiles to the data whereby the Gaussian width $\Gamma_{\text{Gauss}} = 1\ \text{cm}^{-1}$ reflects the resolution of the spectrometer.

The spin polarized density functional theory (DFT) calculations have been performed in the Quantum Espresso (QE) software package [12] using the Perdew-Burke-Ernzehof (PBE) exchange-correlation functional [13] and PAW pseudopotentials [14,15]. The energy cutoffs for the wave functions and the charge density were set to be 85 and 425 Ry, respectively, after convergence tests. For $k$-point sampling, the Monkhorst-Pack scheme was used with a $8 \times 8 \times 8$ grid centered around the $\Gamma$ point. Optimization of the atomic positions in the unit cell was performed until the interatomic forces

 

were smaller than $10^{-6}$ Ry/Å. To treat the van der Waals (vdW) interactions a Grimme-D2 correction [16] is used in order to include long-ranged forces between the layers, which are not properly captured within LDA or GGA functionals. This way, the parameters are obtained more accurately, especially the interlayer distances. Phonon frequencies were calculated at the Γ point using the linear response method implemented in QE. The phonon energies are compiled in Table III together with the experimental values. The eigenvectors of the Raman active modes for both the low- and high-temperature phase are depicted in Fig. 5 of the Appendix.

## III. RESULTS AND DISCUSSION

$CrI_3$ adopts a rhombohedral $R\bar{3}$ ($C_{3i}^2$) crystal structure at low temperatures and a monoclinic $C2/m$ ($C_{2h}^3$) crystal structure at room temperature [3], as shown in Fig. 1. The main difference between the high- and low-temperature crystallographic space groups arises from different stacking sequences with the $CrI_3$ layers being almost identical. In the rhombohedral structure the Cr atoms in one layer are placed above the center of a hole in the Cr honeycomb net of the two adjacent layers. When crossing the structural phase transition at $T_s$ to the monoclinic structure the layers are displaced along the $a$ direction so that every fourth layer is at the same place as the first one. The interatomic distances, mainly the interlayer distance, and the vdW gap, are slightly changed by the structural transition. The crystallographic parameters for both phases are presented in Table I. The numerically obtained values are in good agreement with reported x-ray diffraction data [11].

The vibrational properties of layered materials are typically dominated by the properties of the single layers composing the crystal. The symmetry of a single layer can be described by one of the 80 diperiodic space groups (DG) obtained by lifting translational invariance in the direction perpendicular to the layer [17]. In the case of $CrI_3$, the symmetry analysis revealed that the single layer structure is fully captured by the $p\bar{3}1/m$ ($D_{3d}^1$) diperiodic space group DG71, rather than by $R\bar{3}2/m$ as proposed in Ref. [7].

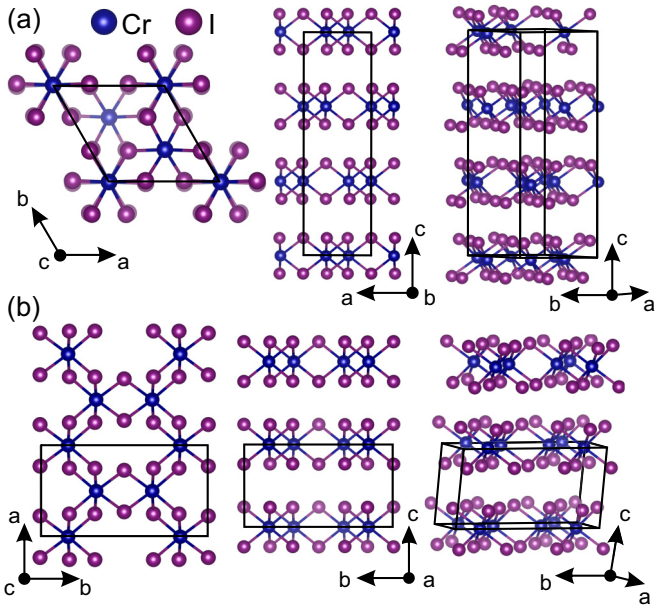


FIG. 1. Schematic representation of (a) the low-temperature $R\bar{3}$ and (b) the high-temperature $C2/m$ crystal structure of $CrI_3$. Black lines represent unit cells.

TABLE I. Calculated and experimental [11] parameters of the crystallographic unit cell for the low-temperature $R\bar{3}$ and high-temperature $C2/m$ phase of $CrI_3$.

| | Space group $R\bar{3}$ | | Space group $C2/m$ | |
|---|---|---|---|---|
| $T$ (K) | Calc. | Expt. [11] | Calc. | Expt. [11] |
| $a$ (Å) | 6.87 | 6.85 | 6.866 | 6.6866 |
| $b$ (Å) | 6.87 | 6.85 | 11.886 | 11.856 |
| $c$ (Å) | 19.81 | 19.85 | 6.984 | 6.966 |
| $\alpha$ (deg) | 90 | 90 | 90 | 90 |
| $\beta$ (deg) | 90 | 90 | 108.51 | 108.68 |
| $\gamma$ (deg) | 120 | 120 | 90 | 90 |

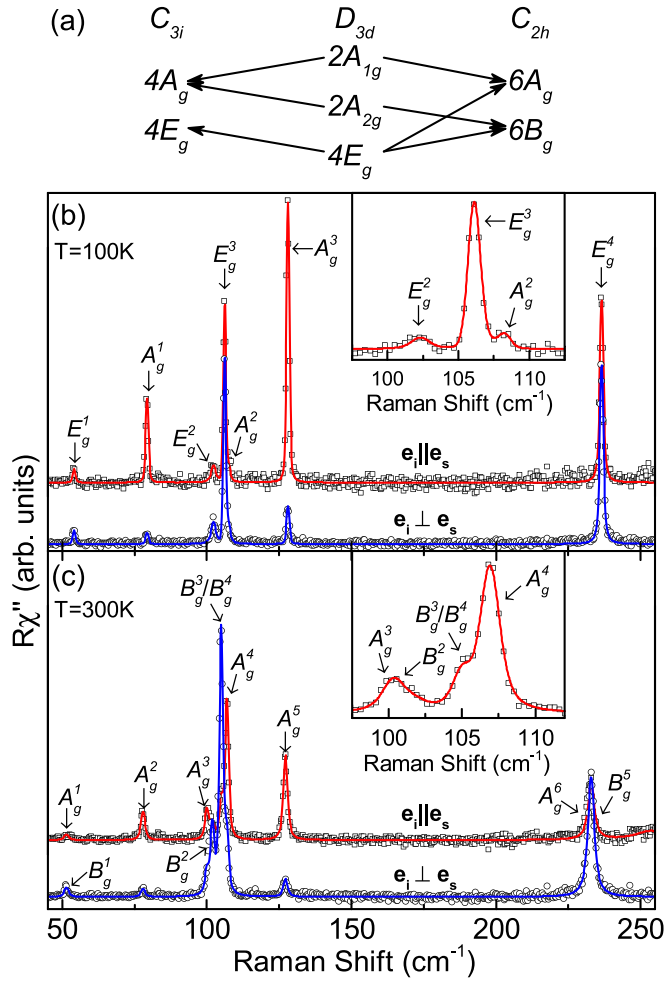


FIG. 2. (a) Compatibility relations for the $CrI_3$ layer and the crystal symmetries. Raman spectra of (b) the low-temperature $R\bar{3}$ and (c) the high-temperature $C2/m$ crystal structure measured in parallel (open squares) and crossed (open circles) polarization configurations at 100 and 300 K, respectively. Red and blue solid lines represent fits of Voigt profiles to the experimental data.

TABLE II. Wyckoff positions of the two types of atoms and their contributions to the Γ-point phonons for the $R\bar{3}$ and $C2/m$ as well as the $p\bar{3}1/m$ diperiodic space group. The second row shows the Raman tensors for the corresponding space groups.

| Space group $R\bar{3}$ | | Diperiodic space group $p\bar{3}1/m$ | | Space group: C2/$m$ | |
|---|---|---|---|---|---|
| Atoms | Irreducible representations | Atoms | Irreducible representations | Atoms | Irreducible representations |
| Cr (6$c$) | $A_g+A_u+E_g+E_u$ | Cr (2$c$) | $A_{2g}+A_{2u}+E_g+E_u$ | Cr (4$g$) | $A_g+A_u+2B_g+2B_u$ |
| I (18$f$) | $3A_g+3A_u+3E_g+3E_u$ | I (6$k$) | $2A_{1g}+A_{1u}+A_{2g}$ $+2A_{2u}+3E_g+3E_u$ | I (4$i$) | $2A_g+2A_u+B_g+B_u$ |
| | | | | I (8$j$) | $3A_g+3A_u+3B_g+3B_u$ |
| $A_g=\begin{pmatrix} a & & \\ & a & \\ & & b \end{pmatrix}$ | | $A_{1g}=\begin{pmatrix} a & & \\ & a & \\ & & b \end{pmatrix}$ | | $A_g=\begin{pmatrix} a & d & \\ & c & \\ d & & b \end{pmatrix}$ | |
| ${}^1E_g=\begin{pmatrix} c & d & e \\ d & -c & f \\ e & f & \end{pmatrix}$ | ${}^2E_g=\begin{pmatrix} d & -c & -f \\ -c & -d & e \\ -f & e & \end{pmatrix}$ | ${}^1E_g=\begin{pmatrix} c & & \\ & -c & d \\ & d & \end{pmatrix}$ | ${}^2E_g=\begin{pmatrix} & -c & -d \\ -c & & \\ -d & e & \end{pmatrix}$ | $B_g=\begin{pmatrix} & e & \\ e & & f \\ & f & \end{pmatrix}$ | |

According to the factor group analysis (FGA) for a single $CrI_3$ layer, six modes ($2A_{1g}+4E_g$) are expected to be observed in the Raman scattering experiment (see Table II). By stacking the layers the symmetry is reduced and, depending on the stacking sequence, FGA yields a total of eight Raman active modes ($4A_g+4E_g$) for the $R\bar{3}$ and 12 Raman active modes ($6A_g+6B_g$) for the $C2/m$ crystal symmetry. The correlation between layer and crystal symmetries for both cases is shown in Fig. 2(a) [18,19].

Figure 2(b) shows the $CrI_3$ single crystal Raman spectra measured at 100 K in two scattering channels. According to the selection rules for the rhombohedral crystal structure (Table II) the $A_g$ modes can be observed only in the parallel polarization configuration, whereas the $E_g$ modes appear in both parallel and crossed polarization configurations. Based on the selection rules the peaks at about 78, 108, and 128 $cm^{-1}$ were identified as $A_g$ symmetry modes, whereas the peaks at about 54, 102, 106, and 235 $cm^{-1}$ are assigned as $E_g$ symmetry. The weak observation of the most pronounced $A_g$ modes in crossed polarizations [Fig. 2(b)] is attributed to the leakage due to a slight sample misalignment and/or the presence of defects in the crystal. The energies of all observed modes are compiled in Table III together with the energies predicted by our calculations and by Ref. [7], and are found to be in good agreement for the $E_g$ modes. The discrepancy is slightly larger for the low energy $A_g$ modes. Our calculations in general agree with those from Ref. [7]. The $A_g^4$ mode of the rhombohedral phase, predicted by calculation to appears at about 195 $cm^{-1}$, was not observed in the experiment, most likely due to its low intensity.

When the symmetry is lowered in the high-temperature monoclinic $C2/m$ phase [Fig. 2(c)] the $E_g$ modes split into an $A_g$ and a $B_g$ mode each, whereas the rhombohedral $A_g^2$ and $A_g^4$ modes are predicted to switch to the monoclinic $B_g$ symmetry. The correspondence of the phonon modes across the phase transition is indicated by the arrows in Table III. The selection rules for $C2/m$ (see Table II) predict that $A_g$ and $B_g$ modes can be observed in both parallel and crossed polarization configurations. Additionally, the sample forms three types of domains which are rotated with respect to each other. We

TABLE III. Phonon symmetries and phonon energies for the low-temperature $R\bar{3}$ and high-temperature $C2/m$ phase of $CrI_3$. The experimental values were determined at 100 and 300 K, respectively. All calculations were performed at zero temperature. Arrows indicate the correspondence of the phonon modes across the phase transition.

| Space group $R\bar{3}$ | | | | | Space group C2/$m$ | | | |
|---|---|---|---|---|---|---|---|---|
| Symm. | Expt. ($cm^{-1}$) | Calc. ($cm^{-1}$) | Calc. ($cm^{-1}$) [7] | | Symm. | Expt. ($cm^{-1}$) | Calc. ($cm^{-1}$) | Calc. [7] ($cm^{-1}$) |
| $E_g^1$ | 54.1 | 59.7 | 53 | ⟶ | $B_g^1$ | 52.0 | 57.0 | 52 |
| | | | | ⟶ | $A_g^1$ | 53.6 | 59.8 | 51 |
| $A_g^1$ | 73.33 | 89.6 | 79 | ⟶ | $A_g^2$ | 78.6 | 88.4 | 79 |
| $E_g^2$ | 102.3 | 99.8 | 98 | ⟶ | $A_g^3$ | 101.8 | 101.9 | 99 |
| | | | | ⟶ | $B_g^2$ | 102.4 | 101.8 | 99 |
| $E_g^3$ | 106.2 | 112.2 | 102 | ⟶ | $B_g^3$ | 106.4[a] | 108.9 | 101 |
| | | | | ⟶ | $A_g^4$ | 108.3 | 109.3 | 102 |
| $A_g^2$ | 108.3 | 98.8 | 88 | ⟶ | $B_g^4$ | 106.4[a] | 97.8 | 86 |
| $A_g^3$ | 128.1 | 131.1 | 125 | ⟶ | $A_g^5$ | 128.2 | 131.7 | 125 |
| $A_g^4$ | – | 195.2 | 195 | ⟶ | $B_g^5$ | – | 198.8 | 195 |
| $E_g^4$ | 236.6 | 234.4 | 225 | ⟶ | $A_g^6$ | 234.6 | 220.1 | 224 |
| | | | | ⟶ | $B_g^6$ | 235.5 | 221.1 | 225 |

[a]Observed as two peak structure.

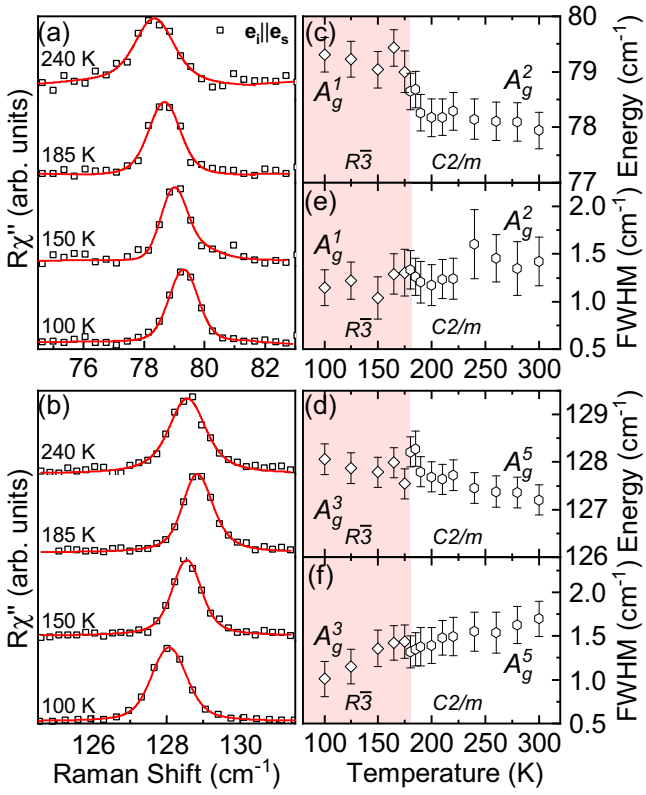


FIG. 3. Temperature dependence of the $A_g^1$ and $A_g^3$ phonon modes of the rhombohedral structure and the corresponding $A_g^2$ and $A_g^5$ modes of the monoclinic structure, respectively. (a) and (b) Raman spectra at temperatures as indicated. The spectra are shifted for clarity. Solid red lines represent Voigt profiles fitted to the data. (c) and (d) and (e) and (f) Temperature dependence of the phonon energies and linewidths, respectively. Both modes show an abrupt change in energy at the phase transition at 180 K.

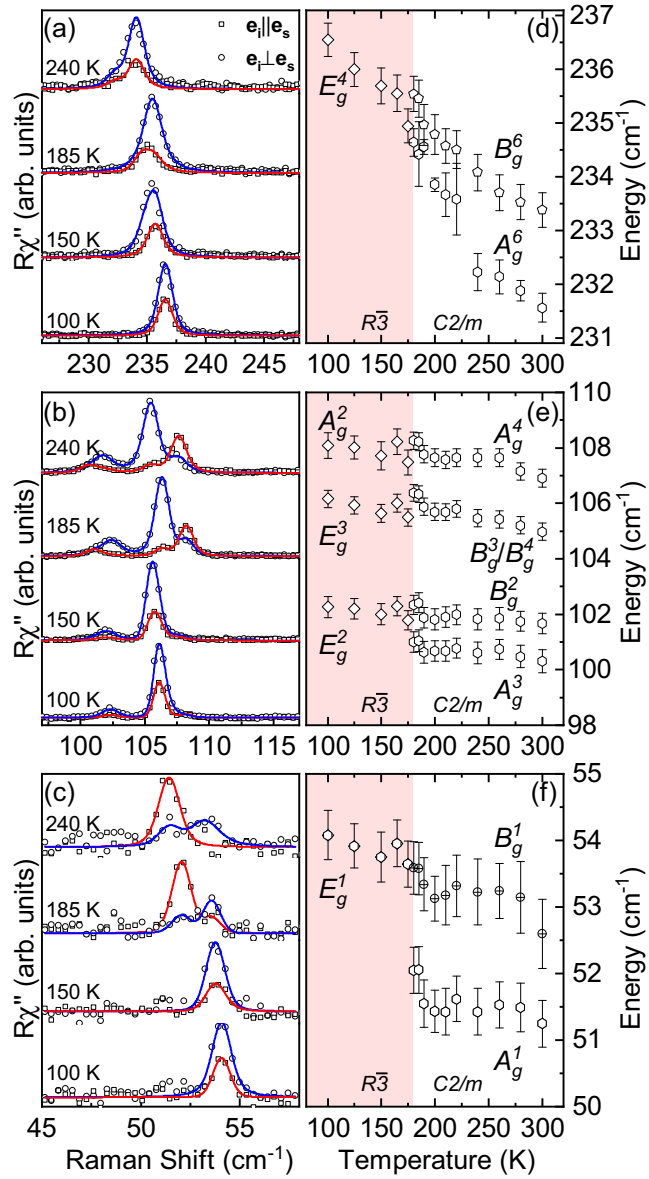


FIG. 4. Temperature dependence of the rhombohedral $A_g^4$ and $E_g$ modes. (a)–(c) Raman spectra in parallel (open squares) and crossed (open circles) light polarizations at temperatures as indicated. The spectra are shifted for clarity. Blue and red solid lines are fits of Voigt profiles to the data. Two spectra were analyzed simultaneously in two scattering channels with the integrated intensity as the only independent parameter. (d)–(f) Phonon energies obtained from the Voigt profiles. Each $E_g$ mode splits into an $A_g$ and a $B_g$ mode above 180 K.

therefore identify the phonons in the $C2/m$ phase in relation to the calculations and find again good agreement of the energies. The $B_g^3$ and $B_g^4$ modes overlap and therefore cannot be resolved separately. As can be seen from the temperature dependence shown below [Fig. 4(b)] the peak at 106 cm$^{-1}$ broadens and gains spectral weight in the monoclinic phase in line with the expectance that two modes overlap. The missing rhombohedral $A_g^4$ mode corresponds to the monoclinic $B_g^5$ mode, which is likewise absent in the spectra.

The temperature dependence of the observed phonons is shown in Figs. 3 and 4. In the low-temperature rhombohedral phase all four $E_g$ modes as well as $A_g^1$ and $A_g^2$ soften upon warming, whereas $A_g^3$ hardens up to $T \approx 180$ K before softening again. Crossing the first-order phase transition from $R\bar{3}$ to $C2/m$ crystal symmetry is reflected in the spectra as a symmetry change and/or renormalization for the non-degenerate modes and lifting of the degeneracy of the $E_g$ modes as shown in Table II. In our samples, this transition is observed at $T_s \approx 180$ K. The splitting of the $E_g$ phonons into $A_g$ and $B_g$ modes at the phase transition is sharp (Fig. 4). The rhombohedral $A_g^1$ and $A_g^3$ phonons show a jump in energy and a small discontinuity in the linewidth at $T_s$ (Fig. 3). Our spectra were taken during warming in multiple runs after cooling to 100 K each time. We found that the temperature dependence for the phonon modes obtained this way was smooth in each phase. McGuire *et al.* [3,20] reported $T_s$ in the range of 220 K, a coexistence of both phases and a large thermal hysteresis. However, they also noted that the first and second warming cycle showed identical behavior and only found a shift of the transition temperature to higher values for cooling cycles. We therefore consider the difference between the reported transition around 220 K and our $T_s \approx 180$ K significant. To some extent this difference may be attributed

to local heating by the laser. More importantly, we find no signs of phase coexistence in the observed temperature range. The spectra for the low-temperature and high-temperature phases are distinctly different (Fig. 2) and the $E_g$ modes exhibit a clearly resolved splitting which occurs abruptly at $T_s$. We performed measurements in small temperature steps (see Figs. 3 and 4). This limits the maximum temperature interval where the phase coexistence could occur in our samples to approximately 5 K, much less than the roughly 30 to 80 K reported earlier [3,20]. We cannot exclude the possibility that a small fraction of the low-temperature phase could still coexist with the high-temperature phase over a wider temperature range, whereby weak peaks corresponding to the remains of the low-temperature $R\bar{3}$ phase might be hidden under the strong peaks of the $C2/m$ phase.

## IV. CONCLUSION

We studied the lattice dynamics in single crystalline $CrI_3$ using Raman spectroscopy supported by numerical calculations. For both the low-temperature $R\bar{3}$ and the high-temperature $C2/m$ phase, all except one of the predicted

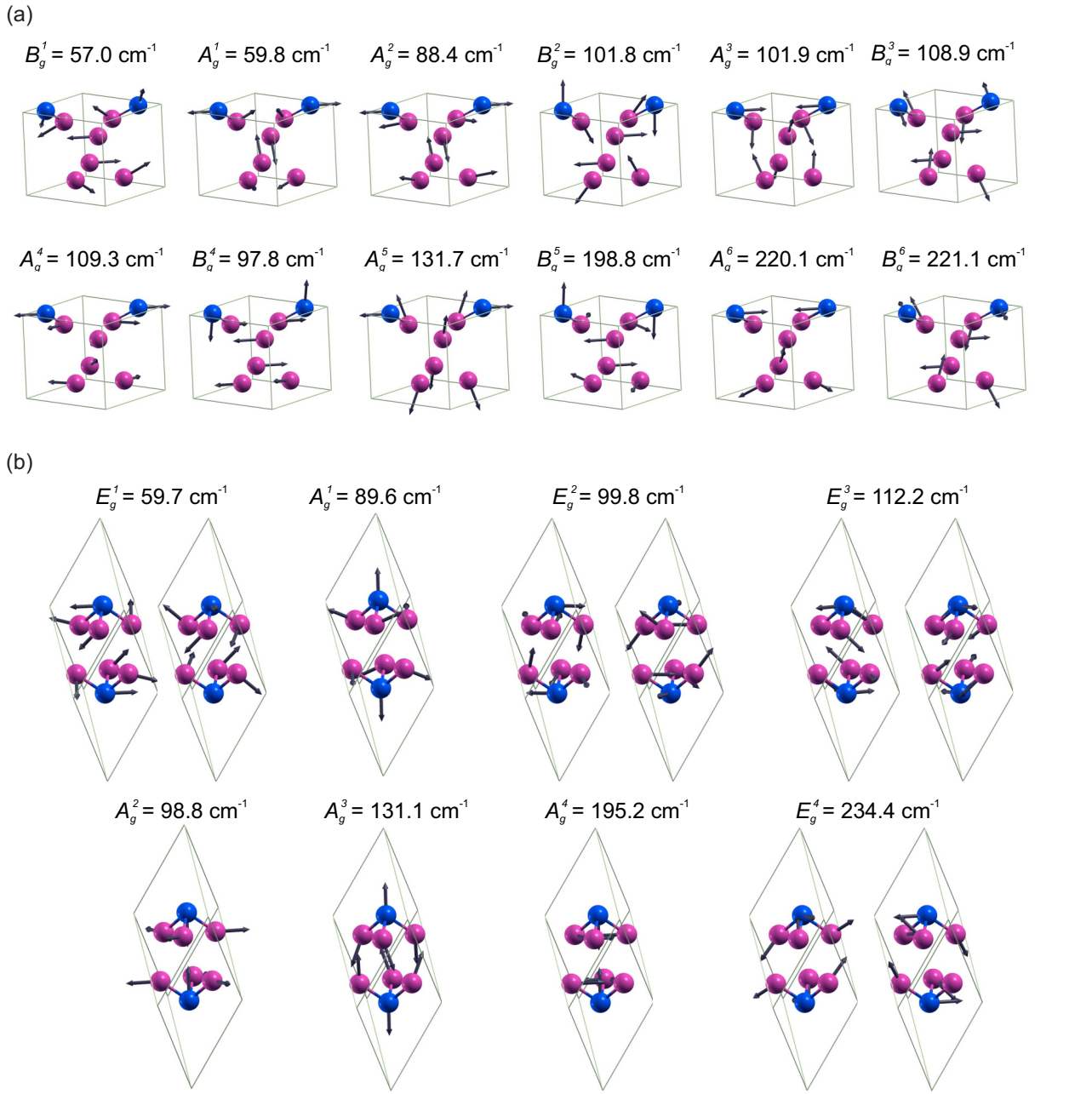


FIG. 5. Raman-active phonons in $CrI_3$ for (a) the monoclinic phase hosting $A_g$ and $B_g$ modes and for (b) the rhombohedral phase hosting $A_g$ and $E_g$ modes. Blue and violet spheres denote Cr and I atoms, respectively. Solid lines represent primitive unit cells. Arrow lengths are proportional to the square root of the interatomic forces. The given energies are calculated for zero temperature.

phonon modes were identified and the calculated and experimental phonon energies were found to be in good agreement. We determined that the symmetry of the single $CrI_3$ layers is $p\bar{3}1/m$. Abrupt changes to the spectra were found at the first-order phase transition which was located at $T_s \approx 180$ K, lower than in previous studies. In contrast to the prior reports we found no sign of phase coexistence over temperature ranges exceeding 5 K.

## ACKNOWLEDGMENTS

The work was supported by the Serbian Ministry of Education, Science and Technological Development under Projects No. III45018 and No. OI171005. DFT calculations were performed using computational resources at Johannes Kepler University, Linz, Austria. Work at Brookhaven was supported by the US Department of Energy, Office of Basic Energy Sciences as part of the Computation Material Science Program (material synthesis and characterization).

S.Dj.M. and N.L. conceived the experiment, performed the experiment, analyzed and discussed the data, and wrote the paper. A.Š. and J.P. calculated the phonon energies, analyzed and discussed the data, and wrote the paper. Y.L. and C.P. synthesized and characterized the samples. M.Š. performed the experiment and analyzed and discussed the data. A.B. and Z.V.P. analyzed and discussed the data and wrote the paper. All authors commented on the manuscript.

## APPENDIX: EIGENVECTORS

In addition to the phonon energies we also calculated the phonon eigenvectors which are shown in Fig. 5(a) for the high-temperature monoclinic phase and in Fig. 5(b) for the low-temperature rhombohedral phase. The energies, as given, are calculated for zero temperature. The relative displacement of the atoms is denoted by the length of the arrows.

[1] E. Navarro-Moratalla, B. Huang, G. Clark *et al.*, Layer-dependent ferromagnetism in a van der Waals crystal down to the monolayer limit, Nature (London) **546**, 270 (2017).

[2] S. Jiang, L. Li, Z. Wang, K. F. Mak, and J. Shan, Controlling magnetism in 2D $CrI_3$ by electrostatic doping, Nat. Nanotechnol. **13**, 549 (2018).

[3] M. A. McGuire, H. Dixit, V. R. Cooper, and B. C. Sales, Coupling of crystal structure and magnetism in the layered, ferromagnetic insulator $CrI_3$, Chem. Mater. **27**, 612 (2015).

[4] J. L. Ladno and J. Fernández-Rossier, On the origin of magnetic anisotropy in two dimensional $CrI_3$, 2D Mater. **4**, 035002 (2017).

[5] W.-B. Zhang, Q. Qu, P. Zhu, and C.-H. Lam, Robust intrinsic ferromagnetism and half semiconductivity in stable two-dimensional single-layer chromium trihalides, J. Mater. Chem. C **3**, 12457 (2015).

[6] J. F. Dillon, Jr. and C. E. Olson, Magnetization, resonance, and optical properties of the ferromagnet $CrI_3$, J. Appl. Phys. **36**, 1259 (1965).

[7] D. T. Larson and E. Kaxiras, Raman Spectrum of $CrI_3$: An *ab initio* study, Phys. Rev. B **98**, 085406 (2018).

[8] N. Lazarević, M. Abeykoon, P. W. Stephens, H. Lei, E. S. Bozin, C. Petrovic, and Z. V. Popović, Vacancy-induced nanoscale phase separation in $K_xFe_{2-y}Se_2$ single crystals evidenced by Raman scattering and powder x-ray diffraction, Phys. Rev. B **86**, 054503 (2012).

[9] H. Ryu, M. Abeykoon, K. Wang, H. Lei, N. Lazarevic, J. B. Warren, E. S. Bozin, Z. V. Popovic, and C. Petrovic, Insulating and metallic spin glass in Ni-doped $K_xFe_{2-y}Se_2$ single crystals, Phys. Rev. B **91**, 184503 (2015).

[10] H. Ryu, K. Wang, M. Opacic, N. Lazarevic, J. B. Warren, Z. V. Popovic, E. S. Bozin, and C. Petrovic, Sustained phase separation and spin glass in Co-doped $K_xFe_{2-y}Se_2$ single crystals, Phys. Rev. B **92**, 174522 (2015).

[11] Y. Liu and C. Petrovic, Three-dimensional magnetic critical behavior in $CrI_3$, Phys. Rev. B **97**, 014420 (2018).

[12] P. Giannozzi, S. Baroni, N. Bonini, M. Calandra, R. Car, C. Cavazzoni, D. Ceresoli, G. L. Chiarotti, M. Cococcioni, I. Dabo, A. D. Corso, S. de Gironcoli, S. Fabris, G. Fratesi, R. Gebauer, U. Gerstmann, C. Gougoussis, A. Kokalj, M. Lazzeri, L. Martin-Samos, N. Marzari, F. Mauri, R. Mazzarello, S. Paolini, A. Pasquarello, L. Paulatto, C. Sbraccia, S. Scandolo, G. Sclauzero, A. P. Seitsonen, A. Smogunov, P. Umari, and R. M. Wentzcovitch, Quantum espresso: A modular and open-source software project for quantum simulations of materials, J. Phys. Condens. Matter **21**, 395502 (2009).

[13] J. P. Perdew, K. Burke, and M. Ernzerhof, Generalized Gradient Approximation Made Simple, Phys. Rev. Lett. **77**, 3865 (1996).

[14] P. E. Blöchl, Projector augmented-wave method, Phys. Rev. B **50**, 17953 (1994).

[15] G. Kresse and D. Joubert, From ultrasoft pseudopotentials to the projector augmented-wave method, Phys. Rev. B **59**, 1758 (1999).

[16] S. Grimme, Semiempirical GGA-type density functional constructed with a long-range dispersion correction, J. Comput. Chem. **27**, 1787 (2006).

[17] E. A. Wood, The 80 diperiodic groups in three dimensions, Bell Syst. Tech. J. **43**, 541 (1964).

[18] W. G. Fateley, N. T. McDevitt, and F. F. Bentley, Infrared and raman selection rules for lattice vibrations: The correlation method, Appl. Spectrosc. **25**, 155 (1971).

[19] N. Lazarević, Z. V. Popović, R. Hu, and C. Petrovic, Evidence of coupling between phonons and charge-density waves in $ErTe_3$, Phys. Rev. B **83**, 024302 (2011).

[20] M. A. McGuire, G. Clark, S. KC, W. M. Chance, G. E. Jellison, V. R. Cooper, X. Xu, and B. C. Sales, Magnetic behavior and spin-lattice coupling in cleavable van der Waals layered $CrCl_3$ crystals, Phys. Rev. Mater. **1**, 014001 (2017).

*Correction:* Missing support information in the Acknowledgment section has been inserted.

# Evidence of spin-phonon coupling in $CrSiTe_3$

A. Milosavljević,[1] A. Šolajić,[1] J. Pešić,[1] Yu Liu (刘育),[2] C. Petrovic,[2] N. Lazarević,[1,*] and Z. V. Popović[1,3]

[1]*Center for Solid State Physics and New Materials, Institute of Physics Belgrade, University of Belgrade, Pregrevica 118, 11080 Belgrade, Serbia*

[2]*Condensed Matter Physics and Materials Science Department, Brookhaven National Laboratory, Upton, New York 11973-5000, USA*

[3]*Serbian Academy of Sciences and Arts, Knez Mihailova 35, 11000 Belgrade, Serbia*

(Received 12 July 2018; published 18 September 2018; corrected 28 March 2019)

We present Raman scattering results on the layered semiconducting ferromagnetic compound $CrSiTe_3$. Four Raman-active modes, predicted by symmetry, are observed and assigned. The experimental results are supported by density functional theory calculations. The self-energies of the $A_g^3$ and the $E_g^3$ symmetry modes exhibit unconventional temperature evolution around 180 K. In addition, the doubly degenerate $E_g^3$ mode shows a clear change of asymmetry in the same temperature region. The observed behavior is consistent with the presence of the previously reported short-range magnetic order and strong spin-phonon coupling.

DOI: 10.1103/PhysRevB.98.104306

## I. INTRODUCTION

Trichalcogenides $CrXTe_3$ ($X$ = Si, Ge) belong to a rare class of quasi-two-dimensional semiconducting materials with a ferromagnetic order, band gaps of 0.4 eV for Si and 0.7 eV for Ge compounds, and Curie temperatures ($T_C$) of 32 and 61 K, respectively [1–6]. Because of their layered structure, due to van der Waals bonding, they can be exfoliated to mono- and few-layer nanosheets, which, together with their semiconducting and magnetic properties, make an ideal combination for applications in optoelectronics and nanospintronics [7–11]. This was further supported by the observation of giant resistivity modulation of $CrGeTe_3$-based devices [12].

From an x-ray diffraction study [1], it was revealed that $CrSiTe_3$ crystals are twined along $c$ axes, the thermal expansion is negative at low temperatures, and the thermal conductivity shows strong magnon-phonon scattering effects. A very small single-ion anisotropy favoring magnetic order along $c$ axes and spin waves was found in $CrSiTe_3$ by elastic and inelastic neutron scattering [13]. Spin-wave measurements suggest the absence of three-dimensional correlations above $T_C$, whereas in-plane dynamic correlations are present up to 300 K. First-principles calculations suggested the possibility of graphenelike mechanical exfoliation for $CrXTe_3$ ($X$ = Si, Ge) single crystals with conserved semiconducting and ferromagnetic properties [14]. The exfoliation of $CrSiTe_3$ bulk to mono- and few-layer two-dimensional crystals onto a $Si/SiO_2$ substrate has been achieved [15] with a resistivity between 80 and 120 K, depending on the number of layers. Critical exponents for $CrSiTe_3$ were also determined from theoretical analysis [16].

Spin-phonon coupling in $CrGeTe_3$ was investigated in Raman scattering experiments [17]. Splitting of the two lowest-energy $E_g$ modes in the ferromagnetic phase has been observed and ascribed to time-reversal symmetry breaking by the spin ordering. Furthermore, the significant renormalization of the three higher-energy modes' self-energies below $T_C$ provided additional evidence of spin-phonon coupling [17]. The external pressure-induced effect on lattice dynamics and magnetization in $CrGeTe_3$ has also been studied [18].

The Raman spectrum of $CrSiTe_3$ single crystals was reported in Ref. [1], where three Raman-active modes have been observed. Similar results have also been presented in Ref. [15] for ultrathin nanosheets of $CrSiTe_3$. Here, we report a Raman scattering study of $CrSiTe_3$ single crystals, with the main focus on phonon properties in the temperature range between 100 and 300 K. Our experimental results are qualitatively different from those previously reported [1,15] but consistent with the results obtained for $CrGeTe_3$ [17,18]. Furthermore, our data reveal the asymmetry of the $E_g^3$ mode, which is suppressed at higher temperatures. The $A_g^3$ and $E_g^3$ symmetry modes exhibit nonanharmonic self-energy temperature dependence in the region around 180 K, related to the strong spin-lattice interaction due to short-range magnetic order [1]. Energies and symmetries of the observed Raman-active modes are in good agreement with theoretical calculations.

## II. EXPERIMENT AND NUMERICAL METHOD

Single crystals of $CrSiTe_3$ and $CrGeTe_3$ were grown as described previously [19]. For a Raman scattering experiment, a Tri Vista 557 spectrometer was used in the backscattering micro-Raman configuration with a 1800/1800/2400 grooves/mm diffraction grating combination. A coherent Verdi G solid-state laser with a 532-nm line was used as the excitation source. The direction of the incident (scattered) light coincides with a crystallographic $c$ axis. Right before being placed in the vacuum, the samples were cleaved in the air. All measurements were performed in a high vacuum ($10^{-6}$ mbar) using a KONTI CryoVac continuous-helium-flow cryostat with a 0.5-mm-thick window. Laser-beam focusing was achieved through a microscope objective with ×50 magnification, a spot size of approximately 8 $\mu$m, and a power

*nenadl@ipb.ac.rs

 

TABLE I. Calculated and experimental crystallographic lattice parameters for $CrSiTe_3$ ($|a| = |b|$), bond lengths, interlayer distance ($d$), and van der Waals (vdW) gap.

| $CrSiTe_3$ | Calculation (Å) | Experiment (Å) [20] |
|---|---|---|
| $a$ | 6.87 | 6.76 |
| $c$ | 19.81 | 20.67 |
| Si-Si | 2.27 | 2.27 |
| Si-Te | 2.52 | 2.51 |
| Cr-Te | 2.77 | 2.78 |
| $d$ | 6.86 | 6.91 |
| vdW gap | 3.42 | 3.42 |

<2 mW on the surface of a sample. All spectra were corrected for the Bose factor.

Density functional theory calculations were performed in the Quantum Espresso software package [21], using the PBE exchange-correlation functional [22], PAW pseudopotentials [23,24], and energy cutoffs for wave functions and the charge density of 85 and 425 Ry, respectively. For $k$-point sampling, the Monkhorst-Pack scheme was used, with a Γ-centered $8 \times 8 \times 8$ grid. Optimization of the atomic positions in the unit cell was performed until the interatomic forces were minimized down to $10^{-6}$ Ry/Å. In order to obtain the parameters accurately, treatment of the van der Waals interactions was included using the Grimme-D2 correction [25]. Phonon frequencies were calculated at the Γ point within the linear response method implemented in Quantum Espresso. Calculated crystallographic properties obtained by relaxing the structures are in good agreement with x-ray diffraction measurements [20]. A comparison between our, calculated, and experimental results is presented in Table I.

## III. RESULTS AND DISCUSSION

### A. Polarization dependence

$CrSiTe_3$ crystallizes in the rhombohedral crystal structure, described by $R\bar{3}$ ($C_{3i}^2$) [26]. Wyckoff positions of atoms, together with each site's contribution to phonons at the Γ point and corresponding Raman tensors, are listed in Table II. The phonon mode distribution obtained by factor-group analysis for the $R\bar{3}$ space group is as follows:

$$\Gamma_{\text{Raman}} = 5A_g + 5E_g,$$
$$\Gamma_{\text{IR}} = 4A_u + 4E_u,$$
$$\Gamma_{\text{Acoustic}} = A_u + E_u.$$

Since the plane of incidence is $ab$, where $|a| = |b|$ [$\angle(a, b) = 120^\circ$], and the direction of light propagation is along $c$ axes, from the selection rules, it is possible to observe all Raman-active modes, i.e., five $A_g$ modes and five doubly degenerate $E_g$ modes. According to the Raman tensors presented in Table II, $A_g$ symmetry modes are observable only in the parallel polarization configuration, whereas $E_g$ symmetry

TABLE II. (a) Type of atoms, Wyckoff positions, each site's contribution to the phonons at the Γ point, and corresponding Raman tensors for the $R\bar{3}$ space group of $CrSiTe_3$. (b) Phonon symmetry, calculated optical phonon frequencies at 0 K, and experimental values for Raman-active (at 100 K) and infrared (IR)-active (at 110 K) [1] $CrSiTe_3$ phonons.

(a) Space group $R\bar{3}$ (No. 148)

| Atom(s) (Wyckoff positions) | Irreducible representations |
|---|---|
| Cr, Si ($6c$) | $A_g + E_g + A_u + E_u$ |
| Te ($18f$) | $3A_g + 3E_g + 3A_u + 3E_u$ |

(b) Raman tensors

$$A_g = \begin{pmatrix} a & 0 & 0 \\ 0 & b & 0 \\ 0 & 0 & c \end{pmatrix} \quad E_g^1 = \begin{pmatrix} c & d & e \\ d & -c & f \\ e & f & 0 \end{pmatrix} \quad E_g^2 = \begin{pmatrix} d & -c & -f \\ -c & -d & e \\ -f & e & 0 \end{pmatrix}$$

| Raman active | | | IR active [1] | | |
|---|---|---|---|---|---|
| Symmetry | Calc. ($cm^{-1}$) | Expt. ($cm^{-1}$) | Symmetry | Calc. ($cm^{-1}$) | Expt. ($cm^{-1}$) |
| $A_g^1$ | 88.2 | – | $A_u^1$ | 91.8 | 91.0 |
| $E_g^1$ | 93.5 | 88.9 | $E_u^1$ | 93.7 | – |
| $E_g^2$ | 96.9 | – | $A_u^2$ | 116.8 | – |
| $E_g^3$ | 118.3 | 118.2 | $E_u^2$ | 117.1 | – |
| $A_g^2$ | 122.0 | – | $A_u^3$ | 202.4 | – |
| $A_g^3$ | 148.0 | 147.4 | $E_u^3$ | 206.2 | 207.9 |
| $A_g^4$ | 208.7 | – | $A_u^4$ | 243.7 | – |
| $E_g^4$ | 219.5 | 217.2 | $E_u^4$ | 365.8 | 370.4 |
| $E_g^5$ | 357.4 | – | | | |
| $A_g^5$ | 508.8 | – | | | |

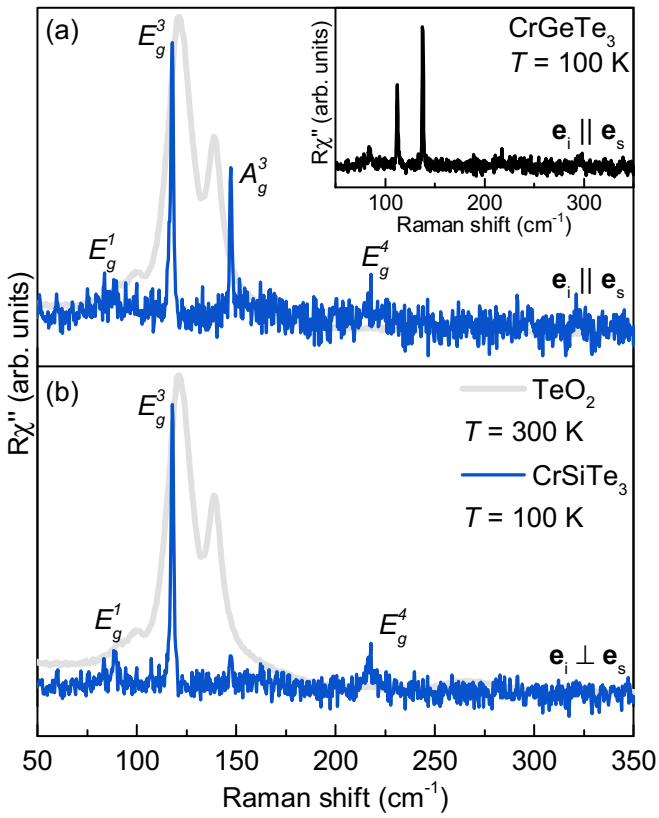


FIG. 1. Raman spectra of $CrSiTe_3$ single crystals measured at 100 K in (a) parallel and (b) cross polarization configurations. The gray line represents the $TeO_2$ spectrum measured at 300 K. Inset: Raman spectrum of $CrGeTe_3$ in the parallel polarization configuration measured at 100 K.

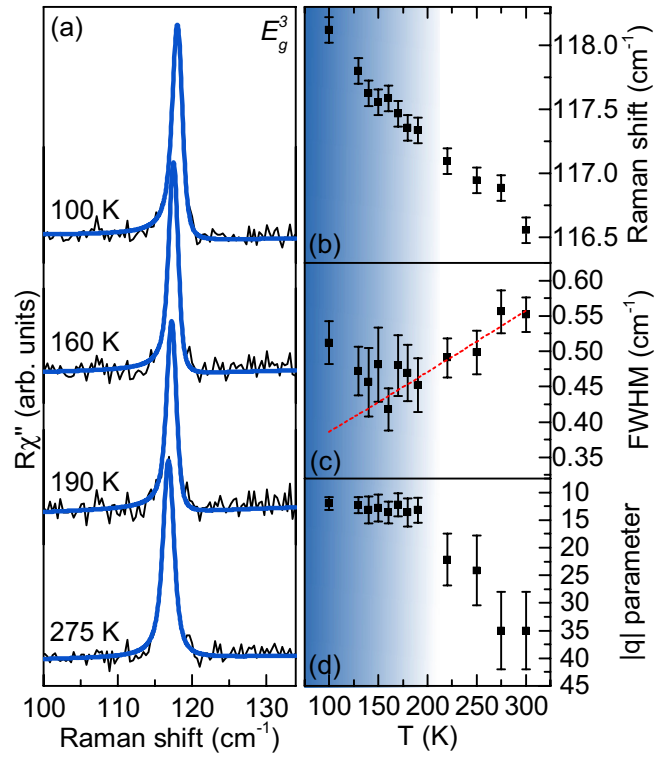


FIG. 2. (a) The $E_g^3$ mode Raman spectra of $CrSiTe_3$ at four temperatures measured in the cross polarization configuration. Blue lines represent line shapes obtained as a convolution of the Fano line shape and Gaussian, calculated to fit the experimetal data. Temperature dependence of (b) the energy, (c) the line width, and (d) the Fano parameter $q$ of the $E_g^3$ mode. The dashed red line represents standard anharmonic behavior [28,29]. All the parameters show a change in tendency around 180 K.

modes can be expected to appear for both in-parallel and cross polarization configurations.

The Raman spectra of $CrSiTe_3$ for two main linear polarization configurations, at 100 K, are shown in Fig. 1. Four peaks can be observed in the spectra, at energies of 88.9, 118.2, 147.4, and 217.2 $cm^{-1}$. Since only the peak at 147.4 $cm^{-1}$ vanishes in the cross polarization configuration, it corresponds to the $A_g$ symmetry mode. The other three modes appear in both parallel and cross polarization configurations and, thereby, can be assigned as $E_g$ symmetry modes (Fig. 1).

In order to exclude the possibility that any of the observed features originate from the $TeO_2$ [17,27], its Raman spectrum is also presented in Fig. 1. It can be noted that no $TeO_2$ contribution is present in our $CrSiTe_3$ data. Furthermore, the observed $CrSiTe_3$ Raman spectra are also consistent with the $CrGeTe_3$ Raman spectra (see inset in Fig. 1), isostructural to $CrSiTe_3$. Five Raman-active modes have been observed for $CrGeTe_3$, two $A_g$ modes, at 137.9 and 296.6 $cm^{-1}$, and three $E_g$ modes, at 83.5, 112.2, and 217.5 $cm^{-1}$, in agreement with the previously published data [17,18]. The main difference in the spectra of $CrSiTe_3$ and $CrGeTe_3$ arises from the change in mass and lattice parameter effects that cause the peaks to shift.

Calculated and observed Raman-active phonon energies are compiled in Table II, together with the experimental energies of the infrared (IR)-active phonons [1], and are found to be in good agreement. Displacement patterns of the $A_g$ and $E_g$ symmetry modes are presented in Fig. 4, in the Appendix.

### B. Temperature dependence

After proper assignment of all the observed $CrSiTe_3$ Raman-active modes we proceeded with temperature evolution of their properties, focusing on the most prominent ones, $E_g^3$ and $A_g^3$. Figure 2(a) shows the spectral region of the doubly degenerate $E_g^3$ mode at an energy of 118.2 $cm^{-1}$, at four temperatures. Closer inspection of the 100 K spectra revealed clear asymmetry of the peak on the low-energy side. The presence of defects may result in the appearance of the mode asymmetry [30], however, they would also contribute to the mode line width and, possibly, the appearance of phonons from the edge of the Brillouin zone in the Raman spectra [29]. The very narrow lines and absence of additional features in the Raman spectra of $CrSiTe_3$ do not support this scenario. The asymmetry may also arise when the phonon is coupled to a continuum [31]. Such a coupling of the $E_g^3$ phonon mode would result in a line shape given by the convolution of a Fano function and a Gaussian, the latter representing the resolution of the spectrometer [29]. Comparison between the Fano line shape convoluted with a Gaussian, the Voigt line shape, and the experimental data at 100 K is presented in Fig. 5, in the

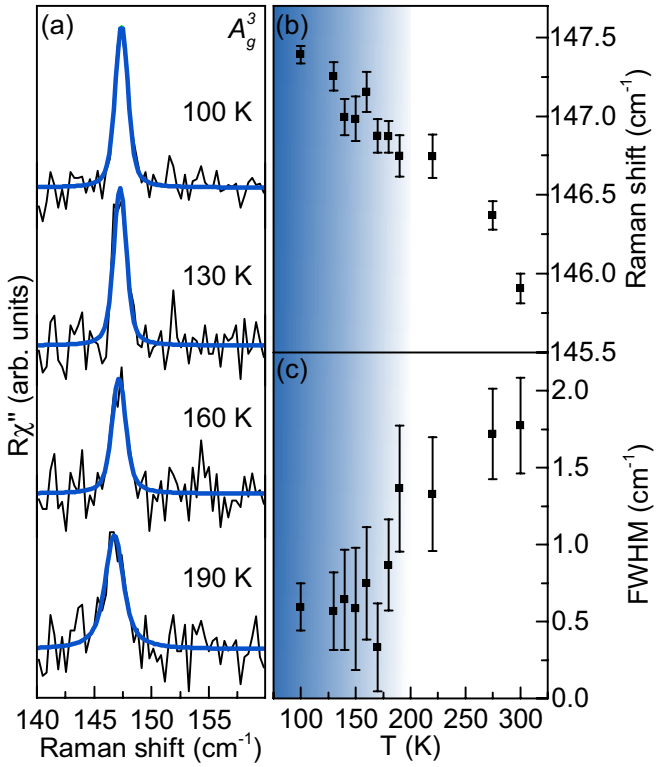


FIG. 3. (a) $A_g^3$ mode Raman spectra of $CrSiTe_3$ at four temperatures measured in the parallel polarization configuration. Blue lines represent Voigt line shapes. (b) Energy and (c) line-width temperature dependence of the $A_g^3$ mode.

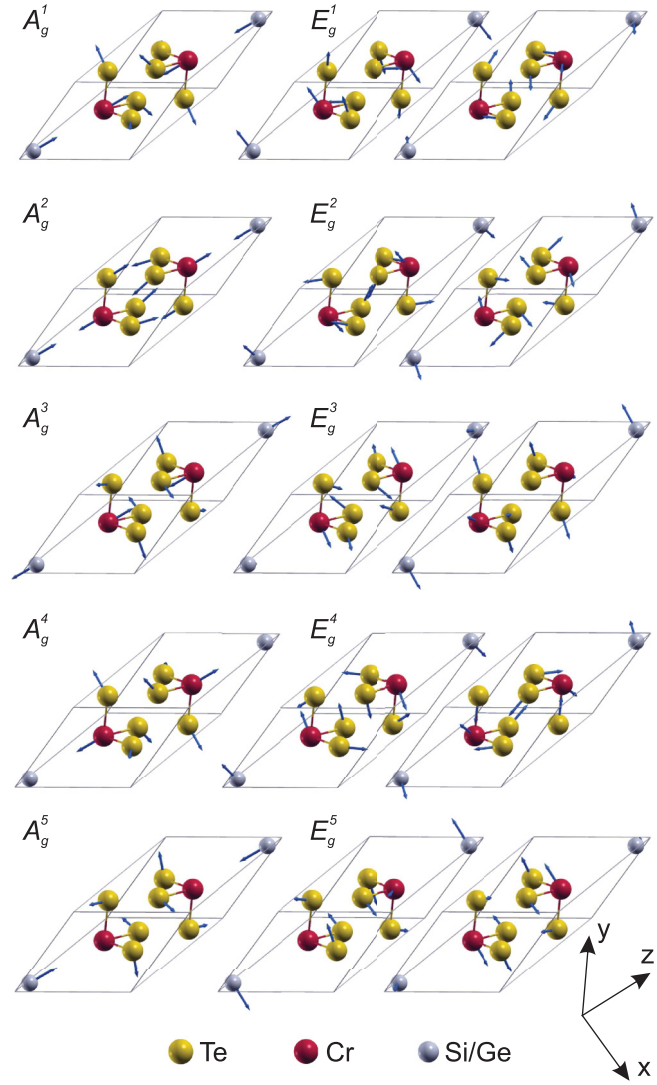


FIG. 4. Unit cell of a $CrSiTe_3$ single crystal (solid lines) with the displacement patterns of the $A_g$ and $E_g$ symmetry modes. Arrow lengths are proportional to the square root of the interatomic forces.

Appendix, with the former yielding better agreement with the experimental data. Furthermore, it fully captures the $E_g^3$ mode line shape at all temperatures under investigation [Figs. 2(a) and 6].

Upon cooling of the sample, the $E_g^3$ mode energy hardens [Fig. 2(b)] with a very small discontinuity in the temperature range around 180 K. Down to the same temperature, the line width monotonically narrows in line with the standard anharmonic behavior [dashed red line in Fig. 2(c)]. Upon further cooling, the line width increased, deviating from the expected anharmonic tendency. This indicates activation of an additional scattering mechanism, e.g., spin-phonon interaction. Figure 2(d) shows the evolution of the Fano parameter, $|q|$. Whereas in the region below 180 K, it increases slightly but continuously, at higher temperatures it promptly goes to lower values and the mode recovers a symmetric line shape. We believe that the observed behavior of the $E_g^3$ mode can be traced back to the short-range magnetic correlations, which, according to Ref. [1], persist up to 150 K, and the strong spin-phonon coupling in $CrSiTe_3$. Similar behavior of the energy and line width, which differs from the conventional anharmonic, as well as the $E_g$ mode Fano-type line shape, was recently reported in $\alpha$-$RuCl_3$ and was interpreted as a consequence of the spin-phonon interaction [32].

Unlike the $E_g^3$ mode, no pronounced asymmetry was observed for the $A_g^3$ mode. As can be seen from Figs. 3(b) and 3(c) both the energy and the line width of the $A_g^3$ mode showed a similar change in tendency in the same temperature region as the $E_g^3$ mode, most likely due to the spin-phonon coupling.

## IV. CONCLUSION

The lattice dynamics of $CrSiTe_3$, a compound isostructural to $CrGeTe_3$, is presented. An $A_g$ and three $E_g$ modes were observed and assigned. The experimental results are well supported by theoretical calculations. The temperature dependences of the energies and line widths of the $A_g^3$ and $E_g^3$ modes deviate from the conventional anharmonic model in the temperature range around 180 K. In addition, the $E_g^3$ mode shows clear Fano resonance at lower temperatures. This can be related to the previously reported short-range magnetic correlations at temperatures up to 150 K [1] and the strong spin-phonon coupling.

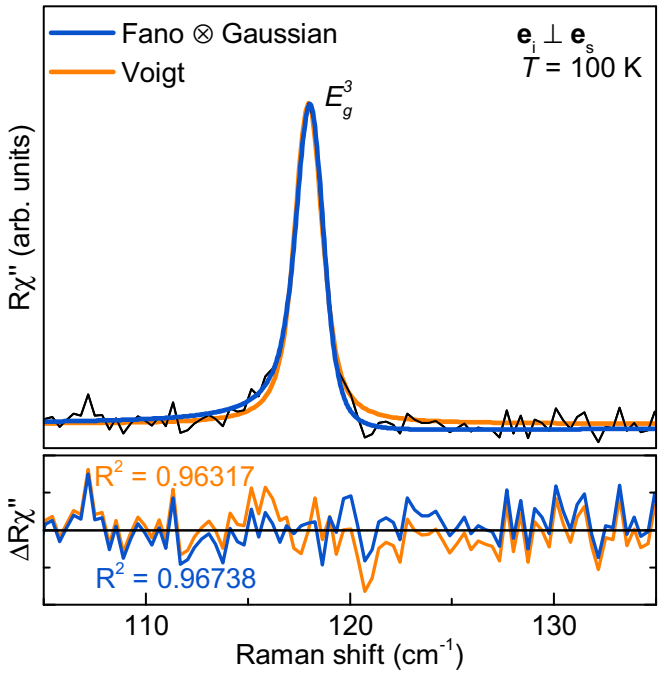


FIG. 5. Analysis of the $E_g^3$ asymmetry. Measured data are shown as the black line. The solid blue line represents the line shape obtained as a convolution of the Fano line shape and a Gaussian, whereas the orange line represents a Voigt line shape, both calculated to fit the experimental data. The Voigt profile deviates from the experimental data at the peak flanks.

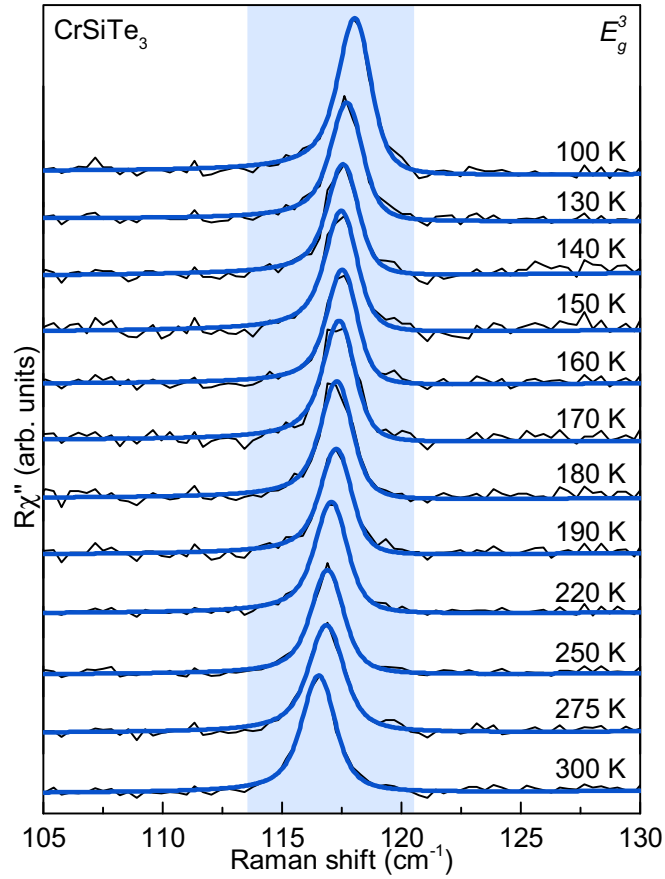


FIG. 6. The $E_g^3$ mode Raman spectra of $CrSiTe_3$ at all temperatures measured in the cross polarization configuration. Blue lines represent calculated spectra obtained as the convolution of the Fano line shape and Gaussian.


## ACKNOWLEDGMENTS

The work was supported by the Serbian Ministry of Education, Science and Technological Development under Projects III45018 and OI171005. DFT calculations were performed using computational resources at Johannes Kepler University, Linz, Austria. Work at Brookhaven was supported by the US Department of Energy, Office of Basic Energy Sciences as part of the Computation Material Science Program (material synthesis and characterization).

A.M. and N.L. conceived and performed the experiment, analyzed and discussed data, and wrote the paper; A.S. and J.P. calculated phonon energies, analyzed and discussed data, and wrote the paper; Y.L. and C.P. synthesized and characterized the samples; Z.V.P. analyzed and discussed data and wrote the paper. All authors commented on the manuscript.


## APPENDIX

### 1. Eigenvectors of Raman-active modes

Figure 4 summarizes the $A_g$ and $E_g$ symmetry mode displacement patterns of a $CrSiTe_3$ single crystal ($R\bar{3}$ space group). Arrow lengths are proportional to the square root of the interatomic forces.

### 2. Asymmetry of the $E_g^3$ line

The peak at 118.2 $cm^{-1}$, which we assigned as the $E_g^3$ symmetry mode, at low temperatures shows a significant asymmetry towards lower energies. The possibility of additional defect-induced features in Raman spectra can be excluded, since the modes are very narrow, suggesting high crystallinity of the sample. Also, the theoretical calculations do not predict additional Raman-active modes in this energy region. On the other hand, coupling of the phonon mode to a continuum may result in an asymmetric line shape described with the Fano function. Due to the finite resolution of the spectrometer it has to be convoluted with a Gaussian ($\Gamma_G = 1\ cm^{-1}$). In Fig. 5 we present a comparison of the line obtained as a convolution of the Fano line shape and a Gaussian (blue line) and a Voigt line shape (orange line) fitted to the experimental data. Whereas the Voigt line shape deviates at the peak flanks, excellent agreement has been achieved for convolution of the Fano line shape and a Gaussian.

### 3. $E_g^3$ mode temperature dependence

Figure 6 shows Raman spectra of $CrSiTe_3$ in the region of the $E_g^3$ mode in the cross polarization configuration at various temperatures. Solid blue lines represent the convolution of the Fano line shape and Gaussian fitted to the experimental data. The asymmetry is the most pronounced below 190 K. Above this temperature, the asymmetry is decreasing, and at high temperatures the peak recovers the fully symmetric line shape.

[1] L. D. Casto, A. J. Clune, M. O. Yokosuk, J. L. Musfeldt, T. J. Williams, H. L. Zhuang, M.-W. Lin, K. Xiao, R. G. Hennig, B. C. Sales, J.-Q. Yan, and D. Mandrus, Strong spin-lattice coupling in $CrSiTe_3$, APL Mater. **3**, 041515 (2015).

[2] X. Zhang, Y. Zhao, Q. Song, S. Jia, J. Shi, and W. Han, Magnetic anisotropy of the single-crystalline ferromagnetic insulator $Cr_2Ge_2Te_6$, Jpn. J. Appl. Phys. **55**, 033001 (2016).

[3] T. Leineweber and H. Kronmuller, Micromagnetic examination of exchange coupled ferromagnetic nanolayers, J. Magn. Magn. Mater. **176**, 145 (1997).

[4] G. Ouvrard, E. Sandre, and R. Brec, Synthesis and crystal structure of a new layered phase: The chromium hexatellurosilicate $Cr_2Si_2Te_6$, J. Solid State Chem. **73**, 27 (1988).

[5] B. Siberchicot, S. Jobic, V. Carteaux, P. Gressier, and G. Ouvrard, Band structure calculations of ferromagnetic chromium tellurides $CrSiTe_3$ and $CrGeTe_3$, J. Phys. Chem. **100**, 5863 (1996).

[6] V. Carteaux, F. Moussa, and M. Spiesser, 2D Ising-like ferromagnetic behaviour for the lamellar $Cr_2Si_2Te_6$ compound: A neutron scattering investigation, Europhys. Lett. **29**, 251 (1995).

[7] N. Sivadas, M. W. Daniels, R. H. Swendsen, S. Okamoto, and D. Xiao, Magnetic ground state of semiconducting transition-metal trichalcogenide monolayers, Phys. Rev. B **91**, 235425 (2015).

[8] K. S. Novoselov, A. K. Geim, S. V. Morozov, D. Jiang, Y. Zhang, S. V. Dubonos, I. V. Grigorieva, and A. A. Firsov, Electric field effect in atomically thin carbon films, Science **306**, 666 (2004).

[9] Q. H. Wang, K. Kalantar-Zadeh, A. Kis, J. N. Coleman, and M. S. Strano, Electronics and optoelectronics of two-dimensional transition metal dichalcogenides, Nat. Nanotechnol. **7**, 699 (2012), review Article.

[10] C. Gong, L. Li, Z. Li, H. Ji, A. Stern, Y. Xia, T. Cao, W. Bao, C. Wang, Y. Wang, Z. Q. Qiu, R. J. Cava, S. G. Louie, J. Xia, and X. Zhang, Discovery of intrinsic ferromagnetism in two-dimensional van der Waals crystals, Nature **546**, 265 (2017).

[11] B. Huang, G. Clark, E. Navarro-Moratalla, D. R. Klein, R. Cheng, K. L. Seyler, D. Zhong, E. Schmidgall, M. A. McGuire, D. H. Cobden, W. Yao, D. Xiao, P. Jarillo-Herrero, and X. Xu, Layer-dependent ferromagnetism in a van der Waals crystal down to the monolayer limit, Nature **546**, 270 (2017).

[12] W. Xing, Y. Chen, P. M. Odenthal, X. Zhang, W. Yuan, T. Su, Q. Song, T. Wang, J. Zhong, S. Jia, X. C. Xie, Y. Li, and W. Han, Electric field effect in multilayer $Cr_2Ge_2Te_6$: A ferromagnetic 2D material, 2D Mater. **4**, 024009 (2017).

[13] T. J. Williams, A. A. Aczel, M. D. Lumsden, S. E. Nagler, M. B. Stone, J.-Q. Yan, and D. Mandrus, Magnetic correlations in the quasi-two-dimensional semiconducting ferromagnet $CrSiTe_3$, Phys. Rev. B **92**, 144404 (2015).

[14] X. Li and J. Yang, $CrXTe_3$ (X = Si, Ge) nanosheets: Two dimensional intrinsic ferromagnetic semiconductors, J. Mater. Chem. C **2**, 7071 (2014).

[15] M.-W. Lin, H. L. Zhuang, J. Yan, T. Z. Ward, A. A. Puretzky, C. M. Rouleau, Z. Gai, L. Liang, V. Meunier, B. G. Sumpter, P. Ganesh, P. R. C. Kent, D. B. Geohegan, D. G. Mandrus, and K. Xiao, Ultrathin nanosheets of $CrSiTe_3$: A semiconducting two-dimensional ferromagnetic material, J. Mater. Chem. C **4**, 315 (2016).

[16] B. Liu, Y. Zou, S. Zhou, L. Zhang, Z. Wang, H. Li, Z. Qu, and Y. Zhang, Critical behavior of the van der Waals bonded high $T_C$ ferromagnet $Fe_3GeTe_2$, Sci. Rep. **7**, 6184 (2017).

[17] Y. Tian, M. J. Gray, H. Ji, R. J. Cava, and K. S. Burch, Magneto-elastic coupling in a potential ferromagnetic 2D atomic crystal, 2D Mater. **3**, 025035 (2016).

[18] Y. Sun, R. C. Xiao, G. T. Lin, R. R. Zhang, L. S. Ling, Z. W. Ma, X. Luo, W. J. Lu, Y. P. Sun, and Z. G. Sheng, Effects of hydrostatic pressure on spin-lattice coupling in two-dimensional ferromagnetic $Cr_2Ge_2Te_6$, Appl. Phys. Lett. **112**, 072409 (2018).

[19] Y. Liu and C. Petrovic, Critical behavior of quasi-two-dimensional semiconducting ferromagnet $Cr_2Ge_2Te_6$, Phys. Rev. B **96**, 054406 (2017).

[20] G. T. Lin, H. L. Zhuang, X. Luo, B. J. Liu, F. C. Chen, J. Yan, Y. Sun, J. Zhou, W. J. Lu, P. Tong, Z. G. Sheng, Z. Qu, W. H. Song, X. B. Zhu, and Y. P. Sun, Tricritical behavior of the two-dimensional intrinsically ferromagnetic semiconductor $CrGeTe_3$, Phys. Rev. B **95**, 245212 (2017).

[21] P. Giannozzi, S. Baroni, N. Bonini, M. Calandra, R. Car, C. Cavazzoni, D. Ceresoli, G. L. Chiarotti, M. Cococcioni, I. Dabo, A. D. Corso, S. de Gironcoli, S. Fabris, G. Fratesi, R. Gebauer, U. Gerstmann, C. Gougoussis, A. Kokalj, M. Lazzeri, L. Martin-Samos, N. Marzari, F. Mauri, R. Mazzarello, S. Paolini, A. Pasquarello, L. Paulatto, C. Sbraccia, S. Scandolo, G. Sclauzero, A. P. Seitsonen, A. Smogunov, P. Umari, and R. M. Wentzcovitch, Quantum espresso: A modular and open-source software project for quantum simulations of materials, J. Phys.: Condens. Matter **21**, 395502 (2009).

[22] J. P. Perdew, K. Burke, and M. Ernzerhof, Generalized Gradient Approximation Made Simple, Phys. Rev. Lett. **77**, 3865 (1996).

[23] P. E. Blöchl, Projector augmented-wave method, Phys. Rev. B **50**, 17953 (1994).

[24] G. Kresse and D. Joubert, From ultrasoft pseudopotentials to the projector augmented-wave method, Phys. Rev. B **59**, 1758 (1999).

[25] G. Stefan, Semiempirical GGA-type density functional constructed with a long-range dispersion correction, J. Comput. Chem. **27**, 1787 (2006).

[26] R. E. Marsh, The crystal structure of $Cr_2Si_2Te_6$: Corrigendum, J. Solid State Chem. **77**, 190 (1988).

[27] N. Lazarević, E. S. Bozin, M. Šćepanović, M. Opačić, Hechang Lei, C. Petrovic, and Z. V. Popović, Probing $IrTe_2$ crystal symmetry by polarized Raman scattering, Phys. Rev. B **89**, 224301 (2014).

[28] M. Opačić, N. Lazarević, M. Šćepanović, H. Ryu, H. Lei, C. Petrovic, and Z. V. Popović, Evidence of superconductivity-induced phonon spectra renormalization in alkali-doped iron selenides, J. Phys.: Condens. Matter **27**, 485701 (2015).

[29] A. Baum, A. Milosavljević, N. Lazarević, M. M. Radonjić, B. Nikolić, M. Mitschek, Z. Inanloo Maranloo, M. Šćepanović, M. Grujić-Brojčin, N. Stojilović, M. Opel, Aifeng Wang, C. Petrovic, Z. V. Popović, and R. Hackl, Phonon anomalies in FeS, Phys. Rev. B **97**, 054306 (2018).

[30] N. Lazarević, M. Radonjić, M. Šćepanović, Hechang Lei, D. Tanasković, C. Petrovic, and Z. V. Popović, Lattice dynamics of $KNi_2Se_2$, Phys. Rev. B **87**, 144305 (2013).

[31] N. Lazarević, Z. V. Popović, Rongwei Hu, and C. Petrovic, Evidence for electron-phonon interaction in $Fe_{1-x}M_xSb_2$ ($M =$ Co and Cr; $0 \leqslant x \leqslant 0.5$) single crystals, Phys. Rev. B **81**, 144302 (2010).

[32] L. J. Sandilands, Y. Tian, K. W. Plumb, Y.-J. Kim, and K. S. Burch, Scattering Continuum and Possible Fractionalized Excitations in $\alpha$-$RuCl_3$, Phys. Rev. Lett. **114**, 147201 (2015).

*Correction:* Missing support information in the Acknowledgment section has been inserted.

Optical and Quantum Electronics (2018) 50:276
https://doi.org/10.1007/s11082-018-1541-x

# Ab-initio calculations of electronic and vibrational properties of Sr and Yb intercalated graphene

**Andrijana Šolajić[1] · Jelena Pešić[1] · Radoš Gajić[1]**

Received: 14 October 2017 / Accepted: 14 June 2018 / Published online: 20 June 2018


**Abstract**
Since the 1960s, Graphite intercalation compounds (GIC) have been extensively studied, showing many new properties and exotic physics. This inspired many to investigate a single or few-layer intercalated graphene. Intercalated graphene has many extraordinary properties and it is different compared to pristine graphene or bulk GICs, with great spectra of characteristics induced by various intercalants. This method opens new possibilities for research and applications in electronics and photonics. Here we present the results of a DFT study on electronic and vibrational properties of the graphene doped with Sr and Yb adatoms, taking into account that only their corresponding bulk compounds have been investigated so far. The calculations were performed in Quantum Espresso software package.

**Keywords** Graphene · DFT · Electronic properties · 2D materials

## 1 Introduction

Since the experimental discovery in Novoselov et al. (2004), graphene has been attracting enormous attention. The relativistic behaviour of the low-energy excitations (the so-called *Dirac fermions*) leads to many interesting effects and the linear electronic dispersion of graphene in the vicinity of the K-point mimics the physics of the massless fermions in quantum electrodynamics, at speed 300 times smaller than the speed of light. Therefore, many unusual properties can be observed in graphene, such are the Klein paradox (Katsnelson et al. 2006) or the anomalous integer quantum Hall effect (Gusynin and Sharapov 2005; Neto et al. 2006) which can be observed at room temperatures (Novoselov et al. 2007).

This article is part of the Topical Collection on Focus on Optics and Bio-photonics, Photonica 2017.

Guest Edited by Jelena Radovanovic, Aleksandar Krmpot, Marina Lekic, Trevor Benson, Mauro Pereira, Marian Marciniak.

✉ Andrijana Šolajić
solajic@ipb.ac.rs

[1] Laboratory for Graphene, Other 2D Materials and Ordered Nanostructures, Center for Solid State Physics and New Materials, Institute of Physics Belgrade, University of Belgrade, Pregrevica 118, Belgrade 11080, Serbia

Graphene has excellent thermal conductivity, high electron mobility (Bolotin et al. 2008) and transparency, and at the same time it is one of the strongest materials known (Lee et al. 2008), about 200 times stronger than structural steel, yet very flexible and stretchable. With all its unique properties, graphene has various potential applications in almost all research fields, especially in electronics and optoelectronics (Ferrari 2015; Blake et al. 2008; Todorović et al. 2015). With high electrical and optical conductivity, it is promising candidate for applications in energy storage (Bonaccorso et al. 2015), detectors (Sassi et al. 2017; Liu et al. 2014), or even for the flexible touch screen technology (Ahn and Hong 2014; Bae et al. 2010). Ultra-thin graphitic films are also well researched for applications in photonics with high transparency and electrical conductivity (Matković et al. 2016).

Already extraordinary characteristics of graphene can be tailored and enhanced in many ways—by various types of disorders, controlling the type of edges (Peres et al. 2006; Wakabayashi et al. 1996, 2009), number of layers, by doping, applying the strain (Levy et al. 2010; Choi et al. 2010; Settnes et al. 2016; Masir et al. 2013), etc. Among them, doping graphene is an excellent way to make graphene suitable for various applications (Sharma and Ahn 2013; Wang et al. 2010; Qu et al. 2010; Jeong et al. 2011; Cui et al. 2011). Especially interesting is intercalation of various species in a few layer graphene (or doping a single layer graphene with adatoms), in a similar manner to the graphite intercalation compounds (GIC). This provides very high level of doping and leads to many interesting effects that are not present in pristine graphene, offering a new way to design various materials with magnetic, highly conductive or superconducting properties. Doping via adsorption is also very convenient, as the graphene can host various adatoms or small molecules while preserving its own structure, and at the same time drastically change its electronic properties. By covering the graphene sheet with the layer of adatoms, significant structural changes are avoided, as the dopant atoms are not fitted in the graphene lattice instead of the carbon atoms. However, adsorbed atoms can strongly affect the electronic properties of graphene, dominantly through the $p_z$ orbitals. Therefore, it is an excellent tool for tuning the properties of graphene in a wide range and obtain new effects. GIC have been extensively researched since the 1960s (Rüdorff 1959; Enoki et al. 2003; Dresselhaus and Dresselhaus 2002), but the interest for them has significantly raised with discovery of the superconductivity in some of the alkali or alkaline earth metal intercalated graphite structures, among which are $CaC_6$ and $YbC_6$ (Weller et al. 2005) with relatively high critical temperatures of $T_c = 11.5$ K and $T_c = 6.5$ K. As research of 2D materials has raised in the last decade, the superconductivity in GIC imposed a question of investigating the monolayer graphene doped with alkali and alkaline earth metal adatoms, searching for the atomically thin superconductors. The electrical characteristics of the doped graphene depend strongly on the species of the used adatom. Reports on related structures suggest the occurrence of superconductivity in some of them, usually with alkali or alkaline earth metals doping, similar to the GICs. The explanation for the emergence of the superconductivity in the alkali doped graphene lies in the electron-phonon coupling that arises from the new intercalant-derived band and the graphene $\pi$-bands at the Fermi level. Among first researched doped graphene structures was Li decorated graphene (Profeta et al. 2012; Pešić et al. 2015), which is superconducting with the critical temperature of $T = 5.9$ K. It can also be enhanced by applying the strain (Pešić et al. 2014). The experimental evidence of superconductivity in the Li doped graphene (Ludbrook 2015) inspired many to search for other 2D superconducting structures (Calandra et al. 2012; Penev et al. 2016; Shimada et al. 2017; Saito et al. 2016). Graphene doped with the Ca atoms is also reported to be superconducting as the doped monolayer (Profeta et al. 2012) and bilayer intercalated graphene (Mazin and Balatsky 2010; Margine et al. 2016), there are also reports for a

few-layer potassium doped graphene (Xue et al. 2012). Among other similar structures, the heavily n-doped graphene was also predicted to be superconducting (Margine and Giustino 2014), the combination of biaxial strain with charge doping, which leads to the superconductor with $T_c$ estimated to be up to 30 K (Si et al. 2013), or the hole-doped graphane which was predicted to be a high $T_c$ superconductor, with a critical temperature in range 60–80 K (Durajski 2015). However, many possible structures based on doped graphene with potential superconducting properties are not considered yet.

In this paper we studied the electronic and vibrational properties of Sr and Yb doped graphene using the density functional theory approach. We were motivated by the fact that both structures are known as superconductors in their corresponding bulk compounds, $YbC_6$ with critical temperature of $T_c = 6.5$ K (Weller et al. 2005) and $SrC_6$ with up to $T_c = 3.03$ K (Calandra and Mauri 2006). We are first to report the results for a monolayer graphene doped with those adatoms.

## 2 Computational details

All calculations were performed using the Quantum Espresso software package (Giannozzi et al. 2009), based on the plane waves and pseudopotentials. We used norm-conserving pseudopotentials (Perdew and Zunger 1981) and LDA exchange-correlation functional. The plane wave energy cutoff is 120 Ry for $SrC_6$-mono and 160 Ry for $YbC_6$-mono. The unit cell for both structures is modelled as $\sqrt{3} \times \sqrt{3}R30°$ supercell of the graphene unit cell, with adatoms positioned in the H-site. This is the favorable adsorption site for both adatoms, according to the DFT study (Nakada and Ishii 2011). The value of the hexagonal cell parameter $a$ is 4.26Å taken theoretically, as there are no experimental realization of those structures. The top and side view of the structures are shown in Fig. 1. In order to avoid interactions between layers, the hexagonal cell parameter $c$ of the unit cell was chosen to be sufficiently large, $c = 11.4$ Å for $SrC_6$-mono and 11.3 Å for $YbC_6$-mono. Prior to any calculations, the ionic positions in systems are fully relaxed to their minimum energy configuration, using the Broyden-Fletcher-Goldfarb-Shanno (BFGS) algorithm. Obtained vertical distance between graphene layer and the adsorbed atom is $h = 2.22$Å for $SrC_6$-mono and $h = 2.25$Å for $YbC_6$-mono. Phonon properties are obtained with the Density

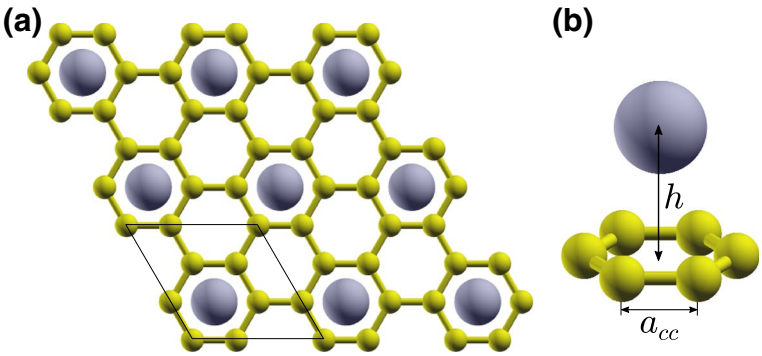


**Fig. 1** **a** Top view of the graphene structure with the adatoms adsorbed in the H-site. Unit cell is marked with the black line, **b** side view of the one hexagon with the adatom above

Functional Perturbation Theory (DFPT) implemented in the PHonon part of the Quantum Espresso software.

## 3 Results and discussion

As we said in Sect. 2, the unit cell for our H-site doped structures is enlarged compared to the pristine graphene. Due to the increase in the size of the primitive cell in direct space, basis vector lengths in reciprocal space are reduced. As a consequence, the K-point of the Brillouin zone of graphene is folded to the Γ point of the Brillouin zone of H-site doped graphene. Brillouin zones of the graphene unit cell and the H-site doped graphene are shown in Fig. 2.

### 3.1 Electronic properties

Electronic dispersions along Γ-M-K-Γ high symmetry points for $SrC_6$-mono and $YbC_6$-mono are shown in Fig. 3. Fermi level is set to zero in all figures. Folding the $\pi$ and $\pi^*$ bands of graphene from K-point to Γ-point, the inner and outer carbon $\pi$ and $\pi^*$ bands are obtained, crossing at the Γ point. For both structures, lower bands from the $\sigma$ bonds in the valence band are almost unaffected, as expected, and they are not shown in figures. The Fermi level is shifted up in both structures. By deposition of adatoms on top of graphene, new interlayer band derived from the Yb or Sr adatoms is formed around the Fermi level, showing a nearly free-electron-like dispersion. They are placed at 2.2 and 1.5 eV below the Fermi level in the $YbC_6$-mono and $SrC_6$-mono, respectively, being partially occupied. The density of states on Fermi level is also raised. The carbon $\pi$ bands are not affected by the presence of the adatoms. Previously unoccupied $\pi^*$ bands now intersect the new up-shifted Fermi level and are strongly hybridized with the new band derived from the adsorbed atoms. In $YbC_6$-mono, 4*f* orbitals coming from the Yb atoms form a set of flat non-dispersive bands, similar to the bulk $YbC_6$ (Csányi et al. 2005). Those flat bands are characteristic for most lanthanides. They are localized at 0.7 eV below the Fermi level with the corresponding peak clearly observed in the density of states. As reported for the bulk $YbC_6$, calculations with the Hubbard+U corrections do not give significant changes and result only in slightly shifting down those bands, so the same is expected for the monolayer. The Dirac points from graphene are folded to the Γ point in the H-site doped graphene, and

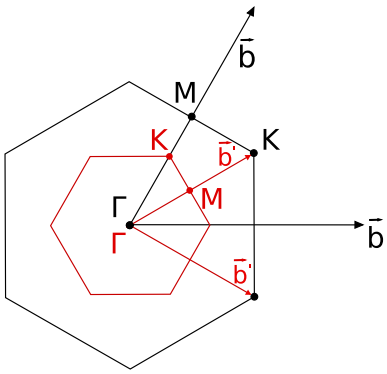


**Fig. 2** Brillouin zones of graphene (black) and the H-site doped graphene (red). (Color figure online)

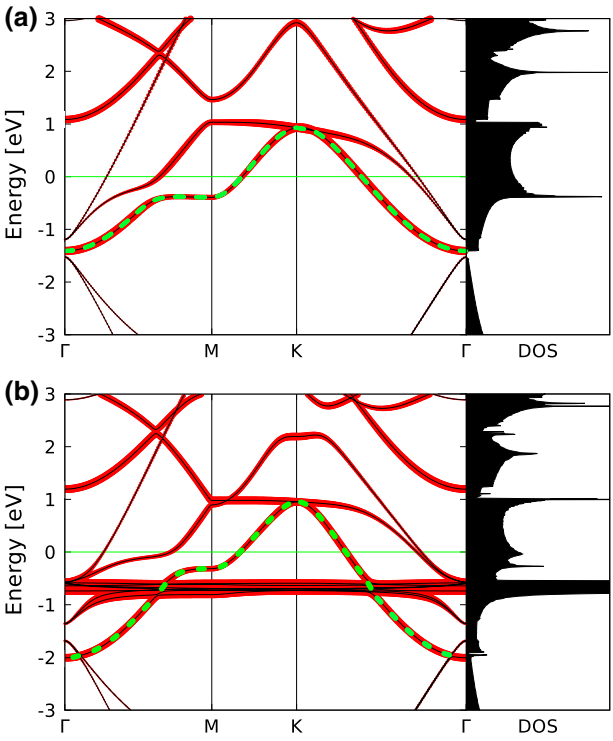


**Fig. 3** Electronic dispersions of **a** $SrC_6$-mono and **b** $YbC_6$ -mono. Thickness of the red lines is proportional to the the Sr/Yb character and the interlayer band is marked in green dotted line. (Color figure online)

they are now below the Fermi level. Due to the adatom presence, the symmetry is broken and a gap is opened. In the $SrC_6$, interlayer band is placed between the $\pi$ and $\pi^*$ and a very small gap can be observed in the density of states, while in the $YbC_6$-mono, the new interlayer band intersect the $\pi$ band and the gap is closed.

### 3.2 Phonon properties

The symmetry group of graphene with adatoms adsorbed in the H-site is $Dg77 = T^{'}C_{6v}$, which is a subgroup of the diperiodic group of graphene, $Dg80 = TD_{6h}$ (Damljanović et al. 2014). In order to connect the phonon modes of the H-site doped graphene with the corresponding phonon modes of graphene, the corresponding irreducible representation of group $Dg77$ of graphene to its subgroup $Dg80$ (Damljanović et al. 2014). The modes from the Γ point, $\Gamma E_{2g}$ and $\Gamma B_{1g}$ correspond to $\Gamma E_2$ and $\Gamma B_1$. For the modes of graphene in the K point, $KA_1^{'}$ corresponds to the modes $A_1$ and $B_2$, $KA_2^{'}$ to $A_2$ and $B_1$, $KE^{'}$ and $KE^{''}$ to $E_1$ and $E_2$ (Altmann and Herzig 1994; Damljanović and Gajić 2012). The modes $A_1$ and $E_1$ are both infrared and Raman active, while $E_2$ modes are only Raman active. The symmetry classification of optical modes and Raman tensors for H-site doped graphene are given in Table 1. The displacement patterns of the $SrC_6$-mono and $YbC_6$-mono, in the Γ point are shown in Fig. 4. Those modes have displacement patterns similar to those of graphene phonons at Γ and K points, which happens due to the Brillouin zone folding. As the K point of graphene is folded to the Γ point of the new Brillouin zone in the H-site doped graphene, the phonon modes in graphene at the Γ and K points correspond to the Γ modes in the H-site doped

**Table 1** Raman tensors and symmetry classification of optical modes

| Raman tensors | | | |
|---|---|---|---|
| Graphene | $A_{1g}$ | $E_{1g}$ | $E_{2g}$ |
| $Dg80 = TD_{6h}$<br>$O_z \parallel C_6$<br>$O_x \parallel C_2'$ | $\begin{pmatrix} a & 0 & 0 \\ 0 & a & 0 \\ 0 & 0 & b \end{pmatrix}$ | $\begin{pmatrix} 0 & 0 & 0 \\ 0 & 0 & c \\ 0 & c & 0 \end{pmatrix}$ $\begin{pmatrix} 0 & 0 & -c \\ 0 & 0 & 0 \\ c & 0 & 0 \end{pmatrix}$ | $\begin{pmatrix} d & 0 & 0 \\ 0 & -d & 0 \\ 0 & 0 & 0 \end{pmatrix}$ $\begin{pmatrix} 0 & -d & 0 \\ -d & 0 & 0 \\ 0 & 0 & 0 \end{pmatrix}$ |
| $A\alpha$ | $A_1$ | $E_1$ | $E_2$ |
| $Dg77 = TC_{6v}$<br>$O_z \parallel C_6$<br>$O_x \parallel \sigma_v$ | $\begin{pmatrix} a & 0 & 0 \\ 0 & a & 0 \\ 0 & 0 & b \end{pmatrix}$ | $\begin{pmatrix} 0 & 0 & c \\ 0 & 0 & 0 \\ c & 0 & 0 \end{pmatrix}$ $\begin{pmatrix} 0 & 0 & 0 \\ 0 & 0 & c \\ 0 & c & 0 \end{pmatrix}$ | $\begin{pmatrix} d & 0 & 0 \\ 0 & -d & 0 \\ 0 & 0 & 0 \end{pmatrix}$ $\begin{pmatrix} 0 & -d & 0 \\ -d & 0 & 0 \\ 0 & 0 & 0 \end{pmatrix}$ |
| Optical modes | | | |
| $A\alpha$ | $\Gamma_{\text{opt}} = 2A_1 + A_2 + 2B_1 + B_2 + 3E_1 + 3E_2$ | | |

structures. This is valid for all H-site doped graphene structures as the unit cell is the type. As the Kohn anomaly is present in graphene at Γ and K points in $E_{2g}$ and $KA_1'$ modes, we expect it to be present in the H-site doped graphene structures for the modes related to these two. Modes with Kohn anomaly can not be calculated precisely using the density functional theory as the DFT is based on the adiabatic Born-Oppenheimer approximation which is in this case broken. Comparing the calculated phonon modes for graphene at K and Γ point, with the corresponding phonon modes at the Γ point of the $SrC_6$ and $YbC_6$ monolayers, we can observe small differences in the corresponding frequencies. Some of these are lower than in pristine graphene and some frequencies are split. For example, frequencies of $E_2$ mode in Sr and Yb doped graphene are 1470 $cm^{-1}$ and 1488 $cm^{-1}$, respectively, while the frequency of $E_{2g}$ in pristine graphene is 1550 $cm^{-1}$; Frequency of $E'$ mode in graphene is 1200 $cm^{-1}$, and corresponding modes in doped graphene are $E_2$ at 1180 $cm^{-1}$ and $E_1$ at 1200 $cm^{-1}$; $E''$ mode in graphene is at 580 $cm^{-1}$, and corresponding modes in doped graphene are $E_2$ at 495 $cm^{-1}$ and $E_1$ at 510 $cm^{-1}$ for $SrC_6$-mono and $E_2$ at 477 $cm^{-1}$ and $E_1$ at 500 $cm^{-1}$ for $YbC_6$-mono. This can be ascribed to the adatoms impact, and in general, it depends on the type of the adatom.

## 4 Conclusion

Using the density functional theory approach, we calculated the electronic and phonon properties of the Sr and Yb doped graphene, in a similar manner to the GICs. Their corresponding bulk compounds have been studied so far and we are first to investigate the monolayer graphene doped with those adatoms. The electronic and phonon properties are of essential interest for electron-phonon coupling as well as the guidelines for experimental research. From the electronic band structure calculations, we can observe a new adatom-derived interlayer band crossing the Fermi level in both structures, which hybridize strongly with the carbon $p_z$ orbitals. Density of states on the Fermi level is also raised. Those results can be indicating a possible superconductivity and can be inspiring for further research of those structures. Displacement patterns calculated in the Γ point are similar to those in the K and Γ point of the pristine graphene, as a consequence of the zone folding effect, but due to the adatoms impact we can observe some differences in frequencies and the splitting of

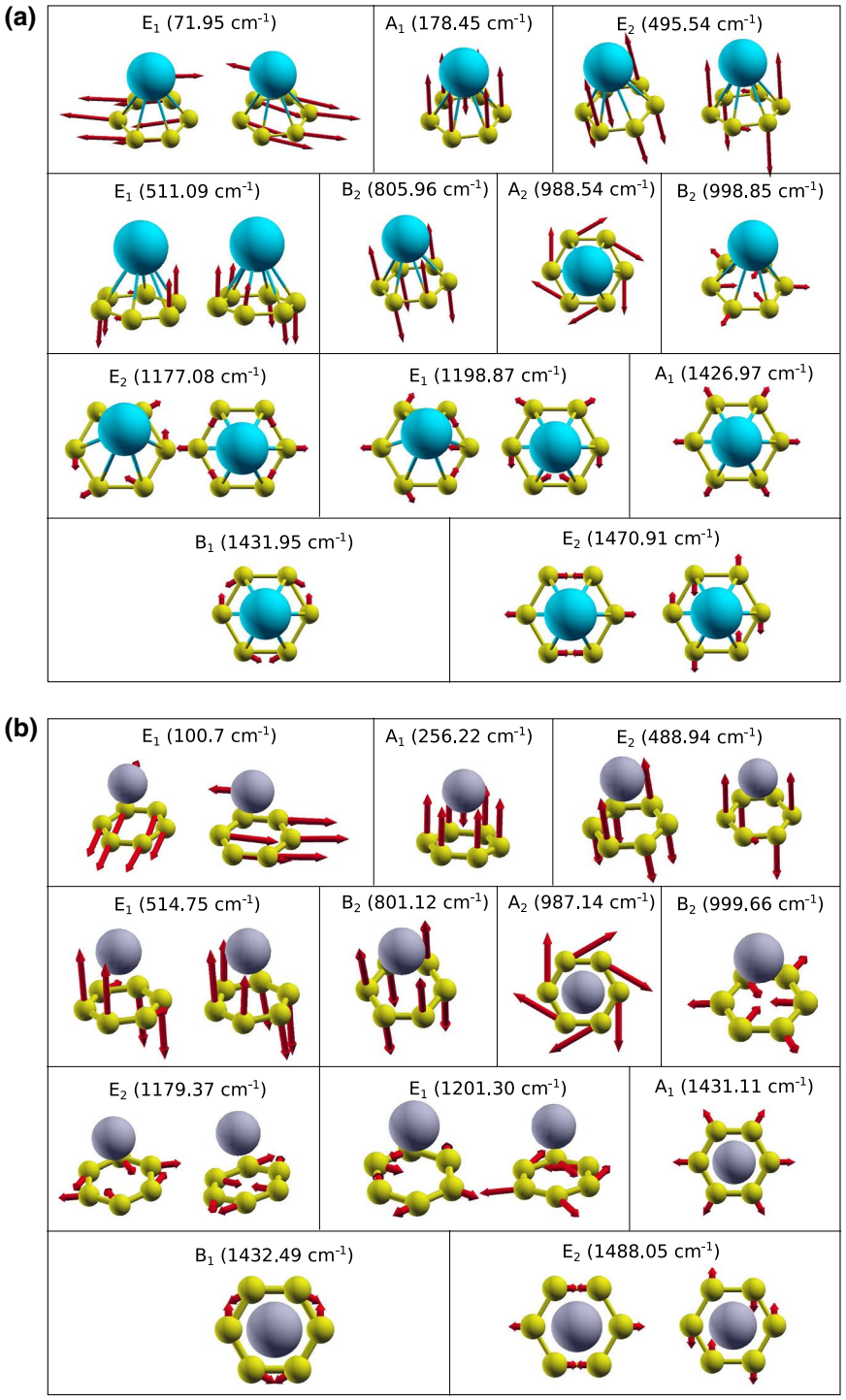


**Fig. 4** Displacement patterns of **a** $SrC_6$-mono and **b** $YbC_6$-mono. Acoustic modes ($\omega = 0$) are not shown in pictures

some modes. The results obtained in this paper are important base for further theoretical and experimental research of those two structures, as well for future research of similar structures of graphene doped with other metal adatoms.

**Acknowledgements** This work is supported by the Serbian MPNTR through Project OI 171005 and by Qatar National Research Foundation through Project NPRP 7-665-1-12.

## References

Ahn, J.H., Hong, B.H.: Graphene for displays that bend. Nat. Nanotechnol. **9**(10), 737–738 (2014)
Altmann, S., Herzig, P.: Point-Group Theory Tables. Oxford Science Publications, Clarendon Press, Oxford (1994)
Bae, S., Kim, H., Lee, Y., Xu, X., Park, J.S., Zheng, Y., Balakrishnan, J., Lei, T., Kim, H.R., Song, Y.I., et al.: Roll-to-roll production of 30-inch graphene films for transparent electrodes. Nat. Nanotechnol. **5**(8), 574–578 (2010)
Blake, P., Brimicombe, P.D., Nair, R.R., Booth, T.J., Jiang, D., Schedin, F., Ponomarenko, L.A., Morozov, S.V., Gleeson, H.F., Hill, E.W., Geim, A.K., Novoselov, K.S.: Graphene-based liquid crystal device. Nano Lett. **8**(6), 1704–1708 (2008)
Bolotin, K., Sikes, K., Jiang, Z., Klima, M., Fudenberg, G., Hone, J., Kim, P., Stormer, H.: Ultrahigh electron mobility in suspended graphene. Solid State Commun. **146**(9), 351–355 (2008)
Bonaccorso, F., Colombo, L., Yu, G., Stoller, M., Tozzini, V., Ferrari, A.C., Ruoff, R.S., Pellegrini, V.: Graphene, related two-dimensional crystals, and hybrid systems for energy conversion and storage. Science **347**(6217), 1246501 (2015)
Calandra, M., Mauri, F.: Possibility of superconductivity in graphite intercalated with alkaline earths investigated with density functional theory. Phys. Rev. B **74**, 094507 (2006)
Calandra, M., Profeta, G., Mauri, F.: Superconductivity in metal-coated graphene. Physica Status Solidi (B) **249**(12), 2544–2548 (2012)
Choi, S.M., Jhi, S.H., Son, Y.W.: Effects of strain on electronic properties of graphene. Phys. Rev. B **81**, 081407 (2010)
Csányi, G., Littlewood, P., Nevidomskyy, A.H., Pickard, C.J., Simons, B.: The role of the interlayer state in the electronic structure of superconducting graphite intercalated compounds. Nat. Phys. **1**(1), 42–45 (2005)
Cui, T., Lv, R., Huang, Z.H., Zhu, H., Zhang, J., Li, Z., Jia, Y., Kang, F., Wang, K., Wu, D.: Synthesis of nitrogen-doped carbon thin films and their applications in solar cells. Carbon **49**(15), 5022–5028 (2011)
Damljanović, V., Kostić R., Gajić R.: Characters of graphenes symmetry group dg80. Physica Scr. **2014**(T162), 014022 (2014)
Damljanović, V., Gajić, R.: Phonon eigenvectors of graphene at high-symmetry points of the brillouin zone. Physica Scr. **2012**(T149), 014067 (2012)
Dresselhaus, M.S., Dresselhaus, G.: Intercalation compounds of graphite. Adv. Phys. **51**(1), 1–186 (2002)
Durajski, A.P.: Influence of hole doping on the superconducting state in graphane. Supercond. Sci. Technol. **28**(3), 035002 (2015)
Enoki, T., Suzuki, M., Endo, M.: Graphite Intercalation Compounds and Applications, pp. 1–456. Oxford University Press, Oxford (2003)
Ferrari, A.C., et al.: Science and technology roadmap for graphene, related two-dimensional crystals, and hybrid systems. Nanoscale **7**, 4598–4810 (2015)
Giannozzi, P., et al.: Quantum espresso: a modular and open-source software project for quantum simulations of materials. J. Phys. Condens. Matter **21**(39), 395–502 (2009)
Gusynin, V.P., Sharapov, S.G.: Unconventional integer quantum hall effect in graphene. Phys. Rev. Lett. **95**, 146801 (2005)
Jeong, H.M., Lee, J.W., Shin, W.H., Choi, Y.J., Shin, H.J., Kang, J.K., Choi, J.W.: Nitrogen-doped graphene for high-performance ultracapacitors and the importance of nitrogen-doped sites at basal planes. Nano Lett. **11**(6), 2472–2477 (2011)
Katsnelson, M., Novoselov, K., Geim, A.: Chiral tunnelling and the klein paradox in graphene. Nat. Phys. **2**(9), 620–625 (2006)

Lee, C., Wei, X., Kysar, J.W., Hone, J.: Measurement of the elastic properties and intrinsic strength of monolayer graphene. Science **321**(5887), 385–388 (2008)

Levy, N., Burke, S.A., Meaker, K.L., Panlasigui, M., Zettl, A., Guinea, F., Neto, A.H.C., Crommie, M.F.: Strain-induced pseudo–magnetic fields greater than 300 tesla in graphene nanobubbles. Science **329**(5991), 544–547 (2010)

Liu, C.H., Chang, Y.C., Norris, T.B., Zhong, Z.: Graphene photodetectors with ultra-broadband and high responsivity at room temperature. Nat. Nanotechnol. **9**(4), 273–278 (2014)

Ludbrook, B.M., et al.: Evidence for superconductivity in li-decorated monolayer graphene. Proc. Nat. Acad. Sci. **112**(38), 11795–11799 (2015)

Margine, E.R., Giustino, F.: Two-gap superconductivity in heavily *n*-doped graphene: Ab initio migdal-eliashberg theory. Phys. Rev. B **90**, 014518 (2014)

Margine, E., Lambert, H., Giustino, F.: Electron-phonon interaction and pairing mechanism in superconducting ca-intercalated bilayer graphene. Sci. Rep. **6**, 21414 (2016)

Masir, M.R., Moldovan, D., Peeters, F.: Pseudo magnetic field in strained graphene: revisited. Solid State Commun. **175**, 76–82 (2013)

Matković, A., Milošević, I., Milićević, M., Tomašević-Ilić, T., Pešić, J., Musić, M., Spasenović, M., Jovanović, D., Vasić, B., Deeks, C., Panajotović, R., Belić, M.R., Gajić, R.: Enhanced sheet conductivity of Langmuir-Blodgett assembled graphene thin films by chemical doping. 2D Mater. **3**(1), 015002 (2016)

Mazin, I., Balatsky, A.: Superconductivity in Ca-intercalated bilayer graphene. Philos. Mag. Lett. **90**(10), 731–738 (2010)

Nakada, K., Ishii, A.: DFT calculation for adatom adsorption on graphene. In: Gong, J.R. (ed.) Graphene Simulation. InTech, Rijeka, Croatia (2011)

Neto, A.H.C., Guinea, F., Peres, N.M.R.: Edge and surface states in the quantum hall effect in graphene. Phys. Rev. B **73**, 205408 (2006)

Novoselov, K.S., Geim, A.K., Morozov, S.V., Jiang, D., Zhang, Y., Dubonos, S.V., Grigorieva, I.V., Firsov, A.A.: Electric field effect in atomically thin carbon films. Science **306**(5696), 666–669 (2004)

Novoselov, K.S., Jiang, Z., Zhang, Y., Morozov, S.V., Stormer, H.L., Zeitler, U., Maan, J.C., Boebinger, G.S., Kim, P., Geim, A.K.: Room-temperature quantum hall effect in graphene. Science **315**(5817), 1379–1379 (2007)

Penev, E.S., Kutana, A., Yakobson, B.I.: Can two-dimensional boron superconduct? Nano Lett. **16**(4), 2522–2526 (2016)

Perdew, J.P., Zunger, A.: Self-interaction correction to density-functional approximations for many-electron systems. Phys. Rev. B **23**, 5048–5079 (1981)

Peres, N.M.R., Neto, A.H.C., Guinea, F.: Conductance quantization in mesoscopic graphene. Phys. Rev. B **73**, 195411 (2006)

Pešić, J., Gajić, R., Hingerl, K., Belić, M.: Strain-enhanced superconductivity in li-doped graphene. EPL (Europhys. Lett.) **108**(6), 67005 (2014)

Pešić, J., Damljanović, V., Gajić, R., Hingerl, K., Belić, M.: Density functional theory study of phonons in graphene doped with Li, Ca and Ba. EPL (Europhys. Lett.) **112**(6), 67006 (2015)

Profeta, G., Calandra, M., Mauri, F.: Phonon-mediated superconductivity in graphene by lithium deposition. Nat. Phys. **8**(2), 131–134 (2012)

Qu, L., Liu, Y., Baek, J.B., Dai, L.: Nitrogen-doped graphene as efficient metal-free electrocatalyst for oxygen reduction in fuel cells. ACS Nano **4**(3), 1321–1326 (2010)

Rüdorff, W.: Graphite Intercalation Compounds. Advances in Inorganic Chemistry and Radiochemistry, pp. 223–266. Academic Press, Cambridge (1959)

Saito, Y., Nojima, T., Iwasa, Y.: Highly crystalline 2d superconductors. Nat. Rev. Mater. **2**, 16094 (2016)

Sassi, U., Parret, R., Nanot, S., Bruna, M., Borini, S., De Fazio, D., Zhao, Z., Lidorikis, E., Koppens, F., Ferrari, A., et al.: Graphene-based mid-infrared room-temperature pyroelectric bolometers with ultrahigh temperature coefficient of resistance. Nature Commun. **8**, 14311 (2017)

Settnes, M., Power, S.R., Jauho, A.P.: Pseudomagnetic fields and triaxial strain in graphene. Phys. Rev. B **93**, 035456 (2016)

Sharma, B.K., Ahn, J.H.: Graphene based field effect transistors: efforts made towards flexible electronics. Solid-State Electron. **89**(Supplement C), 177–188 (2013)

Shimada, N.H., Minamitani, E., Watanabe, S.: Theoretical prediction of phonon-mediated superconductivity with $T_c = 25K$ in Li-intercalated hexagonal boron nitride bilayer. Appl. Phys. Express **10**(9), 093101 (2017)

Si, C., Liu, Z., Duan, W., Liu, F.: First-principles calculations on the effect of doping and biaxial tensile strain on electron-phonon coupling in graphene. Phys. Rev. Lett. **111**, 196802 (2013)

Todorović, D., Matković, A., Milićević, M., Jovanović, D., Gajić, R., Salom, I., Spasenović, M.: Multilayer graphene condenser microphone. 2D Mater **2**(4), 045013 (2015)
Wakabayashi, K., Fujita, M., Kusakabe, K., Nakada, K.: Magnetic structure of graphite ribbon. Czech J. Phys. **46**(4), 1865–1866 (1996)
Wakabayashi, K., Takane, Y., Yamamoto, M., Sigrist, M.: Edge effect on electronic transport properties of graphene nanoribbons and presence of perfectly conducting channel. Carbon **47**(1), 124–137 (2009)
Wang, Y., Shao, Y., Matson, D.W., Li, J., Lin, Y.: Nitrogen-doped graphene and its application in electrochemical biosensing. ACS Nano **4**(4), 1790–1798 (2010)
Weller, T.E., Ellerby, M., Saxena, S.S., Smith, R.P., Skipper, N.T.: Superconductivity in the intercalated graphite compounds $C_6$Yb and $C_6$Ca. Nat. Phys. **1**(1), 39–41 (2005)
Xue, M., Chen, G., Yang, H., Zhu, Y., Wang, D., He, J., Cao, T.: Superconductivity in potassium-doped few-layer graphene. J. Am. Chem. Soc. **134**(15), 6536–6539 (2012)

UNIVERZITET U BEOGRADU

FIZIČKI FAKULTET

Andrijana S. Šolajić

# Ispitivanje uticaja naprezanja na osobine heterostruktura dvodimenzionalnih monohalkogenida IIIA grupe *ab-initio* metodama

doktorska disertacija

Beograd, 2025

UNIVERSITY OF BELGRADE

FACULTY OF PHYSICS

Andrijana S. Šolajić

# Investigation of strain effects on properties of heterostructures based on 2D group IIIA monochalcogenides using *ab-initio* methods

Doctoral dissertation

Belgrade, 2025.

Mentor:
dr Jelena Pešić
Viši naučni saradnik
Institut za fiziku Beograd
Univerzitet u Beogradu

**Članovi komisije:**

dr Božidar Nikolić
Vanredni profesor
Fizički fakultet
Univerzitet u Beogradu

dr Đorđe Spasojević
Redovni profesor
Fizički fakultet
Univerzitet u Beogradu

dr Slavica Maletić
Vanredni profesor
Fizički fakultet
Univerzitet u Beogradu

dr Željko Šljivančanin
Naučni savetnik
Institut za nuklearne nauke Vinča
Univerzitet u Beogradu

dr Vladimir Damljanović
Viši naučni saradnik
Institut za fiziku
Univerzitet u Beogradu

The doctoral dissertation of Andrijana Šolajić
was defended on July 14, 2025.

*What I cannot compute, I do not understand*
- Stefano Baroni (adapted from Richard P. Feynman)

# Zahvalnica

*Ova disertacija je u potpunosti rezultat rada u Centru za fiziku čvrstog stanja i nove materijale, Instituta za fiziku, Univerziteta u Beogradu. Zahvalna sam na pruženoj prilici da ostvarim svoju dugogodišnju želju da se bavim naučnim istraživanjem u Institutu za fiziku.*

*Prvenstveno bih želela da izrazim najdublju zahvalnost mentoru ove disertacije, dr Jeleni Pešić. Njenu dugogodišnju podršku, nesebično zalaganje i inspirativno vodstvo, teško je adekvatno dočarati. Tokom svih godina provedenih na doktorskim studijama, ne samo da mi je velikodušno prenosila svo znanje i iskustvo, već mi je pružala i slobodu da samostalno istražujem i napredujem. Zahvaljujući njenom razumevanju, strpljenju, ali i neverovatnoj sposobnosti da motiviše u trenucima kada je to najpotrebnije, čitav proces doktorskih studija je predstavljao predivan poduhvat i interesantnu avanturu, baš kakvo naučno istraživanje treba da bude. Jelena nije bila samo odličan mentor, već i istinska podrška i prijatelj, na čemu ću joj zauvek biti zahvalna.*

*Veliku zahvalnost dugujem dr Nenadu Lazareviću, šefu Centra za fiziku čvrstog stanja i nove materijale, za bogatu višegodišnju saradnju na brojnim istraživanjima i prilici da učestvujem u njegovim projektima. Ovaj zajednički rad ne samo da je obogatio moje razumevanje u oblasti fizike čvrstog stanja, već mi je pružio i dragoceno iskustvo u numeričkom istraživanju vibracionih svojstava kristalne rešetke, paralelno uz eksperimentalni pristup koje su Nenad i njegove kolege sprovodili. Posebno sam mu zahvalna na prilici da učestvujem u različitim projektima, a naročito na iskustvu koje sam sticala kroz proces pripreme samih projekata, što smatram neprocenjivim za svoj dalji razvoj.*

*Posebno sam zahvalna i dr Vladimiru Damljanoviću na izuzetnoj saradnji tokom izrade zajedničke publikacije, za priliku da učestvujem na međunarodnom projektu kojim rukovodi, kao i na strpljenju za pažljivo čitanje i korekciju ove disertacije. Njegov teorijski pristup, zasnovan na simetrijskim analizama, daje potpuno novu perspektivu na elektronsku strukturu materijala, inspirišući na kreativno razmišljanje i radoznalo otvaranje novih pitanja. Posebno, njegova posvećenost nauci i integritet čine ga mojim velikim naučnim uzorom, na čemu sam mu iskreno zahvalna.*

*Zahvaljujem se dr Kurtu Hingerlu sa Johannes Kepler Univerziteta u Lincu, sa kojim članovi naše laboratorije već godinama uspešno sarađuju. Najveći deo proračuna sprovedenih tokom izrade ove disertacije, obavljen je na serverima Johannes Kepler Univerziteta zahvaljujući nesebičnoj podršci dr Hingerla. Bez ovih računarskih resursa, ovako obimna i detaljna analiza ne bi bila moguća.*

*Zahvalna sam koleginicama dr Ani Milosavljević i dr Sanji Đurđić kao koautorima na mnogim zajedničkim publikacijama, na lepoj saradnji i druženju i razmeni iskustava sa doktorksih studija. Sanji se posebno zahvaljujem za čitanje i korekciju disertacije i veliku podršku u trenucima finalizacije teze. Dr Čedomiru Petroviću i njegovim saradnicima se zahvaljujem na sintezi uzoraka proučavanih u ovim publikacijama.*

*Zahvaljujem se svim kolegama iz Laboratorije za 2D materijale kao i celog Centra za fiziku čvrstog stanja i nove materijale, koji su doprineli lepšem i potpunijem boravku na Institutu, koji mi je tokom godina postao kao druga kuća. Duboku zahvalnost izražavam akademiku Zoranu Popoviću, bivšem šefu Centra za fiziku čvrstog stanja i nove materijale, koji mi je pružio priliku da budem član ovog izuzetnog Centra. Posebno se zahvaljujem mojim dragim koleginicama dr Ivani Milošević i dr Jasni Vujin na svoj pruženoj podršci i prijateljstvu.*

*Zahvalna sam dr Darku Tanaskoviću i dr Željku Šljivančaninu kod kojih sam imala čast da pohađam predmete iz fizike čvrstog stanja i ab-initio metoda, tokom doktorskih studija. Njihova predavanja i stručni pristup ne samo da su mi omogućili da usvojim ključna znanja, već su me inspirisali da dalje produbljujem svoje razumevanje i razvijam veštine neophodne za akademsku i naučnu karijeru.*

*Zahvalna sam i svim nastavnicima i profesorima koji su još od početka školovanja do kraja studiranja produbljivali moju ljubav prema fizici i motivisali me da nastavim tim putem. Posebno bih istakla nastavnike Jovana Todorovića i Mariju Lazarević pored kojih sam izgradila veliku ljubav prema fizici i koji su mi nesebično posvećivali vreme i pažnju. Istakla bih i profesore dr Milana Tadića, dr Vladimira Arsoskog i dr Jelenu Radovanović sa Elektrotehničkog fakulteta, koji su me uveli u fascinantnu oblast kvantne mehanike i 2D materijala i usmerili me na put ka naučnom radu u ovoj oblasti. Zahvaljujem se i dr Radošu Gajiću, bivšem šefu Laboratorije za 2D materijale, za priliku da budem deo njegove laboratorije.*

*Želela bih da se zahvalim i svoj rodbini i prijateljima koji su verovali u mene tokom svih ovih godina, a posebno sestri Branislavi, koja mi je kao mladi naučnik, fizičar, bila uzor još tokom studentskih dana.*

*Konačno, želela bih da se zahvalim svojim roditeljima za bezuslovnu ljubav, uprkos njihovoj ogromnoj želji da od mene naprave inženjera, bratu Gojku koji mi je oduvek bio velika podrška, i Dušanu na ljubavi i strpljenju.*

# Ispitivanje uticaja naprezanja na osobine heterostruktura dvodimenzionalnih monohalkogenida IIIA grupe *ab-initio* metodama

## SAŽETAK

Razvoj nauke o materijalima i fizike čvrstog stanja u 21. veku obeležen je intenzivnim istraživanjima dvodimenzionalnih (2D) materijala. Ovi materijali se ističu jedinstvenim elektronskim, optičkim i mehaničkim svojstvima, uz veliki potencijal za primene u nanoelektronici i optoelektronici. Među njima, monohalkogenidi IIIA grupe ($M^{III}X^{VI}$, gde su M = Ga, In; X = S, Se, Te) izdvajaju se zahvaljujući visokoj pokretljivosti elektrona, sposobnosti apsorpcije svetlosti u širokom spektru i sposobnosti da izdrže velike intenzitete naprezanja. Ipak, njihova hemijska osetljivost, posebno podložnost oksidaciji u kontaktu sa vazduhom, predstavlja značajan izazov za eksperimentalnu primenu. Enkapsulacija odgovarajućim materijalima, poput heksagonalnog bor nitrida (hBN), pokazala se kao efikasno rešenje, pružajući mehaničku i hemijsku zaštitu, uz dodatno poboljšanje elektronskih i optičkih svojstava ovih slojeva.

Jedan od najvažnijih pravaca savremenih istraživanja 2D materijala je primena mehaničkog naprezanja, koje omogućava precizno podešavanje elektronskih i optičkih svojstava, i optimizaciju ovih materijala za različite primene. Kontrolisano naprezanje otvara nove mogućnosti za inženjering energijskog procepa i prilagođavanje svojstava specifičnim primenama, pružajući značajan doprinos fundamentalnim istraživanjima i razvoju uređaja u fleksibilnoj elektronici, optoelektronici i drugim naprednim oblastima.

Cilj ove disertacije je pronalaženje i analiza novih heterostruktura (HS) na bazi $M^{III}X^{VI}$ sloja i hBN-a koje su dinamički stabilne i poseduju superiorna elektronska i optička svojstva. Istraživanje je fokusirano na efekat primene mehaničkog naprezanja na svojstva ovih HS, sa posebnim osvrtom na biaksijalno naprezanje koje omogućava preciznu kontrolu energijskog procepa i poboljšanje optičkih osobina, bez narušavanja simetrije materijala.

Rezultati pokazuju da kombinacija hBN-a sa $M^{III}X^{VI}$ slojevima formira HS sa poboljšanim mehaničkim svojstvima, zahvaljujući zaštitnoj ulozi hBN-a, dok istovremeno omogućava izvanrednu apsorpciju u širokom spektralnom opsegu. HS poput hBN/InTe i hBN/GaTe pokazale su se kao posebno perspektivne, zahvaljujući dobrom poklapanju konstanti rešetke sa hBN-om i manjem energijskom procepu, što rezultuje pojačanom apsorpcijom u vidljivom delu spektra. Ove HS pokazuju veliki potencijal za primene u optoelektronici za različite uređaje poput apsorbera i fotodetektora. Ovi rezultati naglašavaju potencijal za primene u optoelektronici, uključujući apsorbere i fotodetektore, pružajući istovremeno značajne smernice za dalja fundamentalna i eksperimentalna istraživanja.

**Ključne reči**: Teorija funkcionala gustine, 2D materijali, Heterostrukture, Naprezanje
**Naučna oblast**: Fizika
**Oblast istraživanja**: Fizika kondenzovanog stanja materije
**UDK broj**: 538.9

# Investigation of strain effects on properties of heterostructures based on 2D group IIIA monochalcogenides using *ab-initio* methods

## ABSTRACT

The development of materials science and solid-state physics in the 21st century has been marked by intensive research into two-dimensional (2D) materials. These materials are distinguished by their unique electronic, optical, and mechanical properties, with significant potential for applications in nanoelectronics and optoelectronics. Among them, group IIIa monochalcogenides ($M^{III}X^{VI}$, where M = Ga,In; X = S,Se,Te) stand out due to their high electron mobility, ability to absorb light across a wide spectrum, and resilience to high strain intensities. However, their chemical sensitivity, particularly their susceptibility to oxidation upon exposure to air, poses a significant challenge for applications. Encapsulation with suitable materials, such as hexagonal boron nitride (hBN), has proven to be an effective solution, providing mechanical and chemical protection while simultaneously enhancing the electronic and optical properties of these layers.

One of the most important directions in contemporary 2D materials science is the application of mechanical strain, which enables precise tuning of electronic and optical properties as well the optimization of these materials for various applications. Controlled strain opens new possibilities for bandgap engineering and tailoring material properties to specific applications, making significant contributions to fundamental research and the development of devices in flexible electronics, optoelectronics, and other advanced fields.

The goal of this dissertation is to identify and analyze new heterostructures based on $M^{III}X^{VI}$ layers and hBN that are dynamically stable and exhibit superior electronic and optical properties. The research focuses on the effect of mechanical strain on the properties of these heterostructures, with particular emphasis on biaxial strain, which allows precise bandgap control and improvement of optical properties without compromising the symmetry of the materials.

The results demonstrate that combining hBN with $M^{III}X^{VI}$ layers forms heterostructures with enhanced mechanical properties due to the protective role of hBN, while simultaneously achieving exceptional absorption across a broad spectral range. Heterostructures such as hBN/InTe and hBN/GaTe have proven to be particularly promising due to their excellent lattice constant matching with hBN and reduced bandgap, which enhances absorption in the visible light range. These heterostructures show great potential for optoelectronic applications in devices such as absorbers and photodetectors. Additionally, these results provide valuable insights for further fundamental research and serve as guidelines for the experimental realization of these structures.

**Keywords**: Density functional theory, 2D materials, Heterostructures, Strain
**Scientific field**: Physics
**Research area**: Condensed Matter Physics
**UDC number**: 538.9

# Akronimi

2D - Dvodimenzionalni

hBN - heksagonalni bor nitrid

DFT - Teorija funkcionala gustine

DFPT - Perturbaciona teorija funkcionala gustine

HS - Heterostrukture

TMD - Dihalkogenidi prelaznih metala

$M^{III}X^{VI}$ - Monohalkogenidi IIIa grupe

vdW - van der Vals

HEG - Homogeni elektronski gas

LDA - aproksimacija lokalne gustine

GGA - generalizovana gradijentna aproksimacija

QE - Quantum Espresso

# *Sadržaj*

# 1 Uvod

Razvoj nauke o materijalima i fizike čvrstog stanja na početku 21. veka obeležen je intenzivnim istraživanjima niskodimenzionalnih materijala. Posebnu pažnju naučne zajednice privukli su dvodimenzionalni (2D) materijali, zahvaljujući njihovim jedinstvenim svojstvima i širokom spektru mogućih primena. Slojeviti materijali, često nazivani i kvazi-2D materijali, sa slojevitim kristalnim strukturama povezanim slabim van der Valsovim silama, omogućili su istraživačima da eksperimentišu sa pojedinačnim atomskim slojevima, otvarajući nove puteve za fundamentalna i primenjena istraživanja.

Uspešna sinteza grafena 2004. godine označila je prekretnicu u nauci materijala, demonstrirajući stabilnost dvodimenzionalnih materijala u ambijentalnim uslovima, što je dovelo u pitanje ranije teorijske pretpostavke o njihovoj termodinamičkoj nestabilnosti. Otkriće grafena podstaklo je intenzivnu potragu za sličnim 2D materijalima, pa su neznatno kasnije otkriveni brojni drugi 2D materijali, kao što su heksagonalni bor nitrid (hBN) [1, 2], silicen [3, 4], germanen [5, 6], dihalkogenidi prelaznih metala (TMD) [7, 8, 9, 10, 11, 12], emikseni [13, 14], monohalkogenidi IIIA grupe [15, 16, 17, 18].

Posebnu pažnju u oblasti 2D materijala privukle su heterostrukture kod kojih su slojevi različitih materijala povezani slabim van der Valsovim silama. Ove strukture omogućavaju prilagođavanje elektronskih i optičkih svojstava kombinacijom slojeva sa različitim karakteristikama, što im daje prednost u raznovrsnim nanoelektronskim i optoelektronskim primenama [19, 20, 21, 22].

Monohalkogenidi IIIA grupe ($M^{III}X^{VI}$, gde je M = Ga, In; X = S, Se, Te) se poslednjih godina izdvajaju kao važni predstavnici 2D materijala, zahvaljujući direktnom energetskom procepu, visokim vrednostima pokretljivosti elektrona i mogućnosti apsorpcije svetlosti u širokom spektralnom opsegu. Zbog svojih specifičnih elektronskih i optičkih osobina [23], pažnju privlače već decenijama i u obliku tankih filmova. Na primer, FET tranzistori sa InSe slojevima debljine 33 nm dostižu mobilnost od 1055 $cm^2/Vs$ na sobnoj temperaturi [24], što je retko zabeleženo kod mnogih prelaznih TMD poput $MoS_2$ ili $WSe_2$ i uporedivo je sa vrednostima napregnutih silicijumskih MOSFET-ova [25] i tranzistora na bazi crnog fosfora [26]. Ova porodica materijala ima i odlična optička svojstva. Fotodetektori na bazi InSe slojeva imaju dobru apsorpciju u širokom delu spektra, od UV (ultraljubičasto) do bliskog IR (infracrveno), kao i visoku fotoresponzivnost i fotodetekciju [24, 27]. Pokazalo se da su, kao i mnogi drugi materijali sa slojevitom strukturom i

slabim međuslojnim silama, pogodni za eksfolijaciju u monoslojeve.

Monohalkogenidi IIIA grupe se nesumnjivo ističu kao izvanredni kandidati za optoelektronske aplikacije zahvaljujući svojim jedinstvenim svojstvima. Ipak, njihova eksperimentalna primena suočava se sa značajnim izazovima, pre svega zbog izrazite mehaničke i hemijske osetljivosti. Ovi materijali su posebno podložni oksidaciji u kontaktu sa vazduhom, pri čemu studije pokazuju da se strukture debljine jednog sloja gotovo trenutno oksidišu na otvorenom [28, 29, 30, 31]. Ovaj problem se uspešno rešava pasivizacijom odgovarajućim materijalima, koji obezbeđuju enkapsulaciju i mehaničku zaštitu, bez narušavanja željenih karakteristika osnovnog materijala. Heksagonalni bor nitrid (hBN) se pokazao kao izuzetno efikasan za ovu namenu [32, 33] pružajući pouzdanu zaštitu i istovremeno poboljšavajući elektronska i optička svojstva slojeva poput InSe i GaSe. Heterostrukture koje kombinuju monohalkogenide IIIA grupe i hBN posebno se ističu svojim izvanrednim apsorpcionim svojstvima u širokom spektru, od infracrvene do daleke ultraljubičaste oblasti [34]. Njihove mehaničke osobine omogućavaju primenu kontrolisanog naprezanja, što otvara mogućnost preciznog podešavanja energijskog procepa i prilagođavanja svojstava specifičnim aplikacijama. Takve strukture imaju ključnu ulogu u razvoju savremene nanoelektronike, pokazujući potencijal za primenu u tranzistorima sa efektom polja. Istovremeno, heterostrukture na bazi IIIA-VI jedinjenja i grafena pružaju interesantne mogućnosti za nove elektronske primene, uključujući podesive Šotki barijere [35, 36, 37, 38, 39].

Cilj istraživanja ove disertacije je pronalaženje novih heterostruktura na bazi monohalkogenida IIIA grupe koje su dinamički stabilne i poseduju željene karakteristike, čime bi se kvalifikovale kao odlični kandidati za primene u absorberima, fotodetektorima ili tranzistorima. Istraživanje obuhvata analizu njihovih elektronskih i optičkih osobina, kao i mogućnost inženjeringa željenih karakteristika mehaničkim modifikacijama, prvenstveno primenom naprezanja. Monoslojevi $M^{III}X^{VI}$ poseduju izuzetna elektronska i optička svojstva, uključujući visoku pokretljivost elektrona i odličnu apsorpciju u širokom spektralnom opsegu, uz izuzetne elastične osobine i mogućnost istezanja od preko 15% [18, 40, 41]. Monosloj hBN-a je već prepoznat kao izuzetan materijal za zaštitu od atmosferskih uticaja, a zahvaljujući svojim elastičnim osobinama pruža i odličnu mehaničku zaštitu osetljivih $M^{III}X^{VI}$ slojeva, osiguravajući njihovu robusnost. Ovaj izolator sa širokim energijskim procepom ne uvodi značajne kvalitativne promene prilikom formiranja $hBN/M^{III}X^{VI}$ heterostruktura, ali pojačava apsorpciju u određenim delovima spektra.

U okviru istraživanja ispitivana je mogućnost formiranja jedinične ćelije, odnosno poklapanje konstanti rešetki u oba monosloja, vodeći računa o indukovanom naprezanju koje se javlja prilikom formiranja heterostruktura; energija vezivanja, kao i dinamička stabilnost ovih struktura.

Glavni deo istraživanja obuhvata opsežnu analizu elektronskih i optičkih osobina heterostruktura pod uticajem biaksijalnog naprezanja. Ispitivani su jačina sprezanja međuslojeva i prenos naelektrisanja, uticaj intenziteta naprezanja na zonsku strukturu i širinu

energijskog procepa, kao i na optičke osobine poput apsorpcije. Istraživanje se oslanja na numeričke metode zasnovane na osnovnim principima kvantne mehanike - teoriju funkcionala gustine (*density functional theory* - DFT). Ovaj formalizam se široko koristi u fizici, hemiji i nauci o materijalima jer omogućava efikasno rešavanje problema elektronske strukture, pružajući optimalan balans između preciznosti i potrebnih računarskih resursa. Problem višečestičnih sistema u fizici čvrstog stanja i dalje predstavlja izazov - egzaktno rešavanje Šredingerovih jednačina za realistične materijale sa velikim brojem interagujućih atoma i elektrona praktično je neizvodljivo. Polazeći od osnovne ideje, da sve karakteristike sistema interagujućih čestica u svom osnovnom stanju zavise isključivo od funkcionala gustine elektrona, DFT omogućava elegantno rešavanje problema višečestičnih sistema, koji su do tada bili gotovo nerešivi.

Disertacija je organizovana kroz šest poglavlja. Prvo poglavlje pruža kratak uvod. Drugo poglavlje sadrži teorijski pregled i detalje metoda korišćenih u istraživanju. Treće poglavlje pruža opis dvodimenzionalnih monohalkogenida IIIA grupe i pregled postojećih saznanja o njima. Četvrto poglavlje je fokusirano na rezultate istraživanja i podeljeno je u nekoliko potpoglavlja: Rezultati istraživanja hBN/In(Ga)Te i hBN/InSe heterostruktura; uticaj biaksijalnog naprezanja na ove heterostrukture; rezultati istraživanja preostalih heterostruktura hBN-a i $M^{III}X^{VI}$. Peto poglavlje daje kratak pregled preostalih rezultata istraživanja vezanih za 2D i slojevite materijale, ostvarenih tokom doktorskih studija na Institutu za fiziku u Beogradu, dok šesto poglavlje sadrži zaključke istraživanja.

# 2 Teorija funkcionala gustine

Problem opisa višečestičnih sistema već decenijama predstavlja jedno od ključnih pitanja u fizici čvrstog stanja. Rešavanje Šredingerove jednačine postaje veoma složeno za sisteme od već nekoliko čestica, a kod realističnih materijala sa velikim brojem atoma i interagujućih elektrona, egzaktno rešavanje Šredingerovih jednačina praktično je nemoguće zbog ogromnih računarskih zahteva i kompleksnosti. Za opis elektronske strukture postoje brojne numeričke metode, međutim, mnoge od njih se zasnivaju na aproksimativnim rešenjima Šredingerove jednačine i postaju neefikasne za složenije sisteme.

Šezdesetih godina 20. veka, kao odgovor na izazove kvantne mehanike u opisivanju kompleksnih sistema, razvijena je teorija funkcionala gustine (engl. Density Functional Theory - DFT). Prvi korak u ovom smeru načinili su L.H. Tomas i E. Fermi 1927. godine uvodeći teoriju zasnovanu na elektronskoj gustini. Tomas-Fermijeva teorija predstavljala je pionirski pokušaj da se kvantnomehaničko ponašanje elektrona u atomima, molekulima i čvrstim telima opiše korišćenjem elektronske gustine. Iako prilično jednostavna i inovativna, ova teorija zanemarila je ključne kvantne efekte izmene i korelacije, što je značajno ograničilo njenu primenu. Ipak, postavila je stabilne temelje za razvoj modernog DFT-a koji se danas uspešno koristi i kontinuirano unapređuje.

Počeci DFT-a sežu u 1964. godinu, kada su Pjer Hoenberg i Valter Kon u svom radu [42] dokazali da je elektronska gustina osnovnog stanja dovoljna za određivanje svih svojstava kvantnog sistema u osnovnom stanju. Njihove dve fundamentalne teoreme postavile su temelje savremenog DFT-a. Ključna ideja DFT-a zasniva se na činjenici da su sve karakteristike sistema interagujućih čestica u osnovnom stanju funkcional gustine elektrona, $n(\mathbf{r})$. Zahvaljujući ovome, kompleksan sistem interagujućih elektrona može se posmatrati kao sistem neinteragujućih elektrona iste elektronske gustine, tako da se pri određivanju $n(\mathbf{r})$ prelazi na rešavanje jednočestičnih jednačina.

Ovakav pristup privukao je značajnu pažnju naučne zajednice, što je dovelo do proširenja mogućnosti DFT-a i razvoja različitih funkcionala poput LDA, GGA i hibridnih funkcionala. Pojava specijalizovanih softverskih paketa zasnovanih na DFT-u dodatno je ubrzala njegovu primenu u istraživanju materijala. Prednosti DFT-a ogledaju se u njegovom balansu između preciznosti i računske efikasnosti, što ga čini univerzalnim alatom za simulacije širokog spektra materijala. Pored toga, ova teorija ima i univerzalnu metodološku osnovu, budući da ne zahteva konstrukciju posebnih modela za svaku klasu

materijala.

Međutim, i DFT ima određena ograničenja, a posebno u opisivanju jako korelisanih sistema, van der Valsovih interakcija i energijskog procepa u poluprovodnicima. Mnogi prošireni modeli i korekcije razvijeni su sa ciljem da ublaže ove nedostatke, čineći DFT i dalje vodećim alatom u savremenoj nauci o materijalima. Zahvaljujući svojoj praktičnosti i rastućim mogućnostima modernih računara, softveri zasnovani na DFT-u se konstantno razvijaju i unapređuju, a mnogi od njih su otvorenog koda, što omogućava naučnoj zajednici da ih testira, prilagođava svojim potrebama i doprinosi daljem razvoju.

Ovo poglavlje posvećeno je razmatranju teorije na kojoj se zasniva DFT, uz opis ključnih aproksimacija koje su korišćene prilikom proračuna, kao i softvera koji je korišćen.

## 2.1 Višečestični sistemi

Realistični materijali sastoje se od velikog broja elektrona i jezgara koji međusobno interaguju Kulonovim silama. Upravo ove interakcije dovode do složenih problema koje je izuzetno teško tačno rešavati. U opštem slučaju kvantnog sistema sa $N$ elektrona i $M$ jezgara, talasna funkcija sistema zavisi od svih elektronskih i nuklearnih koordinata:

$$\Psi = \Psi(\mathbf{r}_1, \mathbf{r}_2, \ldots, \mathbf{r}_N; \mathbf{R}_1, \mathbf{R}_2, \ldots, \mathbf{R}_M), \tag{2.1}$$

elektronska gustina je određena kao:

$$n(\mathbf{r}) = N \int |\Psi(\mathbf{r}, \mathbf{r}_2, \ldots, \mathbf{r}_N; \mathbf{R}_1, \mathbf{R}_2, \ldots, \mathbf{R}_M)|^2 d\mathbf{r}_2 \ldots d\mathbf{r}_N d\mathbf{R}_1 \ldots d\mathbf{R}_M \tag{2.2}$$

a hamiltonijan sistema se može zapisati kao

$$\hat{H} = \hat{T}_e + \hat{T}_n + \hat{V}_{ee} + \hat{V}_{en} + \hat{V}_{nn}, \tag{2.3}$$

gde su:

$$\hat{T}_e = -\sum_{i=1}^{N} \frac{\hbar^2}{2m_e} \nabla_i^2, \quad \hat{T}_n = -\sum_{I=1}^{M} \frac{\hbar^2}{2M_I} \nabla_I^2 \tag{2.4}$$

$\hat{T}_e$ kinetička energija elektrona i $\hat{T}_n$ kinetička energija jezgara,

$$\hat{V}_{ee} = \frac{1}{2} \sum_{i \neq j} \frac{e^2}{4\pi\epsilon_0 |\mathbf{r}_i - \mathbf{r}_j|}, \; -\hat{V}_{en} = \sum_{i,I} \frac{Z_I e^2}{4\pi\epsilon_0 |\mathbf{r}_i - \mathbf{R}_I|}, \; \hat{V}_{nn} = \frac{1}{2} \sum_{I,J} \frac{Z_I Z_j}{4\pi\epsilon_0 |\mathbf{R}_I - \mathbf{R}_J|} \tag{2.5}$$

su Kulonova interakcija između elektrona, Kulonova interakcija elektrona i jezgara i Kulonova interakcija između jezgara.

Dakle, Šredingerova jednačina za višečestične sisteme ima oblik

$$\left[-\sum_{i=1}^{N}\frac{\hbar^2}{2m_e}\nabla_i^2-\sum_{I=1}^{M}\frac{\hbar^2}{2M_I}\nabla_I^2+\frac{1}{2}\sum_{i\neq j}\frac{e^2}{4\pi\epsilon_0|\mathbf{r}_i-\mathbf{r}_j|}-\right.$$
$$\left.-\sum_{i,I}\frac{Z_I e^2}{4\pi\epsilon_0|\mathbf{r}_i-\mathbf{R}_I|}+\frac{1}{2}\sum_{I,J}\frac{Z_I Z_j}{4\pi\epsilon_0|\mathbf{R}_I-\mathbf{R}_J|}\right]\Psi=E_{tot}\Psi. \tag{2.6}$$

Odavde se jasno vidi zašto se ovakve metode nazivaju i "*ab-initio*" odnosno, "iz prvih principa". Naime, konstante u jednačini 2.6 jesu redukovana Plankova konstanta $\hbar$, masa elektrona $m_e$, masa jezgra $M_I$, naelektrisanje elektrona $e$ i permitivnost vakuuma $\epsilon_0$, koje su već poznate fundamentalne fizičke konstante, nezavisne od materijala koji se proučava. Jednačina dakle, ne sadrži bilo kakve empirijske ili fitovane parametre, pa se metodologija kojom se polazi od njenog rešavanja naziva pristupom iz prvih principa.

Jasno je da za složene sisteme rešavanje takve jednačine zahteva ogromnu računarsku snagu, budući da kompleksnost raste eksponencijalno sa brojem čestica. Značajan deo izazova u ovom problemu dolazi iz međusobnih interakcija elektrona $\hat{V}_{ee}$, jer se taj član ne može jednostavno razložiti na više nezavisnih problema.

Imajući u vidu složenost egzaktnih metoda, razvijene su razne aproksimacije koje omogućavaju rešavanje problema čak i u slučajevima veoma složenih sistema.

Pre razmatranja navedenih aproksimacija, jednačina 2.6 biće zapisana u malo drugačijem obliku, prelaskom na atomske jedinice, koje se najčešće koriste u modelovanju materijala. Ukoliko se za jedinicu energije uvede Ha hartri kao

$$E_{\mathrm{Ha}}=\frac{e^2}{4\pi\epsilon_0 a_0}=27.2114\ \mathrm{eV}=4.3597\cdot 10^{-18}\ \mathrm{J} \tag{2.7}$$

pri čemu je $a_0$ radijus elektronske orbitale atoma vodonika u osnovnom stanju i iznosi $a_0 = 0.529177$ Å. Zajedno sa atomskom jedinicom mase, 1 a.u. $= 9.10938291\cdot 10^{-31}$ kg i usvajanjem naelektrisanja elektrona na $e = 1$, ove jedinice se zovu Hartrijeve atomske jedinice. Jednačina 2.6 sada dobija oblik koji se najčešće koristi u modelovanju materijala:

$$\left[-\sum_{i}\frac{\nabla_i^2}{2}-\sum_{I}\frac{\nabla_I^2}{2M_I}+\frac{1}{2}\sum_{i\neq j}\frac{1}{|\mathbf{r}_i-\mathbf{r}_j|}-\sum_{i,I}\frac{Z_I}{|\mathbf{r}_i-\mathbf{R}_I|}+\frac{1}{2}\sum_{I,J}\frac{Z_I Z_j}{|\mathbf{R}_I-\mathbf{R}_J|}\right]\Psi=E_{tot}\Psi. \tag{2.8}$$

### 2.1.1 Born-Openhajmerova aproksimacija

Jedan od ključnih koncepata u kvantnoj mehanici koji omogućava razdvajanje kretanja elektrona i jezgara u molekulima i čvrstim materijalima jeste Born-Openhajmerova

aproksimacija [43, 44]. Ona je uvedena 1927. godine od strane Maksa Borna i Roberta Openhajmera i značajno je pojednostavila rešavanje kvantnih sistema sa višečestičnim interakcijama. Osnovna ideja Born-Openhajmerove aproksimacije zasniva se na činjenici da su jezgra u atomima i molekulima značajno masivnija od elektrona (nekoliko redova veličine), pa se kreću mnogo sporije. Usled te razlike, kretanje elektrona i kretanje jezgara mogu se posmatrati kao odvojeni procesi. Ujedno, kako se u čvrstim telima i molekulima adsorbovanim na čvrstim površinama jezgra često nalaze na praktično fiksnim i poznatim pozicijama, ona se mogu posmatrati kao "zamrznuta" u određenim položajima.

Pretpostavka da su jezgra dovoljno teška da se praktično ne kreću implicira $M_I = \infty$, pa se član kinetičke energije jezgara može zanemariti, a odbojna Kulonova sila između jezgara smatrati konstantom. Ukoliko se ova konstanta prebaci na desnu stranu jednačine 2.8 i definiše se

$$E = E_{\text{tot}} - \frac{1}{2}\sum_{I\neq J}\frac{Z_I Z_J}{|\mathbf{R}_I - \mathbf{R}_J|}, \tag{2.9}$$

jednačina 2.8 se svodi na

$$\left[-\sum_i \frac{\nabla_i^2}{2} - \sum_{i,I}\frac{Z_I}{|\mathbf{r}_i - \mathbf{R}_I|} + \frac{1}{2}\sum_{i\neq j}\frac{1}{|\mathbf{r}_i - \mathbf{r}_j|}\right]\Psi = E\Psi. \tag{2.10}$$

Tada se talasna funkcija $\Psi$ može posmatrati kao funkcija elektronskih koordinata, $\Psi = \Psi(\mathbf{r}_1, \ldots, \mathbf{r}_N)$, a koordinate jezgara $\mathbf{R}_I$ se posmatraju kao eksterni parametri. Dalje se smatra da se elektroni kreću u statičkom eksternom potencijalu koji generišu jezgra:

$$V_n(\mathbf{r}) = -\sum_I \frac{Z_I}{|\mathbf{r} - \mathbf{R}_I|}. \tag{2.11}$$

Sada se koordinate jezgara pojavljuju isključivo parametarski, pa se može rešavati samo elektronski deo:

$$\left[-\sum_i \frac{\nabla_i^2}{2} + \frac{1}{2}\sum_{i\neq j}\frac{1}{|\mathbf{r}_i - \mathbf{r}_j|} + \sum_i V_n(\mathbf{r}_i)\right]\phi_e(\mathbf{r};\mathbf{R}) = E\phi_e(\mathbf{r};\mathbf{R}), \tag{2.12}$$

Born-Openhajmerova aproksimacija je skoro nezaobilazna u savremenoj kvantnoj mehanici i hemiji materijala, značajno smanjujući kompleksnost problema i omogućavajući precizno izračunavanje elektronskih osobina. Ipak, i ova aproksimacija ima svoja ograničenja, i postoje različiti sistemi u kojima nije validna. Jedan od njih je situacija u kojoj su pokreti jezgara i elektrona zavisni, na primer u slučaju sistema sa veoma malim masama jezgara (npr. vodonik).

### 2.1.2 Model nezavisnih elektrona (Hartrijev model) i Hartri-Fokova aproksimacija

Jedan od prvih pokušaja rešavanja problema višečestičnih kvantnih sistema pomoću pojednostavljenog pristupa potiče od Daglasa Hartrija. Hartri u svom modelu elektrone tretira kao nezavisne i smatra da elektroni ne vide jedan drugi. Talasna funkcija se u ovom modelu aproksimira kao proizvod jednočestičnih talasnih funkcija [45]:

$$\Psi(\mathbf{r}_1, \mathbf{r}_2, \ldots, \mathbf{r}_N) = \phi_1(\mathbf{r}_1) \ldots \phi_N(\mathbf{r}_N), \tag{2.13}$$

a umesto razmatranja Kulonove interakcije među elektronima, smatra se da se svaki elektron kreće u srednjem polju kreiranom od ostalih elektrona:

$$V_H(\mathbf{r}) = \int \frac{n(\mathbf{r}')}{|\mathbf{r} - \mathbf{r}'|}. \tag{2.14}$$

Jednočestične talasne funkcije se tada određuju rešavanjem Hartrijevih jednačina:

$$\left[ -\frac{\nabla_i^2}{2} + V_{ext}(\mathbf{r}) + V_H(\mathbf{r}) \right] \phi_i(\mathbf{r}) = \epsilon_i \phi_i(\mathbf{r}), \tag{2.15}$$

a ukupna energija kao zbir svij dobijenih svojstvenih energija:

$$E = \epsilon_1 + \epsilon_2 + \ldots \epsilon_N. \tag{2.16}$$

Ovaj model iako intuitivan i vrlo jednostavan, zanemaruje važne kvantnomehaničke efekte izmene i korelacije između elektrona. Naime, izmena i korelacija predstavljaju nezaobilazne efekte u opisu interakcija u kvantnim sistemima i javljaju se zbog kvantne prirode elektrona. Izmena se odnosi na kvantno-mehanički princip koji proizilazi iz Paulijevog principa isključenja i simetrije talasne funkcije fermiona. Sa druge strane, korelacija uključuje sve interakcije elektrona koje nisu obuhvaćene izmenom, kao što je elektrostatičko odbijanje među elektronima. Ona dakle uzima u obzir da na kretanje jednog elektrona utiče prisustvo ostalih elektrona, odnosno da je kretanje elektrona korelisano.

Neznatno kasnije, Vladimir Fok razvija unapređen metod za rešavanje višečestičnih problema, zasnovan na Hartrijevom modelu, ali uz dodate efekte izmene među elektronima [46]. Naime, po Paulijevom principu isključenja, dva elektrona ne mogu da zauzimaju isto kvantno stanje, što implicira da višečestična talasna funkcija mora biti antisimetrična. U slučaju dva elektrona, talasna funkcija oblika

$$\Psi(\mathbf{r}_1, \mathbf{r}_2) = \frac{1}{\sqrt{2}} \left[ \phi_1(\mathbf{r}_1)\phi_2(\mathbf{r}_2) - \phi_1(\mathbf{r}_2)\phi_2(\mathbf{r}_1) \right] \tag{2.17}$$

zadovoljava ovaj zahtev. U slučaju više čestica, antisimetrična talasna funkcija ima oblik

Slejterove determinante [47]:

$$\Psi(\mathbf{r}_1, \mathbf{r}_2, \ldots, r_N) = \frac{1}{\sqrt{N!}} \begin{vmatrix} \phi_1(\mathbf{r}_1) & \phi_2(\mathbf{r}_1) & \cdots & \phi_N(\mathbf{r}_1) \\ \phi_1(\mathbf{r}_2) & \phi_2(\mathbf{r}_2) & \cdots & \phi_N(\mathbf{r}_2) \\ \vdots & \vdots & \ddots & \vdots \\ \phi_1(\mathbf{r}_N) & \phi_2(\mathbf{r}_N) & \cdots & \phi_N(\mathbf{r}_N) \end{vmatrix}, \tag{2.18}$$

pri čemu je $\Psi(\mathbf{r}_1, \mathbf{r}_2, \ldots, \mathbf{r}_N)$ talasna funkcija za $N$ elektrona, $\phi_i(\mathbf{r}_j)$ jednočestične talasne funkcije koje opisuju stanje $i$-tog elektrona u koordinati $\mathbf{r}_j$, $\frac{1}{\sqrt{N!}}$ normalizacioni faktor koji osigurava pravilnu normiranost talasne funkcije, dok $|\cdot|$ predstavlja determinantu koja osigurava antisimetričnost talasne funkcije u skladu sa Paulijevim principom isključenja.

Fok uvodi i dodatni član za potencijal izmene,

$$V_X(\mathbf{r}, \mathbf{r}') = -\sum_j \frac{\phi_j^*(\mathrm{r}')\phi_j(\mathrm{r})}{|\mathbf{r} - \mathbf{r}'|}, \tag{2.19}$$

a Hartri-Fokove jednačine koje se izvode minimizacijom ukupne energije E koja odgovara talasnoj funkciji osnovnog stanja, u odnosu na varijacije talasnih funkcija $\phi_i(\mathbf{r})$ u Slejterovoj determinanti, poprimaju oblik:

$$\left[-\frac{\nabla_i^2}{2} + V_{ext}(\mathbf{r}) + V_H(\mathbf{r}) - V_X(\mathbf{r})\right] \phi_i(\mathbf{r}) = \epsilon_i \phi_i(\mathbf{r}). \tag{2.20}$$

Hartri-Fokova aproksimacija daje značajno bolje rezultate u fizici čvrstog stanja, uključujući kvantne efekte izmene koji su važni za precizno opisivanje elektronskih sistema, ali je i dalje zanemaren važan efekat korelacije elektrona. Takođe, računarski je prilično komplikovana za veće sisteme. I pored toga, Hartri-Fokov pristup je predstavljao važnu osnovu za razvoj naprednih metoda, kao što je teorija funkcionala gustine.

## 2.2 Hoenberg-Konove teoreme

Teorija funkcionala gustine (DFT) je jedan od najuspešnijih metoda za istraživanje osnovnih fizičkih osobina materijala. Ovaj metod pojednostavljuje problem rešavanja Šredingerove jednačine za više čestica redukujući ga na efektivno jednočestične i koristeći aproksimacije zasnovane na elektronskoj gustini. DFT počiva na dve fundamentalne teoreme koje su formulisali Hoenberg i Kon [42]:

**Teorema 1.** *Za svaki kvantni sistem interagujućih elektrona u spoljašnjem potencijalu $V_{ext}(\mathbf{r})$, gustina elektrona u osnovnom stanju $n_0(\mathbf{r})$ jednoznačno određuje spoljašnji potencijal $V_{ext}(\mathbf{r})$ do na konstantu.*

Ovo implicira da su sve osobine sistema sadržane u gustini elektrona. Dokaz ove teoreme zasnovan je na svođenju na apsurd:

**Dokaz.** Pretpostavimo da postoje dva eksterna potencijala, $V_{ext}$ i $V'_{ext}$ koji se razlikuju za više od na konstantu, a koji rezultuju istom elektronskom gustinom $n(\mathbf{r})$. Ovi eksterni potencijali su delovi dva hamiltonijana $H$ i $H'$, sa pripadajućim talasnim funkcijama $\Psi$ i $\Psi'$ i odgovarajućim energijama osnovnog stanja, $E_0$ i $E'_0$, respektivno. S obzirom na to da je u pitanju isti sistem elektrona, ova dva hamiltonijana razlikuju se samo u delu koji se odnosi na eksterni potencijal, odnosno, $\hat{H} = \hat{T} + \hat{V}_{ee} + \hat{V}_{ext}$ i $\hat{H}' = \hat{T} + \hat{V}_{ee} + \hat{V}'_{ext}$. Ovde su

$$\hat{T} = -\sum_i \frac{1}{2}\nabla_i^2, \quad \hat{V}_{ee} = \frac{1}{2}\sum_{i\neq j} \frac{1}{|\mathrm{r_i} - \mathrm{r_j}|} \tag{2.21}$$

operator kinetičke energije i operator Kulonove energije, respektivno. Pošto $\Psi$ nije talasna funkcija osnovnog stanja za hamiltonijan $H'$, po varijacionom principu mora važiti

$$E'_0 < \langle\Psi|\, \hat{H}' \,|\Psi\rangle\,, \tag{2.22}$$

odnosno ako zapišemo prethodnu jednačinu malo drugačije,

$$E'_0 < \langle\Psi|\, \hat{H}' \,|\Psi\rangle + \langle\Psi|\, \hat{H} \,|\Psi\rangle - \langle\Psi|\, \hat{H} \,|\Psi\rangle\,, \tag{2.23}$$

dobijamo

$$E'_0 < \langle\Psi|\, \hat{H}' - \hat{H} \,|\Psi\rangle + E_0, \;\; \text{tj.} \;\; E'_0 - E_0 < \langle\Psi|\, \hat{H}' - \hat{H} \,|\Psi\rangle\,. \tag{2.24}$$

Analogno, uzimajući da $\Psi'$ nije talasna funkcija osnovnog stanja za $\hat{H}$, dobija se

$$E_0 - E'_0 < \langle\Psi|\, \hat{H} - \hat{H}' \,|\Psi\rangle\,. \tag{2.25}$$

Sabiranjem prethodne dve jednačine dobija se

$$0 < \int n(\mathbf{r})(V'_{ext} - V_{ext})d\mathbf{r} + \int n(\mathbf{r})(V_{ext} - V'_{ext})d\mathbf{r}, \tag{2.26}$$

odnosno, $0 < 0$, što je kontradikcija. Dakle, tvrdnja da mogu postojati dva različita eksterna potencijala $V_{ext}$ i $V'_{ext}$ koja vode do iste gustine elektrona u osnovnom stanju, $n$ je netačna.

**Teorema 2.** *Za kvantni sistem interagujućih čestica može se definisati funkcional energije $E[n]$ koji zavisi isključivo od gustine $n(\mathbf{r})$. Energija osnovnog stanja sistema odgovara globalnom minimumu funkcionala $E[n]$, dok gustina koja minimizuje funkcional jeste gustina osnovnog stanju sistema $n_0(\mathbf{r})$.*

**Dokaz.** Funkcional ukupne energije sistema definisan je kao:

$$E[n] = F[n] + \int V_{\text{ext}}(\mathbf{r}) n(\mathbf{r})\, d\mathbf{r}, \tag{2.27}$$

gde je $F[n]$ univerzalni funkcional definisan kao:

$$F[n] = \langle \Psi[n] | \hat{T} + \hat{V}_{\text{ee}} | \Psi[n] \rangle, \tag{2.28}$$

pri čemu $\hat{T}$ predstavlja operator kinetičke energije, a $\hat{V}_{\text{ee}}$ operator elektron-elektron interakcije. Neka sistem elektrona u osnovnom stanju ima elektronsku gustinu $n_0(\mathbf{r})$, koja odgovara eksternom potencijalu $V_{ext}(\mathbf{r})$. Energija osnovnog stanja ovakvog sistema je vrednost funkcionala energije za gustinu osnovnog stanja $n_0(\mathbf{r})$. Po varijacionom principu, ta energija je očekivana vrednost hamiltonijana za talasnu funkciju osnovnog stanja $\Psi_0$:

$$E_0 = \langle \Psi_0 | \, \hat{H} \, | \Psi_0 \rangle \, . \tag{2.29}$$

Pretpostavimo da postoji gustina $n'(\mathbf{r}) \neq n_0(\mathbf{r})$, koja odgovara talasnoj funkciji $\Psi'$. Za ovu gustinu, energija $E[n']$ ne može biti manja od energije osnovnog stanja $E_0$, jer ne odgovara osnovnom stanju sistema:

$$E_0 = \langle \Psi_0 | \, \hat{H} \, | \Psi_0 \rangle < \langle \Psi' | \, \hat{H} \, | \Psi' \rangle = E[n']. \tag{2.30}$$

Odavde se može zaključiti da bilo koja druga elektronska gustina različita od gustine osnovnog stanja, dovodi do funkcionala energije čija je vrednost veća od energije koja odgovara gustini osnovnog stanja.

Iako tvrdi postojanje ovako definisanog funkcionala energije, druga Hoenberg-Konova teorema ne govori o tome kako se on definiše, odnosno, ne daje rešenje problema kako se konstruše eksterni potencijal za poznatu elektronsku gustinu osnovnog stanja, pa je i sam funkcional energije u osnovi nepoznat. Polazeći od ovih teorema, Kon i Šam 1965. godine su konstruišući set jednačina uveli Kon-Šamov formalizam [48], koji je omogućio rešavanje problema višečestičnih sistema kroz fiktivni model neinteragujućih čestica. Uopšteno, funkcional energije ovakvog sistema može se izraziti kao:

$$E = F[n] = T[n] + E_{ext}[n] + E_H[n] + E_{xc}[n], \tag{2.31}$$

gde je $T[n]$ kinetička energija elektrona, $E_{ext}[n]$ energija interakcije sa spoljašnjim potencijalom, $E_H[n]$ Hartrijeva energija koja opisuje odbojnu interakciju između elektrona, i $E_{xc}[n]$ energija izmene i korelacije u kojoj su uključeni kvantni efekti. Pretpostavljeni fiktivni sistem neinteragujućih elektrona ima istu elektronsku gustinu kao i realni sistem, a talasna funkcija ovog fiktivnog sistema je antisimetrizovani proizvod jednočestičnih or-

bitala,

$$n(\mathbf{r}) = \sum_{i=1}^{N} |\phi_i(\mathbf{r})|^2, \text{ i zadovoljen je uslov normiranja, } \int n(\mathbf{r}) d\mathbf{r} = N. \tag{2.32}$$

Po Konu i Šamu, ovaj funkcional se sastoji od članova koji su uključeni u aproksimaciju nezavisnih elektrona, plus poslednji član, $E_{xc}[n]$ koji se naziva i izmensko-korelacioni funkcional:

$$E = F[n] = \int n(\mathbf{r}) V_n(\mathbf{r})\, d\mathbf{r} - \sum_i \int \phi_i^*(\mathbf{r}) \frac{\nabla^2}{2} \phi_i(\mathbf{r})\, d\mathbf{r} + \frac{1}{2} \iint \frac{n(\mathbf{r}) n(\mathbf{r}')}{|\mathbf{r} - \mathbf{r}'|}\, d\mathbf{r}\, d\mathbf{r}' + E_{\text{xc}}[n]. \tag{2.33}$$

Prva tri člana koja predstavljaju energiju elektrona u spoljašnjem potencijalu, kinetičku energiju i Hartrijevu energiju su poznati, a izmensko-korelacioni član je taj koji je nepoznat. Ukoliko bi se mogla znati njegova tačna vrednost, tehnički bi bilo moguće odrediti egzaktnu energiju osnovnog stanja sistema $E = F[n]$ koristeći elektronsku gustinu. Ova elektronska gustina osnovnog stanja, $n_0$ je zapravo funkcija koja minimizuje ukupnu energiju, odnosno funkcional $F[n]$:

$$\left. \frac{\delta F[n]}{\delta n} \right|_{n_0} = 0. \tag{2.34}$$

Zahtev da izvod funkcionala bude jednak nuli vodi ka jednačinama talasnih funkcija, $\phi_i(\mathbf{r})$, pomoću kojih se može konstruisati elektronska gustina, a ukoliko se postavi uslov da su talasne funkcije ortonormirane, dobija se jednačina oblika

$$\left[ -\frac{1}{2}\nabla^2 + V_n(\mathbf{r}) + V_{\text{H}}(\mathbf{r}) + V_{\text{xc}}(\mathbf{r}) \right] \phi_i(\mathbf{r}) = \epsilon_i \phi_i(\mathbf{r}), \tag{2.35}$$

Ovde $\nabla^2$ predstavlja laplasijan, $V_n(\mathbf{r})$ eksterni potencijal koji potiče od jezgara, $V_{\text{H}}(\mathbf{r})$ je Hartrijev potencijal, $V_{\text{xc}}(\mathbf{r})$ je izmensko-korelacioni potencijal, $\phi_i(\mathbf{r})$ su jednočestične talasne funkcije (Kon-Šamove orbitale), dok su $\epsilon_i$ energije povezane sa Kon-Šamovim orbitalama. Izmensko-korelacioni član se dobija iz

$$V_{\text{xc}}(\mathbf{r}) = \left. \frac{\delta E_{\text{xc}}[n]}{\delta n} \right|_{n(\mathbf{r})}, \tag{2.36}$$

a forma ovog funkcionala nije poznata. S obzirom na to da se on ne može egzaktno odrediti, vremenom su razvijane različite aproksimacije za opis ovih funkcionala - od najjednostavnije aproksimacije lokalne gustine (LDA), pa sve do različitih hibridnih funkcionala. U odeljku 2.4 će biti više reči o njima, uz detaljniji opis najjednostavnija, ali i najčešća dva korišćena funkcionala: aproksimacija lokalne gustine i aproksimacija uopštenog gradijenta.

## 2.3 Samousaglašeno rešavanje Kon-Šamovih jednačina

Kon-Šamove jednačine omogućavaju rešavanje problema elektronske strukture u teoriji funkcionala gustine, ali se postavlja pitanje kako se u praksi one rešavaju, i kako se iz njih dobija ukupna energija sistema. Kon-Šamove jednačine su date jednačinom 2.35 koju ćemo ponoviti ovde:

$$\left[-\frac{1}{2}\nabla^2 + V_n(\mathbf{r}) + V_{\mathrm{H}}(\mathbf{r}) + V_{\mathrm{xc}}(\mathbf{r})\right]\phi_i(\mathbf{r}) = \epsilon_i\phi_i(\mathbf{r}). \tag{2.37}$$

Neka za izmensko-korelacioni funkcional bude izabrana najjednostavnija aproksimacija lokalne gustine, za koju je potencijal eksplicitno određen jednačinom datom u 2.4. Potencijali jezgara i Hartrijev potencijal su takođe izraženi poznatim jednačinama,

$$V_n(\mathbf{r}) = -\sum_I \frac{Z_I}{|\mathbf{r}-\mathbf{R}_I|}, \quad V_H(\mathbf{r}) = \int \frac{n(\mathbf{r}')}{|\mathbf{r}-\mathbf{r}'|}. \tag{2.38}$$

Kako bi se odredile svojstvene funkcije $\phi_i(\mathbf{r})$ i svojstvene vrednosti $\epsilon_i$, potrebno je prvo znati potencijal $V_{KS} = V_n(\mathbf{r}) + V_{\mathrm{H}}(\mathbf{r}) + V_{\mathrm{xc}}(\mathbf{r})$. Ovo zahteva poznavanje elektronske gustine $n$ od koje potencijali $V_H$ i $V_{xc}$ zavise. A sa druge strane, elektronska gustina zavisi od talasne funkcije $\phi_i$ koja je nepoznata. Ova talasna funkcija dakle, zavisi od ostalih nepoznatih talasnih funkcija $\phi_j$.

Zbog toga rešavanje Kon-Šamovih jednačina zahteva iterativni postupak koji se naziva procedura samousaglašavanja. Ovaj metod omogućava uspostavljanje samousaglašenosti između elektronske gustine i efektivnog potencijala sistema.

Postupak rešavanja Kon-Šamovih jednačina može se predstaviti sledećim koracima:

1. Pretpostavlja se početna gustina elektrona $n^{(0)}(\mathbf{r})$, koja može biti homogena ili proizvoljno zadata. Često se za početnu elektronsku gustinu uzima zbir gustina koje odgovaraju izolovanim atomima koji se nalaze na pozicijama koje odgovaraju pozicijama atoma u razmatranom materijalu.

2. Zatim se pomoću ove početne gustine izračunava efektivni potencijal $V_{\mathrm{eff}}(\mathbf{r})$, koji se sastoji od tri komponente:

$$V_{\mathrm{eff}}(\mathbf{r}) = V_{\mathrm{ext}}(\mathbf{r}) + V_{\mathrm{H}}(\mathbf{r}) + V_{\mathrm{xc}}(\mathbf{r}), \tag{2.39}$$

   gde je $V_{\mathrm{ext}}(\mathbf{r})$ spoljašnji potencijal, $V_{\mathrm{H}}(\mathbf{r})$ Hartrijev potencijal, a $V_{\mathrm{xc}}(\mathbf{r})$ izmensko-korelacioni potencijal definisan kao:

$$V_{\mathrm{xc}}(\mathbf{r}) = \left.\frac{\delta E_{\mathrm{xc}}[n]}{\delta n}\right|_{n(\mathbf{r})}. \tag{2.40}$$

3. Dalje se numerički rešavaju jednočestične Kon-Šamove jednačine:

$$\left[-\frac{1}{2}\nabla^2 + V_{\text{eff}}(\mathbf{r})\right]\phi_i(\mathbf{r}) = \epsilon_i\phi_i(\mathbf{r}), \tag{2.41}$$

gde su $\phi_i(\mathbf{r})$ jednočestične Kon-Šamove orbitale, a $\epsilon_i$ odgovarajuće energijske vrednosti.

4. Elektronska gustina se zatim ažurira na osnovu dobijenih orbitala:

$$n(\mathbf{r}) = \sum_{i=1}^{N} |\phi_i(\mathbf{r})|^2, \tag{2.42}$$

gde $N$ predstavlja broj elektrona u sistemu.

5. Proverava se da li nova gustina $n(\mathbf{r})$ zadovoljava kriterijum konvergencije. Ako je razlika između nove i prethodne gustine manja od unapred zadatog praga $\Delta n(\mathbf{r}) < \epsilon$, proces se zaustavlja. U suprotnom, ažurirana gustina $n(\mathbf{r})$ se koristi kao ulaz za sledeću iteraciju.

Kada se postigne konvergencija, dobija se elektronska gustina osnovnog stanja $n_0(\mathbf{r})$, koja minimizuje funkcional ukupne energije sistema:

$$E[n] = T_s[n] + E_{\text{ext}}[n] + E_{\text{H}}[n] + E_{\text{xc}}[n]. \tag{2.43}$$

Uz ovu gustinu moguće je izračunati mnoge fizičke osobine sistema, uključujući raspodelu naelektrisanja, raspodelu gustine stanja, energiju veze, energijske procese i druge relevantne karakteristike materijala. Šematski prikaz algoritma samousaglašenog rešavanja Kon-Šamovih jednačina prikazan je na slici 2.1.

## 2.4 Izmensko-korelacioni funkcionali

U prethodnim odeljcima je pomenuto da važan član, izmensko-korelacioni funkcional, koji predstavlja sveukupni doprinos izmenskih i korelacionih efekata u ukupnoj energiji sistema, nije egzaktno poznat.

Kako je analitički oblik funkcionala $E_{\text{xc}}[n]$ moguće odrediti samo za najjednostavnije sisteme, poput HEG, vremenom su razvijane mnogobrojne aproksimacije koje omogućavaju praktično korišćenje DFT-a za izučavanje različitih materijala. Navešćemo nekoliko najčešćih aproksimacija koje se u DFT-u koriste:

- **Aproksimacija lokalne gustine (LDA):** Ova aproksimacija se zasniva na modelu HEG i pretpostavlja da vrednost $E_{\text{xc}}[n]$ u tački $\mathbf{r}$ zavisi samo od gustine $n(\mathbf{r})$ u toj

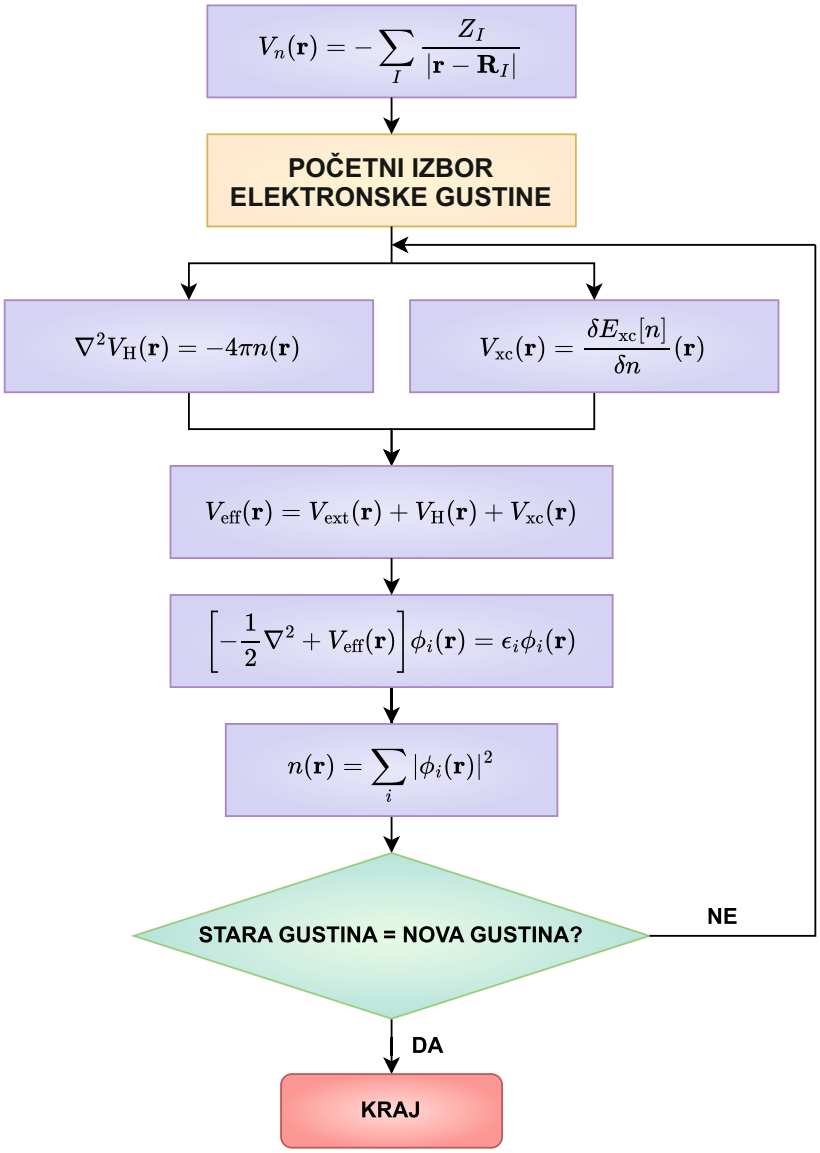


Slika 2.1: Šematski prikaz samousaglašenog postupka za rešavanje Kon-Šamovih jednačina.

tački. LDA je najjednostavnija, ali ima značajna ograničenja, o kojima će kasnije biti reči. Ona ipak dobro funkcioniše za sisteme sa ravnomernom elektronskom gustinom, poput prostih metala.

- **Aproksimacija uopštenog gradijenta (GGA):** GGA unapređuje LDA uključivanjem gradijenata gustine $\nabla n(\mathbf{r})$, pa vrednost funkcionala u tački $\mathbf{r}$ ne zavisi samo od vrednosti gustine u toj tački, već i od njenog gradijenta. Na ovaj način se bolje opisuje prostorna varijacija elektronske gustine i omogućava precizniji opis složenijih sistema kao što su molekuli i različiti heterogeni materijali.

- **Hibridni funkcionali:** Ovi funkcionali kombinuju delove izmenske energije iz Hartri-Fokovog formalizma sa GGA funkcionalima. Time se značajno povećava tačnost u pojedinim sistemima, a posebno u slučaju poluprovodnika i izolatora. Neki od najpoznatijih hibridnih funkcionala su B3LYP [49], HSE03 [50], PBE0 [51].

- **Meta-GGA funkcionali:** Meta-GGA funkcionali pored gustine i njenog gradijenta, uključuju i druge informacije poput Laplasijana gustine ili kinetičke energije [52]. Spadaju među najpreciznije funkcionale, ali i računarski najzahtevnije. Primeri Meta-GGA funkcionala su B95, B98, ISM, PKZB, SCAN i mnogi drugi.

Odabir odgovarajućeg izmensko-korelacionog funkcionala je važan, a često i komplikovan korak u modelovanju željenih materijala. Oni imaju ključnu ulogu u opisivanju mnogih fizičkih i hemijskih svojstava materijala, uključujući energiju vezivanja, energijski procep u poluprovodnicima i izolatorima, interakcije u slojevitim materijalima kod kojih su izražene van der Valsove sile, osobine jako korelisanih sistema. U praksi je potrebno istražiti literaturu za proračune na sličnim materijalima, a često i testirati različite funkcionale na željenom sistemu. Važno je primetiti i da komplikovaniji funkcionali ne dovode obavezno do tačnijih rezultata, u zavisnosti od razmatranih sistema, kao i ispitivanih osobina. Dobro je poznato da LDA i GGA funkcionali potcenjuju energijski procep u poluprovodnicima, a često predviđaju i nulti energijski procep kod materijala koji su izolatori. Na primer, kod jako korelisanih sistema, kao što su Motovi izolatori, energijski procep nije adekvatno opisan pomoću LDA ili GGA, usled činjenice da LDA i GGA nedovoljno tačno opisuju višečestične interakcije među elektronima, pa tako predviđaju da je materijal metal, dok je u stvarnosti izolator. Sa druge strane, hibridni funkcionali takođe imaju svoja ograničenja. Na primer, kod materijala sa visoko lokalizovanim $d$ ili $f$ orbitalama, ni hibridni ni meta-GGA funkcionali ne daju precizne rezultate i za takve sisteme pogodnije je koristiti metode kao što su DFT+U ili teorija dinamičkog srednjeg polja (DMFT), kod kojih je efekat jakih korelacija eksplicitno uključen. Hibridni funkcionali mogu imati problema i u opisivanju metala ili materijala sa veoma malim energijskim procepom [53] - prisustvo Hartri-Fok izmenske energije često dovodi do precenjenog energijskog procepa. Često je PBE funkcional precizniji i u opisivanju svojstava kao što su konstanta rešetke ili energija atomizacije, u odnosu na kompleksnije hibridne funkcionale [53]. Na slici 2.2 prikazana je relativna greška konstante rešetke izračunate

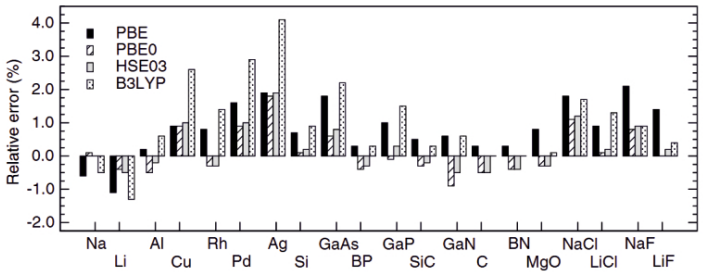


Slika 2.2: Relativna greška izračunate konstante rešetke koristeći PBE, PBE0, HSE03 i B3LYP funkcionale, u odnosu na eksperimentalno dobijene vrednosti. Slika je preuzeta iz [53].

korišćenjem PBE, PBE0, HSE03 i B3LYP funkcionala, u odnosu na eksperimentalno dobijene vrednosti, za različita jedinjenja. Odavde se može videti da u pojedinim slučajevima PBE funkcional daje najpreciznije rezultate, dok kompleksniji funkcionali mogu napraviti pogrešnu procenu za do 4%. Oprez je potreban i kod van der Valsovih sistema. Osim LDA i GGA, ni hibridni i meta-GGA funkcionali nisu dovoljno precizni za opis slojevitih materijala sa slabim vdW silama među slojevima. U ovim slučajevima je pogodnije koristiti funkcionale sa eksplicitnim uključivanjem van der Valsovih interakcija (npr. optB88-vdW), ili standardne funkcionale uz uključene dodatne popravke. Na kraju je potrebno napomenuti i da je nekada potrebno napraviti kompromis u skladu sa razmatranim sistemima - korišćenje kompleksnih funkcionala poput hibridnih zahteva značajno veće računarske resurse čak i prilikom modelovanja jednostavnijih materijala. U slučaju kompleksnijih struktura, nekada je takve proračune praktično nemoguće izvesti. U ovom odeljku će preciznije biti opisane LDA i GGA aproksimacije, koje su, iako jednostavne, uspešne u mnogim primenama i opsežno se koriste i dan danas. Takođe, softverski paketi kao što je Quantum Espresso, o kome će u narednom odeljku biti više reči, imaju implementirane različite popravke i metode (npr. Grimme-D2 [54], Grimme-D3 [55] korekcije za van der Valsove sile, DFT+U [56, 57] za opisivanje jakih korelacija) koje omogućavaju značajno uspešnije korišćenje standardnih funkcionala poput LDA i GGA.

### 2.4.1 Aproksimacija lokalne gustine (LDA)

Aproksimacija lokalne gustine razvijena je 60-tih godina prošlog veka [58, 59, 60], kao prva i najjednostavnija aproksimacija. Zapravo, gotovo sve kompleksnije aproksimacije koje su se vremenom razvijale, zasnovane su na LDA. Centralna ideja za konstrukciju ovakvog funkcionala vezana je za jednostavan sistem, HEG. HEG predstavlja idealizovani kvantnomehanički sistem u kome su elektroni raspoređeni ravnomerno u prostoru, stvarajući konstantnu elektronsku gustinu $n$. Dakle, za razliku od najjednostavnijeg modela slobodnih elektrona, u HEG se uvodi i Kulonova interakcija između elektrona. Za HEG,

izmensku energiju je moguće egzaktno izračunati, dok je za energiju korelacija potrebno korišćenje numeričkih metoda.

LDA je zasnovana upravo na modelu HEGa, pretpostavljajući da se gustina elektrona sporo menja u prostoru. Kod ovog funkcionala, vrednost $E_{\mathrm{xc}}[n]$ u tački $\mathbf{r}$ zavisi samo od gustine $n(\mathbf{r})$ u toj tački. Funkcional $E_{\mathrm{xc}}[n]$ se tada može izraziti kao

$$E_{xc}^{\mathrm{LDA}}[n] = \int \mathrm{d}^3 r\, \epsilon_{xc}[n] n(\mathbf{r}) = E_X + E_C, \tag{2.44}$$

pri čemu je $\epsilon_{xc}[n] = \epsilon_x[n] + \epsilon_c[n]$ gustina izmensko korelacione energije. Ukoliko se posmatra sistem elektronskog gasa, sa $N$ elektrona u zapremini $V$, elektronska gustina je svuda $n = N/V$, a lako se može izvesti izraz za energiju izmene preko elektronske gustine po sledećoj formuli: [44, 61]:

$$E_X = -\frac{3}{4}\left[\frac{3}{\pi}\right]^{\frac{1}{3}} n^{4/3} V. \tag{2.45}$$

Energija korelacija za HEG se ne može jednostavno analitički izraziti kao što je to učinjeno sa izmenskom energijom. U cilju njenog dobijanja, za ovaj model je numeričkim metodama rešavana višečestična Šredingerova jednačina [62]. Zatim su iz dobijenih rezultata uklonjene kinetička, Hartrijeva i izmenska energija, koje su poznate. Ovi rezultati su zatim parametrizovani [58], a dobijena energija korelacija se može izraziti kao:

$$E_C = nV \cdot \begin{cases} 0.0311 \ln r_s - 0.0480 + 0.002 r_s \ln r_s - 0.0116 r_s, & \text{if } r_s < 1, \\ \frac{-0.1423}{1+1.0529\sqrt{r_s}+0.3334 r_s}, & \text{if } r_s \geq 1. \end{cases} \tag{2.46}$$

Ovde $r_s$ predstavlja Vigner-Zajcov radijus, definisan kao radijus sfere centrirane oko svakog elektrona, tako da svaka sfera sadrži tačno jedan elektron, odnosno prosečno rastojanje između elektrona u sistemu sa uniformnom elektronskom gustinom,

$$\frac{4\pi}{3} r_s^3 = \frac{1}{n}. \tag{2.47}$$

Aproksimacije uvedene prilikom konstrukcije ovakvih izmensko-korelacionih funkcionala su, može se reći, drastične. Prvo, pretpostavljeno je da funkcional u datoj tački zavisi od vrednosti gustine isključivo u toj tački, usled čega su mnogi važni efekti zanemareni. Drugo, pretpostavka da je elektronska gustina konstantna u prostoru je ogromna idealizacija i daleko je od stvarne situacije kada su u pitanju realistični sistemi. Ipak, ispostavlja se da za određene vrste materijala, korišćenje LDA iznenađujuće dobro reprodukuje osobine materijala. Jedan od razloga je i činjenica da se greške načinjene u LDA često međusobno poništavaju prilikom proračuna ukupne energije sistema, međuatomske udaljenosti i slično. Takođe, usled višedecenijskog iskustva u korišćenju LDA i opsežnih testiranja ovih funkcionala, poznato je u kakvim oblastima ona pouzdano radi i kakve prednosti i ograničenja nosi, pa zbog svog istorijskog značaja i "zlatnog preseka" između tačnosti i računarske efikasnosti, LDA i dalje uspešno opstaje

kao praktičan i koristan alat u modelovanju materijala.

### 2.4.2 Aproksimacija uopstenog gradijenta (GGA)

LDA funkcionali su i pored svog velikog uspeha sadržali mnoga ograničenja, pa je potreba za razvojem preciznijih funkcionala bila očigledna. Značajan korak napred postignut je krajem 1980tih godina, kada je razvijena generalizovana gradijentna aproksimacija (GGA) [63, 64, 65]. Ovaj funkcional zasnovan je na LDA, ali osim što zavisi od elektronske gustine u datoj tački, zavisi i od njenog gradijenta. Ovi funkcionali postoje u različitim implementacijama, a generalno se definišu u sledećoj formi [66]:

$$E_{xc}^{\mathrm{GGA}}[n^{\uparrow}, n^{\downarrow}] = \int \mathrm{d}^3 r \, n(\mathbf{r}) \, \epsilon_{xc}(n^{\uparrow}, n^{\downarrow}, |\nabla n^{\uparrow}|, |\nabla n^{\downarrow}|, \dots) \tag{2.48}$$

$$\equiv \int \mathrm{d}^3 r \, n(\mathbf{r}) \, \epsilon_x^{\mathrm{hom}}(n) F_{xc}(n^{\uparrow}, n^{\downarrow}, |\nabla n^{\uparrow}|, |\nabla n^{\downarrow}|, \dots). \tag{2.49}$$

Dodatak zavisnosti od gradijenta gustine doneo je značajna unapređenja u odnosu na LDA. To se posebno ogleda u proceni energija i dužina veze, kao i pojedinim mehaničkim osobinama, naročito kod sistema kod kojih se elektronska gustina brzo menja. Kako GGA funkcionali nisu značajno komplikovaniji od LDA funkcionala i zahtevaju neznatno veće računarske resurse, oni su i dalje među najčešće korišćenim funkcionalima, nudeći odličan balans između preciznosti i kompleksnosti. Najpopularnije implementacije GGA su PW91 [63] i PBE [67].

## 2.5 Bazis ravnih talasa

U prethodnim odeljcima opisane su Kon-Šamove jednačine, kao i samousaglašeni postupak za njihovo rešavanje, pomoću kog se dobija konačna elektronska gustina a zatim i željena svojstva materijala. Prilikom implementacije metoda zasnovanih na DFT-u, jedan od ključnih koraka je izbor bazisnih funkcija pomoću kojih će elektronske talasne funkcije biti predstavljene. U praksi se koriste različiti bazisi među kojima su bazis ravnih talasa, lokalizovane atomske orbitale (LCAO), bazis dopunjenih ravnih talasa (*augmented plane wave method, APW*). Ovaj izbor uglavnom zavisi od vrste sistema koji se proučavaju. U fizici čvrstog stanja, za kristalne strukture koje su periodične i "beskonačne", najpogodniji je bazis ravnih talasa, s obzirom na to da su svojstvene funkcije u konstantnom potencijalu upravo ravni talasi. Stoga će u ovom odeljku upravo on biti detaljnije opisan.

U okviru Kon-Šamovog formalizma, elektroni koji se kreću u efektivnom potencijalu $V_{eff}(\mathbf{r})$ zadovoljavaju jednočestičnu jednačinu

$$\hat{H}(\mathbf{r})\phi_i(\mathbf{r}) = \left[-\frac{\hbar^2}{2m_e}\nabla^2 + V_{\text{eff}}(\mathbf{r})\right]\phi_i(\mathbf{r}) = \epsilon_i\phi_i(\mathbf{r}). \tag{2.50}$$

Ukoliko su ova stanja normirana i zadovoljavaju granične uslove u zapremini $\Omega$, svojstvene funkcije se mogu zapisati preko Furijeovog razvoja kao

$$\phi_i(\mathbf{r}) = \sum_{\mathbf{q}} c_{i,\mathbf{q}} \times \frac{1}{\sqrt{\Omega}}\exp(i\mathbf{q}\cdot\mathbf{r}) = \sum_{\mathbf{q}} c_{i,\mathbf{q}} \times |\mathbf{q}\rangle\,, \tag{2.51}$$

gde su $c_{i,\mathbf{q}}$ koeficijenti ekspanzije talasne funkcije u bazisu ortonormiranih ravnih talasa $|q\rangle$ koje zadovoljavaju

$$\langle\mathbf{q}'|\mathbf{q}\rangle \equiv \frac{1}{\Omega}\int_{\Omega} \mathrm{d}\mathbf{r}\, \exp(-i\mathbf{q}'\cdot\mathbf{r})\exp(i\mathbf{q}\cdot\mathbf{r}) = \delta_{\mathbf{q},\mathbf{q}'}. \tag{2.52}$$

Zamenjujući izraz za svojstvene funkcije u jednačinu 2.50, dobija se Šredingerova jednačina u inverznom prostoru:

$$\sum_{\mathbf{q}}\langle\mathbf{q}'|\hat{H}|\mathbf{q}\rangle c_{i,\mathbf{q}} = \varepsilon_i\sum_{\mathbf{q}}\langle\mathbf{q}'|\mathbf{q}\rangle c_{i,\mathbf{q}} = \varepsilon_i c_{i,\mathbf{q}'}. \tag{2.53}$$

Matrični elementi operatora kinetičke energije su

$$\langle\mathbf{q}'|-\frac{1}{2}\nabla^2|\mathbf{q}\rangle = \frac{1}{2}|\mathbf{q}|^2\delta_{\mathbf{q},\mathbf{q}'}. \tag{2.54}$$

Pošto je u kristalnoj strukturi potencijal $V_{eff}(\mathbf{r})$ periodičan, njegov razvoj po Furijeovim komponentama je

$$V_{\text{eff}}(\mathbf{r}) = \sum_m V_{\text{eff}}(\mathbf{G}_m)\exp(i\mathbf{G}_m\cdot\mathbf{r}), \tag{2.55}$$

pri čemu su $\mathbf{G}_m$ vektori recipročne rešetke kristala, a obrnuto je

$$V_{\text{eff}}(\mathbf{G}) = \frac{1}{\Omega_{\text{u.c.}}}\int_{\Omega_{\text{u.c.}}} V_{\text{eff}}(\mathbf{r})\exp(-i\mathbf{G}\cdot\mathbf{r})\,\mathrm{d}\mathbf{r}, \tag{2.56}$$

gde je $\Omega_{uc}$ zapremina primitivne ćelije kristala. Matrični elementi potencijala

$$\langle\mathbf{q}'|V_{\text{eff}}|\mathbf{q}\rangle = \sum_m V_{\text{eff}}(\mathbf{G}_m)\delta_{\mathbf{q}'-\mathbf{q},\mathbf{G}_m} \tag{2.57}$$

su različiti od nule samo ukoliko se $\mathbf{q}$ i $\mathbf{q}'$ razlikuju za neki recipročni vektor rešetke $G_m$. Ukoliko se sada definišu $\mathbf{q} = \mathbf{k} + \mathbf{G}_m$ i $\mathbf{q}' = \mathbf{k} + \mathbf{G}_{m'}$, koji se razlikuju za neki vektor recipročne rešetke, $\mathbf{G}_{m"} = \mathbf{G}_m - \mathbf{G}_{m'}$, Šredingerova jednačina za bilo koje $\mathbf{k}$ se u

matričnom obliku može zapisati kao

$$\sum_{m'} H_{m,m'}(\mathbf{k})c_{i,m'}(\mathbf{k}) = \varepsilon_i(\mathbf{k})c_{i,m}(\mathbf{k}), \tag{2.58}$$

gde su matrični elementi hamiltonijana

$$H_{m,m'}(\mathbf{k}) = \langle \mathbf{k}+\mathbf{G}_m|\hat{H}_{\text{eff}}|\mathbf{k}+\mathbf{G}_{m'}\rangle = \frac{\hbar^2}{2m_e}|\mathbf{k}+\mathbf{G}_m|^2\delta_{m,m'} + V_{\text{eff}}(\mathbf{G}_m - \mathbf{G}_{m'}). \tag{2.59}$$

Prema Blohovoj teoremi, za Šredingerovu jednačinu formulisanu u 2.58, svaka od svojstvenih funkcija za zadato $\mathbf{k}$ je u obliku 2.51, pri čemu je $q$ ograničeno na $\mathbf{q} = \mathbf{k}+\mathbf{G}_m$:

$$\psi_{i,\mathbf{k}}(\mathbf{r}) = \sum_m c_{i,m}(\mathbf{k}) \times \frac{1}{\sqrt{\Omega}} \exp(\mathrm{i}(\mathbf{k}+\mathbf{G}_m)\cdot\mathbf{r}) = \exp(\mathrm{i}\mathbf{k}\cdot\mathbf{r})\frac{1}{\sqrt{N_{\text{u.c.}}}}u_{i,\mathbf{k}}(\mathbf{r}), \tag{2.60}$$

gde je $\Omega = N_{u.c.} \cdot \Omega_{u.c.}$ i definiše se funkcija

$$u_{i,\mathbf{k}}(\mathbf{r}) = \frac{1}{\sqrt{\Omega_{\text{u.c.}}}} \sum_m c_{i,m}(\mathbf{k}) \exp(\mathrm{i}\mathbf{G}_m\cdot\mathbf{r}), \tag{2.61}$$

koja ima periodičnost kristala.

Naravno, potpun bazisni set ravnih talasa, koji uključuje beskonačan broj ravnih talasa, nije moguće koristiti u numeričkim simulacijama. Problem se rešava uvođenjem tzv. energije odsecanja (*cutoff energy*) $E_{cut}$ koja se definiše kao

$$\frac{\hbar^2}{2m}|k+G|^2 \leq E_{cut}. \tag{2.62}$$

Time se u recipročnom prostoru koristi konačan broj ravnih talasa unutar sfere određenog prečnika, a preciznost se kontroliše postupnim povećanjem $E_{cut}$ i proverom konvergencije rezultata.

## 2.6 Pseudopotencijali

Jedna od ključnih tehnika za pojednostavljenje proračuna elektronske strukture je metod pseudopotencijala, a posebno je važan prilikom korišćenja bazisa ravnih talasa. Glavni razlog za njihovo uvođenje leži u činjenici da elektronska talasna funkcija brzo osciluje u blizini jezgra usled jake Kulonove interakcije. Ove brze oscilacije zahtevaju visoku energiju odsecanja za ravne talase, što značajno uvećava broj bazisnih funkcija, pa samim tim zahteva i veće računarske resurse.

Metod pseudopotencijala koristi činjenicu da su elektroni blizu jezgra (*"core" elektroni*) čvrsto vezani za jezgro i samim tim na njih slabo utiče prisustvo okolnih atoma,

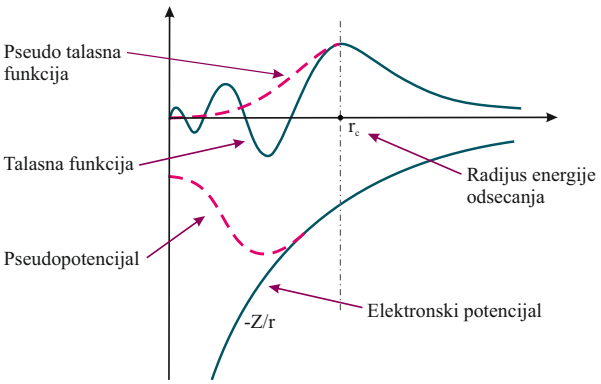


Slika 2.3: Šematski prikaz talasne funkcije i pravog potencijala (tamno zelena linija) i pseudotalasne funkcije i pseudopotencijala (roze linija). Na udaljenosti većoj od $r_c$, pseudotalasne funkcije i pseudopotencijal postaju identične stvarnim.

dok su valentni elektroni oni koji imaju značajnu interakciju sa okolinom, pa su u velikoj meri zaslužni za različita svojstva materijala. To omogućava da se samo valentni elektroni eksplicitno tretiraju, a talasna funkcija u oblasti jezgra postaje glatka, time smanjujući broj potrebnih ravnih talasa. Istovremeno, pseudopotencijal je konstruisan tako da van određene sfere oko jezgra, precizno reprodukuje ponašanje kompletnog elektronskog potencijala kom doprinose svi elektroni, čime se fizičke i hemijske osobine atoma mogu verno opisati. Ilustracija pseudopotencijala i talasne funkcije prikazana je na slici 2.3

Postoje različite klase pseudopotencijala, među kojima su najčešće korišćeni pseudopotencijali sa očuvanom normom (*Norm conserving*) [68, 69], ultrasoft pseudopotencijali [70], i projektor-augmented wave (PAW) metod [71, 72].

Norm-Conserving pseudopotencijali poštuju uslov da je integral kvadrata talasne funkcije isti kao u *all-electron* proračunima, što obezbeđuje visoku pouzdanost za različite elektronske konfiguracije. Ultrasoft pseudopotencijali dozvoljavaju da talasna funkcija bude još glatkija, smanjujući broj potrebnih ravnih talasa i računarsku zahtevnost. Oni međutim, mogu zahtevati kompleksniju formu projektora prilikom izračunavanja očekivanih vrednosti operatora [70]. PAW metod je hibrid koji kombinuje ideju pseudopotencijala sa rekonstrukcijom *all-electron* talasne funkcije. Ovi pseudopotencijali nude visoku tačnost.

Zahvaljujući svojoj praktičnosti koja obezbeđuje smanjenu zahtevnost po pitanju računarskih resursa i dobrom odnosu između tačnosti i efikasnosti, pseudopotencijali su danas standardni alat u DFT-u. Različite klase pseudopotencijala koje su se vremenom razvijale i unapređivale omogućavaju njihovu primenu na gotovo svim tipovima materijala.

## 2.7 Perturbaciona teorija funkcionala gustine (DFPT)

Dinamika kristalne rešetke igra važnu ulogu u fizici čvrstog stanja, s obzirom na to da brojna fizička svojstva materijala zavise od vibracija rešetke: Infracrveni i Ramanovi spektri, specifična toplota, provodljivost toplote, termalna ekspanzija, elektron-fononska interakcija, samo su neki od primera, pa je jasno zašto je teorija koja se odnosi na dinamiku rešetke decenijama proučavana.

Razvoj DFT-a omogućio je napredak i na ovom polju, pa su razvijane različite metode za opis svojstava materijala koji se oslanjaju na dinamiku rešetke.

Veoma istaknut metod koji se danas opsežno koristi je Pperturbaciona teorija funkcionala gustine. Ovaj metod je kao i DFT, zasnovan na *ab initio* principima i omogućava izračunavanje odgovora sistema na perturbativnu promenu potencijala, oslanjajući se na princip linearnog odziva. Ideju su metodološki postavili S. Baroni, P. Giannozzi i A. Testa [73] 1987. godine i kontinuirano su je razvijali, a danas je njihova implementacija [74] dostupna u okviru paketa Quantum Espresso i omogućava precizno izračunavanje fononskih disperzija u celoj Briluenovoj zoni, na efikasan način. U ovom odeljku je dat kratak opis ove implementacije i prateće teorije.

Aproksimacija koja ovde igra ključnu ulogu je Born-Openhajmerova aproksimacija, razmatrana u 2.1.1, koja omogućava razdvajanje kretanja elektrona i jezgara. U okviru ove aproksimacije, Šredingerova jednačina koja opisuje vibraciona svojstva kristalne rešetke, ima sledeći oblik:

$$\left(-\sum_I \frac{\hbar^2}{2M_I}\frac{\partial^2}{\partial \mathbf{R}_I^2} + E(\mathbf{R})\right)\Phi(\mathbf{R}) = \mathcal{E}\Phi(\mathbf{R}), \tag{2.63}$$

gde su $\mathcal{E}$ i $\Phi$ svojstvene vrednosti i svojstvene funkcije, $\mathbf{R}_I$ koordinata I-tog jezgra mase $M_I$, $\mathbf{R}$ predstavlja set svih koordinata jezgara, a $E(\mathbf{R})$ energiju osnovnog stanja interagujućih elektrona koji se kreću u polju fiksnih jezgara (često se ova energija naziva i Born-Openhajmerovom energijom), čiji hamiltonijan ima oblik

$$H_{BO}(\mathbf{R}) = -\frac{\hbar^2}{2m}\sum_i \frac{\partial^2}{\partial \mathbf{r}_i^2} + \frac{e^2}{2}\sum_{i\neq j}\frac{1}{|\mathbf{r}_i - \mathbf{r}_j|} - \sum_{iI}\frac{Z_I e^2}{|\mathbf{r}_i - \mathbf{R}_I|} + E_N(\mathbf{R}), \tag{2.64}$$

gde $Z_I$ prredstavlja naelektrisanje $I$-tog jezgra, $-e$ naelektrisanje elektrona, a $E_N(\mathbf{R})$ Kulonovu interakciju između jezgara,

$$E_N(\mathbf{R}) = \frac{e^2}{2}\sum_{I\neq J}\frac{Z_I Z_J}{|\mathbf{R}_I - \mathbf{R}_J|}. \tag{2.65}$$

Sistem je u ravnotežnom geometrijskom položaju kada je ispunjen uslov da su sile koje deluju na jezgra jednaka nuli:

$$\mathbf{F}_I = -\frac{\partial E(\mathbf{R})}{\partial \mathbf{R}_I} = 0, \tag{2.66}$$

a vibracione frekvencije $\omega$ su određene svojstvenim vrednostima hesijana Born-Openhajmerove energije [74]:

$$\det \left| \frac{1}{\sqrt{M_I M_J}} \frac{\partial^2 E(\mathbf{R})}{\partial \mathbf{R}_I \partial \mathbf{R}_J} - \omega^2 \right| = 0. \tag{2.67}$$

Dakle, za određivanje vibracionih svojstava sistema, kao i optimalne geometrije sistema, potrebno je izračunati prvi i drugi izvod energije $E_N(\mathbf{R})$. Ovde se koristi Helman-Fajnmanova teoremu [75, 76], prema kojoj je prvi izvod svojstvenih vrednosti hamiltonijana $H_\lambda$ koji zavisi od parametra $\lambda$, dat kao očekivana vrednost izvoda hamiltonijana:

$$\frac{\partial E_\lambda}{\partial \lambda} = \left\langle \Psi_\lambda \left| \frac{\partial H_\lambda}{\partial \lambda} \right| \Psi_\lambda \right\rangle, \tag{2.68}$$

gde $\Psi_\lambda$ svojstvena funkcija $H_\lambda$ odgovara svojstvenoj vrednosti $E_\lambda$: $H_\lambda \Psi_\lambda = E_\lambda \Psi_\lambda$. U BO aproksimaciji, koordinate jezgara se ponašaju kao parametri u elektronskom hamiltonijanu 2.64. Sila koja deluje na $I$-to jezgro u osnovnom elektronskom stanju je tada

$$\mathbf{F}_I = -\frac{\partial E(\mathbf{R})}{\partial \mathbf{R}_I} = -\left\langle \Psi(\mathbf{R}) \left| \frac{\partial H_{BO}(\mathbf{R})}{\partial \mathbf{R}_I} \right| \Psi(\mathbf{R}) \right\rangle, \tag{2.69}$$

gde $\Psi(\mathbf{r}, \mathbf{R})$ predstavlja elektronsku talasnu funkciju osnovnog stanja BO hamiltonijana. Hamiltonijan zavisi od $\mathbf{R}$ preko interakcije elektrona i jezgara koja je u sprezi sa elektronskim stepenima slobode samo preko elektronske gustine, pa je prema Helman-Fejnmanovoj teoremi dalje:

$$\mathbf{F}_I = -\int n_{\mathbf{R}}(\mathbf{r}) \frac{\partial V_{\mathbf{R}}(\mathbf{r})}{\partial \mathbf{R}_I} \, \mathrm{d}\mathbf{r} - \frac{\partial E_N(\mathbf{R})}{\partial \mathbf{R}_I}, \tag{2.70}$$

gde je $V_{\mathbf{R}}(\mathbf{r})$ Kulonova interakcija elektrona i jezgara:

$$V_{\mathbf{R}}(\mathbf{r}) = -\sum_{iI} \frac{Z_I e^2}{|\mathbf{r}_i - \mathbf{R}_I|}, \tag{2.71}$$

a $n_{\mathbf{R}}(\mathbf{r})$ elektronska gustina osnovnog stanja, za zadate položaje jezgara $\mathbf{R}$. Hesijan iz jednačine 2.67 se dobija pomoću izvoda sila po koordinatama jezgra kao:

$$\frac{\partial^2 E(\mathbf{R})}{\partial \mathbf{R}_I \partial \mathbf{R}_J} = -\frac{\partial F_I}{\partial \mathbf{R}_J} = \int \frac{\partial n_{\mathbf{R}}(\mathbf{r})}{\partial \mathbf{R}_J} \frac{\partial V_{\mathbf{R}}(\mathbf{r})}{\partial \mathbf{R}_I} d\mathbf{r} + \int n_{\mathbf{R}}(\mathbf{r}) \frac{\partial^2 V_{\mathbf{R}}(\mathbf{r})}{\partial \mathbf{R}_I \partial \mathbf{R}_J} d\mathbf{r} + \frac{\partial^2 E_N(\mathbf{R})}{\partial \mathbf{R}_I \partial \mathbf{R}_J}. \tag{2.72}$$

Može se zaključiti da je za računanje hesijana BO energije potrebno izračunati i elektronsku gustinu $n_{\mathbf{R}}(\mathbf{r})$ kao i njen linearni odziv na perturbaciju pozicija jezgara, $\partial n_{\mathbf{R}}(\mathbf{r})/\partial \mathbf{R}_I$ [77, 78]. Matrica hesijana se najčešće naziva matricom konstanti međuatomskih sila (*interatomic force constants* - IFC).

### 2.7.1 DFPT i linearni odziv

Prema Helman-Fajnmanovoj teoremi, prvi i drugi izvod energije osnovnog stanja imaju sledeći oblik:

$$\frac{\partial E}{\partial \lambda_i} = \int \frac{\partial V_\lambda(\mathbf{r})}{\partial \lambda_i} n_\lambda(\mathbf{r})\, d\mathbf{r}, \tag{2.73}$$

$$\frac{\partial^2 E}{\partial \lambda_i \partial \lambda_j} = \int \frac{\partial^2 V_\lambda(\mathbf{r})}{\partial \lambda_i \partial \lambda_j} n_\lambda(\mathbf{r})\, d\mathbf{r} + \int \frac{\partial n_\lambda(\mathbf{r})}{\partial \lambda_i} \frac{\partial V_\lambda(\mathbf{r})}{\partial \lambda_j}\, d\mathbf{r}. \tag{2.74}$$

Član $\partial n_\lambda(\mathbf{r})/\partial \lambda_i$ koji se javlja u drugom izvodu energije (jednačina 2.74) se linearizacijom Kon-Šamovih jednačina, efektivnog potencijala i elektronske gustine svodi na sledeće [74]:

$$\Delta^\lambda n(\mathbf{r}) = 4\,\mathrm{Re} \sum_{n=1}^{N/2} \psi_n^*(\mathbf{r}) \Delta^\lambda \psi_n(\mathbf{r}), \tag{2.75}$$

gde je operator $\Delta^\lambda$ definisan kao

$$\Delta^\lambda F = \sum_i \frac{\partial F_\lambda}{\partial \lambda_i} \Delta\lambda_i. \tag{2.76}$$

Varijacija Kon-Šamovih orbitala, $\Delta\psi_n(\mathbf{r})$ se dobija pomoću teorije perturbacija prvog reda [79]:

$$(H_{\mathrm{SCF}} - \epsilon_n)|\Delta\psi_n\rangle = -(\Delta V_{\mathrm{SCF}} - \Delta\epsilon_n)|\psi_n\rangle, \tag{2.77}$$

gde je

$$H_{\mathrm{SCF}} = -\frac{\hbar^2}{2m}\frac{\partial^2}{\partial r^2} + V_{\mathrm{SCF}}(r) \tag{2.78}$$

neperturbovani Kon-Šamov hamiltonijan,

$$\Delta V_{\mathrm{SCF}}(r) = \Delta V(r) + e^2 \int \frac{\Delta n(r')}{|r - r'|}\, dr' + \left.\frac{dv_{\mathrm{xc}}(n)}{dn}\right|_{n=n(r)} \Delta n(r) \tag{2.79}$$

je popravka prvog reda za samousaglašeni potencijal, a

$$\Delta\varepsilon_n = \langle\psi_n|\Delta V_{\mathrm{SCF}}|\psi_n\rangle \tag{2.80}$$

varijacija svojstvene vrednosti $\epsilon_n$ Kon-Šamovih jednačina. Jednačina 2.77 se naziva i Šternhajmerova jednačina [79].

Jednačine 2.75-2.79 formiraju set samousaglašenih jednačina za perturbovani sistem, analogno Kon-Šamovim jednačinama.

Perturbaciona teorija funkcionala gustine u ovoj implementaciji predstavlja jedan od najefikasnijih načina za izračunavanje linearnog odziva elektronskog sistema, i ovakva šema linearizovanih Kon-Šamovih jednačina omogućava brzu i preciznu analizu fonon-

skih spektara, kao i proučavanje mnogih perturbativnih efekata u optici, magnetizmu, električnoj polarizaciji.

## 2.8 Quantum ESPRESSO, obrada podataka i prateći softver

### 2.8.1 Quantum ESPRESSO

Quantum ESPRESSO [80, 81] (QE) predstavlja jedan od najkorišćenijih *open-source* softverskih paketa za *ab-initio* proračune elektronske strukture i modelovanja materijala. Naziv „ESPRESSO" izveden je iz engleske skraćenice za opEn Source Package for Research in Electronic Structure, Simulation, and Optimization. Različiti alati iz ovog paketa omogućavaju istraživanje širokog spektra fizičkih i hemijskih svojstava materijala, počevši od osnovnih osobina, elektronske strukture, fononskih spektara, pa sve do proučavanja transportnih koeficijenata, elektron-fononske interakcije, i procesa na površinama.

QE koristi bazis ravnih talasa za reprezentaciju Kon-Šamovih talasnih funkcija, koje su posebno pogodne za modelovanje periodičnih sistema kao što su kristali. Softver koristi i metod pseudopotencijala, pa zajedno ovakav pristup omogućava dobar balans između računarske efikasnosti i dobre tačnosti rezultata. Do sada su implementirani mnogobrojni izmensko-korelacioni funkcionali (od LDA i PBE, pa sve do pojedinih hibridnih funkcionala), a postoji ogroman broj različitih pseudopotencijala generisanih za QE (pseudopotencijali sa očuvanom normom, ultrasoft, PAW...), kako u standardnom obliku, tako i relativističkih za korišćenje u proračunima sa spin-orbitnom interakcijom

Osim toga, implementirane su i različite popravke i dodaci, poput korekcija za van der Valsove sile, DFT+U formalizma i mnogih drugih.

Jedna od ključnih prednosti Quantum ESPRESSO-a je i perturbaciona teorija funkcionala gustine (DFPT), implementirana u modulu `ph.x`, razmatrana u prethodnom odeljku.

Softver se sastoji od više povezanih modula među kojima su istaknuti:

- **PWscf (pw.x):** Glavna rutina za samousaglašeno rešavanje Kon-Šamovih jednačina u bazisu ravnih talasa. Koristi se za proračune elektronske gustine, ukupne energije i optimizaciju geometrije (relaksaciju) sistema. Uz posebne specifikacije u ulaznim fajlovima, koristi se i za proračune od kojih se kasnije obrađuju podaci za dobijanje zonske strukture.

- **CP (cp.x):** Kar-Parinelo molekularna dinamika, pogodna za izučavanje dinamičkog

ponašanja sistema i dobijanje uvida u stabilnost sistema i njegove reakcije na visokim temperaturama

- **PHonon (ph.x):** Modul za perturbacionu teoriju funkcionala gustine, omogućava računanje fononskih spektara, dielektričnih funkcija, elektron-fonon matričnih elemenata i drugih svojstava materijala koja proističu iz vibracija rešetke.
- **PWneb (neb.x):** Implementacija *nudged elastic band* metode za određivanje puteva hemijskih reakcija na atomskom nivou, poput difuzije, adsorpcije, površinskih hemijskih reakcija
- **PostProc (pp.x, projwfc.x, bands.x, dos.x, matdyn.x, itd.):** Skup dodatnih alata za post-procesiranje rezultata među kojima su proračuni gustine stanja (DOS), projekcije talasnih funkcija, mapiranje potencijala u realnom prostoru, itd.
- **TDDFPT (tddfpt.x):** Implementacije vremenski zavisne perturbacione teorije funkcionala gustine
- **EPW (epw.x):** Računanje elektron-fonon interakcije pomoću bazisa Vanijeovih funkcija
- **Atomic:** Alat za generisanje pseudopotencijala,

kao i mnogi drugi (kompletna lista može se naći se na web stranici softvera https://www.quantum-espresso.org/documentation/).

Kod se pokreće iz komandne linije Linux terminala, zahteva ulazne datoteke sa svim potrebnim informacijama o sistemu i željenim parametrima i zasnovan je na *Fortran*-ovom *namelist* formatu, a na na kraju daje odgovarajuće izlazne datoteke.

Za izradu proračuna u ovoj disertaciji, Quantum ESPRESSO je bio najpoželjniji softverski izbor. Pored toga što je zasnovan na ravnim talasima koji su pogodni za opisivanje kristalnih struktura, takođe je: jedan je od najkompletnijih i najbolje održavanih open-source softvera sa višestrukim mogućnostima; odlično optimizovan za paralelno računanje i većina procedura se izvodi na računarskim klasterima sa velikim brojem jezgara, čineći proračune efikasnijim; dostupni su različiti pseudopotencijali i izmensko-korelacioni funkcionali; postoji veliki broj softvera za vizuelizaciju i dalju manipulaciju podacima, koji prepoznaju QE izlazne i ulazne datoteke.

### 2.8.2 Modelovanje 2D struktura i heterostruktura u QE

U svim proračunima korišćen je GGA funkcional u PBE implementaciji. Kao što je u prethodnim odeljcima objašnjeno, GGA funkcionali i pored unapređenja u odnosu na

LDA, imaju tendenciju da precenjuju energijski procep kod poluprovodnika i izolatora. Korišćenje hibridnih funkcionala bi u ovom slučaju rezultovalo preciznijim proračunom energijskog procepa. Ipak, uzevši u obzir da su ovakvi proračuni izuzetno kompleksni i zahtevni po pitanju potrebnih računarskih resursa (izuzetno velika količina RAM memorije) i trajanja proračuna, uz detaljnu analizu postojeće literature, odabran je GGA funkcional kao glavni. Naime, postojeći podaci za dvodimenzionalne monohalkogenide koji su razmatrani u heterostrukturama, ukazuju na to da je najveća razlika u rezultatima dobijenim korišćenjem GGA i hibridnih funkcionala, upravo u širini energijskog procepa, dok su oblici zona veoma slični, kao i ostala svojstva sistema.

QE, kao i većina drugih DFT kodova, razmatra periodične sisteme u 3D prostoru, a jedinična ćelija je ponovljena u sve tri dimenzije do beskonačnosti. Modelovanje 2D materijala u 3D prostoru se sprovodi tako što se u jednom pravcu (neka je to $z$-osa, a materijal je periodičan u $xy$ ravni) dodaje vakuum koji obezbeđuje odsustvo interakcija među periodičnim replikama slojeva modelovanog materijala. Ovaj vakuum se individualno određuje za svaki sistem, a najčešće je to između 15 Å i 25 Å. Tako posmatrana jedinična ćelija sa veoma velikom dužinom duž $z$ ose, u recipročnom prostoru ima Briluenovu zonu koja je praktično dvodimenzionalna. Jedan od najrasprostranjenijih pristupa za generisanje ravnomerno raspoređenih $\mathbf{k}$-tačaka u BZ je *Monkhorst-Pakova* mreža.

Pre bilo kojih proračuna (zonske strukture itd.), sve proučavane heterostrukture su prvo relaksirane, tako da pozicije atoma budu u optimalnom položaju koji obezbeđuje minimum ukupne energije. Optimizacija je izvršena koristeći Brojden-Flečer-Goldfarb-Šanov (BFGS) algoritam [82, 83, 84, 85].

Pošto su kod heterostruktura važne van der Valsove sile kojima su slojevi povezani, korišćena je popravka za van der Valsovu interakciju implementirana kroz Grimme-D2 algoritam [54, 86], koja omogućava precizniji opis interakcija među slojevima i njihove udaljenosti.

#### 2.8.2.1 Određivanje konstanti elastičnosti

Za određivanje konstanti elastičnosti, korišćen je kod Thermo_pw [87], koji koristi QE rutine za proračune različitih svojstava materijala, među kojima su i mehanička svojstva. Ovaj kod računa ne-nulte komponente tenzora napona za zadati set različitih naprezanja, nakon čega računa prvi izvod napona po naprezanju.

U 3D teoriji elastičnosti, tenzor napona $\sigma$ $[N/m^2]$ i tenzor deformacije $\epsilon$ povezani su preko konstanti elastičnosti na sledeći način:

$$\sigma_{ij} = C_{ijkl}\epsilon_{kl}. \tag{2.81}$$

U slučaju 2D materijala, relacija konstantičnosti i tenzora deformacije je data u

sledećem obliku [88]:

$$\hat{\sigma} = \hat{C}\hat{\varepsilon} = \begin{pmatrix} \sigma_{xx} \\ \sigma_{yy} \\ \sigma_{xy} \end{pmatrix} = \begin{pmatrix} C_{11} & C_{12} & 0 \\ C_{12} & C_{22} & 0 \\ 0 & 0 & C_{66} \end{pmatrix} \begin{pmatrix} \varepsilon_{xx} \\ \varepsilon_{yy} \\ 2\varepsilon_{xy} \end{pmatrix}. \tag{2.82}$$

Ovde su $\hat{\sigma}$, $\hat{C}$ i $\hat{\varepsilon}$ tenzor napona, tenzor konstanti elastičnosti, i tenzor naprezanja. U slučaju heksagonalne rešetke, važi $C_{11} = C_{22}$, $C_{12} = C_{21}$, kao i $C_{66} = (C_{11} - C_{12})/2$, pa postoje samo dve nezavisne konstante elastičnosti. Tada su Jangov moduo, Poasonov odnos i moduo smicanja određeni na sledeći način:

$$E_y = C_{11} - \frac{C_{12}^2}{C_{11}}, \quad \nu_{xy} = \frac{C_{12}}{C_{11}}, \quad G_{xy} = C_{66}. \tag{2.83}$$

Moduo sloja za heksagonalne 2D sisteme dat je kao

$$\gamma^{2D} = \frac{C_{11} + C_{12}}{2}. \tag{2.84}$$

Važno je naglasiti da se u 2D materijalima jedinice drugačije izražavaju. Dok su jedinice za tenzor napona i konstante elastičnosti u 3D prostoru date u $N/m^2$, prirodno je da se koriste jedinice $N/m$, pošto u pravcu normalnom na ravan materijala, praktično ne postoji debljina. Često se formalno uvodi pojam "efektivne debljine" kako bi se 2D veličine prevele u 3D radi poređenja. Ipak, fizički, 2D materijali nemaju realnu zapreminu u pravcu normalnom na ravan pa je ova efektivna debljina definisana samo radi pogodnijeg poređenja sa vrednostima za 3D materijale, a ne i fundamentalna veličina. Takođe, ova efektivna debljina nije trivijalna za precizno određivanje, ali se često uzima debljina koju jedan sloj zauzima u jediničnoj ćeliji u 3D materijalu, odnosno rastojanje između dva sloja. Sve vrednosti u poglavlju sa rezultatima, iskazane su u $N/m$.

#### 2.8.2.2 Određivanje optičkih svojstava

U disertaciji su ispitivane pojedine optičke osobine heterostruktura, poput kompleksne dielektrične funkcije i apsoropcije. Kompleksna dielektrična funkcija ima realni i imaginarni deo: $\epsilon(\omega) = \epsilon_R(\omega) + i\epsilon_I(\omega)$. U okviru DFT-a, elektronske pobude se često tretiraju kao jednočestični prelazi između popunjenih i praznih Kon-Šamovih nivoa, uz dodatne aproksimacije. QE u `epsilon.x` modulu koristi aproksimaciju slučajne faze (*Random Phase Approximation (RPA)*) i računa linearni odziv elektrona na pobudu zadatu frekvencijom $\omega$. Detaljna formulacija vezana za ovu implementaciju može se naći u dokumentaciji QE-a [89]. Ovakav pristup omogućava veoma brzo i efikasno određivanje osnovnih optičkih svojstava, ali je važno napomenuti da zanemaruje bilo kakve eksitonske efekte, a matrični elementi uključuju samo međuzonske prelaze poput vertikalnih prelaza u kojima je talasni vektor $\mathbf{k}$ očuvan. Za preciznije rezultate potrebno je koristiti komplek-

snije metode (GW approximation, Bethe-Salpether Equation, non-equilibrium Green's function theory...). U okviru ove teze, optičke osobine su izučavane kvalitativno u cilju određivanja trenda promene za različite jačine naprezanja. Takođe, postojeća literatura pokazuje da za monohalkogenide IIIA grupa kao i za hBN, metodi zasnovani na RPA obezbeđuju korektne rezultate dielektrične funkcije u poređenju sa metodama poput GW [90, 91, 92, 93, 94], pa je ona odabrana za korišćenje u proračunima.

Kao izlazni fajlovi `epsilon.x` proračuna, dobijaju se imaginarni i realni deo dielektrične funkcije. Odatle se može izračunati koeficijent apsorpcije $\alpha(\omega)$ kao:

$$\alpha(\omega) = \sqrt{2}\frac{\omega}{c}\sqrt{\sqrt{\epsilon_R^2(\omega) + \epsilon_I^2(\omega)} - \epsilon_I(\omega)}. \tag{2.85}$$

Indeks prelamanja i koeficijent prigušenja se mogu izraziti kao

$$n(\omega) = \sqrt{\frac{|\epsilon(\omega)| + \epsilon_R(\omega)}{2}}, \quad k(\omega) = \sqrt{\frac{|\epsilon(\omega)| - \epsilon_R(\omega)}{2}}, \tag{2.86}$$

odnosno za imaginarni i realni deo dielektrične funkcije važi

$$\epsilon_R = 2nk, \quad \epsilon_I = n^2 - k^2, \tag{2.87}$$

a refleksija $R(\omega)$ se lako može izraziti preko indeksa prelamanja i koeficijenta prigušenja:

$$R = |r|^2 = \frac{|(n-1) + ik|^2}{|(n+1) + ik|^2}, \tag{2.88}$$

odnosno

$$R = \frac{(n-1)^2 + k^2}{(n+1)^2 + k^2}. \tag{2.89}$$

### 2.8.3 Ostali korišćeni softveri

Za vizuelizaciju struktura korišćeni su VESTA [95] i deo QuantumATK paketa (nekadašnji Atomistix Virtual NanoLab) [96].

VESTA (Visualization for Electronic and STructural Analysis) je sofvterski alat otvorenog koda za vizuelizaciju kristalnih struktura, elektronske gustine, molekula, i drugih srodnih podataka. Softver podržava širok spektar formata datoteka, ima napredne grafičke mogućnosti i mnoštvo podešavanja.

QuantumATK je softverski paket namenjen simulacijama i modelovanju materijala na atomskom nivou, kombinujući kvantno-mehaničke metode poput DFT-a. U istraživanju je korišćen NanoLab, grafički interfejs QuantumAtK-a, koji poseduje različite alate za vizuelizaciju i analizu atomskih struktura, kreiranje i modifikaciju struktura, kao i izvoz

fajlova prilagođen različitim formatima odgovarajućih DFT softvera.

Za obradu dobijenih podataka, konkretno računanje apsorpcije i koeficijenta refleksije, korišćen je programski jezik Python, dok su svi grafici pravljeni u Matplotlib-ovoj biblioteci u Pythonu.

# 3 Dvodimenzionalni materijali i heterostrukture

2D materijali i vdW heterostrukture predstavljaju jedno od najznačajnijih otkrića savremene nauke o materijalima. Kod 2D materijala, debljina je ograničena na jedan ili nekoliko atomskih slojeva, dok se u ravni prostiru u makroskopskim dimenzijama. Njihov atomski tanak oblik omogućava pojavu kvantnih efekata koji nisu prisutni u njihovim trodimenzionalnim pandanima, što rezultuje unikatnim elektronskim, optičkim i mehaničkim svojstvima [97], pa je jasno da su ovi materijali doveli do potpune revolucije u oblasti nano-nauka i omogućili razvoj brojnih novih tehnologija. Počevši od otkrića grafena, koji su 2004. godine mehaničkom eksfolijacijom izolovali iz grafita Andre Geim i Konstantin Novoselov [98], interesovanje za ovu klasu materijala neprestano raste, što je inspirisalo razvoj širokog spektra novih 2D struktura, uključujući silicen, fosforen, germanen, MXene, heksagonalni bor nitrid (hBN), dihalkogenide prelaznih metala (TMD), monohalkogenide IIIA grupe ($M^{III}X^{VI}$, M=In,Ga i X=S,Se,Te) [99, 100]. Neki od primera kristalnih struktura 2D materijala prikazani su na slici 3.1.

Kod 2D materijala prisutna je široka paleta jedinstvenih fenomena koji proizilaze iz njihove atomski tanke strukture i kvantne prirode. Od spinsko-dolinskog sprezanja u TMD [102], preko Izingovih superprovodnika [103, 104, 105], Motovih izolatora [106], do topoloških izolatora [107, 108]. Tokom prethodnih nekoliko godina pronađeni su i prvi magnetni 2D materijali kao što su $CrI_3$ [109], $FePS_3$ [110], $Cr_2Ge_2Te_6$ [111] i mnogi drugi [112, 113, 114, 115]. Primećeni su i spintronički efekti kao što je Rašba cepanje u jednoslojnim monohalkogenidima [116, 117]. Pored toga, ovi materijali često poseduju visoku pokretljivost elektrona i širok opseg apsorpcije svetlosti, što ih čini pogodnim za primenu u fotonaponskim ćelijama, svetlosnim detektorima i fotokatalizatorima za razlaganje vode [118, 119].

Osim fundamentalnih naučnih istraživanja, 2D materijali imaju značajnu potencijalnu primenu u industriji, od razvoja fleksibilnih i prozirnih elektronskih uređaja do unapređenja performansi u energetici i senzorskim tehnologijama [117, 118]. Materijali poput $MoS_2$ i InSe koriste se za fotodetektore visoke osetljivosti, svetlosne emitere i fotonaponske ćelije. Njihova sposobnost da apsorbuju svetlost u širokom spektru talasnih dužina čini ih izuzetno pogodnim za ove uređaje [118, 119]. 2D materijali, kao što su GaTe i GeSe,

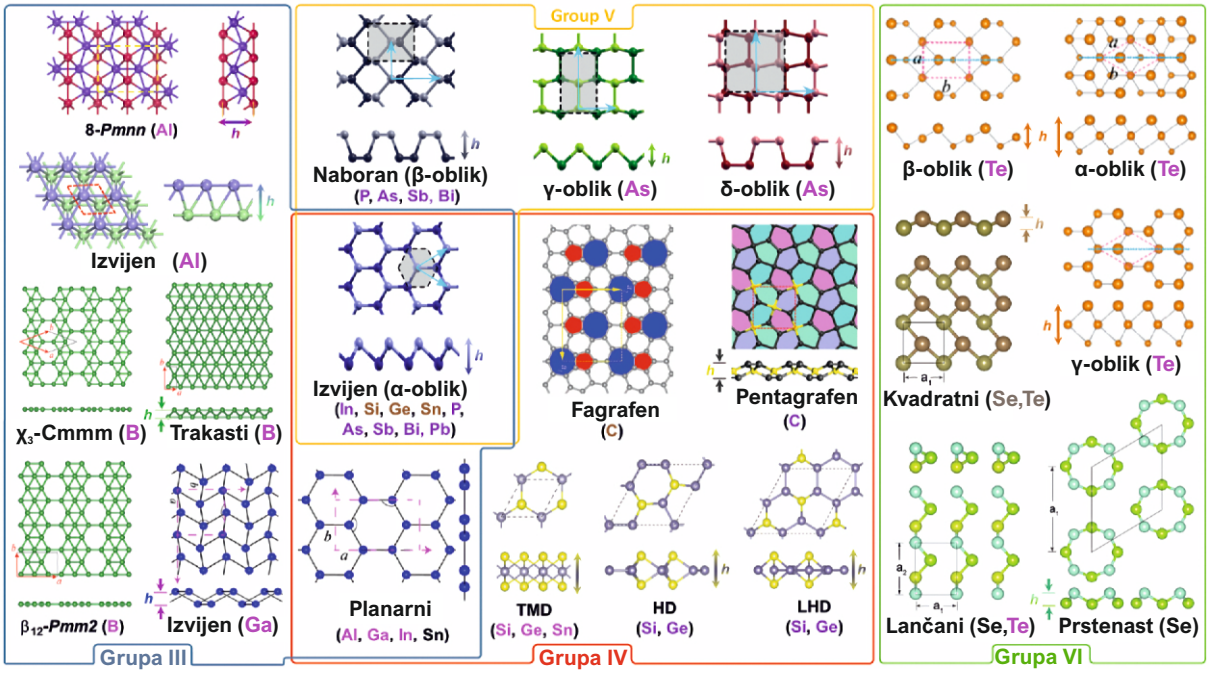


Slika 3.1: Prikaz kristalnih struktura alotropskih oblika različitih glavnih grupa elementarnih 2D materijala. Slika je preuzeta iz [101].

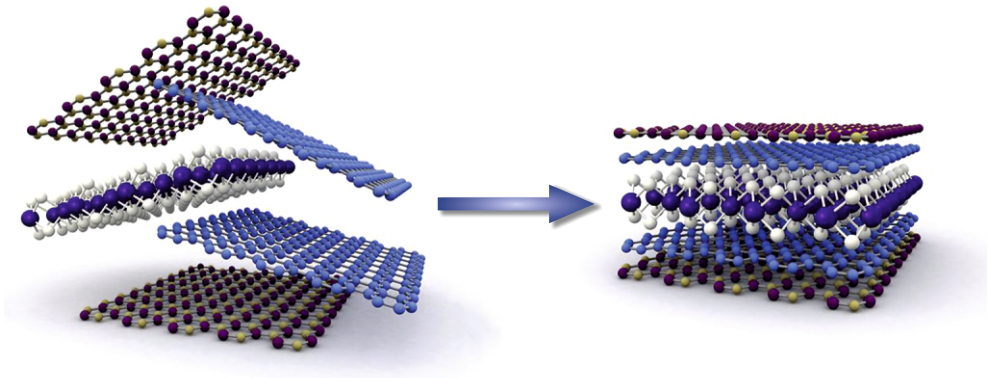

Slika 3.2: Ilustracija heterostrukture sačinjene od nekoliko slojeva 2D materijala. Slika je preuzeta iz [124].

omogućavaju efikasnu fotokatalizu i konverziju sunčeve energije u električnu, dok njihova stabilnost pod naprezanjem povećava trajnost u praktičnim primenama [117]. Magnetni 2D materijali otvaraju nove mogućnosti za spintroničke uređaje poput memorija i spin-tranzistora. Spinsko-dolinsko sprezanje u TMD-ovima može se iskoristiti za inovativne kvantne tehnologije [102, 112]. Visoka osetljivost površine omogućava 2D materijalima primenu u hemijskim i biološkim senzorima, gde se detektuju minimalne promene u hemijskom okruženju [118]. Biokompatibilni 2D materijali poput fosforena, imaju potencijal za detekciju biomolekula u medicinskoj dijagnostici [97, 101]. Materijali poput grafena i heterostruktura TMD-a i grafena ili hBN-a se ističu kao pogodni za fleksibilnu elektroniku [120, 121, 122], dok mnoge heterostrukture pokazuju potencijal za primene u različitim tipovima baterija [123].

Posebno mesto u oblasti 2D materijala i niskodimenzionalnih sistema zauzimaju upravo vdW heterostrukture. Ovi slojeviti sistemi sačinjeni su od različitih 2D materijala složenih u "sendvič" (kao što je prikazano na slici 3.2), čije slojeve povezuju slabe vdW sile, nasuprot jakih kovalentnih veza unutar slojeva. Zahvaljujući takvom načinu slaganja i mnoštvu mogućnosti za materijale "sastojke", moguće je modelovati različite složene sisteme sa željenim elektronskim i optičkim svojstvima. Važno je istaći i činjenicu da formirana heterostruktura nije prost zbir materijala, već da često rezultuje i potpuno novim efektima koji nisu prisutni u materijalima od kojih je sačinjena. Na taj način, heterostrukture otvaraju izuzetno širok spektar mogućih primena, od fleksibilne elektronike i spintronike, do nanooptičkih i kvantnih uređaja. Ovakve strukture pružaju velike mogućnosti za različite manipulacije, pa se promenom vrste materijala, kao i njihovog relativnog rotacionog ugla može precizno podešavati međuslojna interakcija, dovodeći do pojave mnogih fenomena poput topoloških stanja, superprovodnosti ili egzotičnih ekscitonskih efekata.

Jedna od ključnih prednosti 2D materijala koja ih čini posebno atraktivnim je i njihova mogućnost prilagođavanja svojstava pomoću različitih tehnika, poput primene mehaničkog naprezanja, dopiranja [125], ili kombinovanja slojeva različitih materijala u heterostrukture zasnovane na vdW interakcijama [20, 21, 22, 126]. Ove tehnike omogućavaju preciznu kontrolu elektronskih i optičkih svojstava i dodatno otvaraju vrata za primene u nanoelektronici, optoelektronici, fotonici i kvantnim tehnologijama [99, 127].Tokom poslednjih nekoliko godina, inženjering naprezanja je u velikom fokusu istraživanja kao istaknut metod za kontrolisano podešavanje svojstava materijala ili čak izazivanje novih efekata [128, 129, 130, 131, 132]. Na ovaj način se precizno mogu kontrolisati elektronska struktura i energijski procep, kao i optičke osobine. Kod mnogih materijala, usled naprezanja dolazi do tranzicije između direktnog i indirektnog energijskog procepa [133], pojedini pri određenim jačinama naprezanja prelaze iz poluprovodnika u metal [134], a inženjering naprezanja omogućava takođe i modulaciju piezoelektričnih i piezorezistivnih efekata, doprinoseći razvoju fleksibilnih senzora i detektora [135].

Monoslojevi $M^{III}X^{VI}$ grupe se među 2D materijalima posebno ističu usled svojih osobina. Materijali ove grupe poseduju vrlo visoku pokretljivost elektrona - pokazalo se da monoslojevi InSe i GaSe imaju pokretljivost elektrona veću od 1000 $cm^2/(Vs)$ [18, 136], što ih posebno izdvaja od mnogih drugih 2D materijala. Mnogi od njih poseduju i dobru apsorpciju u širokom spektralnom opsegu, a odsustvo inverzionog centra simetrije omogućava pojavu Rašbinog efekta [116, 137, 138], što otvara mogućnosti za njihovu upotrebu u različitim spintroničkim uređajima. Jedna od važnih oblasti gde primena materijala iz $M^{III}X^{VI}$ grupe dolazi do izražaja je fotokatalitičko razlaganje vode za dobijanje vodonika, a primenom naprezanja ili spoljašnjeg električnog polja može se postići dodatna optimizacija efikasnosti solarne konverzije [139, 140].

Ova porodica materijala takođe ima značajan potencijal za kombinovanje sa drugim 2D materijalima, odnosno formiranje heterostruktura. Heterostrukture ovih materijala često

formiraju heterospojeve tipa II, pogodnih za razvoj visokoefikasnih fotonaponskih ćelija i fotodetektora [118, 141]. Primer su heterostruktura GaSe i InSe ili InTe sa materijalima poput grafena ili $MoS_2$ pogodne za različite senzore i svetlosno-aktivne uređaje [15, 118, 142]. Monohalkogenidi IIIA grupe kombinovani sa grafenom ili sličnim materijalima koji imaju Dirakovu disperziju formiraju i Šotkijeve spojeve koji se dodatno mogu kontrolisati primenom naprezanja ili spoljašnjeg električnog polja [36, 143, 144, 145, 146, 147].

Pored brojnih izvanrednih osobina, $M^{III}X^{VI}$ su podložni oksidaciji pri izlaganju vazduhu [28, 29, 148, 149]. Na primer, u slučaju GaSe, oksidacija rezultuje formiranjem tankog sloja na površini, sačinjenog od $Ga_2Se_3$, $Ga_2O_3$ i amorfnog selena [150, 151]. Problem oksidacije je posebno izražen kada su u pitanju tanki slojevi ili monoslojevi pa predstavlja izazov za dalju manipulaciju ovih struktura i ograničava njihove primene u ambijentalnim uslovima.

Zbog toga je pasivizacija ovih materijala adekvatnim zaštitnim slojem od suštinskog značaja za dalja istraživanja i buduću primenu. Zaštitni sloj mora biti pažljivo odabran tako da spreči hemijske reakcije na površini materijala, koje bi mogle degradirati njegove elektronske i optičke karakteristike. Istovremeno, ovaj sloj ne sme značajno uticati na svojstva monohalkogenida, poput elektronske strukture ili mobilnosti elektrona, kako bi se očuvala njihova funkcionalnost u predviđenim primenama.

Materijal koji se posebno istakao za upotrebu u ove svrhe je hBN [152, 153, 154, 155, 156, 157, 158, 159, 160]. Ovaj atomski tanak izolator širokog energijskog procepa poseduje širok spektar izvanrednih svojstava koje ga čine idealnim kandidatom za mehaničku i hemijsku zaštitu osetljivih tankih slojeva - od visoke transparentnosti, preko dobre termalne provodnosti, izuzetnih mehaničkih osobina, do odlične stabilnosti na temperaturama do 1000°C i slabom reaktivnošću sa mnogim hemijskim supstancama, a konstantan napredak na polju fabrikacije 2D materijala omogućava i proizvodnju visokokvalitetnih filmova hBN-a na dimenzijama reda centimetra [161]. Istraživanja takođe pokazuju i da je efikasan kao pasivizator kod $M^{III}X^{VI}$-a [162, 163].

U narednim potpoglavljima biće dat pregled kristalne strukture, najvažnijih osobina i postojećih saznanja o hBN-u i $M^{III}X^{VI}$, koji se koriste u istraživanju u disertaciji.

## 3.1 Heksagonalni bor nitrid (hBN)

hBN pripada grupi slojevitih materijala, po kristalnoj strukturi veoma sličan grafenu. Opisuje ga heksagonalna rešetka sačinjena od atoma bora i azota koji su naizmenično smešteni u saćastoj rešetki, kao što je prikazano na slici 3.3. Kao i kod sličnih vdW materijala, atomi unutar slojeva povezani su jakim kovalentnim vezama, dok su slojevi međusobno povezani vdW interakcijama, što omogućava laku eksfolijaciju hBN-a u monoslojeve. Konstanta rešetke hBN-a je slična kao kod grafena i iznosi $a = 2.49 - 2.51$ Å

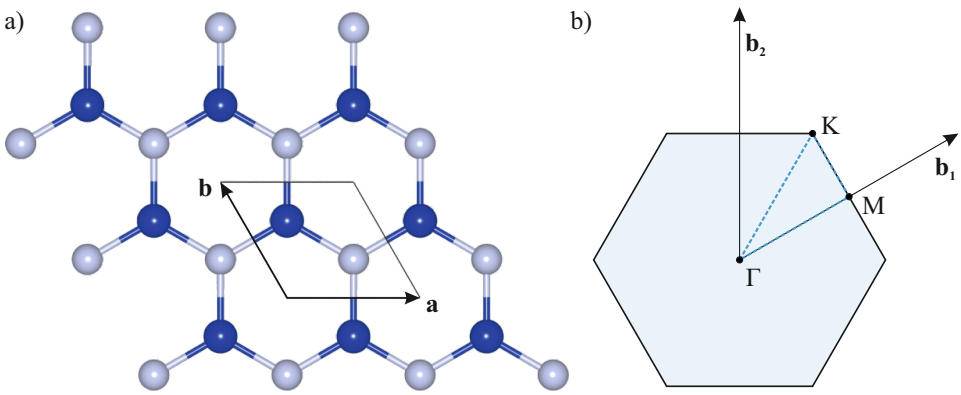


Slika 3.3: (a) Kristalna struktura sloja hBN-a gledano normalno na sloj. Primitivna ćelija je označena punom crnom linijom. (b) odgovarajuća Briluenova zona.

[164, 165, 166, 167]. Zbog sličnosti sa grafenom, uključujući kristalnu strukturu ali i mnoge druge osobine, ovaj materijal se često naziva i "beli grafen" (slojeviti hBN ima belu boju, dok u monosloju ima odličnu transparentnost).

Zahvaljujući jakim kovalentnim vezama između atoma bora i azota, hBN poseduje visoku hemijsku stabilnost, otporan je na oksidaciju i koroziju u različitim hemijskim sredinama i na visokim temperaturama koje prelaze 1000 °C [168, 169, 170], što je od suštinskog značaja za pasivizaciju i zaštitu osetljivih materijala.

Osim toga, hBN se ističe i po izvanrednim mehaničkim osobinama. Jangov moduo hBN-a iznosi oko 275 N/m, a moduo sloja oko 175 N/m, što je konkurentno grafenu koji poseduje Jangov moduo od 340 N/m, odnosno moduo sloja od 206 N/m [171, 172, 173]. Iako poseduje izuzetnu čvrstoću u ravni, hBN ima dobru fleksibilnost na savijanje [172]. Ova kombinacija čvrstoće ali i fleksibilnosti, čini ga idealnim za primene u kojima je potrebno pružiti dodatnu zaštitu materijalima, ili potrebnu čvrstoću ukoliko se koristi kao mehanička podloga za druge 2D materijale.

Još jedno od važnih svojstava koje hBN poseduje je visoka termalna provodnost, koja u monosloju dostiže vrednosti od 751 W/mK na sobnoj temperaturi, što je među najvišim rezultatima zabeleženim kod izolatora i poluprovodnika - preciznije, veće vrednosti imaju samo dijamant i kubni bor nitrid [174]. Zahvaljujući svojim termičkim i mehaničkim svojstvima, hBN se koristi i u nanokompozitima u cilju poboljšanja toplotne provodljivosti i mehaničke otpornosti, u uređajima za odvođenje toplote, kao i u zaštitnim slojevima za metale u korozivnim sredinama [164].

Monosloj hBN-a je po svojoj elektronskoj strukturi izolator širokog direktnog energijskog procepa koji iznosi oko 6 eV [164, 165, 175]. Vrednosti izračunate pomoću DFT-a variraju u opsegu od 4.5 eV do 6 eV u zavisnosti od korišćenog funkcionala [176, 177, 178, 179, 180, 181] i uglavnom su od 4.5-4.7 eV kada se koriste LDA i GGA funkcionali, a oko 6 eV koristeći hibridne funkcionale. Na slici 3.4 prikazana je zonska struktura hBN-a za monosloj, za debljine od dva do pet slojeva, kao i za beskonačan broj slojeva hBN-a, izračunati korišćenjem HSE hibridnog funkcionala [182].

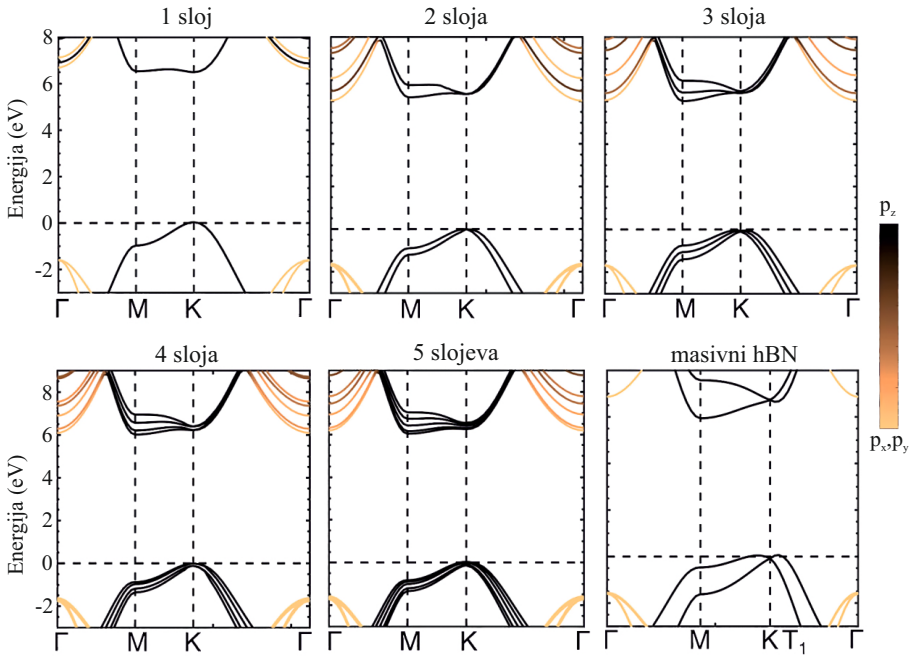


Slika 3.4: Zonska struktura hBN-a u monosloju, debiljine od 2 do 5 slojeva i u masivnom hBN-u. Slika je adaptirana iz [182]

hBN je transparentan za vidljivu svetlost, dok izraženije apsorpcione pikove ima u UV opsegu - najjača apsorpcija je na talasnim dužinama između 200-220 nm. Stoga je pogodan kako za UV fotodetektore, tako i kao zaštitni sloj usled svoje transparentnosti u vidljivom opsegu.

## 3.2 2D monohalkogenidi IIIA grupe

Monohalkogenidi IIIA grupe (InS, InSe, InTe, GaS, GaSe, GaTe) pripadaju grupi slojevitih van der Valsovih kristala, kod kojih su slojevi povezani van der Valsovim silama. Jedan sloj ovih materijala sastoji se od četiri sloja atomskih ravni, raspoređenih prema redosledu X-M-M-X, gde X čine halkogeni atomi (S, Se, Te) a M su atomi IIIA grupe, Ga i In. Atomi u sloju su povezani jakim kovalentnim vezama: Svaki atomi halkogena povezan je sa najbliža tri M atoma u ravni iznad ili ispod njega, a M atomi sa najbliža tri halkogena atoma iz susedne ravni i M atomom naspram njega. Kristalna struktura materijala ove porodice prikazana je na slici 3.5.

Konstante rešetke jednoslojnih $M^{III}X^{VI}$ poređane od najmanje do najveće se u literaturi kreću u vrednostima od 3.61−3.64 Å za GaS, 3.80−3.84 Å za GaSe, 3.91−3.95 Å za InS, 4.06−4.19 Å za InSe, 4.12−4.13 Å za GaTe i 4.36−4.40 Å za InTe [15, 16, 18, 93, 183, 184, 185, 186]. Debljine njihovih slojeva su 4.63−4.65 Å, 4.80−4.82 Å, 5.19 Å, 5.37 Å, 4.99−5.02 Å i 5.56-5.86 Å, za GaS, GaSe, InS, InSe, GaTe i InTe, respektivno

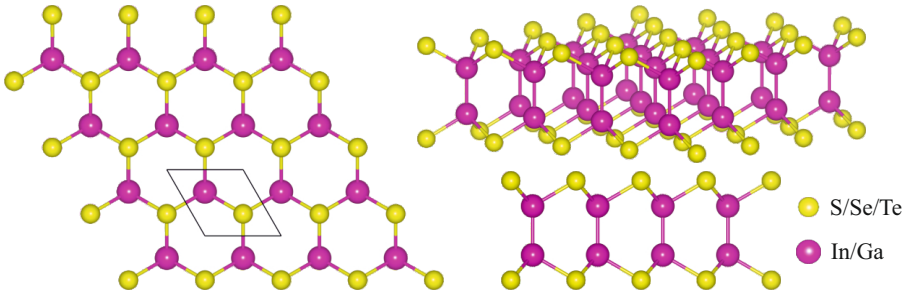


Slika 3.5: Kristalna struktura jednoslojnih monohalkogenida IIIA grupe. Atomi halkogena prikazani su žutom bojom, a atomi IIIA grupe ljubičastom.

[15, 16, 93, 187]. $M^{III}X^{VI}$ su u monoslojevima poluprovodnici sa indirektnim energijskim procepom. Na slici 3.6, prikazane su zonske strukture GaS, GaSe, GaTe, InS, InSe i InTe monoslojeva, računate u [15] korišćenjem HSE06 funkcionala. Energijski procep ima vrednosti od 3.29, 2.77, 2.13, 2.63, 2.30 i 2.07 eV za GaS, GaSe, GaTe, InS, InSe i InTe, respektivno. Neznatno manje vrednosti dobijene korišćenjem hibridnih funkcionala prikazane su i u referencama [183], [93] i [187]. Kod svih struktura, vrh valentne zone pozicioniran je između Γ i M tačke, dok se dno provodne zone kod GaS i GaTe nalazi u M tački, a kod InS, InSe, InTe i GaSe je smešteno u Γ tački. Zonska struktura ovih struktura dobijena korišćenjem LDA i PBE funkcionala je kvalitativno slična kao i kada se koriste hibridni funkcionali. Oblici zona su skoro nepromenjeni, kao i njihovi položaji u valentnoj zoni, a najveća razlika se uočava u smanjenom energijskom procepu za oko 1 eV [187]. Vrednosti energijskog procepa u ovom slučaju kreću se u opsegu 2.35−2.64 eV, 1.80−2.13 eV, 1.42−1.53 eV, 1.66−1.95 eV, 1.39−1.69 eV i 1.33−1.69 eV, za GaS, GaSe, GaTe, InS, InSe i InTe, respektivno [136, 184]. Vrednosti energijskog procepa kao i konstante rešetke, sumirane su u tabeli 3.1. Već je spomenuto da je u ovim materijalima

Tabela 3.1: Konstanta rešetke, debljina sloja, energijski procep računat pomoću HSE funkcionala, kao i energijski procep računat sa LDA i PBE funkcionalima. Vrednosti su prikupljene iz [15, 16, 18, 93, 136, 183, 184, 184, 185, 186, 187].

| | a (Å) | d (Å) | $E_g^{HSE}$ (eV) | $E_g^{LDA/PBE}$ (eV) |
|---|---|---|---|---|
| GaS | 3.61−3.64 | 4.63−4.65 | 3.29 | 2.35−2.64 |
| GaSe | 3.80−3.84 | 4.80−4.82 | 2.77 | 1.80−1.87 |
| GaTe | 4.12−4.13 | 4.99−5.02 | 2.13 | 1.42−1.47 |
| InS | 3.91−3.95 | 5.19 | 2.63 | 1.64−1.76 |
| InSe | 4.06−4.19 | 5.37 | 2.30 | 1.17−1.40 |
| InTe | 4.36−4.40 | 5.56−5.86 | 2.07 | 1.33−1.43 |

zabeležena izuzetno visoka pokretljivost elektrona [18, 24, 136] koja prelazi 1000 $cm^2/(\mathrm{Vs})$. Pored toga, $M^{III}X^{VI}$ poseduju i izvrsne optičke karakteristike. Naime, većina članova ove porodice poseduje značajnu apsorpciju u vidljivom i UV spektru, sa vrednostima koeficijenta apsorpcije od preko $10^4$ $\mathrm{cm}^{-1}$, a u određenim delovima UV spektra do $10^5$ $\mathrm{cm}^{-1}$ [91, 94, 188, 189].

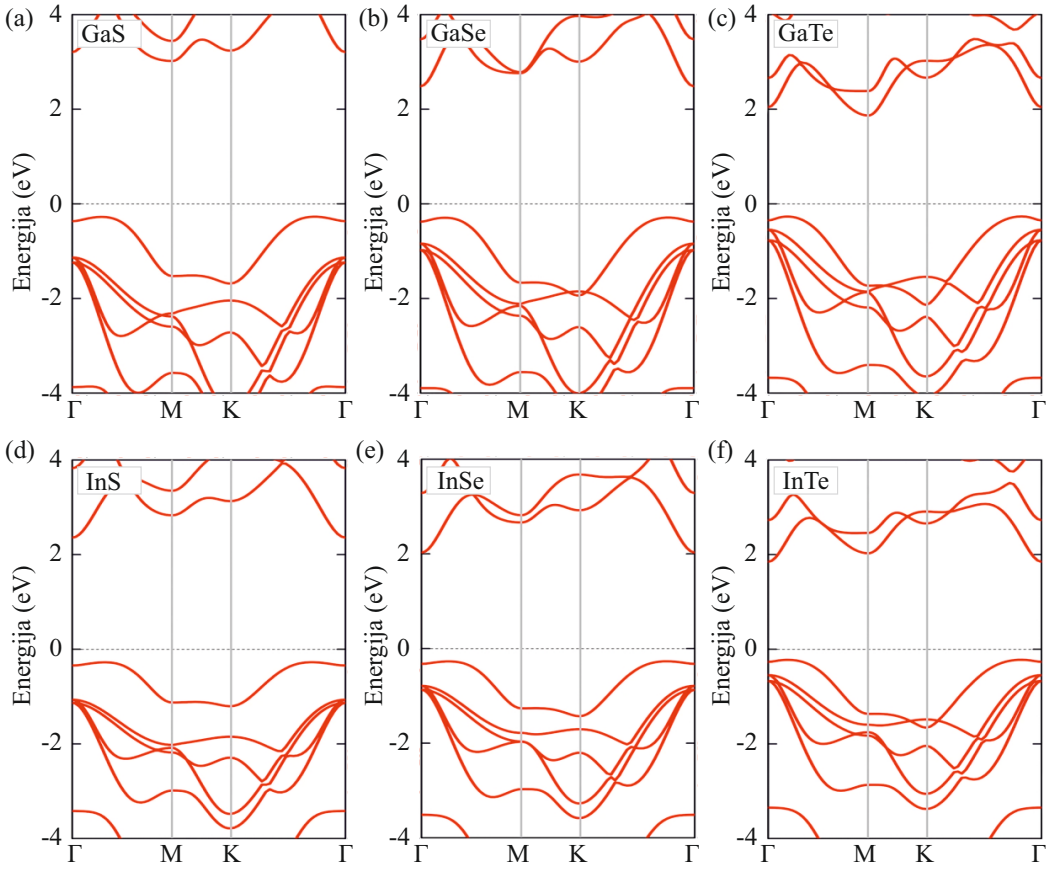


Slika 3.6: Elektronska struktura jednoslojnih (a) GaS, (b) GaSe, (c) GaTe, (d) InS, (e) InSe, (f) InTe, dobijena korišćenjem HSE06 hibridnog funkcionala. Slika je preuzeta i adaptirana iz [15].

Ono što ih, međutim, posebno ističe su i njihova mehanička svojstva. Usled dobrog odnosa čvrstoće i fleksibilnosti, jednoslojni $M^{III}X^{VI}$ mogu da podnesu preko 15% biaksijalnog naprezanja [41] i preko 25% uniaksijalnog naprezanja [18, 40], što pruža impresivne mogućnosti za manipulaciju njihovim osobinama.

Ove izuzetne mehaničke osobine pružaju mogućnost za preciznu kontrolu i podešavanje različitih svojstava ovih materijala putem naprezanja, koje može značajno uticati na njihove osobine. Do izražaja posebno dolazi biaksijalno naprezanje (u vidu istezanja ili sabijanja), kojim se ne narušava simetrija i tip kristalne rešetke, a koje može indukovati značajne promene svojstava materijala. Osim kontrolisane promene širine energijskog procepa, naprezanjem se može izazvati i prelazak sa indirektnog u direktni energijski procep [190, 191], što zajedno sa promenom širine energijskog procepa omogućava poboljšanje apsorpcionih svojstava materijala [192]. Pokazano je da biaksijalno naprezanje jednoslojnog GaTe izaziva značajne promene u energijskom procepu, pri čemu se istezanjem smanjuje širina procepa, a kompresijom povećava optička apsorpcija u UV delu spektra [192]. Uz značajne promene u širini energijskog procepa, zabeleženo je i povećanje fotoluminiscencije u GaSe [189, 193] i InSe [40, 190].

Osim elektronskih i optičkih svojstava, naprezanjem se mogu pojačati i termoelektrične performanse, što je zabeleženo u InTe slojevima [194], interesantan efekat se zapaža kod InSe, kod koga se prilikom primene uniaksijalnog naprezanja od preko 27% duž cik-cak lanca indukuje fazni prelaz i InSe iz heksagonalne strukture prelazi u strukturu sa kvadratnom rešetkom konstante $a = b = 5.32$ Å [40], koja je termodinamički stabilna, a po elektronskoj strukturi je metalna.

## 3.3 Heterostrukture monohalkogenida i hBN-a

Kao što je prikazano, članovi $M^{III}X^{VI}$ grupe poseduju izuzetna svojstva koja ih čine pogodnim za brojne primene u savremenoj tehnologiji. Međutim, njihova primena je često ograničena zbog izrazite podložnosti oksidaciji, koja se javlja pri kontaktu sa vazduhom. U tom kontekstu, hBN se ističe kao ključni zaštitni materijal. Njegova sposobnost da pasivizira površine $M^{III}X^{VI}$ slojeva značajno doprinosi očuvanju njihovih svojstava, dok istovremeno pruža mehaničku stabilnost. Sa svojom visokom transparentnošću u vidljivom delu spektra i širokim energijskim procepom, hBN heterostrukturama omogućava da zadrže svoje elektronske i optičke karakteristike, istovremeno ih štiteći od spoljašnjih uticaja. Zbog svega navedenog, ispitivanje heterostruktura zasnovanih na hBN-u i $M^{III}X^{VI}$ predstavlja važan korak ka razvoju naprednih materijala sa širokim spektrom primena

Prethodna istraživanja su potvrdila teorijski i eksperimentalni potencijal hBN/InSe heterostrukture, koja je razmatrana u teorijskim studijama [34, 195, 196], dok su eksperimentalno demonstrirane heterostrukture sačinjene od slojeva InSe i GaSe, enkapsuliranih

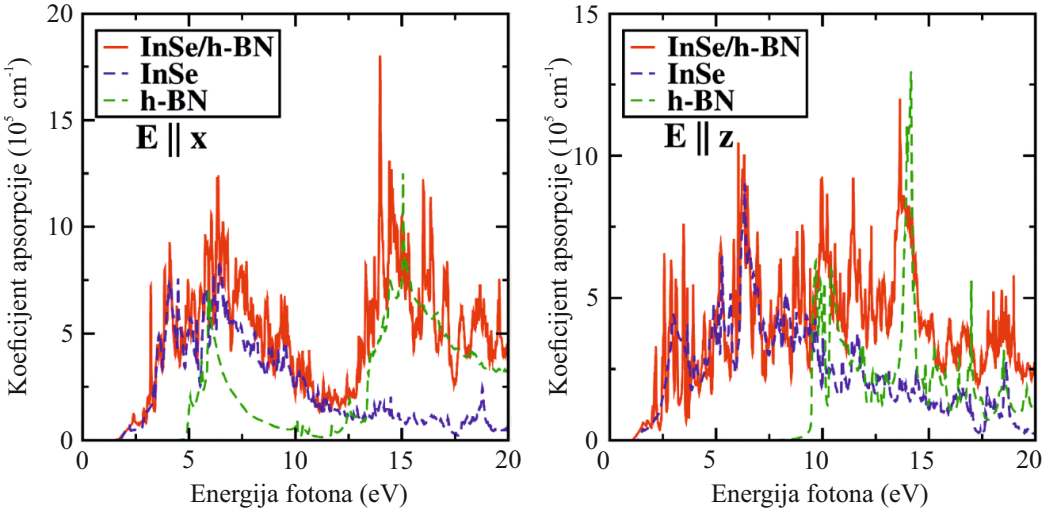


Slika 3.7: Koeficijent apsorpcije hBN/InSe heterostrukture (puna crvena linija), InSe (isprekidana plava linija) i hBN-a (isprekidana zelena linija), za polarizaciju u ravni (levo) i polarizaciju normalnu na ravan (desno). Slika je preuzeta iz [195].

između slojeva hBN-a [162]. Ove studije postavile su osnovu za dublje razumevanje uloge hBN-a kao zaštitnog sloja u stabilizaciji i unapređenju svojstava 2D materijala. Dodatno, ukazale su na potrebu za sistematskim istraživanjem novih kombinacija koje uključuju hBN kako bi se ostvarile optimalne performanse u različitim aplikacijama.

Rezultati ovih istraživanja ukazuju na višestruke prednosti hBN/InSe heterostruktura. Eksperimentalno potvrđene heterostrukture pokazale su da hBN efikasno štiti InSe slojeve od oksidacije i da takve strukture dugo ostaju stabilne u ambijentalnim uslovima [162]. Pred toga, hBN doprinosi i poboljšanju njihovih svojstava.

Uočen je porast apsorpcije u određenim delovima spektra u heterostrukturama, u poređenju sa pojedinačnim slojevima [34, 195], usled doprinosa hBN-a apsorpciji svetlosti, kao i promenama u zonskoj strukturi. Na slici 3.7 prikazani su koeficijenti apsorpcije u hBN/InSe HS, kao i pojedinačnih slojeva hBN-a i InSe. Ovi rezultati ukazuju na potencijalnu primenu ovakvih HS u naprednim optoelektronskim uređajima kao što su fotodetektori i solarne ćelije, gde se zahteva visoka apsorpcija. Pored optičkih svojstava, zapažen je i značajan porast pokretljivosti elektrona. Ispostavlja se da prisustvo hBN-a doprinosi povećanju mehaničke stabilnosti i smanjenju uticaja akustičkih fonona na rasipanje elektrona [196]. Ova svojstva čine hBN/InSe heterostrukture posebno pogodnim za primenu u naprednim nanoelektronskim i optoelektronskim uređajima. S obzirom na značajna poboljšanja koja donosi kombinovanje InSe i hBN-a u HS, istraživanja su usmerena na identifikaciju drugih potencijalnih kombinacija zasnovanih na hBN-u i monohalkogenidima. Prva ideja istraživanja bila je ispitivanje novih potencijalnih heterostruktura koje bi pružile poboljšane osobine i omogućile njihovu primenu u naprednim nanoelektronskim i optoelektronskim uređajima, dok je glavni cilj istraživanje uticaja mehaničkog naprezanja na elektronska, optička i mehanička svojstva ovih HS.

## 3.4 Naprezanje u 2D materijalima

U ovom poglavlju su predstavljeni primeri koji ilustruju značaj i efikasnost primene naprezanja u 2D materijalima. Naprezanje ima značajnu ulogu u savremenim istraživanjima materijala, kako na fundamentalnom nivou, tako i u razvoju inovativnih tehnologija. Kontrolisanom primenom naprezanja moguće je značajno unapređenje elektronskih i optičkih svojstava materijala, uz istovremenu preciznu kontrolu njihovih karakteristika. To omogućava pobuđivanje različitih kvantnih fenomena koji su ključni za razumevanje osnovnih fizičkih procesa u ovim materijalima. Pored toga, naprezanje omogućava optimizaciju mehaničkih svojstava materijala i indukovanje faznih prelaza, što je od posebnog značaja za razvoj novih funkcionalnih materijala sa proširenim mogućnostima primene.

Jedan od najperspektivnijih pravaca u istraživanju materijala je razvoj oblasti „straintronike“ („*straintronics*“), koja se fokusira na korišćenje naprezanja za manipulaciju elektronskim, magnetnim i drugim svojstvima 2D i niskodimenzionalnih materijala [132, 197]. 2D materijali često imaju visok Jangov moduo elastičnosti u kombinaciji sa dobrom fleksibilnošću van ravni, što im daje značajnu prednost u oblasti inženjeringa naprezanjem. Primena naprezanja u 2D materijalima ima višestruki potencijal za najrazličitije primene. Ova oblast donosi inovativne pristupe dizajnu energetski efikasnih i naprednih uređaja, kao što su senzori, memorijski elementi i fleksibilni elektronski sistemi. Od skoro je u fokusu istrživanja primena naprezanja za skladištenje energije, fotokatalizu i elektrolizu: Spomenuto je da se naprezanjem može kontrolisati širina energijskog procepa i pojačati apsorpcija svetlosti, čime se mogu optimizovati fotokatalitičke reakcije. Slično, naprezanjem se indukuju i različite promene u elektronskoj strukturi materijala koje mogu dovesti do optimizacije adsorpcije i bolje katalitičke aktivnosti [198].

Naprezanje se u materijalima može uvesti na različite načine, u zavisnosti od ciljeva istraživanja ili tehničkih zahteva primene. Ključne vrste naprezanja uključuju uniaksijalno, biaksijalno i triaksijalno naprezanje. Uniaksijalno naprezanje podrazumeva deformaciju duž samo jednog pravca, dok biaksijalno uključuje simetričnu deformaciju u dva pravca kristalne rešetke, pri čemu jedinična ćelija materijala ravnomerno menja veličinu, čuvajući svoj oblik i simetriju. Triaksijalno naprezanje se primenjuje duž tri pravca pod uglom od 60° i može proizvesti interesantne efekte, poput pseudo-magnetnih polja u grafenu [199, 200].

Glavni fokus ovog istraživanja je na biaksijalnom naprezanju, koje ima poseban značaj za 2D materijale i tanke filmove. Simetrično naprezanje u oba pravca omogućava precizno podešavanje širine energijskog procepa i potencijalne prelaze između indirektnog i direktnog procepa, što je od izuzetnog značaja za optoelektronske primene, uključujući lasere i fotodetektore. Osim toga, biaksijalno naprezanje može stabilizovati određene faze materijala i indukovati fazne prelaze koji doprinose razumevanju kvantnih fenomena i otvara nove pravce fundamentalnih istraživanja. Uticaj biaksijalnog naprezanja na piezoelektrična i

termoelektrična svojstva pruža dodatne mogućnosti za razvoj inovativnih uređaja, kao što su generatori energije, fleksibilni senzori ili sistemi za skladištenje energije.

Tehnike za uvođenje biaksijalnog naprezanja su raznovrsne i prilagođene su specifičnim zahtevima materijala. Jedan od najčešće korišćenih pristupa je epitaksijalni rast tankih filmova na podlogama sa različitim parametrima kristalne rešetke, pri čemu razlika u konstantama rešetke indukuje homogeno naprezanje. Mikroelektromehanički sistemi (MEMS) omogućavaju preciznu kontrolu naprezanja putem primene sila na uzorak, dok fleksibilni nosači obezbeđuju ravnomerno naprezanje u svim pravcima. Hidrostatički pritisak se koristi za uvođenje izotropnog naprezanja, a kapilarne sile deluju tokom procesa sušenja rastvora materijala u tečnoj fazi. Postoje i mnoge druge tehnike poput manipulacije defektima, kao što je supstituciono dopiranje, koje omogućava uvođenje lokalizovanih naprezanja.

Sve navedene prednosti biaksijalnog naprezanja, u kombinaciji sa raznovrsnim tehnikama njegove implementacije ga pozicioniraju kao važan metod u istraživanju i razvoju materijala, kako u okviru fundamentalnih istraživanja u fizici čvrstog stanja, tako i u razvoju primena u okviru sve značajnije oblasti straintronike. Potencijalne primene obuhvataju napredne elektronske, fotonske i fleksibilne tehnologije, pružajući temelj za dalji tehnološki razvoj.

# 4 Rezultati

Četvrto poglavlje ove doktorske disertacije obuhvata istraživanje HS zasnovanih na monohalkogenidima IIIA grupe i hBN-u, kao i uticaj biaksijalnog naprezanja na njihova elektronska i optička svojstva.

Poglavlje je podeljeno u nekoliko potpoglavlja. U potpoglavlju 4.1 razmatran je način formiranja jedinične ćelije HS i opisana njihova kristalna struktura, uz prikaz detalja proračuna korišćenih u istraživanju. Potpoglavlje 4.2 se bavi novim hBN/InTe i hBN/GaTe HS, koje do sada nisu bile ispitivane, a rezultati su objavljeni u publikaciji [201]. U potpoglavlju 4.3 ispituje se uticaj biaksijalnog naprezanja na ove dve HS, a rezultati istraživanja objavljeni su u [173]. Potpoglavlje 4.4 se odnosi na naprezanje u hBN/InSe HS, koje su prethodno bile teorijski i eksperimentalno ispitivane u svom osnovnom obliku. Rezultati ispitivanja uticaja naprezanja na njihove elektronske i optičke osobine, dobijeni tokom ovog istraživanja, rezultovali su publikacijom [202]. U poslednjem potpoglavlju, 4.5 razmatraju se preostale HS iz porodice hBN/$M^{III}X^{VI}$ .

## 4.1 Modelovanje hBN/$M^{III}X^{VI}$ heterostruktura i izbor vrste naprezanja

Kao što je navedeno u poglavlju 2, kristalnu strukturu hBN i MX slojeva karakteriše heksagonalna jedinična ćelija sa $D_{3h}$ simetrijom. Konstanta rešetke hBN-a iznosi $a = 2.515$Å, dok se konstante rešetke MX monoslojeva kreću od 3.64Å (GaS) do 4.37 Å (InTe). Način konstrukcije jedinične ćelije i poklapanje konstanti rešetki osnovnih materijala igraju ključnu ulogu u istraživanjima HS primenom DFT-a.

Sa jedne strane, važno je minimizovati indukovano naprezanje među slojevima, posebno ako je cilj dodatna modifikacija ovakvih struktura (npr. primenom naprezanja koje dovodi do dodatnog istezanja). Sa druge strane, manja jedinična ćelija ne samo da smanjuje potrebne računarske resurse i vreme izvršavanja proračuna usled manjeg broja atoma u jediničnoj ćeliji.

Sa stanovišta numeričkih proračuna, strukture sa višom simetrijom su jednostavnije i

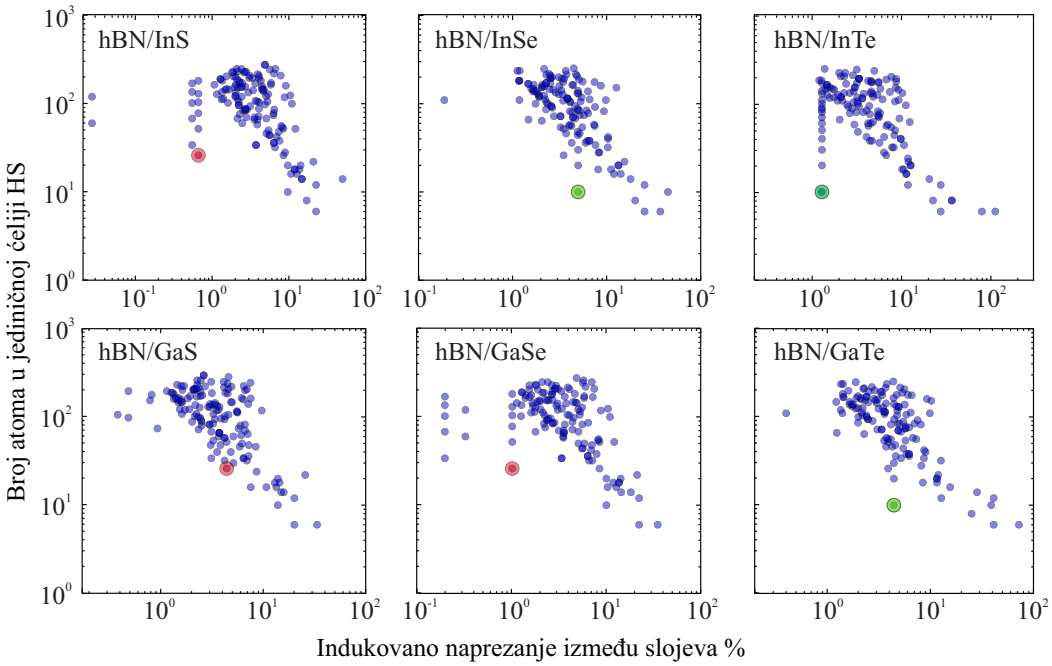


Slika 4.1: Prikaz različitih mogućnosti za formiranje jedinične ćelije HS - odnos broja atoma u ćeliji i indukovanog naprezanja među slojevima.

brže za proračune. Naime, QE, kao i mnogi drugi DFT softveri koristi simetriju kristalne strukture kako bi identifikovao ireducibilnu Briluenovu zonu (IBZ). IBZ predstavlja najmanji deo recipročne rešetke, koji se zahvaljujući simetrijskim operacijama ponavlja u ostatku Briluenove zone. Za zadatu strukturu, softver prepoznaje simetrijske operacije translacije, rotacije i inverzije koje ima zadata struktura. Na osnovu njih se određuje IBZ. Sa praktičnog aspekta, jednostavnije i simetrične strukture su često lakše za fabrikaciju zbog boljeg rasporeda atoma u slojevima i manje mogućnosti za stvaranje defekata, kao i obezbeđivanje konzistentnosti svojstava u različitim serijama proizvedenih uzoraka. A posebno je važno spomenuti i da mnoge karakteristike materijala poput zonske strukture i raspodele elektronskih stanja, karakterističnih oblika elektronske disperzije, optičkih prelaza, direktno zavise od simetrije kristala, pa se njenim narušenjem mogu izgubiti i degradirati važna svojstva materijala . Na slici 4.1 prikazan je odnos između broja atoma u jediničnoj ćeliji i indukovanog naprezanja među slojevima za različite mogućnosti konstrukcije razmatranih HS. Može se uočiti da najmanji broj atoma u jediničnoj ćeliji može biti 8, ali može dostići i preko 500.

Kod HS istraživanih u okviru ovog rada, posebno su značajne tri strukture: hBN/InTe, hBN/GaTe i hBN/InSe. Kod ovih struktura moguće je konstruisati jediničnu ćeliju koja se sastoji od sloja osnovne jedinične ćelije InTe, GaTe ili InSe i sloja hBN superćelije dimenzija $\sqrt{3} \times \sqrt{3}$ jedinične ćelije hBN-a, kao što je prikazano na slici 4.2.

HS sa ovakvim izborom jedinične ćelije zadržavaju heksagonalnu kristalnu strukturu i sadrže samo 10 atoma po jediničnoj ćeliji, uz zadovoljavajuće vrednosti indukovanog naprezanja među slojevima koje ne prelaze 6%. Posebno su samerljivi materijali u hBN/InTe HS – sa konstantama rešetke od $a = 4.37$Å za InTe i $a = 4.35$Å za hBN, in-

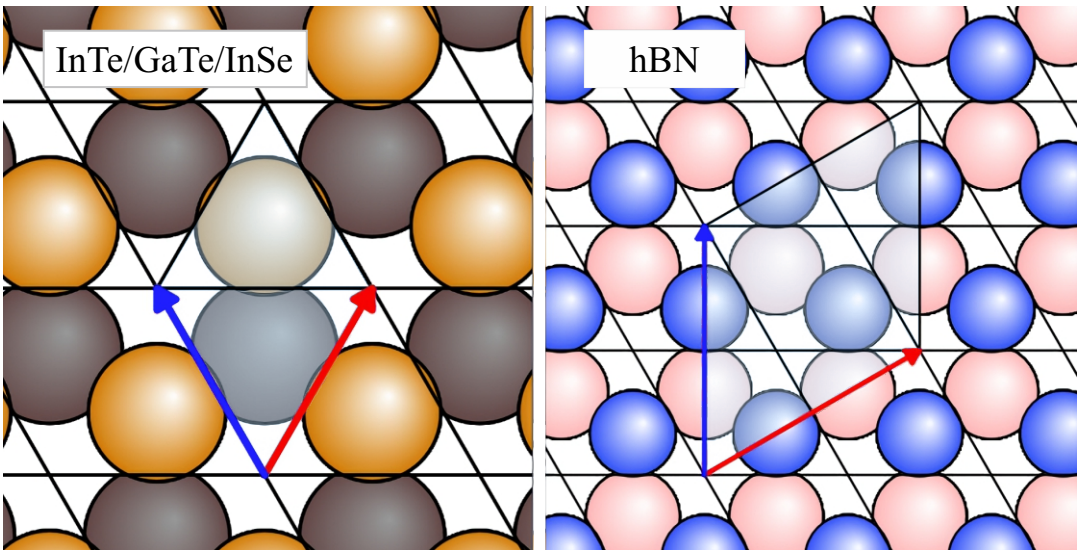


Slika 4.2: Izbor jediničnih ćelija za konstrukciju hBN/InTe, hBN/InSe i hBN/GaTe HS

dukovano naprezanje u ovoj HS iznosi samo 0.8% na sloj InTe i 0.3% na sloj hBN. Ovakav pristup omogućava modelovanje i hBN/GaTe i hBN/InSe HS, uz nešto veće naprezanje među slojevima, ali i dalje u okviru relativno niskih vrednosti koje ne ugrožavaju stabilnost strukture. Složenija situacija kod preostale tri HS prikazana je na slici 4.3.

Tako u slučaju hBN/InS i hBN/GaSe HS, optimalan izbor superćelije sadrži 26 atoma, pri čemu naprezanja ne prelaze 1%. Nasuprot tome, hBN/GaS HS zahteva 34 atoma u jediničnoj ćeliji, uz naprezanje od oko 3%. Ove HS takođe su opisane heksagonalnom kristalnom rešetkom. Jedinična ćelija hBN/GaS sačinjen je od sloja superćelije hBN-a sa konstantom rešetke $3a_{hBN}$ i sloja superćelije GaS sa konstantom rešetke $2a_{GaS}$ i nema rotacije između ova dva sloja. Preostale dve HS, hBN/GaSe i hBN/InSe sastoje se od superćelije hBN-a sa konstantom rešetke $a_{hBN}\sqrt{7}$ i superćelije InSe odnosno GaSe konstante rešetke $a_{(In/Ga)Se}\sqrt{3}$ i rotirana je u odnosu na svoju osnovnu ćeliju za 10.89°.

Fokus u ovom istraživanju je na primeni biaksijalnog naprezanja u modelovanim heterostrukturama, koje omogućava očuvanje simetrije kristalne rešetke, što je od velike važnosti za hBN/$M^{III}X^{VI}$ HS. Ujednačena modifikacija elektronskih i optičkih osobina u svim pravcima koja omogućava precizniju kontrolu energijskog procepa, interakcije između slojeva i doprinosi očuvanju mehaničke stabilnosti HS, od ključnog je značaja za istraživanje ovih heterostruktura.

## Detalji numeričkih proračuna

Svi proračuni su izvršeni korišćenjem softverskog paketa Quantum Espresso, uz primenu izmensko-korelacionog funkcionala PBE i norm-conserving pseudopotencijala. Nakon testiranja konvergencije, izabrane su energije odsecanja (*cut-off energy*) od 86

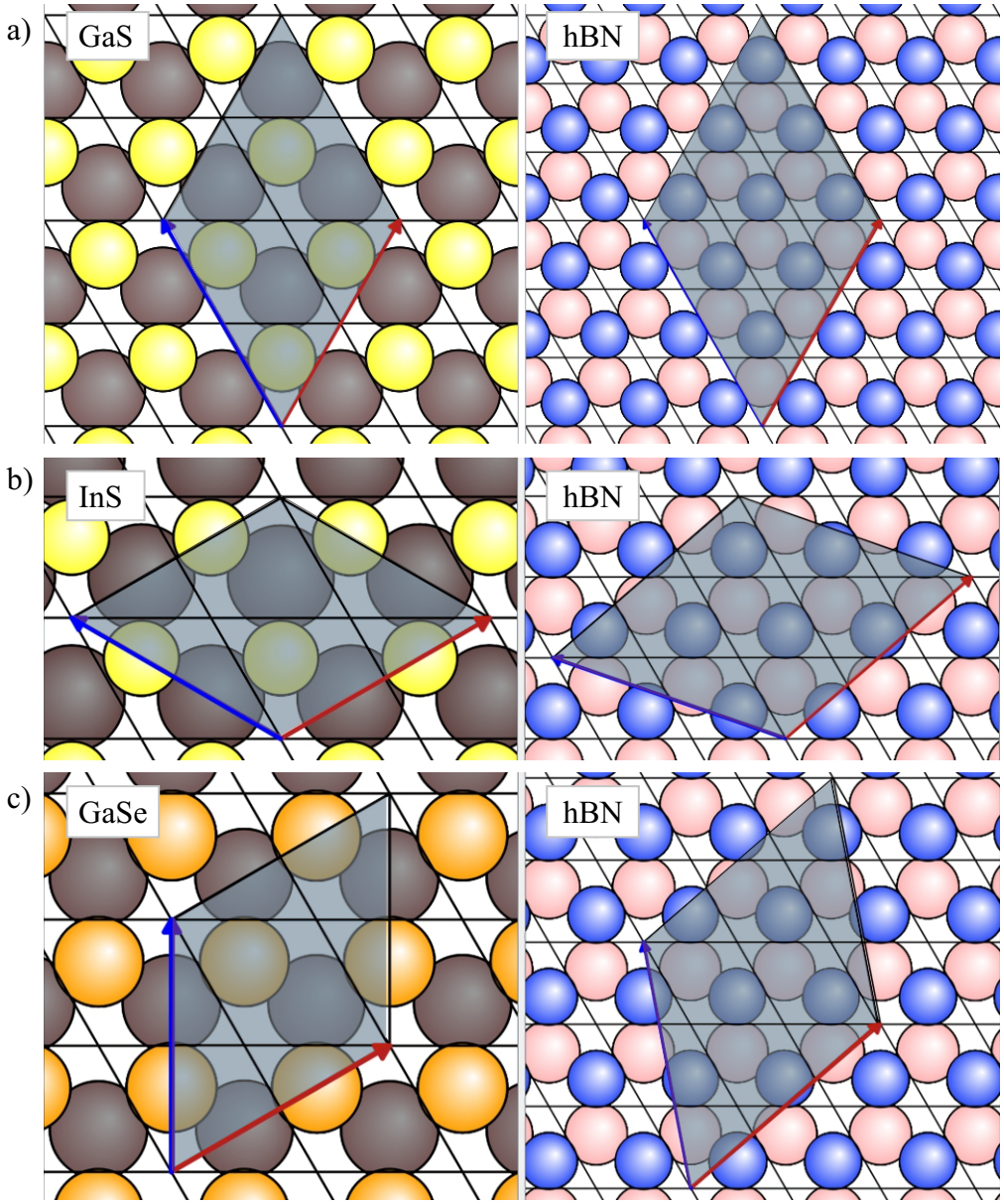


Slika 4.3: Izbor jediničnih ćelija za konstrukciju hBN/InTe, hBN/InSe i hBN/GaTe HS

Ry za hBN/InSe i hBN/GaSe HS, dok su za preostale HS korišćene energije odsecanja od 80 Ry. Za odabir $k$-tačaka u inverznom prostoru primenjena je Monkhorstova šema sa podelom 16x16x1 za proračune geometrijske optimizacije i ukupne energije, dok su za proračune koji zahtevaju finiju podelu (poput projektovane gustine stanja i optičkih karakteristika) korišćene mreže gustine 48x48x1 ili 64x64x1. Zonska struktura izračunata je na 440 $k$-tačaka po $\Gamma - \mathrm{M} - \mathrm{K} - \Gamma$ putanji u BZ.

Pošto QE podrazumeva beskonačan kristal sastavljen od jediničnih ćelija, simulacija dvodimenzionalne strukture postignuta je dodavanjem vakuuma od 20 Å duž $z$-ose, kako bi se eliminisale interakcije periodičnih replika. Za geometrijsku optimizaciju parametara rešetke i pozicija atoma unutar jedinične ćelije korišćen je BFGS algoritam, sa maksimalnim dozvoljenim međuatomskim silama od $10^{-6}$ RyÅ$^{-1}$. Takođe, pošto standardni funkcionali poput GGA ne uključuju van der Valsove sile, u proračunima je uključena Grimme-D2 korekcija radi tačnijeg izračunavanja parametara rešetke. Optičke osobine dobijene su pomoću epsilon.x koda koji koristi aproksimaciju slučajne faze (RPA) i deo je softverskog paketa QE.

## 4.2 hBN/InTe i hBN/GaTe heterostrukture

U slučaju hBN/InTe i hBN/GaTe HS koje su modelovane jediničnom ćelijom od 10 atoma, postoje tri moguća međusobna položaja slojeva: H-top, B-top, i N-top. Kod H-top rasporeda, In ili Ga atom se nalazi u centru hBN šestougaonika. B-top pozicija podrazumeva da se In ili Ga atom nalazi direktno iznad B atoma hBN sloja, dok se kod N-top pozicije In ili Ga atom nalazi iznad N atoma hBN sloja. Šematski prikaz ovih rasporeda slojeva prikazan je na slici 4.4. Kod prethodno ispitivane hBN/InSe HS, pokazano je da je H-top slaganje najpovoljniji način rasporeda slojeva, iako su sve tri konfiguracije eksperimentalno izvodljive sa negativnim energijama adsorpcije od -53.3, -53.2, i -38.6 meV po atomu. Takođe, razlike u zonskoj strukturi između ovih konfiguracija ili nema, ili su zanemarljivo male [34].

Za hBN/InTe i hBN/GaTe HS, koje do sada nisu istraživane, analizirane su pomenute tri moguće konfiguracije slojeva. Da bi se potvrdila stabilnost ovih struktura i pokazala njihova moguća realizacija, izračunate su energije adsorpcije prema sledećoj formuli:

$$E_b = \frac{1}{N}(E_{HS} - E_{In(Ga)Te} - E_{hBN}), \tag{4.1}$$

Gde su $E_{HS}$, $E_{In(Ga)Te}$ i $E_{hBN}$ ukupne energije hBN/In(Ga)Te HS, In(Ga)Te monosloja i hBN sloja, respektivno, dok je $N$ broj atoma u jediničnoj ćeliji HS. Ukoliko je arsorpcija termodinamički povoljnija, energija celog sistema je niža od zbira energija pojedinačnih slojeva, odnosno energija adsorpcije je negativna, a što je veća njena apsolutna vred-

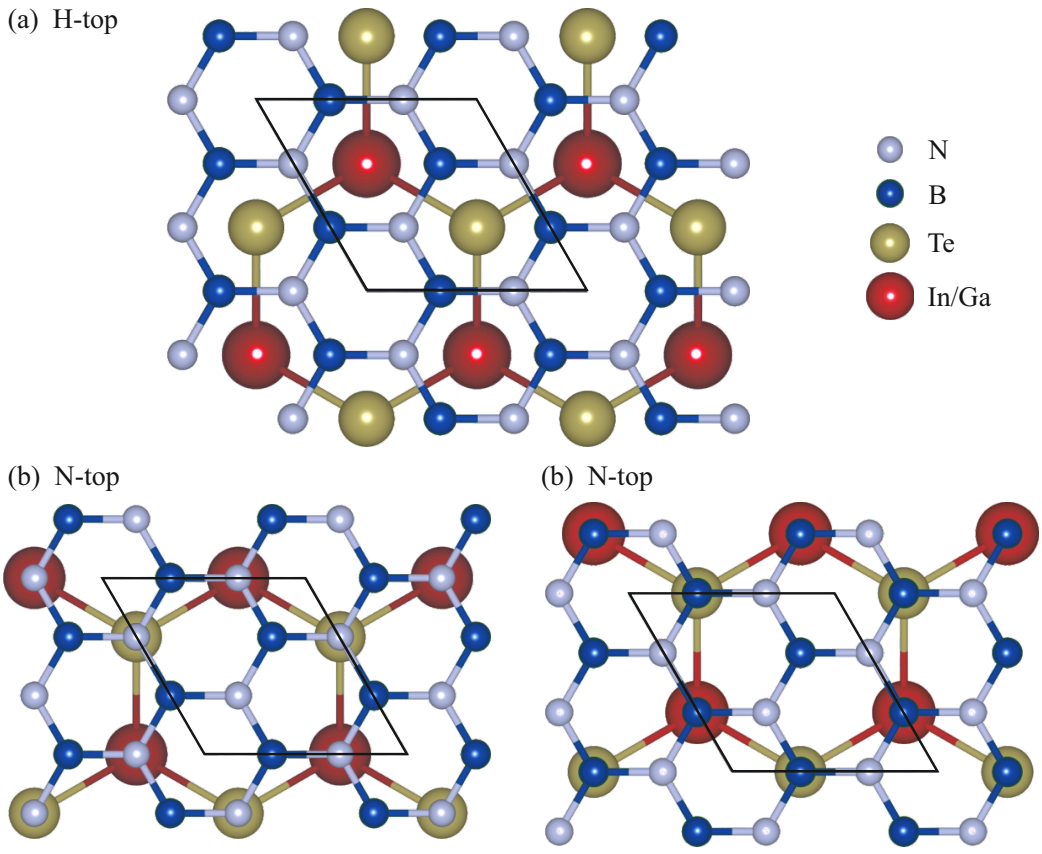


Slika 4.4: Različite mogućnosti slaganja slojeva HS u zavisnosti od položaja In/Ga atoma u odnosu na hBN sloj: (a) H-top, (b) B-Top.

Tabela 4.1: Parametri rešetke, distanca između hBN i InTe odnosno GaTe sloja i energije vezivanja za različite načine slaganja kod hBN/InTe i hBN/GaTe HS.

| | hBN/InTe | | |
|---|---|---|---|
| | H-top | N-top | B-top |
| $a$[Å] | 4.346 | 4.337 | 4.337 |
| $d$[Å] | 3.429 | 3.523 | 3.479 |
| $E_b$[meV] | -26.964 | -25.549 | -25.963 |
| | hBN/GaTe | | |
| | H-top | N-top | B-top |
| $a$[Å] | 4.309 | 4.309 | 4.311 |
| $d$[Å] | 3.451 | 3.516 | 3.503 |
| $E_b$[meV] | -25.562 | -24.176 | -24.661 |

nost, to je arsorpcija jača. Energije adsorpcije za H-top, N-top i B-top konfiguracije, kao i optimizovani parametri rešetke i rastojanje između hBN i InTe, odnosno GaTe sloja, prikazane su u tabeli 4.1. Slično kao i kod hBN/InSe HS, H-top konfiguracija se pokazala kao najstabilnija, sa najvećom energijom adsorpcije po atomu i najnižom ukupnom energijom. Takođe, treba napomenuti da su i ostale konfiguracije podjednako ostvarive, jer imaju negativne energije adsorpcije. Dalje se može zaključiti da zonska struktura praktično ne zavisi od tipa slaganja, što je prikazano na slici 4.5. Sve tri konfiguracije, H-top, N-top i B-top, pokazuju veoma slične zonske strukture, što ukazuje na to da različiti načini slaganja slojeva ne utiču značajno na elektronske osobine ovih HS. U daljem istraživanju korišćen je H-top način slaganja slojeva, koji se izdvaja kao najpovoljniji u pogledu ukupne energije i energije vezivanja.

Kako bismo potvrdili dinamičku stabilnost hBN/InTe i hBN/GaTe HS, izračunata je i njihova fononska disperzija, prikazana na slici 4.6. Doprinos različitih atoma označen je bojama kao na legendi. Može se videti da u disperziji nema negativnih frekvencija koje bi ukazivale na potencijalnu nestabilnost strukture. Male negativne vrednosti u okolini $\Gamma$ tačke se mogu uočiti, a koje su posledice numeričkog problema koji se često javlja prilikom proračuna fonona u 2D materijalima. Može se takođe zaključiti da niskoenergijski modovi potiču prvenstveno od Te atoma, a zatim od In i Ga, što je očekivano usled činjenice da su ovi atomi značajno teži od B i N atoma.

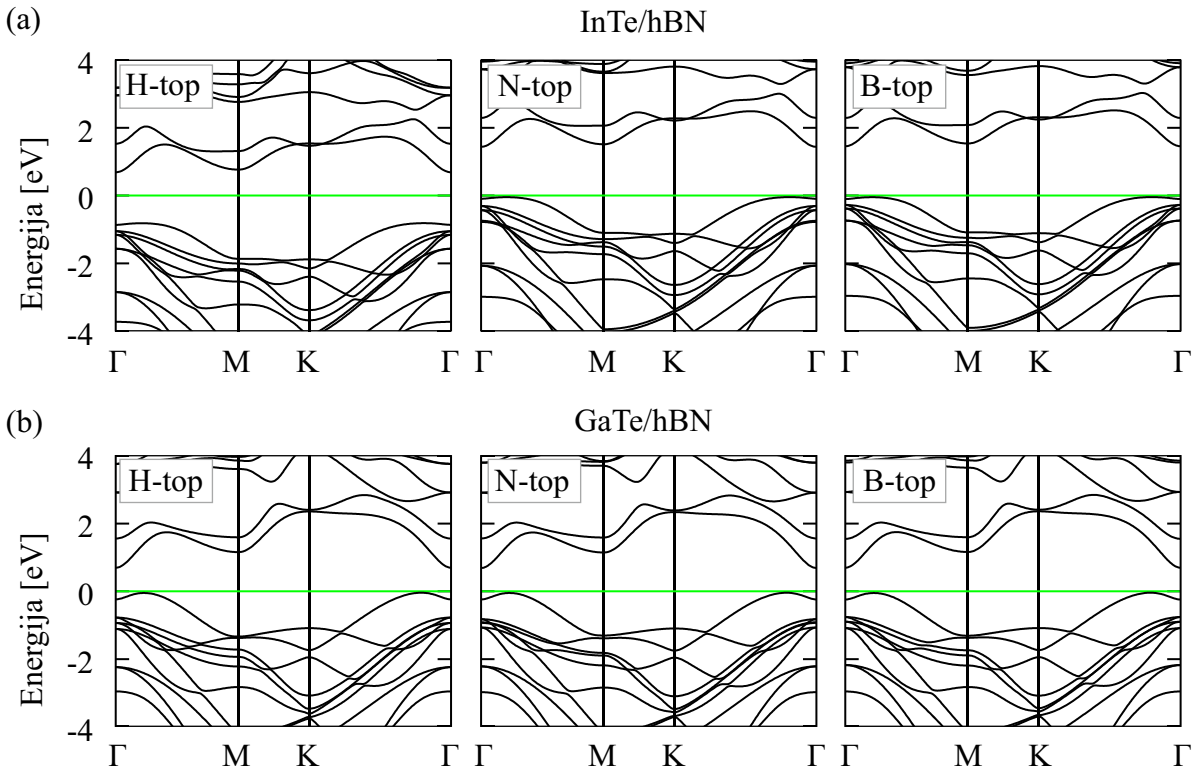


Slika 4.5: Zonska struktura (a) hBN/InTe i (b) hBN/GaTe za različite tipove slaganja slojeva.

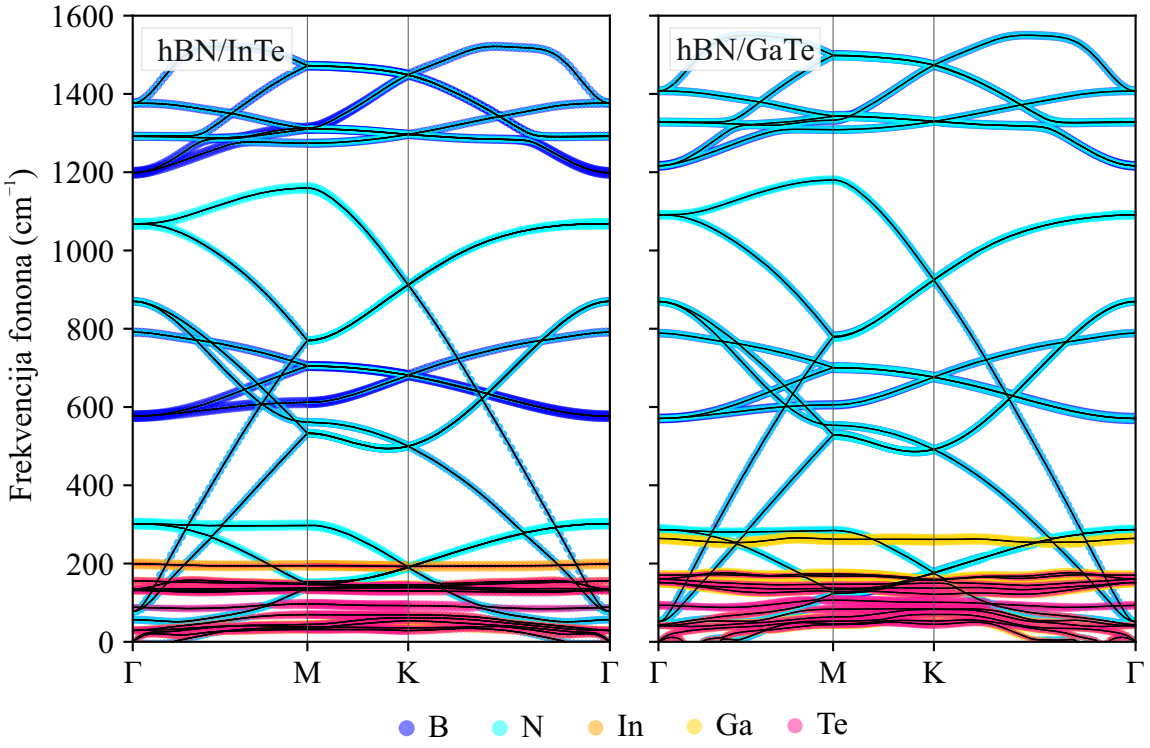


Slika 4.6: Fononska disperzija (a) hBN/InTe i (b) hBN/GaTe HS.

Tabela 4.2: Konstante elastičnosti, Jangov moduo, Poasonov koeficijent, moduo smicanja i moduo sloja za InTe, GaTe, hBN, hBN/InTe, hBN/GaTe strukture. Vrednosti su date u N/m.

| | InTe | GaTe | hBN | hBN/InTe | hBN/GaTe |
|---|---|---|---|---|---|
| $C_{11}$ | 45.36 | 65.62 | 290.77 | 338.30 | 340.00 |
| $C_{12}$ | 11.76 | 15.30 | 63.93 | 72.08 | 75.48 |
| $C_{66}$ | 16.52 | 25.16 | 113.42 | 132.94 | 132.26 |
| $E_y$ | 42.31 | 62.05 | 276.41 | 322.94 | 323.24 |
| $\upsilon_{xy}$ | 0.26 | 0.23 | 0.22 | 0.21 | 0.22 |
| $G_{xy}$ | 16.52 | 25.16 | 113.42 | 132.94 | 132.26 |
| $\gamma^{2D}$ | 28.56 | 40.46 | 177.35 | 205.19 | 207.74 |

### 4.2.1 Mehanička svojstva

Za istraživanje naprezanja u materijalima, važno je prvo ispitati mehaničke osobine materijala. Detaljan opis metoda proračuna konstanti elastičnosti i analiza njihovog međusobnog odnosa predstavljeni su u potpoglavlju 2.8.2.1. S obzirom na to da do sada nema publikovanih rezultata sa osobinama elastičnosti InTe i GaTe monoslojeva, izračunali smo i njihove konstante elastičnosti. Dobijene konstante elastičnosti za jednoslojne InTe i GaTe su u opsegu drugih III-VI monohalkogenida [203]. Konstante $C_{11} = 45.36$ N/m i $C_{12} = 11.76$ N/m za InTe su bliske konstantama jednoslojnog InSe, dok su $C_{11} = 65.62$ N/m i $C_{12} = 15.30$ N/m za GaTe blizu rezultatima za jednoslojni GaSe. Kako bismo potvrdili verodostojnost rezultata, izračunali smo i konstante elastičnosti hBN-a, a dobijene vrednosti su takođe u skladu sa literaturom [171, 172]. Konstante elastičnosti i moduli se značajno povećavaju u formiranim HS. Konstante $C_{11}$ and $C_{12}$ za hBN/InTe su $C_{11} = 338.3$ N/m i $C_{12} = 72.08$ N/m; $C_{11} = 340$ N/m i $C_{12} = 75.48$ za hBN/GaTe, i može se primetiti da su njihove vrednosti otprilike slične zbiru pojedinačnih konstanti svakog sloja u HS. Jangov modul je povećan na $\tilde{3}23$ N/m u HS, što dostiže vrednosti bliske Jangovom modulu grafena (342-366 N/m), a prati ga i moduo sloja od 205-207 N/m u HS, dok je za moduo sloja grafena u opsegu 206-212 N/m [171, 204]). Ovo ukazuje na visoku otpornost na jednosmernu kompresiju kao i na istezanje. Rezultati sugerišu da prisustvo hBN sloja u našim HS ne samo da štiti osetljive slojeve monohalkogenida od oksidacije, već takođe pruža efikasnu mehaničku zaštitu, čineći sistem robustnijim i otpornijim na deformacije.

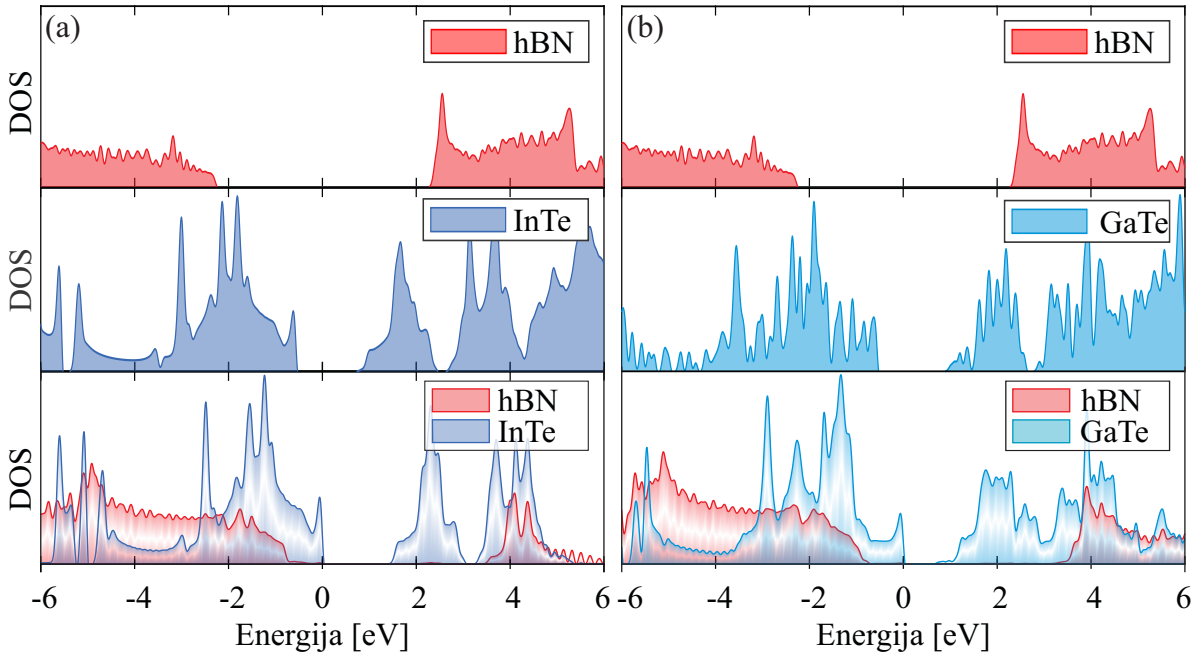


Slika 4.7: Projektovana gustina stanja za (a) hBN, InTe i hBN/InTe HS, (b) hBN, GaTe i hBN/GaTe HS. Udeo hBN-a i InTe odnosno GaTe slojeva, prikazani su crvenim i plavim nijansama kao na legendi.

### 4.2.2 Elektronska struktura

Prema rezultatima proračuna, InTe i GaTe imaju indirektne energijske procepe od $E_g = 1.38$ eV i $E_g = 1.75$ eV, respektivno, dok hBN poseduje veliki direktni energijski procep od 4.63 eV. Ovi rezultati se dobro poklapaju sa prethodnim teorijskim studijama koje koriste PBE funkcional [16, 94, 180, 192]. Prethodne studije na sličnim materijalima, uključujući InSe, pokazale su da korišćenje hibridnih funkcionala kao što je HSE ne menja zonsku strukturu kvalitativno, dok se najznačajnija razlika odnosi na veći energijski procep. Velika razlika u energijskom procepu između InTe/GaTe monoslojeva i hBN-a, kao i njihov međusobni položaj, čine ove HS heterospojevima I vrste. Ovo se takođe može potvrditi uvidom u gustinu stanja monoslojeva hBN, InTe/GaTe, i njihovih HS, kao što je prikazano na slici 4.7.

Na slikama 4.8 i 4.9 prikazane su zonske strukture hBN/InTe i hBN/GaTe HS, razložene po različitim atomskim stanjima. Radi lakšeg poređenja, zonske strukture monoslojeva InTe i GaTe su prikazane uporedo.

Monoslojevi InTe i GaTe su, kao što je prethodno pomenuto, poluprovodnici sa indirektnim energijskim procepom, pri čemu se maksimumi valentne zone nalaze u blizini Γ tačke, dok su minimumi provodne zone u M tački za GaTe i Γ tački za InTe (iako se u ovom slučaju energija u Γ tački veoma blisko poklapa sa energijom u M tački). Nakon formiranja HS, energijski procep se menja, kao i oblici dna provodne zone. U obe HS, minimum provodne zone se nalazi u Γ tački.

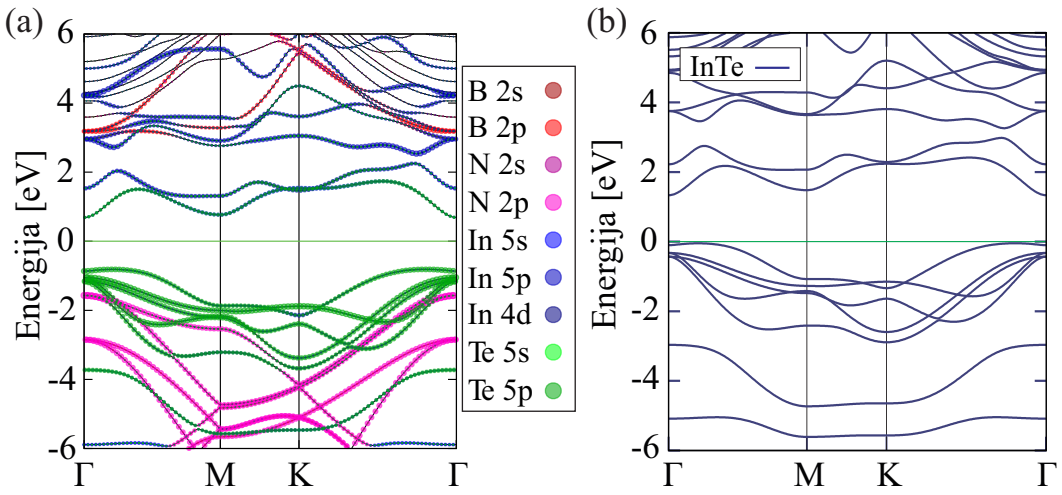


Slika 4.8: Zonska struktura (a) hBN/InTe HS, (b) jednog sloja InTe. Debljina linije označava doprinos određenog stanja/atoma u zonskoj strukturi.

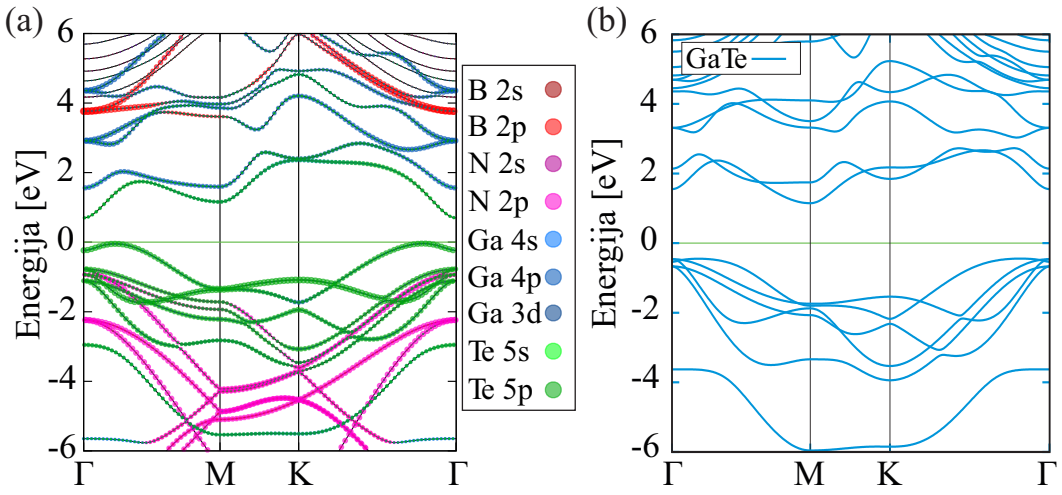


Slika 4.9: Zonska struktura (a) hBN/GaTe HS, (b) jednog sloja GaTe. Debljina linije označava doprinos određenog stanja/atoma u zonskoj strukturi.

Prilikom formiranja hBN/InTe HS, energijski procep je neznatno povećan, sa 1.38 eV u InTe monosloju na 1.54 eV u HS. Ova promena nije značajno vidljiva u zonskoj strukturi, s obzirom na to da su zone u okolini Fermi nivoa slične onima u jednoslojnom InTe. Stanja u okolini Fermi nivoa formirana su gotovo potpuno od InTe, konkretno od stanja Te atoma, dok se doprinos hBN-a uočava ispod -2 eV i iznad 3 eV, slično kao u jednoslojnom hBN-u.

Značajnija razlika uočava se kod hBN/GaTe HS. Energijski procep jednoslojnog GaTe iznosi 1.75 eV, dok je kod HS smanjen na 0.79 eV. U blizini Γ tačke hBN/GaTe HS, uočava se više mešanih stanja na oko -1 eV, koja dolaze od 5p stanja Te atoma i 2p stanja N atoma, kao rezultat interakcije između hBN i GaTe slojeva. Dodatno, valentna zona je značajno pomerena naviše, razdvaja se od prethodno grupisanih stanja u okolini Γ tačke za više od 0.5 eV, čime se značajno smanjuje energijski procep.

Kako širina energijskog procepa direktno utiče na optičke osobine poput apsorpcije, ova promena primećena kod hBN/GaTe može biti veoma značajna sa stanovišta primena u optoelektronici.

### 4.2.3 Optička svojstva

Očekujući sličnu situaciju kao kod hBN/InSe HS, koje su se istakle po velikoj apsorpciji u širokom delu spektra, izračunate su apsorpcione funkcije za hBN/InTe i hBN/GaTe HS. Polazeći od kompleksne dielektrične funkcije, dobijene u okviru RPA aproksimacije, apsorpcioni koeficijent izračunat je po formuli 2.85. Apsorpcioni spektri ovih HS, zajedno sa spektrima njihovih jednoslojnih komponenti, prikazani su na slikama 4.10 i 4.11.

Ovi proračuni omogućavaju poređenje optičkih karakteristika HS i osnovnih materijala koji ih čine, što je ključno za razumevanje potencijalnih primena ovih struktura u optoelektronici. Apsorpcioni spektri pružaju uvid u efikasnost apsorpcije svetlosti i mogu pomoći u identifikaciji talasnih dužina na kojima materijali pokazuju pojačanu optičku aktivnost. Apsorpcioni spektri hBN/InTe i hBN/GaTe pokazuju kombinovane karakteristike svojih osnovnih materijala. Primećuje se da su vrhovi apsorpcije u HS pomereni u odnosu na monoslojeve, usled modifikacije elektronskih stanja u zonskoj strukturi. Obe HS poseduju izvrsna apsorpciona svojstva, pokrivajući vidljivi i UV deo spektra, pri čemu apsorpcija hBN/GaTe HS obuhvata i IR deo spektra. U obe HS, apsorpcioni vrhovi su uglavnom viši i širi od onih kod monoslojeva InTe i GaTe, što ukazuje na poboljšanu apsorpciju u određenim delovima spektra. Posebno se ističe hBN/GaTe, kod koje je apsorpcija u niskoenergetskom opsegu značajnije povećana, što može biti veoma korisno za primene koje zahtevaju efikasnu apsorpciju niskoenergetske svetlosti. S obzirom na to da PBE funkcionali potcenjuju energijski procep, očekivano je da bi proračuni korišćenjem HSE hibridnih funkcionala pomerili apsorpcione spektre ka višim energijama, što bi moglo

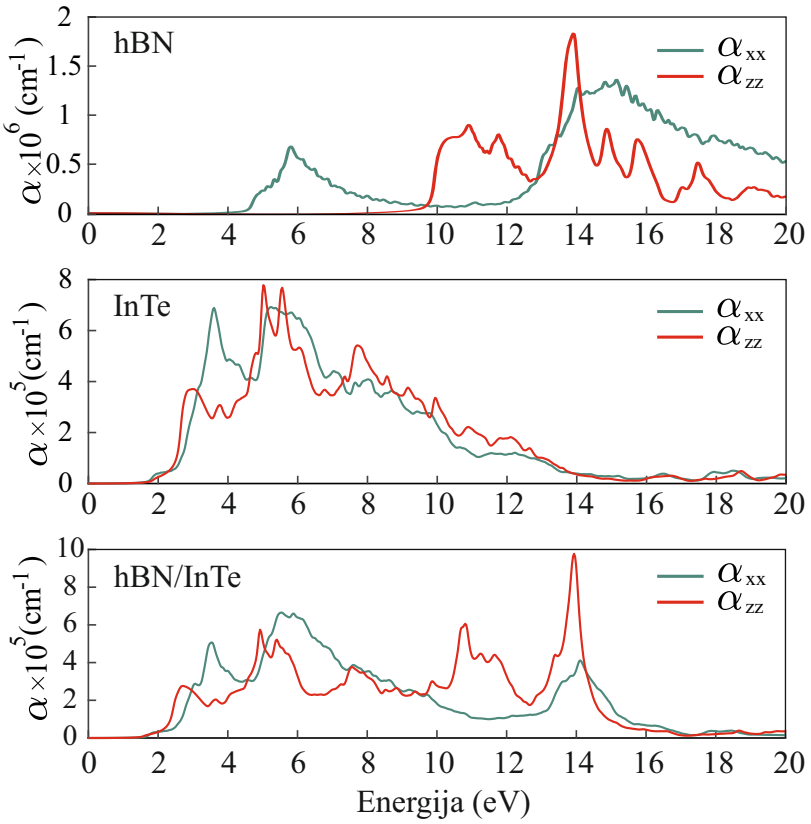


Slika 4.10: Apsorpcija jednoslojnih hBN i InTe, kao i hBN/InTe HS, za polarizacije u ravni ($\alpha_{xx}$) i normalno na ravan ($\alpha_{zz}$).

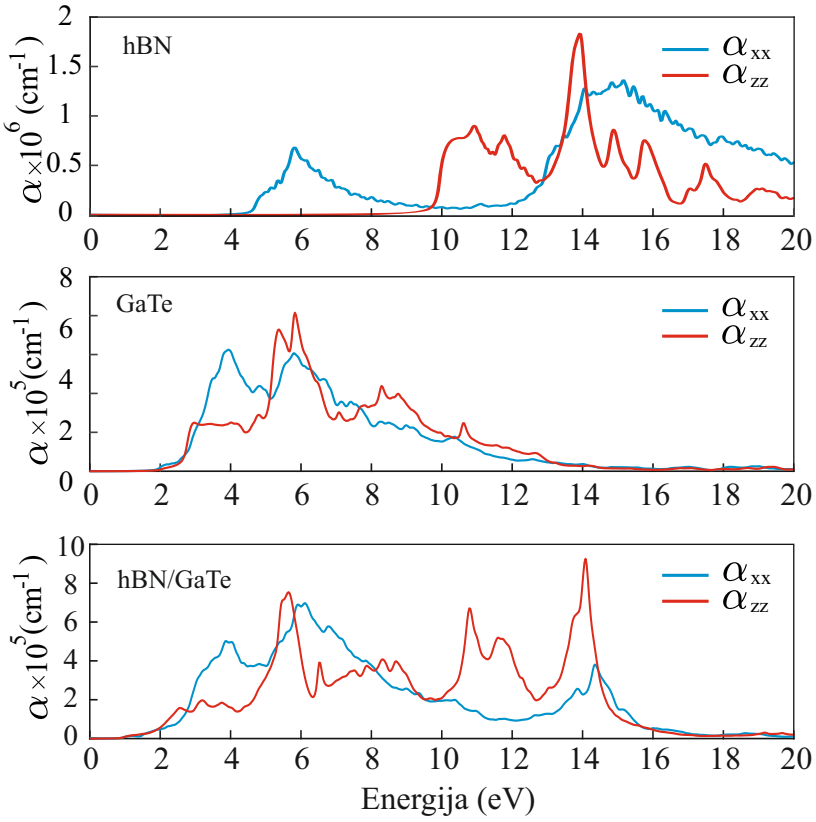


Slika 4.11: Apsorpcija jednoslojnih hBN i GaTe, kao i hBN/GaTe HS, za polarizacije u ravni ($\alpha_{xx}$) i normalno na ravan ($\alpha_{zz}$).

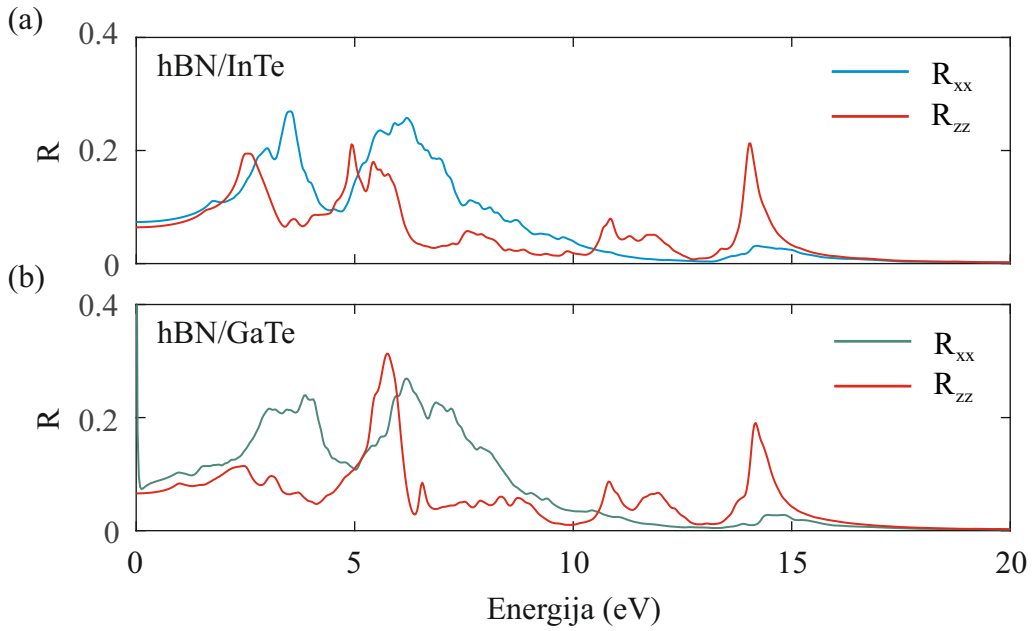


Slika 4.12: Reflektansa (a) hBN/InTe i (b) hBN/GaTe HS, za polarizacije u ravni ($\alpha_{xx}$) i normalno na ravan ($\alpha_{zz}$).

dovesti do smanjenja apsorpcije u IR i vidljivom delu spektra.

Najveći pikovi apsorpcije javljaju se u obe strukture pri energijama oko 6 eV, što je povezano sa InTe odnosno GaTe slojem, kao i pri 11 i 14 eV, gde najveći doprinos dolazi od hBN sloja, sa vrednostima koje dostižu čak $8 \times 10^5$ cm$^{-1}$. Zbog manjeg energijskog procepa u hBN/GaTe HS, apsorpcija u niskoenergetskoj oblasti od 1-2 eV je pojačana u poređenju sa apsorpcijom u hBN/InTe strukturi. Ipak, ova razlika nije velika, što je u skladu sa činjenicom da zonske strukture hBN/InTe i hBN/GaTe nisu značajno različite u kvalitativnom smislu. Naime, smanjenje energijskog procepa kod hBN/GaTe u najvećem delu potiče od jedne izdvojene zone u blizini Fermi nivoa, koja je pomerena naviše.

U energijskom opsegu od 3 do 15 eV, obe HS pokazuju izuzetne vrednosti apsorpcije, koje se kreću u rasponu od $2 \times 10^5$ do $8 \times 10^5$ cm$^{-1}$. Ova karakteristika ih čini odličnim kandidatima za primene u optoelektronici, posebno kao apsorberi u bliskom i dalekom UV spektru, i potencijal za primenu ovih HS u visokoefikasnim fotodetektorima i solarnim ćelijama je značajan.

Analizom apsorpcije za $\alpha_{xx}$ i $\alpha_{zz}$ polarizacije, može primetiti značajna anizotropija apsorpcije, ukazujući na različite preferencijalne orijentacije apsorpcije svetlosti u ovim materijalima.

Dodatna potvrda njihove efikasnosti dolazi iz proračuna reflektanse, koji su prikazani na slici 4.12.

Kao što je prikazano, reflektanse obe HS ne prelaze 30% u bilo kom delu spektra, što ukazuje na to da se značajan deo svetlosti apsorbuje, a samo mali udeo se reflektuje. Posebno su niske reflektanse u niskoenergijskom opsegu, gde iznose oko 10%, što potvrđuje da se većina svetlosti u ovom delu spektra efikasno apsorbuje. Za obe HS, pikovi reflektanse su izraženi na određenim energijama, ukazujući na rezonantne prelaze

unutar struktura.

S obzirom na kvalitativnu sličnost zonskih struktura i apsorpcionih funkcija, reflektanse hBN/InTe i hBN/GaTe HS su takođe slične. Međutim, postoje male razlike u z-polarizaciji kod hBN/GaTe HS, gde se uočava smanjenje vrha reflektanse na oko 2.5 eV, što dovodi do toga da reflektansa u celom opsegu od 0 do 5 eV ostane ispod 10%. Ova karakteristika dodatno potvrđuje potencijal ovih HS za primene u optoelektronici, gde je niska reflektansa poželjna za efikasnu apsorpciju svetlosti. Slično kao i kod apsorpcije, uočljiva je razlika između komponenti reflektanse u zavisnosti od polarizacije. Reflektansa za $z$ polarizaciju generalno pokazuje niže vrednosti u nižim energijskim opsezima u poređenju sa $R_{xx}$, što može biti indikativno za različite odzive materijala na električno polje usmereno duž različitih osa kristalne rešetke.

## 4.3 Uticaj biaksijalnog naprezanja na hBN/InTe i hBN/GaTe heterostrukture

### 4.3.1 Elektronska struktura

Ispitivanje naprezanja fokusirano je na uniformno biaksijalno naprezanje, koje ne dovodi do narušenja simetrije i tipa kristalne rešetke, a može dovesti do značajnih promena u elektronskoj strukturi materijala. Razmatrane su vrednosti naprezanja od -5% (kompresija) do +5% (istezanje), sa korakom od 1%.

Kao što je u prethodnom potpoglavlju navedeno, hBN/InTe i hBN/GaTe HS su poluprovodnici indirektnog energijskog procepa od $E_g = 1.53$ eV i $E_g = 0.76$ eV, respektivno, pri čemu se maksimum valentne zone nalazi u blizini Γ tačke, a minimum provodne zone u Γ tački. Naravno, sa primenjenim naprezanjem, dolazi do značajnih promena ne samo u širini energijskog procepa, već i u obliku određenih zona.

Na slici 4.13 prikazana je zonska struktura hBN/InTe HS projektovana po atomskim stanjima, za vrednosti naprezanja od -5% do +5%. Prvo se uočava značajna promena energijskog procepa, koji se uopšteno gledano, povećava sa primenom kompresivnog naprezanja, a smanjuje prilikom istezanja. Prilikom uvođenja kompresivnog naprezanja, valentna zona postepeno pada ka nižim energijama kako se kompresija povećava, pri čemu se za kompresije jače od 3%, spušta ispod grupe zona smeštene na oko -0.5 eV u Γ tački. Vrh valentne zone tada prelazi u Γ tačku. Što se tiče provodne zone, uočljive su značajne promene. U osnovnom, relaksiranom stanju, minimum provodne zone je u Γ tački, a dno doline u M tački je na vrlo približnoj energiji. Uvođenjem kompresivnog naprezanja, dolina u okolini Γ tačke se održava na približno istim energijama, ali se uočava značajan

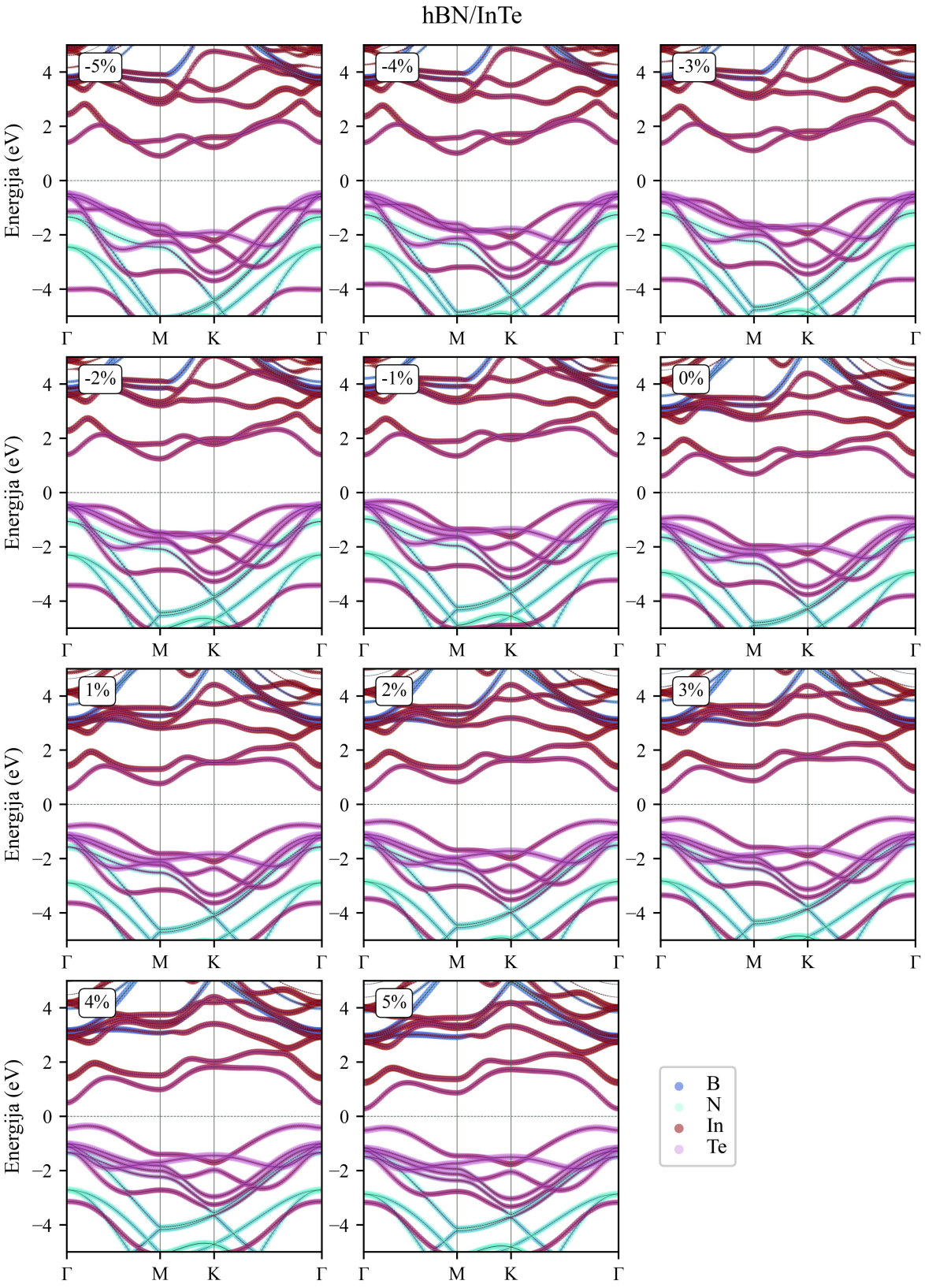


Slika 4.13: Zonska struktura hBN/InTe HS projektovana po atomskim stanjima, za različite vrednosti naprezanja, od -5% do 5%.

pad u energiji M-doline, prilikom čega se minimum provodne zone premešta u M tačku za naprezanja od -2% i intenzivnija. Ovaj komplikovan odnos valentne i provodne zone rezultuje u energijskom procepu koji se povećava do $E_g = 1.69$ eV za -2% kompresivnog naprezanja, nakon čega se polako smanjuje do 1.39 eV, za -5% naprezanja.

U slučaju pozitivnog naprezanja, tj. istezanja, promene su znatno jednostavnije. Valentna zona se pomera ka višim energijama, a dno provodne zone u Γ tački opada u energiji, što dovodi do konstantnog smanjenja energijskog procepa, koji dostiže 0.7 eV za +5% naprezanja.

Do sličnih zaključaka se dolazi se i analizom zonske strukture hBN/GaTe za različita naprezanja, iako je u ovom slučaju odnos naprezanja i zona u okolini Fermi nivoa jednostavniji. Valentna zona ne podleže značajnijoj promeni oblika - sa kompresivnim naprezanjem ona se spušta ka nižim energijama, a prilikom istezanja njena energija raste. Dno provodne zone se pomera ka višim energijama sa porastom intenziteta kompresivnog naprezanja, dok dno M doline ostaje na relativno sličnim energijama. Na -4% naprezanja, energije dna Γ i M doline su praktično izjednačene, odakle dno provodne zone prelazi u Γ tačku. Situacija je obrnuta u slučaju istezanja, pa se tako energija vrha valentne zone pomera ka višim energijama, a dno provodne zone u Γ tački, vidno se spušta ka Fermijevom nivou, što dovodi do značajnog smanjenja energijskog procepa, koji na +5% naprezanja iznosi samo 0.24 eV.

Promene energija dolina u provodnoj zoni koje se uočavaju u zonskim strukturama pri različitim vrednostima naprezanja su bile očekivane, s obzirom na to da su slične uočene u jednoslojnim InTe i GaTe pod dejstvom biaksijalnog naprezanja [187, 192, 205]. Daljom analizom projektovane gustine stanja, prikazanom na slici 4.15 za obe strukture, primećuje se da stanja najbliža Fermi nivou potiču uglavnom od In odnosno Ga i Te stanja. Konkretno, najviša stanja u valentnoj zoni su rezultat doprinosa Te stanja, dok se najniža stanja provodne zone sastoje od In ili Ga, i Te stanja. Može se dakle zaključiti, da se promene u obliku dna provodne zone dešavaju usled uticaja naprezanja na InTe odnosno GaTe sloj, a ne kao svojstvo formirane HS. Ova saznanja ističu važnost teorijskih studija vezanih za naprezanje u HS i njegov efekat na elektronska i optička svojstva, pružajući važne informacije neophodne za modifikaciju njihovih svojstava na željeni način.

### 4.3.2 Optička svojstva

Na slikama 4.16 i 4.17, prikazane su apsorpcione funkcije hBN/InTe i hBN/GaTe HS za različite vrednosti naprezanja od -5% do +5%, za polarizaciju u ravni ($\alpha_{xy}$) i normalno na ravan ($\alpha_z$). Apsorpcione funkcije jasno pokazuju kako promene u naprezanju utiču na optičke osobine materijala, koje su rezultat promene širine energijskog procepa i drugih varijacija u zonskoj strukturi. Kompresivno naprezanje dovodi do blagog širenja pikova i

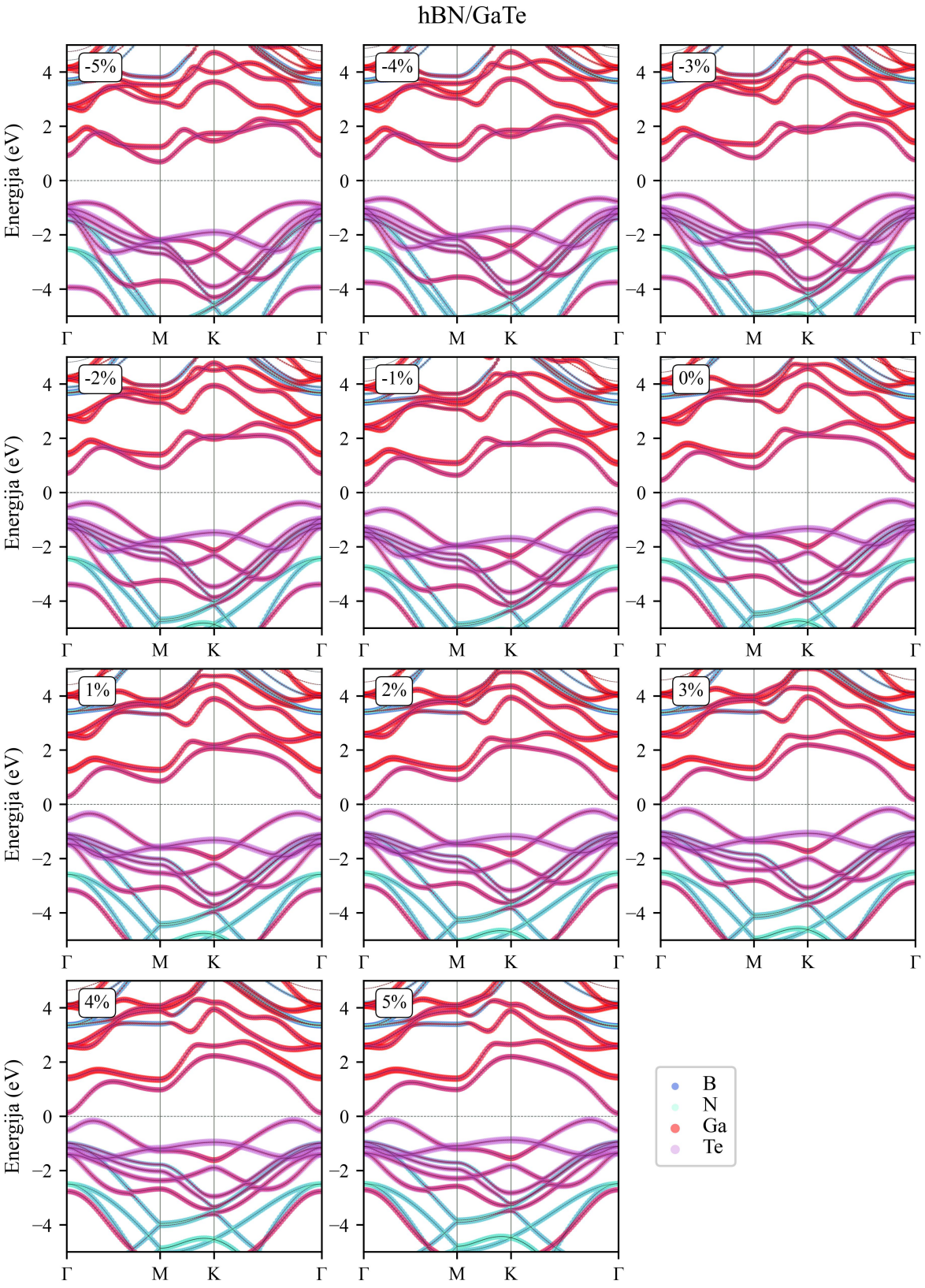


Slika 4.14: Zonska struktura hBN/GaTe HS projektovana po atomskim stanjima, za različite vrednosti naprezanja, od -5% do 5%.

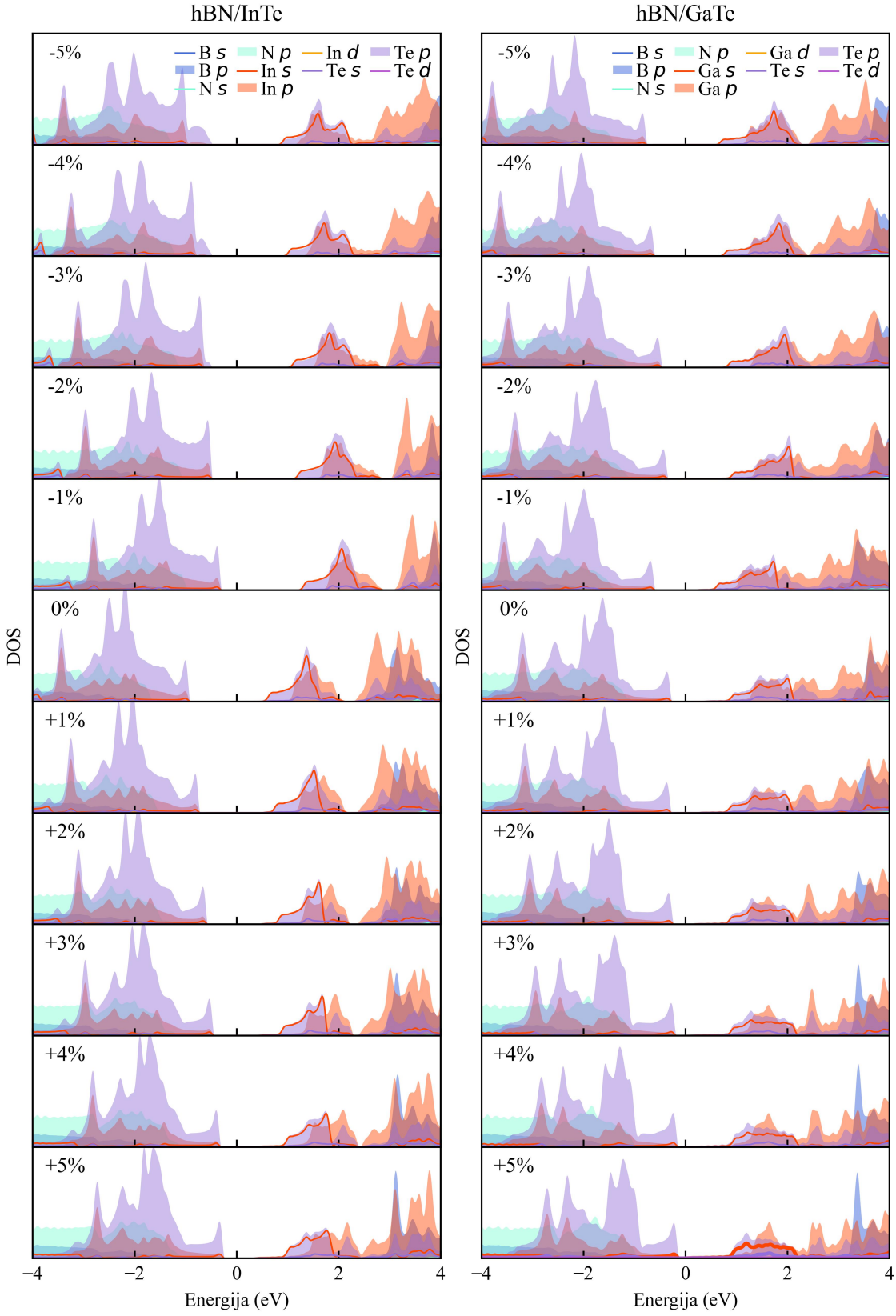


Slika 4.15: Projektovana gustina stanja hBN/InTe i hBN/GaTe HS za različite vrednosti naprezanja.

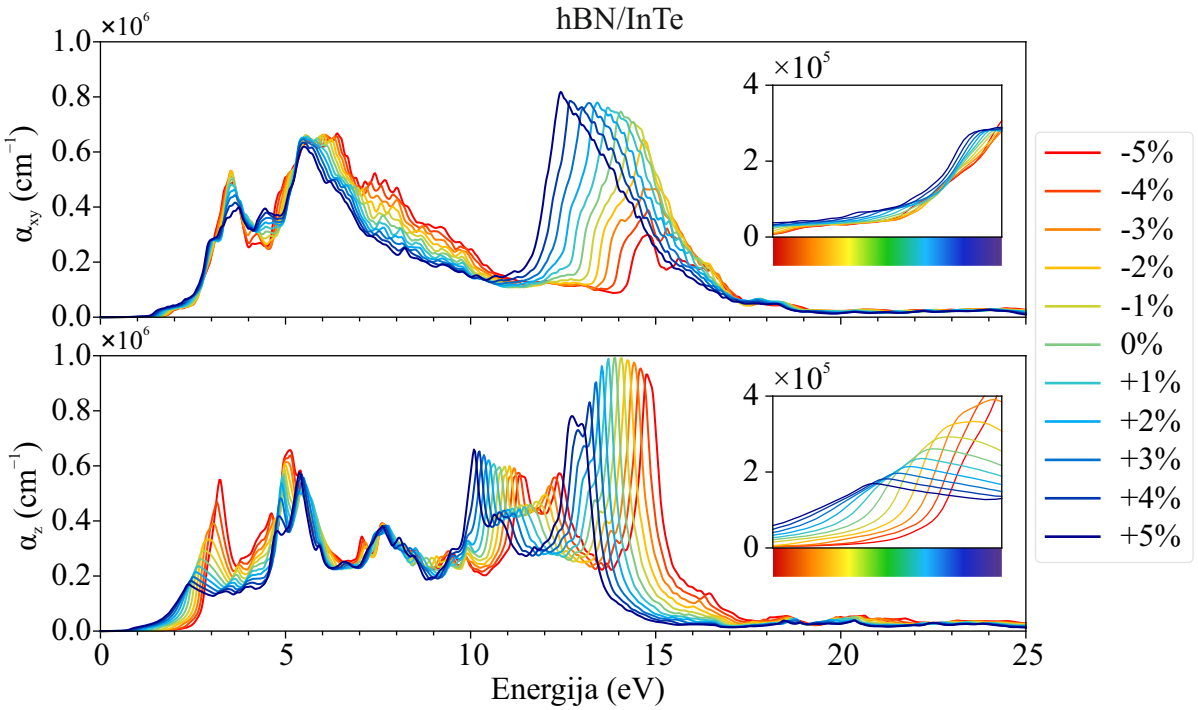


Slika 4.16: Apsorpcija hBN/InTe HS za vrednosti primenjenog naprezanja od -5% do +5%, označene različitim bojama, od crvene (za -5%) ka plavoj (+5%). Inset u grafiku prikazuje uvećanu oblast vidljivog dela spektra.

njihovog pomeranja ka višim energijama, dok sa povećanjem istezanja dolazi do pomeranja pikova ka nižim energijama. Ovo je karakteristika uočena u obe HS, koja je u velikoj meri očekivana, uzevši u obzir trend promene energijskog procepa prilikom naprezanja. Vidljiva promena, uočena kod hBN/InTe, ogleda se u formiranju izraženog pika na oko 3 eV, značajno izraženija u $z$ polarizaciji. Ovaj pik se može pripisati značajnom smanjenju energije dna provodne zone u M dolini, a gotovo se ne može uočiti u hBN/GaTe HS u istim uslovima naprezanja. Na graficima je vidljivo da intenzitet apsorpcije značajno raste posebno u područjima sa izraženim pikovima - oni postaju izraženiji i oštriji. Ovo ukazuje na značaj inženjeringa naprezanja za fino podešavanje optičkih osobina HS, što je posebno značajno u različitim primenama poput fotodetektora i drugih optoelektronskih uređaja. Takođe, razlike u promenama apsorpcije kod $\alpha_{xy}$ i $\alpha_{xy}$ komponenata prilikom naprezanja, ukazuju na anizotropiju materijala u apsorpciji svetlosti, što može biti indikacija različitih mehanizama interakcije svetlosti sa elektronskim stanjima u različitim kristalnim orijentacijama.

Na isti način kao i kod relaksiranih HS, izračunate su reflektanse, za vrednosti naprezanja u analiziranom opsegu. One su prikazane na slikama 4.18 i 4.19. Refleksija i dalje ne prelazi oko 0.3 u bilo kom delu spektra i pri bilo kojoj vrednosti naprezanja, a uglavnom se kreće ispod 0.2, ukazujući na dobru efikasnost u apsorpciji svetlosti. Ono što se može primetiti je trend promene reflektivnosti, koji je takav da prati promene u apsorpciji, pa se sa povećanjem intenziteta apsorpcije, uočava i blagi porast reflektanse. Ipak, ove promene nisu kvantitativno značajne da na bilo koji način umanjuju kvalitet

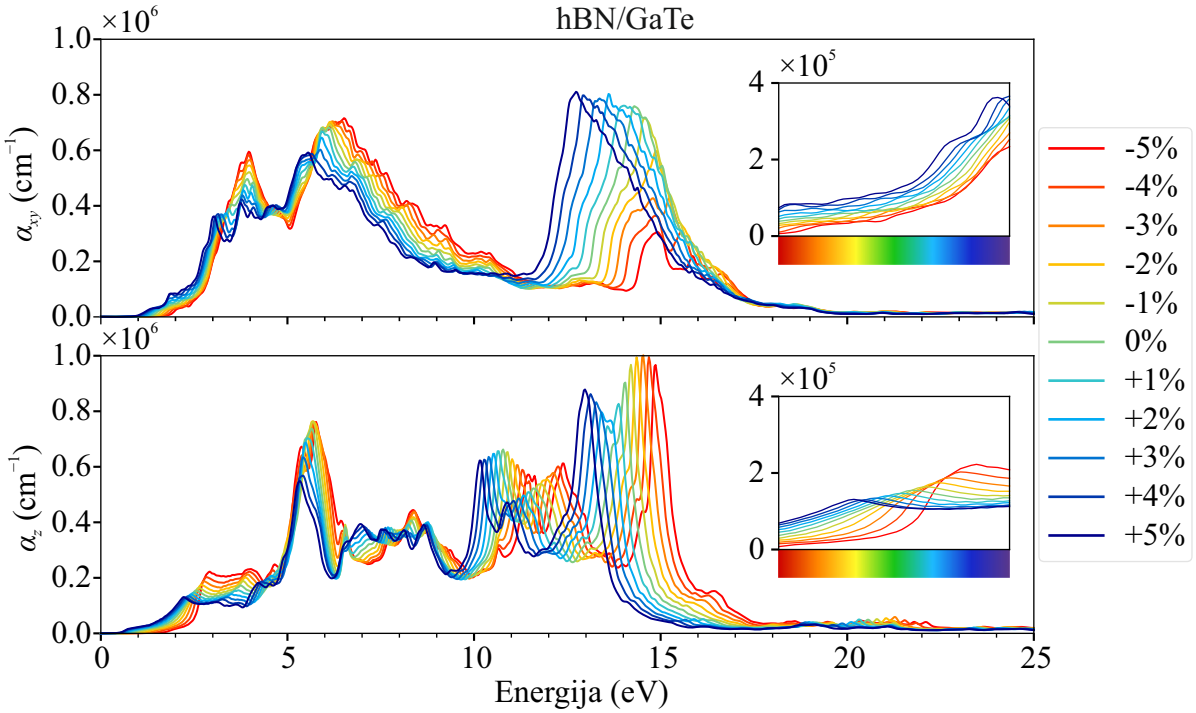


Slika 4.17: Apsorpcija hBN/GaTe HS za vrednosti primenjenog naprezanja od -5% do +5%, označene različitim bojama, od crvene (za -5%) ka plavoj (+5%). Inset u grafiku prikazuje uvećanu oblast vidljivog dela spektra.

struktura po pitanju željenih optičkih karakteristika.

Konačno, može se zaključiti da primena naprezanja u ovim strukturama pruža neverovatnu mogućnost precizne manipulacije ne samo elektronskim već i optičkim svojstvima, što je posebno značajno za primene u fotodetektorima, laserskim rezonatorima ili optičkim filterima.

## 4.4 Uticaj naprezanja na hBN/InSe heterostrukture

hBN/InSe HS su prethodno ispitivane u nekoliko teorijskih studija [34, 206]. Prethodna studija pokazuje da je i kod hBN/InSe HS, energijski najpovoljniji H-top način slaganja [34], kod koga su In atomi pozicionirani ispod centara hBN-ovih šestougaonika, pa se u ovom istraživanju polazi od H-top strukture. Pre manipulacije naprezanjem, HS je prvobitno kompletno relaksirana, optimizujući parametre rešetke, kao i pozicije atoma unutar jedinične ćelije. U relaksiranoj konfiguraciji, konstanta rešetke hBN/InSe HS iznosi $a = 4.29$ Å, što dovodi do 1% naprezanja na sloj hBN-a i 6% naprezanja na sloj InSe. Dobijene vrednosti su slične kao i u slučaju hBN/GaTe struktura, gde se takođe uočava značajna razlika u napregnutosti slojeva-komponenata, a potiče od različitih karakteristika elastičnosti materijala. Konkretno, konstante elastičnosti i moduli hBN-a su približno

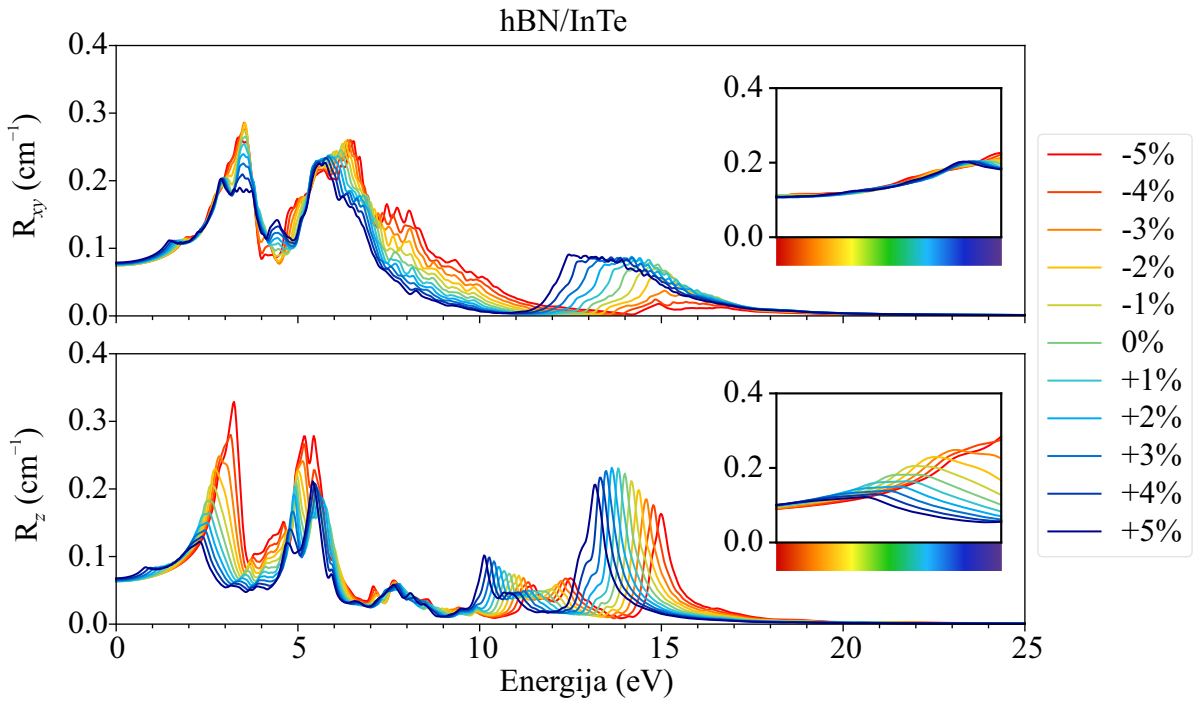


Slika 4.18: Reflektansa hBN/InTe HS za vrednosti primenjenog naprezanja od -5% do +5%, označene različitim bojama, od crvene (za -5%) ka plavoj (+5%). Inset u grafiku prikazuje uvećanu oblast vidljivog dela spektra.

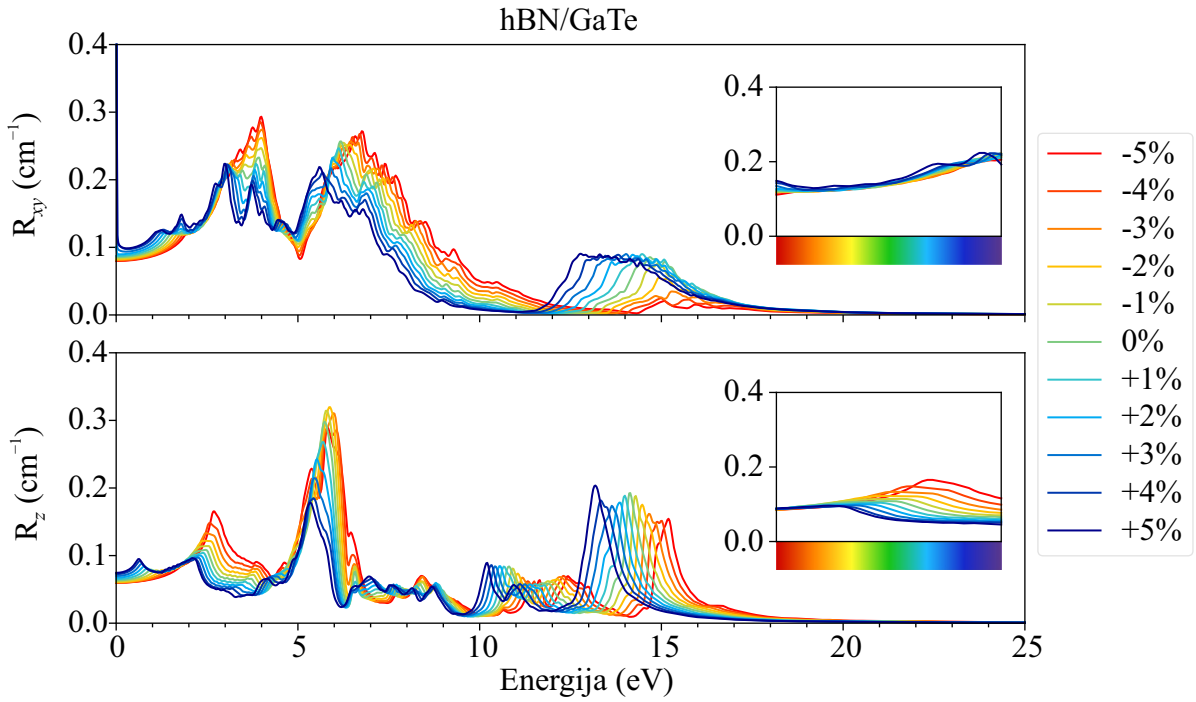


Slika 4.19: Reflektansa hBN/GaTe HS za vrednosti primenjenog naprezanja od -5% do +5%, označene različitim bojama, od crvene (za -5%) ka plavoj (+5%). Inset u grafiku prikazuje uvećanu oblast vidljivog dela spektra.

tri puta veći nego u InSe, pa kako se InSe sloj deformiše lakše, on je podložan većem prilagođavanju u formiranoj HS. Rastojanje između hBN i InSe sloja iznosi 3.29 Å.

Kao i kod hBN/InTe i hBN/GaTe, naprezanje koje je primenjivano je uniformno biaksijalno, uzevši u obzir vrednosti od -6% (kompresija) do +6% (istezanje).

Sa primenjenim naprezanjem, menja se i geometrijska konfiguracija atoma u rešetki. Rastojanje između slojeva se smanjuje do 3.26 Å za -6% naprezanja, a neznatno poraste do 3.30 Å za +6%. Menjaju se i dužine In-Se i In-In veza, koje se skraćuju prilikom kompresije, a izdužuju prilikom istezanja, kao i ugao In-Se-In, koji se smanjuje prilikom kompresije, odnosno širi prilikom istezanja. Očekuje se da ovakve varijacije u geometriji rešetke i dužinama veza, između ostalog dovode do promene u elektronskoj strukturi ovih materijala, pružajući detaljnija saznanja o efektu naprezanja.

### 4.4.1 Elektronska struktura

U relaksiranom stanju, izračunati energijski procep hBN/InSe HS iznosi $E_g = 0.56$ eV i on je vidno manji nego u hBN/InTe i hBN/GaTe HS, što može biti prednost u optoelektronskim primenama u kojima je važan IR/vidljivi deo spektra. U cilju provere rezultata, izračunat je i energijski procep jednoslojnog InSe, za koji je dobijena vrednost od 1.49 eV, što se dobro slaže sa prethodno dobijenim rezultatima koji koriste PBE i njemu slične funkcionale [40, 191, 207]. S obzirom na to da se primenom standardnih GGA funkcionala energijski procep u poluprovodnicima i izolatorima potcenjuje, procenjena greška je u rangu od 0.6 eV do 0.9 eV. Naime, prema postojećoj literaturi [34], energijski procepi dobijeni korišćenjem hibridnih funkcionala iznose 2.37 eV i 1.16 eV za jednoslojni InSe i hBN/InSe HS, respektivno.

Projektovana zonska struktura hBN/InSe za različite vrednosti naprezanja, prikazana je na slici 4.20. Slično kao i kod prethodno razmatranih HS, valentnu zonu čine dominantno stanja In i Se atoma, a energijski procep se širi sa povećanjem kompresivnog naprezanja i smanjuje uz istezanje. Energija vrha valentne zone u Γ tački smeštena između Γ i M tačke blago raste prilikom istezanja, dok istovremeno energija dna provodne zone u Γ tački opada u energiji, pri čemu za 6% naprezanja, energijski procep gotovo iščezava. Kod kompresivnog naprezanja, energija dna provodne zone kontinualno raste, dok se u valentnoj zoni uočava efekat koji prethodno nije primećen u hBN/InTe i hBN/GaTe HS. Naime, vrh valentne zone koji primarno čine stanja Se atoma blago opada, ali se istovremeno stanja u okolini Γ tačke koja su u nenapregnutoj strukturi uočena na oko -0.8 eV, i koja primarno potiču od N atoma hBN-a, izdvajaju naviše. Pri naprezanju od -4%, ova stanja se po energiji izjednačavaju sa stanjima Se atoma, odakle preuzimaju ulogu vrha valentne zone, pa u ovom slučaju vrh provodne zone više ne potiče od InSe sloja, već hBN-a.

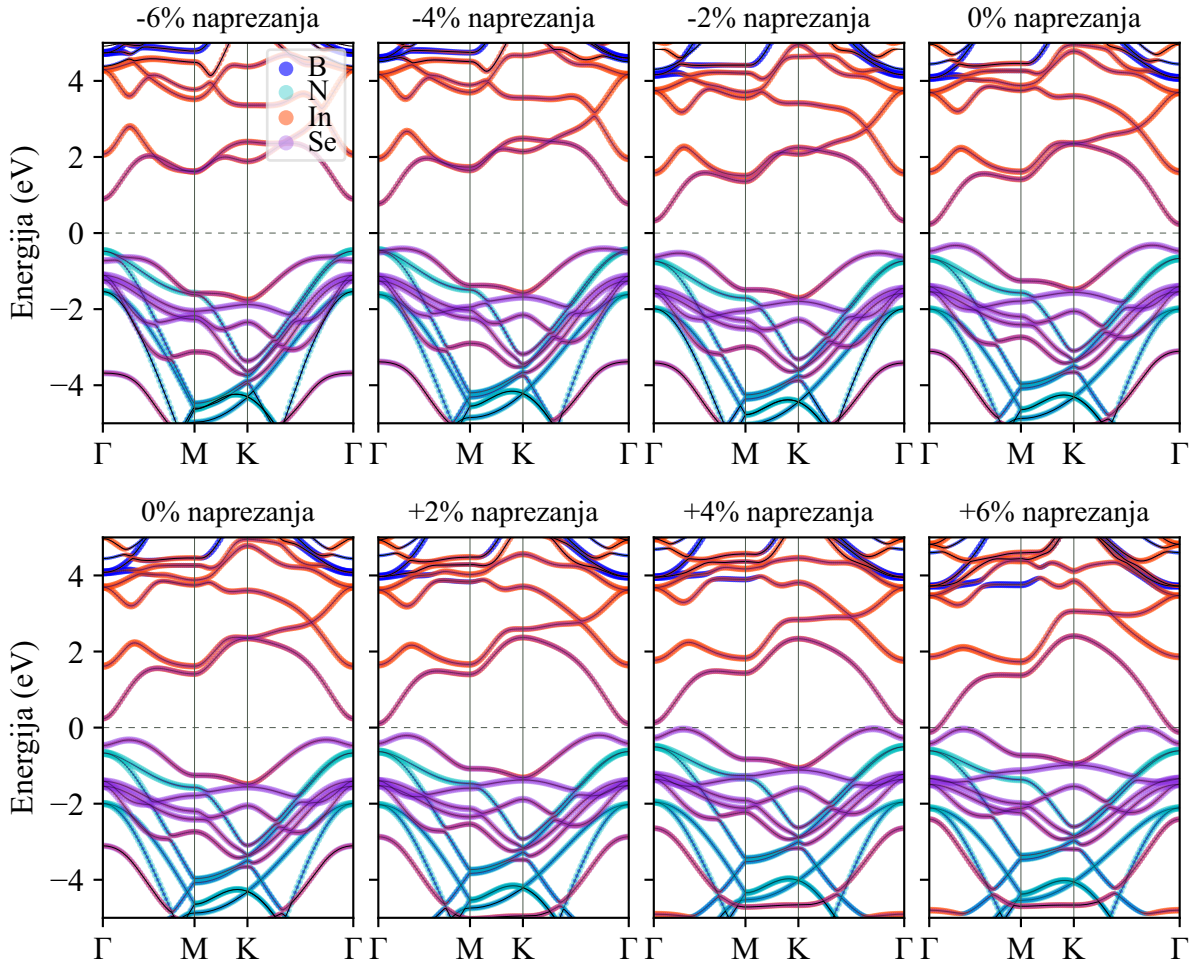


Slika 4.20: Zonska struktura hBN/InSe HS za vrednosti primenjenog naprezanja od -6% do +6%, projektovana po atomskim stanjima.

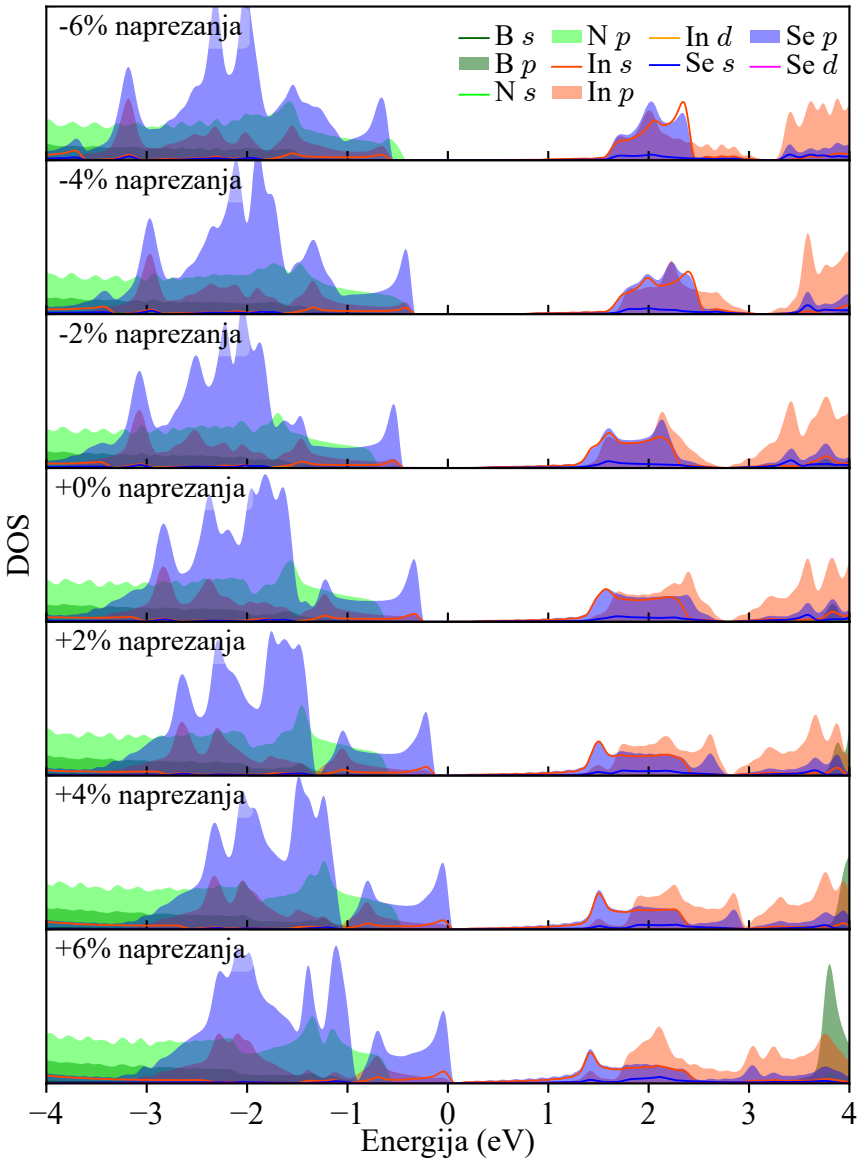


Slika 4.21: Projektovana gustina stanja razdvojena po različitim stanjima atoma u hBN/InSe, za vrednosti primenjenog naprezanja od -6% do +6%, označenih kao u legendi.

Bolji uvid u kompoziciju stanja pruža projektovana gustina stanja, prikazana na slici 4.21. Uočava se da u opsegu od -4% do +6% naprezanja, u okolini Fermi energije dominantno učestvuju stanja In i Se atoma, a prvenstveno Se $p$ stanja ispod Fermi nivoa. Za naprezanja od -4% do -6%, vrh valentne zone uglavnom ima karakter $p$ stanja N atoma.

Zavisnost promene energijskog procepa od jačine naprezanja, predstavljena je na slici 4.22, za sve tri heterostrukture: hBN/InTe, hBN/InSe i hBN/GaTe. Može se uočiti da je trend promene $E_g$ vrlo sličan kao kod hBN/GaTe, tj da se menja skoro linearno u celom opsegu naprezanja, za razliku od hBN/InTe kod koga se ispod -2% naprezanja procep ponovo smanjuje. Takođe se može primetiti da od pomenute tri HS, hBN/InSe ima najmanji energijski procep pri bilo kom intenzitetu naprezanja, što mu može omogućiti prednost sa stanovišta optoelektronskih aplikacija.

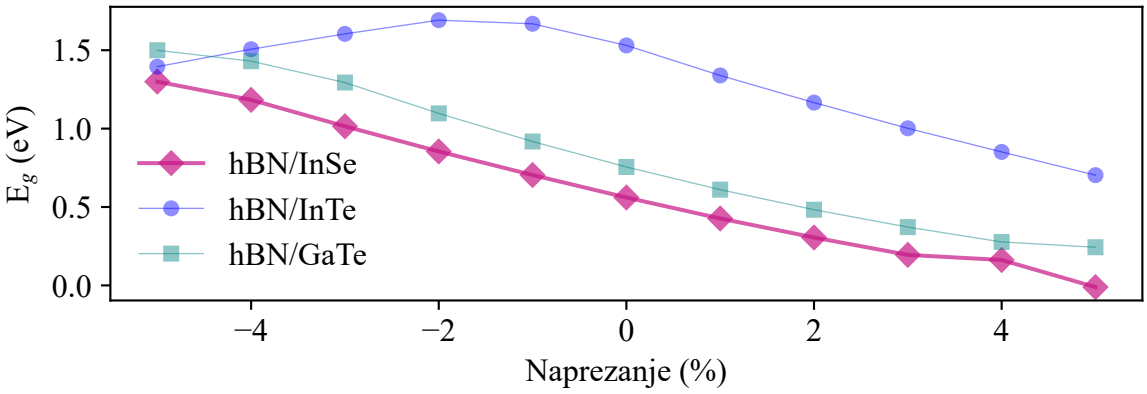


Slika 4.22: Zavisnost energijskog procepa od intenziteta naprezanja za hBN/InSe (ljubičasta linija sa rombovima), hBN/InTe (plava linija sa kružnim markerima) i hBN/GaTe (zelena linija sa kvadratićima).

### 4.4.2 Optička svojstva

Prethodna studija hBN/InSe [34] ističe izvanredne optičke karakteristike ovog materijala, konkretno visoku apsorpciju u širokom delu spektra, slično kao i kod hBN/InTe i hBN/GaTe HS. Fokus ovog istraživanja je na modifikaciji ovih osobina pomoću primenjenog naprezanja, koje bi dovelo do dodatnog poboljšanja apsorpcione funkcije, kao i mogućnosti preciznije kontrole njenih karakteristika. Na način opisan u poglavlju 2.8.2.2, izračunata je apsorpcija hBN/InSe HS, prikazana na slici 4.23, za obe polarizacije. Rezultati su slični kao i kod prethodne dve HS. Potvrđena je izvanredna apsorpcija u veoma širokom delu spektra za strukturu bez primene naprezanja, u kojoj pikovi apsorpcije prelaze $8 \times 10^5$ cm$^{-1}$, a apsorpcija postoji već od IR opsega. Za $xy$ polarizaciju, apsorpcija je posebno izražena u opsegu od 4 eV do 9 eV sa vrednostima oko $4 \times 10^5$ cm$^{-1}$.

Primenom naprezanja, može se uočiti nekoliko značajnih promena i poboljšanja u apsorpciji. U opsegu od 6 do 11 eV, apsorpciona funkcija se blago pomera ka višim energijama prilikom primenjenog kompresivnog naprezanja, ali se istovremeno njen intenzitet pojačava sa većim naprezanjima. Nasuprot tome, kod istog naprezanja, u opsezima od 5 eV do 6 eV kao i 12 do 16 eV, apsorpcija se smanjuje. Prilikom istezanja, u ovim opsezima situacija je obrnuta i pik apsorpcije na 14 eV se širi i pomera ka 12 eV, dok se apsorpcija u opsegu od 6 eV do 11 eV smanjuje. Kod $z$ polarizacije situacija je slična. Apsorpcija se prilikom kompresivnog naprezanja pojačava u oblastima od 2 eV do 5 eV, kao i u pikovima na oko 5.5 eV do 6.5 eV, dok se oblast od 10 eV do 17 eV pomera ka višim energijama. Apsorpcija u vidljivom delu spektra pojačana je prilikom istezanja u $xy$ polarizaciji, dok se u $z$ polarizaciji, apsorpcija na energijama crvenih do žutih nijansi pojačava prilikom istezanja, a od zelene do ljubičaste raste prilikom kompresije.

Ove promene se mogu pripisati promeni energijskog procepa, kao i kompleksnom pon-

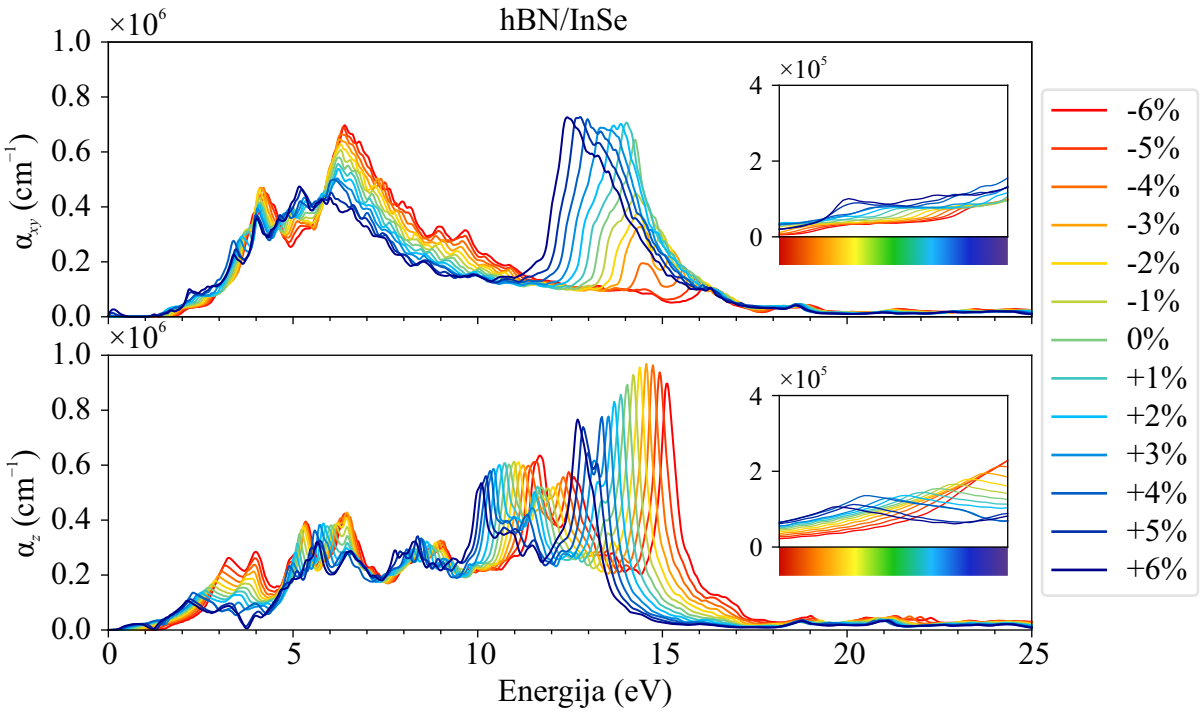


Slika 4.23: Apsorpciona funkcija hBN/InSe HS za vrednosti primenjenog naprezanja od -6% do +6%, označene različitim bojama, od crvene (za -6%) ka plavoj (+6%). Inset u grafiku prikazuje uvećanu oblast vidljivog dela spektra.

ašjanju oblika i pozicija određenih zona, a posebno dna provodne zone i vrha valentne zone.

Izračunata je i reflektansa hBN/InSe HS radi uvida u efikasnost apsorpcije svetlosti, prikazana na slici 4.24. Može se uočiti da maksimalna vrednost reflektanse ne prelazi 0.2, kao i da je u najvećem delu niža od 0.1, što pokazuje izuzetno dobru apsorpcionu moć ovih struktura. Reflektivnost se u najvećem delu opsega pojačava prilikom kompresije, a smanjuje prilikom istezanja. Interesantan je detalj u $xy$ polarizaciji, gde se kod većih intenziteta istezanja, reflektivnost intenzivno povećava na veoma niskim energijama (IR opseg), što se može pripisati iščezavanju energijskog procepa na +5% i +6% naprezanja.

## 4.5 hBN/GaS, hBN/GaSe i hBN/InS heterostrukture

U odeljku 4.1 opisan je način modelovanja hBN/GaS, hBN/GaSe i hBN/InS HS, a njihova kristalna struktura prikazana je na slici 4.25. Sve tri HS su relaksirane pre daljih proračuna i primene naprezanja, kako bi se dobile optimalne konstante rešetke i položaji atoma u jediničnoj ćeliji. Nakon relaksacije, dobijene su konstante rešetki od $a = 7.44$ Å za hBN/GaS, $a = 6.61$ Å za hBN/GaSe i $a = 6.59$ Å za hBN/InS. Zatim je primenjeno uniformno biaksijalno naprezanje od -6% do +6%, sa korakom od 2%, nakon čega su

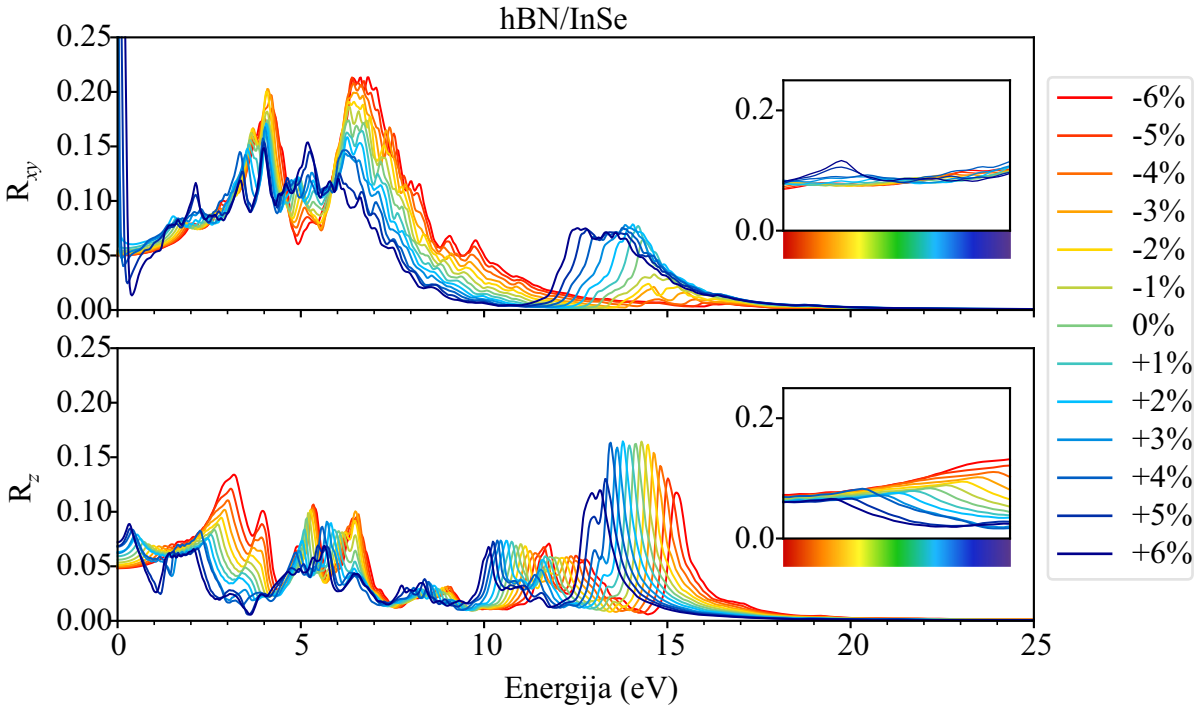


Slika 4.24: Reflektansa hBN/InSe HS za vrednosti primenjenog naprezanja od -6% do +6%, označene različitim bojama, od crvene (za -6%) ka plavoj (+6%). Inset u grafiku prikazuje uvećanu oblast vidljivog dela spektra.

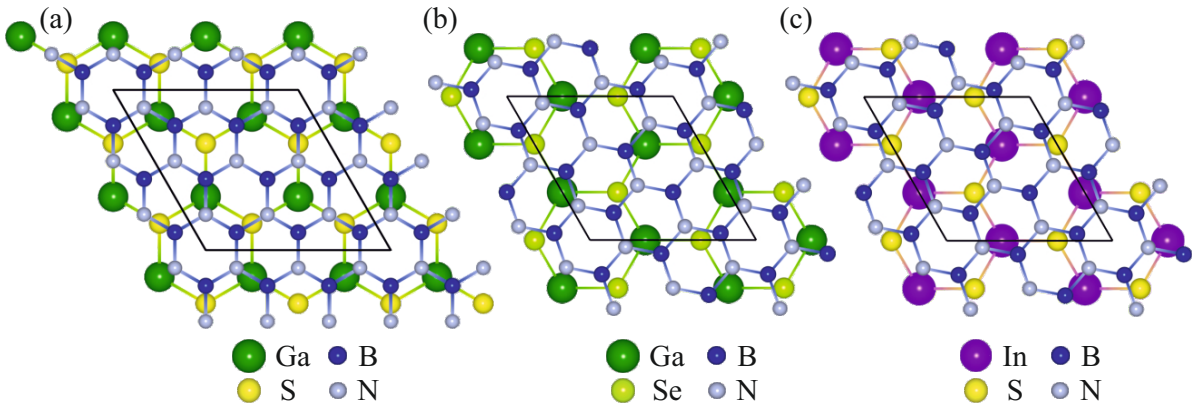


Slika 4.25: Prikaz hBN/GaS, hBN/GaSe i hBN/InS HS, normalno na ravan. Jedinična ćelija je označena crnom linijom.

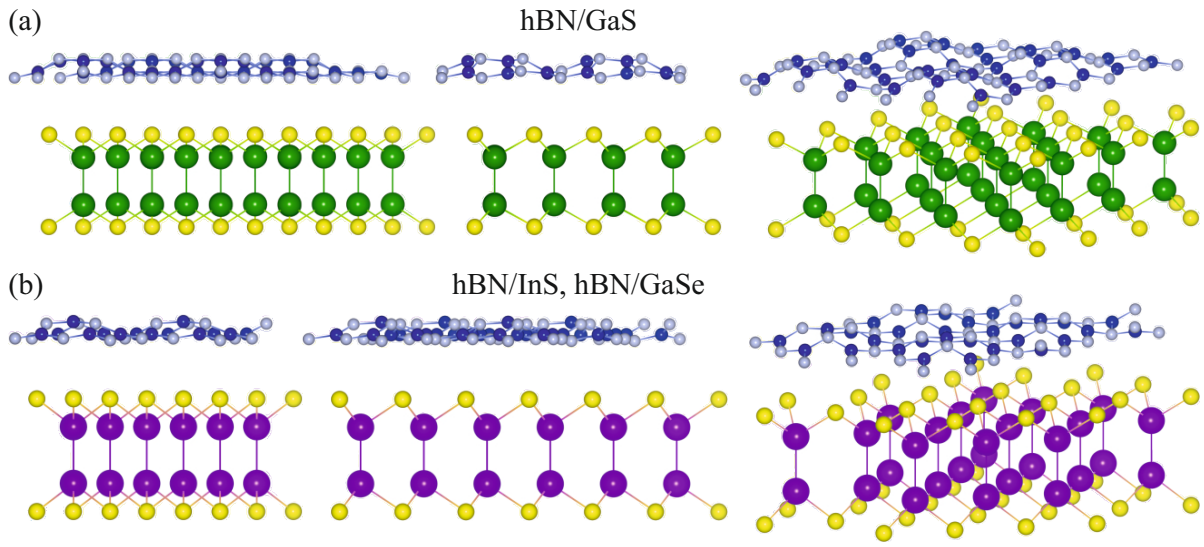


Slika 4.26: Gužvanje hBN-a prilikom kompresivnog naprezanja u (a) hBN/GaS i (b) hBN/GaSe i hBN/InS. Prikazan je slučaj sa 6% kompresivnog naprezanja.

strukture ponovo relaksirane optimizacijom pozicija atoma u ćeliji.

Ono što je uočeno kod ove tri HS prilikom naprezanja, značajno se razlikuje u pogledu geometrije u odnosu na hBN/InSe, hBN/InTe i hBN/GaTe HS. Nakon optimizacije napregnutih HS, pri kompresiji dolazi do "gužvanja" sloja hBN-a, što je prikazano na slici 4.26, gde se formiraju periodične kupaste formacije koje su izdignute. Kod hBN/GaS najviše su izdignuti šestougaonici hBN-a koji su smešteni tako da su N atomi skoro neposredno iznad S/Se atoma, dok su kod hBN/GaSe i hBN/InS na najvećoj visini B atomi smešteni iznad centara šestougaonika GaSe/InS slojeva, sa susedna tri N atoma koji su skoro neposredno iznad S/Se atoma. Efekti gužvanja su pri većim kompresivnim naprezanjima izuzetno izraženi, pa na -6% naprezanja razlika između najnižeg i najvišeg atoma u sloju hBN-a dostiže gotovo 1 Å, dok su pri -2% minimalni. Kod nenapregnutih HS ovaj efekat je gotovo zanemarljiv, iako se ni tada ne postiže idealna ravna konfiguracija hBN-a, kakva se primećuje kod hBN/In(Ga)Te i hBN/InSe.

Kod prethodno razmatranih HS kod kojih su svi atomi $M^{III}X^{VI}$ slojeva smešteni tačno u centrima šestougaonika hBN-a, nikakvo gužvanje nije uočeno. Ovo jasno ukazuje na značaj izbora materijala sa pogodnom samerljivošću konstanti rešetki, kako bi se omogućila konstrukcija minimalnih jediničnih ćelija heterostruktura. Gužvanje sloja doduše, ne znači da struktura nije stabilna - sve konfiguracije su uspešno relaksirane tako da su međuatomske sile manje od $10^{-6}$ RyÅ$^{-1}$, a postoje i mnogi drugi 2D materijali i heterostrukture koji imaju talasaste i naborane strukture. Međutim, kod ispitivanih struktura koje po prirodi jesu idealno ravne, u eksperimentalnoj realizaciji formiranje ovih korugacija bi potencijalno dovela do problema u fabrikaciji strukture, uključujući veću mogućnost pojave različitih defekata prilikom fabrikacije. Izračunata je energija adsorpcije za sve tri HS u relaksiranom, kao i napregnutom stanju. Sve vrednosti su negativne i kreću se u opsegu od -17 do -28 meV, ukazujući na to da je za sve vrednosti

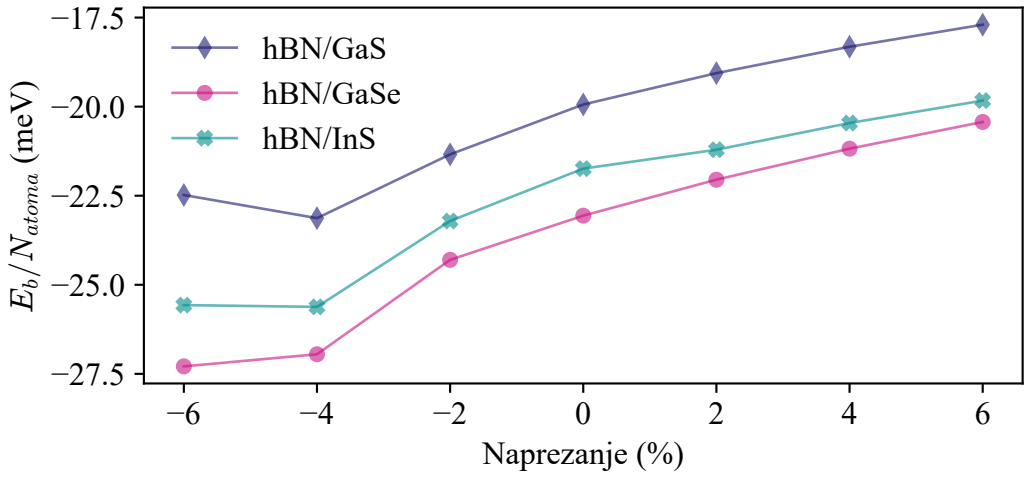


Slika 4.27: Energija vezivanja hBN/GaS, hBN/GaSe i hBN/InSe HS pod različitim intenzitetima naprezanja.

naprezanja energetski povoljnije da se HS formira, iako se jače vezivanje slojeva ostvaruje kod hBN/InTe i hBN/GaTe HS kod kojih se energija adsorpcije kreće u opsegu od -23 do -30 meV. Dinamička stabilnost koja uključuje na primer uticaje vibracija rešetke HS, ispituje se računanjem fononske disperzije za svaku konfiguraciju. Međutim kvalitetni proračuni fononskih disperzija za strukture od oko 30 atoma su računarski vrlo zahtevni i njihovo trajanje se meri u mesecima i često su praćeni problemima nedovoljne numeričke tačnosti. Uzevši sve to u obzir, proračuni fononskih disperzija iz praktičnih razloga nisu sprovedeni.

Formiranje samih heterostruktura u optimizovanom i nenapregnutom stanju, ne dovodi do značajnih promena u geometrijskoj konfiguraciji ovih struktura. Uočava se trend blagog smanjenja debljine $M^{III}X^{VI}$ slojeva, za oko oko 0.1 Å, kao i neznatno skraćivanje In−In odnosno Ga−Ga veza.

U narednim sekcijama biće analizirana elektronska i optička svojstva hBN/InS, hBN/GaS i hBN/GaSe HS i efekti koji proizilaze primenom naprezanja.

### 4.5.1 Elektronska struktura hBN/GaS, hBN/GaSe i hBN/InS

Zonska struktura za različite vrednosti naprezanja, prikazana je na slikama: 4.29 za hBN/GaSe, 4.28 za hBN/GaS i 4.30 za hBN/InS.

U odnosu na odgovarajuće $M^{III}X^{VI}$ slojeve, energijski procep u nenapregnutim HS se ne menja značajno: kod hBN/GaS sa 2.35 eV opada na 1.95 eV, kod hBN/InSe 1.66 na 1.72 eV, a kod hBN/GaSe praktično nepromenjen i iznosi 1.77 eV.

Razmotrićemo prvo hBN/GaSe HS, koja po zonskoj strukturi najviše podseća na

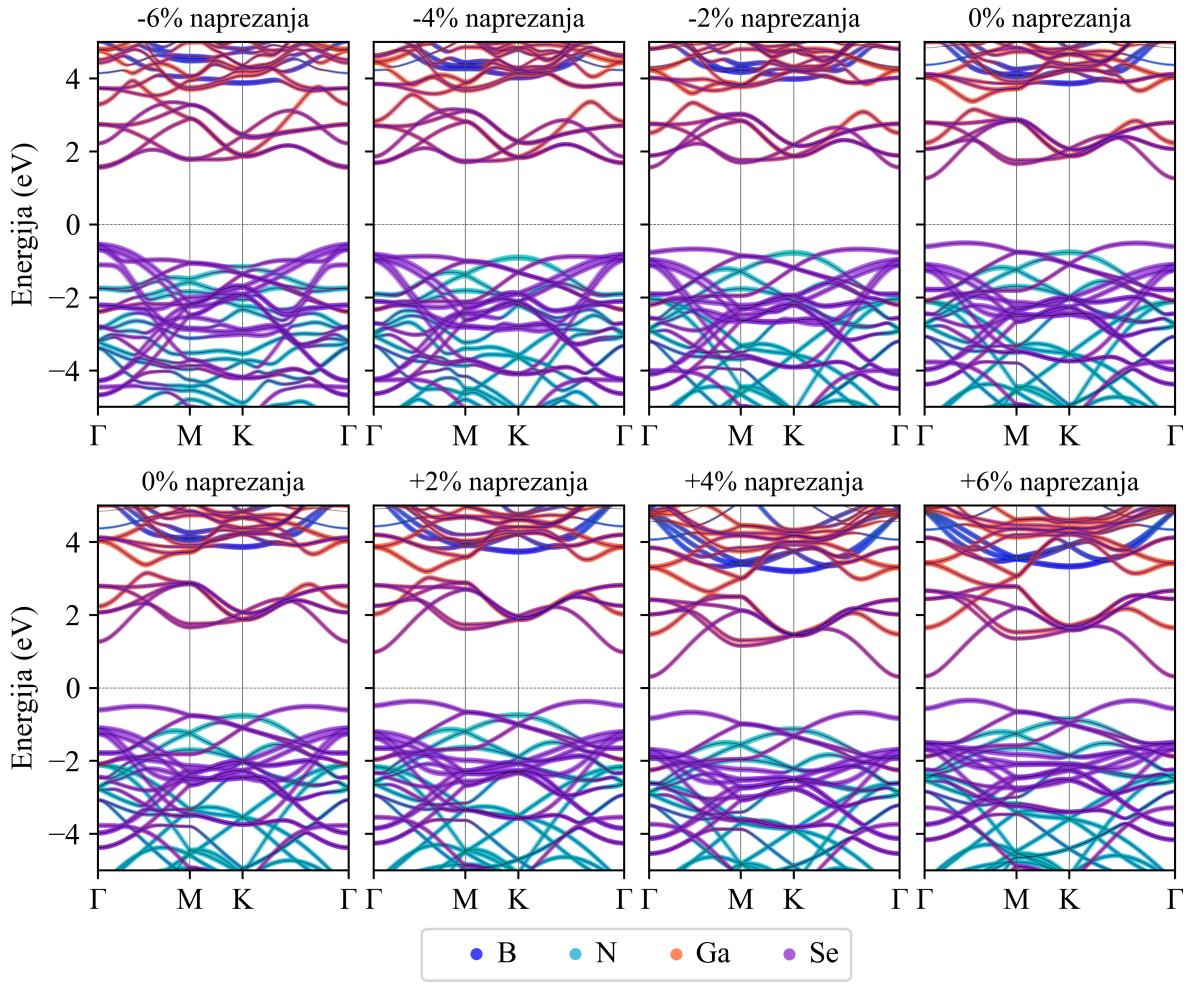


Slika 4.28: Zonska struktura hBN/GaSe HS, za različite vrednosti naprezanja od -6% do 6%.

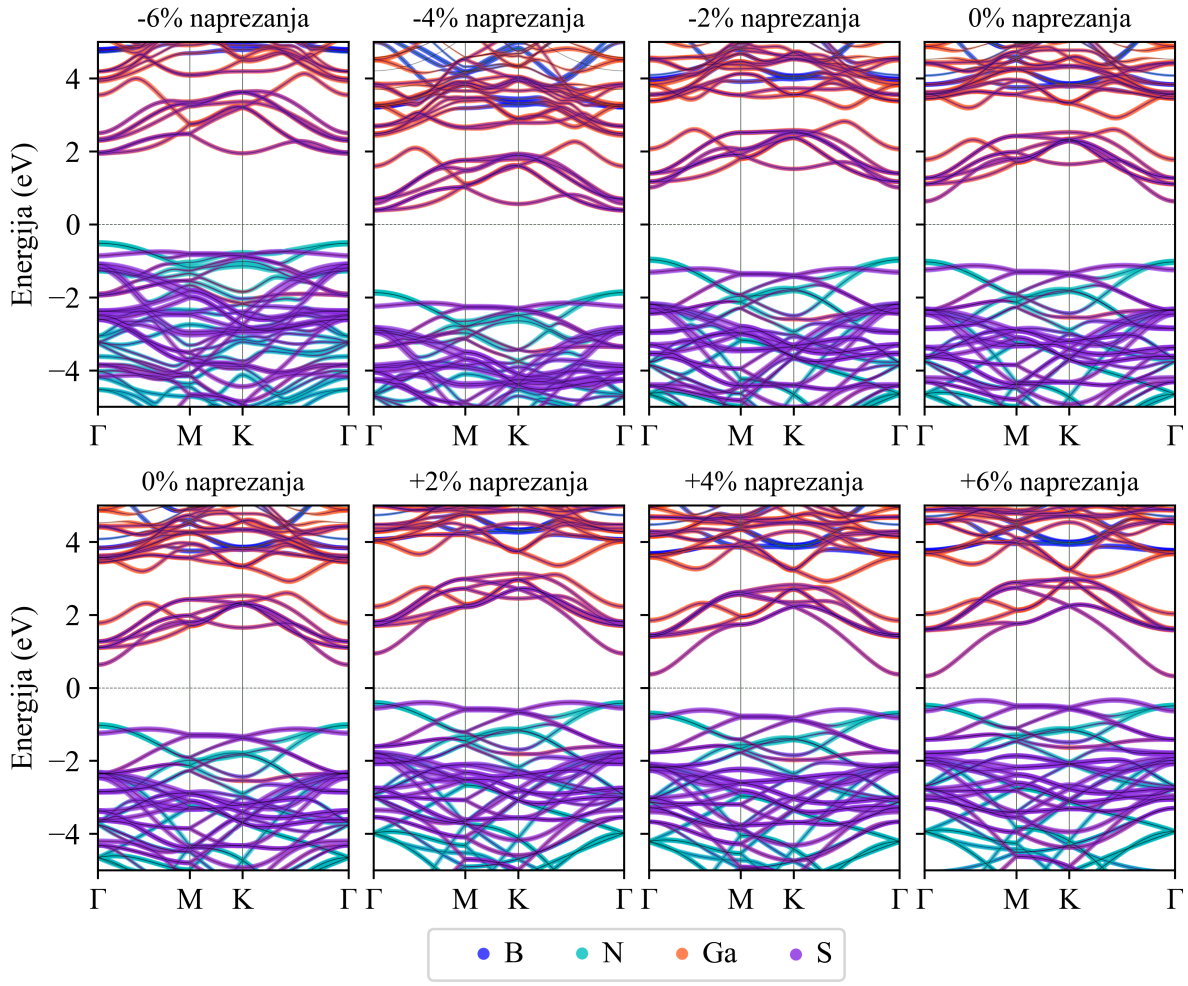


Slika 4.29: Zonska struktura hBN/GaS HS, za različite vrednosti naprezanja od -6% do 6%.

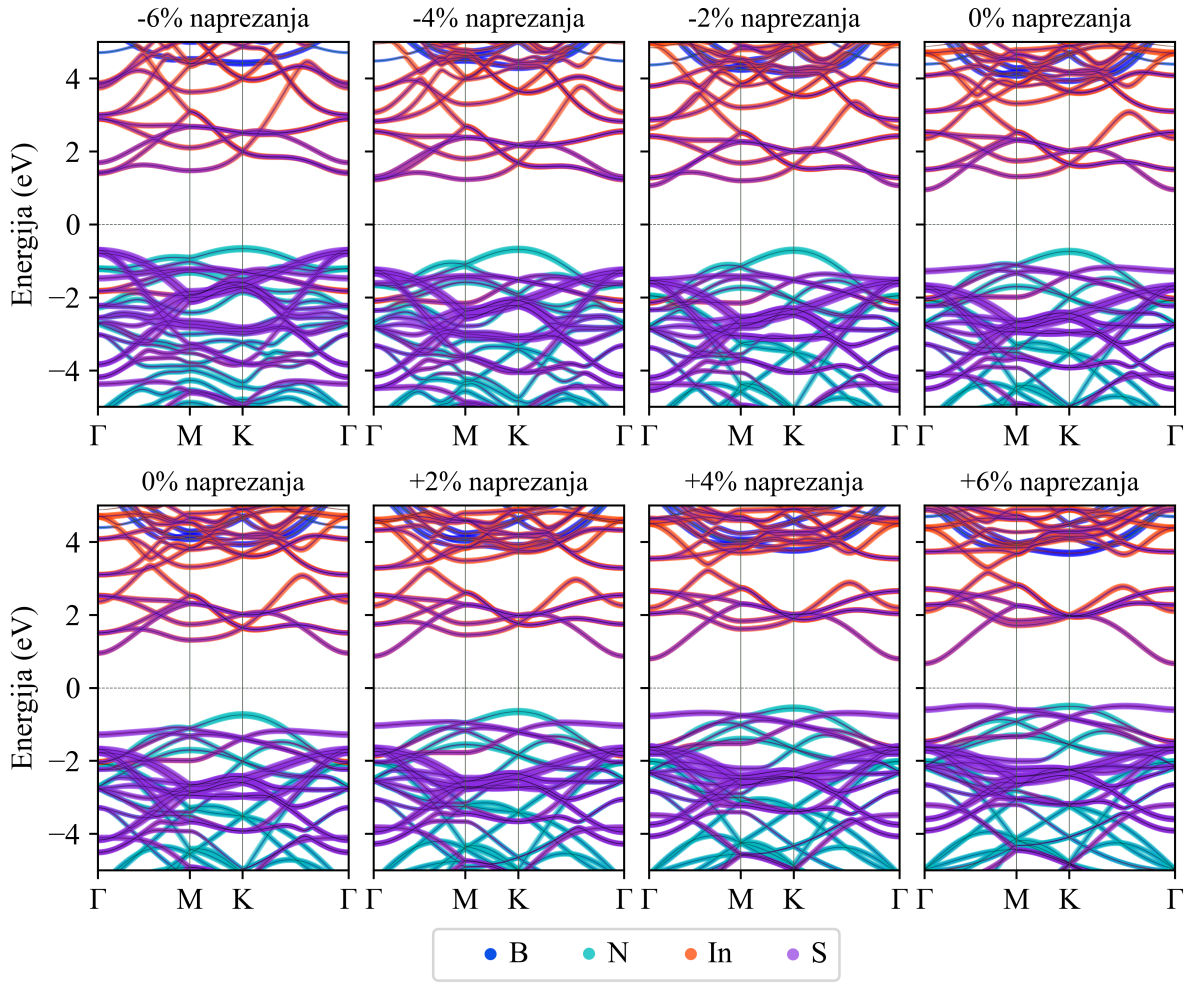


Slika 4.30: Zonska struktura hBN/InS HS, za različite vrednosti naprezanja od -6% do 6%.

zonsku strukturu hBN/InTe i hBN/GaTe ali sa većim energijskim procepom. Ono što je čini značajno drugačijom su stanja N atoma koja su prisutna na već -1 eV kod hBN/GaSe. Vrh valentne zone i dalje dominantno potiče od stanja atoma $M^{III}X^{VI}$ sloja, odnosno od $p$ stanja Se atoma, što se može videti i na projektovanoj gustini stanja prikazanoj na 4.31, i nalazi se između Γ i M tačke kao i između Γ i K tačke (energije su gotovo identične u ove dve tačke), osim za -4% i -6% naprezanja, gde vrh valentne zone prelazi u Γ tačku. Dno provodne zone je u Γ tački i čine ga stanja Ga i Se atoma, a pri naprezanjima od -4% i -6%, dolina u M tački opada sa energijom i njena vrednost je vrlo bliska energiji dna provodne zone. Energijski procep prilikom kompresivnog naprezanja raste do 2.11 eV za intenzitet naprezanja od -6%, a najmanji je za +6% naprezanja i iznosi samo 0.65 eV.

Razmotrimo zonsku strukturu hBN/GaS. Ono što je kod ove HS drugačije od svih prethodno razmatranih HS je međusobni položaj stanja koja potiču od hBN-a i $M^{III}X^{VI}$ sloja. Dok su stanja B i N atoma prethodno istraživanih HS bila udaljena od Fermijevog nivoa, u ovom slučaju, vrh valentne zone pozicioniran u Γ tački čine $p$ stanja N atoma, a energetski blisko su i $p$ stanja S atoma, što se može videti u gustini stanja prikazanoj na slici 4.33. Dno provodne zone jasno je pozicionirano u Γ tački a glavni doprinos imaju stanja Ga i S atoma. Sa primenom kompresivnog naprezanja, vrh valentne zone u Γ tački se dodatno razdvaja od stanja S atoma, a ona se približavaju grupi parova degenerisanih stanja S atoma, smeštenih na oko -2 eV, pa su vrh valentne zone i njena okolina dominantno poreklom od N atoma. Kompresijom se menja i oblik provodne zone i međusobni položaj zona iznad Fermijevog nivoa, pa na -6% dno provodne zone prelazi u K tačku. Energijski procep raste sa većim kompresivnim naprezanjem i za -6% ima vrednost od 2.45 eV. Istezanjem strukture primećuje se suprotan efekat, gde vrh valentne zone iz Γ tačke prelazi na pozicije između Γ i K tačke i između Γ i M tačke, gde su dominantno stanja poreklom od S atoma. Istovremeno se spušta dno provodne zone u Γ tački kome doprinose Ga i S stanja a energijski procep se smanjuje sve do 0.66 eV na +6% naprezanja.

Slično je i sa hBN/InS HS. Razlika u zonama ispod Fermijevog nivoa je i ovde značajna. Valentna zona u sloju InS ima izražene doline u M i K tačkama koje su znatno nižih energija u odnosu na stanja u Γ tački, dok su vrhovi valentne zone između Γ i M tačke i izmedju K i Γ tačke. Ova zona je u HS potisnuta stanjima N atoma koja formiraju vrh valentne zone u K tački, dok je oblik ove zone prilično ravan. Dno provodne zone i dalje se nalazi u Γ tački, ali je energija doline u M tački prilično bliska. Kada se primeni kompresivno naprezanje, zona formirana od N stanja se dodatno izdvaja, usled činjenice da energija najviše zone sa doprinosom $p$ stanja S atoma opada sa porastom kompresivnog naprezanja. Ova pojava je uočljivija posmatranjem projektovane gustine stanja za različite vrednosti naprezanja, prikazane na slici 4.33, gde se vidi da za naprezanja od -6% vrh valentne zone čine $p$ stanja N atoma u K tački, kao i $p$ stanja S atoma u Γ tački. Istovremeno opada energija doline u M tački provodne zone, pa su za naprezanja od -4% i -6% dna provodne zone u Γ i M tački, gotovo istih energija. Energijski procep hBN/InS

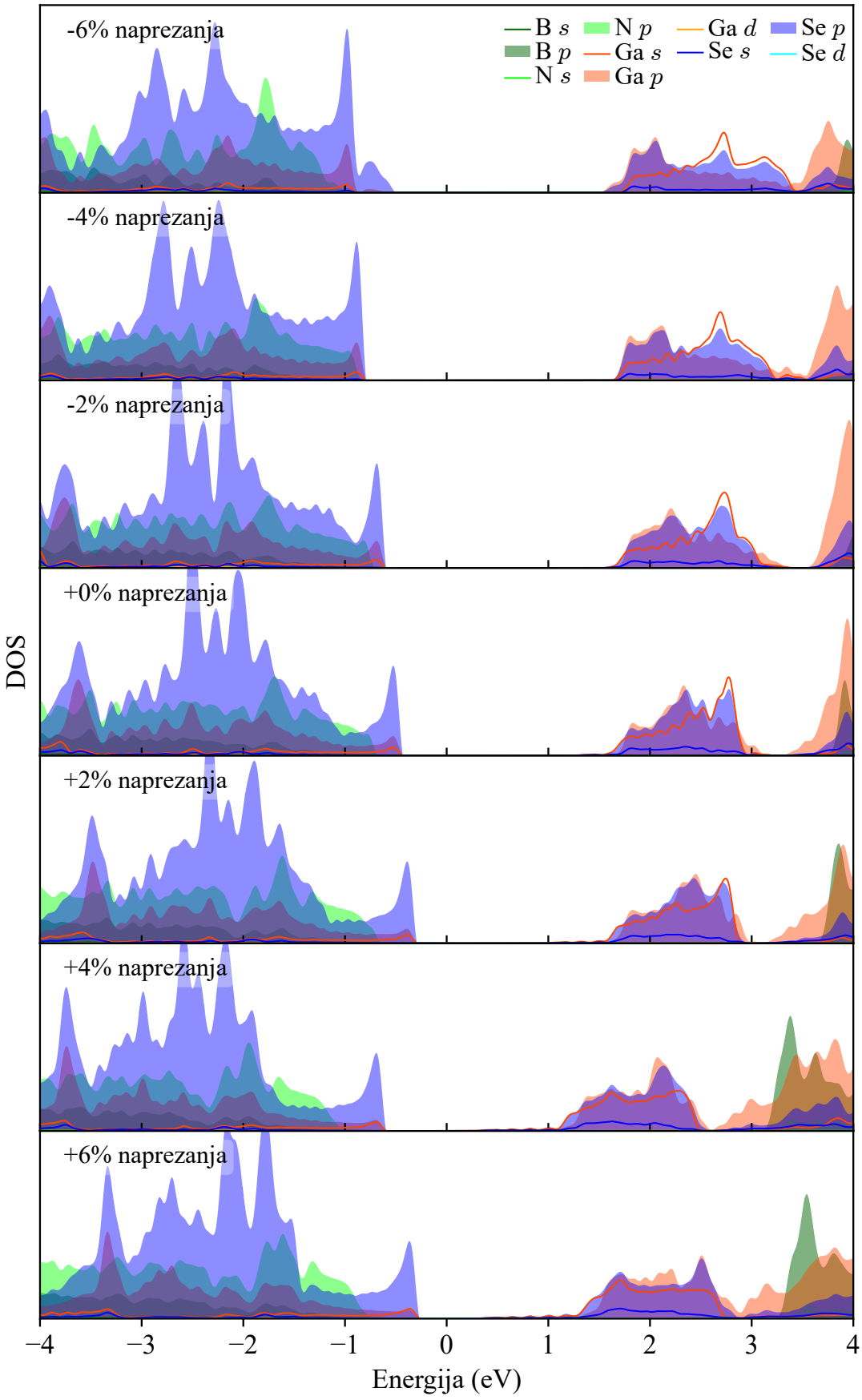


Slika 4.31: Projektovana gustina stanja hBN/GaSe HS za različite vrednosti naprezanja od -6% do +6%. Različita stanja atoma označena su linijama i površinama kao u legendi.

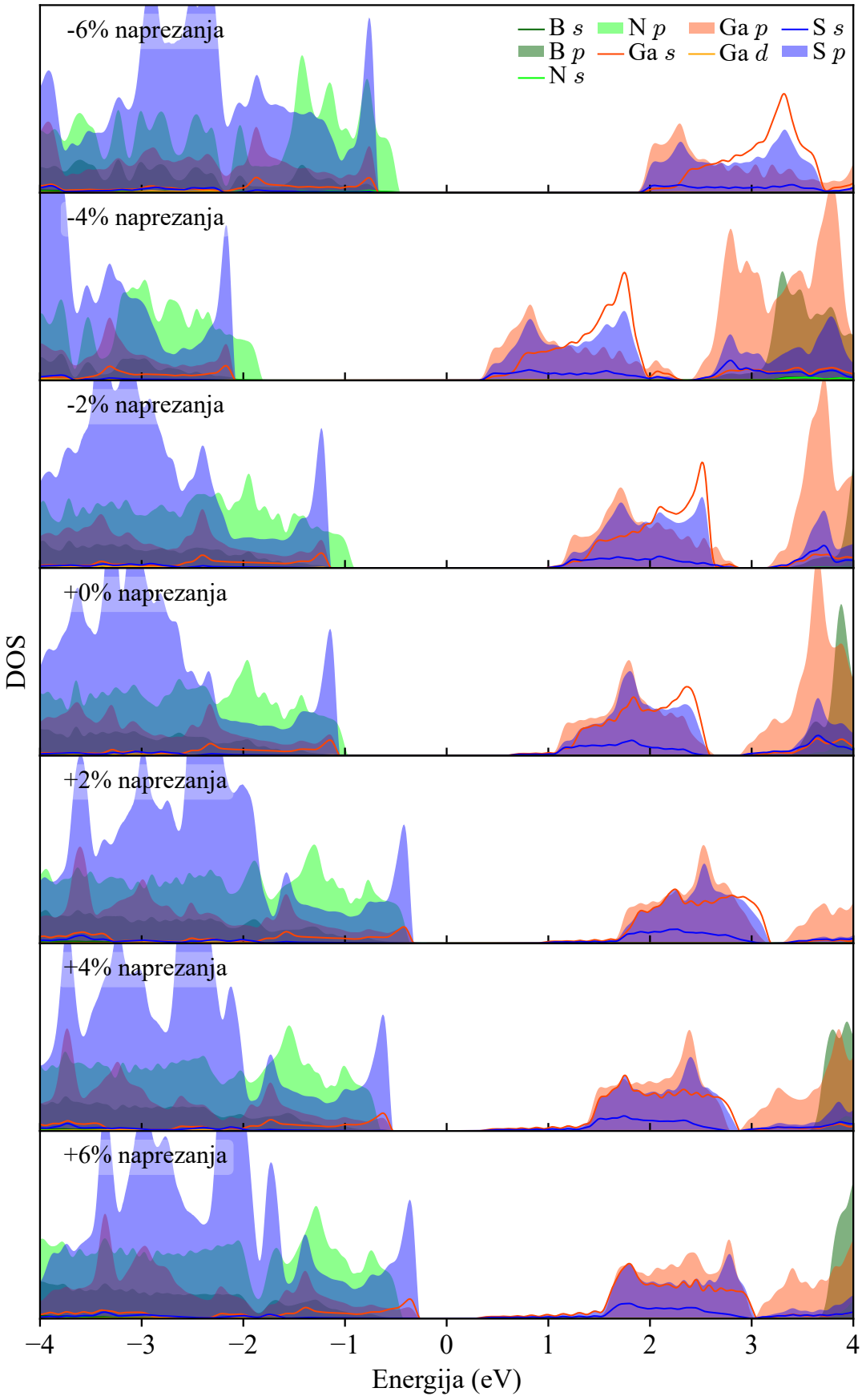


Slika 4.32: Projektovana gustina stanja hBN/GaS HS za različite vrednosti naprezanja od -6% do +6%. Različita stanja atoma označena su linijama i površinama kao u legendi..

za naprezanje od na -6% dostiže 2.01 eV. Kada se struktura isteže, stanja u vrhu valentne zone koja potiču od N atoma, ne menjaju značajno svoju energiju, ali se relativno ravna zona kojom dominiraju $p$ stanja S atoma energijski podiže, izjednačavajući energiju stanja između Γ i M i Γ i K tačaka, sa energijom vrha valentne zone koju formiraju stanja N atoma. Vrh provodne zone u Γ tački se prilikom istezanja dodatno spušta i izdvaja od ostalih stanja, a time se energijski procep smanjuje na 1.16 eV za naprezanje od +6%.

### 4.5.2 Optičke osobine

Značajnije promene u zonskoj strukturi sa primenom naprezanja donose i izmene u optičkim osobinama. Iako se zonska struktura značajnije menja po pitanju udela stanja u okolini Fermijevog nivoa, ni u jednoj od razmatrane tri HS ne dolazi do značajnih razlika u apsorpciji usled promene naprezanja. Apsorpciona funkcija hBN/GaSe HS je prikazana na slici 4.34. Visok koeficijent apsorpcije koji prelazi $10^5$ cm$^{-1}$ u najvećem delu spektra karakterističan je i za ovu HS, a pojedini pikovi dostižu i $8 \times 10^5$ cm$^{-1}$. Kompresijom hBN/GaS dolazi do pojačanja apsorpcije u opsegu od 6 do 15 eV za polarizaciju u ravni, kao i do novoformiranog pika na oko 4 eV za polarizaciju normalnu na ravan, koji raste na $8{\times}10^5$ cm$^{-1}$ za naprezanje od -6%, ali kompresija istovremeno degradira apsorpciju u vidljivom delu spektra. Istezanjem se apsorpcija u vidljivom opsegu pojačava, kao i u opsegu od 11 do 15 eV za polarizaciju u ravni. Izračunati koeficijent refleksije prikazan na slici 4.35 se kreće od 0.1 do 0.3, ukazujući na to da se najviše 30% upadne svetlosti reflektuje.

hBN/GaS i hBN/InS imaju vrlo sličnu apsorpcionu funkciju, prikazanu na slikama 4.36 i 4.37, respektivno. Iako se u zonskoj strukturi ovih HS vidi značajna promena ispod Fermijevog nivoa, gde pri kompresivnom naprezanju stanja N atoma dominiraju vrhom valentne zone, osim malo izraženijeg pika na oko 4 eV, ne postoje drastičnije promene u odnosu na prethodno razmatrane strukture. Ovo sugeriše na to da hBN-ov udeo u zonskoj strukturi u okolini Fermijevog nivoa, nema značaja za apsorpciju. Apsorpciona funkcija i dalje ima sličan oblik kao kod prethodno razmatranih struktura, a vrednosti koeficijenta apsorpcije imaju značajne vrednosti koje su oko $5 \times 10^5$ cm$^{-1}$ u UV opsegu, a nešto niže u vidljivom delu spektra. Pri kompresiji se apsorpciona funkcija pomera ka višim energijama, a pojedini pikovi su pojačani - u oblasti od $4{-}5$ eV, apsorpcija je pojačana za polarizaciju normalnu na ravan, kao i u oblasti od 7 do 13 eV, ali zato potpuno degradira u vidljivom delu spektra usled povećanja energijskog procepa. Istezanjem se apsorpcija u vidljivom opsegu pojačava, a drugih značajnih promena nema, osim blagog pomeranja apsorpcione funkcije ka nižim energijama. Iz izračunate refleksije, prikazane na slikama 4.38 i 4.39, uočava se da ni kod ovih HS vrednost koeficijenta refleksije gotovo da ne prelazi 0.2, osim pikova na $4{-}6$ eV za polarizaciju u ravni i na 13-16 eV za

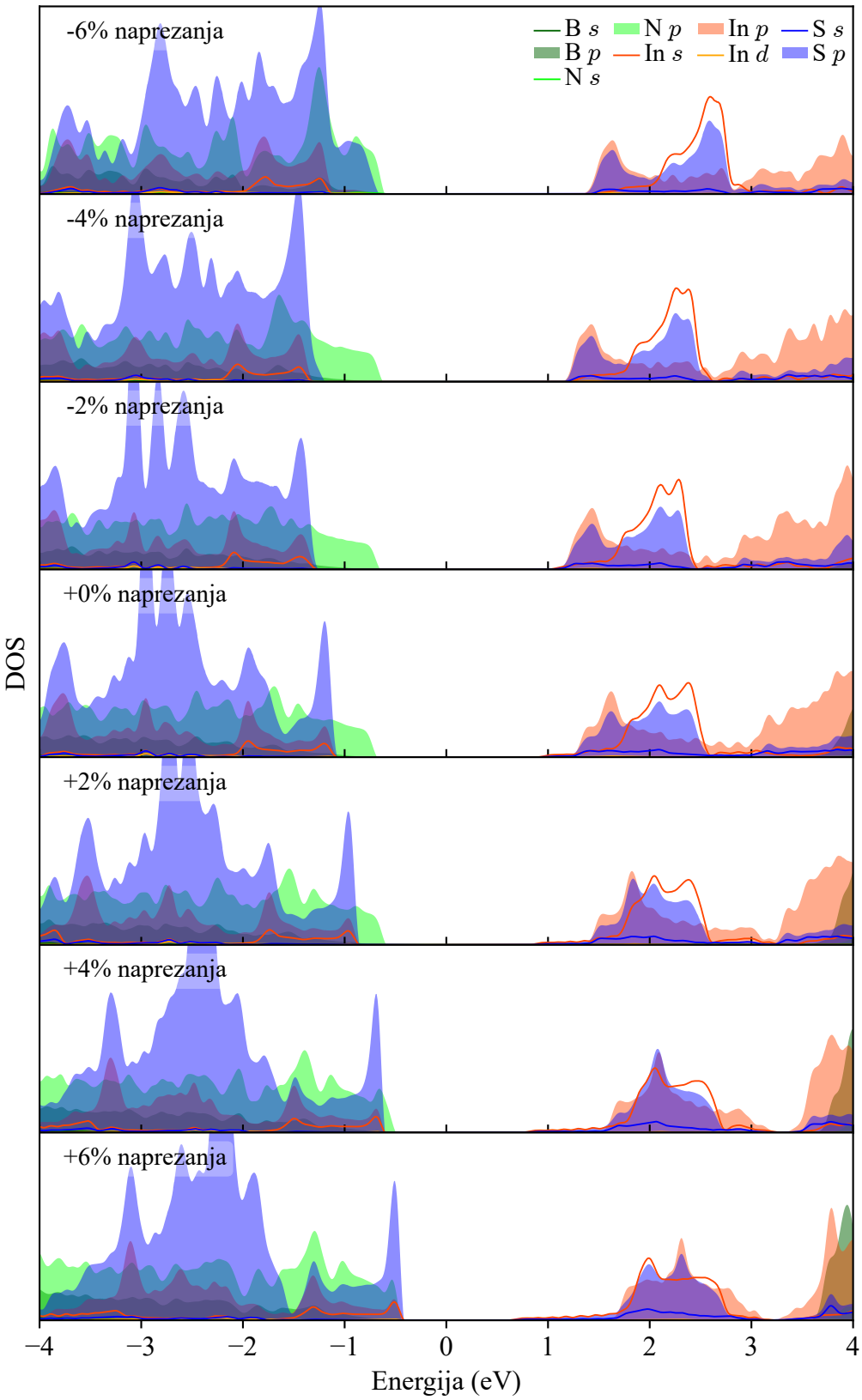


Slika 4.33: Projektovana gustina stanja hBN/InS HS za različite vrednosti naprezanja od -6% do +6%. Različita stanja atoma označena su linijama i površinama kao u legendi.

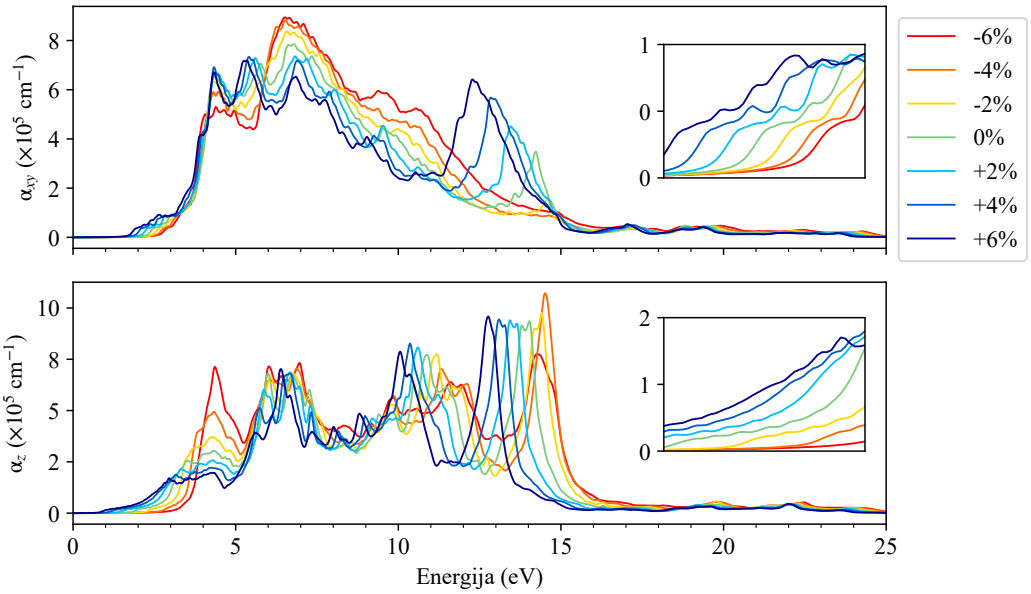


Slika 4.34: Apsorpciona funkcija hBN/GaSe HS za vrednosti primenjenog naprezanja od -6% do +6%, označene bojama kao u legendi. Inset u grafiku prikazuje uvećanu oblast vidljivog dela spektra.

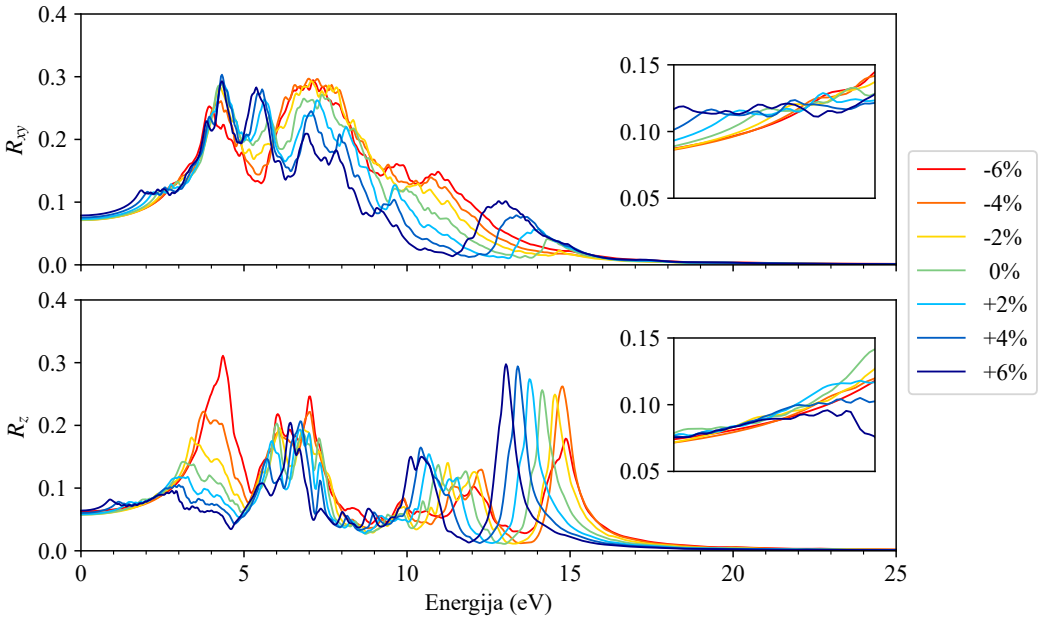


Slika 4.35: Koeficijent refleksije hBN/GaSe HS za vrednosti primenjenog naprezanja od -6% do +6%. Umetnuti grafik prikazuje uvećanu oblast vidljivog dela spektra.

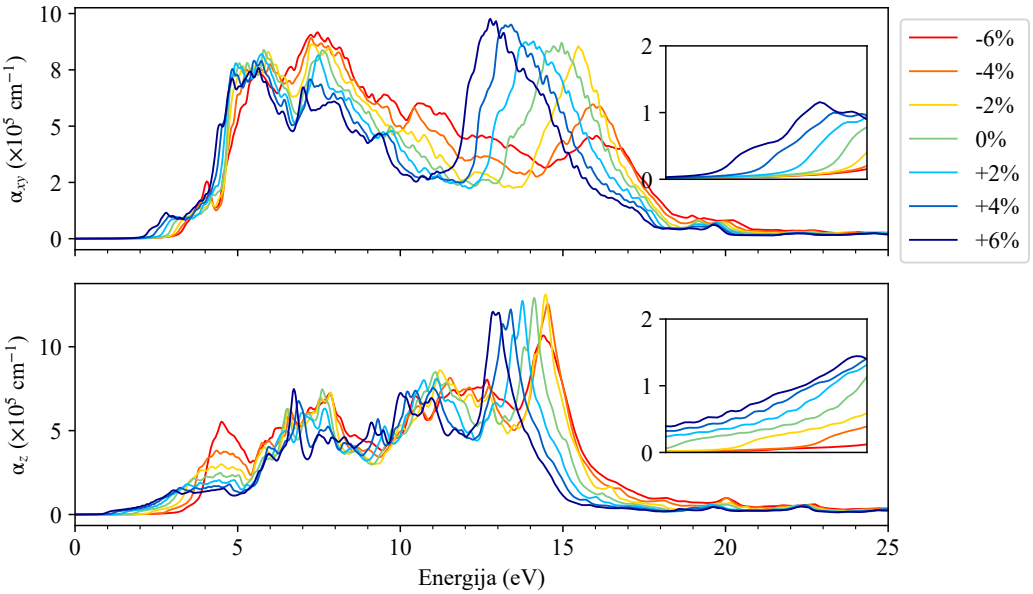


Slika 4.36: Apsorpciona funkcija hBN/GaS HS za vrednosti primenjenog naprezanja od -6% do +6%, označene bojama kao u legendi. Umetnuti grafik prikazuje uvećanu oblast vidljivog dela spektra.

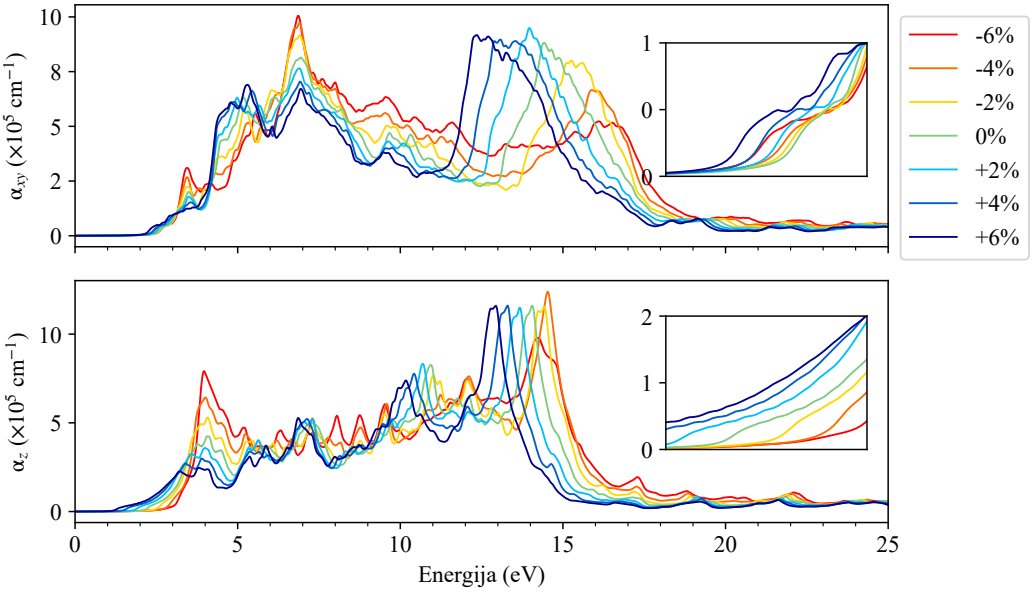


Slika 4.37: Apsorpciona funkcija hBN/InS HS za vrednosti primenjenog naprezanja od -6% do +6%, označene bojama kao u legendi. Umetnuti grafik prikazuje uvećanu oblast vidljivog dela spektra.

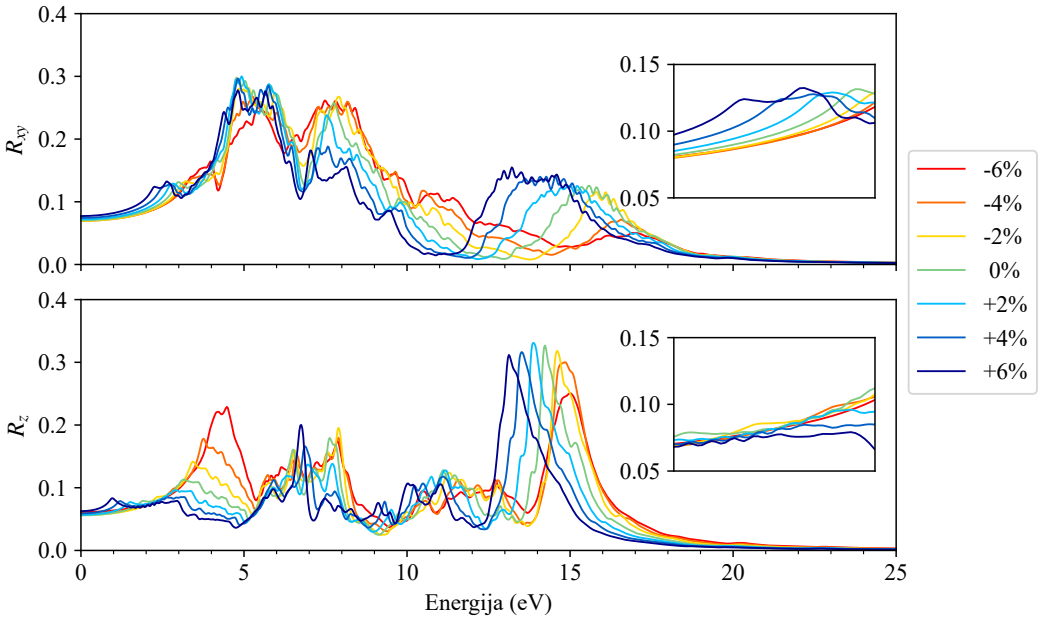


Slika 4.38: Koeficijent refleksije hBN/GaS HS za vrednosti primenjenog naprezanja od -6% do +6%. Umetnuti grafik prikazuje uvećanu oblast vidljivog dela spektra.

polarizaciju normalnu na ravan, pa i ove strukture imaju značajan potencijal za različite optoelektronske primene.

Na kraju se može zaključiti da sve razmatrane HS poseduju poželjne elektronske i optičke osobine i da njihovo formiranje omogućava željeni efekat ojačanja i zaštite $M^{III}X^{VI}$ slojeva, uz očuvanje ili poboljšanje tih osobina. Ove strukture takođe pokazuju značajan potencijal za preciznu kontrolu svojstava primenom biaksijalnog naprezanja, što otvara mogućnosti za njihovu upotrebu u različitim nanoelektronskim i optoelektronskim uređajima. Iako svih šest razmatranih HS imaju slične karakteristike, hBN/InTe, hBN/GaTe i hBN/InSe se izdvajaju kao najperspektivnije zbog odličnog slaganja konstanti rešetki sa konstantom rešetke hBN-a.

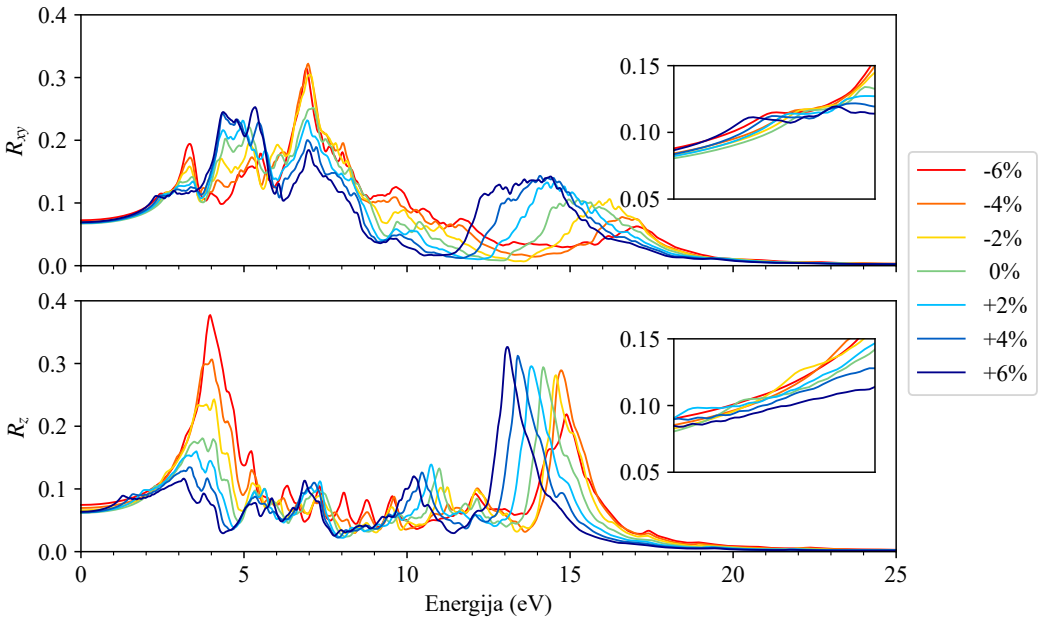


Slika 4.39: Koeficijent refleksije hBN/InS HS za vrednosti primenjenog naprezanja od -6% do +6%. Umetnuti grafik prikazuje uvećanu oblast vidljivog dela spektra.

# 5 Ostali rezultati istraživanja slojevitih i 2D materijala

Tokom rada na doktorskoj disetaciji, istraživani su još i slojeviti i 2D materijali koji će biti predstavljeni u ovom poglavlju. Najveći broj ovih istraživanja je kombinacija numeričkog i eksperimentalnog istraživanja, a teorijski doprinos u ovim istraživanjima uključuje proračune vezane za dinamiku kristalne rešetke, koji su od ključnog značaja za lakše razumevanje i tumačenje spektara dobijenih Ramanovom spektroskopijom. Istraživanja su rezultovala publikacijama koje su navedene u ovom poglavlju. Iako nisu direktno vezane za temu doktorske disertacije, rezultati pružaju širi uvid u ponašanje slojevitih sistema.

## 5.1 "Fortune Teller" disperzija u dvodimenzionalnim materijalima

U istraživanju i analizi elektronske disperzije u materijalima, simetrija ima ključnu ulogu. Ona omogućava predviđanje specifičnih karakteristika u elektronskoj strukturi, poput položaja i prirode tačaka preseka energijskih zona u Briluenovoj zoni, što je od izuzetnog značaja za razumevanje fundamentalnih svojstava materijala, uključujući njihova elektronska, optička i magnetna svojstva. Simetrijska analiza na elegantan način pruža generalizovane zaključke o određenim karakteristikama elektronske strukture koji važe u svim kristalnim rešetkama određene simetrije, a zasnivaju se na univerzalnim zakonima simetrije i nezavisni su od specifičnih aproksimacija i metoda proračuna. Korišćenjem metoda teorije grupa, mogu se identifikovati novi tipovi kvazičestica i elektronskih disperzija koje često nisu očigledne iz direktnih proračuna.

Iako simetrijska analiza predviđa moguće disperzije i generalne karakteristike u elektronskoj strukturi, metode poput DFT-a omogućavaju precizne numeričke proračune zonske strukture, gustine stanja, ali i stabilnosti materijala, pa se kombinacijom ove dve metode može pružiti detaljan uvid u svojstva materijala, otvarajući vrata daljem

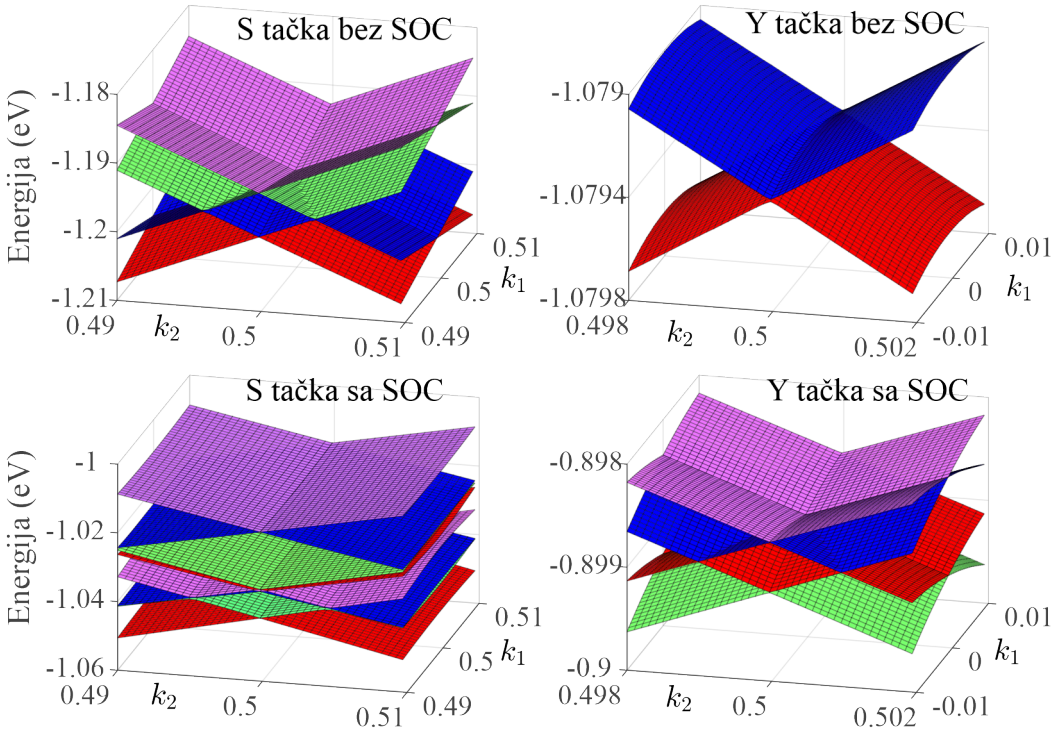


Slika 5.1: Zonska struktura $BiIO_4$ sloja bez i sa SOC, u blizini S i Y tačaka. Uključenjem SOC u proračune, FT disperzija u S tački prelazi u nodalne linije, a degenerisana Dirakova disperzija u Y tački prelazi u FT disperziju.

teorijskom i eksperimentalnom istraživanju novih materijala.

Istraživanja kolege dr Vladimira Damljanovića otkrivaju dve nove vrste elektronskih disperzija, nazvanih "poppy flower" (PF) i "fortune teller" (FT) u dvodimenzionalnim materijalima. Ove disperzije nastaju zahvaljujući specifičnim simetrijski zaštićenim mehanizmima u materijalima sa spin-orbitnom interakcijom (SOC). Kolaboracija sa dr Damljanovićem kombinuje metode teorije grupa sa DFT proračunima kako bi se istražili uslovi i materijali koji podržavaju ove disperzije, a rezultovala je publikacijom:

> Damljanović, V., Nataša Lazić, Andrijana Šolajić, J. Pešić, Božidar Nikolić, and Milan Damnjanović. "Peculiar symmetry-protected electronic dispersions in two-dimensional materials." *Journal of Physics: Condensed Matter* 32, no. 48 (2020): 485501.

U radu se opisuju simetrijska ograničenja potrebna za postojanje PF i FT disperzija. Pronalazi se deset slojnih grupa koje podržavaju PF disperziju, dok se FT disperzije javljaju u dve grupe, a u odredjenim slučajevima opstaju i bez SOC. Analiziraju se karakteristike gustine stanja, pokazujući interesantnu karakteristiku materijala sa FT disperzijom, koja ima konstantnu gustinu stanja blizu Fermijevog nivoa. Pored toga, istražuje se robusnost ovih disperzija pod uticajem narušavanja simetrije, pokazujući na primer, kako deformacije mogu izazvati prelaze iz Dirakovih u PF disperzije. Deo rada bavi se ispitivanjem realističnih materijala koji bi posedovali ovakav tip disperzija. Kao kandidat, identifikovan je i slojeviti $BiIO_4$ materijal kod koga su pomoću DFT-a istraživane

elektronske osobine i mogućnost postojanja monosloja ovog materijala u realnosti. DFT simulacije sugerišu na stabilnost atomski tankog sloja $BiIO_4$ i potvrđuju postojanje FT disperzije u elektronskoj strukturi. Ova stanja su udaljena od Fermijevog nivoa za 0.9 eV, a potrebna su dalja ispitivanja kako bi se karakteristike ovog materijala promenile tako da se Fermijev nivo pomeri na odgovarajuću energiju. Trodimenzionalna zonska struktura $BiIO_4$ u okolini S i Y tačaka, računate bez SOC i sa uključenom SOC je prikazana na slici 5.1.

## 5.2 Slojeviti materijali iz porodica halogenida prelaznih metala i dihalkogenida

Poslednjih godina, slojeviti materijali na bazi halogenida prelaznih metala (poput $CrI_3$, $VI_3$ i $CrSiTe_3$) i dihalkogenida ($Fe_{3-x}GeTe_2$) privlače posebnu pažnju zahvaljujući jedinstvenim magnetnim, elektronskim i vibracionim svojstvima. Ovi materijali omogućavaju istraživanje složenih spin-fononskih i elektron-fononskih interakcija, što ih čini odličnom platformom za proučavanje osnovnih fizičkih fenomena i potencijalnim kandidatima za primene u spintronici.

Magnetni slojeviti materijali, među kojima su $CrI_3$, $VI_3$ i $CrSiTe_3$ predstavljaju idealne sisteme za istraživanje spin-fononskih interakcija i kratkodometnog uređenja. Ovi materijali ispoljavaju jaku zavisnost magnetnih i fononskih svojstava od temperature i strukturnih defekata. Na primer, $CrSi_{0.8}Ge_{0.2}Te_3$ karakterišu složeni efekti defekata na spin-fononske interakcije, a manifestuju se kroz promene u fononskim modovima, detektovane Ramanovom spektroskopijom. Interesantno je i da materijali poput $VI_3$ pokazuju izraženo kratkodometno magnetno uređenje čak i iznad temperature prelaza u feromagnetno stanje, što ukazuje na prisustvo jakih korelacija između spina i rešetke. Pored toga, članovi ovih porodica materijala u dvodimenzionalnoj formi su među prvim pronađenim 2D magnetnim materijalima, što ukazuje na poseban značaj istraživanja ovih materijala.

Još jedan od slojevitih materijala ove porodice koji se ističe je $MnSi_2Te_6$ koji ispoljava dugodometno antiferomagnetno uređenje i karakterišu ga složene interakcije između kristalne rešetke i magnetnog momenta. Ovaj materijal je od posebnog interesa zbog jake spin-fononske interakcije. Među dihalkogenidima prelaznih metala, 1T-$TaS_2$ je poznat po velikom broju faznih prelaza koji su povezani sa talasima gustine naelektrisanja (CDW). Ovaj materijal pokazuje jake korelacije između naelektrisanja i kristalne rešetke, dok eksperimentalni podaci ukazuju na izraženu ulogu fononskih modova u stabilizaciji CDW faze. Specifična svojstva 1T-$TaS_2$ ga čine interesantnim za potencijalne aplikacije u kvantnim računarima.

U istraživanju materijala iz ove porodice, sprovedenih na Institutu za fiziku, primarno

su korišćene tehnike Ramanove spektroskopije i DFT proračuni. Rezultati su objavljeni u sledećim publikacijama:

- Djurdjić-Mijin, S., A. Šolajić, J. Pešić, M. Šćepanović, Y. Liu, A. Baum, Cedomir Petrovic, N. Lazarević, and Z. V. Popović. "Lattice dynamics and phase transition in $CrI_3$ single crystals." *Physical Review B 98*, no. 10 (2018): 104307.

  Fokus istraživanja je na ispitivanju dinamike rešetke i strukturnih faznih prelaza u $CrI_3$ kristalima pomoću Ramanove spektroskopije i teorije funkcionala gustine, sa glavnim ciljem analiziranja vibracionih svojstava i detektovanja faznih prelaza. Rezultati istraživanja daju doprinos razumevanju strukturnih i vibracionih svojstava $CrI_3$, koji ima značajan potencijal za primene u spintroničkim napravama.

- Milosavljević, A., A. Šolajić, J. Pešić, Yu Liu, Cedomir Petrovic, N. Lazarević, and Z. V. Popović. "Evidence of spin-phonon coupling in $CrSiTe_3$." *Physical Review B* 98, no. 10 (2018): 104306.

  Istraživanje je fokusirano na spin-fononsko sprezanje u $CrSiTe_3$, sa ciljem ispitivanja interakcije vibracija rešetke i magnetnog uređenja ovog slojevitog feromagnetnog poluprovodnika. Ramanovom spektroskopijom je utvrđena specifična asimetrija $E_{3g}$ moda na niskim temperaturama povezana sa kratkodometnim magnetnim korelacijama, ukazujući na postojanje jake spinsko-fononske interakcije u ovom materijalu.

- Milosavljević, A., A. Šolajić, S. Djurdjić-Mijin, J. Pešić, B. Višić, Yu Liu, C. Petrovic, N. Lazarević, and Z. V. Popović. "Lattice dynamics and phase transitions in $Fe_{3-x}GeTe_2$." *Physical Review B* 99, no. 21 (2019): 214304.

  U ovom radu, ispitivani su dinamika rešetke i fazni prelazi u $Fe_{3-x}GeTe_2$, kako bi se analizirala svojstva fonona i identifikovale anomalije koje su povezane sa magnetnim faznim prelazima u ovom materijalu. Anomalije u energijama fonona se mogu pripisati spinsko-fononskom sprezanju povezanim sa feromagnetnim-paramagnetnim faznim prelazom dok je poreklo druge i dalje nepoznato.

- Djurdjić Mijin, Sanja, AM Milinda Abeykoon, Andrijana Šolajić, Ana Milosavljević, Jelena Pešić, Yu Liu, Cedomir Petrovic, Zoran V. Popovic, and Nenad Lazarević. "Short-range order in $VI_3$." *Inorganic Chemistry* 59, no. 22 (2020): 16265-16271.

  Još jedan od perspektivnih slojevitih materijala usled postojanja magnetizma u svojoj nisko-dimenzionoj strukturi je $VI_3$. Rezultati ovog istraživanja ukazuju na koegzistenciju kratkodometnog uređenja $P\bar{3}1c$ i dugodometne $R\bar{3}$ faze, a takođe i na postojanje jakog spinsko-fononskog sprezanja kao i kod $CrI_3$.

- Milosavljević, Ana, Andrijana Šolajić, Bojana Višić, Marko Opačić, Jelena Pešić, Yu Liu, Cedomir Petrovic, Zoran V. Popović, and Nenad Lazarević. "Vacancies and spin–phonon coupling in $CrSi_{0.8}Ge0.1Te_3$." *Journal of Raman Spectroscopy* 51, no. 11 (2020): 2153-2160.

Istraživanje se bavi efektima šupljina i spinsko-fononskog sprezanja u vdW feromagnetnom jedinjenju $CrSi_{0.8}Ge0.1Te_3$. Pokazano je da 10% šupljina na Si/Ge mestima redukuje Kirijevu temperaturu, a ponašanje fonona na temperaturama oko 200K ukazuje na postojanje jakog spinsko-fononskog sprezanja. Rezultati pružaju nova saznanja o efektima dopiranja i magnetnim efektima.

- Djurdjić Mijin, S., A. Baum, J. Bekaert, A. Šolajić, J. Pešić, Y. Liu, Ge He et al. "Probing charge density wave phases and the Mott transition in 1T-$TaS_2$ by inelastic light scattering." *Physical Review B* 103, no. 24 (2021): 245133.

  U ovom radu ispituju se CDW faze i Motovi prelazi u 1T-$TaS_2$. Identifikovane su tri CDW faze i izmeren Motov procep od 170-190 meV koji pokazuje temperaturski zavisno ponašanje u C-CDW fazi. Rezultati istraživanja pružaju detaljan uvid u strukturna i elektronska svojstva ovog materijala koji su važni za razumevanje fenomena CDW i Motovog izolatora.

- Lazarević, N., A. Baum, A. Milosavljević, L. Peis, R. Stumberger, J. Bekaert, A. Šolajić et al. "Evolution of lattice, spin, and charge properties across the phase diagram of $FeSe_{1-x}S_x$". *Physical Review B* 106, no. 9 (2022): 094510.

  Ispitivana su vibraciona i spinska svojstva $FeSe_{1-x}S_x$ materijala. Rezultati istraživanja ukazuju na jako sprezanje vibracionih, spinskih, i elektronskih stepena slobode, pružajući nova saznanja o nematičnosti u superprovodnicima na bazi gvožđa.

- Djurdjić Mijin, S., A. Šolajić, J. Pešić, Y. Liu, Cedomir Petrovic, M. Bockstedte, A. Bonanni, Z. V. Popović, and N. Lazarević. "Spin-phonon interaction and short-range order in $Mn_3Si_2Te_6$." Physical Review B 107, no. 5 (2023): 054309.

  Istraživanje obuhvata studiju vibracionih svojstava i spinsko-fononskog sprezanja u $Mn_3Si_2Te_6$. I u ovom materijalu je detektovano jako spinsko-fononsko sprezanje, a uočena su tri fazna prelaza na 142.5 K, 190 K i 285 K, najverovatnije povezana sa kratkodometnim magnetnim uređenjem.

Ova istraživanja pružaju detaljan uvid u složenu povezanost vibracija rešetke, dinamike spina i elektronskih svojstava u slojevitim magnetnim materijalima. Koristeći Ramanovu spektroskopiju zajedno sa teorijom funkcionala gustine, otkrivaju se različiti interesantni fenomeni poput spinsko-fononskog sprezanja, uticaja magnetnog uređenja na dinamiku rešetke i faznih prelaza. Ova saznanja su od velike važnosti za razumevanje fundamentalnih aspekata magnetizma, superprovodnosti i drugih kvantnih fenomena u 2D i slojevitim materijalima. Takvi materijali imaju veliki potencijal za različite primene u magnetoelektronici, spintronici, kvantnom računarstvu i skladištenju podataka, pa svako novo istraživanje ovih materijala doprinosi boljem fundamentalnom razumevanju kvantnih efekata a takođe vodi korak napred ka dizajniranju novih inovativnih uređaja.

# *Glava 6 Zaključak*

U disertaciji su predstavljeni rezultati istraživanja uticaja mehaničkog naprezanja na elektronske, mehaničke i optičke osobine novih heterostruktura zasnovanih na hBN i $M^{III}X^{VI}$ slojevima, koristeći teoriju funkcionala gustine. Dvodimenzionalni monohalkogenidi IIIA grupe ističu se svojim izvrsnim elektronskim i optičkim osobinama, uključujući visoku pokretljivost elektrona i apsorpciju u širokom spektralnom opsegu, dok njihova mehanička fleksibilnost omogućava prilagođavanje svojstava pomoću naprezanja i otvara mogućnosti za primenu u fleksibilnoj elektronici. Međutim, kako su ovi materijali skloni oksidaciji pri kontaktu sa vazduhom, njihova upotreba u uređajima, kao i mogućnost daljeg eksperimentalnog ispitivanja su ograničene. U tom kontekstu, atomski tanak sloj hBN-a se pokazao kao izvrsno rešenje, pružajući efikasnu pasivizaciju i mehaničku zaštitu, uz očuvanje, a u nekim aspektima i poboljšanje elektronskih i optičkih svojstava $M^{III}X^{VI}$ slojeva.

Kako bi se maksimalno iskoristio potencijal ovih struktura, ispitivana je primena naprezanja na ove heterostrukture, u cilju optimizacije i precizne kontrole njihovih osobina. Biaksijalno naprezanje se pokazalo kao posebno efikasan pristup koji omogućava kontrolisano i ravnomerno širenje ili sabijanje kristalne rešetke, uz očuvanje njenog oblika i simetrije. Na ovaj način, svojstva heterostruktura, poput širine energijskog procepa, mogu se linearno menjati bez narušavanja intrinzičnih elektronskih i optičkih karakteristika koje su direktno povezane sa simetrijom materijala, poput specifičnih elektronskih disperzija i optičkih prelaza.

Prethodni eksperimentalni rezultati potvrdili su efikasnost zaštite tankih filmova InSe i GaSe hBN-om, dok teorijske studije ukazuju na izuzetne karakteristike hBN/InSe heterostruktura, uključujući visoku apsorpciju u vidljivom i UV delu spektra, kao i značajno poboljšanu pokretljivost elektrona u InSe i GaSe usled integracije sa hBN slojem. Ova saznanja ukazuju na važnost daljeg istraživanja kako bi se identifikovali slični materijali sa visokim potencijalom za primenu u savremenim tehnologijama.

U istraživanju su ispitivane hBN/InTe, hBN/GaTe, hBN/InSe, hBN/GaSe, hBN/InS i hBN/GaS heterostrukture, koje osim pomenute hBN/InSe, nisu prethodno razmatrane.

Od razmatranih šest heterostruktura, najoptimalnije su pokazale hBN/InTe, hBN/GaTe i hBN/InSe, čije jedinične ćelije sadrže samo 10 atoma, čime se značajno smanjuju računarski zahtevi i kompleksnost modeliranja. Kristalna rešetka ovih het-

erostruktura sastoji se od sloja In(Ga)Te ili InSe i superćelije hBN sloja konstante rešetke $\sqrt{3} \times \sqrt{3} a_{hBN}$ rotirane za 60°. Istraživanja su pokazala da su ove strukture stabilne i da način slaganja slojeva (H-tip, B-tip ili N-tip) nema značajan uticaj na njihova elektronska svojstva, ukupnu energiju sistema ili energiju vezivanja.

Formiranjem ovih heterostruktura dolazi do značajnog poboljšanja mehaničkih osobina u poređenju sa izolovanim slojevima monohalkogenida, pri čemu Jangov modul dostiže vrednosti uporedive sa grafenom. Elektronska svojstva ovih struktura pokazuju umerene do male energijske procepe: 1.54 eV za hBN/InTe, 0.79 eV za hBN/GaTe i 0.56 eV za hBN/InSe, što ih čini pogodnim za različite optoelektronske primene. Optička svojstva ovih heterostruktura takođe su značajno unapređena, pri čemu apsorpcioni koeficijent dostiže redove veličine $10^5\,\mathrm{cm}^{-1}$, a u najvišim pikovima čak prelazi $8 \times 10^5\ \mathrm{cm}^{-1}$. Ove strukture pokazuju širok spektar apsorpcije, pokrivajući vidljivi i UV deo spektra, što ih čini izuzetno atraktivnim za primene u optoelektronskim uređajima poput fotodetektora i solarnih ćelija.

Biaksijalno naprezanje pokazalo se kao moćan alat za preciznu kontrolu i modifikaciju svojstava ovih heterostruktura. Kod hBN/InTe i hBN/GaTe heterostruktura, energijski procep raste sa kompresijom (npr. 1.69 eV pri -2% kompresivnog naprezanja kod hBN/InTe), dok se pri istezanju smanjuje (0.7 eV pri +5%). Kod hBN/GaTe, energijski procep opada na svega 0.24 eV pri istezanju od +5%, što dodatno naglašava potencijal za podešavanje elektronskih svojstava.

Optičke osobine ovih heterostruktura pokazuju značajnu zavisnost od naprezanja. Kod hBN/GaTe, apsorpcija u niskoenergetskom opsegu (1-2 eV) se povećava, dok kod hBN/InTe kompresivno naprezanje pojačava apsorpcione pikove na oko 3 eV u $z$ polarizaciji. Kod hBN/InSe, naprezanje omogućava preciznu kontrolu apsorpcionih karakteristika u širokom spektru energija. Kompresivno naprezanje povećava apsorpciju u UV opsegu, dok istezanje pojačava apsorpciju u infracrvenom i vidljivom delu spektra.

Mehaničke osobine, kao što su konstante elastičnosti i otpornost na deformacije, potvrđuju robustnost ovih struktura. Prisustvo hBN sloja pruža dodatnu mehaničku stabilnost i zaštitu od oksidacije, čineći ih pogodnim za praktične primene u zahtevnim uslovima.

Kod složenijih struktura poput hBN/GaS, hBN/GaSe i hBN/InS, primena kompresivnog naprezanja dovodi do formiranja periodičnih naboranih struktura hBN sloja. Iako ove deformacije ne narušavaju stabilnost struktura, mogu biti izazovne u eksperimentalnoj realizaciji. Uprkos tome, ove heterostrukture zadržavaju dobre optičke osobine i visoke apsorpcione koeficijente u UV opsegu.

Sveobuhvatna analiza uticaja naprezanja na heterostrukture zasnovane na hBN i $M^{III}X^{VI}$ slojevima ne samo da potvrđuje njihovu izvanrednu prilagodljivost i potencijal za primene u fleksibilnoj elektronici, fotonici i optoelektronici, već pruža i ključne uvide u fundamentalnu važnost naprezanja kao univerzalnog alata za inženjering osobina dvodimenzionalnih materijala. Ovo istraživanje pokazuje da biaksijalno naprezanje omogućava

precizno podešavanje elektronskih i optičkih svojstava ovih heterostruktura, otvarajući vrata novim mogućnostima u razvoju tzv. straintronike – revolucionarne oblasti koja se oslanja na kontrolu materijala putem mehaničkih deformacija.

Naprezanje, kao dinamički i visoko kontrolisani parametar, potvrđuje se kao ključni koncept za dizajniranje funkcionalnih materijala sa prilagođenim osobinama. Rezultati ovog istraživanja ne samo da pružaju značajne smernice za eksperimentalnu realizaciju ovih heterostruktura, već postavljaju i čvrstu teorijsku osnovu za buduća istraživanja. Ovi zaključci su relevantni i za širu porodicu 2D materijala, naglašavajući da razumevanje i kontrola naprezanja može igrati centralnu ulogu u kreiranju nove generacije uređaja visokih performansi.

Istraživanje je sprovedeno sa ciljem obezbeđivanja osnova za dalja teorijska i eksperimentalna istraživanja ovih do sada neidentifikovanih struktura, koja će voditi ka integraciji ovih materijala u tehnologije budućnosti. hBN/$M^{III}X^{VI}$ heterostrukture se izdvajaju ne samo po svojoj jedinstvenoj kombinaciji elektronskih, optičkih i mehaničkih osobina, već i po sposobnosti da odgovore na specifične zahteve fleksibilnih i funkcionalnih primena u modernoj tehnologiji. Ovi rezultati ukazuju na izuzetan potencijal naprezanja kao faktora koji ne samo da prilagođava osobine materijala, već ih fundamentalno unapređuje, pružajući mogućnosti za istraživanja koja će oblikovati nauku i tehnologiju u godinama koje dolaze.

Ovaj rad jasno demonstrira da je kontrolisano naprezanje ne samo alat za podešavanje svojstava, već i osnovni princip za projektovanje novih funkcionalnih materijala, čime postaje jedan od stubova savremenih istraživanja u oblasti fizike čvrstog stanja, nanotehnologije i nauke o materijalima. Straintronika, zasnovana na ovim principima, nije samo pravac razvoja, već i vizija budućnosti.

# *Literatura*


[1] Kailiang Zhang, Yulin Feng, Fang Wang, Zhengchun Yang, and John Wang. Two dimensional hexagonal boron nitride (2d-hbn): synthesis, properties and applications. *Journal of Materials Chemistry C*, 5(46):11992–12022, 2017. 1

[2] Li Song, Lijie Ci, Hao Lu, Pavel B Sorokin, Chuanhong Jin, Jie Ni, Alexander G Kvashnin, Dmitry G Kvashnin, Jun Lou, Boris I Yakobson, et al. Large scale growth and characterization of atomic hexagonal boron nitride layers. *Nano letters*, 10(8):3209–3215, 2010. 1

[3] Abdelkader Kara, Hanna Enriquez, Ari P Seitsonen, LC Lew Yan Voon, Sébastien Vizzini, Bernard Aufray, and Hamid Oughaddou. A review on silicene - new candidate for electronics. *Surface science reports*, 67(1):1–18, 2012. 1

[4] Jijun Zhao, Hongsheng Liu, Zhiming Yu, Ruge Quhe, Si Zhou, Yangyang Wang, Cheng Cheng Liu, Hongxia Zhong, Nannan Han, Jing Lu, et al. Rise of silicene: A competitive 2d material. *Progress in Materials Science*, 83:24–151, 2016. 1

[5] Adil Acun, Lijie Zhang, Pantelis Bampoulis, M v Farmanbar, Arie van Houselt, AN Rudenko, M Lingenfelder, G Brocks, Bene Poelsema, MI Katsnelson, et al. Germanene: the germanium analogue of graphene. *Journal of physics: Condensed matter*, 27(44):443002, 2015. 1

[6] Mickael Derivaz, Didier Dentel, Regis Stephan, Marie-Christine Hanf, Ahmed Mehdaoui, Philippe Sonnet, and Carmelo Pirri. Continuous germanene layer on al (111). *Nano letters*, 15(4):2510–2516, 2015. 1

[7] Qiang Fu, Jiecai Han, Xianjie Wang, Ping Xu, Tai Yao, Jun Zhong, Wenwu Zhong, Shengwei Liu, Tangling Gao, Zhihua Zhang, et al. 2d transition metal dichalcogenides: Design, modulation, and challenges in electrocatalysis. *Advanced Materials*, 33(6):1907818, 2021. 1

[8] Yanguang Li, Hailiang Wang, Liming Xie, Yongye Liang, Guosong Hong, and Hongjie Dai. Mos2 nanoparticles grown on graphene: an advanced catalyst for the hydrogen evolution reaction. *Journal of the American Chemical Society*, 133(19):7296–7299, 2011. 1

[9] Andrea Splendiani, Liang Sun, Yuanbo Zhang, Tianshu Li, Jonghwan Kim, Chi-Yung Chim, Giulia Galli, and Feng Wang. Emerging photoluminescence in monolayer mos2. *Nano letters*, 10(4):1271–1275, 2010. 1

[10] Hong Li, Qing Zhang, Chin Chong Ray Yap, Beng Kang Tay, Teo Hang Tong Edwin, Aurelien Olivier, and Dominique Baillargeat. From bulk to monolayer mos2: evolution of raman scattering. *Advanced Functional Materials*, 22(7):1385–1390, 2012. 1

[11] Weijie Zhao, Zohreh Ghorannevis, Leiqiang Chu, Minglin Toh, Christian Kloc, Ping-Heng Tan, and Goki Eda. Evolution of electronic structure in atomically thin sheets of ws2 and wse2. *ACS nano*, 7(1):791–797, 2013. 1

[12] Hai Li, Gang Lu, Yanlong Wang, Zongyou Yin, Chunxiao Cong, Qiyuan He, Lu Wang, Feng Ding, Ting Yu, and Hua Zhang. Mechanical exfoliation and characterization of single-and few-layer nanosheets of wse2, tas2, and tase2. *Small*, 9(11):1974–1981, 2013. 1

[13] Babak Anasori, Maria R Lukatskaya, and Yury Gogotsi. 2d metal carbides and nitrides (mxenes) for energy storage. *Nature Reviews Materials*, 2(2):1–17, 2017. 1

[14] Jinbo Pang, Rafael G Mendes, Alicja Bachmatiuk, Liang Zhao, Huy Q Ta, Thomas Gemming, Hong Liu, Zhongfan Liu, and Mark H Rummeli. Applications of 2d mxenes in energy conversion and storage systems. *Chemical Society Reviews*, 48(1):72–133, 2019. 1

[15] Chongdan Ren, Sake Wang, Hongyu Tian, Yi Luo, Jin Yu, Yujing Xu, and Minglei Sun. First-principles investigation on electronic properties and band alignment of group iii monochalcogenides. *Scientific reports*, 9(1):1–6, 2019. 1, 35, 37, 38, 39

[16] Salih Demirci, N Avazlı, Engin Durgun, and S Cahangirov. Structural and electronic properties of monolayer group iii monochalcogenides. *Physical Review B*, 95(11):115409, 2017. 1, 37, 38, 53

[17] Zhibin Yang and Jianhua Hao. Recent progress in 2d layered iii–vi semiconductors and their heterostructures for optoelectronic device applications. *Advanced Materials Technologies*, 4(8):1900108, 2019. 1

[18] Jianhui Chen, Shuchang Cai, Rui Xiong, Baisheng Sa, Cuilian Wen, Bo Wu, and Zhimei Sun. High-performance iii–vi monolayer transistors for flexible devices. *Physical Chemistry Chemical Physics*, 22(13):7039–7047, 2020. 1, 2, 34, 37, 38, 40

[19] F Withers, O Del Pozo-Zamudio, A Mishchenko, AP Rooney, A Gholinia, K Watanabe, T Taniguchi, SJ Haigh, AK Geim, AI Tartakovskii, et al. Light-emitting diodes by band-structure engineering in van der waals heterostructures. *Nature materials*, 14(3):301–306, 2015. 1

[20] Andre K Geim and Irina V Grigorieva. Van der waals heterostructures. *Nature*, 499(7459):419–425, 2013. 1, 34

[21] KS Novoselov, o A Mishchenko, o A Carvalho, and AH Castro Neto. 2d materials and van der waals heterostructures. *Science*, 353(6298), 2016. 1, 34

[22] Yuan Liu, Nathan O Weiss, Xidong Duan, Hung-Chieh Cheng, Yu Huang, and Xiangfeng Duan. Van der waals heterostructures and devices. *Nature Reviews Materials*, 1(9):1–17, 2016. 1, 34

[23] Kai Xu, Lei Yin, Yun Huang, Tofik Ahmed Shifa, Junwei Chu, Feng Wang, Ruiqing Cheng, Zhenxing Wang, and Jun He. Synthesis, properties and applications of 2d layered m iii x vi (m= ga, in; x= s, se, te) materials. *Nanoscale*, 8(38):16802–16818, 2016. 1

[24] Wei Feng, Wei Zheng, Wenwu Cao, and PingAn Hu. Back gated multilayer inse transistors with enhanced carrier mobilities via the suppression of carrier scattering from a dielectric interface. *Advanced materials*, 26(38):6587–6593, 2014. 1, 38

[25] Leonardo Gomez, I Aberg, and JL Hoyt. Electron transport in strained-silicon directly on insulator ultrathin-body n-mosfets with body thickness ranging from 2 to 25 nm. *IEEE electron device letters*, 28(4):285–287, 2007. 1

[26] Likai Li, Yijun Yu, Guo Jun Ye, Qingqin Ge, Xuedong Ou, Hua Wu, Donglai Feng, Xian Hui Chen, and Yuanbo Zhang. Black phosphorus field-effect transistors. *Nature nanotechnology*, 9(5):372–377, 2014. 1

[27] Srinivasa Reddy Tamalampudi, Yi-Ying Lu, Rajesh Kumar U, Raman Sankar, Chun-Da Liao, Che-Hsuan Cheng, Fang Cheng Chou, and Yit-Tsong Chen. High performance and bendable few-layered inse photodetectors with broad spectral response. *Nano letters*, 14(5):2800–2806, 2014. 1

[28] Mahfujur Rahaman, Raul D Rodriguez, Manuel Monecke, Santos A Lopez-Rivera, and Dietrich R T Zahn. GaSe oxidation in air: from bulk to monolayers. *Semiconductor Science and Technology*, 32(10):105004, sep 2017. 2, 35

[29] Yu Guo, Si Zhou, and Jijun Zhao. Oxidation behaviors of two-dimensional metal chalcogenides. *ChemNanoMat*, 6(6):838–849, 2020. 2, 35

[30] Yu Guo, Si Zhou, Yizhen Bai, and Jijun Zhao. Defects and oxidation of group-iii monochalcogenide monolayers. *The Journal of chemical physics*, 147(10):104709, 2017. 2

[31] Tariq Afaneh, Algene Fryer, Yan Xin, Robert H Hyde, Nalaka Kapuruge, and Humberto R Gutierrez. Large-area growth and stability of monolayer gallium

monochalcogenides for optoelectronic devices. *ACS Applied Nano Materials*, 3(8):7879–7887, 2020. 2

[32] Denis A Bandurin, Anastasia V Tyurnina, L Yu Geliang, Artem Mishchenko, Viktor Zólyomi, Sergey V Morozov, Roshan Krishna Kumar, Roman V Gorbachev, Zakhar R Kudrynskyi, Sergio Pezzini, et al. High electron mobility, quantum hall effect and anomalous optical response in atomically thin inse. *Nature nanotechnology*, 12(3):223–227, 2017. 2

[33] Himani Arora and Artur Erbe. Recent progress in contact, mobility, and encapsulation engineering of inse and gase. *InfoMat*, 3(6):662–693, 2021. 2

[34] Nai-feng Shen, Xiao-dong Yang, Xin-xin Wang, Guang-hou Wang, and Jian-guo Wan. Two-dimensional van der waals heterostructure of indium selenide/hexagonal boron nitride with strong interlayer coupling. *Chemical Physics Letters*, 749:137430, 2020. 2, 40, 41, 48, 64, 66, 69

[35] Hengheng Li, Zhongpo Zhou, and Haiying Wang. Tunable schottky barrier in inte/graphene van der waals heterostructure. *Nanotechnology*, 31(33):335201, 2020. 2

[36] Hengheng Li, Zhongpo Zhou, Kelei Zhang, and Haiying Wang. Schottky barrier modulation of a gate/graphene heterostructure by interlayer distance and perpendicular electric field. *Nanotechnology*, 30(40):405207, 2019. 2, 35

[37] Khang D Pham, Hieu Vu-Quang, and Chuong V Nguyen. Modulation of electronic properties and schottky barrier in the graphene/gas heterostructure by electric gating. *Physica B: Condensed Matter*, 555:69–73, 2019. 2

[38] Khang D Pham, Nguyen N Hieu, Huynh V Phuc, IA Fedorov, CA Duque, B Amin, and Chuong V Nguyen. Layered graphene/gas van der waals heterostructure: controlling the electronic properties and schottky barrier by vertical strain. *Applied Physics Letters*, 113(17):171605, 2018. 2

[39] Xu Gao, Yanqing Shen, Yanyan Ma, Shengyao Wu, and Zhongxiang Zhou. Graphene/gete van der waals heterostructure: Functional schottky device with modulated schottky barriers via external strain and electric field. *Computational Materials Science*, 170:109200, 2019. 2

[40] Ting Hu, Jian Zhou, and Jinming Dong. Strain induced new phase and indirect–direct band gap transition of monolayer inse. *Physical Chemistry Chemical Physics*, 19(32):21722–21728, 2017. 2, 40, 66

[41] M Yagmurcukardes, Ramazan Tuğrul Senger, François M Peeters, and H Sahin. Mechanical properties of monolayer gas and gase crystals. *Physical Review B*, 94(24):245407, 2016. 2, 40

[42] P. Hohenberg and W. Kohn. Inhomogeneous electron gas. *Phys. Rev.*, 136:B864–B871, Nov 1964. 4, 9

[43] JR Oppenheimer and Max Born. Zur quantentheorie der molekeln [on the quantum theory of molecules]. *Annalen der Physik*, 389(20):457–484, 1927. 7

[44] Feliciano Giustino. *Materials modelling using density functional theory: properties and predictions*. Oxford University Press, 2014. 7, 18

[45] Douglas R Hartree. The wave mechanics of an atom with a non-coulomb central field. part i. theory and methods. In *Mathematical Proceedings of the Cambridge Philosophical Society*, volume 24, pages 89–110. Cambridge university press, 1928. 8

[46] Vladimir Fock. Näherungsmethode zur lösung des quantenmechanischen mehrkörperproblems. *Zeitschrift für Physik*, 61:126–148, 1930. 8

[47] John C Slater. The theory of complex spectra. *Physical review*, 34(10):1293, 1929. 9

[48] W. Kohn and L. J. Sham. Self-consistent equations including exchange and correlation effects. *Phys. Rev.*, 140:A1133–A1138, Nov 1965. 11

[49] A Becke. Density-functional thermochemistry. iii. the role of exact exchange j. *Chem. Phys*, 98:5648, 1993. 16

[50] Jochen Heyd, Gustavo E Scuseria, and Matthias Ernzerhof. Hybrid functionals based on a screened coulomb potential. *The Journal of chemical physics*, 118(18):8207–8215, 2003. 16

[51] John P Perdew, Matthias Ernzerhof, and Kieron Burke. Rationale for mixing exact exchange with density functional approximations. *The Journal of chemical physics*, 105(22):9982–9985, 1996. 16

[52] Renxi Liu, Daye Zheng, Xinyuan Liang, Xinguo Ren, Mohan Chen, and Wenfei Li. Implementation of the meta-gga exchange-correlation functional in numerical atomic orbital basis: With systematic testing on scan, rscan, and r2scan functionals. *The Journal of Chemical Physics*, 159(7), 2023. 16

[53] Martijn Marsman, Joachim Paier, A Stroppa, and Georg Kresse. Hybrid functionals applied to extended systems. *Journal of Physics: Condensed Matter*, 20(6):064201, 2008. 16, 17

[54] Stefan Grimme. Semiempirical gga-type density functional constructed with a long-range dispersion correction. *Journal of computational chemistry*, 27(15):1787–1799, 2006. 17, 28

[55] Stefan Grimme, Jens Antony, Stephan Ehrlich, and Helge Krieg. A consistent and accurate ab initio parametrization of density functional dispersion correction (dft-d) for the 94 elements h-pu. *The Journal of chemical physics*, 132(15):154104, 2010. 17

[56] Matteo Cococcioni and Stefano De Gironcoli. Linear response approach to the calculation of the effective interaction parameters in the lda+ u method. *Physical Review B—Condensed Matter and Materials Physics*, 71(3):035105, 2005. 17

[57] Burak Himmetoglu, Renata M Wentzcovitch, and Matteo Cococcioni. First-principles study of electronic and structural properties of cuo. *Physical Review B—Condensed Matter and Materials Physics*, 84(11):115108, 2011. 17

[58] John P Perdew and Alex Zunger. Self-interaction correction to density-functional approximations for many-electron systems. *Physical review B*, 23(10):5048, 1981. 17, 18

[59] John P Perdew. Density-functional approximation for the correlation energy of the inhomogeneous electron gas. *Physical review B*, 33(12):8822, 1986. 17

[60] John P Perdew and Yue Wang. Accurate and simple analytic representation of the electron-gas correlation energy. *Physical review B*, 45(23):13244, 1992. 17

[61] Paul AM Dirac. Note on exchange phenomena in the thomas atom. In *Mathematical proceedings of the Cambridge philosophical society*, volume 26, pages 376–385. Cambridge University Press, 1930. 18

[62] David M Ceperley and Berni J Alder. Ground state of the electron gas by a stochastic method. *Physical review letters*, 45(7):566, 1980. 18

[63] John P Perdew, Kieron Burke, and Matthias Ernzerhof. Generalized gradient approximation made simple. *Physical review letters*, 77(18):3865, 1996. 19

[64] Ales Zupan, Kieron Burke, Matthias Ernzerhof, and John P Perdew. Distributions and averages of electron density parameters: Explaining the effects of gradient corrections. *The Journal of chemical physics*, 106(24):10184–10193, 1997. 19

[65] John P Perdew, Adrienn Ruzsinszky, Gábor I Csonka, Oleg A Vydrov, Gustavo E Scuseria, Lucian A Constantin, Xiaolan Zhou, and Kieron Burke. Restoring the density-gradient expansion for exchange in solids and surfaces. *Physical review letters*, 100(13):136406, 2008. 19

[66] RM Martin. Electronic structure: basic theory and practical methods cambridge university press. *Cambridge Daw MS, Baskes MI (1984) Phys Rev B*, 296443, 2004. 19

[67] John P Perdew, Kieron Burke, and Yue Wang. Generalized gradient approximation for the exchange-correlation hole of a many-electron system. *Physical review B*, 54(23):16533, 1996. 19

[68] DR Hamann, M Schlüter, and C Chiang. Norm-conserving pseudopotentials. *Physical review letters*, 43(20):1494, 1979. 22

[69] David Vanderbilt. Optimally smooth norm-conserving pseudopotentials. *Physical Review B*, 32(12):8412, 1985. 22

[70] David Vanderbilt. Soft self-consistent pseudopotentials in a generalized eigenvalue formalism. *Physical review B*, 41(11):7892, 1990. 22

[71] Peter E Blöchl. Projector augmented-wave method. *Physical review B*, 50(24):17953, 1994. 22

[72] Georg Kresse and Daniel Joubert. From ultrasoft pseudopotentials to the projector augmented-wave method. *Physical review b*, 59(3):1758, 1999. 22

[73] Stefano Baroni, Paolo Giannozzi, and Andrea Testa. Green's-function approach to linear response in solids. *Physical review letters*, 58(18):1861, 1987. 23

[74] Stefano Baroni, Stefano De Gironcoli, Andrea Dal Corso, and Paolo Giannozzi. Phonons and related crystal properties from density-functional perturbation theory. *Reviews of modern Physics*, 73(2):515, 2001. 23, 24, 25

[75] H. Hellmann. *Einführung in die quantenchemie*. F. Deuticke, 1937. 24

[76] Richard Phillips Feynman. Forces in molecules. *Physical review*, 56(4):340, 1939. 24

[77] PD DeCicco and FA Johnson. The quantum theory of lattice dynamics. iv. *Proceedings of the Royal Society of London. A. Mathematical and Physical Sciences*, 310(1500):111–119, 1969. 24

[78] Robert M Pick, Morrel H Cohen, and Richard M Martin. Microscopic theory of force constants in the adiabatic approximation. *Physical Review B*, 1(2):910, 1970. 24

[79] A. Messiah. *Quantum Mechanics*. Number v. 2 in Quantum Mechanics. Elsevier Science, 1961. 25

[80] Paolo Giannozzi, Stefano Baroni, Nicola Bonini, Matteo Calandra, Roberto Car, Carlo Cavazzoni, Davide Ceresoli, Guido L Chiarotti, Matteo Cococcioni, Ismaila Dabo, Andrea Dal Corso, Stefano de Gironcoli, Stefano Fabris, Guido Fratesi, Ralph Gebauer, Uwe Gerstmann, Christos Gougoussis, Anton Kokalj, Michele Lazzeri,

Layla Martin-Samos, Nicola Marzari, Francesco Mauri, Riccardo Mazzarello, Stefano Paolini, Alfredo Pasquarello, Lorenzo Paulatto, Carlo Sbraccia, Sandro Scandolo, Gabriele Sclauzero, Ari P Seitsonen, Alexander Smogunov, Paolo Umari, and Renata M Wentzcovitch. Quantum espresso: a modular and open-source software project for quantum simulations of materials. *Journal of Physics: Condensed Matter*, 21(39):395502 (19pp), 2009. 26

[81] P Giannozzi, O Andreussi, T Brumme, O Bunau, M Buongiorno Nardelli, M Calandra, R Car, C Cavazzoni, D Ceresoli, M Cococcioni, N Colonna, I Carnimeo, A Dal Corso, S de Gironcoli, P Delugas, R A DiStasio Jr, A Ferretti, A Floris, G Fratesi, G Fugallo, R Gebauer, U Gerstmann, F Giustino, T Gorni, J Jia, M Kawamura, H-Y Ko, A Kokalj, E Küçükbenli, M Lazzeri, M Marsili, N Marzari, F Mauri, N L Nguyen, H-V Nguyen, A Otero de-la Roza, L Paulatto, S Poncé, D Rocca, R Sabatini, B Santra, M Schlipf, A P Seitsonen, A Smogunov, I Timrov, T Thonhauser, P Umari, N Vast, X Wu, and S Baroni. Advanced capabilities for materials modelling with quantum espresso. *Journal of Physics: Condensed Matter*, 29(46):465901, 2017. 26

[82] Charles George Broyden. The convergence of a class of double-rank minimization algorithms 1. general considerations. *IMA Journal of Applied Mathematics*, 6(1):76–90, 1970. 28

[83] Roger Fletcher. A new approach to variable metric algorithms. *The computer journal*, 13(3):317–322, 1970. 28

[84] Donald Goldfarb. A family of variable-metric methods derived by variational means. *Mathematics of computation*, 24(109):23–26, 1970. 28

[85] David F Shanno. Conditioning of quasi-newton methods for function minimization. *Mathematics of computation*, 24(111):647–656, 1970. 28

[86] Vincenzo Barone, Maurizio Casarin, Daniel Forrer, Michele Pavone, Mauro Sambi, and Andrea Vittadini. Role and effective treatment of dispersive forces in materials: Polyethylene and graphite crystals as test cases. *Journal of computational chemistry*, 30(6):934–939, 2009. 28

[87] Andrea Dal Corso. Thermo_pw: A set of routines for the calculation of thermophysical properties within density functional theory. `https://dalcorso.github.io/thermo_pw/`. Pristupljeno: 01.01.2025. 28

[88] Li Xue, Yiming Ren, Jun-Rong He, Yuan Zhao, Si-Liu Xu, Yonghong Hu, and Chun-Bo Hua. The mechanical and thermal parameters of two-dimensional hexagonal materials evaluated using elastic properties: monolayer mos2 as an example. *Results in Physics*, 57:107418, 2024. 29

[89] Quantum ESPRESSO Developers. Dielectric properties in quantum espresso: User manual. https://github.com/QEF/q-e/blob/develop/PP/Doc/eps_man.tex, 2025. Accessed: 2025-01-04. 29

[90] Jimin Shang, Longfei Pan, Xiaoting Wang, Jingbo Li, Hui-Xiong Deng, and Zhongming Wei. Tunable electronic and optical properties of inse/inte van der waals heterostructures toward optoelectronic applications. *Journal of Materials Chemistry C*, 6(27):7201–7206, 2018. 30

[91] Thi-Nga Do, Vo T.T. Vi, Nguyen T.T. Binh, Nguyen N. Hieu, and Nguyen V. Hieu. Computational study on strain and electric field tunable electronic and optical properties of inte monolayer. *Superlattices and Microstructures*, 151:106816, 2021. 30, 38

[92] Jaafar Jalilian and Mandana Safari. Electronic and optical properties of $\alpha$-inx (x=s, se and te) monolayer: Under strain conditions. *Physics Letters A*, 381(15):1313–1320, 2017. 30

[93] V. Zólyomi, N. D. Drummond, and V. I. Fal'ko. Electrons and phonons in single layers of hexagonal indium chalcogenides from ab initio calculations. *Phys. Rev. B*, 89:205416, May 2014. 30, 37, 38

[94] Yujie Liao, Huating Liu, Guanghui Yuan, Zongyu Huang, and Xiang Qi. Electronic and optical properties of novel graphene-like inte monolayer: First principle calculations. *Crystal Research and Technology*, 55(12):2000102, 2020. 30, 38, 53

[95] Koichi Momma and Fujio Izumi. Vesta 3 for three-dimensional visualization of crystal, volumetric and morphology data. *Journal of applied crystallography*, 44(6):1272–1276, 2011. 30

[96] Synopsys QuantumATK. Quantumatk, 2023. Available at: https://www.synopsys.com/silicon/quantumatk.html. 30

[97] Andrew J Mannix, Brian Kiraly, Mark C Hersam, and Nathan P Guisinger. Synthesis and chemistry of elemental 2d materials. *Nature Reviews Chemistry*, 1(2):0014, 2017. 32, 33

[98] K. S. Novoselov, A. K. Geim, S. V. Morozov, D. Jiang, Y. Zhang, S. V. Dubonos, I. V. Grigorieva, and A. A. Firsov. Electric field effect in atomically thin carbon films. *Science*, 306(5696):666–669, 2004. 32

[99] Vigneshwaran Shanmugam, Rhoda Afriyie Mensah, Karthik Babu, Sidique Gawusu, Avishek Chanda, Yongming Tu, Rasoul Esmaeely Neisiany, Michael Försth, Gabriel Sas, and Oisik Das. A review of the synthesis, properties, and applications of 2d materials. *Particle & Particle Systems Characterization*, 39(6):2200031, 2022. 32, 34

[100] Pratap Vishnoi, K Pramoda, and CNR Rao. 2d elemental nanomaterials beyond graphene. *ChemNanoMat*, 5(9):1062–1091, 2019. 32

[101] Nicholas R Glavin, Rahul Rao, Vikas Varshney, Elisabeth Bianco, Amey Apte, Ajit Roy, Emilie Ringe, and Pulickel M Ajayan. Emerging applications of elemental 2d materials. *Advanced Materials*, 32(7):1904302, 2020. 33

[102] Xiaodong Xu, Wang Yao, Di Xiao, and Tony F. Heinz. Spin and pseudospins in layered transition metal dichalcogenides. *Nature Physics*, 10(5):343–350, May 2014. 32, 33

[103] J. M. Lu, O. Zheliuk, I. Leermakers, N. F. Q. Yuan, U. Zeitler, K. T. Law, and J. T. Ye. Evidence for two-dimensional ising superconductivity in gated $mos_2$. *Science*, 350(6266):1353–1357, 2015. 32

[104] Yu Saito, Yasuharu Nakamura, Mohammad Saeed Bahramy, Yoshimitsu Kohama, Jianting Ye, Yuichi Kasahara, Yuji Nakagawa, Masaru Onga, Masashi Tokunaga, Tsutomu Nojima, Youichi Yanase, and Yoshihiro Iwasa. Superconductivity protected by spin–valley locking in ion-gated mos2. *Nature Physics*, 12(2):144–149, Feb 2016. 32

[105] Xiaoxiang Xi, Zefang Wang, Weiwei Zhao, Ju-Hyun Park, Kam Tuen Law, Helmuth Berger, László Forró, Jie Shan, and Kin Fai Mak. Ising pairing in superconducting nbse2 atomic layers. *Nature Physics*, 12(2):139–143, Feb 2016. 32

[106] Yijun Yu, Fangyuan Yang, Xiu Fang Lu, Ya Jun Yan, Yong-Heum Cho, Liguo Ma, Xiaohai Niu, Sejoong Kim, Young-Woo Son, Donglai Feng, Shiyan Li, Sang-Wook Cheong, Xian Hui Chen, and Yuanbo Zhang. Gate-tunable phase transitions in thin flakes of 1t-tas2. *Nature Nanotechnology*, 10(3):270–276, Mar 2015. 32

[107] Zaiyao Fei, Tauno Palomaki, Sanfeng Wu, Wenjin Zhao, Xinghan Cai, Bosong Sun, Paul Nguyen, Joseph Finney, Xiaodong Xu, and David H. Cobden. Edge conduction in monolayer wte2. *Nature Physics*, 13(7):677–682, Jul 2017. 32

[108] Xiaofeng Qian, Junwei Liu, Liang Fu, and Ju Li. Quantum spin hall effect in two-dimensional transition metal dichalcogenides. *Science*, 346(6215):1344–1347, 2014. 32

[109] Bevin Huang, Genevieve Clark, Efrén Navarro-Moratalla, Dahlia R. Klein, Ran Cheng, Kyle L. Seyler, Ding Zhong, Emma Schmidgall, Michael A. McGuire, David H. Cobden, Wang Yao, Di Xiao, Pablo Jarillo-Herrero, and Xiaodong Xu. Layer-dependent ferromagnetism in a van der waals crystal down to the monolayer limit. *Nature*, 546(7657):270–273, Jun 2017. 32

[110] Jae-Ung Lee, Sungmin Lee, Ji Hoon Ryoo, Soonmin Kang, Tae Yun Kim, Pilkwang Kim, Cheol-Hwan Park, Je-Geun Park, and Hyeonsik Cheong. Ising-type magnetic ordering in atomically thin feps3. *Nano Letters*, 16(12):7433–7438, Dec 2016. 32

[111] Cheng Gong, Lin Li, Zhenglu Li, Huiwen Ji, Alex Stern, Yang Xia, Ting Cao, Wei Bao, Chenzhe Wang, Yuan Wang, Z. Q. Qiu, R. J. Cava, Steven G. Louie, Jing Xia, and Xiang Zhang. Discovery of intrinsic ferromagnetism in two-dimensional van der waals crystals. *Nature*, 546(7657):265–269, Jun 2017. 32

[112] Kangwon Kim, Soo Yeon Lim, Jae-Ung Lee, Sungmin Lee, Tae Yun Kim, Kisoo Park, Gun Sang Jeon, Cheol-Hwan Park, Je-Geun Park, and Hyeonsik Cheong. Suppression of magnetic ordering in xxz-type antiferromagnetic monolayer nips3. *Nature Communications*, 10(1):345, Jan 2019. 32, 33

[113] Zaiyao Fei, Bevin Huang, Paul Malinowski, Wenbo Wang, Tiancheng Song, Joshua Sanchez, Wang Yao, Di Xiao, Xiaoyang Zhu, Andrew F. May, Weida Wu, David H. Cobden, Jiun-Haw Chu, and Xiaodong Xu. Two-dimensional itinerant ferromagnetism in atomically thin fe3gete2. *Nature Materials*, 17(9):778–782, Sep 2018. 32

[114] Kenneth S. Burch, David Mandrus, and Je-Geun Park. Magnetism in two-dimensional van der waals materials. *Nature*, 563(7729):47–52, Nov 2018. 32

[115] M. Gibertini, M. Koperski, A. F. Morpurgo, and K. S. Novoselov. Magnetic 2d materials and heterostructures. *Nature Nanotechnology*, 14(5):408–419, May 2019. 32

[116] Mohammad Ariapour and Shoeib Babaee Touski. Strain engineering of spin and rashba splitting in group-iii monochalcogenide mx (m = ga, in and x = s, se, te) monolayer. *Journal of Magnetism and Magnetic Materials*, 510:166922, 2020. 32, 34

[117] X. Li, L. Li, and M. Wu. Various polymorphs of group iii–vi (gase, inse, gate) monolayers with quasi-degenerate energies: facile phase transformations, high-strain plastic deformation, and ferroelastic switching. *Materials Today Physics*, 15:100229, 2020. 32, 33

[118] Zhibin Yang and Jianhua Hao. Recent progress in 2d layered iii–vi semiconductors and their heterostructures for optoelectronic device applications. *Advanced Materials Technologies*, 4(8):1900108, 2019. 32, 33, 35

[119] Xingshuai Lv, Wei Wei, Qilong Sun, Fengping Li, Baibiao Huang, and Ying Dai. Two-dimensional germanium monochalcogenides for photocatalytic water splitting with high carrier mobility. *Applied Catalysis B: Environmental*, 217:275–284, 2017. 32

[120] Jongwon Yoon, Woojin Park, Ga-Yeong Bae, Yonghun Kim, Hun Soo Jang, Yujun Hyun, Sung Kwan Lim, Yung Ho Kahng, Woong-Ki Hong, Byoung Hun Lee, and Heung Cho Ko. Highly flexible and transparent multilayer mos2 transistors with graphene electrodes. *Small*, 9(19):3295–3300, 2013. 33

[121] Sang Jin Kim, Kyoungjun Choi, Bora Lee, Yuna Kim, and Byung Hee Hong. Materials for flexible, stretchable electronics: Graphene and 2d materials. *Annual Review of Materials Research*, 45(Volume 45, 2015):63–84, 2015. 33

[122] S. Preethi, Sony Varghese, Kunal Biswas, and N. Vijayalakshmi. Unveiling the properties of layered 2d-based nano-material flexible electronics in biomedical applications: a review. *Journal of Materials Science*, 59(25):11218–11245, Jul 2024. 33

[123] C. He, J. H. Zhang, W. X. Zhang, and T. T. Li. Gese/bp van der waals heterostructures as promising anode materials for potassium-ion batteries. *The Journal of Physical Chemistry C*, 123(9):5157–5163, 2019. 33

[124] K. S. Novoselov, A. Mishchenko, A. Carvalho, and A. H. Castro Neto. 2d materials and van der waals heterostructures. *Science*, 353(6298):aac9439, 2016. 33

[125] Tao Xu, Jingtong Zhang, Yuquan Zhu, Jie Wang, Takahiro Shimada, Takayuki Kitamura, and Tong-Yi Zhang. Two-dimensional polar metal of a pbte monolayer by electrostatic doping. *Nanoscale Horiz.*, 5:1400–1406, 2020. 34

[126] Tianchao Niu and Ang Li. From two-dimensional materials to heterostructures. *Progress in Surface Science*, 90(1):21–45, 2015. Special Issue on Silicene. 34

[127] Xiaolong Liu and Mark C Hersam. 2d materials for quantum information science. *Nature Reviews Materials*, 4(10):669–684, 2019. 34

[128] Yufei Sun and Kai Liu. Strain engineering in functional 2-dimensional materials. *Journal of Applied Physics*, 125(8):082402, 12 2018. 34

[129] Mark A. Bissett, Masaharu Tsuji, and Hiroki Ago. Strain engineering the properties of graphene and other two-dimensional crystals. *Phys. Chem. Chem. Phys.*, 16:11124–11138, 2014. 34

[130] Marwa Mannaï and Sonia Haddad. Twistronics versus straintronics in twisted bilayers of graphene and transition metal dichalcogenides. *Phys. Rev. B*, 103:L201112, May 2021. 34

[131] Sara Postorino, Davide Grassano, Marco D'Alessandro, Andrea Pianetti, Olivia Pulci, and Maurizia Palummo. Strain-induced effects on the electronic properties of 2d materials. *Nanomaterials and Nanotechnology*, 10:1847980420902569, 2020. 34

[132] A A Bukharaev, A K Zvezdin, A P Pyatakov, and Y K Fetisov. Straintronics: a new trend in micro- and nanoelectronics and materials science. *Physics-Uspekhi*, 61(12):1175, dec 2018. 34, 42

[133] Xueping Li, Baoxing Zhai, Xiaohui Song, Yong Yan, Jingbo Li, and Congxin Xia. Two-dimensional janus-in2ste/inse heterostructure with direct gap and staggered band alignment. *Applied Surface Science*, 509:145317, 2020. 34

[134] J. Zhang, X. Y. Lang, Y. F. Zhu, and Q. Jiang. Strain tuned inse/mos2 bilayer van der waals heterostructures for photovoltaics or photocatalysis. *Phys. Chem. Chem. Phys.*, 20:17574–17582, 2018. 34

[135] Feng Li, Tao Shen, Cong Wang, Yupeng Zhang, Junjie Qi, and Han Zhang. Recent advances in strain-induced piezoelectric and piezoresistive effect-engineered 2d semiconductors for adaptive electronics and optoelectronics. *Nano-Micro Letters*, 12(1):106, May 2020. 34

[136] Jianhui Chen, Xiaolin Tan, Peng Lin, Baisheng Sa, Jian Zhou, Yinggan Zhang, Cuilian Wen, and Zhimei Sun. Comprehensive understanding of intrinsic mobility in the monolayers of iii–vi group 2d materials. *Physical Chemistry Chemical Physics*, 21(39):21898–21907, 2019. 34, 38

[137] Mohammad Ariapour and Shoeib Babaee Touski. Spin splitting and rashba effect at mono-layer gate in the presence of strain. *Materials Research Express*, 6(7):076402, 2019. 34

[138] Dat T Do, Subhendra D Mahanti, and Chih Wei Lai. Spin splitting in 2d monochalcogenide semiconductors. *Scientific Reports*, 5(1):17044, 2015. 34

[139] Hongchao Yang, Pei Zhao, Yandong Ma, Xingshuai Lv, Baibiao Huang, and Ying Dai. Janus single-layer group-iii monochalcogenides: a promising visible-light photocatalyst. *Journal of Physics D: Applied Physics*, 52(45):455303, 2019. 34

[140] Houlong L. Zhuang and Richard G. Hennig. Single-layer group-iii monochalcogenide photocatalysts for water splitting. *Chemistry of Materials*, 25(15):3232–3238, 2013. 34

[141] Altaf Ur Rahman, Juliana M. Morbec, Gul Rahman, and Peter Kratzer. Commensurate versus incommensurate heterostructures of group-iii monochalcogenides. *Phys. Rev. Mater.*, 2:094002, Sep 2018. 35

[142] Jimena A. Olmos-Asar, Cedric Rocha Leão, and Adalberto Fazzio. Novel iii-te–graphene van der waals heterojunctions for optoelectronic devices. *RSC Adv.*, 7:32383–32390, 2017. 35

[143] Chen Si, Zuzhang Lin, Jian Zhou, and Zhimei Sun. Controllable schottky barrier in gase/graphene heterostructure: the role of interface dipole. *2D Materials*, 4(1):015027, 2016. 35

[144] Wonjae Kim, Changfeng Li, Ferney A. Chaves, David Jiménez, Raul D. Rodriguez, Jannatul Susoma, Matthias A. Fenner, Harri Lipsanen, and Juha Riikonen. Tunable graphene–gase dual heterojunction device. *Advanced Materials*, 28(9):1845–1852, 2016. 35

[145] Hengheng Li, Zhongpo Zhou, and Haiying Wang. Tunable schottky barrier in inte/graphene van der waals heterostructure. *Nanotechnology*, 31(33):335201, may 2020. 35

[146] Khang D. Pham, Hieu Vu-Quang, and Chuong V. Nguyen. Modulation of electronic properties and schottky barrier in the graphene/gas heterostructure by electric gating. *Physica B: Condensed Matter*, 555:69–73, 2019. 35

[147] Huynh V. Phuc, Victor V. Ilyasov, Nguyen N. Hieu, Bin Amin, and Chuong V. Nguyen. Van der waals graphene/g-gase heterostructure: Tuning the electronic properties and schottky barrier by interlayer coupling, biaxial strain, and electric gating. *Journal of Alloys and Compounds*, 750:765–773, 2018. 35

[148] Daria Hlushchenko, Anna Siudzinska, Joanna Cybinska, Malgorzata Guzik, Alicja Bachmatiuk, and Robert Kudrawiec. Stability of mechanically exfoliated layered monochalcogenides under ambient conditions. *Scientific Reports*, 13(1):19114, 2023. 35

[149] Yu Guo, Si Zhou, Yizhen Bai, and Jijun Zhao. Defects and oxidation of group-iii monochalcogenide monolayers. *The Journal of Chemical Physics*, 147(10):104709, 09 2017. 35

[150] Badreddine Smiri, Rémy Bernardin, Mickael Martin, Hervé Roussel, Jean Luc Deschanvres, Emmanuel Nolot, Névine Rochat, Franck Bassani, Thierry Baron, and Bernard Pelissier. Spectroscopic investigation of oxidation in gase 2d layered materials. *Microelectronic Engineering*, 294:112256, 2024. 35

[151] Alaric Bergeron, John Ibrahim, Richard Leonelli, and Sebastien Francoeur. Oxidation dynamics of ultrathin gase probed through raman spectroscopy. *Applied physics letters*, 110(24), 2017. 35

[152] Vidur Raj, Dipankar Chugh, Lachlan E Black, MM Shehata, Li Li, Felipe Kremer, Daniel H Macdonald, Hark Hoe Tan, and Chennupati Jagadish. Passivation of inp solar cells using large area hexagonal-bn layers. *npj 2D Materials and Applications*, 5(1):12, 2021. 35

[153] Govind Chilkoor, Kalimuthu Jawaharraj, Bhuvan Vemuri, Alex Kutana, Manoj Tripathi, Divya Kota, Taib Arif, Tobin Filleter, Alan B Dalton, Boris I Yakobson, et al. Hexagonal boron nitride for sulfur corrosion inhibition. *ACS nano*, 14(11):14809–14819, 2020. 35

[154] Qiang Li, Qionghua Zhou, Li Shi, Qian Chen, and Jinlan Wang. Recent advances in oxidation and degradation mechanisms of ultrathin 2d materials under ambient conditions and their passivation strategies. *J. Mater. Chem. A*, 7:4291–4312, 2019. 35

[155] Md Rubayat-E Tanjil, Yunjo Jeong, Zhewen Yin, Wyatt Panaccione, and Michael Cai Wang. Ångström-scale, atomically thin 2d materials for corrosion mitigation and passivation. *Coatings*, 9(2), 2019. 35

[156] Govinda Chilkoor, Sushma Priyanka Karanam, Shane Star, Namita Shrestha, Rajesh K. Sani, Venkata K.K. Upadhyayula, Debjit Ghoshal, Nikhil A. Koratkar, M. Meyyappan, and Venkataramana Gadhamshetty. Hexagonal boron nitride: The thinnest insulating barrier to microbial corrosion. *ACS Nano*, 12(3):2242–2252, 2018. PMID: 29432687. 35

[157] Benjamin Sirota, Nicholas Glavin, Sergiy Krylyuk, Albert V Davydov, and Andrey A Voevodin. Hexagonal mote2 with amorphous bn passivation layer for improved oxidation resistance and endurance of 2d field effect transistors. *Scientific reports*, 8(1):8668, 2018. 35

[158] Jongchan Yoon and Zonghoon Lee. Effective passivation of black phosphorus under ambient conditions. *Applied Microscopy*, 47(3):176–186, 2017. 35

[159] Hao-Yu Lan, Rahul Tripathi, Joerg Appenzeller, and Zhihong Chen. Near-ideal subthreshold swing in scaled 2d transistors: The critical role of monolayer hbn passivation. *IEEE Electron Device Letters*, 45(7):1337–1340, 2024. 35

[160] HyunJung Park and Munho Kim. Enhanced performance of self-powered ge schottky photodetectors enabled by 2d hbn monolayer passivation. *Advanced Materials Technologies*, 9(22):2400594, 2024. 35

[161] Yifei Li, Xin Wen, Changjie Tan, Ning Li, Ruijie Li, Xinyu Huang, Huifeng Tian, Zhixin Yao, PeiChi Liao, Shulei Yu, Shizhuo Liu, Zhenjiang Li, Junjie Guo, Yuan Huang, Peng Gao, Lifen Wang, Shulin Bai, and Lei Liu. Synthesis of centimeter-scale high-quality polycrystalline hexagonal boron nitride films from fe fluxes. *Nanoscale*, 13:11223–11231, 2021. 35

[162] Himani Arora, Younghun Jung, Tommaso Venanzi, Kenji Watanabe, Takashi Taniguchi, Rene Hubner, Harald Schneider, Manfred Helm, James C Hone, and Artur Erbe. Effective hexagonal boron nitride passivation of few-layered inse and

gase to enhance their electronic and optical properties. *ACS applied materials & interfaces*, 11(46):43480–43487, 2019. 35, 41

[163] Himani Arora and Artur Erbe. Recent progress in contact, mobility, and encapsulation engineering of inse and gase. *InfoMat*, 2020. 35

[164] Soumyabrata Roy, Xiang Zhang, Anand B. Puthirath, Ashokkumar Meiyazhagan, Sohini Bhattacharyya, Muhammad M. Rahman, Ganguli Babu, Sandhya Susarla, Sreehari K. Saju, Mai Kim Tran, Lucas M. Sassi, M. A. S. R. Saadi, Jiawei Lai, Onur Sahin, Seyed Mohammad Sajadi, Bhuvaneswari Dharmarajan, Devashish Salpekar, Nithya Chakingal, Abhijit Baburaj, Xinting Shuai, Aparna Adumbumkulath, Kristen A. Miller, Jessica M. Gayle, Alec Ajnsztajn, Thibeorchews Prasankumar, Vijay Vedhan Jayanthi Harikrishnan, Ved Ojha, Harikishan Kannan, Ali Zein Khater, Zhenwei Zhu, Sathvik Ajay Iyengar, Pedro Alves da Silva Autreto, Eliezer Fernando Oliveira, Guanhui Gao, A. Glen Birdwell, Mahesh R. Neupane, Tony G. Ivanov, Jaime Taha-Tijerina, Ram Manohar Yadav, Sivaram Arepalli, Robert Vajtai, and Pulickel M. Ajayan. Structure, properties and applications of two-dimensional hexagonal boron nitride. *Advanced Materials*, 33(44):2101589, 2021. 36

[165] N Ooi, A Rairkar, L Lindsley, and J B Adams. Electronic structure and bonding in hexagonal boron nitride. *Journal of Physics: Condensed Matter*, 18(1):97, dec 2005. 36

[166] Klaus Zollner, Martin Gmitra, and Jaroslav Fabian. Heterostructures of graphene and hbn: Electronic, spin-orbit, and spin relaxation properties from first principles. *Phys. Rev. B*, 99:125151, Mar 2019. 36

[167] Willi Auwärter. Hexagonal boron nitride monolayers on metal supports: Versatile templates for atoms, molecules and nanostructures. *Surface Science Reports*, 74(1):1–95, 2019. 36

[168] Jens Eichler and Christoph Lesniak. Boron nitride (bn) and bn composites for high-temperature applications. *Journal of the European Ceramic Society*, 28(5):1105–1109, 2008. Engineering Ceramics '07: From Engineering To Functionality. 36

[169] Nikolaos Kostoglou, Kyriaki Polychronopoulou, and Claus Rebholz. Thermal and chemical stability of hexagonal boron nitride (h-bn) nanoplatelets. *Vacuum*, 112:42–45, 2015. 36

[170] Zheng Liu, Yongji Gong, Wu Zhou, Lulu Ma, Jingjiang Yu, Juan Carlos Idrobo, Jeil Jung, Allan H MacDonald, Robert Vajtai, Jun Lou, et al. Ultrathin high-temperature oxidation-resistant coatings of hexagonal boron nitride. *Nature communications*, 4(1):2541, 2013. 36

[171] R. C. Andrew, R. E. Mapasha, A. M. Ukpong, and N. Chetty. Mechanical properties of graphene and boronitrene. *Phys. Rev. B*, 85:125428, Mar 2012. 36, 52

[172] Qing Peng, Wei Ji, and Suvranu De. Mechanical properties of the hexagonal boron nitride monolayer: Ab initio study. *Computational Materials Science*, 56:11–17, 2012. 36, 52

[173] Andrijana Šolajić and Jelena Pešić. Tailoring electronic and optical properties of hbn/inte and hbn/gate heterostructures through biaxial strain engineering. *Scientific Reports*, 14(1):1081, 2024. 36, 44

[174] Qiran Cai, Declan Scullion, Wei Gan, Alexey Falin, Shunying Zhang, Kenji Watanabe, Takashi Taniguchi, Ying Chen, Elton JG Santos, and Lu Hua Li. High thermal conductivity of high-quality monolayer boron nitride and its thermal expansion. *Science advances*, 5(6):eaav0129, 2019. 36

[175] Guillaume Cassabois, Pierre Valvin, and Bernard Gil. Hexagonal boron nitride is an indirect bandgap semiconductor. *Nature photonics*, 10(4):262–266, 2016. 36

[176] Yoshitaka Fujimoto, Takashi Koretsune, and Susumu Saito. Electronic structures of hexagonal boron-nitride monolayer: strain-induced effects. *Journal of the Ceramic Society of Japan*, 122(1425):346–348, 2014. 36

[177] Wardah Amalia, Pekik Nurwantoro, and Sholihun. Density-functional-theory calculations of structural and electronic properties of vacancies in monolayer hexagonal boron nitride (h-bn). *Computational Condensed Matter*, 18:e00354, 2019. 36

[178] B. Chettri, P.K. Patra, Nguyen N. Hieu, and D.P. Rai. Hexagonal boron nitride (h-bn) nanosheet as a potential hydrogen adsorption material: A density functional theory (dft) study. *Surfaces and Interfaces*, 24:101043, 2021. 36

[179] M. Topsakal, E. Aktürk, and S. Ciraci. First-principles study of two- and one-dimensional honeycomb structures of boron nitride. *Phys. Rev. B*, 79:115442, Mar 2009. 36

[180] Darshana Wickramaratne, Leigh Weston, and Chris G Van de Walle. Monolayer to bulk properties of hexagonal boron nitride. *The Journal of Physical Chemistry C*, 122(44):25524–25529, 2018. 36, 53

[181] Akshay M. Satawara, Gaushiya A. Shaikh, Sanjeev K. Gupta, and P.N. Gajjar. Structural, electronic and optical properties of hexagonal boron-nitride (h-bn) monolayer: An ab-initio study. *Materials Today: Proceedings*, 47:529–532, 2021. Recent Advancements in Materials science and Nanotechnology. 36

[182] Darshana Wickramaratne, Leigh Weston, and Chris G. Van de Walle. Monolayer to bulk properties of hexagonal boron nitride. *The Journal of Physical Chemistry C*, 122(44):25524–25529, 2018. 36, 37

[183] Jianhui Chen, Xiaolin Tan, Peng Lin, Baisheng Sa, Jian Zhou, Yinggan Zhang, Cuilian Wen, and Zhimei Sun. Comprehensive understanding of intrinsic mobility in the monolayers of iii–vi group 2d materials. *Phys. Chem. Chem. Phys.*, 21:21898–21907, 2019. 37, 38

[184] Huazheng Sun, Zhan Wang, and Yong Wang. Band alignment of two-dimensional metal monochalcogenides mxs (m=ga,in; x=s,se,te). *AIP Advances*, 7(9):095120, 09 2017. 37, 38

[185] Chong Sun, Hui Xiang, Bo Xu, Yidong Xia, Jiang Yin, and Zhiguo Liu. Ab initio study of carrier mobility of few-layer inse. *Applied Physics Express*, 9(3):035203, feb 2016. 37, 38

[186] Le Huang, Zhanghui Chen, and Jingbo Li. Effects of strain on the band gap and effective mass in two-dimensional monolayer gax (x = s, se, te). *RSC Adv.*, 5:5788–5794, 2015. 37, 38

[187] Le Huang, Zhanghui Chen, and Jingbo Li. Effects of strain on the band gap and effective mass in two-dimensional monolayer gax (x= s, se, te). *Rsc Advances*, 5(8):5788–5794, 2015. 38, 60

[188] Hamad Rahman Jappor and Majeed Ali Habeeb. Optical properties of two-dimensional gas and gase monolayers. *Physica E: Low-dimensional Systems and Nanostructures*, 101:251–255, 2018. 38

[189] Vo Khuong Dien, Nguyen Thi Han, Wei Bang-Li, Kuang-I Lin, and Ming-Fa Lin. Tuning of the electronic and optical properties of monolayer gase via strain. *Advanced Theory and Simulations*, 6(7):2200950, 2023. 38, 40

[190] Yunhai Li, Xianghong Niu, and Jinlan Wang. Strain-dependent electronic structure and optical properties of monolayer indium selenide: A density functional + tight-binding model + many-body perturbation theory study. *FlatChem*, 15:100092, 2019. 40

[191] Doan Q Khoa, Duy Trinh Nguyen, Chuong V Nguyen, Vo TT Vi, Huynh V Phuc, Le TT Phuong, Bui D Hoi, and Nguyen N Hieu. Modulation of electronic properties of monolayer inse through strain and external electric field. *Chemical Physics*, 516:213–217, 2019. 40, 66

[192] Vo TT Vi, Nguyen N Hieu, Bui D Hoi, Nguyen TT Binh, and Tuan V Vu. Modulation of electronic and optical properties of gate monolayer by biaxial strain and electric field. *Superlattices and Microstructures*, 140:106435, 2020. 40, 53, 60

[193] Yecun Wu, Huei-Ru Fuh, Duan Zhang, Cormac Ó Coileáin, Hongjun Xu, Jiung Cho, Miri Choi, Byong Sun Chun, Xuju Jiang, Mourad Abid, Mohamed Abid, Huajun Liu, Jing Jing Wang, Igor V. Shvets, Ching-Ray Chang, and Han-Chun Wu. Simultaneous large continuous band gap tunability and photoluminescence enhancement in gase nanosheets via elastic strain engineering. *Nano Energy*, 32:157–164, 2017. 40

[194] Min-Shan Li, Kai-Xuan Chen, Dong-Chuan Mo, and Shu-Shen Lyu. Predicted high thermoelectric performance in a two-dimensional indium telluride monolayer and its dependence on strain. *Physical Chemistry Chemical Physics*, 21(44):24695–24701, 2019. 40

[195] Raja Sen, Kasturie Jatkar, and Priya Johari. Modulation of electronic and transport properties of bilayer heterostructures: InSe/$mos_2$ and InSe/*h*-bn as the prototype. *Phys. Rev. B*, 101:235425, Jun 2020. 40, 41

[196] P Kang, V Michaud-Rioux, X-H Kong, G-H Yu, and H Guo. Calculated carrier mobility of h-bn/$\gamma$-inse/h-bn van der waals heterostructures. *2D Materials*, 4(4):045014, sep 2017. 40, 41

[197] Feng Miao, Shi-Jun Liang, and Bin Cheng. Straintronics with van der waals materials. *npj Quantum Materials*, 6(1):59, 2021. 42

[198] Xing Peng, Long Chen, Yifan Liu, Chao Liu, Honglan Huang, Jinbo Fan, Pan Xiong, and Junwu Zhu. Strain engineering of two-dimensional materials for energy storage and conversion applications. *Chemical Synthesis*, 3(4), 2023. 42

[199] Mikkel Settnes, Stephen R. Power, and Antti-Pekka Jauho. Pseudomagnetic fields and triaxial strain in graphene. *Phys. Rev. B*, 93:035456, Jan 2016. 42

[200] Tony Low and F. Guinea. Strain-induced pseudomagnetic field for novel graphene electronics. *Nano Letters*, 10(9):3551–3554, 2010. PMID: 20715802. 42

[201] A Šolajić and J Pešić. Novel wide spectrum light absorber heterostructures based on hbn/in (ga) te. *Journal of Physics: Condensed Matter*, 34(34):345301, 2022. 44

[202] Andrijana Šolajić and Jelena Pešić. Strain-induced modulation of electronic and optical properties in hbn/inse heterostructure. *Optical and Quantum Electronics*, 56(7):1186, 2024. 44

[203] Wenbin Li and Ju Li. Piezoelectricity in two-dimensional group-iii monochalcogenides. *Nano Research*, 8:3796–3802, 2015. 52

[204] Sobhit Singh, Camilo Espejo, and Aldo H Romero. Structural, electronic, vibrational, and elastic properties of graphene/mos 2 bilayer heterostructures. *Physical Review B*, 98(15):155309, 2018. 52

[205] Shoeib Babaee Touski, Mohammad Ariapour, and Manouchehr Hosseini. Electrical and electronic properties of strained mono-layer inte. *Physica E: Low-dimensional Systems and Nanostructures*, 118:113875, 2020. 60

[206] P Kang, V Michaud-Rioux, XH Kong, GH Yu, and H Guo. Calculated carrier mobility of h-bn/$\gamma$-inse/h-bn van der waals heterostructures. *2D Materials*, 4(4):045014, 2017. 64

[207] Khang D Pham, Vo TT Vi, Doan V Thuan, Le TT Phuong, Le T Hoa, Nguyen V Hieu, Chuong V Nguyen, Huynh V Phuc, Hamad R Jappor, Nguyen Q Cuong, et al. Tunable electronic properties of inse by biaxial strain: from bulk to single-layer. *Materials Research Express*, 6(11):115002, 2019. 66

# Spisak objavljenih naučnih radova kandidata korišćenih u disertaciji

[1] A. Šolajić, J, Pešić. "Novel wide spectrum light absorber heterostructures based on hBN/In(Ga)Te", *Journal of Physics: Condensed Matter*. 34(34):345301, 2022.

[2] A. Šolajić, J. Pešić, "Tailoring electronic and optical properties of hBN/InTe and hBN/GaTe heterostructures through biaxial strain engineering", *Scientific Reports*, 14(1):1081, 2024.

[3] A. Šolajić, J. Pešić, "Strain-induced modulation of electronic and optical properties in hBN/InSe heterostructure", *Optical and Quantum Electronics*, 56(7):1186, 2024.

# Biografija

Andrijana Šolajić je rođena 05.05.1991. godine u Beogradu, gde je završila osnovnu školu 2006. godine i Matematičku gimnaziju 2010. godine. Diplomirala je na odseku za Fizičku elektroniku na Elektrotehničkom fakultetu Univerziteta u Beogradu, na smeru Nanoelektronika, optoelektronika i laserska tehnika. Diplomski rad pod nazivom "Elektronska struktura napregnutih grafenskih nanotačaka" odbranila je u junu 2016. godine. Iste godine upisuje master studije na Elektrotehničkom fakultetu Univerziteta u Beogradu, na modulu Nanoelektronika i fotonika. U septembru 2017. godine odbranila je master tezu pod nazivom "Određivanje elektronskih i fononskih svojstava grafena dopiranog stroncijumom i iterbijumom DFT metodom", čime završava master studije sa prosečnom ocenom 10.0. Master rad je kompletno urađen u Centru za fiziku čvrstog stanja i nove materijale Instituta za fiziku u Beogradu, u Laboratoriji za 2D materijale, pod komentorstvom dr Jelene Pešić.

U oktobru 2017. godine upisuje doktorske studije iz oblasti Fizike kondenzovane materije i statističke fizike, na Fizičkom fakultetu Univerziteta u Beogradu, od kada volontira u Centru za fiziku čvrstog stanja i nove materijale, Instituta za fiziku u Beogradu, u Laboratoriji za 2D materijale. U decembru 2018. godine izabrana je u zvanje istraživač pripravnik, od kada je zaposlena u istoj grupi. U januaru 2021. je izabrana u zvanje istraživač saradnik.

U okviru doktorske teze, Andrijana se bavi istraživanjem osobina novih heterostruktura zasnovanih na heksagonalnom bor nitridu (hBN) i monohalkogenidima IIIA grupe pomoću teorije funkcionala gustine. U januaru 2021. izabrana je u zvanje istraživač saradnik.

Andrijana Šolajić je od decembra 2018. do decembra 2019. godine bila angažovana na projektima *"Nanostrukturni multifunkcionalni nanomaterijali i nanokompoziti* (III450018), pod rukovodstvom akademika Zorana V. Popovića i *"Fizika uređenih nanostruktura i novih materijala u fotonici"* (OI171005) pod rukovodstvom dr Radoša Gajića. Od 2020. godine do 2022. godine bila je učesnik PROMIS projekta *"StrainedFeSC - Strain effects in iron chalcogenide superconductors"* pod rukovodstvom dr Nenada Lazarevića. Učestvovala je u međunarodnim projektima bilateralne saradnje: *"Modelling and measuring phase transitions and optical properties for perovskites"* sa Johannes Kepler Univerzitetom u Lincu, Austrija od 2018. - 2020.; *"Synthesis and characterization of ternary Van der Waals* $Mo_xW_{1-x}S_2$ *nanotubes for advanced field emission application"* sa Jožef Stefan Institutom u Ljubljani od 2023 - 2025. godine.

Trenutno je rukovodilac projekta bilateralne saradnje sa Montanuniverzitetom u Leobenu u Austriji, pod nazivom *"Exploring spectroscopic fingerprints of defects and dopants in two dimensional magnetic insulators"* (2024-2026) i učesnik programa multilateralne saradnje u dunavskom regionu pod nazivom *"Nonthermal Phase transitions*

*in 2D Gallium Sulphide for Applications in Next-Generation Devices"* (2023-2025) pod rukovodstvom dr Vladimira Damljanovića.

U septembru 2019. godine učestvovala je na školi *"Summer School on Advanced Materials and Molecular Modelling"* u Ljubljani, gde je pored učešća kao polaznik, imala i zaduženje tutora na praktičnim vežbama.

Bila je član organizacionih odbora nekoliko konferencija: *"The 21st Symposium on Condensed Matter Physics"*, 26-30. jun 2023., Beograd; *"The Workshop Strongly Correlated Electron Systems"*, 9-10. jun 2022., Beograd; *"The 20th Symposium on Condensed Matter Physics"*, 7-11. oktobar 2019., Beograd.

Recenzent je nekoliko radova u međunarodnim časopisima: Physica E: Low-dimensional Systems and Nanostructures, Electronic Structure, Journal of Electronic Materials, Journal of Computational Electronics.

Od marta 2024. godine je član odbora za ravnopravnost i diverzitet Centra za fiziku čvrstog stanja i nove materijale.

Do sada je koautor na 16 radova u međunarodnim časopisima, od čega je prvi autor na 5 radova. Učestvovala je i na višestrukim međunarodnim konferencijama u vidu poster prezentacija. Njena citiranost je 221 prema podacima sa Google Scholar-a, odnosno 160 prema Web of Sience, sa $h$-indeksom 6.

**Spisak publikacija**


1. **A. Šolajić**, J. Pešić, and R. Gajić, "Ab-initio calculations of electronic and vibrational properties of Sr and Yb intercalated graphene," Optical and Quantum Electronics, 2018, doi: 10.1007/s11082-018-1541-x.

2. S. Đurđić Mijin, **A. Šolajić**, J.R. Pešić, M.J. Šćepanović, Y. Liu, A. Baum, Č. Petrović, N.Ž. Lazarević, and Z.V. Popović, "Lattice dynamics and phase transition in CrI3 single crystals," Physical Review B, 2018, doi: 10.1103/PhysRevB.98.104307.

3. A. Milosavljević, **A. Šolajić**, J. Pešić, Y. Liu, Č. Petrović, N. Lazarević, and Z.V. Popović, "Evidence of spin–phonon coupling in CrSiTe3," Physical Review B, 2018, doi: 10.1103/PhysRevB.98.104306.

4. J. Pešić, I. Popov, **A. Šolajić**, V. Damljanović, K. Hingerl, M. Belic, and R. Gajić, "Ab Initio Study of the Electronic, Vibrational, and Mechanical Properties of the Magnesium Diboride Monolayer," Condensed Matter, 2019, doi: 10.3390/condmat4020037.

5. A. Milosavljević, **A. Šolajić**, S. Djurdjić-Mijin, J. Pešić, B. Višić, Y. Liu, Č. Petrović, N. Lazarević, and Z. Popović, "Lattice dynamics and phase transitions in Fe3-xGeTe2," Physical Review B, 2019, doi: 10.1103/physrevb.99.214304.

6. **A. Šolajić**, J. Pešić, and R. Gajić, "Optical and mechanical properties and electron-phonon interaction in graphene doped with metal atoms," Optical and Quantum Electronics, 2020, doi: 10.1007/s11082-020-02300-0.

7. S. Đurđić Mijin, A.M.M. Abeykoon, **A. Šolajić**, A. Milosavljević, J. Pešić, Y. Liu, Č. Petrović, Z.V. Popović, and N. Lazarević, "Short-Range Order in VI3," Inorganic Chemistry, 2020, doi: 10.1021/acs.inorgchem.0c02060.

8. V. Damljanović, N. Lazić, **A. Šolajić**, J. Pešić, B. Nikolić, and M. Damnjanović, "Peculiar symmetry-protected electronic dispersions in two-dimensional materials," Journal of Physics: Condensed Matter, 2020, doi: 10.1088/1361-648X/abaad1.

9. S. Djurdjić Mijin, A. Baum, J. Bekaert, **A. Šolajić**, J. Pešić, Y. Liu, G. He, M.V. Milošević, Č. Petrović, Z. Popović, R. Hackl, and N. Lazarević, "Probing charge density wave phases and the Mott transition in 1T-TaS2 by inelastic light scattering," Physical Review B, 2021, doi: 10.1103/PhysRevB.103.245133.

10. **A. Šolajić**, and J. Pešić, "Novel wide spectrum light absorber heterostructures based on hBN/In(Ga)Te," Journal of Physics: Condensed Matter, 2022, doi: 10.1088/1361-648X/ac7996.

11. J. Pešić, **A. Šolajić**, J. Mitrić, M. Gilić, I. Pešić, N. Paunović, and N. Romčević, "Structural and optical characterization of titanium–carbide and polymethyl methacrylate based nanocomposite," Optical and Quantum Electronics, 2022, doi: 10.1007/s11082-022-03674-z.

12. N. Lazarević, A. Baum, A. Milosavljević, L. Peis, R. Stumberger, J. Bekaert, **A. Šolajić**, J. Pešić, A. Wang, M. Šćepanović, A.M.M. Abeykoon, M.V. Milošević, Č. Petrović, Z.V. Popović, and R. Hackl, "Evolution of lattice, spin, and charge properties across the phase diagram of FeSe1-x Sx," Physical Review B, 2022, doi: 10.1103/PhysRevB.106.094510.

13. S. Djurdjić Mijin, **A. Šolajić**, J. Pešić, Y. Liu, Č. Petrović, M. Bockstedte, A. Bonanni, Z.V. Popović, and N. Lazarević, "Spin-phonon interaction and short-range order in Mn3Si2Te6," Physical Review B, 2023, doi: 10.1103/PhysRevB.107.054309.

14. **A. Šolajić**, and J. Pešić, "Strain-induced modulation of electronic and optical properties in hBN/InSe heterostructure," Optical and Quantum Electronics, 2024, doi: 10.1007/s11082-024-06837-2.

15. **A. Šolajić**, and J. Pešić, "Tailoring electronic and optical properties of hBN/InTe and hBN/GaTe heterostructures through biaxial strain engineering," Scientific Reports, 2024, doi: 10.1038/s41598-024-51303-4.

# Изјава о ауторству

Име и презиме аутора Андријана Шолајић

Број индекса 8005/2017

**Изјављујем**

да је докторска дисертација под насловом

Испитивање утицаја напрезања на особине хетероструктура дводимензионалних монохалкогенида IIIA групе *ab-initio* методама

- резултат сопственог истраживачког рада;
- да дисертација у целини ни у деловима није била предложена за стицање друге дипломе према студијским програмима других високошколских установа;
- да су резултати коректно наведени и
- да нисам кршио/ла ауторска права и користио/ла интелектуалну својину других лица.

**Потпис аутора**

У Београду, _____

_____

# Изјава о истоветности штампане и електронске верзије докторског рада

Име и презиме аутора Андријана Шолајић

Број индекса 8005/2017

Студијски програм Физика

Наслов рада Испитивање утицаја напрезања на особине хетероструктура дводимензионалних монохалкогенида IIIA групе *ab-initio* методама

Ментор др Јелена Пешић

Изјављујем да је штампана верзија мог докторског рада истоветна електронској верзији коју сам предао/ла ради похрањена у **Дигиталном репозиторијуму Универзитета у Београду.**

Дозвољавам да се објаве моји лични подаци везани за добијање академског назива доктора наука, као што су име и презиме, година и место рођења и датум одбране рада.

Ови лични подаци могу се објавити на мрежним страницама дигиталне библиотеке, у електронском каталогу и у публикацијама Универзитета у Београду.

**Потпис аутора**

У Београду, _____

_____

# Изјава о коришћењу

Овлашћујем Универзитетску библиотеку „Светозар Марковић“ да у Дигитални репозиторијум Универзитета у Београду унесе моју докторску дисертацију под насловом:

Испитивање утицаја напрезања на особине хетероструктура дводимензионалних монохалкогенида IIIA групе *ab-initio* методама

која је моје ауторско дело.

Дисертацију са свим прилозима предао/ла сам у електронском формату погодном за трајно архивирање.

Моју докторску дисертацију похрањену у Дигиталном репозиторијуму Универзитета у Београду и доступну у отвореном приступу могу да користе сви који поштују одредбе садржане у одабраном типу лиценце Креативне заједнице (Creative Commons) за коју сам се одлучио/ла.

1. Ауторство (CC BY)

2. Ауторство – некомерцијално (CC BY-NC)

3. Ауторство – некомерцијално – без прерада (CC BY-NC-ND)

4. Ауторство – некомерцијално – делити под истим условима (CC BY-NC-SA)

5. Ауторство – без прерада (CC BY-ND)

6. Ауторство – делити под истим условима (CC BY-SA)

(Молимо да заокружите само једну од шест понуђених лиценци.
Кратак опис лиценци је саставни део ове изјаве).

**Потпис аутора**

У Београду, _____ _____

1. **Ауторство**. Дозвољавате умножавање, дистрибуцију и јавно саопштавање дела, и прераде, ако се наведе име аутора на начин одређен од стране аутора или даваоца лиценце, чак и у комерцијалне сврхе. Ово је најслободнија од свих лиценци.

2. **Ауторство – некомерцијално**. Дозвољавате умножавање, дистрибуцију и јавно саопштавање дела, и прераде, ако се наведе име аутора на начин одређен од стране аутора или даваоца лиценце. Ова лиценца не дозвољава комерцијалну употребу дела.

3. **Ауторство – некомерцијално – без прерада**. Дозвољавате умножавање, дистрибуцију и јавно саопштавање дела, без промена, преобликовања или употребе дела у свом делу, ако се наведе име аутора на начин одређен од стране аутора или даваоца лиценце. Ова лиценца не дозвољава комерцијалну употребу дела. У односу на све остале лиценце, овом лиценцом се ограничава највећи обим права коришћења дела.

4. **Ауторство – некомерцијално – делити под истим условима**. Дозвољавате умножавање, дистрибуцију и јавно саопштавање дела, и прераде, ако се наведе име аутора на начин одређен од стране аутора или даваоца лиценце и ако се прерада дистрибуира под истом или сличном лиценцом. Ова лиценца не дозвољава комерцијалну употребу дела и прерада.

5. **Ауторство – без прерада**. Дозвољавате умножавање, дистрибуцију и јавно саопштавање дела, без промена, преобликовања или употребе дела у свом делу, ако се наведе име аутора на начин одређен од стране аутора или даваоца лиценце. Ова лиценца дозвољава комерцијалну употребу дела.

6. **Ауторство – делити под истим условима**. Дозвољавате умножавање, дистрибуцију и јавно саопштавање дела, и прераде, ако се наведе име аутора на начин одређен од стране аутора или даваоца лиценце и ако се прерада дистрибуира под истом или сличном лиценцом. Ова лиценца дозвољава комерцијалну употребу дела и прерада. Слична је софтверским лиценцама, односно лиценцама отвореног кода.